Nonlinear dynamics and stability of viscous free-surface microcapillary flows in V-shaped channels and on curved surfaces

Thesis by
Nicholas C. White

In Partial Fulfillment of the Requirements for the
Degree of
Doctor of Philosophy

CALIFORNIA INSTITUTE OF TECHNOLOGY
Pasadena, California

2022
Defended May 24, 2022

© 2022

Nicholas C. White
ORCID: 0000-0002-7603-9329

All rights reserved

ACKNOWLEDGMENTS

I am very grateful to the NASA Space Technology and Research Fellowship (Grant no. 80NSSC17K0139) not only for funding my studies from 2017, but also for giving me the opportunity to meet and work with so many amazing people at JPL: Jay Polk, Colleen Marrese-Reading, Nan Yu, Jeff Jewell, Curt Cutler, and Sheng-wey Chiow. I wish to especially thank Jay Polk, for his support and feedback on many early thesis drafts.

I had the privilege of receiving the Philip G. Saffman Graduate Fellowship in my first year, established by Ruth Saffman. I am grateful not only for her financial generosity, but also for the time we spent together. Although I was never able to meet Dr. Saffman, seeing his notes and books and hearing stories about him made me wish I had been able to come to Caltech earlier.

I feel lucky to have had such wonderful labmates, Teddy Albertson, Dillon Chang, Kevin Fiedler, Cheolmin Im, Hiroki Kaifu, Zack Nicolaou, and Chengzhe Zhou, as well as the brilliant summer students Vilda Markeviciute, Kishan Makwana, Ishani Karmarkar, and Lorenzo Van Muñoz. Working together was delightful, and I have missed our interactions in the last few years.

I would like to give special thanks to Teddy Albertson, Chengzhe Zhou, and Yuchen Wei. I certainly learned more from our discussions over the years than from any class or textbook. Even after Teddy and Chengzhe graduated, I frequently mined their theses for insights, and pestered both of them in their post-graduate life to help me understand various problems. And I relied on Yuchen for discussion of every topic, from control theory and differential geometry to software engineering and numerical methods to materials science and fluid and solid mechanics.

I was able to smoothly conduct research thanks to the behind-the-scenes work of the Caltech and APh/MS staff, especially Mabel Chik, Christy Jenstad, Connie Rodriguez, and Jennifer Blankenship. I wish to thank my advisor, Sandra Troian. I also wish to thank the members of my committee, Oscar Bruno, Brent Fultz, Thomas Hou, Beverley McKeon, and Jay Polk, for taking the time to read this thesis.

I am grateful to have had the opportunity to take the outstanding courses taught by Marina Agranov, Philip Hoffman, and Feng-Ying Ming; thanks to them, I can say I am glad I attended Caltech. I am very fortunate to have had many wonderful teachers before graduate school as well; I would particularly like to thank Jens Martin Berling for introducing me to the worlds of mathematics and physics many years ago.

I would also like to express my gratitude to Valentina Quezada, Nancy Lan, and all the staff of the USC Pacific Asia Museum. I highly encourage anyone living in the Pasadena area to visit.

Finally, I could not have completed my graduate studies without the support of my family and my dear friends, Yuhan Chen, Xiuyuan Cheng, John DeBrota, Dongwan Kim, Jarno Sun, Yichen Wu, and Shuyi Zhang.

ABSTRACT

The last two decades have brought a revolution in miniaturization of space technology. Thanks to improved microelectronic sensors and MEMS devices, nanosatellites can perform communication and scientific studies previously limited to large satellites, significantly reducing the financial barriers to space access. But development of a reliable, long-running, small-scale propulsion system for orbital maneuvers remains a key challenge. One solution is the microfluidic electrospray propulsion (MEP) thruster under development at NASA's Jet Propulsion Laboratory (JPL).

This thesis analytically addresses aspects of the MEP system's propellant management, specifically, capillary flow in the groove network delivering fluid propellant from the reservoir to the emitters. Building upon the reduced-order model of viscous capillary flow in straight V-shaped channels ("V-grooves") of Weislogel (1996) and Romero and Yost (1996), we prove stability of steady-state and self-similar flows. Because the MEP design requires an electric field above the grooves and further calls for grooves which curve and bend in three dimensions, we extend earlier V-groove models to include these effects, and also perform stability analyses of the new models. The results not only validate the use of V-grooves as a robust propellant delivery system, but also provide a theoretical basis for the design of future microfluidic devices with compact, three-dimensional designs and electric fields.

In order to lay the groundwork for future studies of early-time behavior of propellant on emitter tips before the Taylor cone necessary for ion emission is formed, we develop the technique of generalized linear stability analysis (Farrell and Ioannou, 1996) of capillary flow of thin viscous films coating curved surfaces (governed by the equation first developed by Roy and Schwartz, 1997). This methodology was first applied to films coating cylinders and spheres by Balestra et al. (2016, 2018); we instead apply the technique and analyze for the first time a viscous-capillary instability arising on a torus coated with a uniform thin film.

Besides the capillary fluid dynamics results, two additional pieces of work are included in the thesis. First, in an unorthodox application of Noether's Theorem to non-Lagrangian gradient flow equations, we show that each variational symmetry of the governing functional induces a constraint on the evolution of the system. Second, to support JPL's efforts to directly detect a "fifth force," we introduce and implement numerical methods for computation of the scalar Cubic Galileon Gravity (CGG) field at solar system scales.

PUBLISHED CONTENT AND CONTRIBUTIONS

Nicholas C. White and Sandra M. Troian. Why capillary flows in slender triangular grooves are so stable against disturbances. Phys. Rev. Fluids, 4(5):054003, 2019. doi:10.1103/PhysRevFluids.4.054003.

Abstract: Ongoing development of fuel storage and delivery systems for space probes, interplanetary vehicles, satellites, and orbital platforms continues to drive interest in propellant management systems that utilize surface tension to retain, channel, and control flow in microgravity environments. Although it has been known for decades that capillary flows offer an ideal method of fuel management, there has been little research devoted to the general stability properties of such flows. In this work, we demonstrate theoretically why capillary flows which channel wetting liquids in slender open triangular channels tend to be very stable against disturbances. By utilizing the gradient flow form of the governing fluid interface equation, we first prove that stationary interfaces in the presence of steady flow are asymptotically nonlinearly and exponentially stable in the Lyapunov sense. We then demonstrate that fluid interfaces exhibiting self-similar Washburn dynamics are transiently and asymptotically linearly stable to small perturbations. This second finding relies on a generalized nonmodal stability analysis due to the non-normality of the governing disturbance operator. Taken together, these findings reveal the robust nature of transient and steady capillary flows in open grooved channels and likely explain the prevalent use of capillary flow management systems in many emerging technologies ranging from CubeSats to point-of-care microfluidic diagnostic systems.

Contribution: NCW carried out analytic and numerical stability analyses, drafted the manuscript, and participated in the revision process.

Nicholas C. White, Sandra M. Troian, Jeffrey B. Jewell, Curt J. Cutler, Sheng-wey Chiow, and Nan Yu. Robust numerical computation of the 3D scalar potential field of the cubic Galileon gravity model at solar system scales. Phys. Rev. D, 102:024033, 2020. doi:10.1103/PhysRevD.102.024033.

Abstract: Direct detection of dark energy or modified gravity may finally be within reach due to ultrasensitive instrumentation such as atom interferometry capable of detecting incredibly small scale accelerations. Forecasts, constraints and measurement bounds can now too perhaps be estimated from accurate numerical simulations of the fifth force and its Laplacian field at solar system scales. The cubic Galileon gravity scalar field model (CGG), which arises in various massive gravity models including the Dvali-Gabadadze-Porrati (DGP) braneworld model, describes modified gravity incorporating a Vainshtein screening mechanism. The nonlinear derivative interactions in the CGG equation suppress the field near regions of high density, thereby restoring general relativity (GR) while far from such regions, field enhancement is comparable to GR and the equation is dominated by a linear term. This feature of the governing equation poses some numerical challenges for computation of the scalar potential, force and Laplacian fields even under stationary conditions. Here we present a numerical method based on finite differences for solution of the static CGG scalar field for a 2D axisymmetric Sun-Earth system and a 3D Cartesian Sun-Earth-Moon system. The method relies on gradient descent of an integrated residual based on the normal attractive branch of the CGG equation. The algorithm is shown to be stable, accurate and rapidly convergent toward

the global minimum state. We hope this numerical study, which can easily be extended to include smaller bodies such as detection satellites, will prove useful to future measurement of modified gravity force fields at solar system scales.

Contribution: NCW developed the numerical iteration method along with JBJ, and performed theoretical analysis of its convergence. NCW designed the numerical meshing scheme, wrote the numerical code, and performed simulations. NCW drafted the manuscript and participated in the revision process.

CONTENTS

* indicates new results

Part I

Background

Chapter 1

INTRODUCTION

1.1 Motivation

The last two decades have brought a revolution in miniaturization of space technology. Beginning with the first nanosatellites in 1998, nearly three thousand satellites weighing under 10kg have since been launched, two of which were sent on interplanetary missions (Kulu, 2020). Thanks to improved microelectronic sensors and MEMS devices, these nanosatellites can perform communication and scientific studies previously limited to large satellites. Because launching material to orbit costs thousands of dollars per kilogram (Jones, 2018), small satellites significantly reduce the financial barriers to space access, in particular making space-based experiments more accessible to universities across the globe.

However, development of a reliable, long-running, small-scale propulsion system for attitude correction and orbital maneuvers remains a key challenge. One solution is the microfluidic electrospray propulsion (MEP) thruster under development at NASA's Jet Propulsion Laboratory (JPL). Electrospray propulsion operates by creating an electric field above a conducting or dielectric liquid propellant; if this electric field is sufficiently strong, it overcomes surface tension and pulls the liquid surface into a cusp or cone, often called a Taylor cone. As the tip of this cone becomes increasingly sharp, the local surface curvature and electric field strength each begin to diverge. After a critical field strength is surpassed, ions or droplets are emitted from the cone, providing propulsive force (Wright and Ferrer, 2015). Electrospray propulsion has been successfully tested on the LISA Pathfinder mission (Ziemer and Merkowitz, 2004), and a number of miniaturized designs are currently being tested, including porous colloid thrusters, in which ionic liquids diffuse through a porous, sponge-like structure to the tips of emitters (Courtney et al., 2012; Legge and Lozano, 2011), and JPL's MEP device, which relies on external propellant flow along grooves on the surface of an emitter needle (see Figures 1.1 and 1.2).

The MEP thruster under development at JPL consists of an array of several hundred emitter needles, each around 200 microns in height, arranged on a flat silicon substrate. Liquid indium propellant is delivered from a reservoir under the substrate to the substrate surface and thence to the emitter needles by means of grooves etched into the substrate surface. A counter-electrode plate sits approximately 50 microns above the emitter array, and has a circular aperture above each emitter; this counter-electrode produces an electric field which is naturally concentrated at the emitter tips, and it is there that Taylor cones form and ultimately emit ions (Figure 1.1).

There is no shortage of hydrodynamic research on Taylor cone formation and the resulting emission process, from Taylor's initial static analysis (Taylor, 1964) and subsequent refinements generalizing the model to include rounded cones (Gomer, 1979; Thompson and Prewett, 1984;

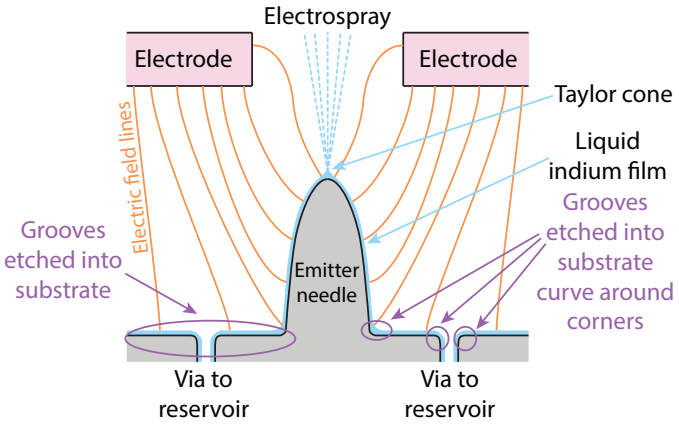

Figure 1.1: Schematic of single emitter on microfluidic electrospray propulsion (MEP) thruster. Liquid indium (blue) is delivered from reservoirs beneath the flat silicon substrate (gray) through vias to the substrate surface, then up the sides of emitter needles. Delivery occurs by capillary action due to triangular grooves etched into the via walls and substrate surface (the grooves themselves are not drawn in the diagram). The voltage gap between a counter electrode with a circular aperture (pink) above the emitter needle generates an electric field (orange lines), which is strongest at the tip of the emitter, at which point a Taylor cone forms and ions or droplets are emitted. This diagram shows a single emitter needle; the actual device has an array of several hundred such emitters.

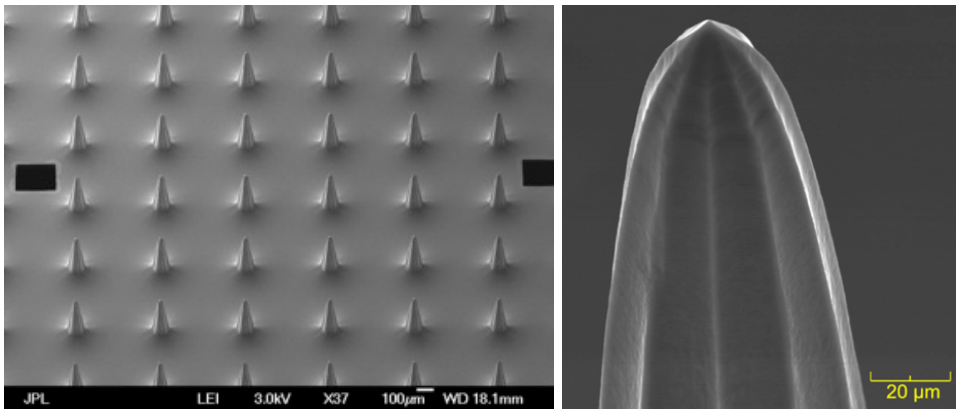

Figure 1.2: Photographs of JPL MEP thruster emitter array. Left: Emitter array on the MEP thruster. Black squares are vias leading to the propellant reservoir. In this photograph, grooves have not yet been etched into the array substrate between the vias and the needles. Note also that the counter electrode is not shown (Marrese-Reading, 2016).
Right: Closeup of emitter needle tip on the MEP thruster (Marrese-Reading, 2016).

Wagner, 1982) and space charge (Mair, 1984), to the identification of self-similar cone sharpening in the inviscid (Zubarev, 2001) and viscous (Betelú et al., 2006) limits.

But understanding the emission process itself is not enough to design a functional electrospray thruster. In particular, a regular, steady, and stable flow of propellant must be delivered to the emission site before and during operation. While large thrusters can rely on electric pumps and

mechanical valves, such components are impractical at micro scales, and instead capillary action can be harnessed to manage propellant flow. This thesis therefore develops new analytic models for a variety of relevant aspects of the MEP propellant management system. These low-order models are developed from first principles and carried out perturbatively based upon our declared assumptions; we endeavor to maintain a modicum of rigor, and avoid ad-hoc addition of terms to existing low-order models.

This thesis focuses on the propellant delivery aspect of the MEP system, specifically, capillary flow in the groove network delivering fluid propellant from the reservoir to the emitters. A reduced-order model of viscous capillary flow in straight V-shaped channels ("V-grooves") has already been developed by Romero and Yost (1996) and Weislogel (1996); this model demonstrates the effectiveness of V-grooves at wicking fluid and motivated the use of V-grooves for propellant transport in the MEP thruster[1]. But the MEP design induces an electric field above the grooves, and further calls for grooves which curve and bend in three dimensions (see Figure 1.1). We extend earlier models to include these effects, and also perform stability analyses of both the original model and the new models. The results not only validate the use of V-grooves as a propellant delivery system, but also provide a theoretical basis for the design of future microfluidic devices with compact, three-dimensional designs and electric fields.

In order to lay the groundwork for future studies of early-time behavior of propellant on emitter tips before the Taylor cone necessary for ion emission is formed, we develop the technique of generalized linear stability analysis (Farrell and Ioannou, 1996a,b) applied to capillary flow of thin viscous films coating curved surfaces (governed by the equation first developed by Roy and Schwartz, 1997). This methodology was first applied to films coating cylinders and spheres by Balestra et al. (2016, 2018); we instead apply the technique and analyze for the first time a viscous-capillary instability arising on a torus coated with a uniform thin film.

The analyses of capillary-driven flow in V-grooves and on curved substrates are primarily motivated by the MEP thruster, but have wide-ranging applications. Various propellant management devices for spacecraft (not only those with electrospray thrusters) already rely upon open channels and corner flow for liquid propellant delivery (Jaekle, 1991, 1997; Rollins et al., 1985). The analytical description of flow dynamics and stability in straight and curved V-groove will enable both more accurate modeling of existing propellant management devices and design of new systems with specific flow requirements. Open channel capillary flow has been applied to heat pipes for cooling microelectronics (Mallik et al., 1992), and in microfluidic lab-on-a-chip devices for medical and chemical assays (Berthier et al., 2015; Oliveira et al., 2019). The curved V-groove analysis in particular could be used to design serpentine heat pipes covering greater surface area, as well as more compact labs-on-chips. Furthermore, such devices with conducting

[1]Fabrication challenges have recently led the MEP thruster design to switch to rounded "U-grooves" rather than sharp V-grooves. The behavior of fluid in U-grooves is qualitatively similar to that in V-grooves, but the latter is far more analytically tractable (Chen et al., 2006). This thesis exclusively analyzes V-grooves, but extension of the results to U-grooves will be discussed briefly in each relevant chapter.

liquids can be designed to use electric fields to direct fluid flow without requiring the addition of extra particles for electrophoresis. The analysis of fluid delivery to emitter needles is directly applicable to electrospray, which is useful not only for space propulsion but also for lithography, deposition, and other aspects of microfabrication (Mackenzie and Smith, 1990). Besides electrospray, the coating of solid substrates with thin liquid films such as lubricants and paints is applicable to a variety of manufacturing processes.[2]

In addition to the capillary fluid dynamics results, two additional pieces of work are included in the thesis. First, in a novel application of Noether's Theorem to non-Lagrangian gradient flow equations, we show that each variational symmetry of the governing functional induces a constraint on the evolution of the system. Second, to support JPL's efforts to directly detect a "fifth force," we introduce and implement numerical methods for computation of the scalar Cubic Galileon Gravity (CGG) field at solar system scales.

1.2 Organization

The thesis is organized as follows. Part I contains background material which is useful for understanding the subsequent results. Chapter 2 discusses the mathematical origin of surface tension, in a slightly unorthodox fashion reflecting the author's intuition. Chapter 3 discusses non-normality and generalized linear stability analysis, as well as Lyapunov stability. Some additional notes on covariant notation and fundamental results in fluid mechanics may be found in Appendix A.

Part II covers capillary flow in slender V-grooves. Chapter 4 introduces the topic and discusses the original reduced-order model describing flow of a wetting liquid in a slender V-groove, following Romero and Yost (1996) and Weislogel (1996). Chapter 5 proves (for the first time) nonlinear exponential stability for steady-state V-groove flows and generalized linear stability for self-similar advancing and receding flows (a subset of the material in this chapter was published in Physical Review Fluids as White and Troian, 2019). Chapter 6 develops a novel extension of the V-groove model to include the effects of external electric fields on a perfectly conducting liquid in a V-groove with conducting walls higher than the fluid thickness. Electric fields are found to enhance the flow rate in grooves, and it is found that fluid above a critical thickness may become unstable, while fluid below that thickness remains stable. Steady state and self-similar solutions are described and analyzed. Chapter 7 describes another new variation of the V-groove model, for grooves following curved trajectories. Grooves with positive curvature are found to enhance the flow rate, while grooves with negative curvature depress it. Steady state and self-similar solutions are again described and analyzed, and stability analyses show that the flow remains stable.

Part III is devoted to thin film flows on curved substrates. Chapter 8 derives the thin film equation on a curved substrate, reproducing the equation first developed by Roy and Schwartz

[2] Indeed, much analytical research in thin film theory has been performed by researchers employed (Orchard, 1963) or funded (O'Brien and Schwartz, 2002; Schwartz and Weidner, 1995) by the paint industry.

(1997) and expanded on by Roy et al. (2002). The result itself is not new, but the derivation differs from earlier work by using covariant notation and showing each step in detail. Chapter 9 describes and analyzes for the first time a viscous capillary instability arising in thin films coating tori (doughnuts). The existence of this instability was first discovered by Roy and Schwartz (1997), in whose nonlinear simulations the instability arose. While similar to instabilities of films uniformly coating cylinders previously studied by Goren (1962), the torus case turns out to be much more complicated, and the limit of tori with infinitely large radii does not converge to the known cylinder result. The reason for the convergence to a different wavenumber is explained analytically.

Part IV contains additional new results in cosmology and mathematical physics. While not directly related to the microfluidic applications of the previous sections, these results require similar analyses of nonlinear PDEs.

Chapter 10 describes the role of variational symmetries in gradient flow PDEs. While Noether's theorem has traditionally been used to find conserved quantities in Lagrangian systems, it is applied here to gradient flow PDEs, which are not Lagrangian. Variational symmetries in these systems correspond to constraints on the evolution vector, and, in certain special cases, give rise to conserved quantities. These symmetry-driven evolutionary constraints may be used as a metric for the validity of numerical simulation. After proving these results, we demonstrate their application to the thermocapillary thin film equation.

Chapter 11 (published in Physical Review D as White et al., 2020) presents a computation of the scalar field from the Cubic Galileon Gravity (CGG) model in the Sun-Earth-Moon system. The CGG model, which arises in various massive gravity models including the Dvali-Gabadadze-Porrati (DGP) braneworld model (Dvali et al., 2000), describes modified gravity incorporating a nonlinear Vainshtein screening mechanism which suppresses the field near regions of high density. The CGG field had previously been computed on galactic and cosmological scales (Barreira et al., 2013; Chan and Scoccimarro, 2009; Li et al., 2013; Schmidt, 2009), where the linear term dominates, and in idealized 2D planetary systems with an artificially large linear term (Hiramatsu et al., 2013). We develop a stable, accurate, and rapidly converging iteration scheme enabling computation of the field in realistic nonlinear-term-dominated systems, and implement it using a nested-grid finite difference scheme to enable high resolution around the Sun, Earth, and Moon, while capturing field variation on a coarser mesh between those bodies.

Chapters describing novel results are marked with * symbols; these are Chapters 5, 6, 7, 9, 10, and 11. All other chapters (Chapters 2 to 4 and 8) provide results based on work by other researchers (although the derivation sometimes differs significantly from the original), and are included to provide context and background for the novel work in this thesis.

We endeavor throughout the thesis to give full derivations to ensure that the results can be reproduced as easily as possible. We also provide several chapters of introductory material in

the hopes that the thesis can be read and understood by a physics graduate student without requiring significant additional reference.

References

G. Balestra, P.-T. Brun, and F. Gallaire. Rayleigh-Taylor instability under curved substrates: An optimal transient growth analysis. Phys. Rev. Fluids, 1(8):083902, 2016. doi:10.1103/PhysRevFluids.1.083902.

G. Balestra, D. M.-P. Nguyen, and F. Gallaire. Rayleigh-Taylor instability under a spherical substrate. Phys. Rev. Fluids, 3(8), August 2018. ISSN 2469-990X. doi:10.1103/PhysRevFluids.3.084005.

A. Barreira, B. Li, W. A. Hellwing, C. M. Baugh, and S. Pascoli. Nonlinear structure formation in the cubic Galileon gravity model. J. Cosmol. Astroparticle Phys., 2013(10):027–027, 2013. doi:10.1088/1475-7516/2013/10/027.

J. Berthier, K. A. Brakke, E. P. Furlani, I. H. Karampelas, V. Poher, D. Gosselin, M. Cubizolles, and P. Pouteau. Whole blood spontaneous capillary flow in narrow v-groove microchannels. Sensor Actuat. B Chem., 206:258–267, 2015. doi:10.1016/j.snb.2014.09.040.

S. I. Betelú, M. A. Fontelos, U. Kindelán, and O. Vantzos. Singularities on charged viscous droplets. Phys. Fluids, 18(5):051706, May 2006. ISSN 1070-6631, 1089-7666. doi:10.1063/1.2204044.

K. C. Chan and R. Scoccimarro. Large-scale structure in brane-induced gravity. II. Numerical simulations. Phys. Rev. D, 80(10):104005, 2009. doi:10.1103/PhysRevD.80.104005.

Y. Chen, M. M. Weislogel, and C. L. Nardin. Capillary-driven flows along rounded interior corners. J. Fluid Mech., 566:235–271, 2006. doi:10.1017/S0022112006001996.

D. G. Courtney, H. Q. Li, and P. Lozano. Emission measurements from planar arrays of porous ionic liquid ion sources. J. Phys. D: Appl. Phys., 45(48):485203, December 2012. ISSN 0022-3727, 1361-6463. doi:10.1088/0022-3727/45/48/485203.

G. Dvali, G. Gabadadze, and M. Porrati. 4D gravity on a brane in 5D Minkowski space. Phys. Lett. B, 485(1-3):208–214, 2000. doi:10.1016/S0370-2693(00)00669-9.

B. F. Farrell and P. J. Ioannou. Generalized Stability Theory. Part II: Nonautonomous operators. J. Atmos. Sci., pages 2041–2053, 1996a. doi:10.1175/1520-0469(1996)053<2041:GSTPIN>2.0.CO;2.

B. F. Farrell and P. J. Ioannou. Generalized Stability Theory. Part I: Autonomous operators. J. Atmos. Sci., 53(14):2025–2040, 1996b. doi:10.1175/1520-0469(1996)053<2025:GSTPIA>2.0.CO;2.

R. Gomer. On the mechanism of liquid metal electron and ion sources. Appl. Phys., 19(4): 365–375, 1979. doi:10.1007/BF00930099.

S. L. Goren. The instability of an annular thread of fluid. J. Fluid Mech., 12(02):309, February 1962. ISSN 0022-1120, 1469-7645. doi:10.1017/S002211206200021X.

T. Hiramatsu, W. Hu, K. Koyama, and F. Schmidt. Equivalence principle violation in Vainshtein screened two-body systems. Phys. Rev. D, 87(6):063525, 2013. doi:10.1103/PhysRevD.87.063525.

D. E. Jaekle. Propellant management device conceptual design and analysis: Vanes. In AIAA/SAE/ASME/ASEE 27th Joint Propulsion Conference, June 24-26, 1991, Sacramento, CA, pages AIAA–91–2172. American Institute of Aeronautics and Astronautics, Reston, VA, 1991. doi:10.2514/6.1991-2172.

D. E. Jaekle. Propellant management device conceptual design and analysis: Galleries. In 33rd AIAA/SAE/ASME/ASEE Joint Propulsion Conference & Exhibit, July 6-9, 1997, Seattle, WA, pages AIAA–97–2811. American Institute of Aeronautics and Astronautics, Reston, VA, 1997. doi:10.2514/6.1997-2811.

H. W. Jones. The recent large reduction in space launch cost. In 48th International Conference on Environmental Systems, Albuquerque, New Mexico, USA, July 2018. doi:2346/74082.

E. Kulu. Nanosats database, 2020. URL `www.nanosats.eu`.

R. S. Legge and P. C. Lozano. Electrospray propulsion based on emitters microfabricated in porous metals. J. Propul. Power, 27(2):485–495, 2011. doi:10.2514/1.50037.

B. Li, G.-B. Zhao, and K. Koyama. Exploring Vainshtein mechanism on adaptively refined meshes. J. Cosmol. Astroparticle Phys., 2013(05):023–023, 2013. doi:10.1088/1475-7516/2013/05/023.

R. A. D. Mackenzie and G. D. W. Smith. Focused ion beam technology: A bibliography. Nanotechnology, 1(2):163–201, October 1990. ISSN 0957-4484, 1361-6528. doi:10.1088/0957-4484/1/2/007.

G. L. R. Mair. Theoretical determination of current-voltage curves for liquid metal ion sources. J. Phys. D: Appl. Phys., 17(11):2323–2330, November 1984. ISSN 0022-3727, 1361-6463. doi:10.1088/0022-3727/17/11/019.

A. K. Mallik, G. P. Peterson, and M. H. Weichold. On the use of micro heat pipes as an integral part of semiconductor devices. J. Electron. Packaging, 114(4):436–442, 1992. doi:10.1115/1.2905477.

C. M. Marrese-Reading. Microfluidic electrospray propulsion (mep) thruster performance with microfabricated emitter arrays for indium propellant. In AIAA. American Institute of Aeronautics and Astronautics, July 2016. ISBN 978-1-62410-406-0. doi:10.2514/6.2016-4738.

S. B. G. O'Brien and L. W. Schwartz. Theory and modeling of thin film flows. Enc. Surf. Colloid Sci., pages 5283–5297, 2002.

N. M. Oliveira, S. Vilabril, M. B. Oliveira, R. L. Reis, and J. a. F. Mano. Recent advances on open fluidic systems for biomedical applications: A review. Mat. Sci. Eng. C, 97:851–863, April 2019. ISSN 09284931. doi:10.1016/j.msec.2018.12.040.

S. E. Orchard. On surface levelling in viscous liquids and gels. Appl. Sci. Res., 11(4-6):451–464, 1963. doi:10.1007/BF03184629.

J. R. Rollins, R. K. Grove, and D. E. Jaekle. Twenty-three years of surface tension propellant management system design, development, manufacture, test, and operation. In A. I. of Aeronautics and V. Astronautics, Reston, editors, AIAA 21st Joint Propulsion Conference, Monterey, CA, July 8-10, 1985, pages AIAA–85–1199, 1985. doi:10.2514/6.1985-1199.

L. A. Romero and F. G. Yost. Flow in an open channel capillary. J. Fluid Mech., 322:109–129, 1996. doi:10.1017/S0022112096002728.

R. V. Roy and L. W. Schwartz. Coating flow over a curved substrate. In Proc. 2nd European Coating Symposium, pages 18–27, Université Louis Pasteur, Strasbourg, 1997. P. G. Bourgin.

R. V. Roy, A. J. Roberts, and M. E. Simpson. A lubrication model of coating flows over a curved substrate in space. J. Fluid Mech., 454:235–261, 2002. ISSN 0022-1120. doi:10.1017/S0022112001007133.

F. Schmidt. Self-consistent cosmological simulations of DGP braneworld gravity. Phys. Rev. D, 80(4):043001, 2009. doi:10.1103/PhysRevD.80.043001.

L. W. Schwartz and D. E. Weidner. Modeling of coating flows on curved surfaces. J. Eng. Math., 29(1):91–103, 1995. doi:10.1007/BF00046385.

G. I. Taylor. Disintegration of water drops in an electric field. Proc. R. Soc. Lond. A, 280(1382): 383–397, July 1964. ISSN 0080-4630, 2053-9169. doi:10.1098/rspa.1964.0151.

S. P. Thompson and P. D. Prewett. The dynamics of liquid metal ion sources. J. Phys. D: Appl. Phys., 17(11):2305–2321, November 1984. ISSN 0022-3727, 1361-6463. doi:10.1088/0022-3727/17/11/018.

A. Wagner. The hydrodynamics of liquid metal ion sources. Appl. Phys. Lett., 40(5):440–442, March 1982. ISSN 0003-6951, 1077-3118. doi:10.1063/1.93100.

M. M. Weislogel. Capillary flow in an interior corner. PhD thesis, Northwestern University, June 1996. URL `https://ntrs.nasa.gov/citations/19970010346`. Also published as NASA Technical Memorandum 107364.

N. C. White and S. M. Troian. Why capillary flows in slender triangular grooves are so stable against disturbances. Phys. Rev. Fluids, 4(5):054003, 2019. doi:10.1103/PhysRevFluids.4.054003.

N. C. White, S. M. Troian, J. B. Jewell, C. J. Cutler, S.-w. Chiow, and N. Yu. Robust numerical computation of the 3D scalar potential field of the cubic Galileon gravity model at solar system scales. Phys. Rev. D, 102:024033, 2020. doi:10.1103/PhysRevD.102.024033.

W. P. Wright and P. Ferrer. Electric micropropulsion systems. Prog. Aerosp. Sci., 74:48–61, April 2015. ISSN 03760421. doi:10.1016/j.paerosci.2014.10.003.

J. K. Ziemer and S. M. Merkowitz. Microthrust propulsion for the LISA mission. In 40th AIAA/ASME/SAE/ASEE Joint Propulsion Conference and Exhibit, Fort Lauderdale, Florida, USA, July 2004. American Institute of Aeronautics and Astronautics. ISBN 978-1-62410-037-6. doi:10.2514/6.2004-3439.

N. M. Zubarev. Formation of conic cusps at the surface of liquid metal in electric field. J. Exp. Theor. Phys. Lett., 73(10):544–548, May 2001. doi:10.1134/1.1387524.

Chapter 2

SURFACE TENSION

Surface tension comprises an integral part of the phenomena discussed in this thesis, so a brief introduction to its mathematical origin will be presented here. This is a macroscopic view of surface tension, in which molecular details are ignored and we simply consider what properties a manifold embedded in a higher dimensional space must have in order to maintain conservation of mass and momentum. The approach is relevant not only in fluid mechanics, but also in other areas of physics such as brane models of cosmology and string theory.

Among the first to study surface tension were Young and Laplace, who at the turn of the 19th century established the relationship between a droplet's curvature and its internal pressure in what is now called the Young-Laplace equation (Maxwell and Strutt, 1911):

$$p = \frac{1}{2}\gamma\left(\frac{1}{r_1} + \frac{1}{r_2}\right). \tag{2.1}$$

Here p is the pressure, γ is the surface tension, and r_1 and r_2 are the principal radii of curvature of the fluid interface. Thus, the smaller a droplet is, the higher is its capillary pressure (pressure due to surface tension).

Young further established the Young equation, which sets the contact angle of a liquid drop on a solid surface surrounded by a gas to be θ, satisfying

$$\gamma_{LG}\cos\theta = \gamma_{SG} - \gamma_{SL}, \tag{2.2}$$

where γ_{LG} represents the surface tension of the liquid-gas interface, γ_{SG} that of the solid-gas interface, and γ_{SL} that of the solid-liquid interface (Maxwell and Strutt, 1911).

Equations (2.1) and (2.2) hold only for static (motionless) fluids with constant surface tension; a more general derivation shows them to be somewhat more complicated, as will be seen shortly.

2.1 Conservation laws and the geometry of surface tension

In this section we will consider the general problem of maintaining conservation of mass and momentum across a smooth surface. We will begin by setting up the mathematics necessary to describe a general surface and conservation laws across that surface. From this general setup, we will gradually impose restrictions, first requiring that the surface be bounded by fluids, next requiring that mass not be transferred across the surface, then requiring that the surface be massless, and finally requiring that it be isotropic. It will be seen how each of these conditions constrains the form of the conservation laws. The final result, the conservation laws for an impenetrable, massless, isotropic surface bounded by fluids, will be recognizable as the classical boundary conditions for immiscible fluids with surface tension.

The results presented here are similar to those of Waxman (1984), and, to a lesser degree, those of Scriven (1960) and Aris (1989). Both Scriven and Aris assume Newtonian fluid stress tensors early in their analyses; Waxman maintains generality by assuming an arbitrary stress tensor, but also keeps the momentum terms (e.g., $\rho u^j u^k$) and shear stress resultant separate from the stress tensor. The derivation presented below will instead keep everything inside a single stress-mass tensor, as Vinokur (1974) did for the bulk Navier-Stokes, before considering specific cases.

2.1.1 Setup

Let $\mathcal{M}$ be some 2+1-dimensional manifold embedded in 3+1 dimensional space, described by $\vec{x} = \vec{\sigma}(\xi, \zeta, t)$. Without loss of generality, we may choose the parametrization of $\vec{\sigma}$ so that the manifold velocity, $u_M^j = \partial_t \sigma^j$, is always normal to the manifold. For now, we assume that the manifold is unbounded (manifolds with edges will be addressed later in Section 2.1.6). Our goal is to enforce conservation of mass and momentum, quantities which may be represented by a stress-mass tensor field, the non-relativistic counterpart of the stress-energy tensor field (Vinokur, 1974). Suppose that the region on one side of the manifold (which we may think of as "below" the manifold) has stress-mass tensor $T_{(1)}^{\Xi\Lambda}$, the other side ("above") has stress-mass tensor $T_{(2)}^{\Xi\Lambda}$, and the manifold itself has stress-mass tensor $S^{\Xi\Lambda}$ (see Figure 2.1), so that the total stress-mass field can be described by

$$T^{\Xi\Lambda} = T_{(1)}^{\Xi\Lambda}\Theta(\vec{x} < \vec{\sigma}) + T_{(2)}^{\Xi\Lambda}\Theta(\vec{x} > \vec{\sigma}) + S^{\Xi\Lambda}\delta(\vec{x} - \vec{\sigma}), \tag{2.3}$$

where Θ is the three-dimensional Heaviside step function and δ is the Dirac delta. We want to know what constraints exist on these three tensors if mass and momentum are to be conserved.

In this section we will use capital Greek letters (Ξ, Λ, ...) to denote the 4D space and time coordinates, lowercase Latin letters (i, j, ...) to denote the 3D spatial coordinates alone, uppercase Latin letters (I, J, ...) to denote 3D spatial coordinates in the manifold-centered coordinate system (to be described), and lowercase Greek letters (μ, ν, ...) to denote the local 2D spatial coordinates on the manifold.

The demand that mass and momentum be conserved can be expressed as $\nabla_\Xi T^{\Xi\Lambda} = 0$ (Misner et al., 1973; Vinokur, 1974). From now on, time and space will be considered separate and metrics will be written only with respect to the spatial coordinates, so that we can write explicitly

Figure 2.1: Cross-section of a 2+1D manifold in 3+1D space, with stress-mass tensor $S^{\Xi\Lambda}$ on the manifold and $T_{(1)}^{\Xi\Lambda}$, $T_{(2)}^{\Xi\Lambda}$ on either side.

$$\partial_t T^{tt} + \nabla_j T^{jt} = 0 \qquad \text{(conservation of mass)}, \tag{2.4a}$$

$$\partial_t T^{ti} + \nabla_j T^{ji} = 0 \qquad \text{(conservation of momentum)}, \tag{2.4b}$$

where ∂_t indicates the usual partial derivative with respect to time and ∇_j the covariant derivative with respect to coordinate j (note that our 3D spaces are always flat and Euclidean). These results hold pointwise even with the stress-mass tensor defined as in Equation (2.3). Angular momentum is typically derived to be $T^{ij} = T^{ji}$, but we will see that this pointwise statement holds only in the bulk.

Note: discontinuous body forces in the stress-mass tensor

The stress-mass tensor provides an elegant encapsulation of the physics of momentum and mass transfer, but discontinuous body forces must be handled carefully. For example, suppose the regions on two sides of a partitioning manifold have conservative force potentials $\Phi_{(1)}$ and $\Phi_{(2)}$. Naïvely, each might be added to the respective region's stress tensor T^{ji} as an additional $\tau^{ji} = g^{ji}\Phi$, so that the contribution to the momentum equation is $\nabla_j \tau^{ji} = \nabla^i \Phi$. This is fine within each region, but leads to problems across the interface, as the two potential terms must be normally continuous, i.e., $n_j \tau^{ji}_{(1)} = n_j \tau^{ji}_{(2)}$. In order to rectify the discontinuity, the body force term in one region (say, region 1) may instead by written as $\tau^{ji}_{(1)} = g^{ji}\Phi_{(1)} + \nabla^i \alpha^j + \nabla^j \alpha^i$, where α^i is a vector field satisfying $\nabla_i \nabla^i \alpha^j + \nabla_i \nabla^j \alpha^i = 0$ in the bulk and $n_i(\nabla^i \alpha^j + \nabla^j \alpha^i) = n^j(\Phi_{(2)} - \Phi_{(1)})$ on the boundary. The bulk body forces will thus not have any effect on the balance across the manifold, and can be ignored. This complication is perhaps the most significant drawback to the approach of bundling all the physics into a single stress-mass tensor.

2.1.2 Integral quantities: Mass and momentum

Let $V_c(t)$ be a comoving control volume enclosing an ε-thin slice around a section of manifold, and $A_c(t)$ be the intersection of $V_c(t)$ with the manifold (as in Figure 2.2). We use "comoving" only to mean with respect to normal motion of the manifold, u^j_M. In particular, the volume does not respect any fluid flow within the manifold. By the Reynolds Transport Theorem (Reynolds, 1903),

$$\begin{aligned} \frac{d}{dt}\int_{V_c} T^{\Xi t} dV &= \int_{V_c} \partial_t T^{\Xi t} dV + \int_{\partial V_c} T^{\Xi t} u^j_c \bar{n}_j dA \\ &= \int_{\partial V_c} \left(-T^{\Xi j} + T^{\Xi t} u^j_c\right) \bar{n}_j dA, \end{aligned} \tag{2.5}$$

where $\bar{n}_j$ is the outward-pointing normal on the surface of V_c (not to be confused with $\hat{n}_j$, the upward pointing normal on the manifold), and u^j_c is the local velocity of the control volume

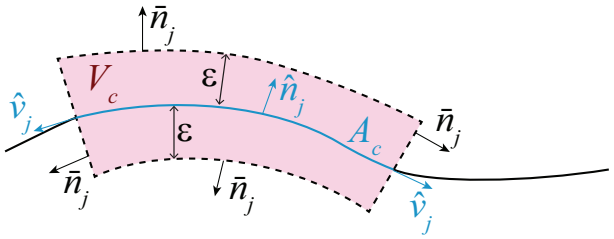

Figure 2.2: Cross-section of a control volume $V_c(t)$ enclosing a section $A_c(t)$ of a manifold with a buffer region of ε on each side. $\bar{n}_j$ represents the outward-pointing normal vectors on the control volume boundary ∂V_c; $\hat{\nu}_j$ are vectors tangent to the manifold at the ends of the control volume; $\hat{n}_j$ represents the upward-pointing normal on the manifold.

boundary. In the limit as $\varepsilon \to 0$, Equation (2.5) reduces to

$$\begin{aligned}\frac{d}{dt}\int_{A_c} S^{\Xi t} dA = \int_{A_c} \left[-\left(T^{\Xi j}_{(2)} - T^{\Xi j}_{(1)}\right) + \left(T^{\Xi t}_{(2)} - T^{\Xi t}_{(1)}\right) u^j_M \right] \hat{n}_j dA \\ + \oint_{\Gamma_c} \left(-S^{\Xi j} + S^{\Xi t} u^j_M \right) \hat{\nu}_j dc. \end{aligned} \tag{2.6}$$

We now must be very careful with the time derivative of the integral on the manifold, as the area of the manifold may be changing in time. The time derivative of the area element is given by $\partial_t dA = u^k_M \hat{n}_k (\nabla_j \hat{n}^j) dA = -2\kappa_m u_M dA$, where κ_m is the mean curvature of the manifold and $u_M = u^k_M \hat{n}_k$ is the magnitude of the manifold's normal velocity (Aris, 1989). Hence,

$$\begin{aligned}\int_{A_c} \left[\partial_t S^{\Xi t} - 2\kappa_m u_M S^{\Xi t} \right] dA = \int_{A_c} \left[-\left(T^{\Xi j}_{(2)} - T^{\Xi j}_{(1)}\right) + \left(T^{\Xi t}_{(2)} - T^{\Xi t}_{(1)}\right) u^j_M \right] \hat{n}_j dA \\ - \oint_{\Gamma_c} S^{\Xi j} \hat{\nu}_j dc, \end{aligned} \tag{2.7}$$

where Γ_c is the closed curve forming the boundary of $V_c \cap \mathcal{M}$ and $\hat{\nu}_j$ is the outward-pointing normal on Γ_c (so that $\hat{\nu}_j$ is in the tangent space of $\mathcal{M}$ at each point). Due to our assumption that the control volume is comoving, we replaced the control volume velocity u^j_c with the manifold velocity $u^j_M = \partial_t \sigma^j$ at the interface.

Next, we apply Stokes's Theorem to convert the Γ_c contour integral into an area integral. If $\hat{\ell}_j$ is the unit tangent to Γ_c, then Stokes's Theorem states that for any vector F^j,

$$\oint_{\Gamma_c} F^j \hat{\ell}_j dc = \int_{A_c} \hat{n} \cdot (\nabla \times F)\, dA = \int_{A_c} \hat{n}_j \varepsilon_{jkr} \partial^k F^r dA. \tag{2.8}$$

Using the fact that $\hat{\nu} = \hat{\ell} \times \hat{n}$, i.e., $\hat{\nu}_j = \varepsilon_{jsp} \hat{\ell}^s \hat{n}^p$,

$$\begin{aligned}\oint_{\Gamma_c} S^{\Xi j} \hat{\nu}_j dc &= \oint_{\Gamma_c} \left(S^{\Xi q} \varepsilon_{qjp} \hat{n}^p \right) \hat{\ell}^j dc = \int_{A_c} \hat{n}_j \varepsilon_{jkr} \partial^k \left(S^{\Xi q} \varepsilon_q{}^r{}_p \hat{n}^p \right) dA \\ &= \int_{A_c} \left[\left(\partial_k - \hat{n}_k \hat{n}^j \partial_j \right) S^{\Xi k} - S^{\Xi j} \hat{n}_j \partial_k \hat{n}^k \right] dA \\ &= \int_{A_c} \left[\nabla_{Sj} S^{\Xi j} - S^{\Xi j} \hat{n}_j \partial_k \hat{n}^k \right] dA \\ &= \int_{A_c} \nabla_{Sj} \left[\left(\delta^j{}_i - \hat{n}^j \hat{n}_i \right) S^{\Xi i} \right] dA, \end{aligned} \tag{2.9}$$

where $\nabla_S \equiv (\nabla - \hat{n}\ \hat{n}\cdot\nabla)$ is the surface gradient (Aris, 1989).

Thus the conservation equation Equation (2.7) can be rewritten as

$$\int_{A_c}\left[\partial_t S^{\Xi t} - 2\kappa_m u_M S^{\Xi t}\right] dA = \int_{A_c}\left\{\left[-\left(T^{\Xi j}_{(2)} - T^{\Xi j}_{(1)}\right) + \left(T^{\Xi t}_{(2)} - T^{\Xi t}_{(1)}\right) u^j_M\right]\hat{n}_j - \nabla_{S j}\left[\left(\delta^j{}_i - \hat{n}^j\hat{n}_i\right) S^{\Xi i}\right]\right\} dA. \tag{2.10}$$

Since the integral was valid regardless of the comoving control volume chosen, then it must be that

$$\begin{aligned}\partial_t S^{\Xi t} - 2\kappa_m u_M S^{\Xi t} = &-\nabla_{S j}\left[\left(\delta^j{}_i - \hat{n}^j\hat{n}_i\right) S^{\Xi i}\right] \\ &+\left[-\left(T^{\Xi j}_{(2)} - T^{\Xi j}_{(1)}\right) + \left(T^{\Xi t}_{(2)} - T^{\Xi t}_{(1)}\right) u^j_M\right]\hat{n}_j.\end{aligned} \tag{2.11}$$

Recall that the conservation of mass and momentum in the entire region had the form $\partial_t T^{\Xi t} = -\nabla_j T^{\Xi j}$. The conservation of mass and momentum on the manifold $\mathcal{M}$ has a similar form, but there is an extra term to account for dilation of the manifold, the divergence term is now a surface divergence (∇_S), and there is an additional forcing term coming from mass and momentum imbalances between the two regions sandwiching $\mathcal{M}$.

2.1.3 Integral quantities: Angular momentum

While conservation of angular momentum can be written for the bulk regions as $T^{ij}_{(1)} = T^{ji}_{(1)}$ and $T^{ij}_{(2)} = T^{ji}_{(2)}$, we need to be a bit more careful on the manifold. Letting X^j be a position vector from an arbitrary origin,

$$\begin{aligned}&\frac{d}{dt}\int_{V_c}\varepsilon_{ijk}X^j T^{kt} dV = \int_{V_c}\varepsilon_{ijk}X^j\partial_t T^{kt} dV + \int_{\partial V_c}\varepsilon_{ijk}X^j T^{kt}u^\ell_c\bar{n}_\ell dA \\ &= -\int_{V_c}\varepsilon_{ijk}X^j\nabla_\ell T^{k\ell} dV + \int_{A_c}\varepsilon_{ijk}X^j\left(T^{kt}_{(2)} - T^{kt}_{(1)}\right)u^\ell_c\bar{n}_\ell dA + \oint_{\Gamma_c}\varepsilon_{ijk}X^j S^{kt}u^\ell_M\hat{\nu}_\ell dc \\ &= -\int_{\partial V_c}\varepsilon_{ijk}X^j T^{k\ell}\bar{n}_\ell dA + \int_{V_c}T^{k\ell}\varepsilon_{ijk}\nabla_\ell X^j dV + \int_{A_c}\varepsilon_{ijk}X^j\left(T^{kt}_{(2)} - T^{kt}_{(1)}\right)u^\ell_M\hat{n}_\ell dA \\ &= \int_{V_c}T^{kj}\varepsilon_{ijk}dV + \int_{A_c}\varepsilon_{ijk}X^j\left[-\left(T^{k\ell}_{(2)} - T^{k\ell}_{(1)}\right) + \left(T^{kt}_{(2)} - T^{kt}_{(1)}\right)u^\ell_M\right]\hat{n}_\ell dA \\ &\quad - \oint_{\Gamma_c}\varepsilon_{ijk}X^j S^{k\ell}\hat{\nu}_\ell dc \\ &= \int_{A_c}S^{kj}\varepsilon_{ijk}dA + \int_{A_c}\varepsilon_{ijk}X^j\left[-\left(T^{k\ell}_{(2)} - T^{k\ell}_{(1)}\right) + \left(T^{kt}_{(2)} - T^{kt}_{(1)}\right)u^\ell_M\right]\hat{n}_\ell dA \\ &\quad - \int_{A_c}S^{k\ell}\varepsilon_{ijk}\nabla_{S\ell}X^j dA - \int_{A_c}\varepsilon_{ijk}X^j\nabla_{S\ell}\left[\left(\delta^\ell{}_m - \hat{n}^\ell\hat{n}_m\right)S^{km}\right] dA,\end{aligned} \tag{2.12}$$

where we have dropped $O(\varepsilon)$ terms in the control volume thickness (keep in mind that ε_{ijk} is the Levi-Civita tensor, not the ε measuring control volume thickness). Since

$$\frac{d}{dt}\int_{A_c}\varepsilon_{ijk}X^j S^{kt} dA = \int_{A_c}\varepsilon_{ijk}X^j\left(\partial_t S^{kt} - 2\kappa_m S^{kt}\right) dV, \tag{2.13}$$

then equating the two expressions yields

$$\begin{aligned}
&\varepsilon_{ijk}X^j\left(\partial_t S^{kt} - 2\kappa_m u_M S^{kt}\right)\\
&= S^{kj}\varepsilon_{ijk} + \varepsilon_{ijk}X^j\left[-\left(T^{k\ell}_{(2)} - T^{k\ell}_{(1)}\right) + \left(T^{kt}_{(2)} - T^{kt}_{(1)}\right)u^\ell_M\right]\hat{n}_\ell\\
&- S^{k\ell}\varepsilon_{ijk}\nabla_{S\ell}X^j - \varepsilon_{ijk}X^j\nabla_{S\ell}\left[\left(\delta^\ell{}_m - \hat{n}^\ell\hat{n}_m\right)S^{km}\right].
\end{aligned} \tag{2.14}$$

Substituting in conservation of momentum, Equation (2.11), yields

$$\begin{aligned}
0 &= S^{kj}\varepsilon_{ijk} - S^{k\ell}\varepsilon_{ijk}\nabla_{S\ell}X^j\\
&= S^{kj}\varepsilon_{ijk} - S^{k\ell}\varepsilon_{ijk}\left(\delta^j_\ell - n_\ell n^j\right)\\
&= \varepsilon_{ijk}n^j S^{k\ell}n_\ell.
\end{aligned} \tag{2.15}$$

That is, $S^{\alpha Y}$, with α being a tangential index and Y being a normal index, must vanish.

To understand this result graphically, consider the two small volume cross-sections depicted in Figure 2.3, each with width W and height H. On the left is a volume in the bulk. Here T^{ji} is a force in direction i acting on the top surface normal to j; similarly for T^{ji} on the bottom (though the direction is reversed). And each side has a T^{ij} term, applying force in the j direction on the faces normal to i. In order for the moments to balance, it must be that

$$\begin{aligned}
0 = &\underbrace{T^{ij}\overbrace{W}^{\text{area}}\overbrace{\frac{H}{2}}^{\text{radius}}}_{\text{right side moment}} + \underbrace{-T^{ij}\overbrace{W}^{\text{area}}\overbrace{\frac{-H}{2}}^{\text{radius}}}_{\text{left side moment}} + \underbrace{-T^{ji}\overbrace{H}^{\text{area}}\overbrace{\frac{-W}{2}}^{\text{radius}}}_{\text{top side moment}} + \underbrace{T^{ji}\overbrace{H}^{\text{area}}\overbrace{\frac{W}{2}}^{\text{radius}}}_{\text{bottom side moment}}\\
&= \left(T^{ij} - T^{ji}\right)\frac{HW}{2}.
\end{aligned} \tag{2.16}$$

This makes it clear that, in the bulk regions, $T^{ij}_{(1)} = T^{ji}_{(1)}$ and likewise for region 2 (Lai et al., 2009).

Consider now the plot on the right. Instead of arbitrary i and j coordinates, we now write α for the coordinate tangent to the manifold and Y normal to it. The setup has 2 key differences: first, the top half has $T^{ij}_{(2)}$ while the bottom half has $T^{ij}_{(1)}$ terms; second, there is an additional force on the right and left sides, provided by $S^{\alpha Y}$ also acting in the Y direction. Note, however, that there is no $S^{Y\alpha}$ counterpart. Counting up the terms, the $T^{ij}_{(1)}$ terms cancel themselves out, as do the $T^{ij}_{(2)}$ terms, leaving the moment balance as only $HS^{\alpha Y} = 0$.

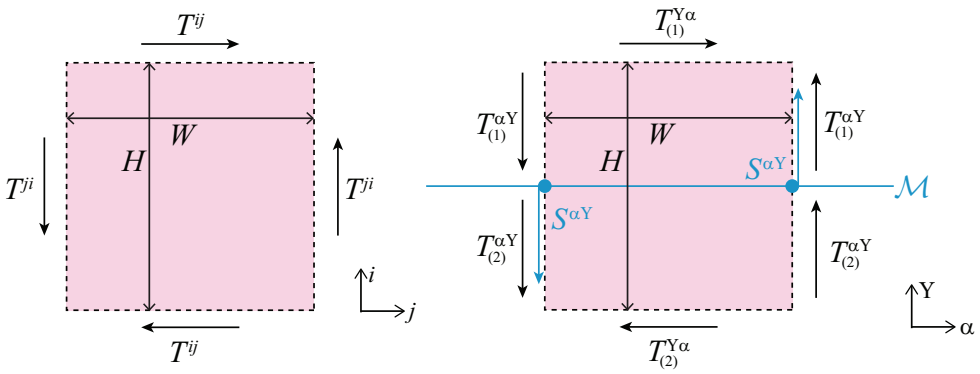

Figure 2.3: Cross-sections of a small volume with width W and height H enclosing a section of a manifold.
Left: A volume in one of the bulk regions. Only the bulk stress tensor T acts on the surfaces.
Right: In this depiction, α is a coordinate tangent to the manifold and Y is normal. The region 1 stress tensor acts on the upper surface, the region 2 stress tensor on the lower surface, and the manifold stress tensor S on the intersection of the volume boundary and the manifold. Note that $S^{Y\alpha}$ does not appear.

2.1.4 Manifold-centered coordinates

Although $S^{\Xi\Lambda}$ is confined to $\mathcal{M}$, we have written it so far with the 3+1 dimensional coordinate system. In order to understand it more clearly, we must look at S in local coordinates on $\mathcal{M}$. We define a new set of manifold-centered coordinates to make projection onto the manifold easier; such local coordinates are frequently used in shell theory (Niordson, 1985). With the manifold being parametrized by ξ and ζ, the two-dimensional local metric is

$$\widetilde{g}_{\mu\nu} = \begin{bmatrix} (\partial_\xi \vec{\sigma} \cdot \partial_\xi \vec{\sigma}) & (\partial_\xi \vec{\sigma} \cdot \partial_\zeta \vec{\sigma}) \\ (\partial_\zeta \vec{\sigma} \cdot \partial_\xi \vec{\sigma}) & (\partial_\zeta \vec{\sigma} \cdot \partial_\zeta \vec{\sigma}) \end{bmatrix}. \tag{2.17}$$

As is usual in differential geometry, the inverse metric will be written with raised indices ($\widetilde{g}^{\mu\nu}$) and raised indices on tensors indicate contraction with the inverse metric. For example, $\widetilde{g}^{\mu\nu} F_{\nu\alpha} \equiv F^{\mu}_{\ \alpha}$.

The shape tensor, or second fundamental form, describes the curvature of $\mathcal{M}$ and can be expressed as

$$\mathrm{I\!I}_{\mu\nu} = \begin{bmatrix} (\partial_{\xi\xi} \vec{\sigma} \cdot \hat{n}) & (\partial_{\xi\zeta} \vec{\sigma} \cdot \hat{n}) \\ (\partial_{\zeta\xi} \vec{\sigma} \cdot \hat{n}) & (\partial_{\zeta\zeta} \vec{\sigma} \cdot \hat{n}) \end{bmatrix} = - \begin{bmatrix} (\partial_\xi \vec{\sigma} \cdot \partial_\xi \hat{n}) & (\partial_\xi \vec{\sigma} \cdot \partial_\zeta \hat{n}) \\ (\partial_\zeta \vec{\sigma} \cdot \partial_\xi \hat{n}) & (\partial_\zeta \vec{\sigma} \cdot \partial_\zeta \hat{n}) \end{bmatrix}, \tag{2.18}$$

where again $\hat{n}$ is the upward-pointing normal on $\mathcal{M}$ (that is, the normal pointing into region 2; see Figure 2.1). Note that $\mathrm{I\!I}$ encodes the mean curvature $\kappa_m = (1/2)\mathrm{I\!I}^{\mu}_{\ \mu}$, and the Gaussian curvature $\kappa_G = \det[\mathrm{I\!I}^{\mu}_{\ \nu}] = 2{\kappa_m}^2 - (1/2)\mathrm{I\!I}^{\mu}_{\ \nu}\mathrm{I\!I}^{\nu}_{\ \mu}$.

Extending this 2D metric to 3D space can be accomplished by defining $\vec{x}(\xi, \zeta, Y) \equiv \vec{\sigma}(\xi, \zeta) +$

$Y\hat{n}(\xi,\zeta)$, yielding a 3D metric (denoted by g without a tilde)

$$g_{IJ} = \begin{bmatrix} \left(1 - Y\mathrm{I\!I}\widetilde{g}^{-1}\right)\widetilde{g}\left(1 - Y\widetilde{g}^{-1}\mathrm{I\!I}\right) & \begin{matrix}0\\0\end{matrix} \\ \begin{matrix}0 & 0\end{matrix} & 1 \end{bmatrix} = \begin{bmatrix} \widetilde{g}_{\mu\nu} - 2Y\mathrm{I\!I}_{\mu\nu} + Y^2\mathrm{I\!I}_{\mu\alpha}\mathrm{I\!I}^{\alpha}{}_{\nu} & \begin{matrix}0\\0\end{matrix} \\ \begin{matrix}0 & 0\end{matrix} & 1 \end{bmatrix} \tag{2.19}$$

(Niordson, 1985) . The new (ξ,ζ,Y) coordinates describe the same bulk 3D space as the original coordinates; they are simply more convenient as the manifold $\mathcal{M}$ now sits at the origin in the Y coordinate.

The Christoffel symbols of this flat 3D g metric are given by

$$\Gamma^{Y}_{YY} = 0 \tag{2.20a}$$

$$\Gamma^{Y}_{\mu Y} = 0 \tag{2.20b}$$

$$\Gamma^{\mu}_{YY} = 0 \tag{2.20c}$$

$$\begin{aligned} \Gamma^{Y}_{\mu\nu} &= \frac{1}{2}g^{YY}\left(g_{Y\mu,\nu} + g_{Y\nu,\mu} - g_{\mu\nu,Y}\right) = -\frac{1}{2}g_{\mu\nu,Y} \\ &= \mathrm{I\!I}_{\mu\nu} - Y\mathrm{I\!I}_{\mu\rho}\mathrm{I\!I}^{\rho}{}_{\nu} \end{aligned} \tag{2.20d}$$

$$\begin{aligned} \Gamma^{\mu}_{Y\nu} &= \frac{1}{2}g^{\mu\mu}\left(g_{\mu Y,\nu} + g_{\mu\nu,Y} - g_{\nu Y,\mu}\right) = \frac{1}{2}g^{\mu\mu}g_{\mu\nu,Y} \\ &= \frac{-\mathrm{I\!I}^{\mu}{}_{\nu} + Y\det\left(\mathrm{I\!I}^{\mu}{}_{\nu}\right)\delta^{\mu}{}_{\nu}}{1 - Y\mathrm{I\!I}^{\mu}{}_{\mu} + Y^2\det\left(\mathrm{I\!I}^{\mu}{}_{\nu}\right)} \\ &= -\mathrm{I\!I}^{\mu}{}_{\nu}\left(1 + Y\mathrm{I\!I}^{\mu}{}_{\mu}\right) + Y\det\left(\mathrm{I\!I}^{\mu}{}_{\nu}\right)\delta^{\mu}{}_{\nu} + O\left((\mathrm{I\!I}Y)^3\right) \end{aligned} \tag{2.20e}$$

$$\Gamma^{\mu}_{\nu\alpha} = \widetilde{\Gamma}^{\mu}_{\nu\alpha} + Y\left(\cdots\right), \tag{2.20f}$$

where $\widetilde{\Gamma}^{\mu}_{\nu\alpha}$ is the Christoffel symbol of the 2D metric $\widetilde{g}_{\mu\nu}$. The covariant derivative in the 3D metric will be denoted by ∇_J.

Surface gradient in local coordinates

Using these results, and letting $\Lambda^{j}{}_{J}$ represent the coordinate transformation, consider the surface gradient of a vector which lives only on the manifold (i.e., which has no Y component):

$$\begin{aligned} \nabla_{Sj}F^i &= \Lambda^{J}{}_{j}\Lambda^{i}{}_{I}\left(\nabla_J - n_J n^K \nabla_K\right)F^I \\ &= \Lambda^{J}{}_{j}\Lambda^{i}{}_{I}\left(\nabla_J F^I - \delta_J{}^{Y}\nabla_Y F^I\right) \\ &= \Lambda^{J}{}_{j}\Lambda^{i}{}_{I}\left(\partial_J F^I + \Gamma^{I}_{J\nu}F^{\nu} - \delta_J{}^{Y}\Gamma^{I}_{Y\nu}F^{\nu}\right) \\ &= \Lambda^{J}{}_{j}\Lambda^{i}{}_{I}\left(\delta^{I}{}_{\beta}\partial_J F^{\beta} + \delta^{I}{}_{\beta}\Gamma^{\beta}_{J\nu}F^{\nu} + \delta^{I}{}_{Y}\Gamma^{Y}_{J\nu}F^{\nu} - \delta^{I}{}_{\beta}\delta_J{}^{Y}\Gamma^{\beta}_{Y\nu}F^{\nu}\right) \\ &= \Lambda^{J}{}_{j}\Lambda^{i}{}_{I}\left(\delta_J{}^{\alpha}\delta^{I}{}_{\beta}\widetilde{\nabla}_{\alpha}F^{\beta} + \delta_J{}^{\alpha}\delta^{I}{}_{Y}\Gamma^{Y}_{\alpha\nu}F^{\nu}\right) \\ &= \Lambda^{\alpha}{}_{j}\Lambda^{i}{}_{\beta}\widetilde{\nabla}_{\alpha}F^{\beta} + \Lambda^{\alpha}{}_{j}\Lambda^{i}{}_{Y}\mathrm{I\!I}_{\alpha\beta}F^{\beta}, \end{aligned}$$

where $\widetilde{\nabla}$ denotes the covariant derivative on $\mathcal{M}$ (as opposed to in the 3D space). The surface gradient of a vector, then, is the manifold-restricted covariant derivative of that vector plus an

extra piece normal to the manifold which is proportional to the second fundamental form. Thus, unlike the covariant derivative, the surface gradient is an operator that lives in the bulk. Even if the vector field F^i is in the tangent bundle of $\mathcal{M}$, its surface gradient may not be.

Now let us compute the surface gradient of a rank 2 tensor, also living exclusively on the manifold:

$$\begin{aligned}\nabla_{Sj}F^{ik} &= \Lambda^J{}_j\Lambda^i{}_I\Lambda^k{}_K\left(\nabla_J - n_J n^R\nabla_R\right)F^{IK} \\ &= \Lambda^\alpha_j\left(\Lambda^i{}_\beta\Lambda^k{}_\lambda\widetilde{\nabla}_\alpha F^{\beta\lambda} + \Lambda^i{}_Y\Lambda^k{}_\lambda\mathrm{I\!I}_{\alpha\nu}F^{\nu\lambda} + \Lambda^i{}_\beta\Lambda^k{}_Y\mathrm{I\!I}_{\alpha\nu}F^{\beta\nu}\right).\end{aligned}$$

The pattern is evident: each additional index yields an additional second fundamental form term.

For a vector with a Y component, e.g. $F^i = f\hat{n}^i$,

$$\begin{aligned}\nabla_{Sj}F^i &= \hat{n}^i\nabla_{Sj}f + f\nabla_{Sj}\hat{n}^i \\ &= \Lambda^\alpha_j\left(\Lambda^i{}_Y\widetilde{\nabla}_\alpha f - \Lambda^i{}_\beta\mathrm{I\!I}_\alpha{}^\beta f\right).\end{aligned} \tag{2.21}$$

Finally, suppose that $U^{i\alpha}$ is a rank 2 tensor whose second component, α, is only tangential, but whose first component, i, may contain both normal and tangential pieces. In this case, it can be written as $U^{i\alpha} = \hat{n}^i\otimes V^\alpha + \Lambda^i{}_\beta F^{\beta\alpha}$ for some V and F. Then

$$\begin{aligned}\nabla_{Sj}\left(\hat{n}^i\otimes V^k\right) &= \hat{n}^i\nabla_{Sj}V^k + V^k\nabla_{Sj}\hat{n}^i \\ &= \Lambda^\alpha_j\left(\Lambda^i{}_Y\Lambda^k{}_\beta\widetilde{\nabla}_\alpha V^\beta + \Lambda^i{}_Y\Lambda^k{}_Y\mathrm{I\!I}_{\alpha\beta}V^\beta - \Lambda^i{}_\nu\Lambda^k{}_\beta\mathrm{I\!I}_\alpha{}^\nu V^\beta\right),\end{aligned} \tag{2.22}$$

and hence

$$\begin{aligned}\nabla_{Sj}U^{ik} &= \Lambda^\alpha_j\left(\Lambda^i{}_Y\Lambda^k{}_\beta\widetilde{\nabla}_\alpha V^\beta + \Lambda^i{}_Y\Lambda^k{}_Y\mathrm{I\!I}_{\alpha\beta}V^\beta - \Lambda^i{}_\nu\Lambda^k{}_\beta\mathrm{I\!I}_\alpha{}^\nu V^\beta\right) \\ &\quad + \Lambda^\alpha_j\left(\Lambda^i{}_\lambda\Lambda^k{}_\beta\widetilde{\nabla}_\alpha F^{\lambda\beta} + \Lambda^i{}_Y\Lambda^k{}_\lambda\mathrm{I\!I}_{\alpha\beta}F^{\beta\lambda} + \Lambda^i{}_\beta\Lambda^k{}_Y\mathrm{I\!I}_{\alpha\nu}F^{\beta\nu}\right).\end{aligned} \tag{2.23}$$

In the case where j and k are contracted,

$$\begin{aligned}\nabla_{Sj}U^{ij} &= \Lambda^i{}_Y\left(\widetilde{\nabla}_\alpha V^\alpha + \mathrm{I\!I}_{\alpha\beta}F^{\beta\alpha}\right) + \Lambda^i{}_\beta\left(\widetilde{\nabla}_\alpha F^{\beta\alpha} - \mathrm{I\!I}_\alpha{}^\beta V^\alpha\right) \\ &= \Lambda^i{}_Y\left(\widetilde{\nabla}_\alpha U^{Y\alpha} + \mathrm{I\!I}_{\alpha\beta}U^{\beta\alpha}\right) + \Lambda^i{}_\beta\left(\widetilde{\nabla}_\alpha U^{\beta\alpha} - \mathrm{I\!I}_\alpha{}^\beta U^{Y\alpha}\right).\end{aligned} \tag{2.24}$$

Note that in the last line we conveniently wrote $U^{Y\alpha}$ to indicate V^α. It should be clear from context when $U^{Y\alpha}$ is used as a tensor and when it is used as a vector.

Time derivatives in local coordinates

Equation (2.11) includes the term $\partial_t S^{\Xi t}$. Care must be taken when translating this term into local coordinates on $\mathcal{M}$, as the coordinates themselves are changing in time.

$$\begin{aligned}\Lambda^Y{}_j \partial_t S^{jt} &= \hat{n}_j \partial_t S^{jt} \\ &= \dot{S}^{Yt} - S^{jt} \partial_t \hat{n}_j \\ &= \dot{S}^{Yt} + S^{\beta t} \widetilde{\nabla}_\beta u_M, \end{aligned} \tag{2.25}$$

and

$$\begin{aligned}\Lambda^\alpha{}_j \partial_t S^{jt} &= \dot{S}^{\alpha t} - S^{jt} \partial_t \Lambda^\alpha_j \\ &= \dot{S}^{\alpha t} - S^{jt} \widetilde{\nabla}^\alpha u_{Mj} \\ &= \dot{S}^{\alpha t} - S^{jt} \widetilde{\nabla}^\alpha \left(u_M \hat{n}_j\right) \\ &= \dot{S}^{\alpha t} - u_M S^{\beta t} \mathrm{I\!I}^\alpha{}_\beta - S^{Yt} \widetilde{\nabla}^\alpha u_M. \end{aligned} \tag{2.26}$$

Here a dot implies a partial derivative in time with respect to fixed coordinates.

2.1.5 Local conservation equations

We can now apply these results to Equation (2.11). Starting with the surface gradient term within that equation, for the $\Xi = t$ case, the surface gradient term is quite simple:

$$\begin{aligned}\nabla_{Sj}\left[\left(\delta^j{}_i - \hat{n}^j \hat{n}_i\right) S^{ti}\right] &= \Lambda^\alpha{}_j \left(\Lambda^j{}_\beta \widetilde{\nabla}_\alpha + \Lambda^j{}_Y \mathrm{I\!I}_{\alpha\beta}\right) S^{t\beta} \\ &= \widetilde{\nabla}_\alpha S^{t\alpha}. \end{aligned} \tag{2.27}$$

In the $\Xi = k$ case,

$$\nabla_{Sj}\left[\left(\delta^j{}_i - \hat{n}^j \hat{n}_i\right) S^{ki}\right] = \Lambda^k{}_Y \left(\widetilde{\nabla}_\alpha S^{Y\alpha} + \mathrm{I\!I}_{\alpha\beta} S^{\beta\alpha}\right) + \Lambda^k{}_\beta \left(\widetilde{\nabla}_\alpha S^{\beta\alpha} - \mathrm{I\!I}_\alpha{}^\beta S^{Y\alpha}\right). \tag{2.28}$$

Substituting in these terms, Equation (2.11) reduces to three equations corresponding to mass conservation, normal stress continuity, and tangential stress continuity. Letting $u_M = u^j_M \hat{n}_j$ (i.e., $u_M = |u^j_M|$) be the normal speed of the manifold,

$$\partial_t S^{tt} - 2\kappa_m u_M S^{tt} = -\widetilde{\nabla}_\alpha S^{t\alpha} - \left(T^{tj}_{(2)} - T^{tj}_{(1)}\right) \hat{n}_j + \left(T^{tt}_{(2)} - T^{tt}_{(1)}\right) u_M \tag{2.29a}$$

$$\begin{aligned}\dot{S}^{Yt} + S^{\beta t} \widetilde{\nabla}_\beta u_M - 2\kappa_m u_M S^{Yt} &= -\widetilde{\nabla}_\alpha S^{Y\alpha} - \mathrm{I\!I}_{\nu\alpha} S^{\nu\alpha} \\ &\quad - \left(T^{Yj}_{(2)} - T^{Yj}_{(1)}\right) \hat{n}_j + \left(T^{Yt}_{(2)} - T^{Yt}_{(1)}\right) u_M \end{aligned} \tag{2.29b}$$

$$\begin{aligned}\dot{S}^{\nu t} - u_M S^{\beta t} \mathrm{I\!I}^\nu{}_\beta - S^{Yt} \widetilde{\nabla}^\nu u_M - 2\kappa_m u_M S^{\nu t} &= -\widetilde{\nabla}_\alpha S^{\nu\alpha} + \mathrm{I\!I}^\nu{}_\alpha S^{Y\alpha} \\ &\quad - \left(T^{\nu j}_{(2)} - T^{\nu j}_{(1)}\right) \hat{n}_j + \left(T^{\nu t}_{(2)} - T^{\nu t}_{(1)}\right) u_M. \end{aligned} \tag{2.29c}$$

These equations are clearly analogous to the bulk conservation equations, Equation (2.4), except that the mass and momentum living on the manifold see the external $T_{(1)}$ and $T_{(2)}$ as additional

sources or sinks of mass and momentum, and some corrections must be made due to the manifold's curvature and motion. The right hand sides of the two momentum equations may be compared to Eqs. (3.5)-(3.6) in Waxman (1984), with $S^{Y\alpha}$ playing the role of Waxman's q^{α}.

Restriction 1: Fluids

Since our main interest is in fluid mechanics, let $T^{\Xi\Lambda}_{(1)}$ be the Cauchy stress-mass tensor (Vinokur, 1974):

$$T^{\Xi\Lambda}_{(1)} = \begin{bmatrix} -\rho & -\rho u^i \\ -\rho u^i & (\tau^{ij} - pg^{ij} - \rho u^i u^j) \end{bmatrix}, \tag{2.30}$$

and similarly for $T_{(2)}$, where u^i is the local fluid velocity, p is pressure, ρ is density, and τ^{ij} is the stress tensor comprising both fluid and additional effects such as electric fields (while it may also contain body forces, such as gravity, these terms will not appear in the manifold equations).

Equation (2.30) is a particular form of the stress-mass tensor that encodes conservation of mass and momentum for fluids (Vinokur, 1974). Plugging $T^{\Xi\Lambda}_{(1)}$ into Equation (2.4) yields the Cauchy momentum equations of fluid dynamics, which in the special case of Newtonian fluids are known as the Navier-Stokes equations. More details may be found in A.2.1.

To consistently require that mass only be transferred to mass and not other types of energy, we make a similar demand on the form of S:

$$S^{\Xi\Lambda} = \begin{bmatrix} -\chi & -\chi u^\alpha & 0 \\ -\chi u^\alpha & \widetilde{S}^{\alpha\beta} - \chi u^\alpha u^\beta & 0 \\ -\chi u_M & \widetilde{S}^{Y\alpha} - \chi u_M u^\alpha & 0 \end{bmatrix}, \tag{2.31}$$

where χ is the mass per unit area of the manifold. The term $\tilde{S}^{Y\alpha}$ is related to the bending moment of the manifold (Waxman, 1984). Note that we have separated the fluid velocity, u^α, which is in the tangent bundle of $\mathcal{M}$, and the manifold velocity u^j_M which acts only normal to the manifold.

The mass conservation, Equation (2.29a), becomes

$$\partial_t \chi - 2\kappa_m u_M \chi + \widetilde{\nabla}_\alpha (\chi u^\alpha) = \rho_{(2)}(u_M - u_{(2)_n}) + \rho_{(1)}(u_{(1)_n} - u_M). \tag{2.32}$$

The normal momentum equation, Equation (2.29b), reduces to

$$\begin{aligned}
&\partial_t(\chi u_M) + \chi u^\beta \widetilde{\nabla}_\beta u_M - 2\kappa_m u_M^2 \chi = \left(\tau_{(2)}^{YY} - \tau_{(1)}^{YY}\right) + \left(p_{(1)} - p_{(2)}\right) \\
&- \rho_{(2)} u_{(2)_n}(u_{(2)_n} - u_M) + \rho_{(1)} u_{(1)_n}(u_{(1)_n} - u_M) \\
&- \widetilde{\nabla}_\alpha\left(\chi u^\alpha u_M\right) + \mathrm{I\!I}_{\nu\alpha}\widetilde{S}^{\nu\alpha} + \widetilde{\nabla}_\alpha S^{Y\alpha} - \mathrm{I\!I}_{\nu\alpha}\chi u^\alpha u^\nu \\
&\implies \chi\partial_t u_M + \chi u^\beta \widetilde{\nabla}_\beta u_M - u_M \widetilde{\nabla}_\beta\left(\chi u^\beta\right) = \left(\tau_{(2)}^{YY} - \tau_{(1)}^{YY}\right) + \left(p_{(1)} - p_{(2)}\right) \\
&- \rho_{(2)}(u_{(2)_n} - u_M)^2 + \rho_{(1)}(u_{(1)_n} - u_M)^2 \\
&- \widetilde{\nabla}_\alpha\left(\chi u^\alpha u_M\right) + \mathrm{I\!I}_{\nu\alpha}\widetilde{S}^{\nu\alpha} + \widetilde{\nabla}_\alpha S^{Y\alpha} - \mathrm{I\!I}_{\nu\alpha}\chi u^\alpha u^\nu \\
&\implies \chi\left(\partial_t u_M + 2u^\beta \widetilde{\nabla}_\beta u_M + \mathrm{I\!I}_{\alpha\beta} u^\alpha u^\beta\right) = \left(\tau_{(2)}^{YY} - \tau_{(1)}^{YY}\right) + \left(p_{(1)} - p_{(2)}\right) \\
&- \rho_{(2)}(u_{(2)_n} - u_M)^2 + \rho_{(1)}(u_{(1)_n} - u_M)^2 + \mathrm{I\!I}_{\nu\alpha}\widetilde{S}^{\nu\alpha} + \widetilde{\nabla}_\alpha S^{Y\alpha},
\end{aligned} \tag{2.33}$$

and the tangential momentum equation, Equation (2.29c), becomes

$$\begin{aligned}
&\partial_t\left(\chi u^\alpha\right) - u_M \chi u^\beta \mathrm{I\!I}^\alpha{}_\beta - 2\kappa_m u_M \chi u^\alpha - \chi u_M \widetilde{\nabla}^\alpha u_M = \tau_{(2)}^{\alpha Y} - \tau_{(1)}^{\alpha Y} \\
&+ \rho_{(2)} u_{(2)}{}^\alpha (u_M - u_{(2)_n}) - \rho_{(1)} u_{(1)}{}^\alpha (u_M - u_{(1)_n}) \\
&+ \widetilde{\nabla}_\beta \widetilde{S}^{\alpha\beta} - \mathrm{I\!I}^\alpha{}_\beta \tilde{S}^{Y\beta} - \widetilde{\nabla}_\beta\left(\chi u^\alpha u^\beta\right) + \chi \mathrm{I\!I}^\alpha{}_\beta u^\beta u_M \\
&\implies \chi\partial_t u^\alpha - 2\chi \mathrm{I\!I}^\alpha{}_\beta u^\beta u_M + \chi u^\beta \widetilde{\nabla}_\beta u^\alpha - \chi u_M \widetilde{\nabla}^\alpha u_M = \tau_{(2)}^{\alpha Y} - \tau_{(1)}^{\alpha Y} \\
&+ \rho_{(2)}(u_{(2)}{}^\alpha - u^\alpha)(u_M - u_{(2)_n}) + \rho_{(1)}(u^\alpha - u_{(1)}{}^\alpha)(u_M - u_{(1)_n}) \\
&+ \widetilde{\nabla}_\beta \widetilde{S}^{\alpha\beta} - \mathrm{I\!I}^\alpha{}_\beta \tilde{S}^{Y\beta}.
\end{aligned} \tag{2.34}$$

All together, the mass and momentum equations are thus

$$\partial_t \chi - 2\kappa_m u_M \chi + \widetilde{\nabla}_\alpha\left(\chi u^\alpha\right) = \rho_{(2)}(u_M - u_{(2)_n}) + \rho_{(1)}(u_{(1)_n} - u_M), \tag{2.35a}$$

$$\begin{aligned}
&\chi\left(\partial_t u_M + 2u^\beta \widetilde{\nabla}_\beta u_M + \mathrm{I\!I}_{\alpha\beta} u^\alpha u^\beta\right) = \mathrm{I\!I}_{\nu\alpha}\widetilde{S}^{\nu\alpha} + \widetilde{\nabla}_\alpha S^{Y\alpha} \\
&+ \left(\tau_{(2)}^{YY} - \tau_{(1)}^{YY}\right) + \left(p_{(1)} - p_{(2)}\right) - \rho_{(2)}(u_{(2)_n} - u_M)^2 + \rho_{(1)}(u_{(1)_n} - u_M)^2,
\end{aligned} \tag{2.35b}$$

$$\begin{aligned}
&\chi\left(\partial_t u^\alpha - 2\mathrm{I\!I}^\alpha{}_\beta u^\beta u_M + u^\beta \widetilde{\nabla}_\beta u^\alpha - u_M \widetilde{\nabla}^\alpha u_M\right) = \widetilde{\nabla}_\beta \widetilde{S}^{\alpha\beta} - \mathrm{I\!I}^\alpha{}_\beta \tilde{S}^{Y\beta} + \left(\tau_{(2)}^{\alpha Y} - \tau_{(1)}^{\alpha Y}\right) \\
&+ \rho_{(2)}(u_{(2)}{}^\alpha - u^\alpha)(u_M - u_{(2)_n}) + \rho_{(1)}(u^\alpha - u_{(1)}{}^\alpha)(u_M - u_{(1)_n}).
\end{aligned} \tag{2.35c}$$

Note that no assumption was made that the interface move at the same velocity as the neighboring fluid, i.e., we did not enforce a kinematic condition. Therefore, mass transfer to and from the interface is possible. Thus the left-hand side of Equation (2.35a) describes the change in density on the manifold due to changes in the area of the manifold itself and convection on the manifold, while the right-hand side describes the transfer of mass between the manifold and the bounding fluids (2) and (1).

Equation (2.35b) describes the transfer of normal momentum between fluids (2) and (1); note in particular that the manifold can indeed transfer momentum normal to itself. The convective derivative has a multiplicative factor of 2; one half is due to fluid convection on the manifold, while the second half is due to the change in direction of the normal vector over time.

Equation (2.35c) describes conservation of tangential momentum; the left-hand side and the last term on the right-hand side simply form the Cauchy momentum equation on the manifold itself; the remaining terms describe transfer of tangential momentum between the manifold and the bounding fluids (2) and (1).

Restriction 2: Fluids and kinematic condition

In the present work, we will omit evaporation and condensation as negligible, and thus can enforce the kinematic condition $u_{(1)_n} = u_{(2)_n} = u_M$. This condition implies that the manifold moves at the same velocity as the fluids bounding it, and so mass is not transferred between the bulk fluids or between the bulk and the manifold. Then,

$$\partial_t \chi - 2\kappa_m u_M \chi + \widetilde{\nabla}_\alpha \left(\chi u^\alpha\right) = 0, \tag{2.36a}$$

$$\chi \left(\partial_t u_M + 2u^\beta \widetilde{\nabla}_\beta u_M + \mathrm{II}_{\alpha\beta} u^\alpha u^\beta\right) = \mathrm{II}_{\nu\alpha} \widetilde{S}^{\nu\alpha} + \widetilde{\nabla}_\alpha S^{Y\alpha} + \tau^{YY}_{(2)} - \tau^{YY}_{(1)} + p_{(1)} - p_{(2)}, \tag{2.36b}$$

$$\chi \left(\partial_t u^\alpha - 2\mathrm{I\!I}^\alpha{}_\beta u^\beta u_M + u^\beta \widetilde{\nabla}_\beta u^\alpha - u_M \widetilde{\nabla}^\alpha u_M\right) = \widetilde{\nabla}_\beta \widetilde{S}^{\alpha\beta} - \mathrm{II}^\alpha{}_\beta \tilde{S}^{Y\beta} + \tau^{\alpha Y}_{(2)} - \tau^{\alpha Y}_{(1)}. \tag{2.36c}$$

Now Equation (2.36a) governs only the mass confined on the manifold. Equation (2.36b) balances the normal acceleration of the manifold with the pressure and normal stress of the outer fluids and the tangential stress of the manifold, which acts normally due to the local curvature. And Equation (2.36c) balances fluid acceleration on the manifold with tangential stresses of the bounding fluids. The momentum equations are now exactly Eqs. (3.5)-(3.6) in Waxman (1984).

Restriction 3: Fluids, kinematic condition, and massless interface

A further simplification comes from assuming that the interfacial manifold is massless ($\chi = 0$), or so thin as to be effectively massless (the interface mass could no longer be negligible if there were a physical membrane, such as an oxidation layer or lipid bilayer on the surface of the fluid). In this case of a massless interface, the conservation equations reduce to

$$0 = \mathrm{II}_{\nu\alpha} \widetilde{S}^{\nu\alpha} + \left(\tau^{YY}_{(2)} - \tau^{YY}_{(1)}\right) + \left(p_{(1)} - p_{(2)}\right) \tag{2.37a}$$

$$0 = \widetilde{\nabla}_\beta \widetilde{S}^{\alpha\beta} + \left(\tau^{\alpha Y}_{(2)} - \tau^{\alpha Y}_{(1)}\right). \tag{2.37b}$$

$\widetilde{S}$ can be decomposed into a diagonal and a trace-free component, $\widetilde{S}^{\nu\alpha} = \gamma \widetilde{g}^{\nu\alpha} + \widetilde{\tau}^{\nu\alpha}$. Without mass or bending moment, it must be the case that $\widetilde{S}^{\nu\alpha} = \widetilde{S}^{\alpha\nu}$ and $\widetilde{S}^{Y\alpha} = 0$ for angular

momentum to be conserved (Waxman, 1984). Thus, the trace-free component $\widetilde{\tau}^{\nu\alpha}$ has only two degrees of freedom. All together,

$$\left(\tau_{(1)}^{YY} - \tau_{(2)}^{YY}\right) + \left(p_{(2)} - p_{(1)}\right) = 2\kappa_m\gamma + \mathrm{I\!I}_{\nu\alpha}\widetilde{\tau}^{\nu\alpha} \tag{2.38a}$$

$$\left(\tau_{(1)}^{\nu Y} - \tau_{(2)}^{\nu Y}\right) = \widetilde{\nabla}^{\nu}\gamma + \widetilde{\nabla}_{\alpha}\widetilde{\tau}^{\nu\alpha}. \tag{2.38b}$$

$\widetilde{\tau}$ is anisotropic, in the sense that it is not invariant under an orthogonal change of coordinates (it is easy to verify by hand that the only matrices of dimension 2 which are invariant under the action of the special orthogonal group $SO(2)$ are multiples of the identity, and hence the only such matrix which is trace-free is the zero matrix). We can imagine several potential sources of anisotropy. The interface may be intrinsically anisotropic, as occurs in nematic liquid crystal interfaces, for example (Rey, 2000).

Alternatively, the interface could gain its "sense of direction" from its own curvature. The simplest nonzero form of $\widetilde{\tau}$ deriving from the curvature would be $\widetilde{\tau}^{\nu\alpha} \propto (\mathrm{I\!I}^{\nu\alpha} - 2\kappa_m\widetilde{g}^{\nu\alpha})$. Indeed, such a deviatoric stress coupled to curvature was proposed by Helfrich (1973) in a model of cell membranes, which also included curvature dependence in the trace of the stress by letting $\gamma = \gamma(\kappa_m, \kappa_G)$. Such higher order curvature terms would be expected to become larger as the system size decreases, and Helfrich gave a rough estimate suggesting they would become relevant at sub-nanometer scales. For fluids without membranes, the Tolman model (Tolman, 1949) describing immiscible fluid interfaces also includes the effect of curvature in γ, but not in the deviatoric $\widetilde{\tau}$. Tolman's coefficient, which also reflects the scale at which this curvature term becomes important, is known as the Tolman length, and is based on the length scale of intermolecular forces for the relevant fluids (Tolman estimated it to be a few nanometers).

For an isotropic fluid interface at scales much larger than the Tolman length, $\widetilde{\tau}$ can be thrown out and the classical boundary conditions for surface tension are recovered (see, e.g., Landau and Lifshitz, 1987):

$$\left(\tau_{(1)}^{YY} - \tau_{(2)}^{YY}\right) + \left(p_{(2)} - p_{(1)}\right) = 2\kappa_m\gamma \tag{2.39a}$$

$$\left(\tau_{(1)}^{\nu Y} - \tau_{(2)}^{\nu Y}\right) = \widetilde{\nabla}^{\nu}\gamma. \tag{2.39b}$$

For motionless bounding fluids, $\tau^{YY} = 0$ and Equation (2.39a) is exactly the Young-Laplace equation. We can interpret Equation (2.39) as the interface manifold locally feeling an isotropic negative pressure γ (which may be a function of temperature, surfactant concentration, etc.), and not being aware of its own curvature at first order. Because the surface tension γ plays for the surface exactly the same role that pressure p plays in the bulk, it can be used to construct a free energy, with interfacial area as its conjugate variable.

2.1.6 Manifolds with edges (contact lines)

We have now seen how to deal with edgeless manifolds, like the surfaces of raindrops and bubbles. Such surfaces were edgeless because they formed the interface between two distinct

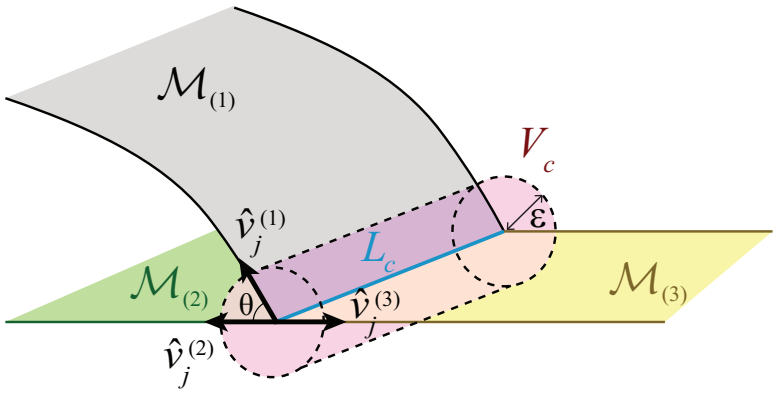

Figure 2.4: A tubular control volume V_c of radius ε enclosing a section L_c of a contact line, where three manifolds ($\mathcal{M}_{(1)}$, $\mathcal{M}_{(2)}$, $\mathcal{M}_{(3)}$) meet. $\hat{\nu}_j^{(N)}$ denotes the normal vector on L_c tangent to manifold $\mathcal{M}_{(N)}$. The contact angle between $\mathcal{M}_{(1)}$ and $\mathcal{M}_{(2)}$ is θ. The contact line L_c is depicted as straight but that need not be the case.

volumetric domains; when there are three volumetric domains, an edge will appear. For example, a water droplet sitting on a table has an edge where the water, air, and solid meet, often referred to as the contact line.

Consider such a contact line formed by intersection of three 2D manifolds, $\mathcal{M}_{(1)}$, $\mathcal{M}_{(2)}$, and $\mathcal{M}_{(3)}$. Let the stress-mass tensor be restricted to the manifolds be given by $S_{(1)}^{\Xi\Lambda}$, $S_{(2)}^{\Xi\Lambda}$, and $S_{(3)}^{\Xi\Lambda}$, and let the stress-mass tensor restricted to the line be given by $B^{\Xi\Lambda}$ (in particular, we ignore the line-bending moment a priori, as we will be assuming a massless line shortly). We can now proceed with an argument similar to that of the previous section, but with the roles of T and S replaced by S and B, respectively.

Consider a comoving tube of radius ε enclosing a section L_c of the contact line, as in Figure 2.4. In the limit as $\varepsilon \to 0$, Equation (2.5) reduces to

$$\frac{d}{dt}\int_{L_c} B^{\Xi t} ds = \sum_{N=1,2,3} \int_{L_c} \left(S_{(\mathsf{N})}^{\Xi j} - S_{(\mathsf{N})}^{\Xi t} u_c^j\right) \hat{\nu}_j^{(\mathsf{N})} ds + \left[\left(-B^{\Xi j} + B^{\Xi t} u_c^j\right) \hat{t}_j\right]_{\partial L_c} + \lim_{\varepsilon \to 0} \sum_{N=1,2,3} \int_{\partial V_c} \left(-T_{(\mathsf{N})}^{\Xi j} + T_{(\mathsf{N})}^{\Xi t} u_c^j\right) \bar{n}_j dA, \tag{2.40}$$

where $\hat{\nu}_j^{(N)}$ is the outward-pointing unit vector normal to the contact line and tangent to $\mathcal{M}_{(\mathsf{N})}$, ds is the measure of an arc-length parametrization of the contact line L_c, and $\hat{t}_j$ is the unit tangent along L_c. Although the surface area of the tube goes to 0 as $\varepsilon \to 0$, we left in the bulk stress tensors $T_{(\mathsf{N})}^{\Xi j}$ because they can form a singularity at a moving contact line if a no-slip boundary condition is imposed. A number of resolutions are possible, including a slip boundary condition, elastic movement of the solid wall, and non-Newtonian stress tensors; a slip condition is perhaps the most plausible and leads to a complicated interface shape near the contact line (Cox, 1986). Let us simply assume that the contact line is motionless and continue from there.

In that case,

$$\int_{L_c} \partial_t B^{\Xi t} ds = \int_{L_c} \left[\partial_s \left(-B^{\Xi j} \hat{t}_j \right) + \sum_{N=1,2,3} S^{\Xi j}_{(\mathsf{N})} \hat{\nu}^{(\mathsf{N})}_j \right] ds. \tag{2.41}$$

The most general form of B is

$$B^{\Xi\Lambda} = \begin{bmatrix} -\beta & -\beta u^\mu \\ -\beta u^\nu & \widetilde{B} \hat{t}^\mu \hat{t}^\nu - \beta u^\mu u^\nu \end{bmatrix}, \tag{2.42}$$

where β is the mass per unit length of the contact line. But let us restrict ourselves from the start to the case where the contact line is massless, so that

$$B^{\Xi\Lambda} = \begin{bmatrix} 0 & 0 \\ 0 & \widetilde{B} \hat{t}^\mu \hat{t}^\nu \end{bmatrix}. \tag{2.43}$$

Note that $\widetilde{B}$, called the line tension, is now a scalar since there is only one spatial degree of freedom on the line. This line tension is analogous to the surface tension, but on a 1-dimensional manifold instead of a 2-dimensional manifold.

Letting α be an arc-length coordinate tangent to the contact line (corresponding to $\hat{t}^j$), and letting μ refer to coordinates normal to it, the conservation of tangent momentum and normal momentum are then

$$0 = -\nabla_s (B^{\alpha\alpha}) + \sum_{N=1,2,3} S^{\alpha j}_{(\mathsf{N})} \hat{\nu}^{(\mathsf{N})}_j \tag{2.44a}$$

$$0 = -\nabla_s (B^{\mu\alpha}) + \sum_{N=1,2,3} S^{\mu j}_{(\mathsf{N})} \hat{\nu}^{(\mathsf{N})}_j, \tag{2.44b}$$

or

$$0 = -\nabla_s \widetilde{B} + \sum_{N=1,2,3} S^{\alpha j}_{(\mathsf{N})} \hat{\nu}^{(\mathsf{N})}_j \tag{2.45a}$$

$$0 = -\kappa \hat{n}^\mu \widetilde{B} + \sum_{N=1,2,3} S^{\mu j}_{(\mathsf{N})} \hat{\nu}^{(\mathsf{N})}_j, \tag{2.45b}$$

where κ is the curvature of L_c and $\hat{n}$ is its normal (parallel to $\partial_s \hat{t}$).

In the simplest case of isotropic manifolds with $S^{ij}_{(\mathsf{N})} = \gamma_{(\mathsf{N})} g^{ij}$, the momentum conservation reduces further to

$$\nabla_s \widetilde{B} = 0 \tag{2.46a}$$

$$\kappa \hat{n}^\mu \widetilde{B} = \sum_{N=1,2,3} \gamma_{(\mathsf{N})} \hat{\nu}^\mu_{(\mathsf{N})}. \tag{2.46b}$$

Equation (2.46a) implies that in this case the line tension $\widetilde{B}$ must be constant. Furthermore, the balance of surface tensions determines the valid $\hat{\nu}_{(\mathsf{N})}$, and in turn the contact angle. For the standard setup of a liquid drop on a flat solid surface, Equation (2.46b) reduces to

$$\kappa \widetilde{B} = \gamma_{SG} - \gamma_{SL} - \gamma_{LG} \cos\theta, \tag{2.47}$$

where θ is the contact angle, and it is in this form that line tension is typically reported (Amirfazli and Neumann, 2004). Setting $\widetilde{B} = 0$, i.e., assuming there is no line tension, recovers Young's Law for the contact angle, Equation (2.2).

Debate remains over both the sign and magnitude of line tension in real systems, and it will not be considered for the work in this thesis. The interested reader is referred to the review article by Amirfazli and Neumann (2004).

References

A. Amirfazli and A. W. Neumann. Status of the three-phase line tension: A review. Adv. Colloid Interface Sci., 110(3):121–141, August 2004. ISSN 00018686. doi:10.1016/j.cis.2004.05.001.

R. Aris. Vectors, Tensors and the Basic Equations of Fluid Mechanics. Dover Publications, New York, 1989. ISBN 9780486661100.

R. G. Cox. The dynamics of the spreading of liquids on a solid surface. part 1. viscous flow. J. Fluid Mech., 168:169–194, 1986. doi:10.1017/S0022112086000332.

W. Helfrich. Elastic properties of lipid bilayers: Theory and possible experiments. Z. Naturforsch. C, 28(11-12):693–703, December 1973. doi:10.1515/znc-1973-11-1209.

W. M. Lai, D. H. Rubin, D. Rubin, and E. Krempl. Introduction to Continuum Mechanics. Elsevier Science, Burlington, MA, 4th edition, 2009. ISBN 9780080942520.

L. D. Landau and E. M. Lifshitz. Fluid Mechanics, volume 6 of Course of Theoretical Physics. Butterworth-Heinemann, 2nd edition, 1987.

J. C. Maxwell and J. W. Strutt. Encyclopædia Britannica (11th Edition), volume 5. Univ. of Cambridge, 1911.

C. W. Misner, K. S. Thorne, and J. A. Wheeler. Gravitation. W. H. Freeman, 1973. ISBN 9780716703440. doi:10.1002/asna.19752960110.

F. I. Niordson. Shell Theory. Applied Mathematics and Mechanics Series. North-Holland, Amsterdam, 1985. ISBN 9780444876409.

A. D. Rey. Young-Laplace equation for liquid crystal interfaces. J. Chem. Phys., 113(23): 10820–10822, December 2000. ISSN 0021-9606, 1089-7690. doi:10.1063/1.1324993.

O. Reynolds. Papers on mechanical and physical subjects, volume III. Cambridge University Press, London, 1903.

L. E. Scriven. Dynamics of a fluid interface equation of motion for Newtonian surface fluids. Chem. Eng. Sci., 12(2):98–108, May 1960. ISSN 00092509. doi:10.1016/0009-2509(60)87003-0.

R. C. Tolman. The effect of droplet size on surface tension. J. Chem. Phys., 17(3):333–337, March 1949. doi:10.1063/1.1747247.

M. Vinokur. A new formulation of the conservation equations of fluid dynamics. Technical Report NASA-TM-X-62415, NASA Ames Research Center Moffett Field, CA, United States, 1974. URL https://ntrs.nasa.gov/citations/19750011505.

A. M. Waxman. Dynamics of a couple-stress fluid membrane. Stud. Appl. Math., 70(1):63–86, February 1984. ISSN 00222526. doi:10.1002/sapm198470163.

Chapter 3

STABILITY ANALYSIS

3.1 Non-normality and generalized linear stability analysis

A central question arising in the study of the behavior of time-dependent ordinary and partial differential equations is whether a given solution is stable. That is, given a known solution for some initial condition, will another solution starting from a nearby initial condition stay close to the first solution, or will their trajectories diverge? The concept of stability analysis may be traced back at least to the 1600s (Leine, 2010), and its application to hydrodynamic problems is nearly as old: as early as 1738, Daniel Bernoulli described stable ("firm") floating bodies: "a minimal arbitrary force makes a body—although put in firm equilibrium—nod a little, but when the force has been undergone [i.e., ceases to act], the body tends again to its natural position, unless the nodding would have exceeded certain bounds" (Bernoulli, 1738, 1747; Leine, 2010). By 1749, Euler was describing hydrodynamic stability with practically modern terminology: "the stability of a floating body in equilibrium is determined by the restoring moment arising when the body has been displaced from equilibrium by an infinitesimally small angle" (Euler, 1749; Leine, 2010).

Bernoulli and Euler both realized that stability must be defined relative to the size of allowed perturbations to a system. The idea of studying how *infinitesimal* perturbations grow or decay naturally leads to linear stability analysis, in which the governing equations of a system are linearized to provide differential equations $\partial_t u(t) = Au(t)$ describing the evolution of infinitesimal perturbations u, A being a matrix or differential operator (note that higher-order derivatives in t such as ∂_t^2 or ∂_t^n may be eliminated by introducing additional variables). As long as the operator A is autonomous (independent of time), then modal linear stability analysis can then be carried out in the following way. For every eigenvector v_i of A with eigenvalue λ_i, $v_i \exp(\lambda_i t)$ is a solution to the evolution equation. Assuming an initial perturbation may be decomposed into the eigenvector basis as $u(0) = \sum_i a_i v_i$, the evolution of u is then given by $u(t) = \sum_i a_i v_i \exp(\lambda_i t)$. If any λ_i is positive, then a perturbation may grow exponentially, a situation described as instability. If all λ_i are negative, then the perturbation decays, satisfying $\lim_{t\to\infty} u(t) = 0$, and the linearized system is thus "stable." When the maximum eigenvalue λ_i is equal to 0, it becomes necessary to included nonlinear terms to determine the stability, despite the infinitesimal perturbations being by definition in the linear regime.

Such modal linear stability analysis appeared at least as early as Maxwell's analysis of flyball governors in steam engines (Leine, 2010; Maxwell, 1868); though Maxwell did not explicitly cast his analysis in terms of eigenvectors and eigenvalues, he connected the stability exponents to the roots of a polynomial which is indeed the characteristic polynomial of the relevant matrix.

Maxwell's problem was a system of ordinary differential equations, but the same methodology was applied to partial differential equations soon afterwards with Lord Rayleigh's 1879 analysis of an initially horizontal fluid interface between two layers of fluid moving in opposite directions parallel to the interface (Rayleigh, 1879). Rayleigh, too, did not explicitly refer to eigenfunctions of the linearized equation, but introduced an ansatz $\cos(\kappa x)\exp(\lambda t)$ to describe perturbations.

Following Rayleigh, modal linear stability analysis was applied to a wide variety of problems in hydrodynamics; historical overviews can be found in Drazin and Reid (2004); Schmid and Henningson (2012). We will skip ahead to the cases where the analysis began to fail in certain hydrodynamic systems, notably in Couette flow, the plane flow induced by an infinitely long channel bounded by two parallel walls separated by a fixed distance, one motionless and one moving at a constant tangent velocity. When Couette flow is inviscid, a naïve computation of the eigenfunctions of the linearized system yields no solutions, and Case (1960) demonstrated that stability can be effectively assessed instead by direct computation of the growth rate of arbitrary perturbations. While Case went on to show that modal linear stability analysis could achieve the same results if a singularity in the operator is dealt with carefully, the first approach of ignoring eigenfunctions and tracking the growth of arbitrary perturbations presaged the methods that would be necessary in later studies.

When viscosity is included, the singularity of Case (1960) is avoided, and here the linearized Navier-Stokes equations are known as the Orr-Sommerfeld equation. In this case, a modal linear stability analysis yields a set of eigenfunctions and corresponding growth rates which depend on the Reynolds number Re. For Couette flow, all modes decay at all Reynolds numbers; i.e., the flow is linearly stable (Romanov, 1973). For Poiseuille flow, which is flow between two parallel motionless walls given fixed pressure boundary conditions to drive the flow, the system is linearly stable for $\mathrm{Re} \lesssim 5772$, and unstable for higher Reynolds numbers (Orszag, 1971). These computations at first seem like a success for modal linear stability theory, but experiments and simulations of the Navier-Stokes equations reveal transition from laminar to turbulent flow at far lower Reynolds numbers: around $\mathrm{Re} = 350$ for Couette flow and $\mathrm{Re} = 1000$ for Poiseuille flow (Trefethen et al., 1993).

Clearly the modal linear stability analysis gives results that differ from observations of the full nonlinear equations. The question then, is whether this failure is simply due to nonlinear effects which cannot be captured by the linearized analysis, or whether some improvement can be made within the linear system. Butler and Farrell (1992) and Reddy et al. (1993) identified the Orr-Sommerfeld operator as *non-normal* under both L_2 and energy density norms, meaning that the operator does not commute with its adjoint and hence has nonorthogonal eigenfunctions. Even for Couette flow, when the operators' eigenvalues are all negative, the linear system can drive certain initial conditions to hundreds or thousands of times their initial size in a finite time before eventually decaying. While the growth is transient and not permanent, the idea is that the linearized system can drive enough amplification of small perturbations to push them into the

nonlinear regime. While simplified low-dimensional models have been developed which indeed prove how transient non-normal growth can induce a transition to nonlinear chaos (Baggett and Trefethen, 1997; Gebhardt and Grossmann, 1994), some disagreement remains over the relative importance of non-normal effects in the onset of real fluid turbulence (Waleffe, 1995). Undisputed, though, is the mathematical fact of transient growth in non-normal systems, which has found a variety of applications.

Non-normal transient growth of perturbations in large-scale (thousands of km) atmospheric flows was first demonstrated by Farrell (1989), who found that the optimal initial perturbations (i.e., those that induce the greatest growth) can lead to cyclone formation. Non-normal growth has also been shown in helically advected magnetic fields, and argued to be a potential source of the large-scale magnetic field distribution of galaxies (Farrell and Ioannou, 1999). In ecology, Neubert and Caswell (1997) took a linear model of nutrient cycles in tropical rainforests which had earlier been shown to be modally stable, and found that the non-normality of the system led to perturbations which could more than double their size over the "transient" period of a century. The same authors later reexamined several nonlinear predator-prey and population models from the ecology literature, finding that non-normality and transient growth are common features. They found in particular that the predation rate has little effect on non-normality, but that it increases significantly with the population growth rate of the prey (Caswell and Neubert, 2005). Asllani et al. (2018) took a more general approach, computing the degree of non-normality in a variety of networks' adjacency matrices, which can be used to model the flow of quantities on the network. While the road transportation networks they studied were nearly normal, they found significant non-normality in microbiological metabolic and transcriptional regulation networks, and in online social networks.

This thesis is concerned with the stability of capillary-driven viscous flows in slender grooves and thin films, and prior research has indeed shown non-normal dynamics to be important in these contexts. One early application was in the spreading of thin films coated with surfactants: experiments had shown the formation of fingering patterns, but classical modal stability analysis found only stable modes. Matar and Troian (1998) showed that the linearized system is highly non-normal, with perturbations able to grow to over 3000 times their initial size. Another example is the gravity-driven flow of a thin viscous film with a contact line down an inclined plane. The moving front of such a film had already been shown to be unstable, leading to finger formation (Troian et al., 1989). A later generalized linear stability analysis using the model of Troian et al. (1989) showed that such films were even more unstable than expected and, in particular, can experience fingering instabilities even on inclines shallower than the limiting critical angle predicted by the modal theory (Bertozzi and Brenner, 1997). Non-normality was subsequently shown to be important in the flow of thin films over a substrate containing bumps, trenches, and other complex topology (Davis and Troian, 2005), and in thermocapillary thin film spreading, in which an external temperature field induces variations in surface tension and hence drives flow (Davis et al., 2003; Tiwari et al., 2007).

As the classical modal linear analysis is insufficient for non-normal and time-dependent systems, the methodology of Lyapunov has increasingly been adopted. Lyapunov (1907) defined a measure of stability in (not necessarily linear) differential equations by measuring the growth of a perturbation as time $t \to \infty$, without predicating that such a perturbation must be an eigenvector; the exponential growth rate of such a perturbation is now known as a Lyapunov exponent. Goldhirsch et al. (1987) generalized the concept of Lyapunov exponents to finite-time growth [as pointed out by Yoden and Nomura (1993), the same definition had earlier been developed by Lorenz (1965) without reference to Lyapunov]. This finite-time Lyapunov exponent methodology was laid out particularly nicely by Farrell and Ioannou (1996a,b) under the title *generalized stability theory*, and the remainder of this section will for the most part follow their derivations and terminology.

To know whether a perturbation is large or small and whether it is growing or decaying requires a method of quantifying its size. It is mathematically convenient (and often physically natural) to define an inner product norm for the purpose of this measurement. The behavior of the system itself does not depend on what tool we use to measure it, but an observer's understanding of the system may vary drastically. In fact, a quantity may even decrease under one inner product norm while increasing under another. The choice of inner product not only determines the size of vectors, but also their orthogonality. The classical method of linear stability analysis rests on simply computing the eigenvalues and eigenvectors of a linear operator, without any reference to inner products or norms. However, assessing growth rates only from the eigenvalues of an operator is implicitly equivalent to choosing an inner product under which the operator is normal, i.e., commutes with its adjoint: $\mathcal{L}\mathcal{L}^\dagger = \mathcal{L}^\dagger\mathcal{L}$ ($\dagger$ represents the adjoint). This normalizing inner product is not necessarily a good choice of measurement, either physically or mathematically; worse, there are cases in which a normalizing inner product does not even exist.

Before continuing with arguments about stability, let us mention a few results from linear algebra which can help us understand the meaning of normality. When two diagonalizable matrices A and B commute, they are in fact simultaneously diagonalizable. That is, there is a basis V such that $V^{-1}AV$ and $V^{-1}BV$ are both diagonal. This in turn implies that A and B have the same set of eigenvectors. Therefore, if a matrix A is normal, then it shares eigenvectors with its adjoint, and the eigenvalues of $A^\dagger$ are complex conjugates of the eigenvalues of A. It is then easy to see that the eigenvectors of A are orthogonal to each other: $Av = \lambda v$ and $Aw = \mu w$ with $\lambda \neq \mu \implies \mu \langle v, w\rangle = \langle v, Aw\rangle = \left\langle A^\dagger v, w\right\rangle = \lambda \langle v, w\rangle \implies \langle v, w\rangle = 0$. Any eigenvectors which share the same eigenvalue can be split up into an orthogonal basis. A matrix A is similar to a normal matrix if and only if A is diagonalizable, i.e., if and only if A has a complete set of eigenvectors which form a basis of the relevant space. Thus for A to fail to be normalizable, i.e., for there to be no inner product such that A is normal, then A must have a set of defective eigenvalues. (These results can be found in linear algebra textbooks such as Horn and Johnson, 1990).

In this section, the inner product between two vectors u and v will be denoted $\langle u, v\rangle$, and the induced norm will be denoted $\|u\|^2 \equiv \langle u, u\rangle$. The operator norm will use the same notation, $\|\mathcal{L}\| \equiv \max_u (\|\mathcal{L}u\|/\|u\|)$. Specific choices of inner product and norm will be specified with subscripts. Except where specified, we will not distinguish matrices from differential operators. In the context of this thesis, generalized linear stability analysis is applied only to differential operators with no singularities, and under L_2 or weighted L_2 inner products, i.e., inner products of the form $\langle u, v\rangle = \int uvw$, where w is some weight function[1]. Some discussion of the conditions required for differential operators may be found in Trefethen and Embree (2005) and references therein.

3.1.1 Autonomous systems

Let us consider the behavior of linear systems of the form

$$\partial_t u = \mathcal{L}u, \tag{3.1}$$

where $\mathcal{L}$ is an *autonomous* linear operator, i.e., one independent of time. For an ordinary differential equation, u in this expression would be a vector and $\mathcal{L}$ a matrix; for a partial differential equation, u would be a function and $\mathcal{L}$ a linear differential or integral operator. Autonomous linear systems frequently arise when linearizing about the steady state of a nonlinear ordinary or partial differential equation (when linearizing about a time-dependent base state, the resulting linear operator is typically also time-dependent, and thus nonautonomous).

Equation (3.1) can be solved formally by $u(t) = \exp(t\mathcal{L})u(0)$ using the operator exponential. Assuming $\mathcal{L}$ is diagonalizable, $u(t = 0)$ can be decomposed into a sum of eigenfunctions v_i of $\mathcal{L}$: $u(0) = \sum_i a_i v_i$, and the time-dependent $u(t)$ can be immediately solved as $u(t) = \sum_i a_i v_i \exp(\lambda_i t)$, where each λ_i is the eigenvalue of v_i. In normal systems, the v_i are all orthogonal, and hence $\|u(t)\|^2 = \sum_i a_i^2 \exp(2\lambda_i t)\|v_i\|^2$. Therefore, it is the eigenvalues λ_i that bound the relative growth rate of $u(t)$. But in non-normal systems, the cross-terms $\langle v_i, v_j\rangle$ do not necessarily vanish for $i \neq j$. In this case, the behavior can be complicated. Even if every λ_i is negative, $u(t)$ can still experience growth due to the cross-terms (Farrell and Ioannou, 1996b).

The time evolution of the magnitude of u, measured with a given inner product norm $\|\cdot\|$, can be written out explicitly without any eigenvector decomposition as

$$\begin{aligned} g(t) = \frac{\|u(t)\|}{\|u(0)\|} = \frac{\|\exp(t\mathcal{L})u(0)\|}{\|u(0)\|} &= \left[\frac{\left\langle \exp(t\mathcal{L}^\dagger)\exp(t\mathcal{L})u(0), u(0)\right\rangle}{\langle u(0), u(0)\rangle}\right]^{1/2} \\ &\leq \|\exp(t\mathcal{L})\|, \end{aligned} \tag{3.2}$$

where $\mathcal{L}^\dagger$ denotes the adjoint of $\mathcal{L}$ under the given inner product and $\|\exp(t\mathcal{L})\|$ uses the operator norm. Equality is achieved for an initial state $u(0) = \arg\max_u (\|\mathcal{L}u\|/\|u\|)$ (Farrell and Ioannou, 1996b).

[1] More complicated inner products, in particular those containing derivatives, such as the H_1 inner product $\langle u, v\rangle_{H_1} = \int (uv + \nabla u \cdot \nabla v)$, are beyond the scope of this work.

The *spectral abscissa* of $\mathcal{L}$, denoted $\beta_{\max}$, is the real part of the eigenvalue of $\mathcal{L}$ with maximum real part, i.e., $\beta_{\max} \equiv \max \operatorname{re} \operatorname{eig} \mathcal{L}$. The spectral abscissa provides a lower bound on the maximum growth of u:

$$\exp\left(\beta_{\max} t\right) \leq \| \exp(t\mathcal{L}) \|. \tag{3.3}$$

Equality holds when $\mathcal{L}$ is normal, in which case the eigenvectors of $\mathcal{L}$ are orthogonal and thus the contribution of each eigenvector to the magnitude measurement is independent of every other eigenvector. In this case, $\exp(\beta_{\max} t) = \| \exp(t\mathcal{L}) \|$, meaning that a vector cannot grow faster than the rate of the spectral abscissa: $g(t) = \|u(t)\|/\|u(0)\| \leq \exp(\beta_{\max} t)$ (Farrell and Ioannou, 1996b).

In general, however, $\exp(\beta_{\max} t)$ is not an upper bound on the growth of vectors. When $\mathcal{L}$ is diagonalizable (i.e., when $\mathcal{L}$ has a complete set of eigenvectors), it can be written as $\mathcal{L} = \mathcal{S}\Lambda\mathcal{S}^{-1}$, with Λ diagonal. Then we can construct a (typically not tight) upper bound on $\| \exp(t\mathcal{L}) \|$:

$$\exp\left(\beta_{\max} t\right) \leq \| \exp(t\mathcal{L}) \| = \| \mathcal{S} \exp(t\Lambda) \mathcal{S}^{-1} \| \leq \| \mathcal{S} \| \| \mathcal{S}^{-1} \| \exp\left(\beta_{\max} t\right). \tag{3.4}$$

Again, when $\mathcal{L}$ is normal, $\mathcal{S}$ is unitary in the given norm, and so the upper bound reduces to $\exp(\beta_{\max} t)$. When $\mathcal{S}$ is not unitary, $\mathcal{L}$ is non-normal, and $u(t)$ may achieve growth exceeding $\exp(\beta_{\max} t)$ (Farrell and Ioannou, 1996b).

The instantaneous growth rate ω is given by

$$\begin{aligned}
\omega &= \frac{\partial \ln g}{\partial t} = \frac{\partial_t \|u(t)\|}{\|u(t)\|} = \frac{\partial_t \left[\langle \exp(t\mathcal{L}) u(0), \exp(t\mathcal{L}) u(0) \rangle \right]^{1/2}}{\|u(t)\|} \\
&= \frac{\langle \mathcal{L} \exp(t\mathcal{L}) u(0), \exp(t\mathcal{L}) u(0) \rangle + \langle \exp(t\mathcal{L}) u(0), \mathcal{L} \exp(t\mathcal{L}) u(0) \rangle}{2\|u(t)\|^2} \\
&= \frac{1}{\|u(t)\|^2} \left\langle \frac{\mathcal{L} + \mathcal{L}^\dagger}{2} u(t), u(t) \right\rangle \\
&\leq \max \operatorname{eig} \left[\frac{\mathcal{L} + \mathcal{L}^\dagger}{2} \right] \equiv \omega_{\max},
\end{aligned} \tag{3.5}$$

where $\omega_{\max}$ is the maximum instantaneous growth rate, known as the *numerical abscissa*. When $\mathcal{L}$ is normal, the eigenvalues of $\mathcal{L}$ and $\mathcal{L}^\dagger$ are complex conjugates, and so $\omega_{\max} = \beta_{\max}$ (Farrell and Ioannou, 1996b). When $\mathcal{L}$ is non-normal, $\beta_{\max} \leq \omega_{\max}$. That $\omega_{\max}$ cannot be less than $\beta_{\max}$ follows immediately from its definition. Letting v be a unit eigenvector of $\mathcal{L}$ corresponding to $\beta_{\max}$, $\omega_{\max} \geq \left\langle (\mathcal{L} + \mathcal{L}^\dagger)/2 v, v \right\rangle = (\langle \mathcal{L}v, v \rangle + \langle v, \mathcal{L}v \rangle)/2 = \beta_{\max}$. Regardless of normality or non-normality, $\lim_{t \to \infty} \omega \leq \beta_{\max}$. Hence, the maximum asymptotic growth rate is the spectral abscissa, while the maximum instantaneous growth rate at $t = 0$ is the numerical abscissa. Indeed, it may be the case that $\beta_{\max} < 0$ while $\omega_{\max} > 0$, indicating transient growth even when all eigenvalues are negative.

It turns out that the initial condition $u(0)$ which induces the maximum growth rate at $t = 0$ (i.e., the mode corresponding to the numerical abscissa) need not be the same as the initial

condition which grows the most between $t = 0$ and a later time t. For any given t, the maximum relative growth achievable at that time is simply $\| \exp(t\mathcal{L})\|$. The initial condition, or *input mode* inducing that maximum is $u_{max,t}(0) = \arg\max_u \| \exp(t\mathcal{L})u\|/\|u\|$. After evolving from $t = 0$ to a later time t, the state of the system may look very different from the initial condition; this *output mode* is given by $v_{max,t}(t) = \exp(t\mathcal{L})u_{max,t}(0)/\| \exp(t\mathcal{L})u_{max,t}(0)\|$. Numerically, the maximum-growth input and output modes can be computed from the singular value decomposition (SVD) of $\exp(t\mathcal{L})$. In particular, if the SVD is given by $\exp(t\mathcal{L}) = U\Lambda V^\dagger$, then the columns of V give the input modes, the columns of U the output modes, and Λ the total relative growth of each non-normal mode at time t (Farrell and Ioannou, 1996b).

Any matrix A which is non-normal under a given inner product and has no defective eigenvalues may be made normal by changing to a particular different inner product (the converse is not true; some matrices, such as the identity and zero matrices, are normal under any inner product). Indeed, when a classical linear stability analysis is carried out, it is implicitly assumed that $\omega_{\max} = \beta_{\max}$, and thus that such a normalizing inner product is being used. But the choice of inner product should not, in general, be arbitrary. For physical systems, there often exists a natural choice of inner product norm which measures energy, volume distribution, or physical height variation of an object. The normalizing inner product is frequently unbalanced, giving certain parts of a physical system much more measurement weight than other parts (as will be seen in the stability analysis of flow in V-grooves, in Chapter 5). In the case of linear stability analysis of nonlinear systems, there may be a natural choice of measurement indicating when a perturbation becomes large enough for nonlinear effects to become important. This occurs, for example, in the destabilization of Couette flow in the laminar-turbulent transition (Butler and Farrell, 1992). In this case, the normalizing inner product may not effectively measure the nonlinear importance of small perturbations, whereas a different choice of inner product allows better prediction of the nonlinear destabilization which may lead to turbulence.

Non-normal operators with significant differences between transient and asymptotic stability are by no means rare occurrences. Chalker and Mehlig (1998) considered random matrices drawn from either a Gaussian ensemble of complex matrices, or from a comparable ensemble of Hermitian (self-adjoint) matrices. For the equation $\partial_t u = (A-1)u$, the normalized expectation value $\sqrt{4\pi}\,\langle u(t), u(t)\rangle$ was equal to $t^{-3/2}$ for the normal matrices and the much slower decaying $t^{-1/2}$ for the general matrices.

Fun Fact: Normal second-order ordinary differential operators

It is well-known (see, e.g., Birkhoff and Rota, 1989) that the Sturm-Liouville operator $\mathcal{L}_{SL} \equiv w^{-1}(x)\partial_x\,[p(x)\partial_x] + w^{-1}(x)q(x)$ is the unique second-order ordinary differential linear operator which is self-adjoint with weight $w(x)$ (given the correct boundary conditions). However it is *not* the unique normal second-order operator; normality is a more general con-

dition than self-adjointness (for example, skew-adjoint operators are also normal). Letting $\mathcal{L} \equiv a(x)\partial_{xx} + b(x)\partial_x + c(x)$, the adjoint with weight $w(x)$ is given by

$$\begin{aligned}\mathcal{L}^\dagger \equiv a(x)\partial_{xx} &+ \left[-b(x) + 2a'(x) + 2a(x)\frac{w'(x)}{w(x)}\right]\partial_x \\ &+ \left[c(x) - b'(x) - b(x)\frac{w'(x)}{w(x)} + a(x)\frac{w''(x)}{w(x)} + 2a'(x)\frac{w'(x)}{w(x)} + a''(x)\right].\end{aligned}$$

Directly computing the commutator $[\mathcal{L}, \mathcal{L}^\dagger]$ yields a result of the form $(f_1)\partial_{xx}+(f_2)\partial_x+(f_3)$, where each f is a somewhat complicated expression. Solving for $f_1 = f_2 = f_3 = 0$ yields three distinct cases:

Case 1: $\mathcal{L}$ is Sturm-Liouville, i.e., $a(x) = p(x)/w(x)$, $b(x) = p'(x)/w(x)$. This is the only case in which $c(x)$ is a free function.

Case 2: $\mathcal{L}$ is skew-adjoint plus a constant (denoted c_1 here). In this case,

$$\begin{aligned}\mathcal{L} &= b(x)\partial_x + \frac{1}{2}\left[b'(x) + b(x)\frac{w'(x)}{w(x)}\right] + c_1 \\ \mathcal{L}^\dagger &= -b(x)\partial_x - \frac{1}{2}\left[b'(x) + b(x)\frac{w'(x)}{w(x)}\right] + c_1.\end{aligned}$$

Case 3: $\mathcal{L}$ has the following specific form:

$$\begin{aligned}\mathcal{L} = &\frac{1}{w(x)}\partial_x[p(x)\partial_x] + c_1\sqrt{\frac{p(x)}{w(x)}}\left[\partial_x + \frac{p'(x)}{4p(x)} + \frac{w'(x)}{4w(x)}\right] + c_2 \\ &+ \frac{p''(x)}{4w(x)} - \frac{[p'(x)]^2}{16p(x)w(x)} + \frac{p'(x)w'(x)}{8w^2(x)} - \frac{5p(x)[w'(x)]^2}{16w^3(x)} + \frac{p(x)w''(x)}{4w^2(x)} \\ \mathcal{L}^\dagger = &\frac{1}{w(x)}\partial_x[p(x)\partial_x] - c_1\sqrt{\frac{p(x)}{w(x)}}\left[\partial_x + \frac{p'(x)}{4p(x)} + \frac{w'(x)}{4w(x)}\right] + c_2 \\ &+ \frac{p''(x)}{4w(x)} - \frac{[p'(x)]^2}{16p(x)w(x)} + \frac{p'(x)w'(x)}{8w^2(x)} - \frac{5p(x)[w'(x)]^2}{16w^3(x)} + \frac{p(x)w''(x)}{4w^2(x)}.\end{aligned}$$

In this final case, $\mathcal{L}$ is a sum of a Sturm-Liouville operator with a specific value of q and a skew-adjoint operator (the terms with coefficient c_1). Incidentally, balancing the operator leaves only a single functional degree of freedom, p, along with two constants. Clearly this form is quite tuned and should not be expected to arise as often as Sturm-Liouville operators. In general, given a second-order operator which is not Sturm-Liouville, it is very likely to be non-normal.

Example: An autonomous ODE

To get a better intuitive picture of normality and non-normality, let us consider a 2×2 matrix, based on an example from Farrell and Ioannou (1996b):

$$A = \begin{bmatrix} -1 & 6 \\ 0 & -2 \end{bmatrix}. \tag{3.6}$$

Being upper triangular, A clearly has eigenvalues -1 and -2, and it has corresponding eigenvectors $\{1, 0\}$ and $\{-6, 1\}$. The spectral abscissa is hence $\beta_{\max} = -1$. The transient operator is given by

$$\frac{A + A^\dagger}{2} = \begin{bmatrix} -1 & 3 \\ 3 & -2 \end{bmatrix}, \tag{3.7}$$

which has eigenvalues $(-3 \pm \sqrt{37})/2$. Thus the numerical abscissa is $\omega_{\max} = (-3 + \sqrt{37})/2 \approx 1.54$. Because $\omega_{\max} > 0$, the system $\partial_t u = Au$ will undergo transient growth for certain initial $u(0)$. The initial condition which grows the most at any time may be computed numerically and turns out to be $u_{max} \approx \{0.334, 0.943\}$.

The maximum growth $G(t) = \max_{u(0)} \|u(t)\|/\|u(0)\|$ is shown in Figure 3.1 (orange line), with the evolution of the magnitudes of the two eigenvectors, $\exp(-t)$ and $\exp(-2t)$, shown in green and blue, respectively. Keep in mind that $G(t)$ does not plot a single trajectory; instead at each time it shows the maximum growth by any initial condition.

The left and center columns of Figure 3.2 show the evolution u_{max} (red) and the two eigenvectors (green and blue) over time, while the right column shows the optimal input and output modes at each time (orange). The unit circle is denoted by the dotted black line. It is clear from the first column that while the two eigenvectors quickly decay to the origin over time, u_{max} follows a curved trajectory, moving far to the right before turning around and falling back into the origin. The middle column aims to elucidate this behavior by displaying the decomposition u_{max} (red arrow) into its eigenvector components (green and blue arrows). The key fact is that the eigenvectors are nonorthogonal and, counterintuitively, the sum of two shrinking nonorthogonal vectors may actually grow. The right column displays the optimal input and output modes at each time, labeled V and U, respectively. At $t = 0$, the two points coincide, and represent the point which experiences the fastest growth rate (the numerical abscissa). But the initial condition that induces fastest growth at $t = 0$ is not the same as the one which grows the most overall; it is evident from the plot that the initial condition which grows the most at $t = 0.656$ is much higher in y than the point which induces the fastest $t = 0$ growth. Finally, note from the last plot of the right column that the optimal output mode at late times coincides with the least-stable eigenvector. Thus, at late times, the modal stability result is restored.

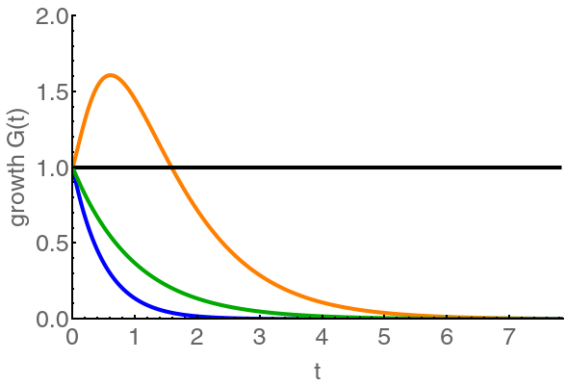

Figure 3.1: Maximum growth achievable at any time (orange line), as compared to the growth of the two eigenvectors (blue and green lines), for the autonomous system $\partial_t u = Au$, for $A = [-1, 6; 0 - 2]$. Note that the orange line does not represent the magnitude of a single initial condition evolved over time. Rather, at each time t, the orange line gives the greatest magnitude of any initial condition up to that time.

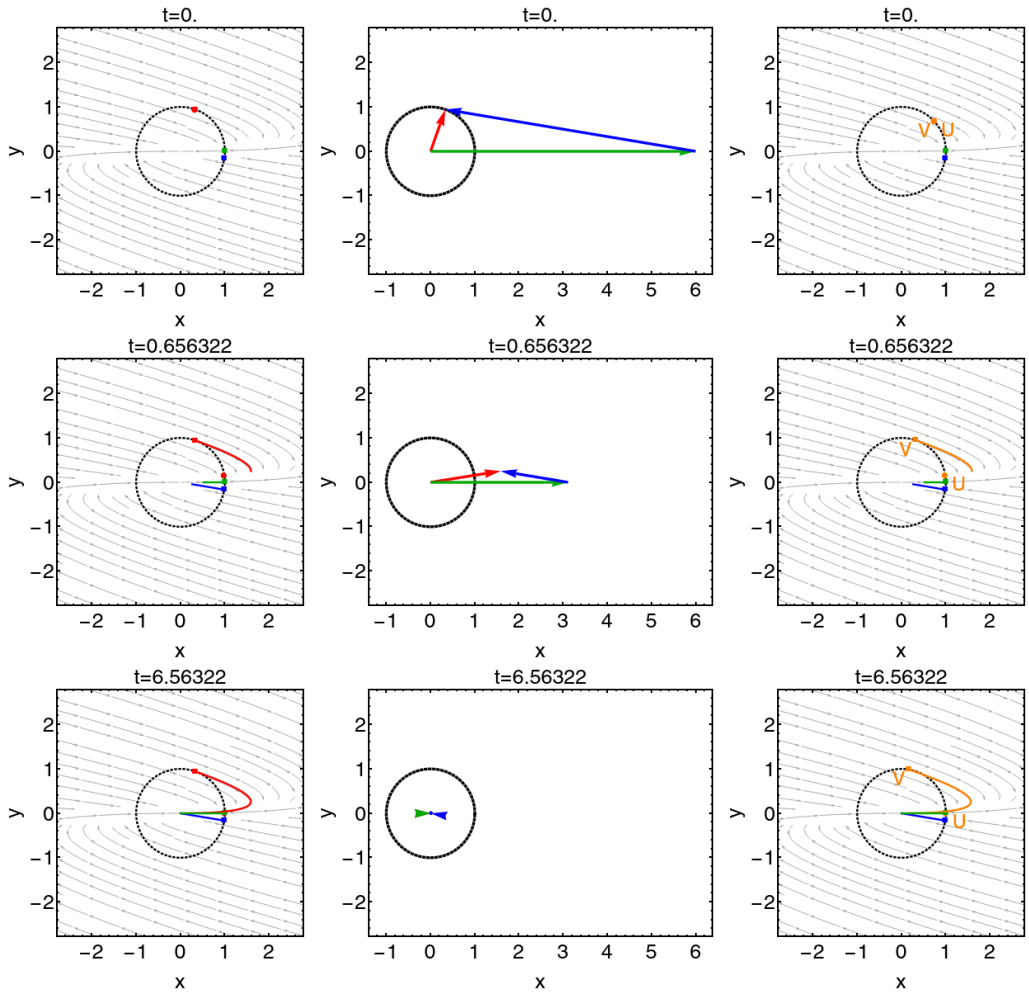

Figure 3.2: Evolution of the autonomous system $\partial_t u = Au$, for $A = [-1, 6; 0 - 2]$. The top row displays time $t = 0$, the center row $t = 0.656$, and the bottom row $t = 6.56$.
Left column: Background gray arrows display a stream plot of A. The eigenvector $\{1, 0\}$ is shown as a green dot on the unit circle (dotted line), and the evolution of the corresponding initial condition $u(0) = \{1, 0\}$ over time is the green line emerging from that dot. The second eigenvector $\{0.986, -0.164\}$ is shown as a blue dot on the unit circle (dotted line), and its evolution over time is the blue line emerging from that dot. The red dot indicates an initial condition of $u(0) = \{0.334, 0.943\}$, and the curved red line is its corresponding evolution.
Middle column: The red arrow now represents the evolution of the initial condition $u(0) = \{0.334, 0.943\}$ (as did the red line in the left column). The horizontal green and tilted blue arrows show the eigenvector decomposition of the red arrow. These plots aim to emphasize that the sum of two shrinking vectors is a transiently growing vector.
Right column: Green and blue lines represent the eigenvectors, as before. The orange dots now represent the optimal input mode V and output mode U at each time. The orange line displays the maximum growth achieved at any time.

3.1.2 Nonautonomous systems

When a linear operator $\mathcal{L}(t)$ is time-dependent, it is still possible to perform generalized stability analysis. In this case the formal exponential solution $u(t) = \exp(t\mathcal{L})u(0)$ used for autonomous systems is no longer valid, but one can still define a linear propagation operator $\Phi(t)$ such that $u(t) = \Phi(t)u(0)$. It thus still makes sense to ask how the magnitude of an initial state $u(0)$ evolves in time:

$$g(t) = \frac{\|u(t)\|}{\|u(0)\|} = \frac{\|\Phi(t)u(0)\|}{\|u(0)\|} \leq \|\Phi(t)\|. \tag{3.8}$$

Furthermore, we can still ask what input mode (initial condition) will lead to the greatest growth at time t by computing the SVD of $\Phi(t)$. Again, if the SVD is given by $\Phi(t) = U\Lambda V^\dagger$, then the columns of V give the input modes, the columns of U the output modes, and Λ the total relative growth of each non-normal mode at time t (Farrell and Ioannou, 1996a).

The numerical abscissa may be defined in a manner similar to the autonomous case:

$$\omega_{\max} = \max_{u(0)} \left[\frac{\partial_t \|u(t)\|}{\|u(t)\|}\right]_{t=0} = \max \operatorname{eig}\left[\frac{\mathcal{L}(0) + \mathcal{L}^\dagger(0)}{2}\right], \tag{3.9}$$

though it now merely determines the maximum growth rate at $t = 0$ and not necessarily at all times. But as $\mathcal{L}(t)$ changes in time, the late-time evolution depends on earlier states, and so even if the limit as $t \to \infty$ of $\mathcal{L}(t)$ is well-defined, the spectral abscissa based on its eigenvalues does not necessarily provide useful information. Instead, the entire evolution history must be taken into account, and the corresponding asymptotic value of interest is the first Lyapunov exponent (Farrell and Ioannou, 1996a):

$$\lambda = \lim_{t\to\infty} \sup \frac{\ln(\|\Phi(t)\|)}{t}. \tag{3.10}$$

Example: A nonautonomous ODE

Let us again consider a 2×2 matrix similar to the previous static example, but we now add time dependence by letting the matrix rotate at a fixed speed ρ:

$$A(t) = \begin{bmatrix} \cos(\rho t) & \sin(\rho t) \\ -\sin(\rho t) & \cos(\rho t) \end{bmatrix} \begin{bmatrix} -1 & 6 \\ 0 & -2 \end{bmatrix} \begin{bmatrix} \cos(\rho t) & -\sin(\rho t) \\ \sin(\rho t) & \cos(\rho t) \end{bmatrix}. \tag{3.11}$$

$A(t)$ still has the eigenvalues -1 and -2, and the transient operator is again given by

$$\frac{A(0) + A(0)^\dagger}{2} = \begin{bmatrix} -1 & 3 \\ 3 & -2 \end{bmatrix}, \tag{3.12}$$

so that the numerical abscissa is unchanged from the autonomous example: $\omega_{\max} = (-3 + \sqrt{37})/2 \approx 1.54$.

We consider a slowly-varying case with $\rho = 0.1$ and quickly-varying case with $\rho = 1$. The slowly-varying case has behavior somewhat similar to the static case. The maximum growth at

any time is plotted in Figure 3.3; the transient growth and slow decay are clearly resemble the static results in Figure 3.1. Figure 3.4 shows the evolution at three times: $t = 0$, $t = 0.656$, and $t = 6.56$, just like the static case in Figure 3.2. Again, the optimal input mode moves upwards as time progresses, and the optimal output mode decays at a rate close to the least-stable eigenvalue at late times. Indeed, because the timescale of A's variation is $O(10)$ while the timescale of the spectral and numerical abscissae of $A(t)$ at any given time is $O(1)$, it is to be expected that the operator's variation has a relatively small effect.

The quickly-varying case is completely different. Figure 3.5 shows the maximum growth, which keeps increasing ad infinitum. Figure 3.6 shows the optimal input and output modes over time; the evolution trajectory is far outside the frame in the third plot. The first Lyapunov exponent can be numerically computed, and is approximately $\lambda \approx 0.8$; which is positive and far different from the spectral abscissa $\beta_{\max} = -1$.

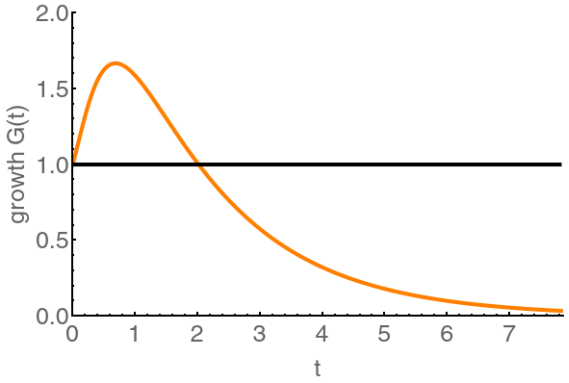

Figure 3.3: Maximum growth achievable at any time (orange line) for the nonautonomous system $\partial_t u = A(t)u$ in the slowly-varying case $\rho = 0.1$. Note that the orange line does not represent the magnitude of a single initial condition evolved over time. Rather, at each time t, the orange line gives the greatest magnitude of any initial condition up to that time.

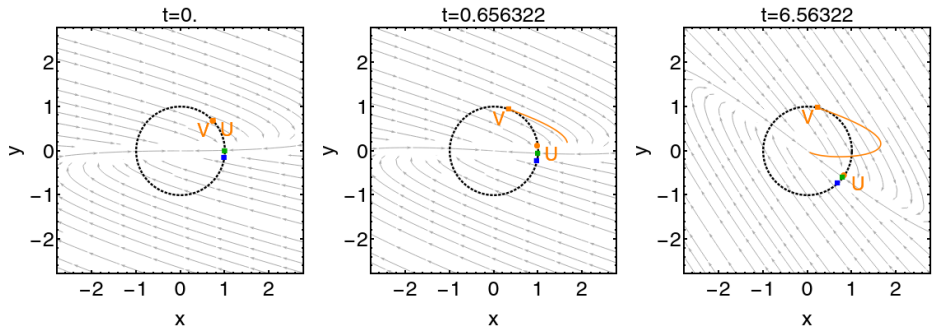

Figure 3.4: Evolution of the nonautonomous system $\partial_t u = A(t)u$, for the slowly-varying case $\rho = 0.1$. The first plot displays time $t = 0$, the second $t = 0.656$, and the last $t = 6.56$. Background gray arrows display a stream plot of $A(t)$ (note that it rotates in time). Green and blue dots represent the eigenvectors of $A(t)$ at each time. The orange dots represent the optimal input mode V and output mode U at each time. The orange line displays the maximum growth achieved at any time.

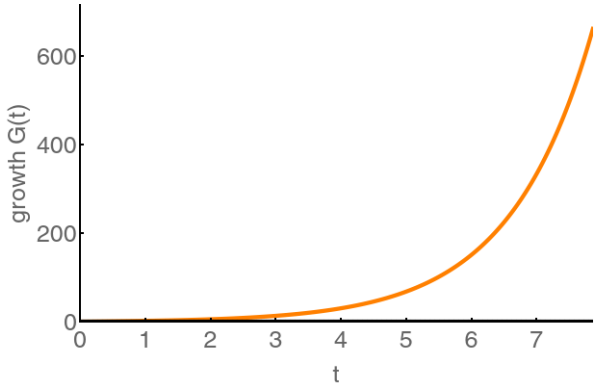

Figure 3.5: Maximum growth achievable at any time (orange line) for the nonautonomous system $\partial_t u = A(t)u$ in the quickly-varying case $\rho = 1$. Note that the orange line does not represent the magnitude of a single initial condition evolved over time. Rather, at each time t, the orange line gives the greatest magnitude of any initial condition up to that time.

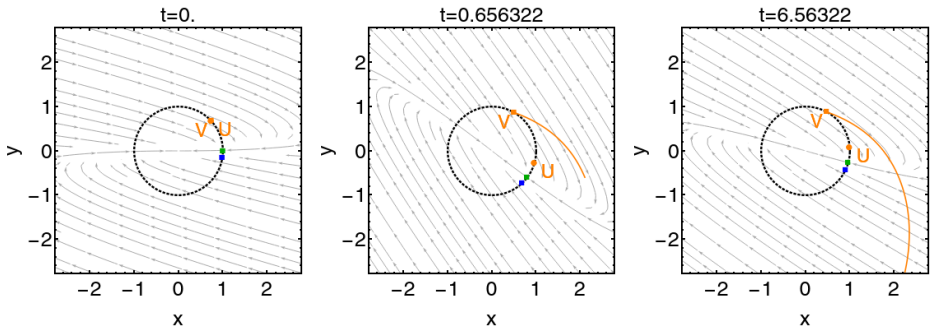

Figure 3.6: Evolution of the nonautonomous system $\partial_t u = A(t)u$, for the quickly-varying case $\rho = 1$. The first plot displays time $t = 0$, the second $t = 0.656$, and the last $t = 6.56$. Background gray arrows display a stream plot of $A(t)$ (note that it rotates in time). Green and blue dots represent the eigenvectors of $A(t)$ at each time. The orange dots represent the optimal input mode V and output mode U at each time. The orange line displays the maximum growth achieved at any time.

3.2 Nonlinear stability analysis with Lyapunov's direct method

The linear methods described in Section 3.1 can be applied to nonlinear equations via linearization; stability results are then valid only for sufficiently small perturbations around the base state. One method of proving stability of larger perturbations is Lyapunov's direct method (La Salle and Lefschetz, 1961). Consider an ordinary or partial differential equation

$$\partial_t u = \mathcal{N}[u], \tag{3.13}$$

where $\mathcal{N}[u]$ represents some nonlinear function of u and its spatial derivatives, and let $u = u_0$ be the steady state of interest, with $\mathcal{N}[u_0] = 0$. A function or functional $\mathfrak{F}[u]$ is said to be a *Lyapunov function(al)* if (La Salle and Lefschetz, 1961)

1. $\mathfrak{F}[u]$ is continuous and has continuous partial (functional) derivatives in a ball Ω around u_0,
2. $\mathfrak{F}[u_0] = 0$,
3. $\mathfrak{F}[u] > 0$ for $u \in \Omega$ and u_0 is an isolated minimum,
4. $\partial_t \mathfrak{F}[u] = \mathcal{N}[u](\delta\mathfrak{F}/\delta u) \leq 0$ for all $u \in \Omega$.

In this context, "isolated minimum" means that u_0 is the only local minimum in Ω or its closure (including ∞ if necessary). If a Lyapunov functional exists, then an initial condition $u \in \Omega$ will not leave Ω. If $\partial_t \mathfrak{F}[u] < 0$ for all $u \in \Omega \setminus \{u_0\}$ holds, then u will asymptotically approach the steady state u_0, a situation we will call "stable" (note that in the dynamical systems literature, this condition is typically referred to instead as asymptotic stability). If Ω spans the entire space of u, then the system has *global stability*.

Geometrically, the Lyapunov functional generates a scalar landscape for different states of the system, analogous to an energy landscape (though the functional need not correspond to a physical energy). The requirement that u_0 be the only minimum implies that the landscape has a bowl-like shape. Then, so long as $\partial_t \mathfrak{F}[u] \leq 0$, any initial state cannot escape upwards in the bowl, and if $\partial_t \mathfrak{F}[u] < 0$ for all $u \in \Omega \setminus \{u_0\}$, then any initial state will keep traveling down the bowl, asymptotically approaching u_0. (The requirement that Ω be a ball prevented, for example, Ω consisting of a region minus a single point at a second steady state u_1 having $\mathfrak{F}[u_1] > 0$. In such a case, the condition $\partial_t \mathfrak{F}[u] < 0$ for $u \in \Omega \setminus \{u_0\}$ would be insufficient to prove convergence to u_0, as the system might converge instead to u_1).

If one hopes to show that a steady state is stable, clearly a Lyapunov functional operating within as large an Ω as possible would be ideal, so as to cover as many perturbations as possible. In this sense, nonlinear stability is preferable to linear stability. Unfortunately, even when Lyapunov functionals do exist they are not always easy to find.

While this thesis relies only on generalized linear stability analysis and Lyapunov's direct method as described above, other stability analyses, such as adjoint methods, pseudospectral analysis, and resolvent analysis, are likely to be useful for extending this work. A few notes on such alternatives may be found in Appendix B.

References

M. Asllani, R. Lambiotte, and T. Carletti. Structure and dynamical behavior of non-normal networks. Sci. Adv., 4(12):eaau9403, December 2018. ISSN 2375-2548. doi:10.1126/sciadv.aau9403.

J. S. Baggett and L. N. Trefethen. Low-dimensional models of subcritical transition to turbulence. Phys. Fluids, 9(4):1043–1053, 1997. ISSN 10706631. doi:10.1063/1.869199.

D. Bernoulli. Commentationes de statu aequilibrii corporum humido insidentium. Comment. Acad. Scient. Imp. Petrop., X:147–163, 1738, 1747.

A. L. Bertozzi and M. P. Brenner. Linear stability and transient growth in driven contact lines. Phys. Fluids, 9(3):530–539, March 1997. ISSN 1070-6631, 1089-7666. doi:10.1063/1.869217.

G. Birkhoff and G. C. Rota. Ordinary Differential Equations. Introductions to higher mathematics. John Wiley & Sons, New York, 1989. ISBN 9780471500209.

K. M. Butler and B. F. Farrell. Three-dimensional optimal perturbations in viscous shear flow. Phys. Fluids A - Fluid, 4(8):1637–1650, August 1992. ISSN 0899-8213. doi:10.1063/1.858386.

K. M. Case. Stability of inviscid plane Couette flow. Phys. Fluids, 3(2):143, 1960. ISSN 00319171. doi:10.1063/1.1706010.

H. Caswell and M. G. Neubert. Reactivity and transient dynamics of discrete-time ecological systems. J. Differ. Equ. Appl., 11(4-5):295–310, April 2005. ISSN 1023-6198, 1563-5120. doi:10.1080/10236190412331335382.

J. T. Chalker and B. Mehlig. Eigenvector statistics in non-Hermitian random matrix ensembles. Phys. Rev. Lett., 81(16):3367–3370, October 1998. ISSN 0031-9007, 1079-7114. doi:10.1103/PhysRevLett.81.3367.

J. M. Davis and S. M. Troian. Generalized linear stability of noninertial coating flows over topographical features. Phys. Fluids, 17(7):072103, July 2005. ISSN 1070-6631, 1089-7666. doi:10.1063/1.1945627.

J. M. Davis, B. J. Fischer, and S. M. Troian. A General Approach to the Linear Stability of Thin Spreading Films, pages 79–106. Springer Berlin Heidelberg, Berlin, Heidelberg, 2003. ISBN 978-3-540-45095-5.

P. G. Drazin and W. H. Reid. Hydrodynamic Stability. Cambridge Mathematical Library. Cambridge University Press, 2004. ISBN 9780521525411.

L. Euler. Scientia navalis seu tractatus de construendis ac dirigendis, volume 1. Academiae Scientarum, St. Petersburg, 1749.

B. F. Farrell. Optimal Excitation of Baroclinic Waves. J. Atmos. Sci., 46 (9):1193–1206, May 1989. ISSN 0022-4928, 1520-0469. doi:10.1175/1520-0469(1989)046<1193:OEOBW>2.0.CO;2.

B. F. Farrell and P. J. Ioannou. Generalized Stability Theory. Part II: Nonautonomous operators. J. Atmos. Sci., pages 2041–2053, 1996a. doi:10.1175/1520-0469(1996)053<2041:GSTPIN>2.0.CO;2.

B. F. Farrell and P. J. Ioannou. Generalized Stability Theory. Part I: Autonomous operators. J. Atmos. Sci., 53(14):2025–2040, 1996b. doi:10.1175/1520-0469(1996)053<2025:GSTPIA>2.0.CO;2.

B. F. Farrell and P. J. Ioannou. Optimal excitation of magnetic fields. Astrophys. J., 522(2): 1079–1087, September 1999. ISSN 0004-637X, 1538-4357. doi:10.1086/307662.

T. Gebhardt and S. Grossmann. Chaos transition despite linear stability. Phys. Rev. E, 50(5): 3705–3711, 1994. ISSN 1063651X. doi:10.1103/PhysRevE.50.3705.

I. Goldhirsch, P.-L. Sulem, and S. A. Orszag. Stability and Lyapunov stability of dynamical systems: A differential approach and a numerical method. Physica D: Nonlin. Phen., 27(3): 311–337, August 1987. ISSN 01672789. doi:10.1016/0167-2789(87)90034-0.

R. A. Horn and C. R. Johnson. Matrix Analysis. Cambridge University Press, Cambridge, 1990. ISBN 9780521386326. doi:10.1017/9781139020411.

J. La Salle and S. Lefschetz. Stability by Liapunov's Direct Method, with Applications. Academic Press, New York and London, 1961.

R. I. Leine. The historical development of classical stability concepts: Lagrange, Poisson and Lyapunov stability. Nonlinear Dynam., 59(1-2):173–182, January 2010. ISSN 0924-090X, 1573-269X. doi:10.1007/s11071-009-9530-z.

E. N. Lorenz. A study of the predictability of a 28-variable atmospheric model. Tellus, 17(3): 321–333, August 1965. ISSN 00402826, 21533490. doi:10.1111/j.2153-3490.1965.tb01424.x.

A. Lyapunov. Problème général de la stabilité du mouvement. Ann. Fac. Sci. Toulouse Math., 2e série, 9:203–474, 1907. doi:10.5802/afst.246.

O. K. Matar and S. M. Troian. Growth of non-modal transient structures during the spreading of surfactant coated films. Phys. Fluids, 10(5):9–11, 1998. doi:10.1063/1.869645.

J. C. Maxwell. I. On governors. Proc. R. Soc. Lond., 16:270–283, December 1868. ISSN 0370-1662, 2053-9126. doi:10.1098/rspl.1867.0055.

M. G. Neubert and H. Caswell. Alternatives to resilience for measuring the responses of ecological systems to perturbations. Ecology, 78(3):653–665, April 1997. ISSN 0012-9658. doi:10.1890/0012-9658(1997)078[0653:ATRFMT]2.0.CO;2.

S. A. Orszag. Accurate solution of the Orr-Sommerfeld stability equation. J. Fluid Mech., 50(4): 689–703, December 1971. ISSN 0022-1120, 1469-7645. doi:10.1017/S0022112071002842.

L. Rayleigh. On the stability, or instability, of certain fluid motions. Proc. Lond. Math. Soc., s1-11(1):57–72, November 1879. ISSN 00246115. doi:10.1112/plms/s1-11.1.57.

S. C. Reddy, P. J. Schmid, and D. S. Henningson. Pseudospectra of the Orr-Sommerfeld operator. SIAM J. Appl. Math., 53(1):15–47, February 1993. doi:10.1137/0153002.

V. A. Romanov. Stability of plane-parallel Couette flow. Func. Anal. Appl., 7(2):137–146, 1973. ISSN 0016-2663, 1573-8485. doi:10.1007/BF01078886.

P. J. Schmid and D. S. Henningson. Stability and Transition in Shear Flows. Applied Mathematical Sciences. Springer, New York, 2012. ISBN 9781461301851. doi:10.1007/978-1-4613-0185-1.

N. Tiwari, Z. Mester, and J. M. Davis. Stability and transient dynamics of thin liquid films flowing over locally heated surfaces. Phys. Rev. E, 76(5), November 2007. ISSN 1539-3755, 1550-2376. doi:10.1103/PhysRevE.76.056306.

L. N. Trefethen and M. Embree. Spectra and Pseudospectra: The Behavior of Nonnormal Matrices and Operators. Princeton University Press, Princeton and Oxford, 2005. ISBN 9780691119465.

L. N. Trefethen, A. E. Trefethen, S. C. Reddy, and T. A. Driscoll. Hydrodynamic stability without eigenvalues. Science, 261:30, 1993. doi:10.1126/science.261.5121.578.

S. M. Troian, E. Herbolzheimer, S. A. Safran, and J. F. Joanny. Fingering instabilities of driven spreading films. Europhys. Lett., 10(1):25–30, September 1989. ISSN 0295-5075, 1286-4854. doi:10.1209/0295-5075/10/1/005.

F. Waleffe. Transition in shear flows. Nonlinear normality versus non-normal linearity. Phys. Fluids, 7(12):3060–3066, 1995. ISSN 1070-6631. doi:10.1063/1.868682.

S. Yoden and M. Nomura. Finite-time Lyapunov stability analysis and its application to atmospheric predictability. J. Atmos. Sci., 50(11):1531–1543, June 1993. ISSN 0022-4928, 1520-0469. doi:10.1175/1520-0469(1993)050<1531:FTLSAA>2.0.CO;2.

Part II

Capillary flow in V-grooves

Chapter 4

INTRODUCTION TO V-GROOVE FLOW

Note: portions of this chapter are adapted from published work (White and Troian, 2019).

4.1 Background and motivation

With modern day advances in microfabrication techniques, capillary action is being used as a reliable form of flow control in numerous microfluidic devices as well, some involving capillary action through porous substrates like paper or polymer films, and others relying on a combination of capillary action, positive displacement pumping and electrophoresis. The number of such applications is multiplying rapidly with emphasis on disposable inexpensive platforms beneficial to global public health (Yager et al., 2006), drug discovery screening (Dittrich and Manz, 2006) and specialized fluid based logic circuitry (Prakash and Gershenfeld, 2007; Thorsen et al., 2002).

While flow in enclosed capillaries is the most well-known capillary action, wetting liquids will in fact rapidly and spontaneously creep along open surfaces containing grooves, interior corners, crevices, or roughened areas, a process known as wicking. Since the late 1960s, researchers have been incorporating this passive and reliable method of flow control in the design of novel propellant management devices able to store, channel, and meter fuel in microgravity environments (Hartwig, 2016, 2017; Jaekle, 1991; Levine et al., 2015; Rollins et al., 1985). Such systems have significantly extended mission lifetimes of spacecraft and satellites, enabling future interplanetary explorations as well. Modern propellant management systems consist of combinations of sponges, traps, troughs, vanes, and wicks to channel propellant flow by capillary action, systems which have been investigated extensively (Collicott and Chen, 2010; Darr et al., 2017; Jaekle, 1991, 1997; Weislogel, 2001; Weislogel et al., 2002). Shown in Figure 4.1 are two common structures designed in such a way that the liquid film thickness is much smaller than the streamwise flow distance, a limiting ratio which leads to considerable simplification of the governing equations of motion. However, even though the mechanism describing internal capillary flow, whereby a liquid column spontaneously fills the interior of a slender capillary tube, was well-understood by the 1920s, the mechanism driving spontaneous capillary flow along an open grooved channel required a half century more to be deduced.

Ongoing efforts to miniaturize fluid management systems for many different applications continue to drive interest in the fundamentals of free-surface capillary flow along structured substrates. Besides the aforementioned propellant management applications, open capillary grooves are now being used for heat pipes to cool microelectronics, as open flows in each corner of a triangular cross-section heat pipe provide a large surface area from which to evaporate (Mallik et al., 1992). Open channels are also being explored for biomedical lab-on-a-chip devices. Experiments by Berthier et al. (2015) showed that even viscous fluids such as blood and alginate

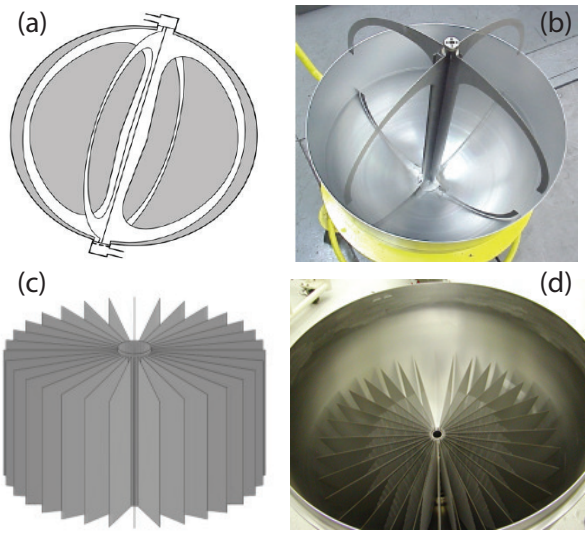

Figure 4.1: Two types of propellant management devices (PMDs) often found in satellite fuel tanks and used for passively routing propellant within open grooved channels. (a) Sketch and (b) fabricated structure showing vane-type PMDs. (c) Sketch and (d) fabricated structure showing sponge type PMDs (see Jaekle, 2011).

solutions are quickly wicked into V-shaped grooves. An overview of open-channel microfluidic biomedical devices may be found in the review article by Oliveira et al. (2019).

This chapter will first briefly review flow in closed capillaries, and then cover the derivation of the low-order V-groove flow equation developed by Weislogel (1996) and Romero and Yost (1996). Subsequent chapters will introduce new work: the first comprehensive stability analysis of flow in straight V-grooves (Chapter 5), the behavior of conducting liquids in V-grooves under the influence of an external electric field (Chapter 6), and the behavior of liquids in V-grooves with curved backbones (Chapter 7).

4.1.1 Closed capillaries: Static equilibrium

The principle of capillary action in enclosed tubes has been well-known for centuries (Maxwell and Strutt, 1911), and is familiar to many of us from the classic drinking straw experiment. In that experiment, a straw of radius r is placed vertically in a large (radius $\gg r$) container of water (see Figure 4.2).

In static equilibrium, the Navier-Stokes equations reduce to $\nabla p = \rho\vec{g}$, $\vec{g}$ being the gravitational acceleration vector. Taking gravity to operate along the z-axis, $p = p_{\text{ext}} - \rho g z$, where $z = 0$ at the fluid interface of the container, g is the magnitude of gravitational acceleration and p_{ext} is the pressure of the surrounding vacuum or air; this is the well-known hydrostatic pressure (Landau and Lifshitz, 1987). (Since $\rho_{\text{air}} \ll \rho_{\text{water}}$, hydrostatic variations in pressure in the air can be neglected). Taking the fluid interface of the container (away from the straw) to have negligible mean curvature, the normal stress balance Equation (2.39) is simply $p_{\text{ext}} - (p_{\text{ext}} - \rho g z)|_{z=0} = 0$.

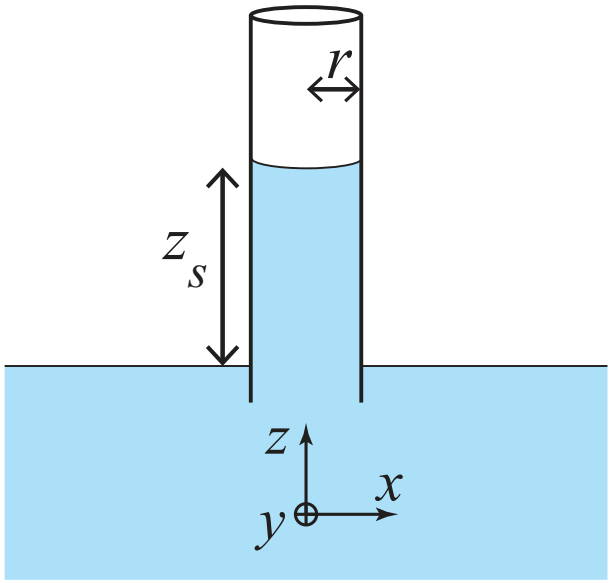

Figure 4.2: A closed capillary tube (or drinking straw) of radius r in a reservoir. z_s measures the height of the fluid meniscus in the tube from the reservoir surface.

If the straw is wetting, i.e., is of a material that forms a contact angle of $\theta < 90^\circ$ between water and air, then a concave interface will be formed. In static equilibrium, this interface conforms approximately to the surface of a sphere of radius $r \sec\theta$, and hence has mean curvature $\kappa_m \approx \cos\theta / r$. The interface balance Equation (2.39) then implies $p_{\text{ext}} - (p_{\text{ext}} - \rho g z)|_{z=z_g} = 2\kappa_m \gamma \approx 2\gamma \cos\theta / r$, where z_g is the height of the fluid in the straw. Hence,

$$z_g = \frac{2\gamma \cos\theta}{r \rho g}. \tag{4.1}$$

Note that details of how to measure the height of the fluid and the non-spherical surface curvature due to gravity were ignored; as we implicitly assumed $r \ll z_g$, or $r \ll \sqrt{\gamma/(\rho g)}$, called the capillary length (Probstein, 1994). For water, which has $\rho_{\text{water}} = 10^3$ kg/m^3 and surface tension $\gamma \approx 0.072$ N/m (Dean, 1999), the capillary length comes out to approximately 0.27 cm. For straws with larger radii, a more careful analysis would be necessary to compute an accurate height.

4.1.2 Closed capillaries: dynamics

In order to achieve the static equilibrium just described, fluid motion must occur. And, in the limit of zero gravity (more specifically, in the limit of zero Bond number, $\text{Bo} = \rho g r^2/\gamma \to 0$), there is no steady state; the fluid will rise indefinitely.

Washburn (1921) appears to have been the first to derive the dynamics of capillary-driven flow of a Newtonian liquid in an enclosed tube. Neglecting inertia and gravity and assuming

unidirectional flow, the Navier-Stokes equations reduce to

$$0 = \partial_z w, \tag{4.2a}$$

$$0 = \partial_x p = \partial_y p, \tag{4.2b}$$

$$0 = -\partial_z p + \mu(\partial_{xx} + \partial_{yy})w, \tag{4.2c}$$

where w is velocity in the z direction, with boundary conditions

$$w|_{x^2+y^2=r^2} = 0, \tag{4.3a}$$

$$\langle w \rangle_{z=z_s} = \partial_t z_s, \tag{4.3b}$$

where z_s is the position of the fluid meniscus in z (the height of the fluid in the straw; see Figure 4.2) and $\langle w \rangle$ is the average velocity across the tube.[1] The solution in the bulk is given by

$$w = (2/r^2)(r^2 - x^2 - y^2)\partial_t z_s, \tag{4.4a}$$

$$\partial_z p = \frac{-2\gamma \cos\theta / r}{z_s}; \tag{4.4b}$$

the velocity w has the parabolic cross-section typical of Poiseuille flow and the constant pressure gradient is set by the capillary pressure divided by the fluid height. Balancing the momentum equation, Equation (4.2c), yields $2\gamma\cos\theta/(rz_s) = \mu(8/r^2)\partial_t z_s$, and hence

$$z_s = \sqrt{\left(\frac{r\cos\theta}{2}\right)\left(\frac{\gamma}{\mu}\right)t}, \tag{4.5}$$

a result now known as the Washburn relation. Washburn broadened the application of his relation by modeling porous media as collections of intertwined tubes and predicting that fluid fronts in such media would also be proportional to $\sqrt{t\gamma/\mu}$. Indeed, the Washburn scaling has since been successful in describing a variety of capillary transport phenomena, ranging from blood flow in microvascular hemodynamics (Jones, 1969; Skalak et al., 1989) to oil extraction from porous rocks (Wooding and Morel-Seytoux, 1976) to capillary water uptake in wood (Johansson and Kifetew, 2010), among others.

When gravity is included, the moving front no longer advances with the Washburn relation but instead as

$$z_s = z_g\left[1 + \mathcal{W}\left(-e^{-1-(gr^2\rho t)/(8z_g\mu)}\right)\right], \tag{4.6}$$

where z_g is the asymptotic height from Equation (4.1) and $\mathcal{W}$ is the Lambert W function, or product log, defined by $x = \exp[\mathcal{W}(x)]\mathcal{W}(x)$ (Probstein, 1994). The time scale is thus revealed

[1] Note that imposing the no-slip boundary condition, $w|_{x^2+y^2=r^2} = 0$, like this implies that the fluid cannot actually wet the walls of the tube! In reality, both the unidirectional flow and no-slip wall assumptions are simplifications, but as long as the length of the fluid in the tube is much greater than the radius of the tube (i.e., $z_s \gg r$), these issues can be ignored. For more information on the problem of the no-slip boundary condition and the advance of a fluid's leading edge on a solid, see Cox (1986).

to be $t_g = 8z_g\mu/(\rho g r^2) = 8\gamma\cos\theta\mu/(\rho g^2 r^3)$. At early times $t \ll t_g$, the result can be expanded as

$$z_s = \sqrt{\left(\frac{r\cos\theta}{2}\right)\left(\frac{\gamma}{\mu}\right)t} - \frac{\rho g r^2}{12\mu}t + O(t^{3/2}), \tag{4.7}$$

recovering the gravity-free solution at lowest order, while at late times $t \gg t_g$ it asymptotically approaches z_g as

$$z_s = z_g\left[1 - e^{-1-(gr^2\rho t)/(8z_g\mu)}\right] + O\left(e^{-2(gr^2\rho t)/(8z_g\mu)}\right). \tag{4.8}$$

4.1.3 Open capillary flow

Two features of closed capillary flow stand out in the prior derivations. First, a threshold pressure $p_{threshold} = -2\gamma\cos\theta/r$ is required to push fluid into the capillary. Such a threshold pressure was achievable with a large fluid reservoir, but would make transfer of fluid from small capillaries to larger ones impractical. Second, when gravity acts parallel to the capillary, the height to which fluid can be transported is limited. This second issue could be avoided by means of tapering capillaries, but the threshold pressure requirement at the base would remain. A simpler solution, both conceptually and from a manufacturing standpoint, is the use of open V-grooves (see Figure 4.3a). As shall be seen shortly, open V-grooves allow a fluid to reach effectively arbitrarily small radii of curvature, and hence arbitrarily low pressure, eliminating both the threshold pressure and the limit on flow height against gravity. Indeed, such grooves were proposed in by Concus and Finn (1969) to explain how trees can carry water to their topmost leaves despite the fact that their xylem conduits are too wide to allow closed capillary flow to great heights.

The theoretical study of flow in V-grooves appears to begin with Concus and Finn (1969), who studied the equilibrium shape of free fluid surfaces in sharp wedges. They found the contact angle conditions necessary for a fluid to fill a V-groove, and also discovered that the equilibrium surfaces are unbounded even in the presence of gravity, implying that fluid with with a contact angle below the requisite value can flow arbitrarily far into a V-groove, even against gravity. Ayyaswamy et al. (1974) then determined a semi-analytical series solution for the streamwise velocity profile in a 2D cross-section of a fluid in a V-groove with a circular free surface. While not a full equation of motion, this result demonstrated that the friction factor coefficient $2D_h^2/\overline{w}$, where D_h is a hydraulic diameter proportional to the groove width and $\overline{w}$ is the mean streamwise velocity, increases with fluid contact angle θ but has a non-monotonic relationship with interior groove half angle α. In the mid-1990s, Weislogel (1996), Romero and Yost (1996), and Dong and Chatzis (1995) independently developed a low-order, one-dimensional partial differential equation to describe the flow and found self-similar solutions in which the fluid advances as $t^{1/2}$, incidentally the same power as the Washburn relation for closed capillaries. This differential equation was first order in time and second order in z, the axial variable, describing the height of the fluid in the groove as a nonlinear diffusion process.

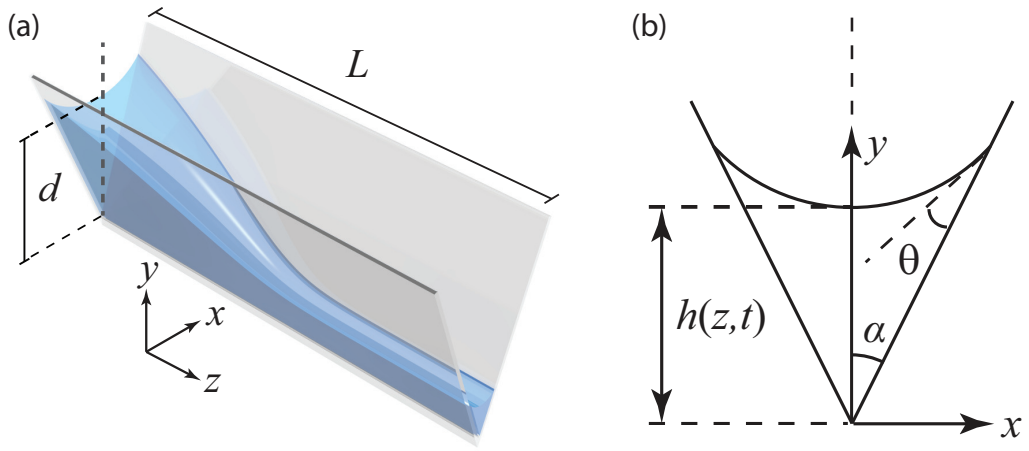

Figure 4.3: Diagrams of V-groove flow system. (a) Schematic of a wetting liquid film ($0 \leq \theta < \pi/2$) flowing within a slender open triangular groove with constant cross-section. The inlet midline film thickness at the origin is denoted by $d = h(x = 0, z = 0, t)$ (note that we follow Weislogel's convention of measuring the midline film thickness, rather than Romero and Yost's convention of the film thickness at the wall) and the channel length by L where $d/L \ll 1$. (b) Cross-sectional view of the flow geometry depicted in (a) where $h(z, t)$ denotes the local midline film thickness, α is the groove internal half angle (note that we follow Weislogel's convention of α being the internal groove half angle, rather than Romero and Yost's convention of α being the exterior groove angle), r_c is the radius of curvature of the liquid interface and θ is the contact angle of the liquid wetting the channel sidewalls, which is assumed constant.

All three arrived at the same resulting equation by throwing out convective terms (i.e., assuming purely viscous flow), and making the key assumption that the groove is much longer than it is wide or deep, thus ignoring axial surface curvature. Romero and Yost (1996) explicitly assumed unidirectional flow; although this was an oversimplification, it provided a shortcut to the end result. Dong and Chatzis (1995) implicitly made a similar shortcut. Weislogel (1996) carried out a formal perturbation analysis, setting the model on firm theoretical footing.

Experimental studies of V-grooves have been performed with various fluids, including solder (Rye et al., 1996, 1998), silicone oil (Weislogel, 1996), methanol (Chen et al., 2009), acetone (Deng et al., 2014), and blood (Berthier et al., 2015), confirming the $t^{1/2}$ spreading rate predicted by earlier theoretical studies.

4.2 Model for free surface capillary flow in slender open V-grooves

We now derive the slender-limit model of flow in V-grooves, following Weislogel (1996) and Romero and Yost (1996).

4.2.1 Slender limit form of the hydrodynamic equations

In order to conserve mass and momentum, an incompressible Newtonian liquid of constant density must satisfy the continuity and Navier-Stokes equations given by the set of coupled equations

$$\nabla \cdot \vec{u} = 0, \tag{4.9}$$

$$\rho \left[\frac{\partial \vec{u}}{\partial t} + (\vec{u} \cdot \nabla) \vec{u} \right] = -\nabla p + \mu \nabla^2 \vec{u} + \rho \vec{g}, \tag{4.10}$$

where the velocity field in Cartesian coordinates is represented by $\vec{u} = (u, v, w)$, the fluid pressure by $p(x, y, z)$, the gravitational acceleration by $\vec{g}$ and the constant fluid density by ρ. Assuming flow in a slender channel such that $\varepsilon = d/L \ll 1$ and a dominant balance between the pressure gradient and the viscous force per unit volume leads to the characteristic scalings and nondimensional variables listed in Table 4.1 along with the corresponding Bond number (Bo), capillary number (Ca) and Reynolds number (Re) in the slender limit. The x, y, and z directions, the d and L scales, and other geometric variables are shown on the diagram in Figure 4.3.

To order ε^2, the rescaled forms of Equations (4.9) and (4.10) are then given by

$$0 = \frac{\partial U}{\partial X} + \frac{\partial V}{\partial Y} + \frac{\partial W}{\partial Z}, \tag{4.11a}$$

$$\varepsilon^3 \mathrm{Re} \frac{DU}{DT} = \frac{\mathrm{Bo}}{\mathrm{Ca}} G_x - \frac{\partial P}{\partial X} + \varepsilon^2 \Delta U, \tag{4.11b}$$

$$\varepsilon^3 \mathrm{Re} \frac{DV}{DT} = \frac{\mathrm{Bo}}{\mathrm{Ca}} G_y - \frac{\partial P}{\partial Y} + \varepsilon^2 \Delta V, \tag{4.11c}$$

$$\varepsilon \mathrm{Re} \frac{DW}{DT} = \frac{1}{\varepsilon} \frac{\mathrm{Bo}}{\mathrm{Ca}} G_z - \frac{\partial P}{\partial Z} + \Delta W, \tag{4.11d}$$

where the substantial derivative D/DT and the Laplacian derivative Δ, respectively, are given by

$$\frac{D}{DT} = \frac{\partial}{\partial T} + U \frac{\partial}{\partial X} + V \frac{\partial}{\partial Y} + W \frac{\partial}{\partial Z}, \tag{4.12a}$$

$$\Delta = \frac{\partial}{\partial X^2} + \frac{\partial}{\partial Y^2} + \varepsilon^2 \frac{\partial}{\partial Z^2}, \tag{4.12b}$$

and $\vec{G} = \vec{g}/g$. In the limits where $\varepsilon^2 \ll 1$, ε and $\mathrm{Re} \ll 1$, the governing equations reduce to the form:

$$\frac{\partial U}{\partial X} + \frac{\partial V}{\partial Y} + \frac{\partial W}{\partial Z} = 0, \tag{4.13a}$$

$$\frac{\partial P}{\partial X} = \frac{\partial P}{\partial Y} = 0, \tag{4.13b}$$

$$\frac{\partial P}{\partial Z} + \frac{\mathrm{Ca}^{-1}}{\widehat{R}} B = \frac{\partial^2 W}{\partial X^2} + \frac{\partial^2 W}{\partial Y^2}, \tag{4.13c}$$

where $B = \varepsilon^{-1} \mathrm{Bo} \widehat{R} (-G_z)$ is the rescaled Bond number, written with $(-G_z)$ to suggest gravity in the $-z$ direction. When subject to the slender limit, the flow is therefore inertia-free and the fluid pressure is constant throughout the (x, y) plane. The pressure gradient driving the flow, which will stem solely from capillary forces and gravity in the z direction, can therefore only vary along the streamwise axis and can only be counterbalanced the viscous force set in play by the no-slip boundary condition applied along the groove sidewalls, namely $U = V = W = 0$ at all liquid/solid interfaces.

Quantity	Scaling	Rescaled variable
Slender parameter		$\varepsilon = d/L \ll 1$
Coordinates	$x_c = d$	$X = x/x_c$
	$y_c = d$	$Y = y/y_c$
	$z_c = L$	$Z = z/z_c$
Velocity	$u_c = \varepsilon^2\gamma\mathrm{Ca}/\mu$	$U = u/u_c$
	$v_c = \varepsilon^2\gamma\mathrm{Ca}/\mu$	$V = v/v_c$
	$w_c = \varepsilon\gamma\mathrm{Ca}/\mu$	$W = w/w_c$
Pressure	$p_c = \gamma\mathrm{Ca}/(\varepsilon L)$	$P = p/p_c$
Time	$t_c = \mu L/(\varepsilon\gamma\mathrm{Ca})$	$T = t/t_c$
		$\tau = \ln(T)$
Interface midline thickness	$y_c = d$	$H = h(z,t)/y_c$
Interface shape	$y_c = d$	$\Sigma = \sigma(x,z,t)/y_c$
Interface radius of curvature	$y_c = d$	$R = r_c/y_c$
Stationary state midline thickness		$H_S(Z)$
Self-similar variable		$\eta = Z/\sqrt{T}$
Self-similar state midline thickness		$S(\eta)$
Bond number		$\mathrm{Bo} = \rho g d^2/\gamma$
Rescaled Bond number		$B = \varepsilon^{-1}(-G_z)\mathrm{Bo}\widehat{R}$
		$= (-G_z)\varepsilon^{-1}(\rho g d^2\gamma^{-1})\widehat{R}$
Slender limit capillary number		$\mathrm{Ca} = \mu w_c/(\varepsilon\gamma) = \Phi$
Reynolds number		$\mathrm{Re} = \rho w_c d/\mu$
		$= (\varepsilon\rho\gamma d/\mu^2)\mathrm{Ca}$

Table 4.1: Characteristic scalings (lower case) and nondimensional variables (uppercase) used to describe dimensionless system shown in Figure 4.3.

4.2.2 Boundary conditions at the liquid interface

The two (dimensional) boundary conditions specifying the jump in normal and shear stresses across the gas/liquid interface $\sigma(x,z,t)$ are given by

$$\left[\hat{n}\cdot(\widetilde{\tau}-p\mathbb{I})\cdot\hat{n}+\gamma(\nabla_s\cdot\hat{n})\right]_{y=\sigma(x,z,t)}=0, \tag{4.14a}$$

$$\left[\hat{t}_{i=1,2}\cdot\widetilde{\tau}\cdot\hat{n}\right]_{y=\sigma(x,z,t)}=0, \tag{4.14b}$$

where $\mathbb{I}$ is the 3×3 identity matrix, $\widetilde{\tau}=\mu[\nabla\vec{u}+(\nabla\vec{u})^T]$ denotes the shear stress tensor, $\nabla_s=\nabla-\hat{n}(\hat{n}\cdot\nabla)$ denotes the surface gradient operator and the triad $(\hat{n},\hat{t}_1,\hat{t}_2)$ denotes the three unit vectors representing directions normal and tangent to the moving interface with the convention that $\hat{n}$ points away from the interface. In rescaled units, these unit vectors are given by

$$\hat{N}=\frac{1}{[1+(\partial_X\Sigma)^2+\varepsilon^2(\partial_Z\Sigma)^2]^{1/2}}\begin{pmatrix}-\partial_X\Sigma\\1\\-\varepsilon\partial_Z\Sigma\end{pmatrix}, \tag{4.15a}$$

$$\hat{T}_1=\frac{1}{[1+(\partial_X\Sigma)^2]^{1/2}}\begin{pmatrix}1\\\partial_X\Sigma\\0\end{pmatrix}, \tag{4.15b}$$

$$\hat{T}_2=\frac{1}{[1+\varepsilon^2(\partial_Z\Sigma)^2]^{1/2}}\begin{pmatrix}0\\\varepsilon\partial_Z\Sigma\\1\end{pmatrix}, \tag{4.15c}$$

where $\Sigma(X,Z,T)=\sigma(x,z,t)/d$ denotes the nondimensional interface function and subscripts denote differentiation with regard to the rescaled coordinates. Specifying a system for which the fluid pressure derives solely from variations in the local interface curvature of the flowing liquid, the interfacial surface tension γ is everywhere constant since the liquid is isothermal and contains no surfactant-like additives, and that the liquid remains in contact with a passive quiescent gas of negligible viscosity and density with gauge pressure set to zero, the jump in normal stress is then strictly due to capillary forces and the liquid interface is a surface of vanishing shear stress. To order $O(\varepsilon^2)$ then, these dimensionless boundary conditions reduce to the form

$$0=-P-\mathrm{Ca}^{-1}\left(\frac{\partial_X^2\Sigma}{[1+(\partial_X\Sigma)^2]^{3/2}}\right)+O(\varepsilon^2) \tag{4.16a}$$

$$=-P-\mathrm{Ca}^{-1}\mathsf{K}(Z,T)+O(\varepsilon^2), \tag{4.16b}$$

$$0=\partial_Y W-(\partial_X\Sigma)\partial_X W+O(\varepsilon^2), \tag{4.16c}$$

$$\begin{aligned}0=&\left[1-(\partial_X\Sigma)^2\right](\partial_Y U+\partial_X V)\\&+2(\partial_X\Sigma)(-\partial_X U+\partial_Y V)\\&-(\partial_Z\Sigma)\left[\partial_X W+(\partial_X\Sigma)\partial_Y W\right]+O(\varepsilon^2),\end{aligned} \tag{4.16d}$$

where K(Z) represents the local curvature of the interface function Σ (defined to be positive for a wetting liquid). It is clear from Equation (4.16b) that the curvature function K can in general only depend on (Z,T) since according to Equation (4.13b), the pressure P is independent of (X,Y). This then requires that the cross-sectional shape of the liquid interface be described by a curve with constant curvature. This restriction limits the shape either to a flat interface or one described by a segment of a circle. Since the liquid must also satisfy a prescribed contact angle set by the particulars of the liquid/solid interaction, a flat profile is disallowed and $\Sigma(Z,T)$ must therefore trace out a circular arc of constant curvature. The nondimensional radius of curvature of the gas/liquid interface is then given by $R(Z,T) = H(Z,T)\,\sin\alpha/(\cos\theta - \sin\alpha)$, or likewise, the interface curvature is described by $K(Z,T) = 1/R(Z,T) = (\cos\theta - \sin\alpha)(\csc\alpha)H^{-1}(Z,T)$. (This relation differs slightly from that originally derived by Romero and Yost, 1996, who adopted a sign convention for K opposite to ours and chose the reference liquid thickness to be the height of the fluid intersecting the groove wall, not the inlet midline film thickness.) According to Equation (4.16a), the capillary pressure is then given by

$$P(Z,T) = -\frac{\mathrm{Ca}^{-1}}{\widehat{R}(\alpha,\theta)H(Z,T)}, \tag{4.17}$$

where

$$\widehat{R}(\alpha,\theta) = \frac{\sin\alpha}{\cos\theta - \sin\alpha}. \tag{4.18}$$

The Concus-Finn condition $\alpha + \theta < \pi/2$ for liquid imbibition yields $\widehat{R}(\alpha,\theta) > 0$, or likewise $P(Z,T) < 0$, consistent with a liquid interface with positive curvature. The case $\alpha + \theta > \pi/2$ is not relevant to our study since it ultimately leads to dewetting configurations resulting in a cascade instability resembling a linear array of primary, secondary, and tertiary droplets (Yang and Homsy, 2007).

4.2.3 Interface midline equation $H(Z,T)$ for capillary flow in slender open V-grooves

The fact that the interface shape can only be a segment of a circle, and is therefore independent of the local coordinates (X,Y), leads to simplification of the expression for the streamwise volumetric flux $Q(Z,T)$. The relevant variables are then scaled by H according to

$$\widetilde{X} = \frac{X}{H} \quad \text{and} \quad \widetilde{Y} = \frac{Y}{H}, \tag{4.19}$$

$$\widetilde{W}(\widetilde{X},\widetilde{Y}) = \left[-\frac{\mathrm{Ca}^{-1}}{\widehat{R}}\left(\frac{\partial H}{\partial Z} + BH^2\right)\right]^{-1} W, \tag{4.20}$$

$$\widetilde{\Sigma}(\widetilde{X}) = 1 + \widehat{R} - \sqrt{\widehat{R}^2 - \widetilde{X}^2}. \tag{4.21}$$

This rescaling allows for solution of $\widetilde{W}$ independently of the local value of H. As a result, the flux factor

$$\Gamma(\alpha,\theta) = \iint \widetilde{W}\, d\widetilde{X}\, d\widetilde{Y} \tag{4.22}$$

depends only on α and θ and need only be computed numerically once (note that the flux factor, $\Gamma(\alpha,\theta)$, is inversely proportional to the friction factor of Ayyaswamy et al. [1974]). The dimensionless streamwise flux which traverses the local cross-sectional area A can then be re-expressed as

$$Q(Z,T) = \iint_A W \; dXdY \tag{4.23}$$

$$= -\frac{\mathrm{Ca}^{-1}}{\widehat{R}(\alpha,\theta)}\Gamma(\alpha,\theta)H^2\left(\frac{\partial H}{\partial Z} + BH^2\right), \tag{4.24}$$

where $A = \widehat{A}(\alpha,\theta)H^2$ and

$$\widehat{A} = \frac{\cos\theta\sin\alpha\cos(\alpha+\theta) - (\pi/2-\alpha-\theta)\sin^2\alpha}{(\cos\theta-\sin\alpha)^2} \tag{4.25}$$

(Romero and Yost, 1996; Weislogel, 1996). As first derived in Appendix 2 of Lenormand and Zarcone (1984), the streamwise gradient in liquid flux is directly related to the temporal variation in the liquid cross-sectional area through the relation $\partial A/\partial T = -\partial Q/\partial Z$, which yields the governing nonlinear diffusion equation for the midline height $H(Z,T)$, namely

$$\widehat{A}(\alpha,\theta)\frac{\partial H^2}{\partial T} = \frac{\mathrm{Ca}^{-1}}{\widehat{R}(\alpha,\theta)}\Gamma(\alpha,\theta)\frac{\partial}{\partial Z}\left(H^2\frac{\partial H}{\partial Z} + BH^4\right). \tag{4.26}$$

Without loss of generality and to recast this equation into parameter-free form, the remaining scaling for the streamwise velocity is chosen to be $w_c = (\varepsilon\gamma/\mu)\Phi$, where $\Phi(\alpha,\theta) = \mathrm{Ca}$ (see Table 1) is defined by

$$\Phi(\alpha,\theta) = \frac{\Gamma(\alpha,\theta)}{\widehat{A}(\alpha,\theta)\,\widehat{R}(\alpha,\theta)}. \tag{4.27}$$

The fact that the capillary number, Ca, depends only on geometric factors may at first seem odd. The formulation of $\mathrm{Ca} = \mu w_c/(\varepsilon\gamma)$ measures the relative importance of capillarity to whatever force is driving the fluid to move at velocity w_c. In this case, the fluid is driven by capillary forces alone; thus $w_c \propto \gamma/\mu$, and γ and μ drop out of the formula for Ca. In other words, because there is nothing to compare the capillary forces to, the capillary number becomes a geometric factor. The following work uses $\Phi(\alpha,\theta)$ instead of Ca to avoid confusion.

The resulting interface equation is then given by

$$\frac{\partial H^2}{\partial T} - \frac{\partial}{\partial Z}\left(H^2\frac{\partial H}{\partial Z} + BH^4\right) = 0, \tag{4.28}$$

subject to the constraint that $H(Z,T)$ is everywhere always positive. As noted by Weislogel and Lichter (1998), Equation (4.28) is equivalent to the foam drainage equation derived by Verbist et al. (1996).

Except when explicitly specified otherwise, the rest of this work will consider only the case of negligible gravity, i.e., $\mathrm{Bo}/(\varepsilon\Phi) \ll 1$ (or, for a groove oriented perpendicular to gravity, $\mathrm{Bo}/\Phi \ll 1$), so that

$$\frac{\partial H^2}{\partial T} - \frac{\partial}{\partial Z}\left(H^2\frac{\partial H}{\partial Z}\right) = 0. \tag{4.29}$$

In Figure 4.4 are plotted the scaled functions $\widehat{A}(\alpha,\theta)$, $\widehat{R}(\alpha,\theta)$, $\Gamma(\alpha,\theta)$ and $\Phi(\alpha,\theta)$ for four values of the liquid contact angle $\theta = 0^\circ$, 20°, 40° and 60° as a function of increasing groove internal half angle α. While $\widehat{A}(\alpha,\theta)$, $\widehat{R}(\alpha,\theta)$ and $\Gamma(\alpha,\theta)$ are of order $O(10)$ or less, the values of $\Phi(\alpha,\theta)$ are far smaller and tend toward $O(10^{-2})$ or less. Note too that since $\widehat{R}(\alpha,\theta)$ and $\Gamma(\alpha,\theta)$ are non-negative functions for systems obeying the Concus-Finn condition, the direction of the liquid flux specified by Equation (4.23) is then strictly determined by the sign of the local interface slope $\partial H/\partial Z$ in the absence of gravity. Interfaces with $\partial H/\partial Z < 0$ engender a positive local flux Q and vice versa. A vanishing local flux will result whenever $\partial H/\partial Z = 0$.

The form of Equation (4.29) falls within a class known as the porous medium equation (PME) generally given by $\partial C(Z,T)/\partial T = \partial^2 C^m/\partial Z^2$, where $C(Z,T)$ is a non-negative scalar function and m is a constant larger than one (Newman, 1984; Otto, 2001; Ralston, 1984; Vázquez, 2007). As discussed in (Vázquez, 2007), this nonlinear diffusion equation describes the relaxation of the order parameter $C(Z,T)$ relevant to various phenomena which arise in different branches of science and mathematics and exhibiting properties such as scale invariance and self-similarity. To help track the energy flow associated with the evolution of C, Newman (1984) outlined a general method for constructing Lyapunov functionals for systems sustaining traveling wave solutions. He used that method to establish the actual rate of convergence of an initial configuration to solutions exhibiting self-similarity. Ralston (1984) complemented this work by showing that Newman's choice of Lyapunov function allowed proof that initial conditions with finite mass converge to self-similar solutions asymptotically in time. When applied to our system, these results indicate that self-similar states which result from the spreading of an initial finite drop within a slender open V-groove are asymptotically globally stable. However, despite longstanding interest in the porous medium equation and wicking phenomena in general, there has been no prior study of which we are aware of the general stability of stationary or transient solutions corresponding to unconstrained volume states.

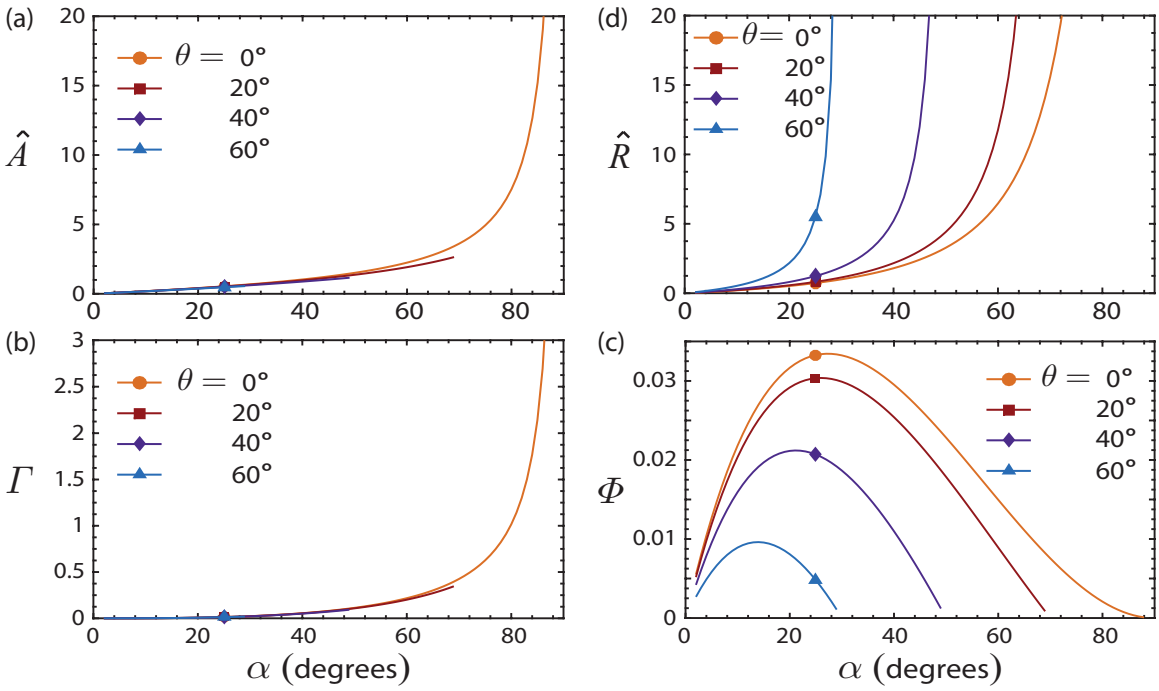

Figure 4.4: H-independent functions pertinent to capillary flow of a Newtonian liquid film with constant contact angle θ in a slender open V-groove with half opening angle α satisfying the Concus-Finn condition $\alpha + \theta < \pi/2$. Plotted are the functions (a) $\widehat{A}(\theta, \alpha)$, (b) $\widehat{R}(\theta, \alpha)$, (c) $\Gamma(\theta, \alpha)$, and (d) $\Phi(\theta, \alpha)$ described in the text.

4.3 Notable solutions

4.3.1 Stationary states for time-independent Dirichlet, Neumann, and volume conditions

Stationary states of Equation (4.29) correspond to those solutions for which $\partial H^2/\partial T = 0$, which reduces the governing equation to a second order, ordinary differential equation requiring two boundary conditions. So long as the interface slope does not vanish, such stationary interfaces $H_S(Z)$ are possible because the subsurface flow of liquid establishes a balance between the local capillary and viscous stresses generates a constant flux Q_o, which according to Equation (4.26) is given by

$$Q_o = -\frac{\mathrm{Ca}^{-1}}{\widehat{R}(\alpha,\theta)}\Gamma(\alpha,\theta)H_S^2\frac{dH_S}{dZ} \tag{4.30}$$

$$= -\widehat{A}(\alpha,\theta)H_S^2\frac{dH_S}{dZ}. \tag{4.31}$$

The general form of these stationary solutions is then represented by

$$H_S = \left[\text{const} - \frac{3Q_oZ}{\widehat{A}(\alpha,\theta)}\right]^{1/3} > 0 \tag{4.32}$$

described by a power law decrease of $Z^{1/3}$ for positive flux and power law increase for negative flux. Particular solutions, of course, require specification of two boundary conditions for setting

the values of const and Q_o. For a V-groove with fixed corner angle and liquid contact angle (i.e., constant value of $\widehat{A}(\alpha,\theta)$) extending between endpoints Z_1 and Z_2, stationary solutions H_S correspond to

$$H_S = \left[H_1^3 - \frac{3Q_S}{\widehat{A}(\alpha,\theta)}(Z - Z_1) \right]^{1/3} \tag{4.33}$$

for Dirichlet and Neumann conditions $H_S(Z_1) = H_1$ and $Q_2 = Q_S$, respectively. Alternatively, Dirichlet conditions imposed at both endpoints, such that $H_S(Z_1) = H_1$ and $H_S(Z_2) = H_2$, yield

$$H_S(Z) = \left[H_2^3 \frac{Z - Z_1}{Z_2 - Z_1} + H_1^3 \frac{Z_2 - Z}{Z_2 - Z_1} \right]^{1/3}. \tag{4.34}$$

Note from Equation (4.17) and the scaling for the streamwise flow speed w_c that specification of the boundary film thickness is equivalent to specification of the boundary fluid pressure. Solutions H_S to Equation (4.32) can also be generated subject to constant flux Q_S at one boundary ($Q_1 = Q_S$ or $Q_2 = Q_S$) and conservation of volume V_S, which sets the constant value C_S in the implicit relation :

$$V_S = \widehat{A} \int_{Z_1}^{Z_2} H^2(Z) dZ \tag{4.35}$$

$$= \frac{3^{5/3} \widehat{A}^{1/3}}{5Q_S} \left[(C_S - Q_S Z_1)^{5/3} - (C_S - Q_S Z_2)^{5/3} \right]. \tag{4.36}$$

Likewise, constant volume and fixed liquid height at one endpoint yield similar forms.

Representative solutions $H_S(Z)$ are plotted in Fig. 4.5 for Dirichlet conditions which pin the inlet height to $H_1 = 1.0$ and pin the outlet height H_2 to the five values shown. From the expression for the flux given by Equation (4.30), it is evident that the solution with $H_2 = 1.33$, which exhibits interface slope values dH/dZ which are everywhere positive, describes a stationary solution with net streamwise flux $Q_S < 0$, i.e., net flow directed from right to left. The uniform solution $H_2(Z) = 1.0$ clearly then represents a case with no flux and no subsurface flow, i.e., a quiescent liquid filament. The remaining curves with negative interface slopes throughout the domain correspond to stationary solutions with positive flux, i.e., net flow directed from left to right. Other boundary conditions yield similar shapes with characteristic scaling $Z^{1/3}$.

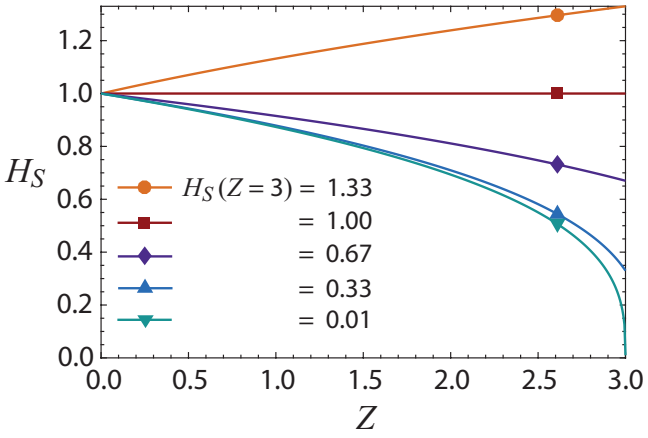

Figure 4.5: Representative stationary solutions subject to Dirichlet conditions $H_S(Z_1) = H_1 = 1.0$ and $H_S(Z_2) = H_2 =$ 0.01, 0.33, 0.67, 1.00, and 1.33 for the range $Z \in [Z_1, Z_2] = [0, 3.0]$.

4.3.2 Self-similar spreading and draining solutions with fixed boundary pressure

Previous studies have delineated the conditions leading to existence and uniqueness of self-similar solutions as well as the attraction of spatially confined initial distributions toward self-similar base states (Vázquez, 2007). Here we focus on volume non-conserving positive states $S(\eta)$ consistent with time-independent Dirichlet boundary conditions imposed at the domain endpoints, namely $S(0) = 1$ and $S(\eta \to \eta_B) = \text{const}$ where η_B denotes a location far downstream of the origin. The Dirichlet condition at the origin can be set to unity without loss of generality since as evident from Equation (4.42), a rescaling involving a multiplicative factor of $S(0)$ leaves the governing equation unchanged.

In general, for self-similarity to hold, there can be no intrinsic length or time scale imposed on the flow, in contrast to the steady state solutions examined in the previous section which depend on the groove length $Z_2 - Z_1$. A simple scaling analysis of Equation (4.29) reveals that self-similar solutions may be possible whenever $T << L^2/H \sim O(L/\varepsilon)$. To find such solutions, it is convenient to expand and rewrite Equation (4.29) in the form

$$\frac{\partial H}{\partial T} - \frac{H}{2}\frac{\partial^2 H}{\partial Z^2} - \left(\frac{\partial H}{\partial Z}\right)^2 = 0. \tag{4.37}$$

The ansatz $H_{\text{sim}}(\eta, T)$ defined by

$$H_{\text{sim}}(\eta) = T^{2\beta-1} S(\eta) \quad \text{where} \tag{4.38}$$

$$\eta = \frac{Z}{T^\beta} \quad \text{for } \beta > 0, \tag{4.39}$$

allows for a large class of self-similar solutions (Vázquez, 2007; Weislogel and Lichter, 1998)

satisfying the general second order nonlinear differential equation

$$\frac{S}{2}S_{\eta\eta} + (S_\eta)^2 + \beta\eta S_\eta + (1-2\beta)S = 0. \tag{4.40}$$

Inspection of the asymptotic behavior of $S(\eta)$ as $\eta \to \infty$ helps ascertain what range of exponents β are required for bounded non-terminating (i.e., $S > 0$) states such that $S_{\eta\eta}$ and S_η asymptotically approach zero as $\eta \to \infty$. While the first two terms on the left side of Equation (4.40) then vanish identically, care must be taken with regard to the third term which couples an increasingly large value of η with an increasingly small term S_η. Balancing the third and fourth terms yields the proper asymptotic scaling, namely $dS/S \sim [(2\beta-1)/\beta]d\eta/\eta$, and hence $S(\eta \to \infty) \sim \eta^{(2\beta-1)/\beta}$. Therefore, only the range $0 < \beta \leq 1/2$ yields bounded non-terminating self similar states.

Boundary conditions also impose constraints on the allowable values of the exponent β. For example, enforcement of constant liquid volume $V \simeq \int_{Z_1}^{Z_2} H^2 dZ = T^{5\beta-2}\int_{Z_1}^{Z_2} S^2 d\eta$ is only consistent with $\beta = 2/5$. According to Equation (4.30), enforcement of a constant flux boundary condition $Q = -\widehat{A}(\alpha/\theta)H^2(\partial H/\partial Z) = \text{const} = -\widehat{A}(\alpha/\theta)T^{3\beta-2}S^2 S_\eta$ is only consistent with $\beta = 3/5$. Clearly then, a constant flux boundary condition (Neumann condition) is therefore inconsistent with bounded solutions.[2]

In what follows, we restrict attention to the value $\beta = 1/2$, which accords with the Washburn relation and allows enforcement of time-independent Dirichlet boundary conditions. For this category of solutions, the nondimensional flux defined in Equation (4.23) is represented by

$$Q(\eta, T) = -\frac{\widehat{A}(\alpha,\theta)}{T^{1/2}}S^2\frac{\partial S}{\partial \eta}. \tag{4.41}$$

The self-similar solution $S(\eta)$ then satisfies the equation:

$$SS_{\eta\eta} + \eta S_\eta + 2(S_\eta)^2 = 0. \tag{4.42}$$

To ascertain the interface shape of these solutions, we numerically solved Equation (4.42) by rewriting the second order equation as a system of first order equations and using the ODE45 solver in Matlab (Mat, 2015). Shown in Fig. 4.6 are representative solutions for receding, uniform, advancing, and terminating states $S(\eta)$ satisfying the far field Dirichlet conditions shown. According to Equation (4.41), solutions with $S_\eta > 0$ correspond to states with net liquid flux to the left, designated *receding states*, while solutions with $S_\eta < 0$ correspond to a net liquid flux to the right, designated *advancing* states. The solution for which S_η vanishes everywhere, which corresponds to a zero flux solution in self-similar coordinates, is designed a

[2]When gravity in the Z-direction is included [see Equation (4.28)], the only admissible self-similar constant is $\beta = 1/3$. This indeed leads to bounded self-similar states, but requires a boundary condition of the form $P(0) \propto T^{1/3}$ or $Q(0) \propto T^{-4/3}$. If gravity is perpendicular to the flow direction, the governing equation picks up corrections similar to those in Chapter 7 and admits only $\beta = 1/2$ (see Appendix C). Thus, the Washburn-like $T^{1/2}$ spreading would be maintained with Dirichlet pressure boundary conditions.

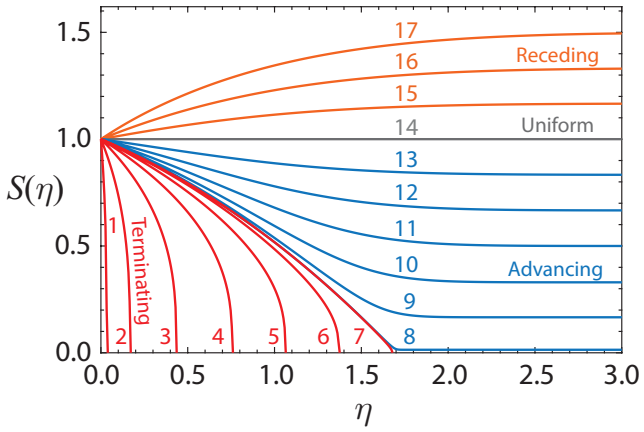

Figure 4.6: Representative self-similar solutions $S(\eta)$ with pressure boundary condition, for terminating (1-7), advancing (8-13), uniform (14) and receding (15-17) states. The computational domain used in numerically solving for these solutions was $[0 \leq \eta \leq 80]$. (Only the range $[0 \leq \eta \leq 3.0]$ is shown in the figure since the downstream behavior remains essentially unchanged beyond that value.) All solutions satisfy the Dirichlet condition $S(\eta = 0) = 1$ at the origin. Solutions 1-7 exhibit interface slopes at the origin given by $S_\eta(0)$ =-10, -2, -0.8, -0.5, -0.4, -0.36, and -0.3492. Solutions 8-13 satisfy far field Dirichlet conditions given, respectively, by $S(80) = 0.01$, 0.17, 0.33, 0.5, 0.67 and 0.83. (Resulting values for the interface slopes at the origin are $S_\eta(0) =$ -0.3491, -0.3418, -0.3185, -0.2745, -0.2090, and -0.1185, respectively.) The line denoted by 14 represents a uniform solution where $S(\eta) = 1.0$. Solutions 15-17 satisfy far field Dirichlet conditions given, respectively, by $S(80) =$ 1.17, 1.33 and 1.5. (Resulting values for the interface slopes at the origin are $S_\eta(0) =$ 0.1485, 0.3283 and 0.5451, respectively.)

uniform state. It represents an exception in that it is the only solution which satisfies volume conservation. Solutions whose advancing front are characterized by a vanishing value of $S(\eta)$ are likewise designated *terminating* states. The numerical solutions indicate that solutions undergo termination only when the interface slope at the origin $S_\eta(0) \lesssim -0.349$. It should be noted that there is a unique terminating solution with finite slope (and hence finite flux) at $S = 0$; all other terminating solutions are not physically accessible without some additional physics to describe behavior at the termination point.

4.3.3 Self-similar converging and receding solutions with fixed boundary flux

Satisfying a flux condition at $\eta = 0$ requires self-similar exponent $\beta = 3/5$. In this case, Equation (4.40) reduces to

$$S_Q S_{Q\eta\eta} + \frac{6}{5}\eta S_{Q_\eta} + 2(S_{Q_\eta})^2 - \frac{2}{5}S_Q = 0. \tag{4.43}$$

Because $S_Q = T^{-1/5}H$, there is no solution with $\lim_{\eta\to\infty} H = const. \in (0, \infty)$. In fact, there is also no smooth, nontrivial solution with $\lim_{\eta\to\infty} S_Q = const. \in [0, \infty)$; this can be seen from Equation (4.43) itself, as the $S_Q S_{Q\eta\eta}$ and $S_{Q_\eta}^2$ terms must vanish in such a limit, which in turn forces $S_{Q_\eta} \propto \eta^{1/3}$.

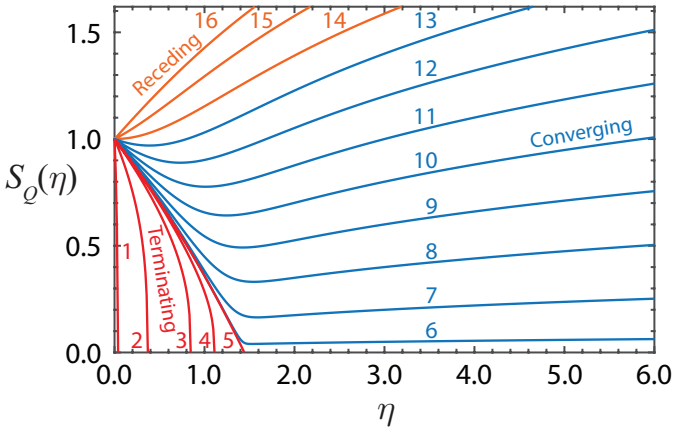

Figure 4.7: Representative self-similar solutions $S_Q(\eta)$ with flux boundary condition for terminating (1-5), converging (6-13), and receding (14-16) states. The computational domain used in numerically solving for these solutions was $[0 \leq \eta \leq 80]$. (Only the range $[0 \leq \eta \leq 6.0]$ is shown in the figure). Solutions satisfy $S_Q(\eta = 0) = 1$ at the origin. Solutions 1-5 exhibit interface slopes at the origin given by $S_{Q_\eta}(0)$ =-10, -1, -0.59, -0.55, and -0.5398. Solutions 6-13 exhibit interface slopes at the origin given, respectively, by $S_{Q_\eta}(0)$ = -0.5396, -0.5358, -0.5215, -0.4931, -0.4467, -0.3778, -0.2817, and -0.1537. And solutions 14-16 have exhibit initial slopes $S_{Q_\eta}(0) = 0$, 0.2187, and 0.4733.

Solutions therefore fall into three categories, shown in Figure 4.7. Terminating solutions, like those in the $\beta = 1/2$ system, reach $S_Q = 0$ at finite η, and only one such solution has finite flux at the termination point. Second, converging solutions have negative slope (and positive flux) at $\eta = 0$ but positive slope (negative flux) at large η. Receding solutions have uniformly positive slope, and hence represent flux from large η back to $\eta = 0$.

4.3.4 Capillary rise against gravity

While flow in a closed capillary of constant radius reaches a finite height $z_g = (2\gamma \cos\theta)/(r\rho g)$ described in Equation (4.1), the front of liquid flow in a V-groove rising against gravity has no finite limit. Indeed, it is this ability to transport liquid to arbitrary heights that motivated Concus and Finn (1969) to suggest it as a mechanism of transpiration in trees.

The static form of Equation (4.28) is given by $H_G^2 \partial_Z H_G + B H_G^4 = 0$, and hence has solution

$$H_G(Z) = \frac{H_0}{1 + BZH_0}, \tag{4.44}$$

where H_0 is the fluid thickness at $Z = 0$ (Verbist et al., 1996). Although $\lim_{Z\to\infty} H_G(Z) = 0$, H_G is positive for all finite Z. And the total volume remains finite:

$$v_G = (Ld^2) \int_{Z=0}^{\infty} \widehat{A} H_G^2 dZ = (Ld^2)\widehat{A}H_0/B = (\widehat{A}\Gamma/\widehat{R})h_0\gamma/(\rho g), \tag{4.45}$$

which is comparable to the closed-capillary volume of $(2\pi \cos\theta)r\gamma/(\rho g)$. In other words, the V-groove and the closed capillary have similar limits on the amount of fluid they can raise against

gravity, but the V-groove distributes that constant volume in a long, narrow thread which can reach arbitrary heights.

4.4 Discussion

4.4.1 Limitations

A few limitations of the V-groove model are obvious from the derivation.

First, if Re is too large (due to high density, low viscosity, or a large groove), then ignoring inertial terms will become invalid. If the inertial terms are too large to ignore but still smaller than the viscous terms, it may be possible to add them in perturbatively, in the manner of the inertial thin film equation (Oron et al., 1997; Roberts, 1997). That said, the relative magnitude of inertial flux corrections is in fact $O(\varepsilon \mathrm{Re}\Gamma)$, because the first-order inertial corrections to streamwise velocity involve solving $\nabla^2 \widetilde{W}_1 = O(\widetilde{W})$, where $\widetilde{W}$ is the viscous streamwise velocity which integrates to Γ (see Appendix C for more details). As an example, let us take values for liquid indium (viscosity $\mu = 1.60 \times 10^{-3}$ Pa s, surface tension $\gamma = 0.57$ N/m, and density $\rho = 7000$ kg/m^3 [Assael et al.; Chentsov et al., 2012; 2011]) and a V-groove with $\alpha = 45°$, $\theta = 15°$, $d = 5\mu$m, $L = 200\mu$m. Then, $\Phi \approx 0.024$, $\Gamma \approx 0.078$, and thus $\varepsilon \mathrm{Re} \approx 0.12$ and $\varepsilon \mathrm{Re}\Gamma \approx 0.0090 \ll 1$.

The slender limit derivation also assumed that $\partial_z h \sim d/L$, i.e., local variations in slope must be gentle; even for a very thin film in a groove, the existence of a steep slope will break the slender limit assumption.

The Van der Waals forces due to the solid walls of the groove become important in the extremely thin film limit, typically as $d \approx O(0.01\ \mu\mathrm{m})$; such forces may be attractive or repulsive, depending on the sign of the Hamaker constant, and thus may either incite or help prevent rupture (Oron et al., 1997). The application of V-grooves as conduits for propellant delivery to microemitters, which motivates this thesis, calls for grooves several microns deep, well outside the range in which Van der Waals forces are significant. Even in a deep groove, a more accurate treatment of the interface shape very close to the termination point of self-similar solutions would also need to take Van der Waals forces into consideration.

The reduced V-groove model is also predicated on the assumption that the liquid contact angle θ is a constant equal to the equilibrium (static) contact angle θ_S. In reality the dynamic contact angle at a moving triple line (i.e., contact line) separating gas, liquid, and solid media is a function of not only θ_S but also the local capillary number based on the speed of the contact line. In the limit of small capillary number, Cox (1986) derived a general equation relating the dynamic contact angle θ_D to the static angle θ_S, the local capillary number Ca, and a coefficient b reflecting the log ratio of the slip length to the characteristic interface length. Cox's equation is

$$g(\theta_D) = g(\theta_S) + b\,\mathrm{Ca} \tag{4.46}$$

where the function g is well approximated by $\theta^3/9$ for small contact angles typical of highly

wetting liquids. Accordingly, it can be shown that for $\theta_S^3 \gg \mathrm{Ca}$, the dynamic angle is given by

$$\theta_D \approx \theta_S + 3b\left(\frac{\mathrm{Ca}}{\theta_S^3}\right) + O\left(\frac{\mathrm{Ca}^2}{\theta_5^S}\right), \tag{4.47}$$

while for $\theta_S^3 \ll \mathrm{Ca}$, the dynamic angle is given by

$$\theta_D \approx (9b\mathrm{Ca})^{1/3} + O\left(\frac{\theta_S^3}{\mathrm{Ca}^{2/3}}\right). \tag{4.48}$$

In the V-groove model, the contact angle is relevant only for the motion of the contact line up and down the sidewalls of the groove (there is no contact line in the streamwise direction). From the scaling relations discussed in Section 4.2.1, this sidewall flow is characterized by the velocity scale εw_c, where w_c is the representative flow speed in the streamwise direction. The relevant capillary number for contact line motion along the sidewalls is therefore $\mathrm{Ca}_{\mathrm{wall}} = \varepsilon w_c \mu/\gamma = \varepsilon^2\Phi$ (see Table 4.1), where Φ is of order 10^{-2} as indicated in Fig. 4.4(d). From Cox's relation, when $\theta_S^3 \gg \mathrm{Ca}_{\mathrm{wall}}$, then $\theta_D \approx \theta_S + O(\varepsilon^2)$ and the dynamic correction to the static angle can therefore be ignored within the slender channel approximation. When $\theta_S^3 \ll \mathrm{Ca}_{\mathrm{wall}}$, then $\theta_D \approx (9b\varepsilon^2\Phi^2)$. Straightforward Taylor expansion of the functions describing the interface curvature radius $\widehat{R}$ and interface shape Σ reveals that each function reduces to the sum of a constant and a term proportional to θ_S^2, i.e., these functions contain no linear term in θ_S. Additionally, the functions representing the cross-sectional area $\widehat{A}$ and flux Γ, which are nonsingular functionals of Σ, also contain no linear term in θ_S. The overall dynamic correction to the static angle can then be shown to be of order $\varepsilon^{4/3}$. Therefore, so long as $\mathrm{Ca}_{\mathrm{wall}}$ remains small, the governing equation given by Equation (4.29) remains unchanged. The value $b = \ln(\epsilon^{-1})$, where ϵ is the ratio of the slip length to the characteristic interface length at which the angle is measured. Cox estimates values of ϵ to be 10^{-2} to 10^{-6} in order to fit experimental data from silicone oil flowing in a glass tube of radius 1mm (Cox, 1986; Hoffman, 1975). While the value would depend in general on material parameters, the slip length should not in principle fall below the molecular length, and so for a typical V-groove a few microns deep it should be expected that $\epsilon \gtrsim (1\ \text{Å})/(1\ \mu\text{m}) = 10^{-4}$, yielding $b \lesssim 10$. While a fully numerical model incorporating a velocity-dependent contact angle can certainly be developed for flows at higher capillary numbers (Bracke et al., 1989; Joos et al., 1990), such an extension precludes analytic solutions for base states and is beyond the scope of this work.

Evaporation was excluded from the model, but is important in applications such as heat pipes. To include evaporation, Equation (4.29) can be modified to read $\partial_T H^2 = \partial_Z(H^2\partial_Z H) - E(H,Z)$, where $E(H,Z)$ is a dimensionless evaporation rate function which depends on the temperature distribution within the film, and must be solved simultaneously (Markos et al., 2006). A solution for a groove with a linear temperature gradient boundary condition was computed by Markos et al. (2006), and their work can be extended to other boundary conditions.

At the microscale, manufacturing constraints may prevent the production of perfect V-grooves. In particular, if the manufactured walls are not smooth, various complications could arise. First,

the contact line may become pinned (stuck) at a wall defect, preventing the interface from rising higher in the groove. A model of fluid with symmetrical pinned edges in a V-groove was proposed by Romero and Yost (1996), in which the contact angle varies instead of the fluid thickness. The resulting model is qualitatively similar to the unpinned V-groove model, and in particular represents a 1-dimensional nonlinear diffusion PDE. If the scale of roughness is very small compared to the groove, then it may be treated as an averaged quantity. In this case, the contact angle, θ, typically becomes smaller (Quéré, 2008) and the no-slip wall condition may be replaced by an effective slip condition (Sarkar and Prosperetti, 1996), resulting in a decreased flux factor (i.e., a smaller Γ). If the manufactured walls are not perfectly straight but instead curved, then the linear relationship between fluid thickness and interface radius of curvature would be broken, i.e., it would no longer be the case that $p \propto h^{-1}$, and the cross-sectional area would also no longer be proportional to h^2. Such a case is likely analytically tractable for simple wall shapes (of the form $y = x^{const}$ for example), but would necessitate a complete rederivation of the model. Furthermore, manufacturing perfectly sharp corners may be impossible; this is discussed in the following section.

4.4.2 Rounded V-grooves (U-grooves)

Manufacturing V-grooves with perfectly sharp corners is challenging at the microscale, one of the reasons for which variations on the V-groove geometry have been investigated. Chen, Weislogel, and Nardin (2006) generalized the model to V-shaped grooves with rounded bottoms (assumed to be circular sections) instead of sharp corners, which we will refer to as "U-grooves." Above the rounded bottom, the upper portion of each groove was assumed to have straight walls like the and V-groove. It was found that the governing equations remained similar to the V-groove equation, but included some nonlinear terms which could not be expressed in closed form (although the authors did construct an approximate closed form solution containing only polynomial fractions). However, the authors identified several limiting cases, such as nearly-rectangular grooves and highly rounded "crescent-like" grooves, in which the model could be approximated with a simple polynomial expression. In these cases, the model remained a nonlinear diffusion equation similar to the V-groove equation, but with a different exponent. Tang et al. (2015) considered asymmetrical V-grooves, with a sharp corner but with one wall slightly curved. This model also contained a nonlinear term with no closed form expression, and solutions were computed numerically.

These models are derived from the same $\partial A/\partial T = -\partial Q/\partial Z$ equation as the V-groove, but the dependence of A and Q on H are different. Most importantly, the cross-sectional shape of the fluid changes with H, unlike the V-groove, where the cross-sectional shape simply scales to larger or smaller sizes as H varies. This means that the cross-sectional area A is no longer quadratic in H, but instead follows some complicated (though still closed-form-expressible) nonlinear function of H. The streamwise flux, however, must be computed numerically for each different cross-sectional shape, and hence leads to an inexpressible nonlinear function.

Despite the complexity of these models, their dynamics remain qualitatively similar to those of the V-groove. In particular, both exhibit self-similar solutions with the same $t^{1/2}$ spreading behavior as the V-groove. The spreading profile in the U-grooves of Chen et al. (2006) appears steeper than that of the V-groove, resembling the terminating solutions 5 and 6 in Figure 4.7.

References

MATLAB and Statistics Toolbox Release 2015a, The MathWorks, Inc., Natick, MA, USA, 2015. URL `https://www.mathworks.com/products/matlab.html`.

M. J. Assael, I. J. Armyra, J. Brillo, S. V. Stankus, J. Wu, and W. A. Wakeham. Reference data for the density and viscosity of liquid cadmium, cobalt, gallium, indium, mercury, silicon, thallium, and zinc. J. Phys. Chem. Ref. Data, 41(3), 2012. ISSN 0047-2689. doi:10.1063/1.4729873.

P. S. Ayyaswamy, I. Catton, and D. K. Edwards. Capillary flow in triangular grooves. J. Appl. Mech., 41:332–336, 1974. doi:10.1115/1.3423288.

J. Berthier, K. A. Brakke, E. P. Furlani, I. H. Karampelas, V. Poher, D. Gosselin, M. Cubizolles, and P. Pouteau. Whole blood spontaneous capillary flow in narrow v-groove microchannels. Sensor Actuat. B Chem., 206:258–267, 2015. doi:10.1016/j.snb.2014.09.040.

M. Bracke, F. De Voeght, and P. Joos. The kinetics of wetting: The dynamic contact angle, volume 79 of Trends in Colloid and Interface Science III, Progress in Colloid & Polymer Science. Steinkopff-Verlag Heidelberg, 1989. doi:10.1007/BFb0116200.

Y. Chen, M. M. Weislogel, and C. L. Nardin. Capillary-driven flows along rounded interior corners. J. Fluid Mech., 566:235–271, 2006. doi:10.1017/S0022112006001996.

Y. Chen, L. S. Melvin, S. Rodriguez, D. Bell, and M. M. Weislogel. Capillary driven flow in micro scale surface structures. Microelectron. Eng., 86(4):1317–1320, 2009. doi:10.1016/j.mee.2009.02.016.

V. P. Chentsov, V. G. Shevchenko, A. G. Mozgovoi, and M. A. Pokrasin. Density and surface tension of heavy liquid-metal coolants: Gallium and indium. Inorg. Mater. Appl. Res., 2(5): 468–473, 2011. doi:10.1134/S2075113311050108.

S. H. Collicott and Y. Chen. Studies of the wetting of gaps in weightlessness. Microgravity Sci. Tec., 22:487–498, 2010. doi:10.1007/s12217-010-9233-6.

P. Concus and R. Finn. On the behavior of a capillary surface in a wedge. Proc. Natl. Acad. Sci. USA, 63(2):292, 1969. doi:10.1073/pnas.63.2.292.

R. G. Cox. The dynamics of the spreading of liquids on a solid surface. part 1. viscous flow. J. Fluid Mech., 168:169–194, 1986. doi:10.1017/S0022112086000332.

S. R. Darr, C. F. Camarotti, J. W. Hartwig, and J. N. Chung. Hydrodynamic model of screen channel liquid acquisition devices for in-space cryogenic propellant management. Phys. Fluids, 29:017101, 2017. doi:10.1063/1.4973671.

J. A. Dean. Lange's Handbook of Chemistry. McGraw-Hill, New York, 15th edition, 1999. ISBN 0070163847.

D. Deng, Y. Tang, J. Zeng, S. Yang, and H. Shao. Characterization of capillary rise dynamics in parallel micro v-grooves. Int. J. Heat Mass Trans., 77:311–320, 2014. doi:10.1016/j.ijheatmasstransfer.2014.05.003.

P. S. Dittrich and A. Manz. Lab-on-a-chip: Microfluidics in drug discovery. Nat. Rev. Drug. Discov., 5(3):210–218, 2006. doi:10.1038/nrd1985.

M. Dong and I. Chatzis. The imbibition and flow of a wetting liquid along the corners of a square capillary tube. J. Colloid Interface Sci., 172(2):278–288, 1995. doi:10.1006/jcis.1995.1253.

J. W. Hartwig. A detailed historical review of propellant management devices for low gravity propellant acquisition. In Proceedings of the 52nd AIAA/SAE/ASEE Joint Propulsion Conference, Salt Lake City, UT, July 25-27, 2016, pages AIAA–16–4772. American Institute of Aeronautics and Astronautics, Reston, VA, 2016. doi:10.2514/6.2016-4772.

J. W. Hartwig. Propellant management devices for low-gravity fluid management: Past, present, and future applications. J. Spacecr. Rockets, 54:808–824, 2017. doi:10.2514/1.A33750.

R. L. Hoffman. A study of the advancing interface. J. Colloid Interface Sci., 50(2):14, 1975. doi:10.1016/0021-9797(75)90225-8.

D. E. Jaekle. Propellant management device conceptual design and analysis: Vanes. In AIAA/SAE/ASME/ASEE 27th Joint Propulsion Conference, June 24-26, 1991, Sacramento, CA, pages AIAA–91–2172. American Institute of Aeronautics and Astronautics, Reston, VA, 1991. doi:10.2514/6.1991-2172.

D. E. Jaekle. Propellant management device conceptual design and analysis: Galleries. In 33rd AIAA/SAE/ASME/ASEE Joint Propulsion Conference & Exhibit, July 6-9, 1997, Seattle, WA, pages AIAA–97–2811. American Institute of Aeronautics and Astronautics, Reston, VA, 1997. doi:10.2514/6.1997-2811.

D. E. Jaekle. PMD Technology, 2011. URL `https://www.pmdtechnology.com`.

J. Johansson and G. Kifetew. Ct-scanning and modelling of the capillary water uptake in aspen, oak and pine. Eur. J. Wood Prod., 68:77 – 85, 2010. doi:10.1007/s00107-009-0359-4.

R. T. Jones. Blood flow. Annu. Rev. Fluid Mech., 1(1):223–244, 1969. doi:10.1146/annurev.fl.01.010169.001255.

P. Joos, P. van Remoortere, and M. Bracke. The kinetics of wetting in a capillary. J. Colloid Interface Sci., 136:189 – 197, 1990. doi:10.1016/0021-9797(90)90089-7.

L. D. Landau and E. M. Lifshitz. Fluid Mechanics, volume 6 of Course of Theoretical Physics. Butterworth-Heinemann, 2nd edition, 1987.

R. Lenormand and C. Zarcone. Role of roughness and edges during imbibition in square capillaries. In Proceedings of the 59th Annu. Tech. Conference & Exhibit, Houston, TX, Sept. 16-19, 1984, pages SPE–13264. American Institute of Mining, Metallurgical and Petroleum Engineers, Inc., Englewood, CO, 1984. doi:10.2118/13264-MS.

D. Levine, B. Wise, R. Schulman, H. Gutierrez, D. Kirk, N. Turlesque, W. Tam, M. Bhatia, and D. Jaekle. Surface tension and contact angle analysis with design of propellant measurement apparatus. J. Propul. Power, 31(1):429–443, 2015. doi:10.2514/1.B35213.

A. K. Mallik, G. P. Peterson, and M. H. Weichold. On the use of micro heat pipes as an integral part of semiconductor devices. J. Electron. Packaging, 114(4):436–442, 1992. doi:10.1115/1.2905477.

M. Markos, V. S. Ajaev, and G. M. Homsy. Steady flow and evaporation of a volatile liquid in a wedge. Phys. Fluids, 18(9):092102, September 2006. ISSN 1070-6631, 1089-7666. doi:10.1063/1.2347529.

J. C. Maxwell and J. W. Strutt. Encyclopædia Britannica (11th Edition), volume 5. Univ. of Cambridge, 1911.

W. I. Newman. A Lyapunov functional for the evolution of solutions to the porous medium equation to self-similarity. I. J. Math. Phys., 25(10):3120–3123, 1984. doi:10.1063/1.526028.

N. M. Oliveira, S. Vilabril, M. B. Oliveira, R. L. Reis, and J. a. F. Mano. Recent advances on open fluidic systems for biomedical applications: A review. Mat. Sci. Eng. C, 97:851–863, April 2019. ISSN 09284931. doi:10.1016/j.msec.2018.12.040.

A. Oron, S. H. Davis, and S. G. Bankoff. Long-scale evolution of thin liquid films. Rev. Mod. Phys., 69(3):931–980, 1997. doi:10.1103/RevModPhys.69.931.

F. Otto. The geometry of dissipative evolution equations: The porous medium equation. Commun. Part. Diff. Eq., 26(1-2):101–174, 2001. doi:10.1081/PDE-100002243.

M. Prakash and N. Gershenfeld. Microfluidic bubble logic. Science, 315(5813):832–835, 2007. doi:10.1126/science.1136907.

R. F. Probstein. Physicochemical Hydrodynamics: An Introduction. John Wiley & Sons, New York, 1994. ISBN 9780471010111.

D. Quéré. Wetting and Roughness. Annu. Rev. Mater. Res., 38(1):71–99, August 2008. ISSN 1531-7331, 1545-4118. doi:10.1146/annurev.matsci.38.060407.132434.

J. Ralston. A Lyapunov functional for the evolution of solutions to the porous medium equation to self-similarity. II. J. Math. Phys., 25(10):3124–3127, 1984. doi:10.1063/1.526029.

A. J. Roberts. Low-dimensional modelling of dynamics via computer algebra. Comput. Phys. Commun., 100(3):215–230, March 1997. ISSN 00104655. doi:10.1016/S0010-4655(96)00162-2.

J. R. Rollins, R. K. Grove, and D. E. Jaekle. Twenty-three years of surface tension propellant management system design, development, manufacture, test, and operation. In A. I. of Aeronautics and V. Astronautics, Reston, editors, AIAA 21st Joint Propulsion Conference, Monterey, CA, July 8-10, 1985, pages AIAA–85–1199, 1985. doi:10.2514/6.1985-1199.

L. A. Romero and F. G. Yost. Flow in an open channel capillary. J. Fluid Mech., 322:109–129, 1996. doi:10.1017/S0022112096002728.

R. R. Rye, J. A. Mann, and F. G. Yost. The flow of liquids in surface grooves. Langmuir, 12 (2):555–565, 1996. doi:10.1021/la9500989.

R. R. Rye, F. G. Yost, and E. J. O'Toole. Capillary flow in irregular surface grooves. Langmuir, 14(14):3937–3943, 1998. doi:10.1021/la9712247.

K. Sarkar and A. Prosperetti. Effective boundary conditions for Stokes flow over a rough surface. J. Fluid Mech., 316:223–240, June 1996. ISSN 0022-1120, 1469-7645. doi:10.1017/S0022112096000511.

R. Skalak, N. Ozkaya, and T. C. Skalak. Biofluid mechanics. Annu. Rev. Fluid Mech., 21(1): 167–200, 1989. doi:10.1146/annurev.fl.21.010189.001123.

Y. Tang, X. Chen, and Y. Huang. Capillary flow rate limitation in asymmetry open channel. Chinese J. Aeronaut., 28(3):720–728, 2015. doi:10.1016/j.cja.2015.04.019.

T. Thorsen, S. J. Maerkl, and S. R. Quake. Microfluidic large-scale integration. Science, 298 (5593):580–584, 2002. doi:10.1126/science.1076996.

J. L. Vázquez. The Porous Medium Equation: Mathematical Theory. Oxford Science Publications. Clarendon Press, 2007. ISBN 9780198569039. doi:10.1093/acprof:oso/9780198569039.001.0001.

G. Verbist, D. Weaire, and A. M. Kraynik. The foam drainage equation. J. Phy. Condens. Matter, 8(21):3715–3731, May 1996. ISSN 0953-8984, 1361-648X. doi:10.1088/0953-8984/8/21/002.

E. W. Washburn. The dynamics of capillary flow. Phys. Rev., XVII(3):273 – 283, 1921. doi:10.1103/PhysRev.17.273.

M. M. Weislogel. Capillary flow in an interior corner. PhD thesis, Northwestern University, June 1996. URL `https://ntrs.nasa.gov/citations/19970010346`. Also published as NASA Technical Memorandum 107364.

M. M. Weislogel. Capillary flow in containers of polygonal section. AIAA Journal, 39(12):2320 – 2326, 2001. doi:10.2514/2.1237.

M. M. Weislogel and S. Lichter. Capillary flow in an interior corner. J. Fluid Mech., 373: 349–378, 1998. doi:10.1017/S0022112098002535.

M. M. Weislogel, M. A. Sala, and S. H. Collicott. Analysis of tank PMD rewetting following thrust resettling. In 40th AIAA Aerospace Sciences Meeting & Exhibit, Reno, NV, January 14-17,2002, 2002. doi:10.2514/6.2002-757.

N. C. White and S. M. Troian. Why capillary flows in slender triangular grooves are so stable against disturbances. Phys. Rev. Fluids, 4(5):054003, 2019. doi:10.1103/PhysRevFluids.4.054003.

R. A. Wooding and H. J. Morel-Seytoux. Multiphase fluid flow through porous media. Annu. Rev. Fluid Mech., 8(1):233–274, 1976. doi:10.1146/annurev.fl.08.010176.001313.

P. Yager, T. Edwards, E. Fu, K. Helton, K. Nelson, M. R. Tam, and B. H. Weigl. Microfluidic diagnostic technologies for global public health. Nature, 442(7101):412–418, 2006. doi:10.1038/nature05064.

L. Yang and G. M. Homsy. Capillary instabilities of liquid films inside a wedge. Phys. Fluids, 19:044101, 2007. doi:10.1063/1.2716632.

Chapter 5

STABILITY OF V-GROOVE FLOW

Note: portions of this chapter are adapted from published work (White and Troian, 2019).

5.1 Introduction

Although V-groove flow theory has formed the foundation of numerous applications, from propellant management (Jaekle, 1991) to heat pipes (Mallik et al., 1992), there has never been a comprehensive analysis of the stability and robustness of the V-groove equations. Until now, only a few narrow special cases of stability have been studied.

One such special case is the instability associated with high-speed convective flow in open grooves. This convective instability has been studied by Haake et al. (2010) in rectangular grooves, We et al. (2013) in V-grooves, and Tang et al. (2015) in asymmetrical V-grooves. However, not only are these models based on convective flow, but they also assume unidirectional flow, and would require a perturbation analysis to establish their regimes of validity.

Other special cases are analyses of the droplet formation of nonwetting liquids in V-grooves (Langbein, 1990; Yang and Homsy, 2007), and the "dryout" instability of thermocapillary flow in V-grooves (Yang and Homsy, 2006).

For viscous flow of wetting fluids in V-grooves, Romero and Yost (1996) presented a surface energy formulation, showing that a fluid with sufficiently small contact angle will fill a groove, but offering no further insight into its behavior or stability. Weislogel (2001) demonstrated the linear stability of a static, unmoving fluid in a filled groove by adding small sinusoidal perturbations.

In this paper, a general stability analysis of the partial differential equations governing V-groove flow is presented for the three most important regimes: steady state flow, self-similar spreading flow, and self-similar draining flow. All of these regimes are shown to be stable, a result which justifies the use of the perturbative V-groove flow model and provides a new incentive for the use of V-grooves in microfluidic devices.

5.2 Nonlinear stability of steady states

We first examine the time-asymptotic nonlinear stability of stationary solutions by appealing to a Lyapunov analysis. In particular, we construct a Lyapunov energy function (akin to a potential energy function in classical mechanics) to determine whether and how rapidly arbitrary disturbances equilibrate back to the stationary solutions H_S. A similar approach to asymptotic stability has previously been used to characterize disturbance decay governed by nonlinear diffusion dynamics (Kern and Felderhof, 1977). Here we show that the capillary flow in a bounded domain with time-independent boundary conditions has a uniquely determined stationary solu-

tion which is dynamically stable. This implies that any initial distribution which maintains the condition $H(Z,T) > 0$ for all time will ultimately evolve toward the stationary state. Furthermore, it is shown that initial states satisfying Dirichlet boundary conditions are *globally stable* - that is, any initial distribution $H(Z,0) > 0$ will converge to the stationary state. For all sets of boundary conditions posed, we show that the convergence to the stationary state is exponential in time so long as it satisfies the positivity condition $H(Z,T) > 0$.

Recall that the equation of motion of flow in the V-groove was given by Equation (4.37) as

$$\frac{\partial H}{\partial T} = \frac{H}{2}\frac{\partial^2 H}{\partial Z^2} + \left(\frac{\partial H}{\partial Z}\right)^2. \tag{5.1}$$

In order to find a Lyapunov functional for Equation (5.1), we first try recasting it into gradient flow form (Cahn and Taylor, 1994; Giacomelli and Otto, 2001)

$$\frac{\partial G(Z,T)}{\partial T} = \frac{\partial}{\partial Z}\left\{M(G)\frac{\partial}{\partial Z}\left(\frac{\delta \mathfrak{F}}{\delta G}\right)\right\}, \tag{5.2}$$

where $M(G)$ is the so-called mobility function and $\delta\mathfrak{F}/\delta G$ denotes the functional derivative of $\mathfrak{F}(H)$ with respect to G. The gradient flow form is a useful first step in the search for a Lyapunov functional to prove stability. Note that not all PDEs can be put into gradient flow form, and furthermore the existence of a gradient flow functional does not guarantee stability.

By introducing $G(H) = H^2(Z,T)$ (the mapping from H to G is one-to-one since H is strictly positive), and letting $M = 1/3$, Equation (5.1) can be re-expressed in gradient flow form as

$$\frac{\partial G}{\partial T} = \frac{\partial}{\partial Z}\left\{\frac{1}{3}\frac{\partial}{\partial Z}\left(\frac{\delta \mathfrak{F}}{\delta G}\right)\right\} = \frac{\partial}{\partial Z}\left[\frac{1}{3}\frac{\partial R}{\partial Z}\right] \tag{5.3}$$

where the functional $\mathfrak{F}$ is given by

$$\mathfrak{F}(G) = \int_{Z_1}^{Z_2}\left(\frac{2}{5}G^{5/2} - G_S^{3/2}G + \frac{3}{5}G_S^{5/2}\right)dZ \tag{5.4}$$

and $R(G) = \delta\mathfrak{F}(G)/\delta G$ is

$$R(G) = (G^{3/2} - G_S^{3/2}) = (H^3 - H_S^3). \tag{5.5}$$

This functional was found in reverse: first noting that $\partial H/\partial T = \partial_Z[(1/3)\partial_Z G^{3/2}]$, integrating $\int G^{3/2}dG$ yields $G^{5/2}$. Because the extra G_S terms are canceled by the Z-derivatives, there exists a large family of valid gradient flow functionals of the form $c_1G^{5/2} + c_2G_S^{3/2}G + c_3G_S^{5/2}$. In fact, choosing instead a mobility function $M(G) = G^a$ for some a yields an even larger family of possible functionals $\mathfrak{F}$. But most of these functionals, while valid bases for the gradient flow form, are useless for proving stability. The particular $\mathfrak{F}$ defined in Equation (5.4) turns out to be compatible with the boundary conditions of interest and have the necessary properties to demonstrate stability of the system, as outlined below.

Recall from Section 3.2 that for $\mathfrak{F}(G)$ to represent a Lyapunov functional around the steady state G_S, it must have an isolated minimum at G_S, and it must approach that steady state, i.e., $\partial_T \mathfrak{F}(G) \leq 0$.

We first show that $\mathfrak{F}(G_S)$ is a minimum by showing that $\delta\mathfrak{F}(G_S) = 0$ (implying G_S is extremal) and $\delta^2\mathfrak{F}(G_S) > 0$ (implying G_S is a minimum):

$$\delta\mathfrak{F}(G)|_{G_S} = \int_{Z_2}^{Z_1} \left.\frac{\delta\mathfrak{F}}{\delta G}\right|_{G_S} \delta G \, dZ \tag{5.6}$$

$$= \int_{Z_2}^{Z_1} R(G)|_{G_S} \, \delta G \, dZ = 0 \text{ and} \tag{5.7}$$

$$\left.\delta^2\mathfrak{F}(G)\right|_{G_S} = \int_{Z_2}^{Z_1} \left.\frac{\delta^2\mathfrak{F}}{\delta G^2}\right|_{G_S} (\delta G)^2 \, dZ \tag{5.8}$$

$$= \int_{Z_2}^{Z_1} \frac{3}{2} G_S^{1/2} (\delta G)^2 \, dZ > 0. \tag{5.9}$$

We next show that $\mathfrak{F}$ decreases in time, assuming either Dirichlet boundary conditions (corresponding to $R|_{Z_1,Z_2} = 0$) or Neumann boundary conditions (corresponding to $(\partial R/\partial Z)|_{Z_1,Z_2} = 0$).

$$\begin{aligned}
\frac{\partial\mathfrak{F}(G)}{\partial T} &= \int_{Z_1}^{Z_2} \left(\frac{\delta\mathfrak{F}}{\delta G}\right) \frac{\partial G}{\partial T} dZ \\
&= \int_{Z_1}^{Z_2} R \frac{\partial G}{\partial T} dZ \\
&= \int_{Z_1}^{Z_2} \frac{R}{3} \frac{\partial}{\partial Z} \left[\frac{\partial R}{\partial Z}\right] dZ \\
&= \left[\frac{R}{3}\frac{\partial R}{\partial Z}\right]_{Z_1}^{Z_2} - \int_{Z_1}^{Z_2} \frac{1}{3} \left[\frac{\partial R}{\partial Z}\right]^2 dZ \\
&= -\int_{Z_1}^{Z_2} \frac{1}{3} \left[\frac{\partial R}{\partial Z}\right]^2 dZ \leq 0.
\end{aligned} \tag{5.10}$$

Hence $\mathfrak{F}(G)$ is indeed a Lyapunov functional, and the system is locally stable. Note that we made use of the Dirichlet or Neumann boundary conditions to get rid of the boundary term, $[(R/3)(\partial R/\partial Z)]_{Z_1}^{Z_2}$. Given different boundary conditions, this term would not necessarily vanish, and the system would not necessarily be stable.

$\mathfrak{F}$ can be re-expressed in terms of the interface function H:

$$\mathfrak{F}(H) = \int_{Z_1}^{Z_2} \left(\frac{2}{5}H^5 - H_S^3 H^2 + \frac{3}{5}H_S^5\right) dZ. \tag{5.11}$$

and hence

$$\frac{\partial\mathfrak{F}(H)}{\partial T} = -\frac{1}{3}\int_{Z_1}^{Z_2} \left[\frac{\partial}{\partial Z}(H^3 - H_S^3)\right]^2 dZ \leq 0, \tag{5.12}$$

where the final equality holds only for initial states $H(Z,T)$ exactly equal to the stationary state solutions $H_S(Z)$. The flow described is locally asymptotically stable in the Lyapunov sense, i.e., arbitrary initial distributions $H(Z,T)$ decay in time toward the stationary solution H_S.

To prove global stability, we must show that each stable stationary state H_S is unique, i.e., $\mathfrak{F}$ has a unique minimum. Suppose that in addition to the already specified steady state solution H_S there exists another steady solution H_{S2} satisfying the same boundary conditions. Since H_{S2} is time independent, it must satisfy the relation $\partial\mathfrak{F}(H_{S2})/\partial T = -(1/3)\int_{Z_1}^{Z_2}[\partial(H_{S2}^3 - H_S^3)/\partial Z]^2 dZ = 0$. Clearly this is possible only if $H_{S2} = (H_S^3 + C_o)^{1/3}$, where the constant C_o must equal zero in order for H_{S2} to satisfy the same boundary conditions as H_{S2}. Thus $H_{S2} = H_S$, and we have shown that the solution H_S is indeed unique.

The proof above requires that both the stationary $H_S(Z)$ and transient $H(Z,T)$ solutions be everywhere strictly positive. For solutions satisfying Dirichlet boundary conditions, these requirements are easily met. Consider any positive initial state $H(Z,T=0)$ which redistributes its height in time according to Equation (5.1). Were there a point within the domain where $H(Z,T) \to 0$, then the local interface would have to satisfy $\partial H/\partial T < 0$ and the local curvature $\partial^2 H/\partial Z^2$ would have to become sufficiently negative to satisfy the balance of terms in Equation (5.1). The local interface would then have to develop a local protrusion (negative curvature) and not a local dimple leading to rupture (positive curvature), in contradiction to the assumption of positive curvature required at that local minimum. Therefore, all positive initial states remain positive in time. For Dirichlet conditions then, stationary solutions $H_S(Z)$ are *globally* stable. For the remaining stationary solutions subject to a Neumann boundary condition, it may become the case that too high a flux condition leads to one or more points where the local film thickness vanishes. In the vicinity of such points, the local interface slope will become increasingly large and eventually violate the slender limit approximation. Perhaps more importantly, disjoining pressure effects, known to modify the flow in ultrathin regions of a liquid film, must then be incorporated into the model interface equation (Schwartz et al., 2001; Teletzke et al., 1987). In such cases then, the proof above only establishes asymptotic stability, not global asymptotic stability.

Next, we demonstrate an even stronger statement regarding the asymptotic stability of stationary states, namely that the stationary solutions H_S represent *exponentially stable* equilibria of Equation (5.1). A useful relation for the function $R(Z)$ defined in Equation (5.5) can be obtained by first applying the Poincaré-Friedrichs inequality in one dimension (Smith et al., 2016) according to which

$$\int_{Z_1}^{Z_2}\left(\frac{dR}{dZ}\right)^2 dZ \geq \frac{1}{(Z_2 - Z_1)^2}\int_{Z_1}^{Z_2} R^2(Z)dZ \tag{5.13}$$

subject to the constraint that there is some interior point Z^* in the bounded domain $Z_1 \leq Z^* \leq Z_2$ where $R(Z^*) = 0$. This must always be the case, however, since $H(Z,T)$ must satisfy the same boundary conditions as H_S. Given that $H(Z,T)$ and $H_S(Z)$ are strictly positive throughout the domain, it is possible to construct an upper bound on $\partial\mathfrak{F}/\partial T$ in Equation (5.12) as follows:

$$\begin{aligned}
\frac{\partial \mathfrak{F}(H)}{\partial T} &= -\frac{1}{3}\int_{Z_1}^{Z_2}\left[\frac{\partial}{\partial Z}(H^3 - H_S^3)\right]^2 dZ \\
&\leq -\frac{1}{3(Z_2-Z_1)^2}\int_{Z_1}^{Z_2}(H^3 - H_S^3)^2 dZ \\
&\leq -\frac{1}{3\,\mathcal{C}\,(Z_2-Z_1)^2}\int_{Z_1}^{Z_2}(H^3 - H_S^3)^2 \times \\
&\left\{\frac{2H^3 + 4H^2H_S + 6HH_S^2 + 3H_S^3}{5(H^2 + HH_S + H_S^2)^2}\right\} dZ \\
&= -\frac{1}{3\,\mathcal{C}\,(Z_2-Z_1)^2}\int_{Z_1}^{Z_2}\left(\frac{2}{5}H^5 - H_S^3H^2 + \frac{3}{5}H_S^5\right) dZ \\
&= -\frac{\mathfrak{F}(H)}{3\,\mathcal{C}\,(Z_2-Z_1)^2},
\end{aligned}$$

where $\mathcal{C}$, which is strictly positive, is defined as

$$\mathcal{C} = \max_{T,Z}\left\{\frac{2H^3 + 4H^2H_S + 6HH_S^2 + 3H_S^3}{5(H^2 + HH_S + H_S^2)^2}\right\} \tag{5.14}$$

(the boundedness of $\mathcal{C}$ will be discussed momentarily). The final inequality sought is then given by

$$\frac{\mathfrak{F}(H,T)}{\mathfrak{F}(H,T=0)} \leq \exp\left\{\frac{-T}{3\mathcal{C}(Z_2-Z_1)^2}\right\}, \tag{5.15}$$

which confirms that the Lyapunov free energy of any disturbed state $H(Z,T)$ satisfying the same boundary conditions as the initial stationary state will decay back to the stationary state H_S at least as fast as an exponential with a decay rate that scales with the square of the spatial domain size. This proof applies to all categories of stationary solutions discussed in Chapter 4. For disturbance functions subject either to two Dirichlet conditions or one Dirichlet condition and one Neumann (constant flux) or constant volume condition, the proof is trivial since either $R(Z_1)$ or $R(Z_2)$ vanishes identically. For solutions H_S that correspond to fixed flux Q_S at one boundary and constant volume V_S, the proof above also applies since there always exists an interior point $Z_1 \leq Z^* \leq Z_2$ where $R\,(Z^*) = 0$. This follows because two solutions H and H_S cannot have the same constant volume unless the functions $H(Z,T)$ and $H_S(Z)$ undergo at least one crossing point within the domain.

5.2.1 Boundedness of $\mathcal{C}$ and dryout

We now address the boundedness of $\mathcal{C}$. In particular, we must show that $\mathcal{C}$ is bounded from above. We will also consider the conditions in which dryout, i.e., $H(Z,T) = 0$, might occur somewhere in the groove; if dryout occurs, the governing equation [Equation (5.1)] no longer applies, violating the premise in which stability is analyzed.

We first note that the constant $\mathcal{C}$ given by Equation (5.14), namely

$$\mathcal{C} = \max_{T,Z}\left\{\frac{2H^3 + 4H^2H_S + 6HH_S^2 + 3H_S^3}{5(H^2 + HH_S + H_S^2)^2}\right\} \tag{5.16}$$

satisfies the condition $\mathcal{C} \geq 0$ for $H(Z,T) > 0$ and $H_S(Z) > 0$. Assuming $H_S(Z)$ and $H(Z,T)$ remain bounded, then the function in brackets is observed to decrease monotonically with H and H_S since the derivatives

$$\frac{\partial}{\partial H}\left(\frac{2H^3+4H^2H_S+6HH_S^2+3H_S^3}{5(H^2+HH_S+H_S^2)^2}\right) = \tag{5.17}$$

$$-\frac{2H\left(H^3+3H^2H_S+6HH_S^2+5H_S^2\right)}{5\left(H^2+HH_S+H_S^2\right)^3} \tag{5.18}$$

and

$$\frac{\partial}{\partial H_S}\left(\frac{2H^3+4H^2H_S+6HH_S^2+3H_S^3}{5(H^2+HH_S+H_S^2)^2}\right) = \tag{5.19}$$

$$-\frac{3H_S^2\left(H^2+3HH_S+H_S^2\right)}{5\left(H^2+HH_S+H_S^2\right)^3} \tag{5.20}$$

are strictly negative. The largest possible value of the bracketed term in $\mathcal{C}$ is attained when that ratio is evaluated at the minima of $H_S(Z)$ and $H(Z,T)$ (which do not necessarily occur at the same point Z). It then follows that

$$\mathcal{C} \leq \left(\frac{2H_{\text{min}}^3+4H_{\text{min}}^2H_{S,\text{min}}+6H_{\text{min}}H_{S,\text{min}}^2+3H_{S,\text{min}}^3}{5(H_{\text{min}}^2+H_{\text{min}}H_{S,\text{min}}+H_{S,\text{min}}^2)^2}\right) \leq \frac{3}{5}\frac{1}{H_{S,\text{min}}}, \tag{5.21}$$

where H_{min} and $H_{S,\text{min}}$ denote H and H_S evaluated at their respective minima. Therefore, since $H_S(Z,T) > 0$ at all times, $\mathcal{C} < \infty$, and

$$\frac{\partial \ln[\mathfrak{F}(H)]}{\partial T} \leq -\frac{5H_{S,\text{min}}}{9\left(Z_2-Z_1\right)^2}. \tag{5.22}$$

We now consider when dryout can occur, i.e., when $H(Z,T)$ can go to 0, as well as whether $H(Z,T)$ can approach infinity.

Consider the behavior of Equation (5.1) in the vicinity of local extrema. Any local minimum of H will satisfy $\partial H/\partial Z = 0$, $\partial^2 H/\partial Z^2 \geq 0$ and thus $\partial H/\partial T \geq 0$, which leads to an increase in thickness due to the diffusive nature of the underlying equation of motion. Similarly, a local maximum of H cannot further increase in value. Therefore, any new extrema beyond those present in the initial condition can only be reached by possible extrema at the boundaries. For those solutions satisfying Dirichlet conditions at both endpoints of the domain, H can therefore never attain a new minimum below the minimum value of the initial condition nor attain a new maximum above the maximum value of the initial condition. This behavior guarantees that $\mathcal{C}$ will always remain bounded (from above and below). Similarly, so long as the initial condition satisfies $H(Z,T=0) > 0$, no dryout can occur either.

To assess the case of a Neumann, or flux, boundary condition, we recast Equation (5.1) not in terms of the local variable $H(Z,T)$ but the local flux $Q(Z,T) = -H^2\partial H/\partial Z =$

$-(1//3)\partial H^3/\partial Z^3$ by first multiplying Equation (5.1) by $-H/2$ followed by differentiation by Z, which yields

$$\frac{\partial Q}{\partial T} = \frac{\partial}{\partial Z}\left(H\frac{\partial Q}{\partial Z}\right) = H\frac{\partial^2 Q}{\partial Z^2} + \frac{\partial H}{\partial Z}\frac{\partial Q}{\partial Z}\,. \tag{5.23}$$

Adopting a similar argument as above, for any case requiring constant liquid volume, the prescribed fluxes at the endpoint must be equal, thereby imposing Dirichlet conditions on the flux Q. It then follows that $Q(Z,T)$ can never exceed the extrema present in the initial condition $Q(Z,T=0)$, which therefore precludes H from becoming arbitrarily large; hence $\mathcal{C}$ is again bounded below at all times. However, a sufficiently large flux condition with a thin initial film could drive the film thickness at that endpoint to 0, which in turn would make the boundary condition impossible to continue satisfying.

For cases subject to one Dirichlet and one flux boundary condition, the only way in which H might approach infinity is if the flux boundary condition is made very large. However, this would give rise either to an arbitrarily large internal flux extremum, which is disallowed by the previous argument, or an arbitrarily large flux of liquid at the boundary subject to the Dirichlet condition. For the latter case, the divergence in H at one endpoint would be driven by the flux condition at the other endpoint, such that the system would approach infinite volume and the Lyapunov functional would therefore not decrease as required. Hence, such a situation cannot occur, and H is therefore bounded above at all times and $\mathcal{C}$ bounded below at all times. And, again, a large flux condition with a thin initial film could create dryout at that endpoint, making the boundary condition impossible to satisfy.

Finally, for the case of a Dirichlet boundary condition coupled with a requirement of constant volume, were H to approach infinity at one boundary, the flux there would also diverge and be matched by identical divergence at the other end point in order to satisfy constant volume. But according to Equation (5.23), an interior flux minimum would have to undergo increase thus increasing the minimum slope of H^3, which would eventually violate the constraint of constant volume. Hence, in this case as well, H cannot diverge at any point in time and $\mathcal{C}$ therefore remains bounded below at all times. Furthermore, the second endpoint cannot decrease if it is a local minimum, and hence dryout cannot occur if the initial condition satisfies $H(Z,T=0)>0$.

In conclusion, setting a very large flux condition with a very thin initial film may cause dryout at that endpoint and make the boundary condition unsatisfiable, violating the premise of the analysis. With the exception of that situation, all stationary states, irrespective of the boundary conditions considered above, are exponentially stable. Furthermore, with the exception of dryout, the bracketed term in Equation (5.14) is strictly positive and bounded both above and below.

5.2.2 Aside: Exponential stability of the porous medium equation

The proof of exponential stability for non-rupturing states can be generalized from the V-groove equation to the n-dimensional porous medium equation (PME), $\partial_t \rho = \nabla^2 \rho^m$ with $m>1$, and Dirichlet boundary conditions on a bounded star-shaped domain Ω. Let ρ_S be the steady state

solution with the same boundary conditions, i.e., $\nabla^2 \rho_S^m = 0$. As with the V-groove, we can put the PME into gradient flow form, defining

$$\mathfrak{F}(\rho) \equiv \int_\Omega \mathcal{F}(\rho) d^n x = \int_\Omega \left[\frac{1}{m+1} \rho^{m+1} - \rho_S^m \rho + \frac{m}{m+1} \rho_S^{m+1} \right] d^n x,$$
$$R(\rho) \equiv \frac{\delta \mathfrak{F}}{\delta \rho} = \rho^m - \rho_S^m,$$

so that $\partial_t \rho = \nabla \cdot \nabla R(\rho)$ [note that this differs from Otto's gradient flow formulation of the PME (Otto, 2001), which is based on different boundary conditions, namely, ρ decaying to 0 at infinity]. Then,

$$\partial_t \mathfrak{F}(\rho) = \int_\Omega R(\rho) \partial_t \rho d^n x = -\int_\Omega \left[\nabla \left(\rho^m - \rho_S^m \right) \right]^2 d^n x < 0.$$

This demonstrates nonlinear, but not exponential, stability, and is similar to a result shown by Kern and Felderhof (1977). Using the Poincaré-Friedrichs inequality (Smith et al., 2016),

$$\partial_t \mathfrak{F}(\rho) \leq -a \int_\Omega \left(\rho^m - \rho_S^m \right)^2 d^n x \leq -\frac{a \mathfrak{F}(\rho)}{\mathcal{C}},$$

where a is a constant set only by the shape of Ω (Smith et al., 2016) and $\mathcal{C}$ is given by

$$\mathcal{C} \equiv \max_{t,\Omega} \left\{ \frac{\mathcal{F}(\rho)}{\left(\rho^m - \rho_S^m \right)^2} \right\} = \max_{t,\Omega} \left\{ \frac{\frac{1}{m+1} \rho^{m+1} - \rho_S^m \rho + \frac{m}{m+1} \rho_S^{m+1}}{\left(\rho^m - \rho_S^m \right)^2} \right\}.$$

Thus, if $\mathcal{C}$ is positive and bounded above, $\mathfrak{F}(\rho)$ will decay exponentially.

As with the specialized V-groove case, we proceed by showing that the argument of $\mathcal{C}$ is decreasing in ρ and ρ_S. Suppose m is rational, i.e., $m = p/q$, where $p > q > 0$ and $p, q \in \mathbb{Z}$. Let $w \equiv \rho^{1/q}$ and $w_S \equiv \rho_S^{1/q}$, where the positive real root is taken. Then,

$$\begin{aligned}
&\frac{\partial}{\partial \rho} \left[\frac{\mathcal{F}(\rho)}{\left(\rho^m - \rho_S^m \right)^2} \right] = \frac{-\frac{m-1}{m+1} \rho^{2m} + 2(m-1) \rho^m \rho_S^m - \frac{2m^2}{m+1} \rho^{m-1} \rho_S^{m+1} + \rho_S^{2m}}{\left(\rho^m - \rho_S^m \right)^3} \\
=& \frac{-q(p-q) w^{2p} + 2(p^2 - q^2) w^p w_s^p - 2p^2 w^{p-q} w_S^{p+q} + q(p+q) w_S^{2p}}{q(p+q)(w^p - w_S^p)^3} \\
=& -\frac{(w - w_S)^3}{(w^p - w_S^p)^3} \left\{ \sum_{j=0}^{p-q-1} \frac{(j+1)(j+2)}{2} w^j w_S^{2p-3-j} \right. \\
&+ \sum_{j=p-q}^{p-3} \frac{(p-q)}{q(p+q)} \left[-\frac{2p+q}{2} j^2 + \left(2p^2 - \frac{3}{2} q - 3p \right) j \right. \\
&\qquad \left. \left. - (p-1)(p^2 - pq - 2p - q) \right] w^j w_S^{2p-3-j} \right. \\
&\left. + \sum_{j=\max(p-q, p-2)}^{2p-3} \frac{(p-q)(j-2p+1)(j-2p+2)}{2(p+q)} w^j w_S^{2p-3-j} \right\} \leq 0
\end{aligned}$$

and

$$\frac{\partial}{\partial \rho_S}\left[\frac{\mathcal{F}(\rho)}{\left(\rho^m-\rho_S^m\right)^2}\right]=\frac{-m\frac{m-1}{m+1}\rho^{m+1}\rho_S^{m-1}+m\rho^m\rho_S^m-m\rho\rho_S^{2m-1}+\frac{m-1}{m+1}\rho_S^{2m}}{(\rho^m-\rho_S^m)^3}$$

$$=\frac{-p(p-q)w^{p+q}w_S^{p-q}+p(p+q)w^pw_S^p-p(p+q)w^qw_S^{2p-q}+p(p-q)w_S^{2p}}{q(p+q)(w^p-w_S^p)^3}$$

$$=-\frac{(w-w_S)^3}{(w^p-w_S^p)^3}\left\{\sum_{j=0}^{q-1}\frac{p(p-q)}{2q(p+q)}\frac{(j+1)(j+2)}{2}w^jw_S^{2p-3-j}\right.$$

$$+\sum_{j=q}^{p-3}\frac{p}{p+q}\left[-j^2+(p+q-3)j-\frac{1}{2}\left(q^2+pq-3p-3q+4\right)\right]w^jw_S^{2p-3-j}$$

$$\left.+\sum_{j=\max(p-2,q)}^{2p-3}\frac{p(p-q)}{2q(p+q)}\left(p+q-1-j\right)\left(p+q-2-j\right)w^jw_S^{2p-3-j}\right\}\leq 0.$$

In both cases, it is easy[1] to verify that every coefficient is nonpositive, and so the expression itself must be nonpositive. Because neither of these expressions has a singularity, we can extend the results from rational m to real m. Therefore, $\mathcal{C}$ is bounded above by its argument's value at $\rho\to 0$, $\rho_S\to\min_\Omega\rho_S$, i.e.,

$$\mathcal{C}\leq\frac{m}{m+1}\left[\min_\Omega\rho_S\right]^{-(m-1)}$$

and

$$\frac{\partial\ln[\mathfrak{F}(\rho)]}{\partial t}\leq -a\frac{m+1}{m}\left[\min_\Omega\rho_S\right]^{(m-1)}.$$

Hence, the PME in a bounded domain with Dirichlet boundary conditions is exponentially stable, as long as the steady state solution ρ_S is everywhere positive. In one dimension, the Poincaré-Friedrichs inequality holds for Neumann boundary conditions as well as Dirichlet, and so the result holds for Neumann boundary conditions in that case.

This result differs from that of Newman (1984) and Ralston (1984), who used a Lyapunov functional to show how a finite mass spreading in an infinite domain under the PME approaches self-similarity. Our result is similar to that of Kern and Felderhof (1977), who showed nonlinear (but not exponential) stability with a Lyapunov functional for a more general class of generalized

[1] Note that the minus sign is outside the braces, so one needs to show that each summand within the braces is nonnegative. Note also that each sum goes over a different set of indices j, so there is no adding terms between the different sums.
Each term in braces has three sums. Keeping in mind that $p>q$, the first summand is simply (positive const.)$\times(j+1)(j+2)$, which is clearly positive.
The second summand is quadratic in j, with negative quadratic term. Thus, it suffices to show that the term is positive for j at the extrema ($p-q$ and $p-3$ for the ∂_ρ equation; q and $p-3$ for the ∂_{ρ_s} equation). Substituting in these values indeed yields positive expressions.
The third summand contains a positive term times a product of two integers which differ by 1: $(j-2p+1)(j-2p+2)$ in the ∂_ρ equation and $(p+q-j-1)(p+q-j-2)$ in the ∂_{ρ_s} equation. Such products are clearly nonnegative (since there is no positive and negative integer pair which differ by 1).

diffusion equations with Dirichlet boundary conditions in a bounded domain; our contribution is to demonstrate exponential stability for the PME.

Note that for the U-grooves of Chen et al. (2006), the limiting cases of the nearly-rectangular groove and the highly rounded crescent-like groove both fall into the PME class, and hence have steady states with exponential nonlinear stability. The general U-groove equation does not fall into this class, but it does remain a nonlinear diffusion equation and hence exhibits nonlinear stability (though perhaps not exponential) via the proof by Kern and Felderhof (1977).

5.3 Generalized linear stability of self-similar states

Having demonstrated stability of steady states, we now proceed to self-similar spreading and draining states. Of course even if the fluid begins by spreading in a self-similar fashion from one end of a groove of finite length, it will eventually reach the other end and approach the steady state, as we have just proven. But during the initial spreading, before the fluid is "aware" that it is in a finite groove and not an infinitely long groove, we may ask whether this self-similar solution itself is locally stable. That is, can a small perturbation to the self-similar $t^{1/2}$ spreading cause the fluid to enter a different regime, perhaps with a different shape or spreading velocity? As the V-groove equation in self-similar coordinates is no longer amenable to Lyapunov analysis, we turn instead to a generalized linear stability analysis to answer this question.

Recall that the self-similar solutions to Equation (5.1) with a Dirichlet pressure (or height) boundary condition were governed by Equation (4.42), i.e.,

$$SS_{\eta\eta} + \eta S_\eta + 2(S_\eta)^2 = 0. \tag{5.24}$$

Given that the base state solutions to Equation (5.24) include advancing and receding states which vary in the self-similar variable, we appeal to a transient stability analysis to investigate their behavior. The stability of terminating solutions shown in Figure 4.6, however, will not be examined in this work because the point of termination requires that additional terms be included in the governing equation of motion to relieve the diverging stress known to occur at a moving contact line. Stability analyses for terminating solutions could be performed either by including a thin precursor film ahead of the contact line or by allowing a slip boundary condition near the termination point (Davis and Troian, 2003, 2004; Davis et al., 2006). Our approach will prove stability for all non-terminating self-similar base states, including films which have arbitrarily thin, yet nonzero, thickness ahead of the termination point. But since we do so while omitting Van der Waals terms, which are important below ≈ 0.01 microns, our result cannot be considered a true precursor film stability analysis.

To begin, we linearize the general solution according to

$$H(\eta, \tau) = S(\eta) + \delta H(\eta, \tau), \tag{5.25}$$

where $S(\eta)$ satisfies Equation (5.24) with the given boundary conditions, $\delta H(\eta, \tau)$ represents the infinitesimal non-modal disturbance function, and $\tau = \ln(T)$. Substituting this form into

Equation (5.1) yields the governing linear disturbance equation to order δH:

$$\frac{\partial \delta H}{\partial \tau} = \mathcal{L}[\delta H], \tag{5.26}$$

with

$$\mathcal{L} = \frac{S}{2}\frac{\partial^2}{\partial \eta^2} + \left(2S' + \frac{\eta}{2}\right)\frac{\partial}{\partial \eta} + \frac{1}{2}S'', \tag{5.27}$$

where primes denote differentiation by η. It can be shown that $\mathcal{L}$ has no positive eigenvalues for non-terminating solutions of S, i.e., the spectral abscissa $\beta_{\max}[\mathcal{L}] < 0$ (this fact will be proven later). Recall from Section 3.1, however, that this implies asymptotic stability under all inner product norms but only implies transient stability under the normalizing inner product. The normalizing inner product in this case turns out to be the L_2 inner product with integration weight $W = S^3 \exp\left(\int \frac{\eta}{S} d\eta\right)$. That is,

$$\int S^3 \exp\left(\int \frac{\eta}{S} d\eta\right) \delta H_1 \mathcal{L}[\delta H_2] d\eta = \int S^3 \exp\left(\int \frac{\eta}{S} d\eta\right) \delta H_2 \mathcal{L}[\delta H_1] d\eta. \tag{5.28}$$

This weight does not appear to correspond to any simple physical quantities. Furthermore, the nonlinear terms in Equation (5.1) have the simple forms HH'' and $(H')^2$, so that this norm will not likely be useful to determine when a perturbation becomes large enough for nonlinear effects to be important. Worst of all, this integration weight diverges as $\eta \to \infty$. This means that it effectively measures only very distant perturbations and ignores perturbations near $\eta = 0$, despite the fact that we should be most concerned about instability in the dynamic region at small η. Therefore, we must determine the transient stability of the system under a more useful norm rather than simply using the spectral abscissa to claim that the flow is stable.

Three natural choices of inner product immediately come to mind. First is simply the L_2 inner product. This measures physical height variations and gives no preference to different values of η. From a physical standpoint, one would be concerned about a fluid instability causing thinning or overfilling of the groove, which is measured by the fluid height. The second choice is the L_2 inner product with weight S^2. The integral $\int \delta H^2 S^2$ can be viewed as an L_2 inner product over the variation of H^2, which is proportional to the local cross-sectional area. Thus, this inner product measures volumetric deviations, rather than height deviations. A third natural choice would be the $\mathcal{H}_2$ inner product, $\langle \delta H_1, \delta H_2 \rangle = \int (\partial_\eta \delta H_1)(\partial_\eta \delta H_2) d\eta$. This inner product would be most appropriate for determining when the $(H')^2$ nonlinear term becomes significant, and can also be viewed as measuring velocity deviations, since the local average velocity is proportional to H'. The downside is that the $\mathcal{H}_2$ adjoint of $\mathcal{L}$ cannot be written in closed form.

In the following, we prove that linear perturbations to the self-similar spreading and draining states are asymptotically stable, and, under the L_2 inner product, transiently stable. Under the L_2 norm, the adjoint is given by:

$$\mathcal{L}^\dagger = \frac{S}{2}\frac{\partial^2}{\partial \eta^2} - \left(\frac{\eta}{2} + \frac{dS}{d\eta}\right)\frac{\partial}{\partial \eta} - \left(\frac{1}{2} + \frac{d^2 S}{d\eta^2}\right). \tag{5.29}$$

5.3.1 Generalized stability of volume non-conserving self-similar solutions

In what follows, we examine the generalized linear stability of self-similar non-terminating states on the finite domain $0 \leq \eta \leq \eta_B$. Recall from Section 3.1 that the fastest growth rate of perturbations is given by the numerical abscissa, $\omega_{\max}$, which is the least stable eigenvalue of the transient operator $(\mathcal{L} + \mathcal{L}^\dagger)/2$. Computing this transient operator using the non-normal linear operator $\mathcal{L}$ from Equation (5.27), we see that

$$\frac{\mathcal{L} + \mathcal{L}^\dagger}{2} = \frac{\partial}{\partial \eta}\left(\frac{S(\eta)}{2}\frac{\partial}{\partial \eta}\right) - \frac{1}{4}\left(1 + \frac{\partial^2 S}{\partial \eta^2}\right) \tag{5.30}$$

$$= \frac{S}{2}\frac{\partial^2}{\partial \eta^2} + \frac{1}{2}\frac{\partial S}{\partial \eta}\frac{\partial}{\partial \eta} - \frac{1}{4}\left(1 + \frac{\partial^2 S}{\partial \eta^2}\right), \tag{5.31}$$

which satisfies a Sturm-Liouville eigenvalue equation where

$$\left(\frac{\mathcal{L} + \mathcal{L}^\dagger}{2}\right) G(\eta, \tau) = \lambda\, G(\eta, \tau), \tag{5.32}$$

provided $S(\eta) > 0$ and S, $dS/d\eta$ and $d^2S/d\eta^2$ are continuous within the interval $0 \leq \eta \leq \infty$. As a result, the eigenvalues λ are strictly real and the corresponding eigenfunctions form a complete orthogonal set of basis functions. According to the definitions in Equation (3.5) then, if it can be shown that all the eigenvalues of $(\mathcal{L} + \mathcal{L}^\dagger)/2$ are strictly negative, then $\omega_{\max} < 0$ and disturbance growth is suppressed.

Note that the linear stability of the uniform state $S(\eta) = 1$, first shown by Weislogel (2001), is relatively easy to see. From the definitions given by Equations (5.31) and (5.32)), the relevant operator sum reduces to $(1/2)\,(\partial^2/\partial\eta^2) - (1/4)$, which is self-adjoint and therefore normal and whose eigenvalues are strictly real, negative and given by $-[(1/2)(n\pi/L)^2 + 1/4]$ for $n = 1$, 2, etc. According to Equation (5.32), the least stable disturbance $\delta G(\eta, \tau)$ will evolve in time according to $\exp\{-[(1/2)(n\pi/L)^2 + 1/4]\,\tau\}$ and therefore decay away, restoring the system back to the initial uniform self-similar state.

Proceeding to the self-similar advancing and draining states, we first note a lemma which will aid in the proofs.

Note: Sturm-Liouville sign convention

In the introduction to stability analysis in Section 3.1, we considered eigenvalue problems of the form $\partial_t u = \mathcal{L}u = \lambda u$ with a positive sign convention, so that $\lambda > 0$ implied instability and $\lambda < 0$ implied stability. However, Sturm-Liouville problems are traditionally written with a negative eigenvalue convention, as $\mathcal{L}u = -\mu u$. In order to maintain consistency with the remainder of the thesis, we continue to use a positive eigenvalue convention. But for the Sturm-Liouville lemma below, we write out both explicitly as $\mathcal{L}u = \lambda u = -\mu u$, with μ representing the negative-sign Sturm-Liouville eigenvalue.

Lemma 1. *Given a second order Sturm-Liouville eigenvalue equation of the form* $(P\,G_\eta)_\eta + Q\,G = \lambda G = -\mu G$ *where* $P > 0$, $G \neq 0$, μ *is real, and* $G(0) = G(\eta_B) = 0$, *then* $\mu_{min} > (-Q)_{min}$, *i.e.,* $\lambda_{max} < Q_{max}$

where subscripts denote differentiation with respect to the domain coordinate η.

In order for G to satisfy homogeneous conditions at the boundary points, it must be the case that there exists an extremum within the domain $[0, \eta_B]$ where $G_\eta(\eta^*) = 0$. Without loss of generality, the first such extremum from the origin may be assumed to be a local maximum in G for $G > 0$. (Note that G can always be made positive at this point by multiplying the local value by -1 and still remain an eigenfunction). Because PG_η must change sign on either side of this maximum, then at some point in its vicinity, $(PG_\eta)_\eta < 0$. This yields the relation $\mu > -Q(\eta^*)$, which therefore implies $\mu_{\min} > -Q(\eta^*) \geq (-Q)_{\min}$, where $(-Q)_{\min}$ denotes the smallest value of $-Q$ within the domain.

Transient and asymptotic stability of advancing solutions $S(\eta)$

We first examine the stability of advancing self-similar solutions shown in Figure 4.6. These solutions are all characterized by a downstream boundary value smaller than the inlet value, namely $S(\eta_B) = \text{const} < S(0) = 1$, and an inlet slope which is always negative, namely $S_\eta(0) < 0$. Here and in what follows, η_B represents the coordinate where the downstream boundary condition is applied.

Establishing that such states are linearly stable requires a finding that the largest eigenvalue of $(\mathcal{L} + \mathcal{L}^\dagger)/2$, namely $\lambda_{\max}$, is negative, which can be satisfied by

$$\lambda_{\max} < Q_{\max} = -(1 + S^{\min}_{\eta\eta})/4 < 0, \tag{5.33}$$

which in turn requires that $S^{\min}_{\eta\eta} > -1$. This minimum value can occur either at some interior point η_{int} or at the boundary points $\eta = 0, \eta_B$, which shall be examined separately. When the minimum value $S^{\min}_{\eta\eta}$ occurs at the downstream boundary point η_B, the inequality is easily satisfied for all solutions S, whether advancing or receding, since as evident from Figure 4.6, all the self-similar solutions asymptote to a uniform thickness, which therefore yields values $S_{\eta\eta}(\eta \to \eta_B) \to 0 > -1$.

When $S^{\min}_{\eta\eta}$ occurs at an interior point η_{int}, it will then be the case that $S^{\min}_{\eta\eta\eta}(\eta_{\text{int}}) = 0$. Differentiation of Equation (4.42) then yields the corresponding third order equation evaluated at the point η_{int}

$$\left[\left(\frac{S_\eta}{S^2} \right) [\, -S + (\eta + 2S_\eta)\,(\eta + 5S_\eta)\,] \right]_{\eta = \eta_{\text{int}}} = 0 \tag{5.34}$$

whose solutions are given by

$$S_\eta(\eta_{\text{int}}) = 0 \quad \text{or} \tag{5.35}$$

$$= \frac{-7\eta_{\text{int}} \pm \sqrt{9\eta_{\text{int}}^2 + 40S(\eta_{\text{int}})}}{20}, \tag{5.36}$$

which, when substituted into Equation (4.42), provides the value of the curvature at that interior point, namely

$$S_{\eta\eta}(\eta_{\text{int}}) = 0 \quad \text{or} \tag{5.37}$$

$$= -\frac{1}{5} + \frac{3\eta_{\text{int}}^2 \pm \eta_{\text{int}}\sqrt{9\eta_{\text{int}}^2 + 40S(\eta_{\text{int}})}}{50S(\eta_{\text{int}})}. \tag{5.38}$$

The minimal value of this relation is attained for the negative root, which as shown is always less than -1:

$$\begin{aligned} S_{\eta\eta}^{\min}(\eta_{\text{int}}) &= -\frac{1}{5} + \frac{3\eta_{\text{int}}^2 - \eta_{\text{int}}\sqrt{9\eta_{\text{int}}^2 + 40S(\eta_{\text{int}})}}{50S(\eta_{\text{int}})} \\ &= -\frac{1}{5} + \frac{3}{50}\ \frac{\eta_{\text{int}}}{\sqrt{S(\eta_{\text{int}})}}\ \left(\sqrt{\frac{\eta_{\text{int}}^2}{S(\eta_{\text{int}})}} - \sqrt{\frac{\eta_{\text{int}}^2}{S(\eta_{\text{int}})} + \frac{40}{9}}\right) \\ &\geq -\frac{1}{5} + \frac{3}{50}\ \times \left(-\frac{20}{9}\right) \qquad (5.39) \\ &> -1. \qquad (5.40) \end{aligned}$$

The last inequality derives from the general relation $\eta(\sqrt{\eta^2} - \sqrt{\eta^2 + k}) \geq -k/2$ for η and k real and positive.

When the minimum value of $S_{\eta\eta}$ occurs at the origin, evaluation of Equation (4.42) subject to the Dirichlet condition $S(0) = 1$ yields the criterion for stability, namely $S_{\eta\eta}(0) = -2S_\eta^2(0) > -1$. Since advancing solutions always exhibit negative slopes at the origin, this criterion can be rewritten as $S_\eta(0) > -1/\sqrt{2}$. That is, so long as every non-terminating solution satisfies $S_\eta(0) > -1/\sqrt{2}$, then said solutions are stable. We therefore must prove that all solutions with initial condition $S_\eta(0) \leq -1/\sqrt{2}$ are terminating solutions. Our numerical results show that in order for advancing solutions to remain strictly positive throughout the domain $[0, L\eta_B]$ and not yield a termination point, it must be the case that $S_\eta(0) \gtrsim -0.349$, which is clearly greater than $-1/\sqrt{2}$. The result can also be proven analytically using the following geometric argument.

Since $S_{\eta\eta}(0) = -2S_\eta^2(0) < 0$ while $S_\eta(\eta_B) = 0$, there must occur at least one inflection point in the domain $[0, \eta_B]$. Consider the first such inflection point at position η_p where $S_{\eta\eta}(\eta_p) = 0$. As shown in Fig. 5.1, since $S(\eta_p)$ lies below the extended line $1 + \eta_p S_\eta(0)$, then $S(\eta_p) < 1 + \eta_p S_\eta(0) = 1 - 2S_\eta(\eta_p)S_\eta(0) < 1 - 2S_\eta^2(0)$. These relations are found by noting that $S_\eta(\eta_p) = -\eta_p/2$ from Equation (4.42) and that $S_\eta(\eta_p) < S_\eta(0)$ where both slopes are negative. This then establishes that $S_\eta(0) > -1/\sqrt{2}$, which is proof that advancing solutions are linearly stable at all times.

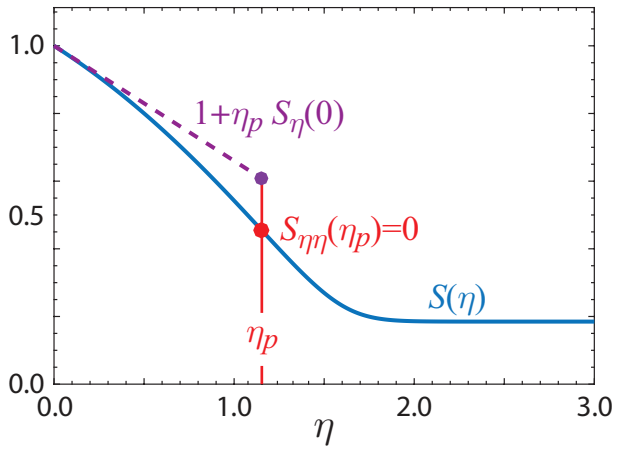

Figure 5.1: Representative self-similar solution $S(\eta)$ (blue solid line) for advancing state. The (red) dot designates the point η_P where there occurs the first inflection point away from the origin where $S_{\eta\eta}(\eta_p) = 0$. The (purple) dashed line represents a linear extension of the Taylor expansion of $S(\eta)$ about the origin to the point η_P.

Transient and asymptotic stability of receding solutions $S(\eta)$

We next examine the stability of receding solutions which are characterized by a downstream boundary value larger than the inlet condition, namely $S(\eta_B) = \text{const} > S(0) = 1$, and inlet slopes which are always positive, namely $S_\eta(0) > 0$. In order to make use of the lemma above, we first apply a change of variable to Equation (5.32) such that $G(\eta)$ is replaced by the product $S(\eta)G(\eta) > 0$. Straightforward calculation yields yet another Sturm-Liouville eigenvalue equation with weighting factor $S^2(\eta)$:

$$\left(\frac{\mathcal{M}+\mathcal{M}^\dagger}{2}\right) G(\eta,\tau) = \lambda S^2(\eta) G(\eta,\tau), \tag{5.41}$$

where

$$\left(\frac{\mathcal{M}+\mathcal{M}^\dagger}{2}\right) = \frac{\partial}{\partial\eta}\left(\frac{S^3}{2}\frac{\partial}{\partial\eta}\right) - \frac{S}{4}\left(\eta S_\eta + S\right). \tag{5.42}$$

The lemma applies here as well with an adjustment for the weighting factor, $\lambda_{\max} < (Q/S^2)_{\max}$, yielding the result

$$\lambda_{\max} < \max\left\{-\frac{1}{4S}\left(\eta S_\eta + S\right)\right\}. \tag{5.43}$$

Since for receding solutions all terms in the expression $S(\eta S_\eta + S)$ are strictly positive, then $\lambda_{\max}$, and hence $\omega_{\max}$, are strictly negative. This demonstration establishes that receding solutions are transiently and asymptotically linearly stable to any infinitesimal disturbances G satisfying homogeneous Dirichlet boundary conditions.

5.3.2 Numerical results and comparison to analytic bounds

Our numerical results for the operator exponential governing transient growth are next compared to analytic bounds derived above. Derivatives were constructed using second-order fi-

nite differences. (In discrete form, these operators are simply square matrices.) Homogeneous Dirichlet boundary conditions were enforced by directly reducing the operator matrices. The numerical abscissa $\omega_{\max}$ was obtained by identifying the largest eigenvalue of the corresponding reduced operator matrix $(\mathcal{L}+\mathcal{L}^\dagger)/2$ according to which $\omega_{\max}=\lambda_{\max}$. The spectral abscissa $\beta_{\max}$ was obtained by identifying the largest eigenvalue of the reduced matrix $\mathcal{L}$. The quantity $\ln(\|\exp(\mathcal{L}\tau)\|)$, representing the maximum instantaneous disturbance amplification, was obtained from the operator norm $\|\cdot\|$ given by the matrix maximum singular value. Shown in Fig. 5.2 are the numerical results for these three quantities plotted alongside the analytic bounds for $\lambda_{\max}$ given by $\max\{-(S/4)(\eta S_\eta+S)\}$ for receding solutions and $\max\{-(1+S_{\eta\eta})/4\}=-(1+S_{\eta\eta}^{\min})/4$ for advancing solutions.

As predicted, the values of $\ln\|\exp(\mathcal{L}\tau)\|$ for all times τ fall intermediate between the analytic upper bound, namely $\max\{-(S/4)(\eta S_\eta+S)\}$ for receding solutions or $-(1+S_{\eta\eta}^{\min})/4$ for advancing solutions, and the analytic lower bound given by $\beta_{\max}$. The numerical results also confirm that as $\tau\to\infty$, the slope of the function $\ln\|\exp(\mathcal{L}\tau)\|$ exactly equals the value $\beta_{\max}$, as must be the case since the asymptotic decay rate of disturbances is dictated by the eigenvalue of $\mathcal{L}$ with maximum real part.

The numerical results in Fig. 5.2 (and similar studies not shown of other receding and advancing states) reveal that there is no transient nor asymptotic growth of disturbances. Furthermore, the suppression of disturbances as quantified by $\ln\|\exp(\mathcal{L}\tau)\|$ asymptotes to the eigenvalue $\beta_{\max}$ already at early times $\tau<9.0$. The sudden drop off in the value $\ln\|\exp(\mathcal{L}\tau)\|$ observed near $\tau=8$ in Fig. 5.2(b) simply reflects onset of increased damping of disturbances incurred in the thin precursor film. All results presented were computed using spatial domains $0\le\eta\le\eta_B$ where $5\le\eta_B\le80$ with fixed mesh size ranging from 0.05 to 0.005. As shown in Fig. 5.3, a domain length of 80 was sufficiently long to ensure numerical convergence irrespective of mesh size. Note that the analytic bounds (dashed lines) are not sharp, and hence the numerical stability result does not approach those bounds. As the domain length increases, more and more of the film is flat, and the numerical abscissa appears to approach the flat-film value of $-1/4$.

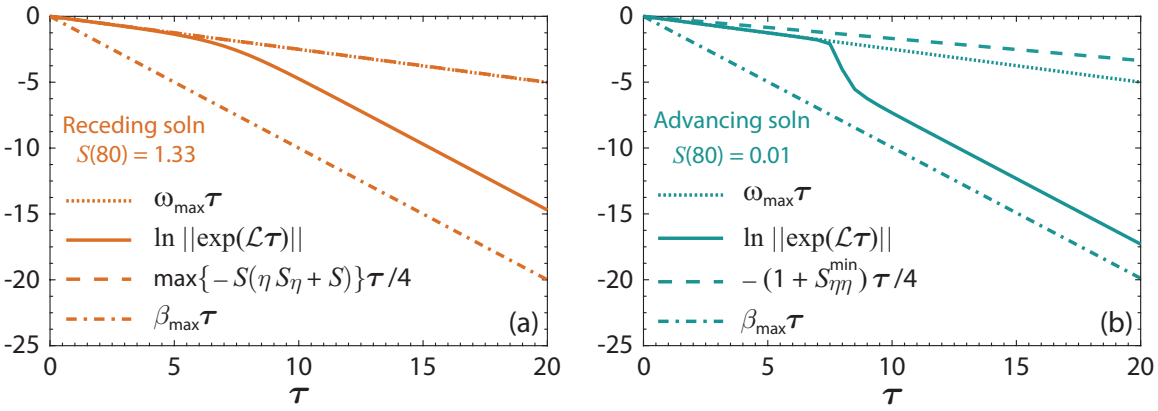

Figure 5.2: Analytic bounds and numerical results confirming transient and asymptotic stability of representative receding and advancing self-similar states shown in Figure 4.6.
Left: Results for receding state subject to Dirichlet condition $S(\eta = 80) = 1.33$. Note that lines depicting the numerical abscissa ($\omega_{\max}\tau$) and analytic bound ($\max\{-S(\eta S_\eta + S)\}\tau/4$) lie almost exactly on top of each other.
Right: Results for advancing state with Dirichlet condition $S(\eta = 80) = 0.01$.

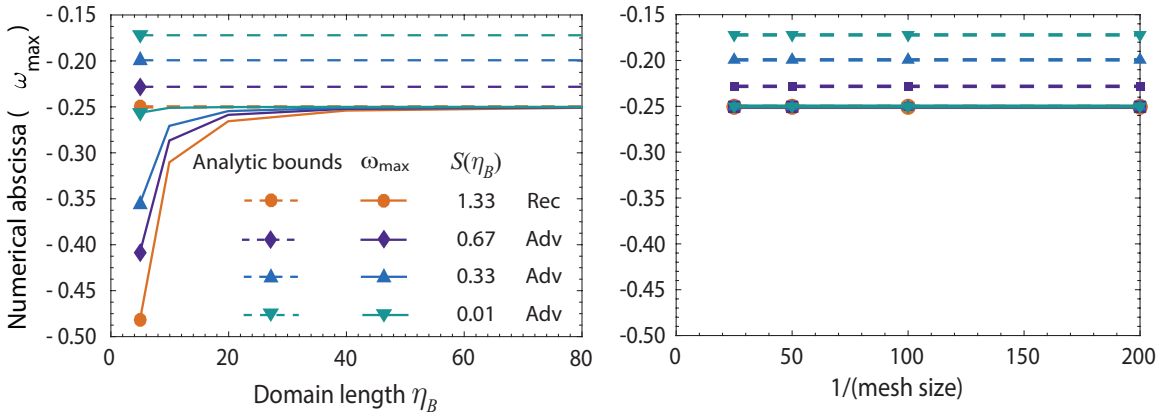

Figure 5.3: Results of convergence studies as a function of the domain length η_B (left, with mesh size), and of the inverse mesh size (right, with domain length $\eta_B = 80$). The labels Rec and Adv refer, respectively, to receding and advancing self-similar solutions shown in Figure 4.6. The analytic bound for the receding solution is given by $\max -(S/4)(\eta S_\eta + S)$, as defined in Equation (5.43). The analytic bounds for the advancing solutions are given by $(1 + S^{\min}_{\eta\eta})/4$, as defined in Equation (5.33).

5.4 Conclusion

In this chapter, we have examined the global and linear stability of solutions describing inertia-free flow of a thin wetting Newtonian film within an open slender V-groove of constant cross-section with constant liquid contact angle. The study is limited to flow states for which the interface function representing the local film thickness is always strictly positive thereby ruling out rupture states. The results furthermore require that the slender approximation be everywhere satisfied, which in turn sets an upper bound on the interface slope, namely, $(\partial h/\partial z)^2 \sim (d/L)^2 \sim O(\varepsilon^2)$. This constraint can be viewed as a low-pass filtering requirement which prevents low-frequency modes or disturbances from ever generating high-frequency modes. Consequently, neither the base states nor disturbances applied to these base states can trigger streamwise capillary waves. As noted by Yang and Homsy (2006), flow caused by streamwise curvature can also not be neglected in the limit $(\theta + \alpha) \to \pi/2$.

The steady state stability analysis was extended to the general PME, and in particular demonstrated exponential nonlinear stability for the limiting cases of nearly-rectangular and highly rounded crescent-like grooves of Chen et al.'s (2006) U-groove model. The general case of the U-groove does not fall into the PME class but remains a nonlinear diffusion equation, and hence exhibits nonlinear stability around the steady state. An analysis of the self-similar spreading solutions of the U-groove equation would likely require a numerical approach and is beyond the scope of this work.

The relevant base states for stability analysis include stationary interface states $H_S(Z)$ and self-similar states $S(\eta)$ which adopt the (dimensionless) Washburn scaling $\eta = Z/T^{1/2}$. The stationary states allow for various boundary conditions imposed at the ends of the channel including Dirichlet-Dirichlet, Dirichlet-Neumann (i.e., flux condition), Neumann-constant volume or Dirichlet-constant volume. The self-similar states are volume non-conserving and result from application of Dirichlet boundary conditions. By exploiting an analogy with other gradient flow equations and examining the asymptotic behavior of the corresponding Lyapunov function, it was shown that (strictly positive) stationary interface solutions represent exponentially stable equilibrium points. Disturbances of any type decay away exponentially fast to restore the system back to the initial stationary state. The second important result is that advancing, uniform and receding self-similar states satisfying Washburn dynamics are both transiently and asymptotically linearly stable to infinitesimal perturbations. This finding required implementation of a generalized non-modal linear stability analysis, since the non-constant nature of the self-similar states naturally gives rise to non-normal disturbance operators.

These two results provide motivation to use V-grooves as conduits for propellant delivery in the microfluidic electrospray propulsion (MEP) system, as they can avoid spontaneous overflow or dryout. But the analysis relied upon a straight V-groove with no external forces. The real MEP system will have regions with ambient electric fields, and also regions where the V-grooves must bend and curve in order to deliver the propellant fluid to the emitter needles. The next

chapter, Chapter 6, will consider the effect of electric fields on the V-groove flow and stability, and Chapter 7 will analyze curved V-grooves.

References

J. W. Cahn and J. E. Taylor. Surface motion by surface diffusion. Acta Metall. Mater., 42(4): 1045–1063, 1994. doi:10.1016/0956-7151(94)90123-6.

Y. Chen, M. M. Weislogel, and C. L. Nardin. Capillary-driven flows along rounded interior corners. J. Fluid Mech., 566:235–271, 2006. doi:10.1017/S0022112006001996.

J. M. Davis and S. M. Troian. Influence of attractive van der Waals interactions on the optimal excitations in thermocapillary-driven spreading. Phys. Rev. E, 67:016308, 2003. doi:10.1103/PhysRevE.67.016308.

J. M. Davis and S. M. Troian. Influence of boundary slip on the optimal excitations in thermocapillary driven spreading. Phys. Rev. E, 70:046309, 2004. doi:10.1103/PhysRevE.70.046309.

J. M. Davis, D. E. Kataoka, and S. M. Troian. Transient dynamics and structure of optimal excitations in thermocapillary spreading: Precursor film model. Phys. Fluids, 18(9):092101, 2006. doi:10.1063/1.2345372.

L. Giacomelli and F. Otto. Variational formulation for the lubrication approximation of the hele-shaw flow. Calc. Var. Partial Dif., 13(3):377–403, 2001. doi:10.1007/s005260000077.

D. Haake, J. Klatte, A. Grah, and M. E. Dreyer. Flow rate limitation of steady convective dominated open capillary channel flows through a groove. Microgravity Sci. Tec., 22(2): 129–138, 2010. doi:10.1007/s12217-009-9164-2.

D. E. Jaekle. Propellant management device conceptual design and analysis: Vanes. In AIAA/SAE/ASME/ASEE 27th Joint Propulsion Conference, June 24-26, 1991, Sacramento, CA, pages AIAA–91–2172. American Institute of Aeronautics and Astronautics, Reston, VA, 1991. doi:10.2514/6.1991-2172.

W. Kern and B. U. Felderhof. Stability of nonlinear diffusion. Z. Phys. B. Con. Mat., 28(2): 129–134, 1977. doi:10.1007/BF01325451.

D. Langbein. The shape and stability of liquid menisci at solid edges. J. Fluid Mech., 213: 251–265, 1990. doi:10.1017/S0022112090002312.

A. K. Mallik, G. P. Peterson, and M. H. Weichold. On the use of micro heat pipes as an integral part of semiconductor devices. J. Electron. Packaging, 114(4):436–442, 1992. doi:10.1115/1.2905477.

W. I. Newman. A Lyapunov functional for the evolution of solutions to the porous medium equation to self-similarity. I. J. Math. Phys., 25(10):3120–3123, 1984. doi:10.1063/1.526028.

F. Otto. The geometry of dissipative evolution equations: The porous medium equation. Commun. Part. Diff. Eq., 26(1-2):101–174, 2001. doi:10.1081/PDE-100002243.

J. Ralston. A Lyapunov functional for the evolution of solutions to the porous medium equation to self-similarity. II. J. Math. Phys., 25(10):3124–3127, 1984. doi:10.1063/1.526029.

L. A. Romero and F. G. Yost. Flow in an open channel capillary. J. Fluid Mech., 322:109–129, 1996. doi:10.1017/S0022112096002728.

L. W. Schwartz, R. V. Roy, R. R. Eley, and S. Petrash. Dewetting patterns in a drying liquid film. J. Colloid Interface Sci., 224:363–374, 2001. doi:10.1006/jcis.2000.7312.

F. Smith, T. Fearn, and S. Bullett. Advanced Techniques In Applied Mathematics. Ltcc Advanced Mathematics Series. World Scientific Publishing Company, 2016. doi:10.1142/q0007.

Y. Tang, X. Chen, and Y. Huang. Capillary flow rate limitation in asymmetry open channel. Chinese J. Aeronaut., 28(3):720–728, 2015. doi:10.1016/j.cja.2015.04.019.

G. F. Teletzke, H. T. Davis, and L. E. Scriven. How liquids spread on solids. Chem. Eng. Commun., 55:41 – 81, 1987. doi:10.1080/00986448708911919.

Y. Wei, X. Chen, and Y. Huang. Flow rate limitation in open wedge channel under microgravity. Sci. China: Phys. Mech. Astron., 56(8):1551–1558, 2013. doi:10.1007/s11433-013-5086-5.

M. M. Weislogel. Capillary flow in interior corners: The infinite column. Phys. Fluids, 13(11): 3101–3107, 2001. doi:10.1017/S0022112098002535.

N. C. White and S. M. Troian. Why capillary flows in slender triangular grooves are so stable against disturbances. Phys. Rev. Fluids, 4(5):054003, 2019. doi:10.1103/PhysRevFluids.4.054003.

L. Yang and G. M. Homsy. Steady three-dimensional thermocapillary flows and dryout inside a v-shaped wedge. Phys. Fluids, 18:042107, 2006. doi:10.1063/1.2193471.

L. Yang and G. M. Homsy. Capillary instabilities of liquid films inside a wedge. Phys. Fluids, 19:044101, 2007. doi:10.1063/1.2716632.

Chapter 6

ELECTRIFIED CAPILLARY FLOW OF A PERFECTLY CONDUCTING FILM IN A SLENDER V-GROOVE CHANNEL: STEADY STATE, SELF SIMILAR, AND GENERALIZED STABILITY ANALYSIS

6.1 Introduction

The microfluidic electrospray propulsion (MEP) thruster operates by creating electric field above emitter needles, and hence inducing the formation of liquid metal cones which subsequently emit ions or droplets. The electric field will be concentrated at the emitter tips, and weaker but still existent on the emitter sides and array floor (simply due to these regions being farther from the electrodes), where the propellant delivery V-grooves are located. Hence we seek to understand the effect of an electric field on the flow behavior and stability of a conducting liquid in a V-groove.

Electric fields are known to destabilize conducting liquid films on flat surfaces, and thus the question immediately arises of whether and when such a phenomenon can occur in V-groove flow, potentially impairing the functionality of applications such as the MEP. The effect in flat films has been known since at least the time of Zeleny (1914), who observed the disintegration of droplets of hydrochloric acid upon exposure to strong electric fields. Tonks (1935) provided perhaps the first theoretical analysis, explicitly balancing capillary pressure, the Maxwell pressure induced by an electric field on the surface of a conducting liquid, and gravity, and thus giving an estimate of the required field strength for a bump-like perturbation of a given length to be unstable. Frenkel (1936) extended the work of Tonks by performing a formal linear stability analysis, arriving at the same critical field strength $E_{crit.} = 2\sqrt{\pi}(g\rho\gamma)^{1/4}$ required to induce instability with a sinusoidal perturbation wavelength proportional to the size of Tonks's bump. Notably, their results showed that for a flat film of infinite extent under a uniform electric field, the system will always be unstable if there is no gravity. But the weaker the electric field, the longer the wavelength of unstable perturbations, and hence a bounded system may be stable. While these original results were computed for an inviscid fluid, the same behavior and critical field strength apply to viscous films as well (de Surgy et al., 1993). We will see in this chapter that, even in the absence of gravity, V-groove flow is not unstable at arbitrary low electric fields due to the capillary pressure penalty of increasing the fluid thickness in the groove. However, for sufficiently high electric fields, the system will destabilize.

The Weislogel (1996) and Romero and Yost (1996) model can be extended fairly easily to include additional forces or stresses, as long as the system obeys the slender limit. Additional forces will introduce extra terms in the bulk and/or boundary condition equations, and further turn induce a change in the fluid interface shape, which will no longer necessarily be circular. Thus, while the integrated continuity equation $\partial A/\partial T = -\partial Q/\partial Z$ will still hold, the computation of

the flux Q and the cross-sectional area A may be modified. These modifications are typically semi-analytic; that is, a numerical approach may be needed to solve for A and Q across a range of parameters, just as it was necessary to numerically solve for the flux constant Γ for a range of α and θ values in the original model (note that in the specific cases considered in this work, we show the correction to A to be small and leave it out).

The first study including extra forces the basic V-groove flow model was the addition of gravity by Weislogel (1996), as discussed in Chapter 4. An external tangential shear stress was introduced by Su and Lai (2004), who developed it as a general model without considering specific applications. They performed numerical simulations with a monotonically increasing or decreasing shear stress, to show how flow spreading from a constant-pressure or constant-flux boundary condition could be sped up or slowed down. Yang and Homsy (2006) produced a similar model (apparently independently) in order to describe V-groove flow with a thermocapillary effect, wherein a varying temperature field induces a varying surface tension strength, and hence a tangential Marangoni stress on the interface. Yang and Homsy (2006) considered only configurations with stationary interface (which may still have underlying flow), and showed that certain temperature fields can induce a stationary state with regions where the film thickness $H \to 0$, i.e., the film dries out. Della Rocca and Troian (2013) constructed a model of a perfectly conducting fluid flowing in a V-groove with the addition of an electric field, under the assumption that the field is independent of the liquid interface and groove shape and determined only by far-field conditions. Such a model might be relevant in the thick-film regime, in which the fluid nearly fills the V-groove.

In this work, we develop a novel model of the thin-film limit of V-groove flow of a perfectly conducting liquid under an electric field and study both its base state behavior and its stability. Our model is developed as an extension of the model of Weislogel (1996) and Romero and Yost (1996), and similarly produces a nonlinear second-order partial differential equation (PDE) describing the evolution of fluid interface midline thickness, h, in time (t) and in z, an axial dimension along the groove. We will consider only electric fields weak enough that the sensitivity to fluid thickness of the capillary pressure at the interface is greater than Maxwell pressure. The reason for this is that capillary pressure increases with the fluid interface midline thickness h, while Maxwell pressure decreases. Hence the capillary effect induces stability and "self-regulation," as regions that are thick with fluid will have high pressure and push the excess towards thinner regions. The Maxwell pressure, on the other hand, induces a positive feedback driving thick regions to become thicker and thicker. As long as the thickness (h) sensitivity of the capillary pressure is greater than that of the Maxwell pressure, i.e., $|\partial p_{\text{capillary}}/\partial h| > |\partial p_{\text{Maxwell}}/\partial h|$, then the fluid will remain in the self-regulating regime and a slender-limit model approach can be effective. In order to construct an analytic form of the Maxwell pressure, p_{Maxwell}, the fluid thickness is assumed to be small relative to the depth of the groove; specifically, $(d/b)^2 \ll 1$, where d is the characteristic fluid thickness and b is the groove depth. The limits of this regime and exact conditions for the threshold thickness at which it is violated will be

discussed. Note also that, due to the slender limit assumption, the pressure will be taken to be constant in the cross-section of the groove. That is, although capillary and Maxwell pressure are applied at the fluid interface, their effect will extend throughout the depth of the fluid.

An electric field will produce a normal stress if the liquid is a perfect conductor or perfect dielectric, and both normal and tangential stresses if the fluid is instead a leaky dielectric due to the accumulation of of charge on the interface (Saville, 1997). We will first outline the derivation of the general equation of motion for a liquid in a V-groove with an electric field, without assumptions about the electrical characteristics of the liquid. We will then fully develop the case of a perfectly conducting liquid in a groove with perfectly conducting walls, that being the relevant application.

Section 6.2 will develop the equations of motion for flow in a V-groove under a general electric field, without assumptions about the conductivity of the fluid or substrate, and without assumptions about the fluid thickness relative to the groove depth. Section 6.3 will derive an approximate expression for the electric field distribution in a V-shaped groove with perfectly conducting walls and liquid, and Section 6.4 will combine these results into an equation of motion for a perfectly conducting fluid in a perfectly conducting V-groove with depth much greater than the fluid thickness. Section 6.5 will demonstrate stationary and self-similar solutions. In Section 6.6, we perform a nonlinear stability analysis of stationary solutions and a non-normal linear stability analysis of self-similar solutions, following the methodology of Chapter 5. Section 6.7 will provide numerical support for some of the approximations used in the model, determining the regimes of validity. Section 6.8 will conclude and discuss a few remaining issues.

6.2 V-groove model with Maxwell stress

The V-groove flow model of Weislogel (1996) and Romero and Yost (1996) is generalized to include an electric field. Let the interior half angle of a straight V-groove be denoted α (note that we follow Weislogel's convention of α being the internal groove half angle, rather than Romero and Yost's convention of α being the exterior groove angle), and the wetting angle of the fluid against the wall be θ (Figure 6.1). An electric field is produced by some means far above the fluid interface. The characteristic length of the groove is L, which is much longer than the fluid interface midline thickness h, the latter characterized by its maximum, d.

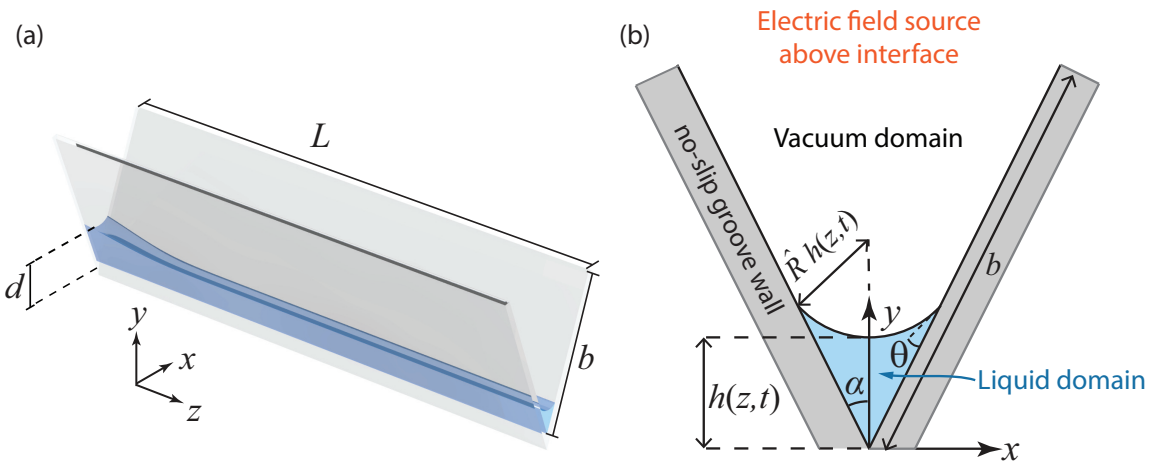

Figure 6.1: Diagrams of V-groove flow system with electric field. (a) Schematic of a perfectly conducting, wetting liquid film ($0 \leq \theta < \pi/2$) flowing within a slender open triangular groove with constant cross-section and perfectly conducting walls. The maximum midline film thickness is denoted by $d = h(x = 0, z = 0, t)$ (note that we follow Weislogel's convention of measuring the midline film thickness, rather than Romero and Yost's convention of the film thickness at the wall) and the channel length by L where $(d/L)^2 \ll 1$. The groove depth, measured along the wall, is denoted by b. (b) Cross-sectional view of the flow geometry depicted in (a) where $h(z,t)$ denotes the local midline film thickness, α is the groove interior half angle (note that we follow Weislogel's convention of α being the internal groove half angle, rather than Romero and Yost's convention of α being the exterior groove angle), $\hat{R}h$ is the radius of curvature of the liquid interface and θ is the contact angle of the liquid wetting the channel sidewalls, which is assumed constant.

6.2.1 Key model assumptions

Several important assumptions underlie the model developed in the following sections, restricting its domain of validity.

The first set of assumptions is exactly those required for the viscous V-groove model without an electric field, described in Chapter 4. The liquid is assumed to be Newtonian and incompressible, as well as isothermal. The geometry is assumed to satisfy the slender limit, in which the slender parameter, $\varepsilon = (d/L)$, satisfies $\varepsilon^2 \ll 1$, where d is the characteristic fluid thickness and L is the characteristic groove length scale. Working in the slender limit allows the pressure to be approximated as constant in the cross-section of the groove; thus, although the capillary and Maxwell forces are applied at the interface, the resulting pressure extends throughout the depth of the fluid. The fluid is assumed to be sufficiently thick that Van der Waals forces between the fluid and wall [which are important in the extremely thin film limit, typically for $d \lesssim O(0.01\ \mu\text{m})$] may be ignored. The region outside the liquid is assumed to be a vacuum. The liquid is assumed to be purely viscous, i.e., all inertial effects are ignored. This condition is valid when $\varepsilon \text{Re} \Gamma = \varepsilon^2 \rho \gamma d \Phi \Gamma / \mu^2 \ll 1$, where $\varepsilon = (d/L)$ is the slender parameter, ρ is fluid density, γ is surface tension, μ is dynamic viscosity, and Γ is a geometric factor depending on

α and θ. $\Phi = \mathrm{Ca}$ is the slender limit capillary number, which will be shown later to reduce to a geometric factor depending only on α and θ. Numerical results show that $\Phi < 0.0335$, a bound which was computed numerically [see Figure 6.3]. In this work, the characteristic fluid thickness d is taken to be the maximum fluid thickness. Furthermore, the thickness of the fluid is assumed to be much smaller than the length scale of axial variations. Note that, given ρ, μ, and γ of a particular liquid, the film being sufficiently thin (i.e., having small enough $d \ll [\mu^2 L^2/(\Phi\Gamma\gamma\rho)]^{1/3}$) is sufficient to ensure the noninertial condition is satisfied. As an example, consider liquid indium (viscosity $\mu = 1.60 \times 10^{-3}$ Pa s, surface tension $\gamma = 0.57$ N/m, and density $\rho = 7000$ kg/m^3 [Assael et al.; Chentsov et al., 2012; 2011]) and a groove with interior half angle $\alpha = 45^\circ$, fluid contact angle $\theta = 15^\circ$, $d = 5\mu$m, $L = 200\mu$m. Then $\Phi \approx 0.024$, $\Gamma \approx 0.078$, and thus $\varepsilon\mathrm{Re} \approx 0.12$ and $\varepsilon\mathrm{Re}\Gamma \approx 0.009 \ll 1$. Water (viscosity $\mu = 10^{-3}$Pa s, surface tension with air $\gamma = 0.07$ N/m, density $\rho = 1000$ kg/m^3 [Batchelor, 2000]) in a groove of the same dimensions would have $\varepsilon\mathrm{Re} \approx 0.005$ and $\varepsilon\mathrm{Re}\Gamma \approx 0.0004 \ll 1$.

The internal groove half angle, α, is assumed to be constant, as is the liquid wetting angle, θ. In particular, corrections due to the dynamic variation of θ with fluid velocity are not considered. The fluid is assumed to be isothermal, and its density, ρ, viscosity, μ, and surface tension, γ, are similarly assumed to be constant.

In this work, gravitational effects are ignored; specifically, it is assumed that the Bond number $\mathrm{Bo} = \rho g d^2/\gamma \ll \varepsilon\Phi$, where g is gravitational acceleration. This can be achieved with a sufficiently thin film, or with a thicker film in a low gravity environment. As an example, taking values for liquid indium and a groove with $\alpha = 45^\circ$, $\theta = 15^\circ$, $d = 5\mu$m, $L = 200\mu$m, and using Earth gravity of $g = 9.8$ m/s^2, then $\mathrm{Bo}/(\varepsilon\Phi_0) \approx 0.005 \ll 1$. Water in a groove of the same dimensions would have $\mathrm{Bo}/(\varepsilon\Phi_0) \approx 0.006 \ll 1$.

Additional assumptions specific to the electric field model of this work are also required. The electric field distribution outside the groove is assumed to be time-independent, and slow-varying along the groove axis; specifically, the it is assumed that the variation in the electric field measured at the top of the groove has a length scale of at least $O(L)$. This assumption will be applied in Section 6.2, in which the blueprint of deriving a reduced order model for flow in a V-groove with an electric field is presented, without assumptions on the electrical properties of the liquid itself.

Following the generalized derivation in Section 6.2, a specific derivation is carried out from Section 6.3 onward, requiring additional constraints on the electric field and material properties of the system. It will be assumed that both the liquid and the groove walls are perfect conductors, and further that the thickness d of the film is smaller than the groove depth, b; specifically, $(d/b)^2 \ll 1$. These assumptions will allow analytic determination of the relevant electric field distributions, and further are relevant to the MEP device, which uses a liquid metal propellant and a substrate which has been precoated with liquid metal. A smoothness condition for the transverse variation across the groove of the outside electric field will also be required, details of

which are discussed in Section 6.3. It will be assumed that the thickness (h) sensitivity of the capillary pressure is greater than that of the Maxwell pressure, i.e., $|\partial p_{\text{capillary}}/\partial h| > |\partial p_{\text{Maxwell}}/\partial h|$; electric fields exceeding this value are likely to cause fluid breakup and prevent flow in the groove. This constraint can be expressed as $\psi_0^{\text{outer}} < (\alpha/\pi)\sqrt{(2b^2/\epsilon_0)[\gamma/(d\widehat{R})][1/(m\widehat{C})(b/d)^m}$ [Equation (6.47)], where ψ_0^{outer} is the first term in a cosine transform of the electric potential at the top of the groove, ϵ_0 is the permittivity of free space, $\widehat{R}(\alpha,\theta)$ is a geometric factor determining the interface curvature, $m = (\pi/\alpha) - 2$ is the Maxwell pressure exponent in the groove, and $\widehat{C}$ is an $O(1)$ geometric factor reflecting the groove shape and external electric field. Finally, it will be assumed that the electric field does not induce a significant change in the cross-sectional interface shape, and hence assumed that one can use the cross-sectional area, flux factor, and capillary pressure of the V-groove with no electric field. This assumption is evaluated numerically in Section 6.7 to confirm its validity.

Note that the analysis does not assume that the electric field and liquid interface are independent; rather, the electric field depends on the liquid thickness and is updated accordingly, affecting in turn the Maxwell pressure on the liquid. However, due to the slender limit and slow-varying electric field assumptions, the axial curvature of the interface is assumed not to affect the electric field. For systems not subject to the slender limit, the feedback between interface shape of a conducting liquid and electric field distribution can lead to rapid interface acceleration and the formation of conic liquid structures; see, for example, Albertson and Troian (2019); Zhou and Troian (2021).

6.2.2 Bulk equations

The continuity and Navier-Stokes equations are given by

$$\nabla \cdot \vec{u} = 0, \tag{6.1}$$

$$\rho\left[\frac{\partial \vec{u}}{\partial t} + (\vec{u}\cdot\nabla)\,\vec{u}\right] = -\nabla p + \mu\nabla^2\vec{u} \tag{6.2}$$

where the velocity field in Cartesian coordinates is represented by $\vec{u} = (u, v, w)$, the fluid pressure by $p(x, y, z)$, and the constant fluid density by ρ. Note that additional bulk forces due to the electric field would arise in Equation (6.2) if the permittivity within the fluid varied (e.g., due to density or temperature variations), or if there were free charges (such as in an ionic liquid) (Landau and Lifshitz, 1984); we do not consider these cases.

We nondimensionalize just as in Chapter 4, and relevant quantities are listed in Table 6.1. Note in particular that we set the characteristic velocity and time scales using the capillary pressure, rather than the Maxwell pressure, because of the requirement that capillary pressure thickness sensitivity dominate Maxwell pressure thickness sensitivity (a condition which will be satisfied if the capillary pressure is sufficiently large compared to the Maxwell pressure). The capillary pressure is thus the natural reference for nondimensionalizing velocity and other variables.

Quantity	Scaling	Rescaled variable
Slender parameter		$\varepsilon = d/L; \quad \varepsilon^2 \ll 1$
Thin film parameter (film thickness/groove depth)		$\delta = d/b; \quad \delta^2 \ll 1$
Coordinates	$x_c = d$	$X = x/x_c$
	$y_c = d$	$Y = y/y_c$
	$z_c = L$	$Z = z/z_c$
Polar coordinates	r, β	
Velocity	$u_c = \varepsilon w_c$	$U = u/u_c$
	$v_c = \varepsilon w_c$	$V = v/v_c$
	$w_c = \varepsilon\gamma \mathrm{Ca}/\mu$	$W = w/w_c$
Streamwise flux	$q_c = d^2 w_c$	$Q = [\int_\Omega w dx dy]/q_c$
Stress tensor (in vacuum)	$\widetilde{\tau}_{\mathsf{vac.}}$ (Eq. 6.6)	
Stress tensor (in liquid)	$\widetilde{\tau}_{\mathsf{liq.}}$ (Eq. 6.7)	
Electric potential (in vacuum)	ψ_c	$\Psi = \psi/\psi_c$
Electric potential (in liquid)		$\Psi^{\mathsf{liq.}} = \psi^{\mathsf{liq.}}/\psi_c$
Relative permittivity		$\epsilon_r = \epsilon_{\mathsf{liq.}}/\epsilon_0$
Interface electric field strength		$\chi(Z) = [(\mathrm{We}\widehat{R})/2](\psi_0^{\mathsf{outer}}(z)/\psi_c)^2 \widehat{C}$
Electric field	$E_c = (\psi_c/b)(\pi/\alpha)(d/b)^{[\pi/(2\alpha)]-1}$	
Pressure	$p_c = \mu w_c/(\varepsilon d)$	$P = p/p_c$
Rescaled pressure		$\overline{P} = P\mathrm{Ca}\widehat{R}$
Time	$t_c = L/w_c$	$T = t/t_c$
Interface midline thickness	$y_c = d$	$H = h(z,t)/y_c$
Interface shape	$y_c = d$	$\Sigma(X,Z,T) = \sigma(x,z,t)/y_c$
Stationary state midline thickness		$H_S(Z)$
Self-similar variable		$\eta = Z/\sqrt{T}$
Self-similar state midline thickness		$S(\eta)$
Reynolds number		$\mathrm{Re} = \rho w_c d/\mu$
Slender limit capillary number		$\mathrm{Ca} = w_c\mu/(\varepsilon\gamma) = \Phi(\alpha,\theta)$

Electric Weber number	$\mathrm{We} = \epsilon_0 E_c^2 d/\gamma = \mathrm{Ca}\epsilon_0 E_c^2 (d\varepsilon)/(w_c \mu)$
Maxwell pressure exponent	$m = (\pi/\alpha) - 2$
Electric geometric factor (Eq. 6.36)	$\widehat{C}(\alpha, \theta, \text{electrode geom.}) = O(1)$

Table 6.1: Characteristic scalings and nondimensional variables used to describe dimensionless system shown in Figures 6.1 and 6.4. Note that $\psi_0^{\text{outer}}(z)$ denotes the 0th order term in a cosine transform of the applied electric field at the top of the groove, $r = b$ (see Section 6.3.2).

The dimensionless forms of Equations (6.1) and (6.2) are then given by

$$0 = \partial_X U + \partial_Y V + \partial_Z W, \tag{6.3a}$$

$$\varepsilon^3 \mathrm{Re} \frac{DU}{DT} = -\partial_X P + \varepsilon^2 \left[\partial_{XX} + \partial_{YY} + \varepsilon^2 \partial_{ZZ}\right] U, \tag{6.3b}$$

$$\varepsilon^3 \mathrm{Re} \frac{DV}{DT} = -\partial_Y P + \varepsilon^2 \left[\partial_{XX} + \partial_{YY} + \varepsilon^2 \partial_{ZZ}\right] V, \tag{6.3c}$$

$$\varepsilon \mathrm{Re} \frac{DW}{DT} = -\partial_Z P + \left[\partial_{XX} + \partial_{YY} + \varepsilon^2 \partial_{ZZ}\right] W, \tag{6.3d}$$

where D/DT is the dimensionless material derivative

$$\frac{D}{DT} = \partial_T + U\partial_X + V\partial_Y + W\partial_Z. \tag{6.4}$$

In the limits where $\varepsilon^2 \ll 1$, $\varepsilon\,\mathrm{Re} \ll 1$, the governing equations, Equation (6.3), then reduce to

$$\partial_X U + \partial_Y V + \partial_Z W = 0, \tag{6.5a}$$

$$\partial_X P = 0 + O(\varepsilon^2), \tag{6.5b}$$

$$\partial_Y P = 0 + O(\varepsilon^2), \tag{6.5c}$$

$$\partial_Z P = \partial_{XX} W + \partial_{YY} W + O(\varepsilon^2). \tag{6.5d}$$

6.2.3 Boundary conditions at the liquid interface

The two (dimensional) boundary conditions specifying the jump in normal and tangential stresses across the gas/liquid interface $\sigma(x, z, t)$ can be written in terms of the stress tensor inside the liquid, $\widetilde{\tau}_{\text{liq.}}$, and the vacuum region stress tensor $\widetilde{\tau}_{\text{vac.}}$. (Note that $\widetilde{\tau}$ here represents the full stress tensor including the pressure, not the deviatoric stress tensor.)

Letting the electric field in the vacuum region be represented by ψ and the electric field within the liquid be represented by $\psi^{\text{liq.}}$, the stress tensors become

$$\widetilde{\tau}_{\text{vac.}ij} = \epsilon_0 \left[\nabla_i \psi \nabla_j \psi - \frac{1}{2}\delta_{ij} \nabla_k \psi \nabla_k \psi\right] \tag{6.6}$$

$$\widetilde{\tau}_{\text{liq.}ij} = \mu[\nabla_i u_j + \nabla_j u_i] - p\delta_{ij} + \epsilon_{\text{liq.}} \left[\nabla_i \psi^{\text{liq.}} \nabla_j \psi^{\text{liq.}} - \frac{1}{2}\delta_{ij} \nabla_k \psi^{\text{liq.}} \nabla_k \psi^{\text{liq.}}\right] \tag{6.7}$$

where δ_{ij} is the identity matrix (Saville, 1997). The external pressure has, without loss of generality, been set to a reference pressure of 0.

The interfacial stress balance conditions are then

$$\left[\hat{n}\cdot(\widetilde{\tau}_{\text{liq.}}-\widetilde{\tau}_{\text{vac.}})\cdot\hat{n}+\gamma(\nabla_s\cdot\hat{n})\right]_{y=\sigma(x,z,t)}=0, \tag{6.8a}$$

$$\left[\hat{t}_{i=1,2}\cdot(\widetilde{\tau}_{\text{liq.}}-\widetilde{\tau}_{\text{vac.}})\cdot\hat{n}\right]_{y=\sigma(x,z,t)}=0, \tag{6.8b}$$

where $\nabla_s=(\nabla-\hat{n}(\hat{n}\cdot\nabla))$ is the surface gradient operator, and the triad $(\hat{n},\hat{t}_x,\hat{t}_z)$ is the three unit vectors representing directions normal and tangent to the moving interface with the convention that $\hat{n}$ points away from the fluid.

In rescaled units, the unit vectors are given by

$$\hat{N}=\frac{1}{[1+(\partial_X\Sigma)^2+\varepsilon^2(\partial_Z\Sigma)^2]^{1/2}}\begin{pmatrix}-\partial_X\Sigma\\1\\-\varepsilon\partial_Z\Sigma\end{pmatrix}, \tag{6.9a}$$

$$\hat{T}_X=\frac{1}{[1+(\partial_X\Sigma)^2]^{1/2}}\begin{pmatrix}1\\\partial_X\Sigma\\0\end{pmatrix}, \tag{6.9b}$$

$$\hat{T}_Z=\frac{1}{[1+\varepsilon^2(\partial_Z\Sigma)^2]^{1/2}}\begin{pmatrix}0\\\varepsilon\partial_Z\Sigma\\1\end{pmatrix}, \tag{6.9c}$$

where $\Sigma(X,Z,T)=\sigma(x,z,t)/d$ denotes the nondimensional interface function and subscripts denote differentiation with regard to the rescaled coordinates.

To order $O(\varepsilon^2)$ then, the dimensionless normal boundary condition reduces to the form

$$\begin{aligned}0=&-P|_{Y=\Sigma(X,Z,T)}-\mathrm{Ca}^{-1}\left(\frac{\partial_X^2\Sigma}{[1+(\partial_X\Sigma)^2]^{3/2}}\right)\\&+\frac{\mathrm{We}}{\mathrm{Ca}}\left\{\left[\frac{1}{2}\left|\nabla\Psi\right|^2-\left(\hat{N}\cdot\nabla\Psi\right)^2\right]-\epsilon_r\left[\frac{1}{2}\left|\nabla\Psi^{\text{liq.}}\right|^2-\left(\hat{N}\cdot\nabla\Psi^{\text{liq.}}\right)^2\right]\right\}_{Y=\Sigma(X,Z,T)}+O(\varepsilon^2)\end{aligned} \tag{6.10a}$$

$$=\left[-P-\mathrm{Ca}^{-1}K(X,Z,T)+P_{\text{Maxwell}}\right]_{Y=\Sigma(X,Z,T)}+O(\varepsilon^2), \tag{6.10b}$$

where P_{Maxwell} is the total Maxwell pressure (defined by the term with the coefficient We/Ca) (Landau and Lifshitz, 1984) and $K(X,Z,T)$ is the dimensionless mean curvature of the interface function $\Sigma(X,Z,T)$ (defined to be positive for a wetting liquid). According to Equation (6.5b), the pressure P is independent of (X,Y), and thus the quantity $(P_{\text{Maxwell}}-\mathrm{Ca}^{-1}K)$ must also be a function of Z alone. In the absence of an electric field, this condition would imply that K is a function of Z alone and thus that the interface is a circular section. However, that is no longer the case here, and a nonzero Maxwell pressure breaks the circularity of $\Sigma(X,Z,T)$.

The tangential boundary conditions meanwhile become

$$0 = \left[\frac{\partial_Y W - (\partial_X \Sigma)\partial_X W}{\sqrt{1+(\partial_X \Sigma)^2}}\right]_{Y=\Sigma(X,Z,T)} - \frac{\mathrm{We}}{\mathrm{Ca}}\left[\left(\varepsilon^{-1}\hat{T}_Z \cdot \nabla\Psi\right)\left(\hat{N}\cdot\nabla\Psi\right) - \epsilon_r\left(\varepsilon^{-1}\hat{T}_Z\cdot\nabla\Psi^{\mathsf{liq.}}\right)\left(\hat{N}\cdot\nabla\Psi^{\mathsf{liq.}}\right)\right]_{Y=\Sigma(X,Z,T)} + O(\varepsilon^2), \tag{6.11a}$$

$$0 = \left[\left(\hat{T}_X \cdot \nabla\Psi\right)\left(\hat{N}\cdot\nabla\Psi\right) - \epsilon_r\left(\hat{T}_X\cdot\nabla\Psi^{\mathsf{liq.}}\right)\left(\hat{N}\cdot\nabla\Psi^{\mathsf{liq.}}\right)\right]_{Y=\Sigma(X,Z,T)} + O(\varepsilon^2). \tag{6.11b}$$

6.2.4 Surface shape

In principle, we next must determine the shape of the fluid surface. In particular, the cross-sectional surface must satisfy the ordinary differential equation $\partial_X P = 0$, with the sides satisfying the contact angle condition $\partial_X \Sigma(X,Z,T)|_{wall} = \cot(\alpha+\theta)\mathsf{sign}(X)$. If P_{Maxwell} were independent of $\Sigma(X,Z,T)$ and X, then the result would be a segment of a circle. But for a conducting or dielectric film, that will not be the case.

However, it turns out to be sufficient for our case of interest (specifically, for a conducting fluid which is thin compared to the height of the groove walls) to approximate the surface as a circular segment. For a more accurate model, the surface shape would need to be computed numerically. Writing P_{Maxwell} as a functional $P_{\mathsf{Maxwell}}[\Sigma, X]$ and calling the midline interface thickness H, i.e., $\Sigma(X=0,Z,T) = H(Z,T)$, the surface would need be computed for each given H. Solving $\partial_X(P_{\mathsf{Maxwell}} - \mathrm{Ca}^{-1}K) = 0$ with the aforementioned contact angle boundary conditions and the additional condition $\Sigma(X=0,Z,T) = H(Z,T)$ will yield the desired result, as long as P_{Maxwell} is not dependent on Z-derivatives of $\Sigma(X,Z,T)$. While we will carry out such an analysis for the curved-backbone V-groove problem in Chapter 7, we do not do so here, as the resulting correction is small; see Section 6.7 for a numerical quantification of the errors induced by this approximation. From now on, we will assume that the surface is a circular section and the pressure is a function of H and Z alone, i.e., $P = P[H,Z]$.

6.2.5 Flux

To compute the cross-sectional flux, it is necessary to solve

$$\frac{\partial P[H,Z]}{\partial Z} = \left(\partial_{XX} + \partial_{YY}\right) W, \tag{6.12a}$$

$$0 = W|_{wall}, \tag{6.12b}$$

$$0 = \left[\left(\hat{\mathcal{T}}_Z - \nabla W\right)\cdot\hat{N}\right]_{Y=\Sigma(X,Z,T)}, \tag{6.12c}$$

for $(X,Y) \in \Omega(Z,T)$, the cross-sectional liquid domain. Here $\hat{\mathcal{T}}$ represents the boundary stress term in Equation (6.11a), which would arise for a leaky dielectric fluid. As with the pressure, let us assume that $\hat{\mathcal{T}}_Z \cdot \hat{N} = \mathcal{T}_{NZ}$ is a function of Z and H alone; the same simplifying assumption was made by Su and Lai (2004) and Yang and Homsy (2006) (although their interfacial stresses did not arise from electric effects). Note that the leaky dielectric model includes an equation

of motion for free charges on the fluid interface (Saville, 1997), and it would take additional work to validate the assumption that the motion of such charges does not induce a significant X-dependence of the shear stress. We make this simplifying assumption here in order to provide a blueprint for how one might proceed with a leaky dielectric; from Section 6.3 onward, we will consider only perfectly conducting fluids and not leaky dielectrics.

Decomposing the streamwise velocity as $W = -(\partial P[H,Z]/\partial Z)\overline{M}_1 + H^{-1}\mathcal{T}_{NZ}[H,Z]\overline{M}_2$, Equation (6.12) then becomes

$$-1 = (\partial_{XX} + \partial_{YY})\,\overline{M}_1, \tag{6.13a}$$

$$0 = \overline{M}_1|_{wall}, \tag{6.13b}$$

$$0 = \left[\nabla \overline{M}_1 \cdot \hat{N}\right]_{Y=\Sigma(X,Z,T)}, \tag{6.13c}$$

and

$$0 = (\partial_{XX} + \partial_{YY})\,\overline{M}_2, \tag{6.14a}$$

$$0 = \overline{M}_2|_{wall}, \tag{6.14b}$$

$$1 = \left[H^{-1}\nabla \overline{M}_2 \cdot \hat{N}\right]_{Y=\Sigma(X,Z,T)}, \tag{6.14c}$$

again to be solved for $(X,Y) \in \Omega(Z,T)$, the cross-sectional liquid domain. Just as in Chapter 4, these equations can be solved once for a given α and θ by scaling the domain Ω by H. An example of the resulting streamwise velocity factors $\overline{M}_1$ and $\overline{M}_2$ for a groove of $\alpha = 30^\circ$, $\theta = 15^\circ$, is shown in Figure 6.2.

The resulting flux is then

$$Q(Z,T) = \int_{\Omega(Z,T)} W = -H^4\Gamma(\alpha,\theta)\partial_Z P + H^3\Gamma_T(\alpha,\theta)\mathcal{T}_{NZ}, \tag{6.15}$$

where $\Omega(Z,T)$ represents the cross-sectional liquid domain (Figure 6.1 b), $\Gamma(\alpha,\theta)$ is the same constant geometric flux factor as in Chapter 4 (also shown in Figure 6.3) defined by $\Gamma(\alpha,\theta) = [\int_\Omega \overline{M}_1 dXdY]/H^4$, and $\Gamma_T(\alpha,\theta) = [\int_\Omega \overline{M}_2 dXdY]/H^3$ is a geometric flux factor coming from solving Equation (6.14) for the tangential-stress-driven component of the streamwise velocity.

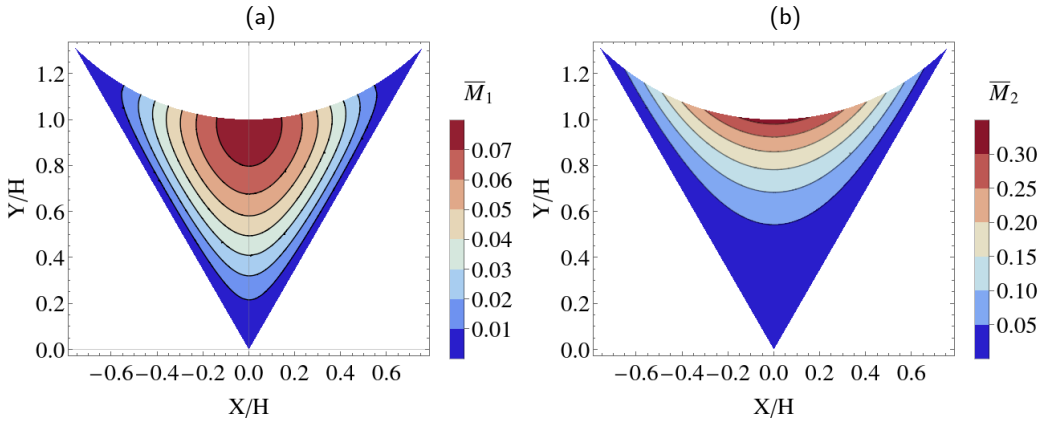

Figure 6.2: Contour plots of streamwise velocity factors $\overline{M}_1$ and $\overline{M}_2$, defined by Equations (6.13) and (6.14), in a slender V-groove with groove half angle $\alpha = 30°$ and fluid contact angle $\theta = 15°$. Results are plotted on coordinates normalized by H, i.e., $\{X/H, Y/H\}$. Note that the color scales differ between (a) and (b).
(a) Streamwise velocity factor, $\overline{M}_1$, computed according to Equation (6.13). Note that this is identical to the velocity factor arising in a groove without an electric field.
(b) Streamwise velocity factor, $\overline{M}_2$, computed according to Equation (6.14), arising due to tangential stresses. Note that such a streamwise velocity correction would arise in the case of a leaky dielectric fluid, which produces tangential stresses. However, the main result of this work will consider only perfectly conducting fluids, and hence the streamwise velocity will consist only of the $\overline{M}_1$ term, without $\overline{M}_2$.

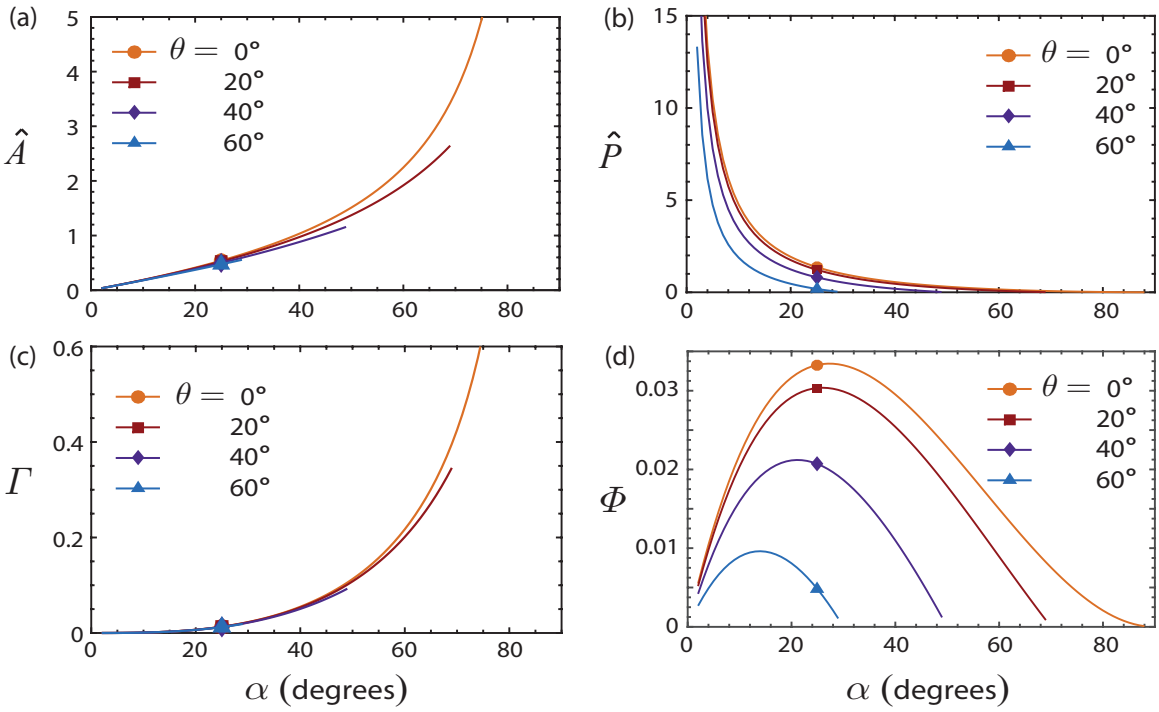

Figure 6.3: Geometric functions pertinent to capillary flow of a Newtonian liquid film with constant contact angle θ in a straight V-groove with internal groove half angle α satisfying the Concus-Finn condition $\theta + \alpha < \pi/2$.
(a) $\widehat{A}(\theta, \alpha)$, defined by Equation (6.17)
(b) $\widehat{P}(\theta, \alpha) = 1/\widehat{R}(\theta, \alpha)$, defined by Equation (6.38)
(c) $\Gamma(\theta, \alpha)$, defined by Equation (4.22)
(d) $\Phi(\theta, \alpha) = \Gamma(\alpha, \theta)\widehat{P}(\alpha, \theta)/\widehat{A}(\alpha, \theta)$. Note that according to the nondimensionalization scheme of this work, $\mathrm{Ca} = \Phi$.
These geometric functions were plotted earlier in Chapter 4, Figure 4.4, and are included again for convenience. Note that because the system satisfies the Concus-Finn condition, data at higher θ is cut off earlier at $\alpha = \pi/2 - \theta$.

6.2.6 Combined equation

Using the integrated conservation of mass equation $\partial_T A = -\partial_Z Q$, with $A = \widehat{A}H^2$ (due to the assumption that the interface deviates only negligibly from a circular section), the general V-groove equation of motion becomes

$$\frac{\partial H^2}{\partial T} = \frac{\Gamma}{\widehat{A}}\partial_Z \left[H^4 \partial_Z P - \frac{\Gamma_T}{\Gamma} H^3 \mathcal{T}_{NZ} \right], \tag{6.16}$$

where P is the pressure due to capillary and Maxwell forces and $\mathcal{T}_{NZ}$ is the tangential stress in the case of a leaky dielectric. $\Gamma(\alpha, \theta)$ and $\widehat{A}(\alpha, \theta)$ are positive geometric factors dependent only on the internal groove angle, α, and the wetting angle, θ (see Chapter 4 for more details). $\Gamma(\alpha, \theta)$ must be computed numerically by solving the streamwise velocity Poisson equation, Equation (6.13), in the cross-sectional liquid domain (Figure 6.1 b); the result is plotted in Figure 6.3 (c). The cross-sectional area factor can be expressed in closed form as

$$\widehat{A} = \frac{\cos\theta \sin\alpha \cos(\alpha + \theta) - (\pi/2 - \alpha - \theta)\sin^2\alpha}{(\cos\theta - \sin\alpha)^2}. \tag{6.17}$$

The tangential stress term matches that found by Yang and Homsy (2006) in the thermocapillary problem; Γ_T would also have to be computed numerically by solving the Laplacian equation for tangential-stress-induced streamwise velocity, Equation (6.14).

We will now specialize to the case of a perfect conductor, meaning that $\mathcal{T}_{NZ} = 0$, and

$$\frac{\partial H^2}{\partial T} = \frac{\Gamma}{\widehat{A}}\partial_Z \left[H^4 \partial_Z P \right], \tag{6.18}$$

where $P(Z,T) = P_{\text{capillary}}(X,Z,T) + P_{\text{Maxwell}}(X,Z,T)$ (note that $P_{\text{capillary}}$ and P_{Maxwell} may individually vary in X, i.e., transversely across the groove, but their sum must be constant in X). All that remains is to determine the expression for P for a given system.

6.3 Electric field distribution in conducting groove with thin fluid

The previous section laid out the methodology for constructing the model. While a general derivation was presented to cover the cases of the fluid being a perfect conductor, dielectric, or leaky dielectric, we now consider only perfectly conducting fluids, meaning that $\mathcal{T}_{NZ} = 0$. We will also consider only specific electric fields. In order for the model to be valid, the electric fields must remain in the long wavelength limit. Thus, the groove and electrode geometry must be slowly-varying in the z dimension.

A variety of geometries may be considered; here we will concentrate on a perfectly conducting fluid in a groove whose walls are much higher than the fluid thickness. While in principle A and Q will depend on H in a complicated manner than can be determined only numerically, when the fluid is very thin in the corner of the groove, i.e., $(d/b)^2 \ll 1$, the electric field's influence will be near the power-law solution for an electric field in a wedge. In this limit, H also becomes separable from the cross-sectional area expression, A, and the flux, Q, yielding a semi-analytic solution with H dependence in closed form expressions, rather than numerical functions.

6.3.1 Electric field slow variation assumptions

The electric potential must be Laplacian in the vacuum region, i.e.,

$$\nabla^2\psi = \partial_{xx}\psi + \partial_{yy}\psi + \partial_{zz}\psi = 0. \tag{6.19}$$

We consider only electric fields which are slow-varying in z, i.e., along the groove axis. Specifically, we require that at the top of the groove, the length scale of electric field variations in z is $\geq O(L)$, the characteristic groove length scale. Thus, for example, a counter-electrode at the top of the groove with $O(d)$ length scale variations in its geometry or potential would be disallowed. If the slow-varying condition holds, then the electric potential in the vacuum region of the groove may be nondimensionalized as

$$\partial_{XX}\Psi + \partial_{YY}\Psi + \varepsilon^2\partial_{ZZ}\Psi = 0, \tag{6.20}$$

where $\Psi = \psi/\psi_c$, $X = x/d$, $Y = y/d$, $Z = z/L$, and $\varepsilon = d/L$ (see Table 6.1), so that the electric field can be considered in 2D "slices," satisfying $\partial_{XX}\Psi + \partial_{YY}\Psi = 0$ up to $O(\varepsilon^2)$ corrections.

We further consider only fields which are sufficiently smooth in the transverse direction across the groove. Specifically, letting $\psi^{\text{outer}}(\beta)$ be the electric field distribution on a circular section a distance b from the groove corner (i.e., the field distribution at the top of the groove), with β being the angular coordinate (see Figure 6.4), and letting ψ_k^{outer} be the cosine transform of ψ^{outer} with wavenumber k, it is assumed that $|\psi_0^{\text{outer}}/\psi_k^{\text{outer}}| > (d/b)^{2(k-1)}\ \forall k$. That is, the 0th wavenumber, representing a constant far-field potential at radial distance $r = b$ from the groove corner, does not need to be larger than higher-order ψ_k^{outer} modes, but needs to be only $(d/b)^{2(k-1)}$ times their size. As the film gets thinner compared to the groove depth, (d/b) gets smaller and the constraint is loosened. Intuitively, this condition may be understood as the requirement that the liquid film interface does not "see" any variations in the far-field potential; the thinner the film, the more leeway there is for far-field details to get washed out inside the groove. The distance b at which the "outside" electric potential is defined is either the diagonal depth of the groove wall or the distance to the nearest charge or counter-electrode (in the case that such a charge or counter-electrode is placed lower than the groove wall depth).

6.3.2 Electric field in a 2D wedge

Note that the analysis in this section will be carried out in dimensional variables, with a fixed fluid midline height of $h = d$. Consider a wedge with opening half angle α and an outer radial limit b, as in Figure 6.4. Assume the walls and fluid interface are perfect conductors (and hence have $\psi = 0$), and the outer boundary has some potential distribution $\psi|_{r=b} = \psi^{\text{outer}}(\beta)$. In polar coordinates (r, β), we must then solve

$$\nabla^2\psi = \partial_{rr}\psi + \frac{1}{r}\partial_r\psi + \frac{1}{r^2}\partial_{\beta\beta}\psi = 0 \tag{6.21}$$

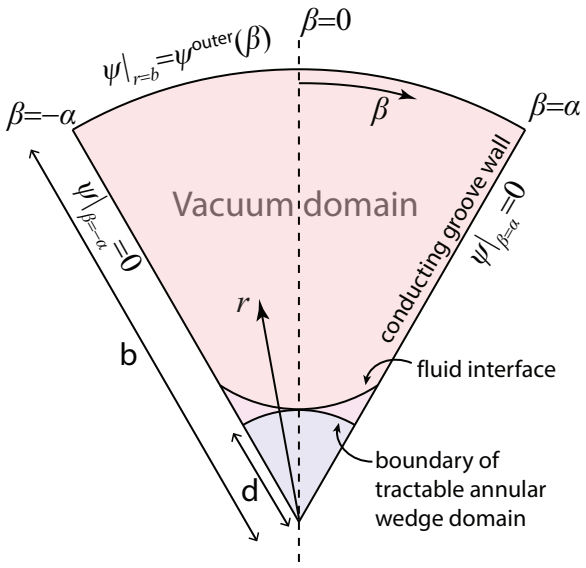

Figure 6.4: Cross-sectional schematic of the system depicted in Figure 6.1 (b), with quantities relevant to the electric field solution in a 2D wedge emphasized. The system is described in polar coordinates $\{r, \beta\}$, with $\beta = 0$ at the center of the groove and $\beta = \pm\alpha$ being the groove walls. The groove walls are grounded, so that $\psi|_{\beta=\pm\alpha} = 0$, and the electric potential at the top of the groove, a distance b from the corner, is $\psi|_{r=b} = \psi^{\text{outer}}(\beta)$. The boundary of the annular wedge domain, tracing out $r = d$, is shown, as is the fluid interface, shown with interface midline thickness d. Note that the variables shown in this diagram are dimensional.

with boundary conditions

$$\psi_{\beta=\pm\alpha} = 0 \tag{6.22a}$$

$$\psi_{r=b} = \psi^{\text{outer}}(\beta) \tag{6.22b}$$

$$\psi_{r=\sigma(\beta)} = 0, \tag{6.22c}$$

where $r = \sigma(\beta) = d \times \Sigma(\beta)$ is the fluid interface.[1]

Solving Equation (6.21) with only the wall condition Equation (6.22a) by separation of variables yields

$$\psi = \sum_{j=-\infty}^{\infty} c_j r^{(j+1/2)(\pi/\alpha)} \cos\left[\left(j + \frac{1}{2}\right)\frac{\pi}{\alpha}\beta\right], \qquad \sigma(\beta) \le r \le b. \tag{6.23}$$

Solving for c_j such that the field vanishes at the fluid surface is analytically intractable, even when the surface has a simple shape such as a semicircle, and thus a numerical approach will be necessary. However, we can analytically determine the scaling of the electric field gradient in the limit of a distant electrode, so long as the fluid interface is sufficiently well-behaved. To do

[1] Note that in reality the interface depends on z and t as well, having the form $\sigma(\beta, z, t) = d \times \Sigma(\beta, Z, T)$. However, since we are solving in 2D "slices" due to the assumptions that the electric field is time-independent and slow-varying in Z, we simplify notation by omitting z and t from σ in this section.

so, we will first solve for the field in the tractable case of a homogeneous Dirichlet condition on a circular boundary with negative-curvature (instead of the realistic fluid interface, which has positive curvature and is not circular), forming an annular wedge domain. The following section will show that when $\delta = (d/b) \ll 1$, the Maxwell pressure scales as $(d/b)^{(\pi/\alpha)-2}$, where b is the distance to the outside electric field (defined as the groove wall length or the distance to the nearest charge or counter-electrode, whichever is shorter) and d is the inner radius of the annulus. In the subsequent section, the annular wedge analysis will be extended to the case of a more general fluid interface, where it will be shown that the dominant contribution to the Maxwell pressure still scales as $(d/b)^{(\pi/\alpha)-2}$. This scaling result will be verified numerically in Section 6.7.

Electric field in a 2D annular wedge

To find the annular wedge solution, we solve for $c_j^{\text{a.w.}}$ using the boundary conditions $\psi_{\text{a.w.}}|_{r=b} = \psi^{\text{outer}}(\beta)$ and $\psi_{\text{a.w.}}|_{r=d} = 0$. Defining

$$\psi_k^{\text{outer}} = \frac{1}{\alpha}\int_{-\alpha}^{\alpha} \cos\left[\left(k+\frac{1}{2}\right)\frac{\pi}{\alpha}\beta\right]\psi^{\text{outer}}(\beta)d\beta, \tag{6.24}$$

the outer and inner boundary constraints become

$$\psi_k^{\text{outer}} = c_k^{\text{a.w.}} b^{(k+1/2)(\pi/\alpha)} + c_{-k-1}^{\text{a.w.}} b^{-(k+1/2)(\pi/\alpha)}, \tag{6.25a}$$

$$0 = c_k^{\text{a.w.}} d^{(k+1/2)(\pi/\alpha)} + c_{-k-1}^{\text{a.w.}} d^{-(k+1/2)(\pi/\alpha)}, \tag{6.25b}$$

yielding

$$c_k^{\text{a.w.}} = \frac{b^{-(k+1/2)(\pi/\alpha)}}{1-\delta^{2(k+1/2)(\pi/\alpha)}}\psi_k^{\text{outer}} \tag{6.26}$$

and

$$\begin{aligned}\psi_{\text{a.w.}} &= \sum_{j=0}^{\infty}\left[\frac{1}{1-\delta^{2(j+1/2)(\pi/\alpha)}}\left(\frac{r}{b}\right)^{(j+1/2)(\pi/\alpha)} + \frac{1}{1-\delta^{-2(j+1/2)(\pi/\alpha)}}\left(\frac{r}{b}\right)^{-(j+1/2)(\pi/\alpha)}\right] \\ &\qquad \times \psi_j^{\text{outer}}\cos\left[\left(j+\frac{1}{2}\right)\frac{\pi}{\alpha}\beta\right] \\ &= \sum_{j=0}^{\infty}\frac{\delta^{(j+1/2)(\pi/\alpha)}}{1-\delta^{2(j+1/2)(\pi/\alpha)}}\left[\left(\frac{r}{d}\right)^{(j+1/2)(\pi/\alpha)} - \left(\frac{r}{d}\right)^{-(j+1/2)(\pi/\alpha)}\right]\psi_j^{\text{outer}}\cos\left[\left(j+\frac{1}{2}\right)\frac{\pi}{\alpha}\beta\right]\end{aligned} \tag{6.27}$$

We are interested in the behavior of the field near the fluid surface, i.e., at $r = d$. By the assumption that $d < b$, the lowest powers of $\delta = (d/b)$ will dominate the result. The ratio in magnitude of the kth term in the series to the 0th term then has order $\delta^{k(\pi/\alpha)}|\psi_k^{\text{outer}}/\psi_0^{\text{outer}}|$, which is $\leq \delta^{2k}|\psi_k^{\text{outer}}/\psi_0^{\text{outer}}|$, where we have used the fact that $\alpha < \pi/2$ (α must be less than $\pi/2$ for the substrate to form a groove instead of a plane or an external corner). Therefore, so long as $|\psi_k^{\text{outer}}/\psi_0^{\text{outer}}| < O(\delta^{-2(k-1)})$ (the smoothness condition which we assumed a priori),

then the 0th order term will dominate the series and all higher order terms will be at most $O(\delta^2)$. The electric field near the inner annulus surface is then well-approximated by

$$\psi_{\text{a.w.}} = \left[\left(\frac{r}{b}\right)^{(1/2)(\pi/\alpha)} - \delta^{(\pi/\alpha)}\left(\frac{r}{b}\right)^{-(1/2)(\pi/\alpha)}\right]\psi_0^{\text{outer}}\cos\left[\left(\frac{1}{2}\right)\frac{\pi}{\alpha}\beta\right]\left[1+O(\delta^2)\right]. \quad (6.28)$$

The Maxwell pressure of the annular wedge solution at $r = d$,$\beta = 0$ is then given by

$$\begin{aligned}
p_{\text{a.w.}}|_{r=d,\beta=0} &= -\frac{1}{2}\epsilon_0\left[(\partial_r\psi_{\text{a.w.}})^2 + \frac{1}{r^2}(\partial_\beta\psi_{\text{a.w.}})^2\right]\Big|_{r=d} \\
&= -\frac{\epsilon_0(\psi_0^{\text{outer}})^2}{b^2}\frac{\pi^2}{8\alpha^2}\left[\left(\frac{r}{b}\right)^{(\pi/\alpha)-2} + \left(\frac{r}{b}\right)^{-(\pi/\alpha)-2}\delta^{2(\pi/\alpha)} + \left(\frac{r}{b}\right)^{-2}\delta^{(\pi/\alpha)}\cos\left(\frac{\pi\beta}{\alpha}\right)\right]_{r=d,\beta=0} \\
&= -\frac{\epsilon_0(\psi_0^{\text{outer}})^2}{b^2}\frac{\pi^2}{4\alpha^2}\delta^{(\pi/\alpha)-2}\left[1+\cos\left(\frac{\pi\beta}{\alpha}\right)\right]_{\beta=0}\left[1+O(\delta^2)\right] \\
&= -\frac{\epsilon_0(\psi_0^{\text{outer}})^2}{b^2}\frac{\pi^2}{2\alpha^2}\left(\frac{d}{b}\right)^{(\pi/\alpha)-2}\left[1+O(\delta^2)\right]. \quad (6.29)
\end{aligned}$$

Note in particular that $p_{\text{a.w.}}|_{r=d}$ scales as $\delta^{(\pi/\alpha)-2} = (d/b)^{(\pi/\alpha)-2}$. Note also that the pressure of the annular wedge solution differs from the pressure of the pure wedge solution evaluated at $r = d$ (the latter has an extra multiplicative factor of $1/4$).

Electric field in a 2D wedge with a nontrivial fluid interface

Having solved the annular wedge solution, we now consider the general solution to the electric potential ψ satisfying Equation (6.21) and boundary equations Equations (6.22a) to (6.22c). But because it is difficult to deal with a boundary condition on $r = \sigma(\beta)$, we instead construct an equivalent boundary condition $\psi_{r=d} = \psi^{\text{inner}}(\beta)$. That is, $\psi^{\text{inner}}(\beta)$ is the boundary condition on the annular wedge domain which gives a solution with $\psi|_{r=\sigma(\beta)} = 0$.

In the same manner as ψ_k^{outer}, we define

$$\psi_k^{\text{inner}} = \frac{1}{\alpha}\int_{-\alpha}^{\alpha}\cos\left[\left(k+\frac{1}{2}\right)\frac{\pi}{\alpha}\beta\right]\psi^{\text{inner}}(\beta)d\beta, \quad (6.30)$$

and the outer and inner boundary constraints become

$$\psi_k^{\text{outer}} = c_k b^{(k+1/2)(\pi/\alpha)} + c_{-k-1}b^{-(k+1/2)(\pi/\alpha)}, \quad (6.31a)$$

$$\psi_k^{\text{inner}} = c_k d^{(k+1/2)(\pi/\alpha)} + c_{-k-1}d^{-(k+1/2)(\pi/\alpha)}, \quad (6.31b)$$

yielding

$$c_k = \frac{b^{-(k+1/2)(\pi/\alpha)}}{1-\delta^{2(k+1/2)(\pi/\alpha)}}\left[\psi_k^{\text{outer}} - \delta^{(k+1/2)(\pi/\alpha)}\psi_k^{\text{inner}}\right]. \quad (6.32)$$

Comparing the magnitudes of a term with $k \neq 0$ to the 0 term:

$$\begin{aligned}
\left|\frac{c_k d^{(k+1/2)(\pi/\alpha)}}{c_0 d^{(0+1/2)(\pi/\alpha)}}\right| &= \frac{\delta^{(k+1/2)(\pi/\alpha)}[1-\delta^{2(0+1/2)(\pi/\alpha)}]}{\delta^{(0+1/2)(\pi/\alpha)}[1-\delta^{2(k+1/2)(\pi/\alpha)}]}\left|\frac{\psi_k^{\text{outer}} - \delta^{(k+1/2)(\pi/\alpha)}\psi_k^{\text{inner}}}{\psi_0^{\text{outer}} - \delta^{(0+1/2)(\pi/\alpha)}\psi_0^{\text{inner}}}\right| \\
&= O(\delta^2)\times\left|\frac{1-\delta^{(k+1/2)(\pi/\alpha)}\psi_k^{\text{inner}}/\psi_k^{\text{outer}}}{1-\delta^{(0+1/2)(\pi/\alpha)}\psi_0^{\text{inner}}/\psi_0^{\text{outer}}}\right|. \quad (6.33)
\end{aligned}$$

The annular boundary $r = d$ and the true interface boundary $r = \sigma(\beta) = d\Sigma(\beta)$ are a distance $O(d)$ apart. If $\Sigma(\beta)$ is sufficiently smooth, then it may be the case that $\lim_{\delta\to 0} \psi_k^{\mathsf{inner}}/\psi_k^{\mathsf{outer}} < O(\delta^{-k(\pi/\alpha)})$, and hence that the kth series term is $O(\delta^2)$ smaller than the 0th series term. This would be nontrivial to prove, and indeed would not be true if $\Sigma(\beta)$ were to have a sharp corner or cusp. The contact line, where the interface meets the wall, is certainly not smooth if $\theta > 0$; however, being an internal rather than external corner, it is not expected to lead to a singularity inducing an arbitrarily large electric field (Jackson, 2012). We will take it as an assumption here that the interface is smooth and that the contact line does not significantly affect the electric field, and later confirm the results numerically. Therefore, the field near the fluid surface can be approximated using only the $k = 0$ and $k = -1$ terms:

$$\begin{aligned}
\psi &= \left\{ \left[\left(\frac{r}{b}\right)^{(1/2)(\pi/\alpha)} - \delta^{(\pi/\alpha)} \left(\frac{r}{b}\right)^{-(1/2)(\pi/\alpha)} \right] \psi_0^{\mathsf{outer}} + \delta^{(1/2)(\pi/\alpha)} \left(\frac{r}{b}\right)^{-(1/2)(\pi/\alpha)} \psi_0^{\mathsf{inner}} \right\} \\
&\times \cos\left[\left(\frac{1}{2}\right) \frac{\pi}{\alpha}\beta \right] \left[1 + O(\delta^2)\right] \\
&= \delta^{\pi/(2\alpha)} \left\{ \left[\left(\frac{r}{d}\right)^{(1/2)(\pi/\alpha)} - \left(\frac{r}{d}\right)^{-(1/2)(\pi/\alpha)} \right] \psi_0^{\mathsf{outer}} + \delta^{-(1/2)(\pi/\alpha)} \left(\frac{r}{d}\right)^{-(1/2)(\pi/\alpha)} \psi_0^{\mathsf{inner}} \right\} \\
&\times \cos\left[\left(\frac{1}{2}\right) \frac{\pi}{\alpha}\beta \right] \left[1 + O(\delta^2)\right], \quad \sigma(\beta) \le r \ll b. \qquad (6.34)
\end{aligned}$$

Evaluating ψ at the fluid interface $r = d\Sigma(\beta)$,

$$0 = \psi|_{r=d\Sigma(\beta)} = \left\{ O(\delta^{(1/2)(\pi/\alpha)})\psi_0^{\mathsf{outer}} + O(\delta^0)\psi_0^{\mathsf{inner}} \right\} \cos\left[\left(\frac{1}{2}\right) \frac{\pi}{\alpha}\beta \right] \left[1 + O(\delta^2)\right]. \qquad (6.35)$$

In order for ψ to vanish at the fluid surface, it must then be the case that $\psi_0^{\mathsf{inner}} = O(\delta^{(1/2)(\pi/\alpha)})$, yielding the same scaling as the annular wedge solution. In other words, despite all the ugly calculations, we conclude that we can use the Maxwell pressure from an annular wedge as a good approximation to the Maxwell pressure for a different fluid interface shape in a wedge, so long as the fluid is sufficiently shallow compared to the wedge depth and the assumptions of sufficiently smooth fluid interface and outside electric field distribution hold. In the remainder of this work, we will approximate Maxwell pressure as

$$p_{\mathsf{Maxwell}}|_{r=h,\beta=0} = \widehat{C} p_{\mathsf{a.w.}}|_{r=h,\beta=0} = -\frac{\epsilon_0 (\psi_0^{\mathsf{outer}})^2}{b^2} \frac{\pi^2}{2\alpha^2} \left(\frac{h}{b}\right)^{(\pi/\alpha)-2} \widehat{C} \left[1 + O(\delta^2)\right], \qquad (6.36)$$

where $\widehat{C}$ is an $O(1)$ correction to the annular wedge pressure. Note that by adopting the annular wedge solution at $r = h$, we are explicitly taking into account the way the electric field changes as the fluid thickness changes.

6.4 Equation of motion for perfectly conducting thin film in a V-groove

As shown in the previous section, $P_{\text{Maxwell}} \propto (h/b)^{(\pi/\alpha)-2} = [(d/b)H]^{(\pi/\alpha)-2}$. In nondimensional form, the midline Maxwell pressure is given by

$$\begin{aligned} P_{\text{Maxwell}} &= -\frac{1}{p_c}\frac{\epsilon_0(\psi_0^{\text{outer}})^2}{b^2}\frac{\pi^2}{2\alpha^2}\left(\frac{h}{b}\right)^{(\pi/\alpha)-2}\widehat{C} + O(\delta^2) \\ &= -\left[\frac{d}{\gamma \text{Ca}}\frac{\epsilon_0\psi_c^2}{b^2}\frac{\pi^2}{2\alpha^2}\left(\frac{d}{b}\right)^{(\pi/\alpha)-2}\right]\left(\frac{\psi_0^{\text{outer}}}{\psi_c}\right)^2\widehat{C}\left(\frac{h}{d}\right)^{(\pi/\alpha)-2} + O(\delta^2) \\ &= -\frac{1}{2\text{Ca}}\left[\frac{d}{\gamma}\epsilon_0 E_c^2\right]\left(\frac{\psi_0^{\text{outer}}}{\psi_c}\right)^2\widehat{C}H^{(\pi/\alpha)-2} + O(\delta^2) \\ &= -\frac{1}{\widehat{R}\text{Ca}}\left[\frac{\text{We}\widehat{R}}{2}\left(\frac{\psi_0^{\text{outer}}}{\psi_c}\right)^2\widehat{C}\right]H^{(\pi/\alpha)-2} + O(\delta^2) \\ &= -\frac{1}{\widehat{R}\text{Ca}}\chi(Z)\times H^m, \end{aligned} \tag{6.37}$$

where

$$\widehat{R} = \frac{\sin\alpha}{\cos\theta - \sin\alpha} \tag{6.38}$$

is the interface radius of curvature factor (see Chapter 4), and

$$m = \left(\frac{\pi}{\alpha} - 2\right) \in (0, \infty) \tag{6.39}$$

is the Maxwell pressure exponent. The factor χ, given by

$$\chi(Z) = \frac{1}{2}\left(\frac{\widehat{R}d}{\gamma}\right)\left[\frac{\epsilon_0(\psi_0^{\text{outer}})^2}{b^2}\frac{\pi^2}{\alpha^2}\right]\left(\frac{d}{b}\right)^{(\pi/\alpha)-2}\widehat{C} = \frac{\text{We}\widehat{R}}{2}\left(\frac{\psi_0^{\text{outer}}(Z)}{\psi_c}\right)^2\widehat{C}, \tag{6.40}$$

encapsulates the far-field electric field variation in Z (that is, the variation in Z of the electric field outside the groove) in the form of $\psi_0^{\text{outer}}(Z)$, the first term in a cosine transform of the outer electric field at $r = b$. $\chi(Z)$ also contains the electric Weber number (Maxwell-capillary ratio), and is independent of H. The value of $\chi(Z)$ will depend on details of the electric field outside the groove, and would have to be computed numerically for any given system.

Note that Equation (6.37) is simply the midline ($\beta = 0$) Maxwell pressure of the annular wedge solution at $r = h$ with multiplicative $O(1)$ correction $\widehat{C}$, and recast in nondimensional units.

Because $\alpha < \frac{\pi}{2}$ (i.e., because the geometry is that of a groove instead of an external corner), the exponent m is positive, and hence P_{Maxwell} decreases with H, i.e., $\partial P_{\text{Maxwell}}/\partial H < 0$. That is, fluid that is higher in the groove (and closer to the electrode) will have lower pressure.

The overall pressure is then given by

$$P = P_{\text{capillary}} + P_{\text{Maxwell}} = \frac{1}{\text{Ca}\widehat{R}}\left[-\frac{1}{H} - \chi(Z)H^m\right] + O(\delta^2). \tag{6.41}$$

Note that the deviation of the fluid surface from a circular section implies that the nondimensional capillary pressure is no longer exactly $-1/H$; for a sufficiently thin film, however,

this is a good approximation (see Section 6.7 for quantification of the error induced by this approximation).

It is convenient now to define a rescaled pressure

$$\overline{P} = \mathrm{Ca}(\alpha,\theta)\widehat{R}(\alpha,\theta)P = \overline{P}_{\mathsf{capillary}} + \overline{P}_{\mathsf{Maxwell}} = -\frac{1}{H} - \chi(Z)H^m, \tag{6.42}$$

where, similarly, $\overline{P}_{\mathsf{capillary}} = \mathrm{Ca}\widehat{R}P_{\mathsf{capillary}}$ and $\overline{P}_{\mathsf{Maxwell}} = \mathrm{Ca}\widehat{R}P_{\mathsf{Maxwell}}$.

In terms of the rescaled pressure $\overline{P}$ defined by Equations (6.41) and (6.42), the governing equation of motion becomes

$$\frac{\partial H^2}{\partial T} = -\frac{\partial}{\partial Z}\left[H^4\left(-\frac{\partial \overline{P}}{\partial Z}\right)\right] = -\frac{\partial}{\partial Z}\left[H^4\frac{\partial}{\partial Z}\left(\frac{1}{H} + \chi(Z)H^m\right)\right], \tag{6.43}$$

where $m = (\pi/\alpha) - 2 \in (0,\infty)$ and $\chi(Z) = (\mathrm{We}\widehat{R}/2)(\psi_o^{\mathsf{outer}}(z)/\psi_c)^2\widehat{C}$, and we have used the fact that $\mathrm{Ca} = \Phi(\alpha,\theta) = \Gamma/(\widehat{R}\widehat{A})$.

Equation (6.43) is the reduced-order evolution equation of fluid interface midline thickness we have sought. Keep in mind that it applies only to a perfectly conducting fluid in a groove with perfectly conducting walls, and requires that the fluid thickness d be less than the characteristic length L and the groove height b, specifically, $(d/L)^2 \ll 1$ and $(d/b)^2 \ll 1$. It was further assumed that the internal groove angle, α, and contact angle, θ, were constant, that inertial and gravitational terms could be ignored, and that the applied electric field is constant in time and slow-varying in z. Furthermore, it was assumed that the electric field is sufficiently weak that the thickness sensitivity of the Maxwell pressure ($\partial P_{\mathsf{Maxwell}}/\partial H$) is less than that of the capillary pressure ($\partial P_{\mathsf{capillary}}/\partial H$); this requirement will be expressed as $\chi < \chi_{\mathsf{thresh.}}$ and explained shortly. For more details on the assumptions required for the above equation to be in the regime of validity, see Section 6.2.1.

For large H, P_{Maxwell} may dominate the capillary pressure, making the overall pressure $P = P_{\mathsf{Maxwell}} + P_{\mathsf{capillary}}$ satisfy $\partial P/\partial H < 0$. In this case, the equation of motion $\partial_T(H^2) = \partial_Z\left(H^4\partial_Z P\right)$ will become anti-diffusive and ill-posed, and breakup or instability is expected. But for small H, $P_{\mathsf{Maxwell}} \to 0$ in a groove, and so the capillary terms will dominate and the equation of motion should be diffusive. Therefore, we expect that there will be a threshold thickness (which is dependent on the strength of the applied field), above which the fluid in the groove is unstable. Rather than define a local threshold thickness, it is convenient to define a worst-case threshold thickness based on the location with the greatest electric field $\chi_{\mathsf{max}} = \max_Z \chi(Z)$. Then, the threshold thickness is computed by

$$0 = \frac{\partial}{\partial H}\left(\frac{1}{H} + \chi_{\mathsf{max}}H^m\right)_{H=H_{\mathsf{thresh.}}} = -H_{\mathsf{thresh.}}^{-2} + m\chi_{\mathsf{max}}H_{\mathsf{thresh.}}^{m-1}$$

$$\implies H_{\mathsf{thresh.}} = \left(m\chi_{\mathsf{max}}\right)^{-1/(m+1)}. \tag{6.44}$$

The threshold thickness also defines a threshold pressure

$$\begin{aligned}\overline{P}_{\text{thresh.}} &= -\frac{1}{H_{\text{thresh.}}} - \chi_{\text{max}} H_{\text{thresh.}}^{m} \\ &= -\left(m\chi_{\text{max}}\right)^{1/(m+1)} - \chi_{\text{max}}\left(m\chi_{\text{max}}\right)^{-m/(m+1)} \\ &= -\left(m^{1/(m+1)} + m^{-m/(m+1)}\right)\chi_{\text{max}}^{1/(m+1)} \\ &= -\left(1+m\right)m^{-m/(m+1)}\chi_{\text{max}}^{1/(m+1)}. \end{aligned} \tag{6.45}$$

Alternatively, given a maximum fluid thickness $H_{\text{max}} = \max_Z H(Z)$ in the groove, one can define a threshold electric field strength above which the system is ill-posed:

$$\begin{aligned} H_{\text{max}} &= \left(m\chi_{\text{thresh.}}\right)^{-1/(m+1)} \\ \implies \chi_{\text{thresh.}} &= H_{\text{max}}^{-(m+1)} m^{-1}. \end{aligned} \tag{6.46}$$

Recalling that the equation of motion is well-posed only when $\chi < \chi_{\text{thresh.}} = H_{\text{max}}^{-(m+1)} m^{-1}$. Assuming d is the maximum fluid thickness, $H_{\text{max}} = 1$, and $\chi_{\text{thresh.}} = m^{-1}$. The constraint on the characteristic electric potential at the groove top to ensure the fluid remains in the well-posed regime is then

$$\psi_0^{\text{outer}} < \frac{\alpha}{\pi}\sqrt{\frac{2b^2}{\epsilon_0}\frac{\gamma}{d\widehat{R}}\frac{1}{m\widehat{C}}\left(\frac{b}{d}\right)^m}. \tag{6.47}$$

In the special case of a constant electric field, $\chi(Z) = \chi_0$ [note that χ_0 is so named simply to indicate that it is a constant; not to refer to $\chi(Z=0)$], the equation of motion Equation (6.43) can be rewritten as

$$\frac{\partial H^2}{\partial T} = \frac{\partial^2}{\partial Z^2}\left[\frac{1}{3}H^3 - \chi_0\frac{m}{m+4}H^{m+4}\right]. \tag{6.48}$$

The $\widehat{C}$ factor

The exact value of $(\nabla\Psi|_{Y=H})^2$ depends on the geometric factors α and θ, as well as the form of the electric field at the top of the groove; these details lead to an $O(1)$ deviation, $\widehat{C}$, from the annular wedge solution.

The case of a groove covered by a flat electrode of constant potential ψ_c located at $y = b$ was tested numerically (see Section 6.7), with internal groove half angles of $\alpha \in \{15°, 30°, 45°, 60°, 75°\}$ and contact angles $\theta \in \{10°, 15°, 30°, 45°, 60°\}$. $\widehat{C}$ increased with θ and decreased with α, ranging from a minimum of $\widehat{C} = 0.45$ for $(\alpha = 75°, \theta = 10°)$ to a maximum of 1.15 for $(\alpha = 15°, \theta = 60°)$.

6.4.1 Estimate of MEP threshold values

We can make some order-of-magnitude estimates of the critical fluid interface midline thickness in grooves on the MEP emitter. Suppose the counter-electrode sits a height ℓ above the array

substrate floor and has voltage gap V_0, and the grooves on the substrate floor have depth b. The electric field at the floor is then approximately V_0/ℓ. Since the electric potential in the groove goes as $\psi \approx \psi_0^{\text{outer}}(r/b)^{\pi/(2\alpha)}$, ψ_0^{outer} can be approximated by matching the field strength at the groove top with the field at the substrate floor.

$$\begin{aligned} \frac{V_0}{\ell} &\approx \frac{\pi}{2\alpha}\frac{\psi_0^{\text{outer}}}{b} \\ \implies \psi_0^{\text{outer}} &\approx \frac{2\alpha}{\pi}\frac{V_0}{\ell}b. \end{aligned} \tag{6.49}$$

The Maxwell pressure at the fluid surface is then

$$p_{\text{Maxwell}} \approx -\frac{\epsilon_0(\psi_0^{\text{outer}})^2}{b^2}\frac{\pi^2}{2\alpha^2}\left(\frac{h}{b}\right)^{(\pi/\alpha)-2}\widehat{C} = -2\epsilon_0\left(\frac{V_0}{\ell}\right)^2\left(\frac{h}{b}\right)^{(\pi/\alpha)-2}\widehat{C}, \tag{6.50}$$

where we used the annular wedge solution, Equation (6.29), and the overall pressure at the surface is

$$p \approx -\frac{\gamma}{\widehat{R}(\alpha,\theta)h} - 2\epsilon_0\left(\frac{V_0}{\ell}\right)^2 b^{-m}h^m, \tag{6.51}$$

where $\widehat{R}(\alpha,\theta) = \sin\alpha/(\cos\theta - \sin\alpha)$ is the surface curvature factor, $m = (\pi/\alpha) - 2$, and we have taken $\widehat{C}$ to be 1 (since $\widehat{C}$ is O(1) and we are constructing an order of magnitude estimate).

The threshold thickness is then given by

$$\begin{aligned} 0 &= \frac{\gamma}{\widehat{R}(\alpha,\theta)h_{\text{thresh.}}^2} - 2\epsilon_0\left(\frac{V_0}{\ell}\right)^2 b^{-m}mh_{\text{thresh.}}^{m-1} \\ \implies h_{\text{thresh.}} &= \left[b^m\frac{\gamma}{m\widehat{R}(\alpha,\theta)}\frac{1}{2}{\epsilon_0}^{-1}\left(\frac{\ell}{V_0}\right)^2\right]^{1/(m+1)}. \end{aligned} \tag{6.52}$$

Solving for V_0,

$$V_{\text{thresh.}} = \sqrt{\frac{\ell^2}{2\epsilon_0 d}\left(\frac{b}{d}\right)^m\frac{\gamma}{m\widehat{R}(\alpha,\theta)}}, \tag{6.53}$$

where we have substituted in d, the maximum fluid midline thickness, for $h_{\text{thresh.}}$ to then yield the threshold voltage $V_{\text{thresh.}}$ above which the equation of motion is ill-posed and instability is expected.

Let us substitute in $\epsilon_0 \approx 8.85 \times 10^{-12}$ F/m, the permittivity of free space, and $\gamma \approx 0.57$ N/m, the surface tension of liquid indium (Chentsov et al., 2011; Tiesinga et al., 2019).

Let the counter-electrode be 250 microns from the substrate surface. Supposing typical grooves are $b = 10$ microns deep, the maximum film thickness in the thin film regime is perhaps $d = 3$ microns. Using these values, a set of $V_{\text{thresh.}}$ is shown in Table 6.2 for a variety of internal groove half angles α and contact angles θ. Note that $1/(m\widehat{R})$ is monotonically decreasing in both α and θ, and so larger α or θ will always lead to smaller threshold voltage. Results are reported to

	$\theta = 0°$	$\theta = 15°$	$\theta = 50°$
$\alpha = 15°$	5700 kV	5570 kV	4110 kV
$\alpha = 30°$	144 kV	139 kV	77 kV
$\alpha = 45°$	39 kV	37 kV	
$\alpha = 60°$	19 kV	16 kV	
$\alpha = 75°$	10 kV		

Table 6.2: Approximate values of threshold counter-electrode voltage $V_{\text{thresh.}}$ [Equation (6.53)] for MEP values: permittivity of free space $\epsilon_0 = 8.85 \times 10^{-12}$ F/m (Tiesinga et al., 2019), liquid indium surface tension $\gamma \approx 0.57$ N/m (Chentsov et al., 2011; Tiesinga et al., 2019), grooves of depth $b = 10$ microns and film thickness $d = 3$ microns, and a flat counter-electrode a distance 250 microns above the top of the groove. These values are order of magnitude estimates, having omitted the $O(1)$ multiplicative correction factor $\widehat{C}$. Results are reported to the nearest kV not to imply accuracy, but merely in order to make the results distinguishable from one another. Results are shown for $\alpha \in \{15°, 30°, 45°, 60°, 75°\}$ and $\theta \in \{0°, 15°, 50°\}$ (note that results can be reported only within the valid regime in which the Concus-Finn condition, $\alpha + \theta < \pi/2$, is satisfied).

the nearest kV not because that is the known accuracy of the MEP system (it is not; we have omitted the $O(1)$ factor $\widehat{C}$), but in order to distinguish the results for different geometries from each other.

Grooves of different internal angles show stark differences, ranging from $V_{\text{thresh.}} \approx 5700$kV for $\alpha = 15°$ to $V_{\text{thresh.}} \approx 10$kV for $\alpha = 75°$. This is due both to the power $m = (\pi/\alpha) - 2$ being larger for narrow grooves (for $\alpha = 15°$, $m = 10$; for $\alpha = 75°$, $m = 0.4$) and due to $\widehat{R}$ being smaller for narrow grooves (for $\alpha = 15°, \theta = 0°$, $\widehat{R} \approx 0.35$; for $\alpha = 75°, \theta = 0°$, $\widehat{R} \approx 28$).

While the results of Table 6.2 are only order of magnitude approximationes, they are all larger than the typical MEP running values of 4-5kV (Marrese-Reading, 2016). This rough analysis therefore suggests that the film in the groove will likely exit the regime in which is it very thin compared to groove depth before it exceeds the threshold thickness at which one would need to worry about electrocapillary instability. However, a more detailed numerical study would be a worthwhile future research effort. In particular, the exact values of $\widehat{C}$, α, and θ should be applied.

6.5 Analysis of equation of motion

6.5.1 Effect of electric field on flux

Given a V-groove with fixed pressure boundary conditions, an external electric field enhances the flux, i.e., induces a higher flux than that groove would experience without an electric field. This property holds regardless of the variation of the electric field in Z, so long as the threshold thickness of the fluid in the groove is not exceeded.

To see this result, note first that, for a fixed pressure $\overline{P}$ and a fluid thickness $H < H_{\text{thresh.}}$,

$$\left.\frac{\partial H}{\partial \chi}\right|_{\overline{P}} = \frac{H^m}{\partial \overline{P}/\partial H} > 0. \tag{6.54}$$

In particular, the addition of an electric field means a thicker film is necessary to achieve the same pressure that would be achieved by capillary pressure alone without an electric field.[2] Hence for Dirichlet pressure boundary conditions $\overline{P}_1$ and $\overline{P}_2$ at Z_1 and Z_2, increasing the electric field enhances the flux.

For Dirichlet fluid thickness (H) boundary conditions, the reverse is true. If the electric field is increased and the boundaries adjusted to maintain a constant thickness H, the pressure gradient and flux become smaller than they would be without an electric field. In the case of a constant electric field $\chi(Z) = \chi_0$ [note that χ_0 is so named simply to indicate that it is a constant; not to refer to $\chi(Z = 0)$], and thickness boundary conditions $H(Z_A) = H_A$, $H(Z_B) = H_B$, the resulting flux can be computed exactly

$$\begin{aligned} Q &= \frac{1}{Z_B - Z_A}\int_{Z_A}^{Z_B} Q dZ = -\frac{\Gamma}{Z_B - Z_A}\int_{Z_A}^{Z_B} H^4 \partial_Z P dZ = -\frac{\Gamma}{Z_B - Z_A}\int_{H_A}^{H_B} H^4 \partial_H P dH \\ &= \frac{\widehat{A}}{Z_B - Z_A}\left[\frac{H_A^3 - H_B^3}{3} - \frac{m\chi_0}{m+4}\left(H_A^{m+4} - H_B^{m+4}\right)\right]. \end{aligned} \tag{6.55}$$

Clearly $(H_A^3 - H_B^3)$ and $-(H_A^{m+4} - H_B^{m+4})$ have opposite signs, and hence the electric field depresses the flux given the same fluid thickness boundary conditions.

6.5.2 Numerical analysis

In the following sections, stationary and self-similar solutions will be discussed and numerical solutions presented. The numerical solutions are computed by solving the relevant second-order ordinary differential equations (ODEs) as boundary value problems.

Stationary solutions, all of which assume constant electric field strength, were computed by solving Equation (6.57) using the ode45 solver in MATLAB (Mat, 2015) on a domain with 500 points. The system was solved with a shooting method. The boundary condition at $Z = 0$ was fixed, a slope $\partial_Z H|_{Z=0}$ was posited, and the system was solved forward to $Z = 5$. The resulting $H(Z = 5)$ was compared to the desired boundary condition, and the initial slope was adjusted accordingly. The process was repeated until the absolute error on the $Z = 5$ boundary condition thickness was less than 10^{-7}. Self-similar solutions were solved by the same procedure, but using Equation (6.59) and on a domain of length 40 and with 2000 elements. The domain and element sizes were chosen based on the results of Section 5.3.2.

[2] Regardless of whether $H < H_{\text{thresh.}}$ or $H > H_{\text{thresh.}}$, a fluid in a V-groove with an electric field will experience lower pressure than one without, and hence require a thicker film to achieve the same pressure. This is qualitatively similar to the behavior of the perfectly conducting thin film equation with an external electric field. However, when comparing two V-grooves that both experience an electric field, the one with the stronger electric field will have a thicker film at a given pressure only if H is less than the threshold thickness of the weaker field.

Terminating self-similar solutions were computed by solving Equation (6.59) with the ode45 solver in MATLAB (Mat, 2015) on a domain with 2000 points. This system was also solved with a shooting method, but in reverse: first, a termination point η_c was posited, the system was solved backwards from $\eta = \eta_c$ to $\eta = 0$, and the resulting pressure $\overline{P}(\eta = 0)$ or fluid thickness $H(\eta = 0)$ was compared to the corresponding boundary condition. η_c would then be adjusted, and the process continued until the absolute error on the $\eta = 0$ boundary condition thickness was less than 10^{-7}.

6.5.3 Stationary solutions

Stationary (i.e., time-independent) solutions can be found by solving Equation (6.43) with $\partial_T H = 0$, i.e.,

$$0 = \frac{\partial}{\partial Z}\left[H_S^4 \frac{\partial}{\partial Z}\left(\frac{1}{H_S} + \chi(Z) H_S^m\right)\right], \tag{6.56}$$

or, in the case of a constant electric field $\chi(Z) = \chi_0$,

$$0 = \frac{\partial^2}{\partial Z^2}\left[\frac{1}{3}H_S^3 - \chi_0 \frac{m}{m+4} H_S^{m+4}\right]. \tag{6.57}$$

[Recall that χ is defined by Equation (6.40) and captures the ratio of electric field strength, $\epsilon_0 E^2$, to capillary pressure, $\gamma/d\widehat{R}$]. Such solutions have a stationary fluid interface and constant flux which may be nonzero . For a review of stationary solutions without electric fields, see Chapter 4. The right-hand side of Equation (6.43) is a second-order ordinary differential equation (ODE), and thus requires two boundary conditions to specify, which may be Dirichlet pressure or fluid thickness boundary conditions, a constant flux boundary condition, a constant volume condition, etc. Because there is a one-to-one map between pressure and fluid thickness for $H < H_{\text{thresh.}}$, Dirichlet pressure and Dirichlet thickness boundary conditions are equivalent. However, when performing a comparison between systems with different electric field strengths, there is no obviously "better" choice of whether to compare pressure or thickness conditions; one or the other may be more convenient depending on the experimental setup. In what follows, we use fluid thickness boundary conditions as the canonical comparison (comparative plots with pressure boundary conditions may be found in Section 6.9). Although stationary solutions can be found for general functions $\chi(Z)$, here we consider only the special case of a constant electric field $\chi(Z) = \chi_0$.

Figure 6.5 shows plots of stationary solutions given a constant external electric field, with various fluid thickness (H) boundary conditions and electric field strengths, for $\alpha = 30^\circ$. Figure 6.6 shows similar plots for $\alpha = 60^\circ$. Note that since the nondimensionalization of the problem is based upon geometric quantities Γ, $\widehat{A}$, and $\widehat{R}$, then the nondimensionalization of the 30° and 60° grooves differs. Furthermore, the constant electric field strengths χ_0 shown are chosen as $\chi_0 = \{0,\ 0.2,\ 0.4,\ 0.6,\ 0.8,\ 0.9\} \times \chi_{\text{thresh.}}$, where $\chi_{\text{thresh.}}$ is defined relative to each groove geometry with $H_{\text{max}} = 1$; specifically, $\chi_{\text{thresh.}}(\alpha = 30^\circ) = 0.25$ and $\chi_{\text{thresh.}}(\alpha = 60^\circ) = 1$.

Consider again the example values in Section 6.4.1, namely, permittivity of free space $\epsilon_0 \approx 8.85\times10^{-12}$ F/m (Tiesinga et al., 2019), liquid indium surface tension $\gamma \approx 0.57$ N/m (Chentsov et al., 2011), and a flat counter-electrode with potential V_0 a distance $\ell = 250$ microns above the groove. Taking groove depth $b = 10$ microns and fluid thickness $d = 3$ microns implied that $\chi = \chi_{\text{thresh.}}$ when $V_0 \approx 77$ kV for $\alpha = 30°, \theta = 50°$ and $V_0 \approx 16$ kV for $\alpha = 60°, \theta = 15°$. Using these values, the dimensionless interface profiles shown in Figure 6.5 would then correspond to $V_0 \in \{0,\ \sqrt{0.2},\ \sqrt{0.4},\ \sqrt{0.6},\ \sqrt{0.8},\ \sqrt{0.9}\} \times 77$ kV $\approx \{0,\ 34,\ 49,\ 60,\ 69,\ 73\}$ kV. The dimensionless interface profiles shown in Figure 6.6 would in turn correspond to $V_0 \in \{0,\ \sqrt{0.2},\ \sqrt{0.4},\ \sqrt{0.6},\ \sqrt{0.8},\ \sqrt{0.9}\} \times 16$ kV $\approx \{0,\ 7,\ 10,\ 12,\ 14,\ 15\}$ kV.

Each plot in Figures 6.5 and 6.6 shows a different set of Dirichlet fluid thickness (H) boundary conditions; within each plot, different lines represent different electric field strengths. It is immediately noticeable that higher field strengths lead to thinner films, given the same H boundary conditions. This phenomenon arises due to the opposing signs of the integrated $H^4\partial_H P_{\text{capillary}}$ and $H^4\partial_H P_{\text{Maxwell}}$ terms in Equation (6.48). Note also that, while the stationary solution without an electric field follows the power $Z^{1/3}$ (see Chapter 4 for a review of such solutions), the solution with an electric field is clearly more complicated. In particular, the stationary solutions with an electric field can have both convex and concave regions within a single domain (this is only a statement of lengthwise curvature; the fluid surface transverse to the groove remains a circular section at all times).

While the results in the $\alpha = 30°$ groove (Figure 6.5) and the $\alpha = 60°$ groove (Figure 6.6) are qualitatively similar, the film interfaces in the $\alpha = 60°$ groove experience a bigger difference between $\chi_0 = 0$ and $\chi_0 = 0.9\chi_{\text{thresh.}}$ than those in the narrow groove (look at the gap between the blue $\chi_0 = 0$ line and the grey $\chi_0 = 0.9\chi_{\text{thresh.}}$ line around $Z = 2.5$, for example). This occurs because $m(\alpha = 30°) = 4$ while $m(\alpha = 60°) = 1$, so that the electric field strength decays faster in the narrow $30°$ groove than in the wide $60°$ groove.

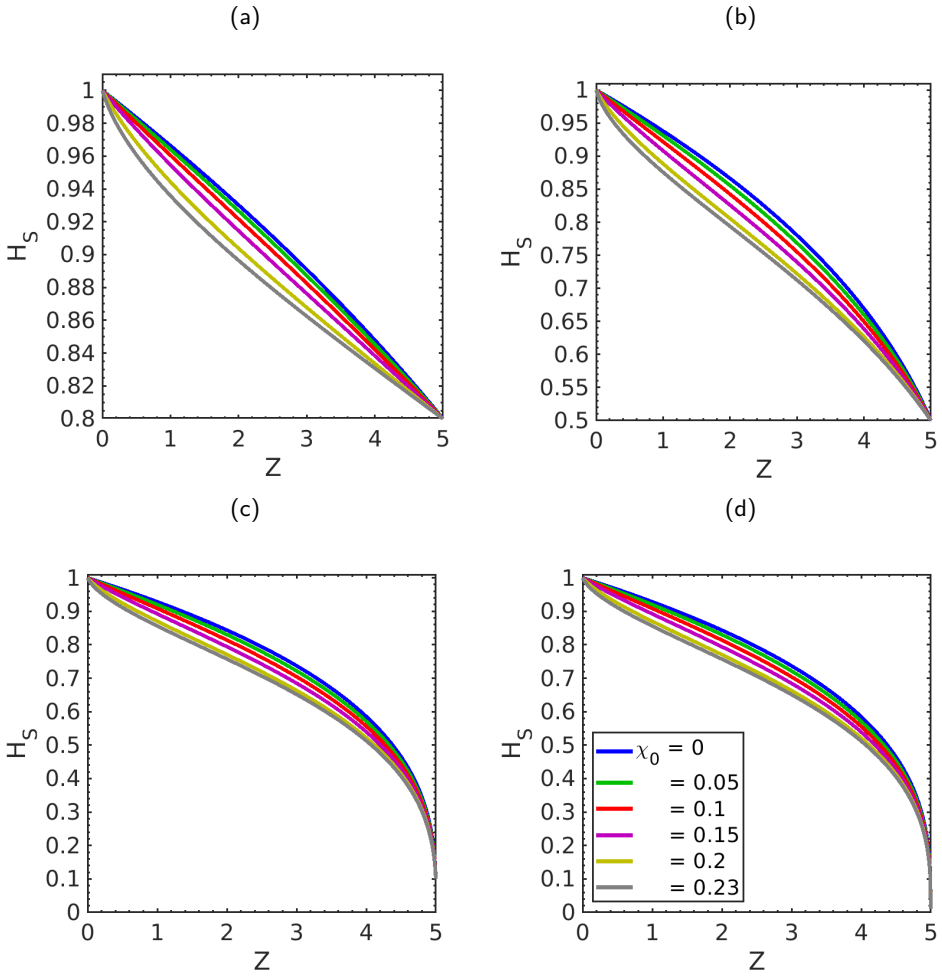

Figure 6.5: Representative stationary solutions of flow of conducting liquids in V-grooves with constant applied electric field, with internal groove half angle $\alpha = 30°$, and Dirichlet fluid thickness (H) boundary conditions, according to Equation (6.57). Results are plotted for grooves with 5 different values of nondimensional electric field, $\chi_0 \in \{0, 0.05, 0.1, 0.15, 0.2, 0.225\}$ corresponding to $(\chi_0/\chi_{\text{thresh.}}) \in \{0, 0.2, 0.4, 0.6, 0.8, 0.9\}$, where $\chi_{\text{thresh.}}$ is the maximum electric field strength for which $H_S(0) = 1 < H_{\text{thresh.}}$ [see Equation (6.44)]. The horizontal axis is Z, the axial coordinate along the groove, and the vertical axis is H_S, the nondimensional midline fluid thickness. All plotted solutions have boundary condition $H_S(0) = 1$, and the boundary condition at $H_S(5)$ is varied between the plots:
(a) $H_S(5) = 0.8$, (b) $H_S(5) = 0.5$, (c) $H_S(5) = 0.1$, (d) $H_S(5) = 0.01$.

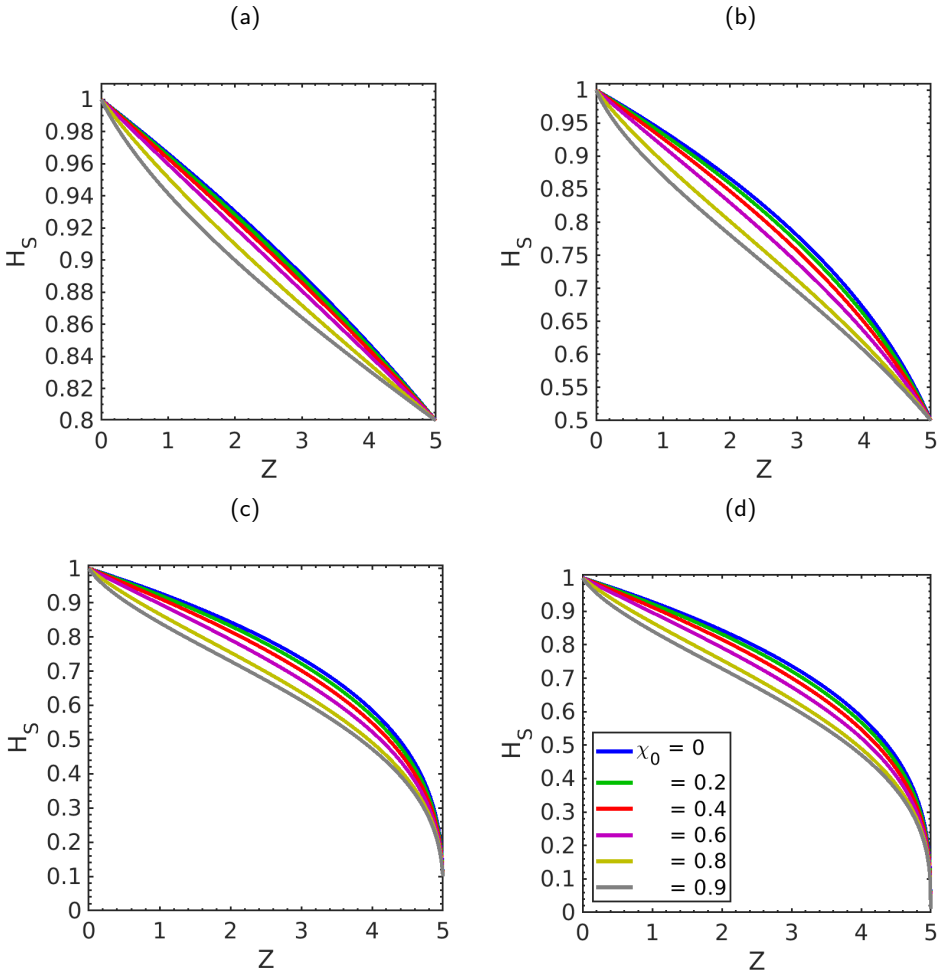

Figure 6.6: Representative stationary solutions of flow of conducting liquids in V-grooves with constant applied electric field, with internal groove half angle $\alpha = 60°$, and Dirichlet fluid thickness (H) boundary conditions, according to Equation (6.57). Results are plotted for grooves with 5 different values of nondimensional electric field, $\chi_0 \in \{0, 0.2, 0.4, 0.6, 0.8, 0.9\}$ corresponding to $(\chi_0/\chi_{\text{thresh.}}) \in \{0, 0.2, 0.4, 0.6, 0.8, 0.9\}$, where $\chi_{\text{thresh.}}$ is the maximum electric field strength for which $H_S(0) = 1 < H_{\text{thresh.}}$ [see Equation (6.44)]. The horizontal axis is Z, the axial coordinate along the groove, and the vertical axis is H_S, the nondimensional midline fluid thickness. All plotted solutions have boundary condition $H_S(0) = 1$, and the boundary condition at $H_S(5)$ is varied between the plots:
(a) $H_S(5) = 0.8$, (b) $H_S(5) = 0.5$, (c) $H_S(5) = 0.1$, (d) $H_S(5) = 0.01$.

6.5.4 Symmetry analysis and self-similar solution

Given an arbitrary electric field distribution $\chi(Z)$, the PDE Equation (6.43) has only one symmetry, time translation, represented by the symmetry operator $v_1 = \partial_T$ (if χ is constant in Z, a Z-translation symmetry $v_3 = \partial_Z$ exists as well). But if the electric field distribution follows a power law, i.e., $\chi(Z) = \chi_c Z^\nu$ for some constant χ_c and ν, then there is an additional scaling symmetry represented by the operator $v_2 = \left(2 + \frac{\nu}{1+m}\right) T\partial_T + Z\partial_Z - \frac{\nu}{1+m} H\partial_H$. This scaling symmetry leaves the quantities $\eta = Z/T^{(m+1)/[\nu+2(m+1)]}$ and $J = HT^{\nu/[\nu+2(m+1)]}$ invariant. In the special case $\nu = -2(m+1)$, T and HZ^{-2} are invariant. (Note that the result could be generalized from Z to $[Z - Z_0]$, but we may choose the origin anywhere we like without loss of generality).[3]

Therefore, when $\chi(Z) \propto Z^\nu$ with $\nu \neq -2(m+1)$, there exists a self-similar solution which solves

$$\frac{2}{\nu + 2(m+1)} J\left[\nu J + (1+m)\eta J'\right] = -2J(J')^2 - J^2 J' + \chi_c \eta^{\nu-2} J^{m+2}\left[\nu(\nu-1)J^2 + m(m+3)\eta^2 (J')^2 + 2\nu(m+2)\eta J J' + m\eta^2 J J''\right], \quad (6.58)$$

where $J' = \partial J(\eta)/\partial\eta$.

Recall that in the case without electric field, there was a family of self-similar solutions; here, the Maxwell pressure term constrains the result to a single self-similar solution. Because the self-similar solution is a second-order ordinary differential equation, it requires two boundary conditions to specify fully. These boundary conditions are typically set at $\eta = 0$ and $\eta = \infty$, because a boundary condition at $\eta = const.$ would reflect a boundary condition at $Z = const. \times T^{(m+1)/[\nu+2(m+1)]}$, i.e., a growing domain.

Note that boundary conditions on η correspond to both boundary conditions and initial/final conditions on Z and T, due to the combination of Z and T into a single variable. The $J(\eta = 0)$ boundary condition corresponds to both $Z = 0$ and $T = \infty$, while the $J(\eta = \infty)$ boundary condition corresponds to $Z = \infty$ and $T = 0$. Thus, self-similar solutions correspond to constant initial conditions $J(0) = 0^{\nu/[\nu+2(m+1)]} H(Z, T = 0)$ (which is finite for $\nu = 0$, 0 for $\nu > 0$, and infinite for $\nu < 0$) and to $T \to \infty$ conditions $J(\infty) = \infty^{\nu/[\nu+2(m+1)]} H(Z, T = \infty)$ (which is finite for $\nu = 0$, 0 for $\nu < 0$, and infinite for $\nu > 0$). The finite-time initial condition $H(Z, T_0) = H_i(Z)$ corresponds to $J(\eta) = T_0^{\nu/[\nu+2(m+1)]} \times H_i(T_0^{(m+1)/[\nu+2(m+1)]}\eta)$. Thus, an

[3] The symmetries of the PDE were found by the prolongation method, in which symmetries are posited in their most general form, these general symmetry operators are applied to the PDE, and the resulting differential equations are solved. Details of the methodology may be found in the textbook by Olver (1986); a more application-focused introduction is given by Hydon (2000). While that methodology allowed confirmation that time translation and scaling symmetries (and Z-translation, if χ is constant) are the only continuous symmetries of Equation (6.43), a much simpler method can be employed to find the symmetries. Time translation symmetry can be seen immediately by noting that there is no explicit T appearing in the equation; similarly for Z if $\chi = const.$. As for the scaling symmetry, one can proceed by making the scaling substitutions $H \to \lambda_1 H$, $Z \to \lambda_2 Z$, $T \to \lambda_3 T$ and noting that the original equation is recovered when $\lambda_1 = \lambda_2^{\nu/(m+1)}$ and $\lambda_3 = \lambda_2^{[2+\nu/(1+m)]}$.

initial condition $H(Z,T_0) = H_i(Z)$ is a part of a self-similar solution only if $T_0^{\nu/[\nu+2(m+1)]} \times H_i(T_0^{(m+1)/[\nu+2(m+1)]}\eta)$ satisfies the self-similar equation of motion, Equation (6.58).

A boundary condition on J corresponds to a boundary condition on $HT^{\nu/[\nu+2(m+1)]}$. Hence it is only for particular values of ν that useful physical boundary conditions will fit the self-similarity. In particular, the action of v_2 on $\overline{P}$ yields $v_2\overline{P} = \frac{\nu}{1+m}\overline{P}$, while $v_2 H = -\frac{\nu}{1+m}H$ and $v_2 Q = -\frac{3\nu+(m+1)}{m+1}Q$. A boundary condition is compatible with the self-similarity when the action of v_2 on the relevant quantity vanishes, i.e., when the boundary condition is invariant under the symmetry (Hydon, 2000). Thus, Dirichlet pressure or interface thickness boundary conditions require $\nu = 0$, and constant flux boundary conditions require $\nu = -(m+1)/3$. The latter is somewhat "fine-tuned"; one would have to carefully implement an electric field which decays in Z at the correct rate in order for a constant-flux boundary condition to yield a self-similar solution. But the Dirichlet pressure or thickness boundary condition is compatible with $\nu = 0$, or a constant electric field, which is likely to arise often in applications. Furthermore, with a constant external electric field, $\eta = Z/T^{1/2}$, i.e., the Washburn-like $T^{1/2}$ spreading is produced. In the case of a constant electric field strength $\chi(Z) = \chi_0$, the self-similar equation Equation (6.58) simplifies to

$$\begin{aligned} S'' &= -\left(\frac{S'}{S}\right)\frac{\eta + [2 - m(3+m)\chi_0 S^{m+1}]S'}{1 - m\chi_0 S^{m+1}} \\ &= -\left(\frac{S'}{S}\right)\left\{\eta + 2S' + \frac{m\chi_0}{1 - m\chi_0 S^{m+1}}\left[\eta - (m+1)S'\right]\right\}, \end{aligned} \tag{6.59}$$

where we have denoted the self-similar solution by $S(\eta) = H(Z/T^{1/2})$, and denoted η-derivatives by $S' = \partial_\eta S$.

Representative solutions of Equation (6.59) are shown in Figure 6.7. Advancing solutions (blue) represent flow from the origin $Z = 0$ towards $Z = \infty$, and have a well defined finite limit at $S(\infty)$. Receding solutions (orange) represent flow from $Z = \infty$ back towards $Z = 0$. The uniform solution with constant $S = 1$ (gray) has no flux. Terminating solutions (red) begin with $S > 0$ but reach $S = 0$ at a finite value of η. It should be noted that for each unique χ_0 and α there is a unique terminating solution with finite slope (and hence finite flux) at $S = 0$; all other terminating solutions are not physically accessible without some additional physics to describe behavior at the termination point.

Each plot of Figure 6.7 uses a different set of initial slope conditions $\partial_\eta S$ in order to construct a representative set of self-similar solutions for the relevant electric field strength χ_0 and internal groove half angle α. The top row represents solutions with internal groove half angle $\alpha = 30°$, corresponding to $m = 4$ and $\chi_{\text{thresh.}} = 0.25$ (computed with respect to an assumed $S_{\text{max}} = 1$, for consistency with the rest of this work). The bottom row represents solutions with internal groove half angle $\alpha = 60°$, corresponding to $m = 1$ and $\chi_{\text{thresh.}} = 1$ (also computed with respect to an assumed $S_{\text{max}} = 1$, for consistency). Each column represents self-similar solutions with a different electric field strength, $\chi_0 \in \{0, 0.4, 0.8\} \times \chi_{\text{thresh.}}$. $\chi_{\text{thresh.}}$ is computed with

respect to $S_{\text{max}} = 1$, for consistency; it is for this reason that only one receding solution is shown for $\alpha = 30^\circ$ with $\chi_0 = 0.8\chi_{\text{thresh.}}$ (higher receding solutions would exit the well-posed regime).

While the self-similar solutions are qualitatively similar with and without an electric field, some differences stand out. While the terminating solutions and lower advancing solutions have negative second derivative ($\partial_{\eta\eta} S < 0$) for small η when no electric field is applied, stronger electric fields flatten out the slope and even push it to $\partial_{\eta\eta} S > 0$. This effect is larger for the narrow $\alpha = 30^\circ$ than for the $\alpha = 60^\circ$ groove, due to the larger exponent m (4 vs. 1). Receding solutions also differ; as the electric field increases, the distance over which receding solutions transition from increasing slope to nearly flat becomes shorter, leading to an increasingly sharp "corner." This effect is again more pronounced in the narrow, $\alpha = 30^\circ$ groove, and will be discussed more shortly.

Figure 6.8 shows plots of self-similar solutions under a constant external electric field [i.e., solutions of Equation (6.59)], with various Dirichlet thickness (S) boundary conditions and electric field strengths, for $\alpha = 30^\circ$. Figure 6.9 shows similar plots for $\alpha = 60^\circ$. In the case of advancing solutions [plots (a)-(d)], for which $S(0) > S(\infty)$, stronger electric fields yield thinner films, just as with the stationary solutions. Furthermore, stronger electric fields yield a greater $\partial_{\eta\eta} S$ near $\eta = 0$; in particular, it can be seen in plots (c)-(d) that the solution with no electric field has negative axial interface curvature ($\partial_{\eta\eta} S < 0$) while the solution with an electric field has positive axial interface curvature ($\partial_{\eta\eta} S > 0$) near $\eta = 0$.

Receding solutions [plots (e)-(f)] show a different behavior, in which solutions with electric fields approach the thickness $S = 1$ faster than the solution without electric field. As the electric field strength, χ_0, increases the transition from a positive slope to a nearly flat interface occurs over a shorter distance, yielding an increasingly sharp "corner." Mathematically, this effect arises due to the denominator $(1 - m\chi_0 S^{m+1})$ in Equation (6.59) becoming smaller as $S \to H_{\text{thresh.}}$, leading to large-magnitude negative value of $\partial_{\eta\eta} S$. Put another way, the self-similar equation can be written as

$$0 = \frac{1}{2}\eta\partial_\eta(S^2) + \partial_\eta\left[S^4\frac{\partial\overline{P}}{\partial S}\partial_\eta S\right] = \eta S S' + \frac{\partial}{\partial S}\left[S^4\frac{\partial\overline{P}}{\partial S}\right](S')^2 + S^4\frac{\partial\overline{P}}{\partial S}S''. \tag{6.60}$$

As $(\partial\overline{P}/\partial S) \to 0$, the equation approaches a singular perturbation problem (Bender and Orszag, 1999), leading to a small region with a different scaling in which S'' is very large.

The self-similar solutions in the V-groove with $\alpha = 60^\circ$ (Figure 6.9) are qualitatively similar to those with $\alpha = 30^\circ$ (Figure 6.8). But, as with the stationary solutions, the gap between the $\chi_0 = 0$ interface and the $\chi_0 = 0.9\chi_{\text{thresh.}}$ interface is larger for the wide 60° groove than for the narrow 30° groove. This is attributable to the electric field exponent difference; $m(\alpha = 30^\circ) = 4$ and $m(\alpha = 60^\circ) = 1$, so that the electric field decays faster in the narrow groove than the wide groove.

Note that the results in (c) and (d) for advancing states thinning to $S = 0.1$ and $S = 0.01$, respectively, decrease to those thicknesses and do not rupture. Depending on the system parameters, $S = 0.1$ or $S = 0.01$ may be approaching the regime in which Van der Waals forces between the fluid and wall become relevant; such effects are omitted from the present model but would typically contribute to preventing rupture.

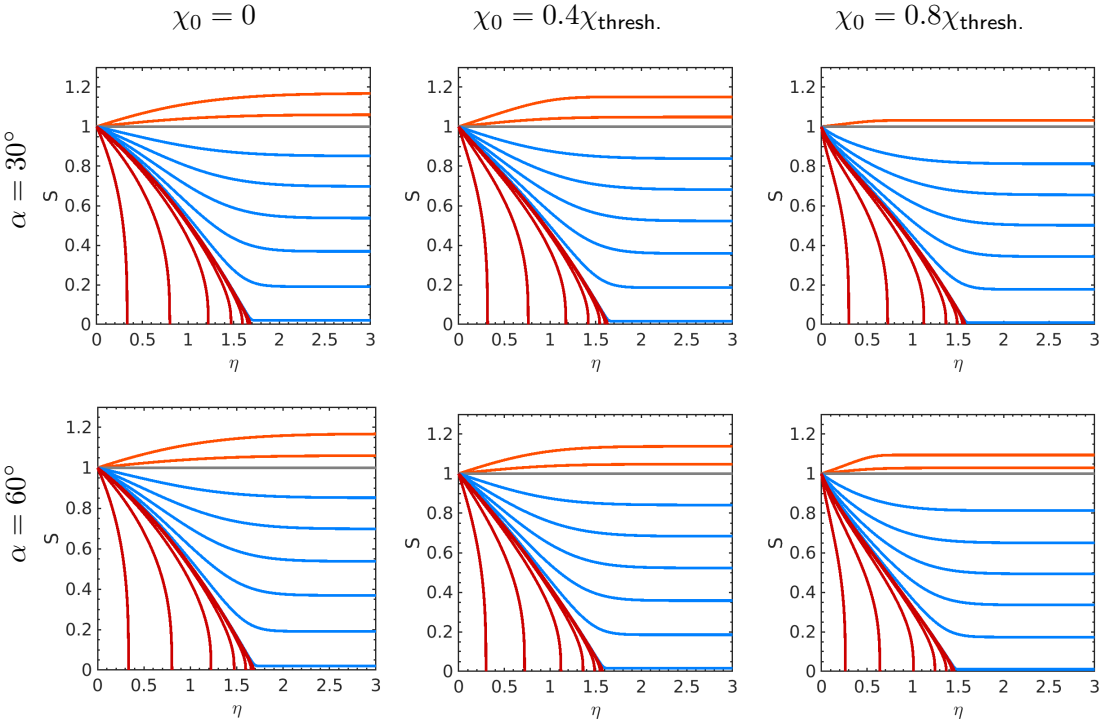

Figure 6.7: Representative self-similar solutions $S(\eta)$ with Dirichlet fluid thickness (S) boundary condition, for terminating (red), advancing (blue), uniform (gray) and receding (orange) states. The computational domain used in numerically solving for these solutions was $[0 \leq \eta \leq 5]$. (Only the range $[0 \leq \eta \leq 3.0]$ is shown in the figure since the downstream behavior remains essentially unchanged beyond that value.) All solutions satisfy the Dirichlet condition $S(\eta = 0) = 1$ at the origin. Each plot uses a different set of initial slope conditions $\partial_\eta S$ in order to construct a representative set of self-similar solutions for the relevant electric field strength χ_0 and internal groove half angle α.

The top row represents solutions with internal groove half angle $\alpha = 30°$, corresponding to $m = 4$ and $\chi_{\text{thresh.}} = 0.25$ (computed with respect to an assumed $S_{\text{max}} = 1$, for consistency with the rest of this work). The bottom row represents solutions with internal groove half angle $\alpha = 60°$, corresponding to $m = 1$ and $\chi_{\text{thresh.}} = 1$ (also computed with respect to an assumed $S_{\text{max}} = 1$, for consistency).

Each column represents self-similar solutions with a different electric field strength, $\chi_0 \in \{0, 0.4, 0.8\} \times \chi_{\text{thresh.}}$. $\chi_{\text{thresh.}}$ is computed with respect to $S_{\text{max}} = 1$, for consistency; it is for this reason that only one receding solution is shown for $\alpha = 30°$ with $\chi_0 = 0.8\chi_{\text{thresh.}}$ (higher receding solutions would exit the well-posed regime). Note also that the boundary conditions are not chosen consistently between the different cases; instead, a set of boundary conditions was chosen in each case in order to produce a clear set of differing solutions.

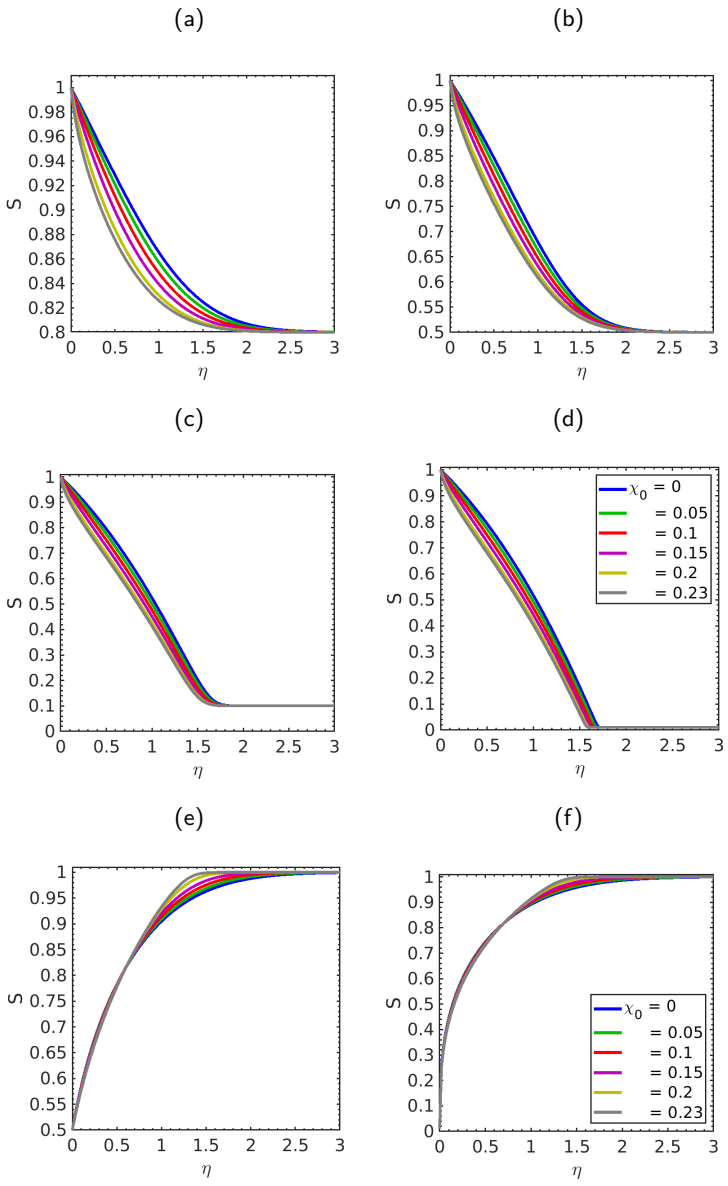

Figure 6.8: Representative self-similar solutions of flow of conducting liquids in V-grooves with constant applied electric field, with internal groove half angle $\alpha = 30^\circ$, and Dirichlet fluid thickness (S) boundary conditions, according to Equation (6.59). Results are plotted for grooves with 5 different values of nondimensional electric field, $\chi_0 \in \{0, 0.05, 0.1, 0.15, 0.2, 0.225\}$ corresponding to $(\chi_0/\chi_{\text{thresh.}}) \in \{0, 0.2, 0.4, 0.6, 0.8, 0.9\}$, where $\chi_{\text{thresh.}}$ is the maximum electric field strength for which $S(0) = 1 < H_{\text{thresh.}}$ [see Equation (6.44)]. The horizontal axis is Z, the axial coordinate along the groove, and the vertical axis is S, the nondimensional midline fluid thickness. Results were computed for $Z \in [0, 40]$, but plotted only for $Z \in [0, 3]$, because the remainder of the solution is nearly constant.
Plots (a)-(d) depict advancing solutions, with $S(0) = 1$, and varying boundary condition $S(40)$: (a) $S(40) = 0.8$, (b) $S(40) = 0.5$, (c) $S(40) = 0.1$, (d) $S(40) = 0.01$.
Plots (e)-(f) depict receding solutions, with $S(40) = 1$, and varying boundary condition $S(0)$: (e): $S(0) = 0.5$, (f): $S(0) = 0.01$.

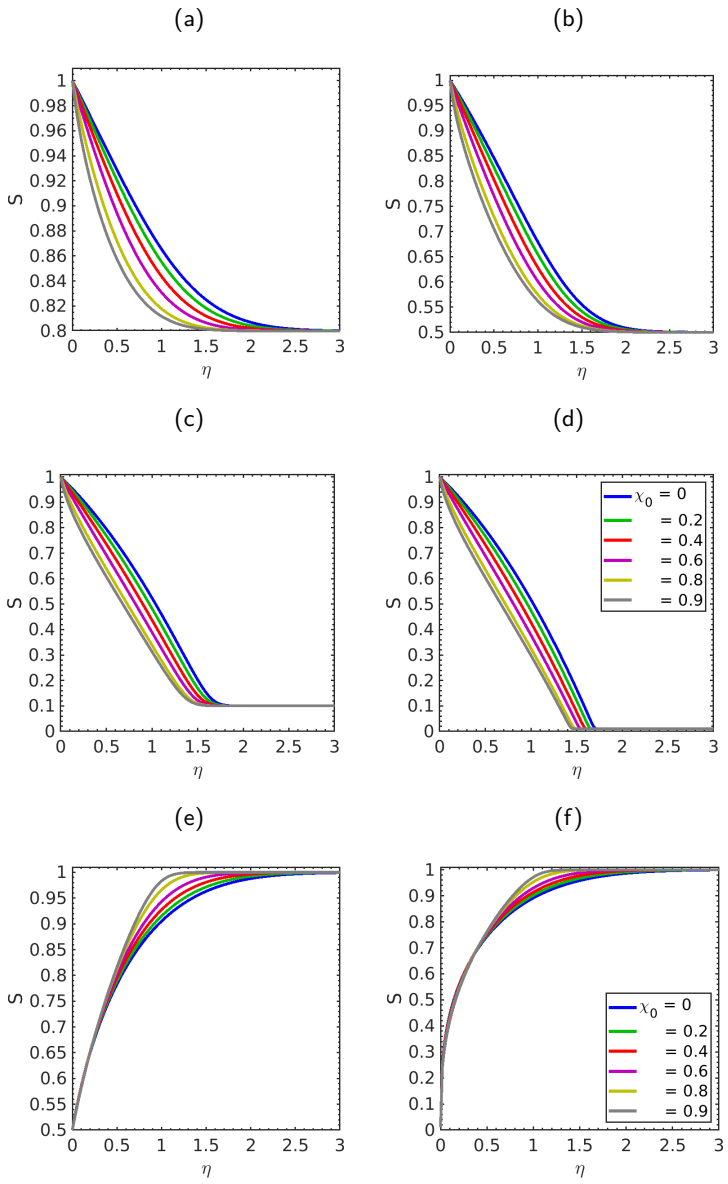

Figure 6.9: Representative self-similar solutions of flow of conducting liquids in V-grooves with constant applied electric field, with internal groove half angle $\alpha = 60°$, and Dirichlet fluid thickness (S) boundary conditions, according to Equation (6.59). Results are plotted for grooves with 5 different values of nondimensional electric field, $\chi_0 \in \{0, 0.2, 0.4, 0.6, 0.8, 0.9\}$ corresponding to $(\chi_0/\chi_{\text{thresh.}}) \in \{0, 0.2, 0.4, 0.6, 0.8, 0.9\}$, where $\chi_{\text{thresh.}}$ is the maximum electric field strength for which $S(0) = 1 < H_{\text{thresh.}}$ [see Equation (6.44)]. The horizontal axis is Z, the axial coordinate along the groove, and the vertical axis is S, the nondimensional midline fluid thickness. Results were computed for $Z \in [0, 40]$, but plotted only for $Z \in [0, 3]$, because the remainder of the solution is nearly constant.
Plots (a)-(d) depict advancing solutions, with $S(0) = 1$, and varying boundary condition $S(40)$: (a) $S(40) = 0.8$, (b) $S(40) = 0.5$, (c) $S(40) = 0.1$, (d) $S(40) = 0.01$.
Plots (e)-(f) depict receding solutions, with $S(40) = 1$, and varying boundary condition $S(0)$: (e): $S(0) = 0.5$, (f): $S(0) = 0.01$.

6.6 Stability analysis

6.6.1 Nonlinear stability analysis: Stationary, quiescent state

We first consider the nonlinear stability of the stationary state with no-flux boundary conditions, i.e., the state for which the fluid has zero flux and is quiescent. This state has a constant pressure ($\partial_Z \overline{P} = 0$). With a constant electric field, constant pressure is equivalent to constant interface midline thickness [as seen in the solutions in Figure 6.5 (a) and Figure 6.6 (a)], but for general fields that is not the case; a quiescent fluid may have a nontrivial thickness variation.

Letting $G = H^2$, Equation (6.43) becomes

$$\frac{\partial G}{\partial T} = \partial_Z \left[-G^2 \partial_Z \left(G^{-1/2} + \chi G^{m/2} \right) \right]. \tag{6.61}$$

We then define a Lyapunov functional $\mathfrak{F}_Q$ by

$$\mathfrak{F}_Q = \int_{Z_1}^{Z_2} \left\{ 2 \left[G_Q^{1/2} - G^{1/2} \right] + \frac{2}{m+2} \chi \left[G_Q^{(m+2)/2} - G^{(m+2)/2} \right] \right\}, \tag{6.62}$$

where $G_Q = H_Q^2$ is the stationary solution for some given pressure.

The functional derivatives are given by

$$\frac{\delta \mathfrak{F}_Q}{\delta G} = -G^{-1/2} - \chi G^{m/2} = \overline{P}_0 \tag{6.63}$$

$$\begin{aligned} \frac{\delta^2 \mathfrak{F}_Q}{\delta G^2} &= \frac{1}{2} G^{-3/2} \left(1 - m\chi G^{(m+1)/2} \right) \\ &= \frac{1}{2} H^{-3} \left(1 - \frac{\chi}{\chi_{\mathsf{max}}} \left[\frac{H}{H_{\mathsf{thresh.}}} \right]^{m+1} \right), \end{aligned} \tag{6.64}$$

where we have denoted the pressure by $\overline{P}_0$ to emphasize that it is constant ($\partial_Z \overline{P}_0 = 0$). In the last line, we have substituted in $G = H^2$ and used the relation $H_{\mathsf{thresh.}} = (m\chi_{\mathsf{max}})^{-1/(m+1)}$ in order to make clear that a sufficient condition for the second functional derivative $\delta^2 \mathfrak{F}_Q / \delta G^2$ to be positive is to have $H < H_{\mathsf{thresh.}}$ (note that by definition, $\chi < \chi_{\mathsf{max}}$). Thus, when H is below the threshold thickness, $\mathfrak{F}_Q$ is convex, implying that it has an isolated minimum.

Furthermore, $\mathfrak{F}_Q$ is always decreasing:

$$\begin{aligned} \frac{\partial \mathfrak{F}_Q}{\partial T} &= \int_{Z_1}^{Z_2} \frac{\delta \mathfrak{F}_Q}{\delta G} \frac{\partial G}{\partial T} dZ = \int_{Z_1}^{Z_2} \frac{\delta \mathfrak{F}_Q}{\delta G} \partial_Z \left(G^2 \partial_Z \frac{\delta \mathfrak{F}_Q}{\delta G} \right) dZ \\ &= \left[G^2 \frac{\delta \mathfrak{F}_Q}{\delta G} \partial_Z \frac{\delta \mathfrak{F}_Q}{\delta G} \right]_{Z_1}^{Z_2} - \int_{Z_1}^{Z_2} G^2 \left(\partial_Z \frac{\delta \mathfrak{F}_Q}{\delta G} \right)^2 \\ &= \left[\frac{\delta \mathfrak{F}_Q}{\delta G} Q \right]_{Z_1}^{Z_2} - \int_{Z_1}^{Z_2} G^2 \left(\partial_Z \frac{\delta \mathfrak{F}_Q}{\delta G} \right)^2 \\ &= - \int_{Z_1}^{Z_2} \left(\partial_Z \frac{\delta \mathfrak{F}_Q}{\delta G} \right)^2 < 0. \end{aligned} \tag{6.65}$$

Note that the boundary term vanished because $G^2 \partial_Z (\delta \mathfrak{F}_Q / \delta G) = Q$, the flux, which was assumed to be 0 at the boundaries.

Thus, because the Lyapunov functional $\mathfrak{F}_Q$ is convex and decreasing, a quiescent film satisfying $H < H_{\mathsf{thresh.}}$ is nonlinearly stable.

Comparison to thin film instability

While the previous section proved stability of quiescent states mathematically, we still may wish to understand intuitively why the V-groove is stable under an electric field while a thin film on a flat plate is unstable. Turning to linear stability analysis of the quiescent state will help to provide intuition. The key is the fact that the V-groove capillary pressure is $\propto h^{-1}$ (the exponent is not important; the lack of derivatives is important), while the thin film capillary pressure is $\propto \nabla^2 h$. In both cases, the Maxwell pressure is proportional to a function of h alone with no derivatives. Thus, the wavelength of a perturbation does not induce any difference between Maxwell and capillary pressure for the V-groove, while long wavelengths on thin films induce a weakening of the capillary pressure relative to the Maxwell pressure.

More explicitly, let us linearize the V-groove equation with a constant electric field strength $\chi(Z) = \chi_0$ by writing $H = H_0 + \delta H$, with H_0 constant. Then,

$$\begin{aligned} 2H_0 \frac{\partial \delta H}{\partial T} &= -H_0^4 \left(-\frac{1}{H_0^2} + \chi_0 m H_0^{m-1} \right) \frac{\partial^2 \delta H}{\partial Z^2} \\ \implies \frac{\partial \delta H}{\partial T} &= -\frac{H_0}{2} \left(1 - \chi_0 m H_0^{m+1} \right) K^2 \delta H, \end{aligned} \tag{6.66}$$

where we have performed a Fourier transform of Z to K. Clearly the wavenumber K is irrelevant to the question of whether the system is stable or not; all that matters is the sign of $(1 - \chi_0 m H_0^{m+1}$, i.e., whether H_0 is greater than or less than $H_{\text{thresh.}}$.

But the thin film equation on a flat plate under an electric field is given by (Kim et al., 1992)

$$\frac{\partial H}{\partial T} = -\frac{1}{3} \nabla \cdot \left[H^3 \nabla \left(\varepsilon^2 \nabla^2 H + \frac{\mathrm{We}}{2} \nabla \Psi \cdot \nabla \Psi \right) \right], \tag{6.67}$$

where we have applied the V-groove nondimensionalization for consistency of comparison (thus yielding the extra factor of ε^2 in front of the capillary term). Linearizing about a sinusoidal perturbation δH yields a perturbed electric field $\Psi_0 + \Psi_1 \delta H$, and hence

$$\begin{aligned} \frac{\partial \delta H}{\partial T} &= -\frac{1}{3} H_0^3 \varepsilon^2 \nabla \cdot \left[\nabla \left(\nabla^2 \delta H + \varepsilon^{-2} \mathrm{We} \{ \nabla \Psi_0 \cdot \nabla \Psi_1 \} \delta H \right) \right] \\ \implies \frac{\partial \delta H}{\partial T} &= \frac{1}{3} H_0^3 \varepsilon^2 \left[-K^4 + \left(\varepsilon^{-2} \mathrm{We} \nabla \Psi_0 \cdot \nabla \Psi_1 \right) K^2 \right] \delta H. \end{aligned} \tag{6.68}$$

Thus, long wavelength (small wavenumber K) perturbations are unstable, due to the higher power of K on the capillary pressure term. For a full derivation of the stability of a thin film under an electric field, see de Surgy et al. (1993) (who did not use the thin film equation explicitly but performed a linear stability analysis of the full Navier-Stokes equations and took both thick and thin limits, yielding the thin film equation result in the latter case) or Kim et al. (1992), who included inertial effects and gravity for a thin film on an inclined plane under an electric field.

While this linear analysis provides intuition, the nonlinear stability analysis presented above was more general, as it allowed non-infinitesimal perturbations and arbitrary electric fields.

6.6.2 Nonlinear stability analysis: Stationary interface with non-zero fluid flux and constant electric field

For the case of a stationary interface with non-zero fluid flux (or a stationary interface shape with different boundary values of the pressure), finding a Lyapunov functional is more challenging, since the boundary terms are no longer trivial. In this case, we consider only a constant external electric field with $\chi(Z) = \chi_0$, and follow an analysis similar to that in Section 5.2.

Letting $G = H^2$, Equation (6.43) becomes

$$\begin{aligned}\frac{\partial G}{\partial T} &= \partial_Z\left[-G^2\partial_Z\left(G^{-1/2} + \chi_0 G^{m/2}\right)\right] \\ &= \partial_Z\left[\left(\frac{1}{2}G^{1/2} - \frac{m}{2}\chi_0 G^{(m+2)/2}\right)\partial_Z G\right] \\ &= \frac{1}{3}\partial_Z\left\{\partial_Z\left[\left(G^{3/2} - G_S^{3/2}\right) - \frac{3m}{m+4}\chi_0\left(G^{(m+4)/2} - G_S^{(m+4)/2}\right)\right]\right\},\end{aligned} \tag{6.69}$$

where $G_S = H_S^2$ is the stationary solution for the given pressure, midline thickness, or flux boundary conditions. We now define a Lyapunov functional $\mathfrak{F}$ by

$$\begin{aligned}\mathfrak{F}[G] = \int_{Z_1}^{Z_2}\Bigg\{&\left[\frac{2}{5}G^{5/2} - G_S^{3/2}G + \frac{3}{5}G_S^{5/2}\right] \\ &- \frac{3m\chi_0}{(m+4)(m+6)}\left[2G^{(m+6)/2} - (m+6)G_S^{(m+4)/2}G + (m+4)G_S^{(m+6)/2}\right]\Bigg\}dZ.\end{aligned} \tag{6.70}$$

The functional derivatives are given by

$$\frac{\delta\mathfrak{F}}{\delta G} = \left(G^{3/2} - G_S^{3/2}\right) - \frac{3m}{m+4}\chi_0\left(G^{(m+4)/2} - G_S^{(m+4)/2}\right) \tag{6.71}$$

$$\frac{\delta^2\mathfrak{F}}{\delta G^2} = \frac{3}{2}G^{1/2} - \frac{3m}{2}\chi_0 G^{(m+2)/2}. \tag{6.72}$$

Note that $\mathfrak{F}[G_S] = 0$ and $(\delta\mathfrak{F}/\delta G)|_{G=G_S} = 0$. $\mathfrak{F}$ is convex when $(\delta^2\mathfrak{F}\delta G^2) > 0$:

$$\begin{aligned}\frac{\delta^2\mathfrak{F}}{\delta G^2} > 0 &\iff G < (m\chi_0)^{-2/(m+1)} \\ &\iff H < (m\chi_0)^{-1/(m+1)} = H_{\text{thresh.}}.\end{aligned} \tag{6.73}$$

Finally, $\mathfrak{F}$ is always decreasing:

$$\begin{aligned}\frac{\partial\mathfrak{F}}{\partial T} &= \int_{Z_1}^{Z_2}\frac{\delta\mathfrak{F}}{\delta G}\frac{\partial G}{\partial T}dZ = \int_{Z_1}^{Z_2}\frac{\delta\mathfrak{F}}{\delta G}\partial_{ZZ}\frac{\delta\mathfrak{F}}{\delta G}dZ \\ &= \left[\frac{\delta\mathfrak{F}}{\delta G}\partial_Z\frac{\delta\mathfrak{F}}{\delta G}\right]_{Z_1}^{Z_2} - \frac{1}{3}\int_{Z_1}^{Z_2}\left(\partial_Z\frac{\delta\mathfrak{F}}{\delta G}\right)^2 \\ &= -\frac{1}{3}\int_{Z_1}^{Z_2}\left(\partial_Z\frac{\delta\mathfrak{F}}{\delta G}\right)^2 < 0.\end{aligned} \tag{6.74}$$

Note that the boundary term vanishes in the case of a pressure or thickness boundary condition because $(\delta\mathfrak{F}/\delta G)|_{G=G_S} = 0$, and in the case of a flux boundary condition because $\partial_Z(\delta\mathfrak{F}/\delta G) = -3(Q - Q_S)$, Q_S being the stationary flux.

Therefore, for the case of a constant electric field, $H_{\text{thresh.}}$ is not only the threshold thickness below which the equation of motion is well-posed; it is also the threshold thickness below which the system exhibits Lyapunov stability around a stationary solution with pressure or flux boundary conditions.

6.6.3 Generalized linear stability analysis: Self-similar states

Following the methodology of Chapter 5, we perform a generalized linear stability analysis of self-similar states with constant electric field $\chi(Z) = \chi_0$. We linearize according to

$$H(\eta, \tau) = S(\eta) + \delta H(\eta, \tau), \tag{6.75}$$

where $\tau = \ln(T)$, $S(\eta)$ is the self-similar state obeying the given boundary conditions, and $\delta H(\eta, \tau)$ represents the infinitesimal non-modal disturbance function. Substituting this into Equation (6.43) yields the governing linear disturbance equation to order δH,

$$\frac{\partial \delta H}{\partial \tau} = \mathcal{L}\delta H, \tag{6.76}$$

with

$$\begin{aligned}\mathcal{L} = &\frac{S}{2}\left[1 - m\chi_0 S^{m+1}\right]\partial_{\eta\eta} + \left[\frac{\eta}{2} + 2S' - m(3+m)\chi_0 S^{m+1}S'\right]\partial_\eta \\ &+ \frac{S''}{2} - \frac{m}{2}\chi_0 S^m\left[(m+1)(m+3)(S')^2 + (m+2)SS''\right].\end{aligned} \tag{6.77}$$

The transient operator is then given by

$$\begin{aligned}\frac{\mathcal{L} + \mathcal{L}^\dagger}{2} = &\frac{S}{2}\left[1 - m\chi_0 S^{m+1}\right]\partial_{\eta\eta} + \frac{S'}{2}\left[1 - m(2+m)\chi_0 S^{m+1}\right]\partial_\eta \\ &- \frac{1}{4}\left\{1 + S'' + m\chi_0 S^m\left[(m+1)(m+2)(S')^2 + mSS''\right]\right\}.\end{aligned} \tag{6.78}$$

Parameter sweeps testing linear stability for a variety of half angles α and initial and final fluid thickness conditions $S_a = S(\eta = 0)$ and $S_b = S(\eta = \eta_b)$ were performed. Fluid thickness was set to $S_a = 1$ and various $S_b \in \{0.01, 0.1, 0.5, 0.8, 1\}$ for self-similar advancing solutions, and vice versa for receding solutions . System parameters were set to α from 15° to 75°, and χ_0 from 0 to $0.9 \times \chi_{\text{thresh.}}$, where $\chi_{\text{thresh.}}$ is the maximum electric field strength for which $S(0) = 1 < H_{\text{thresh.}}$ (see Equation (6.44)). In all cases, the system was both transiently and asymptotically stable, with numerical abscissa less than -0.18 and spectral abscissa below -0.81 (see Chapter 3 and Chapter 5 for reviews of generalized linear stability analysis and numerical and spectral abscissae). In the nondimensionalized system, the timescale of comparison is 1; hence the numerical abscissa of $O(-0.1)$ may be considered slightly weak stability, as perturbations decay on a timescale of $O(10)$.

A subset of these results is shown in Figure 6.10, which displays plots of the numerical abscissa for advancing, (a), and receding, (b), systems, with $\chi_0 = 0.9 \times \chi_{\text{thresh.}}$. The advancing case

shows little variation between different interior groove angles; this result is likely due to the fact that the majority of the fluid is very thin in the groove and hence feels little effect from the electric field. The slightly greater stability of narrow (small α) grooves is likely attributable to the faster decay of the electric field within those grooves. The receding states, on the other hand, have most of their fluid at a large thickness, and so are less stable than the advancing solutions. Furthermore, as noted in Section 6.5.4, receding solutions at large χ_0 develop a sharp "corner" effect, where $S'' \ll 0$. An inspection of the constant term in the transient operator, Equation (6.78), suggests that as S'' becomes more negative, the upper bound on the eigenvalue of the operator (i.e., the upper bound on the numerical abscissa) increases. This effect thus likely explains why receding states are less stable than advancing states, and why narrow grooves with small α (which have a sharper "corner") should be less stable than wide grooves, as reflected in Figure 6.10 (b).

To gain some intuition for why the numerical abscissa remains near $-(1/4)$ for advancing states, even as $\chi \to \chi_{\text{thresh.}}$, consider the simplest case of $S = S_0 = const.$. In this case, the transient operator is given by

$$\begin{aligned} \frac{\mathcal{L} + \mathcal{L}^\dagger}{2} &= \frac{S_0}{2}\left[1 - m\chi_0 S_0^{m+1}\right]\partial_{\eta\eta} - \frac{1}{4} \\ &= \frac{S_0}{2}\left[1 - \frac{\chi_0}{\chi_{\text{thresh.}}}\right]\partial_{\eta\eta} - \frac{1}{4}. \end{aligned} \tag{6.79}$$

Thus, for $\chi_0 \leq \chi_{\text{thresh.}}$, the numerical abscissa is at most $-1/4$. As the wavelength of perturbations decreases, the eigenvalue of $(\mathcal{L} + \mathcal{L}^\dagger)/2$ becomes more negative. But as soon as $\chi_0 > \chi_{\text{thresh.}}$, suddenly short wavelengths instead increase the eigenvalue. Indeed, for any $\chi_0 > \chi_{\text{thresh.}}$, the numerical abscissa is unbounded, indicating an ill-posed PDE. For more complicated base states $S(\eta)$, the bounds vary slightly, but the same qualitative behavior applies as long as S'' is not highly negative (i.e., the qualitative behavior applies for advancing states, not receding states).

While a full stability analysis was carried out only for $\chi_0 \leq 0.9\chi_{\text{thresh.}}$, exploratory results suggest that the numerical abscissae for advancing states indeed remain negative up to $\chi_0 = 0.99\chi_{\text{thresh.}}$, but the numerical abscissae of certain receding states may become positive around $\chi_0 \gtrsim 0.96\chi_{\text{thresh.}}$. A more detailed study would be required to determine the exact cutoff, with special care taken to accurately capture the increasingly sharp "corner." It is safe to say, however, that the self-similar states are transiently and asymptotically stable for $\chi_0 \leq 0.9\chi_{\text{thresh.}}$.

Linear stability analysis was performed in MATLAB by second-order central finite difference on a domain $\eta \in [0, 40]$ with 2000 points, based on the length and mesh fineness found to be sufficient for straight V-grooves in Section 5.3.2. The transient operator was constructed in matrix form using second-order finite difference operators, and the maximum eigenvalue was found using MATLAB's built-in `eig` function, which computes exact matrix eigenvalues (the matrices were sufficiently small that approximate eigensystem methods were not required).

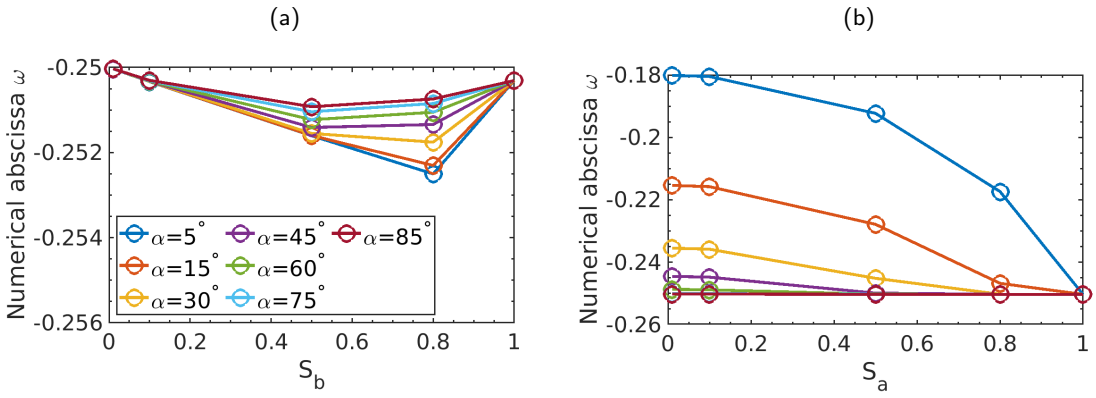

Figure 6.10: Representative numerical abscissae for self-similar solutions of flow in V-grooves with constant applied electric field, computed by finding the largest eigenvalue of the transient linear operator in self-similar coordinates, Equation (6.78). Results for advancing solutions (a) and receding solutions (b) are shown Numerical abscissae are computed for interior groove half angle $\alpha \in \{5°, 15°, 30°, 45°, 60°, 75°, 85°\}$ and electric field strength $\chi_0(\alpha)/\chi_{\text{thresh.}}(\alpha) = 0.9$, where $\chi_{\text{thresh.}}(\alpha)$ is the ($\alpha-$dependent) maximum electric field strength for which $S(0) = 1$ is in the well-posed regime [see Equation (6.46)]. Results are shown in nondimensional variables, and each case (each α) is nondimensionalized independently. Results were computed with domain length 40 and the mesh size was taken to be 0.02, following Chapter 5. The horizontal axis describes the fluid thickness boundary condition, while the vertical axis is the numerical abscissa, ω (see Chapter 3).
(a) Self-similar advancing solutions with Dirichlet fluid thickness boundary conditions $S(0) = S_a = 1$ and $S(40) = S_b \in \{0.01, 0.1, 0.5, 0.8, 1\}$.
(b) Self-similar receding solutions with Dirichlet fluid thickness boundary conditions $S(0) = S_a \in \{0.01, 0.1, 0.5, 0.8, 1\}$ and $S(40) = S_b = 1$.

6.7 Numerical validation

In the analysis above, the deviation of the fluid surface from a circular section was ignored, and furthermore the interface pressure was approximated as $\overline{P} = -1/H - \chi_0 H^m$. Ignoring the surface correction led to the flux parameter $[\int_\Omega \overline{M}_1 dX dY]/H^4$ (from Equation (6.13)) being approximated as $\Gamma(\alpha, \theta)$ and the cross-sectional area of the fluid being approximated as $A = \widehat{A} H^2$. To justify these approximations, we perform numerical tests.

Consider a V-groove with tall walls, capped by a flat electrode with constant potential $\Psi_{electrode}$ at a height $y = b$ above the groove corner (see cross-section in Figure 6.11). We use a flat electrode specifically in order to violate the annular wedge solution and mimic a realistic applied electric field. We continue to assume that the fluid and groove walls are perfect conductors.

In this case, the fluid interface shape and flux factor depend on two quantities: $(h/b) = (d/b)H$ (the fluid interface midline thickness divided by the electrode height) and $\Psi_{electrode}$, the electric potential strength. For each pair $\{(h/b), \Psi_{electrode}\}$, we can compute the surface shape which satisfies $\partial_X \overline{P} = 0$, along with the electric potential distribution in the groove. This results in a cross-sectional liquid domain $\Omega_{\text{num.}}(\alpha, \theta, \Psi_{electrode}, H)$ with a different shape from the

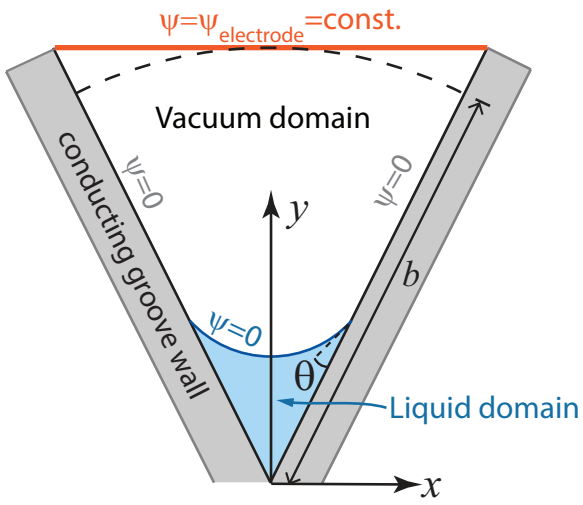

Figure 6.11: Cross-sectional schematic of numerical test system, based on the more general system depicted in Figure 6.1, but with the addition of a flat electrode at $y = b$. The conducting groove walls and conducting fluid interface are grounded at $\psi = 0$, while the electrode potential is fixed at $\psi = \psi_{electrode}$. The fluid interface is allowed to freely deviate from a circular section, but the contact angle θ remains fixed.

prior assumed $\Omega(\alpha, \theta)$. The normalized fluid velocity $\overline{M}_1$ can then be solved by the Poisson equation in Equation (6.13), but in $\Omega_{\text{num.}}$ instead of Ω, then yielding a numerical flux factor $\Gamma_{\text{num.}} = \int_{\Omega_{\text{num.}}} \overline{M}_1 dX dY / H^4$. Similarly, the cross-sectional area $A_{\text{num.}} = \int_{\Omega_{\text{num.}}} 1 dX dY$ can be computed. From new fluid interface, the mean curvature $K_{\text{num.}}$ can be computed, along with the capillary pressure $P_{\text{capillary,num.}} = -2\text{Ca}K_{\text{num.}}$, and the Maxwell pressure $P_{\text{Maxwell,num.}} == -[\text{We}/(2\text{Ca})][\nabla\Psi]^2|_{Y=H}$. These values can then be compared to the simpler values assumed in the analytic model. An overview of these variables can be found in Table 6.3.

Variable	Value in analytic model	Variable name in numerical validation
Cross-sectional liquid domain	$\Omega(\alpha,\theta)$	$\Omega_{\text{num.}}(\alpha,\theta,\Psi_{electrode},H)$
Cross-sectional area	$\widehat{A}(\alpha,\theta)H^2=\int_\Omega 1dXdY$	$A_{\text{num.}}=\int_{\Omega_{\text{num.}}}1dXdY$
Flux factor	$\Gamma(\alpha,\theta)$ $=[\int_\Omega \overline{M}_1 dXdY]/H^4$	$\Gamma_{\text{num.}}$ $=[\int_{\Omega_{\text{num.}}}\overline{M}_1 dXdY]/H^4$
Liquid interface mean curvature	$K=1/(2\widehat{R}H)$	$K_{\text{num.}}(\alpha,\theta,\Psi_{electrode},H)$
Capillary pressure	$P_{\text{capillary}}=-2\text{Ca}K=-(\text{Ca}\widehat{R})^{-1}/H$	$P_{\text{capillary,num.}}=-2\text{Ca}K_{\text{num.}}$
Maxwell pressure	P_{Maxwell} $=-(\text{Ca}\widehat{R})^{-1}\chi H^m$	$P_{\text{Maxwell,num.}}$ $=-[\text{We}/(2\text{Ca})][\nabla\Psi]^2\vert_{Y=H}$
Rescaled pressure	$\overline{P}=(\text{Ca}\widehat{R})P=-1/H-\chi H^m$	$\overline{P}_{\text{num.}}$

Table 6.3: Variables arising in numerical validation of the analytical model.

6.7.1 Numerical validation methodology

The true (non-circular) cross-sectional fluid interface and corresponding electric field and flux values were computed using the finite element method in COMSOL (Com, 2017). Geometry corresponding to Figure 6.11 was implemented and given a triangular mesh by COMSOL, in which elements on the interface and within the liquid domain were chosen to have length at most 7.5% of the center fluid thickness, and elements in the vacuum domain were allowed length at most 5% of the total domain height b.

The initial geometry was set up with the liquid domain having a circular interface, as would be the case without an electric field. The electrostatic equation $\nabla^2\Psi=0$ was set up in the vacuum domain, with boundary conditions $\Psi|_{\text{walls, interface}}=0$ and $\Psi|_{y=b}=\Psi_{electrode}$. At the top corners of the vacuum domain, the electrode with potential $\Psi_{electrode}\neq 0$ meets the wall with potential $\Psi=0$. This was resolved only at the level of the smallest finite element, with length at most $0.05b$; finer resolution of these interior corners is not expected to have a significant effect on the electric field far from the corners.

In order to naturally produce an interface in which the sum of capillary pressure and Maxwell pressure remains constant in x, a time-dependent non-inertial 2D incompressible fluid equation was solved in the liquid domain. Using COMSOL's built-in arbitrary Lagrangian-Eulerian (ALE) moving mesh algorithm. Specifically, a 2D incompressible fluid satisfying $\nabla\cdot[U,V]=0$, $\nabla^2[U,V]=-\nabla P$ was solved, with no-slip wall boundary conditions ($U|_{wall}=V|_{wall}=0$). The interface boundary conditions were set by $2\hat{n}\cdot(\nabla[U,V])\cdot\hat{n}-P=2K+\text{We}(\nabla\Psi)^2$ and $\hat{n}\cdot(\nabla[U,V]+\nabla[U,V]^T)\cdot\hat{t}=0$ at the fluid interface, where $\hat{n}$ and $\hat{t}$ represent normal and tangent unit vectors at the fluid interface and K is the interface mean curvature (see Chapter 2

for a review of fluid mechanics boundary conditions). A kinematic condition (see Chapter 2 for a review) was set, imposing that the fluid interface must move according to the velocity of the fluid, specifically, $\partial_T \Sigma(X,T) + U\partial_X \Sigma(X,T) = V$ at the fluid interface, where $Y = \Sigma(X,T)$ represents the interface. COMSOL was directed to simultaneously solve the electrostatic equation in the vacuum region (with the updated fluid interface) and the fluid equations in the fluid region. The result was that the fluid interface was continually adjusted until the capillary and Maxwell pressures were constant on the interface.

Once the interface shape was determined, the Poisson equation for the streamwise velocity, Equation (6.13), was computed in the liquid domain to determine the flux factor $\Gamma_{\text{num.}} = \overline{Q}/H^4$. The cross-sectional area $A_{\text{num.}}$ was also computed. While the interface was no longer circular, H was still taken to be the midline thickness of the fluid.

In order to compare the numerical results to the theoretical model, it was necessary to numerically determine the constant χ_0. This was accomplished by fitting all numerically computed Maxwell pressures (with all values of h and θ) for a given groove angle α onto the line $\chi_0 H^m$, as in Figure 6.12. χ_0 is the only parameter which was fit from the numerical results (more specifically, $\widehat{C}$, the deviation of the Maxwell pressure from the annular wedge solution, is the value which is fit, and in turn determines χ_0). Note that it is because of this fitting methodology that systems with very small and very large values of θ appear to have a larger error than those with middling values of θ. The error could be reduced by fitting a separate χ_0 for each value of θ. Thus, if one knows what material and what groove angle will be used, as well as the external electric field (or shape of the electrode) a priori, one can compute a more accurate χ_0 and have a lower error in the theoretical model.

Numerical validation results

A parameter sweep was performed for thin films varying between $h/b = (d/b)H \in [10^{-4}, 10^{-1}]$, with $\alpha = \in \{15^\circ, 30^\circ, 45^\circ, 60^\circ, 75^\circ\}$ and $\theta \in \{10^\circ, 15^\circ, 30^\circ, 45^\circ, 60^\circ\}$. In each case, the electrode potential was set to $\Psi_{electrode} = 1/\sqrt{m 0.1^m}$. This electric field strength was chosen in order to make $h_{\text{thresh.}} \approx 0.1b$. That is, the electric field was set to approximately the highest value accessible for $(h/b) = 0.1$ under the constraints of the model.[4]

First, the Maxwell pressure, $-\overline{P}_{\text{Maxwell}}$, at the fluid surface was computed. Two example plots comparing $\overline{P}_{\text{Maxwell}}$ to h/b are shown in Figure 6.12, for the extreme values of $\alpha = 15^\circ$ and $\alpha = 75^\circ$. In each case, it can be seen that the numerical results (X's) indeed confirm the dominant $\overline{P} \propto H^m$ scaling of the theoretical model (solid lines). Note that, due to the large (10^{30}) range of Figure 6.12 (a), no difference is visible between the different values of θ. However, they are not exactly the same; $P_{\text{Maxwell}}(\alpha = 15^\circ, \theta = 60^\circ)/P_{\text{Maxwell}}(\alpha = 15^\circ, \theta = 10^\circ) \approx 1.38$.

[4] The highest electric field value, and hence $h_{\text{thresh.}}$, were not known a priori due to the fluid interface shape being unknown. The choice $h = 0.1b$ turned out to range from around 1 to 1.3 times $h_{\text{thresh.}}$. It is for this reason that Figures 6.13 and 6.14 show some data points with values of $H/H_{\text{thresh.}}$ exceeding 1.

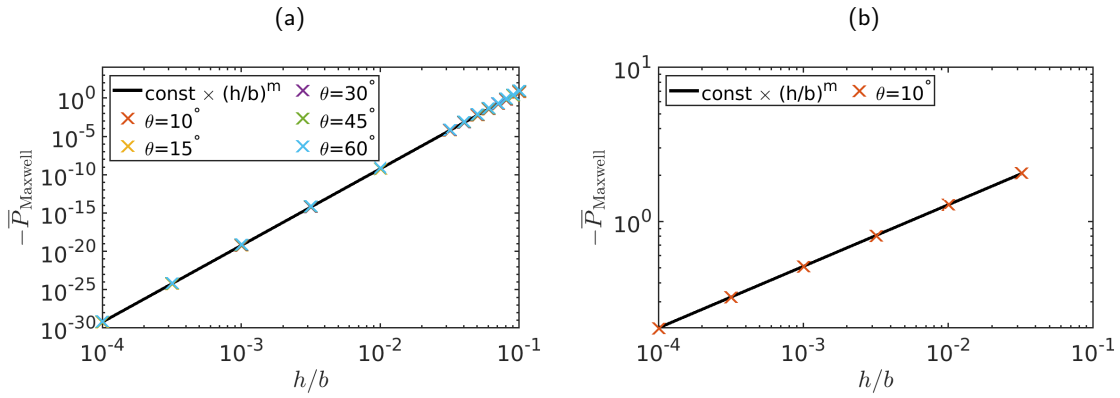

Figure 6.12: Log-log plots of rescaled Maxwell pressure, $\overline{P}_{\text{Maxwell}}$, against rescaled film midline thickness, h/b, for $\alpha = 15^\circ$ (left) and $\alpha = 75^\circ$ (right). X's denote data computed numerically in a cross-sectional domain with a flat electrode of constant potential (Figure 6.11) using the finite element method software COMSOL, as described in Section 6.7.1. Solid lines denote the theoretically predicted power law $\overline{P}_{\text{Maxwell}} \propto (h/b)^m$, with $m = (\pi/\alpha) - 2$.
(a) Interior groove half angle $\alpha = 15^\circ$, with contact angles $\theta \in \{10^\circ, 15^\circ, 30^\circ, 45^\circ, 60^\circ\}$. Note that the results for different contact angles are indistinguishable. For $\alpha = 15^\circ$, $m = 10$.
(b) Interior groove half angle $\alpha = 75^\circ$, with contact angles $\theta = 10^\circ$ (larger values of θ were not considered because of the necessity of satisfying the Concus-Finn condition, $\alpha + \theta < \pi/2 = 90^\circ$). For $\alpha = 75^\circ$, $m = 0.4$.

For the parameter range considered, the error in the approximation of the flux factor Γ as compared to the numerically computed flux factor $\Gamma_{\text{num.}} = \overline{Q}/H^4$ and in the approximation of the cross-sectional area $\widehat{A}H^2$ compared to the numerically computed $A_{\text{num.}}$ are shown in Figure 6.13. Plots in the left column fix the wetting angle $\theta = 10^\circ$ and show results for various α, while plots in the right column fix the internal groove half angle at $\alpha = 15^\circ$ and vary θ. Even when $H > H_{\text{thresh.}}$, the error in the flux factor remains below 1.1%, while the error in the cross-sectional area reaches at most 1.7%. Thus, Γ and $\widehat{A}$ appear to be fairly good approximations.

Next, the top row of Figure 6.14 displays the relative error in the pressure approximation $\overline{P} = -1/H - \chi H^m$ as compared to the numerically computed pressure $\overline{P}_{\text{num.}}$. Again, the plot on the left fixes $\theta = 10^\circ$ and varies α, while the plot on the right fixes $\alpha = 15^\circ$ and varies θ. So long as $H < H_{\text{thresh.}}$, the error remains below approximately 3%. While it quickly grows for $H > H_{\text{thresh.}}$, especially for large wetting angles, at that point the film thickness is outside of the model regime.

The plots in the bottom row of Figure 6.14 display the Maxwell pressure as a fraction of the total pressure. These results reveal that the small errors in the pressure approximation are not due simply to the Maxwell pressure being small compared to the capillary pressure. Indeed, for $\theta = 10^\circ$ and $\alpha = 60^\circ$ (left column, purple), the Maxwell force contributes up to half of the pressure, but the error is $< 1\%$.

We therefore conclude that the model approximations are indeed reasonable for the regime in which $(h/b) \leq 0.1$.

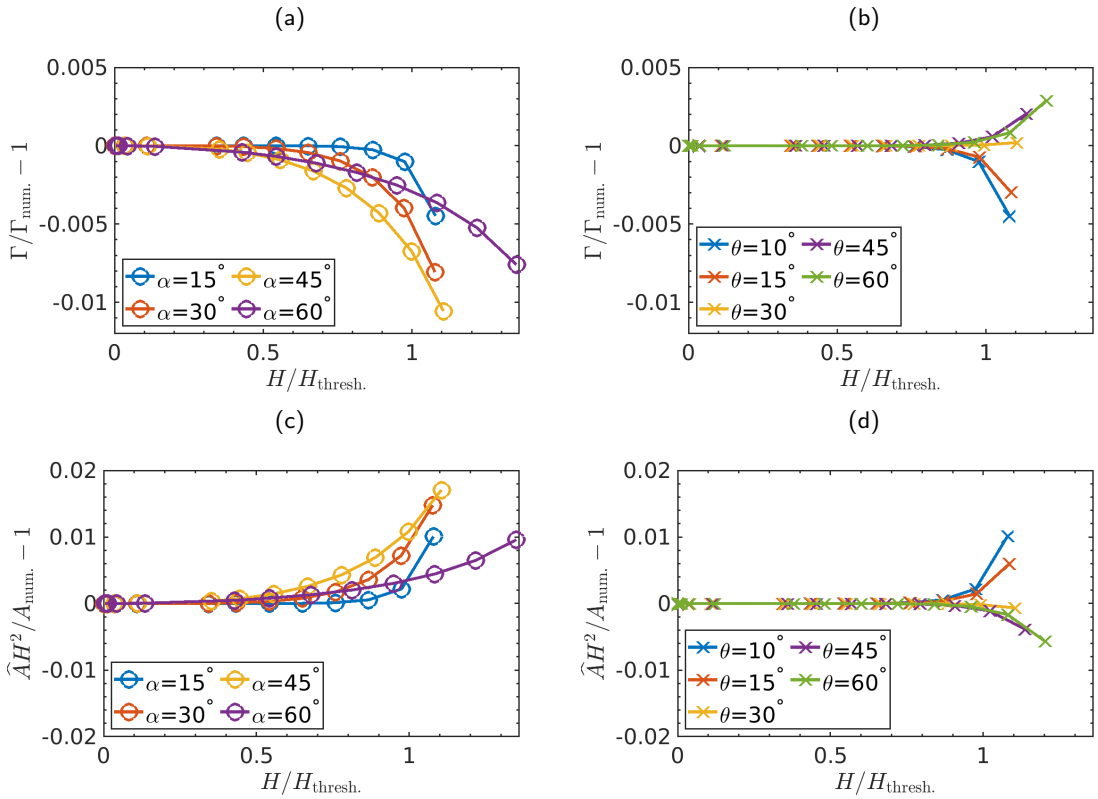

Figure 6.13: Flux factor (Γ) and cross-sectional area ($\widehat{A}$) approximation errors relative to numerical results computed in a cross-sectional domain with a flat electrode of constant potential (Figure 6.11) using the finite element method software COMSOL, as described in Section 6.7.1. Such errors arise due to neglecting the effect of a non-circular fluid interface in the derivation of the equations of motion.

The horizontal axis tracks $H/H_{\text{thresh.}}$ as the electric potential strength $\Psi_{electrode}$ is held fixed, where $H_{\text{thresh.}}$ is the threshold fluid thickness defined in Equation (6.44). In each simulation, the point of maximal H is $h = 0.1b$ ($H = h/d = 0.1b/d$), where b is the distance to the electrode. Plots in the left column [(a),(c)] fix the contact angle $\theta = 10°$ and vary the interior groove half angle α; plots in the right column [(b),(d)] fix $\alpha = 15°$ and vary θ.

Top row [(a)-(b)]: Relative flux factor error, $(\Gamma - \Gamma_{\text{num.}})/\Gamma_{\text{num.}}$, due to approximating the cross-sectional flux parameter as $\Gamma(\alpha, \theta)$ (see Figure 6.3 and Chapter 4) without considering the effect of a non-circular fluid interface. The numerical result, $\Gamma_{\text{num.}} = \overline{Q}/H^4$, with $\overline{Q}$ being the numerically computed streamwise flux.

Bottom row [(c)-(d)]: Relative cross-sectional area error, $(\widehat{A}H^2 - A_{\text{num.}})/A_{\text{num.}}$, due to approximating the cross-sectional area as $\widehat{A}(\alpha, \theta)H^2$. The numerical result, $A_{\text{num.}}$, is determined by numerically integrating the cross-sectional domain.

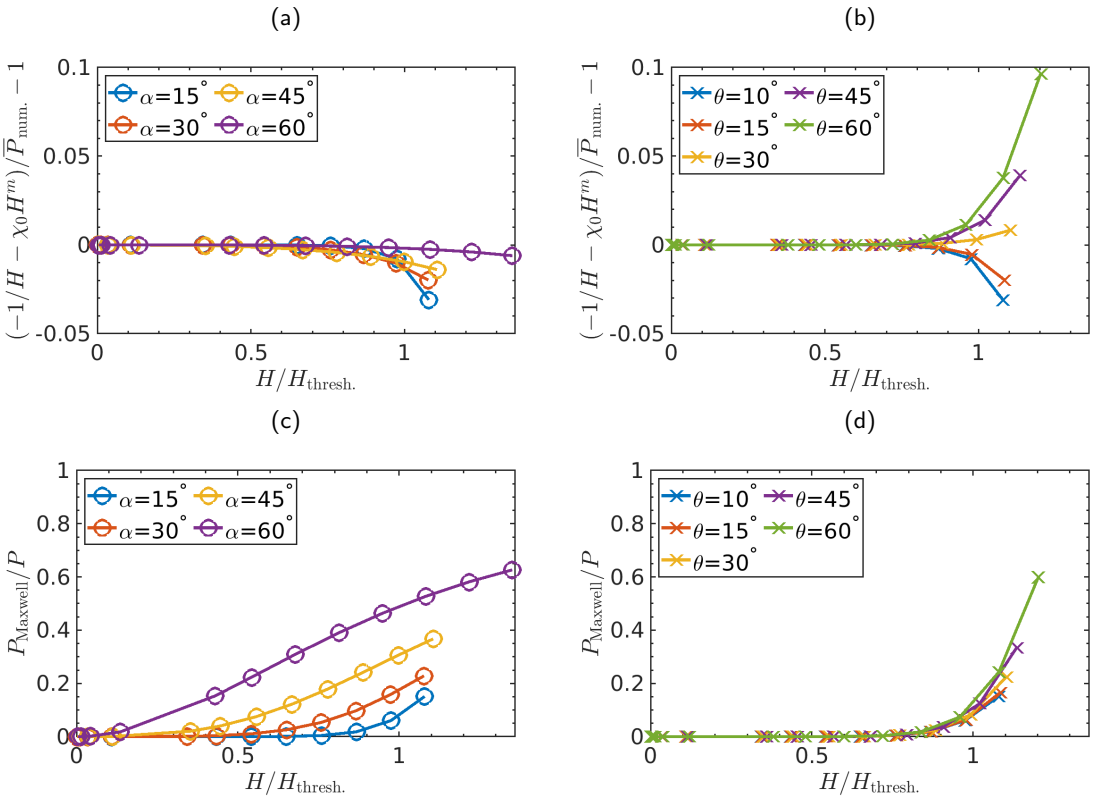

Figure 6.14: Quantities related to pressure computed in a cross-sectional domain with a flat electrode of constant potential (Figure 6.11) using the finite element method software COMSOL, as described in Section 6.7.1.
The horizontal axis tracks $H/H_{\text{thresh.}}$ as the electric potential strength $\Psi_{electrode}$ is held fixed, where $H_{\text{thresh.}}$ is the threshold fluid thickness defined in Equation (6.44). In each simulation, the point of maximal H is $h = 0.1b$ ($H = h/d = 0.1b/d$), where b is the distance to the electrode. Plots in the left column [(a),(c)] fix the contact angle $\theta = 10°$ and vary the interior groove half angle α; plots in the right column [(b),(d)] fix $\alpha = 15°$ and vary θ.
Top row [(a)-(b)]: Relative pressure error, $(-1/H - \chi_0 H^m - \overline{P}_{\text{num.}})/\overline{P}_{\text{num.}}$, due to approximating the pressure as $-1/H - \chi_0 H^m$ without considering the effect of a non-circular fluid interface. $\overline{P}_{\text{num.}}$ is the numerically computed rescaled pressure (including both capillary and Maxwell pressure).
Bottom row [(c)-(d)]: Relative contribution of Maxwell pressure to total pressure in the numerically computed system: $P_{\text{Maxwell,num.}}/P_{\text{num.}} = P_{\text{Maxwell,num.}}/(P_{\text{capillary,num.}} + P_{\text{Maxwell,num.}})$.

6.8 Discussion

We have derived a new low-order model for slender viscous flow of a perfectly conducting fluid in a V-groove subject to an external electric field, under the assumptions outlined in Section 6.2.1. It was shown that the application of an electric field enhances the flux. In the special case of an electric field which is constant in Z, we have shown that stationary solutions with fluid below a threshold thickness are nonlinearly stable, that a self-similar Washburn-like family of self-similar solutions exists, and that these self-similar solution are both transiently and asymptotically stable

when the fluid is below $0.9\times$ the threshold thickness.

It should be noted that the threshold thickness is conservative, and in reality is likely slightly higher due to axial (lengthwise) curvature of the fluid helping surface tension hold the fluid in the groove. As our slender limit approach of the V-groove model ignores lengthwise curvature, this correction is not captured. Yang and Homsy (2006) did introduce an approximation for lengthwise curvature in their model, although they did not include all relevant $O(\varepsilon^2)$ terms.

Errors associated with the approximation of the fluid interface as a circular section and the approximation of the electric field were discussed in Section 6.7, for $(d/b) \lesssim 0.1$. While the errors were found to be small for the case of a flat, lid-like electrode covering the groove, the errors may vary for different external electric fields. However, based on the analysis in Section 6.3.2, so long as the electric field is sufficiently smooth, such errors are expected to remain $O([d/b]^2)$.

A fully rigorous determination of the electric field distribution would require not only explicit restrictions on the smoothness of the external electric field and the shape of the fluid interface, but also a careful analysis at the contact line, where the fluid interface meets the wall. For contact angle $\theta > 0$, this point represents a sharp interior corner. Being an interior corner rather than an exterior corner, a singularity with an arbitrarily large electric field in the vicinity is not expected (Jackson, 2012). However, the electric field will be affected; hence finer analytical and numerical work in that region would be worthwhile to make a more accurate determination of the exact electric field distribution.

The most significant limitation to the model is the requirement that the fluid be thin compared to the depth of the groove. This assumption was required in order for an analytic approximation of the electric field to be tractable. For fluid filled near to the top of the groove, a numerical computation of the external field would be required; the most notable complication would arise where at the edges of the groove, which, being exterior corners, would amplify the local electric field (if the groove is conducting, which we assume to be the case). A low-order model could still be developed in that regime, following the blueprint of Section 6.2, but it would likely result in both $P_{\text{capillary}}$ and P_{Maxwell} being nontrivial numerical functions of H and the external field strength.

Similarly, adapting the model to curved-bottom U-grooves would also likely require $P_{\text{capillary}}$ and P_{Maxwell} to be computed as numerical functions of H. In particular, the sensitivity of the Maxwell pressure to fluid thickness would likely be lower when the fluid remained near the rounded bottom of the groove than when the fluid began to fill the groove. Once the fluid completely covered the rounded interior corner, an appropriately shaped groove would appear to the electric field to be a V-groove, and thus the $P_{\text{Maxwell}} \propto H^m$ electric field approximation might again be applicable.

The assumption that the groove walls were perfect conductors determined the form of the electric

field. Such an assumption is relevant if the groove is etched into a conducting substrate, and may also apply if the substrate is not conducting but maintains a thin, precoated film of liquid metal. In the latter case, dewetting of residual liquid metal could lead to nonconductive patches on the groove walls, and would require additional study. If the groove walls are assumed to be perfect insulators, an issue arises at the sharp corners of the fluid cross-section as the electric field would approach a singularity there. Such a situation would likely result in the contact angle θ changing to decrease the sharpness of the fluid corners, and further analysis would be required in that case.

A few rules of thumb are transferable from the thin V-groove regime model to the thick V-groove regime and U-groove models. It should still be the case that the Maxwell pressure increases in magnitude as the fluid becomes thicker, and hence a threshold thickness above which the fluid destabilizes should be expected. And it will still be the case that, for fixed pressure boundary conditions, the presence of an electric field enhances the flux. However, the $h^{(\pi/\alpha)-2}$ scaling of the Maxwell pressure will likely no longer be applicable.

Besides having ambient electric fields, the MEP feed system also has a complex geometry which the V-grooves must traverse, first rising vertically from the reservoir, then curving to travel horizontally across the array substrate floor, and again curving upwards to scale the emitter needles. The coming chapter will address the issue of such curved V-grooves.

6.9 Appendix: Additional plots

Additional plots similar to those in Figures 6.5, 6.6, 6.8 and 6.9, but with Dirichlet pressure boundary conditions rather than Dirichlet fluid thickness boundary conditions are shown.

6.9.1 Stationary plots

Figure 6.15 shows plots of stationary solutions given a constant external electric field, with various pressure ($\overline{P}$) boundary conditions and electric field strengths, for $\alpha = 30^\circ$. Figure 6.16 shows similar plots for $\alpha = 60^\circ$. Note that since the nondimensionalization of the problem is based upon geometric quantities Γ, $\widehat{A}$, and $\widehat{R}$, then the nondimensionalization of the 30° and 60° grooves differs. Furthermore, the constant electric field strengths χ_0 shown are chosen as $\chi_0 = \{0, 0.2, 0.4, 0.6, 0.8, 0.9\} \times \chi_{\text{thresh.}}$, where $\chi_{\text{thresh.}}$ is defined relative to each groove geometry with $H_{\text{max}} = 1$.

Each plot in Figures 6.15 and 6.16 shows a different set of Dirichlet pressure ($\overline{P}$) boundary conditions; within each plot, different lines represent different electric field strengths. It is immediately noticeable that higher field strengths lead to thicker films, given the same $\overline{P}$ boundary conditions (opposite behavior from the case of H boundary conditions). Indeed, it is a general rule that the fluid must be thicker in the presence of an electric field in order to achieve the same pressure it would have without an electric field. Note also that, while the stationary solution without an electric field follows the power $Z^{1/3}$ (see Chapter 4 for a review of such solutions), the solution with an electric field is more complicated. In particular, the stationary solution with

an electric field can have both convex and concave regions within a single domain (this is only a statement of lengthwise curvature; the fluid surface transverse to the groove remains a circular section at all times).

Because the Maxwell pressure scales as H^m (with $m > 0$) and the capillary pressure as H^{-1}, then the relative strength of the electric field is smaller as H is smaller. Hence, the difference between interfaces with and without electric fields is smaller at low H than at high H.

While the results in the $\alpha = 30^\circ$ groove (Figure 6.15) and the $\alpha = 60^\circ$ groove (Figure 6.15) are qualitatively similar, the film interfaces in the $\alpha = 60^\circ$ groove experience a bigger difference between $\chi_0 = 0$ and $\chi_0 = 0.9\chi_{\text{thresh.}}$ than those in the narrow groove. This result arises because $m(\alpha = 30^\circ) = 4$ while $m(\alpha = 60^\circ) = 1$; thus the narrow groove can achieve a large change in pressure with only a small change in fluid thickness.

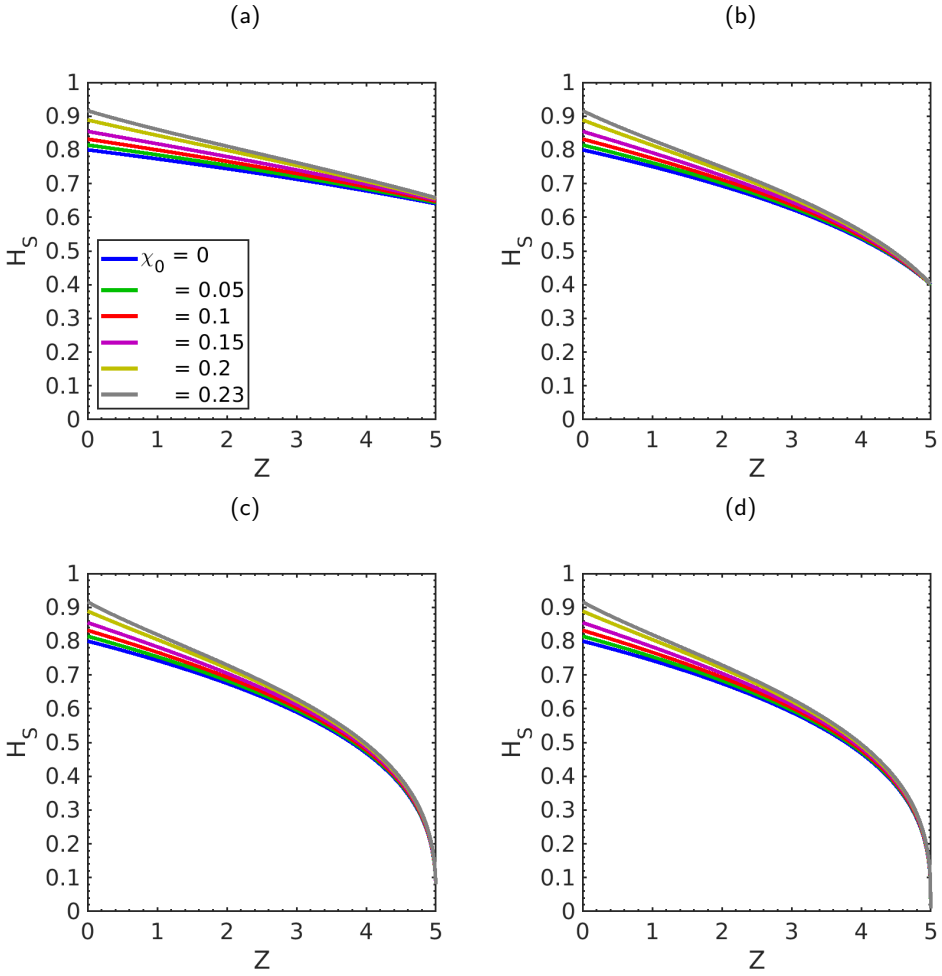

Figure 6.15: Representative stationary solutions of flow of conducting liquids in V-grooves with constant applied electric field, with internal groove half angle $\alpha = 30°$, and Dirichlet pressure ($\overline{P}$) boundary conditions, according to Equation (6.57). Results are plotted for grooves with 5 different values of nondimensional electric field, $\chi_0 \in \{0, 0.05, 0.1, 0.15, 0.2, 0.225\}$ corresponding to $(\chi_0/\chi_{\text{thresh.}}) \in \{0, 0.2, 0.4, 0.6, 0.8, 0.9\}$, where $\chi_{\text{thresh.}}$ is the maximum electric field strength for which $H(0) = 1 < H_{\text{thresh.}}$ [see Equation (6.44)]. The horizontal axis is Z, the axial coordinate along the groove, and the vertical axis is H_S, the nondimensional midline fluid thickness. All plotted solutions have boundary condition $\overline{P}(0) = -(1+m)/m = -1.25$, and the boundary condition at $\overline{P}(5)$ is varied between the plots:
(a) $\overline{P}(5) = 1.25 \times \overline{P}(0) = -1.5625$, (b) $\overline{P}(5) = 2 \times \overline{P}(0) = -2.5$, (c) $\overline{P}(5) = 10 \times \overline{P}(0) = -12.5$, (d) $\overline{P}(5) = 100 \times \overline{P}(0) = -125$.

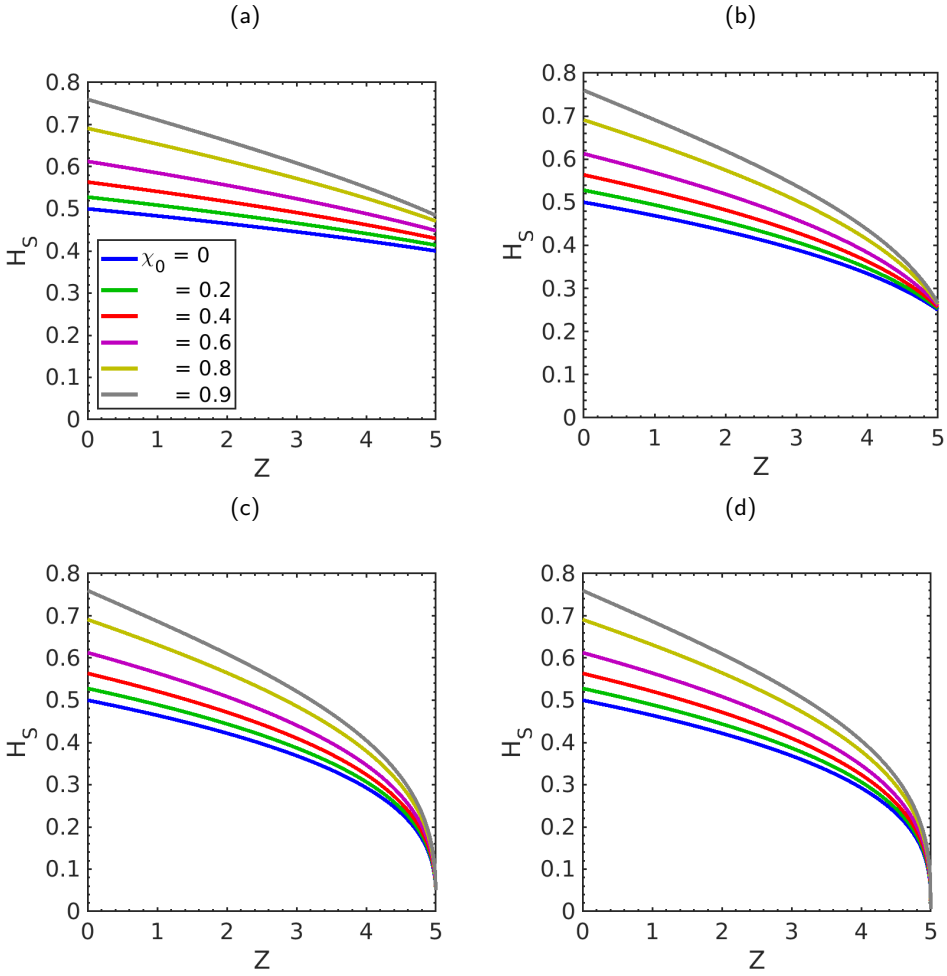

Figure 6.16: Representative stationary solutions of flow of conducting liquids in V-grooves with constant applied electric field, with internal groove half angle $\alpha = 60^\circ$, and Dirichlet pressure ($\overline{P}$) boundary conditions, according to Equation (6.57). Results are plotted for grooves with 5 different values of nondimensional electric field, $\chi_0 \in \{0, 0.2, 0.4, 0.6, 0.8, 0.9\}$ corresponding to $(\chi_0/\chi_{\text{thresh.}}) \in \{0, 0.2, 0.4, 0.6, 0.8, 0.9\}$, where $\chi_{\text{thresh.}}$ is the maximum electric field strength for which $H(0) = 1 < H_{\text{thresh.}}$ [see Equation (6.44)]. The horizontal axis is Z, the axial coordinate along the groove, and the vertical axis is H_S, the nondimensional midline fluid thickness. All plotted solutions have boundary condition $\overline{P}(0) = -(1+m)/m = -2$, and the boundary condition at $\overline{P}(5)$ is varied between the plots:
(a) $\overline{P}(5) = 1.25 \times \overline{P}(0) = -2.5$, (b) $\overline{P}(5) = 2 \times \overline{P}(0) = -4$, (c) $\overline{P}(5) = 10 \times \overline{P}(0) = -20$, (d) $\overline{P}(5) = 100 \times \overline{P}(0) = -200$.

6.9.2 Self-similar plots

Figure 6.17 shows plots of self-similar solutions under a constant external electric field [i.e., solutions of Equation (6.59)], with various Dirichlet pressure ($\overline{P}$) boundary conditions and electric field strengths, for $\alpha = 30^\circ$. Figure 6.18 shows similar plots for $\alpha = 60^\circ$. In the case of advancing solutions [plots (a)-(d)], for which $S(0) > S(\infty)$, stronger electric fields yield thicker films (again, opposite to the behavior when comparing against fixed thickness boundary conditions). Furthermore, stronger electric fields yield a greater $\partial_{\eta\eta} S$ near $\eta = 0$; in particular, it can be seen in plots (c)-(d) that the solution with no electric field has negative axial interface curvature ($\partial_{\eta\eta} S < 0$) while the solution with an electric field has positive axial interface curvature ($\partial_{\eta\eta} S > 0$) near $\eta = 0$. Receding solutions [plots (e)-(f)] similarly have thicker films when the electric field is increased.

In plots (b)-(d), the interfaces with different electric field strengths appear to be converge to nearly identical thicknesses. Because the Maxwell pressure scales as S^m (with $m > 0$) and the capillary pressure as S^{-1}, then the relative strength of the electric field is smaller as S is smaller. Hence, the difference between interfaces with and without electric fields is smaller at low S than at high S.

The self-similar solutions in the V-groove with $\alpha = 60^\circ$ (Figure 6.18) are qualitatively similar to those with $\alpha = 30^\circ$ (Figure 6.17). But, as with the stationary solutions, the gap between the $\chi_0 = 0$ interface and the $\chi_0 = 0.9\chi_{\text{thresh.}}$ interface is larger for the wide 60° groove than for the narrow 30° groove.

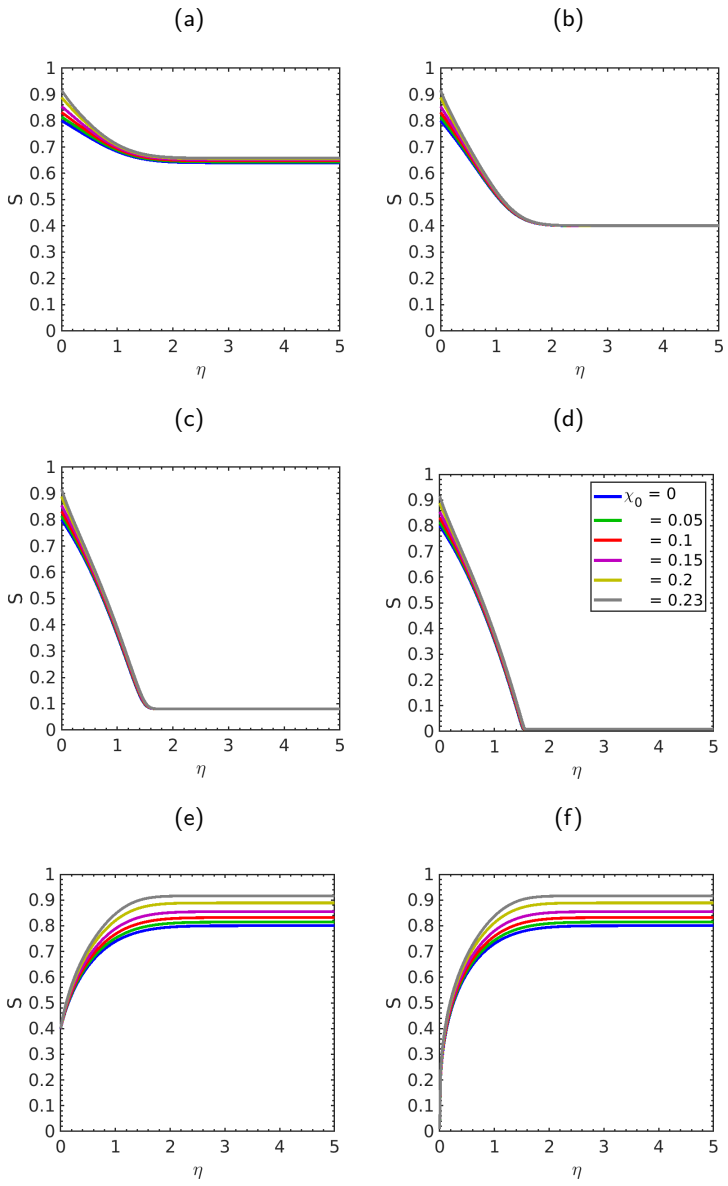

Figure 6.17: Representative self-similar solutions of flow of conducting liquids in V-grooves with constant applied electric field, with internal groove half angle $\alpha = 30°$, and Dirichlet pressure ($\overline{P}$) boundary conditions, according to Equation (6.59). Results are shown for 5 different values of nondimensional electric field, $\chi_0 \in \{0, 0.05, 0.1, 0.15, 0.2, 0.225\}$ corresponding to $(\chi_0/\chi_{\text{thresh.}}) \in \{0, 0.2, 0.4, 0.6, 0.8, 0.9\}$, where $\chi_{\text{thresh.}}$ is the maximum electric field strength for which $S(0) = 1 < H_{\text{thresh.}}$ [see Equation (6.44)]. The horizontal axis is $\eta = Z/T^{1/2}$, the self-similar coordinate; the vertical axis is S, the nondimensional midline fluid thickness. Results were computed for $\eta \in [0, 40]$, but only $\eta \in [0, 3]$ is shown, as the remainder is nearly constant. Plots (a)-(d) depict advancing solutions, with $\overline{P}(0) = -(1+m)/m = -1.25$, and varying boundary condition $\overline{P}(40)$: (a) $\overline{P}(40) = 1.25 \times \overline{P}(0) = -1.5625$, (b) $\overline{P}(40) = 2 \times \overline{P}(0) = -2.5$, (c) $\overline{P}(40) = 10 \times \overline{P}(0) = -12.5$, (d) $\overline{P}(40) = 100 \times \overline{P}(0) = -125$.
Plots (e)-(f) depict receding solutions, with $\overline{P}(40) = -(1+m)/m = -1.25$, and varying boundary condition $\overline{P}(0)$: (e) $\overline{P}(0) = 2 \times \overline{P}(0) = -2.5$, (f) $\overline{P}(0) = 100 \times \overline{P}(0) = -125$.

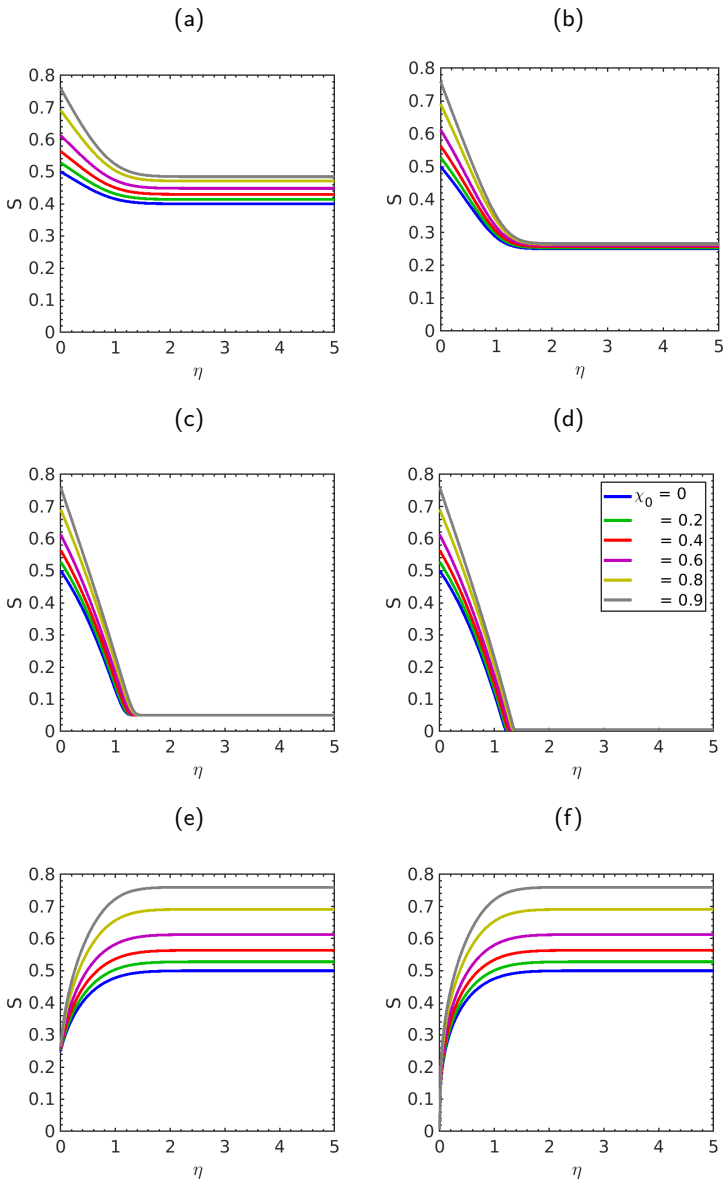

Figure 6.18: Representative self-similar solutions of flow of conducting liquids in V-grooves with constant applied electric field, with internal groove half angle $\alpha = 60°$, and Dirichlet pressure ($\overline{P}$) boundary conditions, according to Equation (6.59). Results are shown for 5 different values of nondimensional electric field, $\chi_0 \in \{0, 0.2, 0.4, 0.6, 0.8, 0.9\}$ corresponding to $(\chi_0/\chi_{\text{thresh.}}) \in \{0, 0.2, 0.4, 0.6, 0.8, 0.9\}$, where $\chi_{\text{thresh.}}$ is the maximum electric field strength for which $S(0) = 1 < H_{\text{thresh.}}$ [see Equation (6.44)]. The horizontal axis is $\eta = Z/T^{1/2}$, the self-similar coordinate, and the vertical axis is S, the nondimensional midline fluid thickness. Results were computed for $\eta \in [0, 40]$, but only $\eta \in [0, 3]$ is shown, as the remainder is nearly constant.
Plots (a)-(d) depict advancing solutions, with $\overline{P}(0) = -(1+m)/m = -2$, and varying boundary condition $\overline{P}(40)$: (a) $\overline{P}(40) = 1.25 \times \overline{P}(0) = -2.5$, (b) $\overline{P}(40) = 2 \times \overline{P}(0) = -4$, (c) $\overline{P}(40) = 10 \times \overline{P}(0) = -20$, (d) $\overline{P}(40) = 100 \times \overline{P}(0) = -200$.
Plots (e)-(f) depict receding solutions, with $\overline{P}(40) = -(1+m)/m = -2$, and varying boundary condition $\overline{P}(0)$: (e) $\overline{P}(0) = 2 \times \overline{P}(0) = -4$, (f) $\overline{P}(0) = 100 \times \overline{P}(0) = -200$.

References

MATLAB and Statistics Toolbox Release 2015a, The MathWorks, Inc., Natick, MA, USA, 2015. URL https://www.mathworks.com/products/matlab.html.

COMSOL Inc. Multiphysics V5.3a, Burlington, MA, USA, 2017. URL https://www.comsol.com.

T. G. Albertson and S. M. Troian. Electrified cone formation in perfectly conducting viscous liquids: Self-similar growth irrespective of Reynolds number. Phys. Fluids, 31(10):102103, October 2019. ISSN 1070-6631, 1089-7666. doi:10.1063/1.5123742.

M. J. Assael, I. J. Armyra, J. Brillo, S. V. Stankus, J. Wu, and W. A. Wakeham. Reference data for the density and viscosity of liquid cadmium, cobalt, gallium, indium, mercury, silicon, thallium, and zinc. J. Phys. Chem. Ref. Data, 41(3), 2012. ISSN 0047-2689. doi:10.1063/1.4729873.

G. K. Batchelor. An Introduction to Fluid Dynamics. Cambridge Mathematical Library. Cambridge University Press, 2000. doi:10.1017/CBO9780511800955.

C. M. Bender and S. A. Orszag. Advanced Mathematical Methods for Scientists and Engineers I: Asymptotic Methods and Perturbation Theory. Advanced Mathematical Methods for Scientists and Engineers. Springer, 1999. ISBN 9780387989310. doi:10.1007/978-1-4757-3069-2.

V. P. Chentsov, V. G. Shevchenko, A. G. Mozgovoi, and M. A. Pokrasin. Density and surface tension of heavy liquid-metal coolants: Gallium and indium. Inorg. Mater. Appl. Res., 2(5): 468–473, 2011. doi:10.1134/S2075113311050108.

G. N. de Surgy, J.-P. Chabrerie, O. Denoux, and J.-E. Wesfreid. Linear growth of instabilities on a liquid metal under normal electric field. J. Phys. II, 3(8):1201–1225, August 1993. ISSN 1155-4312, 1286-4870. doi:10.1051/jp2:1993192.

G. Della Rocca and S. M. Troian. (unpublished), 2013.

Y. I. Frenkel. About the Tonks theory of liquid surface rupture by a uniform electric field in vacuum. Zh. Eksp. Teor. Fiz, 6(4):347–350, 1936.

P. E. Hydon. Symmetry Methods for Differential Equations: A Beginner's Guide. Cambridge Texts in Applied Mathematics. Cambridge University Press, 2000. ISBN 9780521497862. doi:10.1017/CBO9780511623967.

J. D. Jackson. Classical Electrodynamics. Wiley, 3rd edition, 2012. ISBN 9788126510948.

H. Kim, S. G. Bankoff, and M. J. Miksis. The effect of an electrostatic field on film flow down an inclined plane. Phys. Fluids A - Fluid, 4(10):2117–2130, October 1992. ISSN 0899-8213. doi:10.1063/1.858508.

L. D. Landau and E. M. Lifshitz. Electrodynamics of Continuous Media, volume 8 of Course of Theoretical Physics. Pergamon Press, Oxford, 2nd edition, 1984.

C. M. Marrese-Reading. Microfluidic electrospray propulsion (mep) thruster performance with microfabricated emitter arrays for indium propellant. In AIAA. American Institute of Aeronautics and Astronautics, July 2016. ISBN 978-1-62410-406-0. doi:10.2514/6.2016-4738.

P. J. Olver. Applications of Lie groups to differential equations. Graduate Texts in Mathematics. Springer-Verlag New York, 1986. ISBN 9780387962504. doi:10.1007/978-1-4684-0274-2.

L. A. Romero and F. G. Yost. Flow in an open channel capillary. J. Fluid Mech., 322:109–129, 1996. doi:10.1017/S0022112096002728.

D. A. Saville. Electrohydrodynamics: The Taylor-Melcher leaky dielectric model. Annu. Rev. Fluid Mech., 29(1):27–64, 1997. doi:10.1146/annurev.fluid.29.1.27.

S.-K. Su and C.-L. Lai. Interfacial shear-stress effects on transient capillary wedge flow. Phys. Fluids, 16(6):2033–2043, June 2004. doi:10.1063/1.1714791.

E. Tiesinga, P. Mohr, D. Newell, and B. Taylor. 2018 codata recommended values of the fundamental constants of physics and chemistry, 2019-06-03 04:06:00 2019. URL `https://tsapps.nist.gov/publication/get_pdf.cfm?pub_id=928211`.

L. Tonks. A theory of liquid surface rupture by a uniform electric field. Phys. Rev., 48(6): 562–568, September 1935. ISSN 0031-899X. doi:10.1103/PhysRev.48.562.

M. M. Weislogel. Capillary flow in an interior corner. PhD thesis, Northwestern University, June 1996. URL `https://ntrs.nasa.gov/citations/19970010346`. Also published as NASA Technical Memorandum 107364.

L. Yang and G. M. Homsy. Steady three-dimensional thermocapillary flows and dryout inside a v-shaped wedge. Phys. Fluids, 18:042107, 2006. doi:10.1063/1.2193471.

J. Zeleny. The electrical discharge from liquid points, and a hydrostatic method of measuring the electric intensity at their surfaces. Phys. Rev., 3(2):69–91, February 1914. ISSN 0031-899X. doi:10.1103/PhysRev.3.69.

C. Zhou and S. M. Troian. Multiplicity of inertial self-similar conical shapes in an electrified liquid metal. Phys. Rev. Applied, 15(4):044001, April 2021. ISSN 2331-7019. doi:10.1103/PhysRevApplied.15.044001.

Chapter 7

INFLUENCE OF BACKBONE CURVATURE ON CAPILLARY FLOW AND STABILITY IN OPEN V-GROOVE CHANNELS

7.1 Introduction

Passive capillary wicking is a central feature of many modern propellant management devices (PMDs) (Hartwig, 2016, 2017; Jaekle, 1991; Levine et al., 2015; Rollins et al., 1985). In particular, free-surface flow in V-grooves is a frequent feature of PMDs, in addition to other applications such as heat pipes for cooling microelectronics (Cotter, 1984; Mallik et al., 1992; Peterson et al., 1993; Qu et al., 2017). As these devices are increasingly miniaturized, such as in CubeSats and other microsatellites, curving or coiling the backbones of their interior fluid channels becomes an effective way to reduce device size. Indeed, the microfluidic electrospray propulsion (MEP) thruster under development at NASA calls for delivery of fluid from a reservoir underneath the emitter array, across the array substrate floor, and up the sides of emitter needles, a path which cannot feasibly be made a straight line. In order to model and assess such systems, it is necessary to understand the flow behavior and stability properties of flow in a V-groove with an curved backbone, an example of which is shown in Figure 7.1.

The study of liquids with free surfaces in V-grooves appears to have begun with Concus and Finn (1969), who studied the equilibrium shapes of fluid free surfaces in sharp interior corners with interior angle 2α. They found that the fluid contact angle, θ, must satisfy $\theta + \alpha < \pi/2$ for equilibrium solutions to exist, and also discovered that the equilibrium surfaces are unbounded even in the presence of gravity, implying that fluid with with a contact angle below the requisite value can flow arbitrarily far into a V-groove. Ayyaswamy et al. (1974) determined a semi-

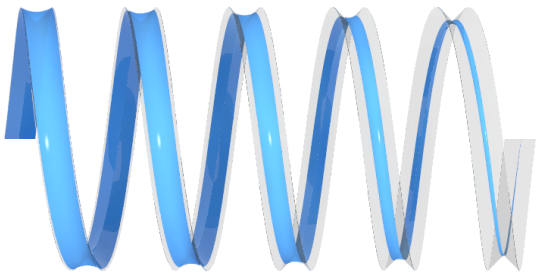

Figure 7.1: Wetting fluid (blue) flowing in a helical V-groove, a system which can be simulated using the present work's reduced-order model.

analytical series solution for the streamwise velocity profile in a 2D cross-section of a fluid in a V-groove with a circular free surface. While not a full equation of motion, this result demonstrated that the friction factor coefficient $2D_h^2/\overline{w}$, where D_h is a hydraulic diameter proportional to the groove width and $\overline{w}$ is the mean streamwise velocity, increases with fluid contact angle θ but has a non-monotonic relationship with interior groove angle α. A dynamical model of viscous V-groove flow was later developed independently by Dong and Chatzis (1995), Romero and Yost (1996), and Weislogel and Lichter (1996; 1998), which described viscous liquids satisfying the Concus-Finn contact angle condition and which included the streamwise friction factor of Ayyaswamy et al. in determining a capillary-driven equation of motion. (see Chapter 4 for a review of this model).

Significant research has been devoted to the study of incompressible laminar flows in closed, curved pipes. Dean (1927) computed the equations of motion in a pipe of circular cross-section which is not straight but instead has a small constant curvature (i.e., the radius of curvature is much larger than the pipe radius) and a constant streamwise pressure gradient. Dean found that such curvature induces a secondary cross flow of magnitude $O(\mathrm{Re}\ dk)$, where $\mathrm{Re} = \rho u d/\mu$ is the Reynolds number, d is pipe diameter, and k is pipe curvature. The flow is then not unidirectional but instead forms twin helical structures within the pipe. The correction to the streamwise velocity has magnitude $O(\mathrm{Re}^2 dk)$ and results in a given pressure gradient producing lower streamwise flux in a curved pipe than a straight pipe. This effect arises due to interaction between inertial and viscous forces. In inviscid fluids, Dean's secondary flow does not arise (Berger et al., 1983), and in viscous fluids at zero Reynolds number ($\mathrm{Re} = 0$), no cross flow whatsoever occurs and the solution is unidirectional (Chadwick, 1985; Dean, 1927). Similar results have been found in pipes with non-circular cross-sections. Rectangular pipes at nonzero Reynolds number have been shown to generate secondary flow similar to that of Dean (Norouzi and Biglari, 2013). Torsion (twisting) out of plane of the curvature in circular cross-section pipes has been considered in addition to curvature alone, and found to have a positive or negative effect on flux at $O(\varepsilon^2)$, with ε being the ratio of pipe curvature to pipe diameter, depending on the Reynolds number (Wang, 1981b). Although no cross flow occurs in a gently curved pipe at $\mathrm{Re} = 0$, the unidirectional flow solution does differ from that of a straight pipe, with the result that, at $O(\varepsilon)$ (first order in the ratio of radius of curvature to pipe radius), the center of streamwise flow (the point of maximum flow speed) is shifted towards the interior of curves. Furthermore, the cross-sectional flux is slightly enhanced at $O(\varepsilon^2)$ as compared to a straight pipe with identical pressure gradient (Chadwick, 1985). Analyses of $\mathrm{Re} = 0$ flow in rectangular and elliptical curved pipes have shown that the center of streamwise flow shifts towards the interior of curves, as with circular pipes (Wang, 2012). However, whether flux is enhanced or suppressed as compared to straight pipes depends on the aspect ratio of the pipe cross-section. In the analysis of the present work, inertial terms are negligible, and hence the Dean effect is also negligible. However, as in the results of Chadwick (1985) and Wang (2012), we will find that curvature of the V-groove induces a change in the flux via a modification of streamwise

flow.

Flows in closed pipes lack a free surface, limiting how directly they can be compared to V-groove flow, but free-surface flows in curved geometries have also been investigated. For example, Stokes et al. (2013) analyzed gravity-driven shallow inertial flow in helical open channels, approximately 0.5m in diameter. At this scale surface tension was ignored, and the change in shape of the interface was driven by inertial forces, with the result that the fluid layer was thicker on the outside of curves than on the inside. In the present work, the shape of the fluid interface will be affected by the groove curvature, but this effect will be driven by surface tension and not by inertia.

The effect of substrate curvature on capillary-driven free-surface flows has been investigated in the context of thin films coating curved substrates. A model for such curved thin film flows was first constructed by Schwartz and Weidner (1995), and a more accurate result was developed with rigorous perturbation theory by Roy et al. (2002). Rumpf and Vantzos (2013) rederived the result of Roy et al. from a different starting point by identifying the gradient flow form of the thin film equation. The direct influence of substrate curvature on fluid interface shape, and hence capillary pressure, and the existence of changes in local volume element and flux in a curvilinear coordinate system are all factors which also arise in the curved V-groove. The qualitative rule that fluid thins where substrate curvature is negative and thickens where it is positive (Roy et al., 2002) will be shown to apply to the V-groove system as well. And the general approach to developing the equations of motion by perturbative expansion in the low curvature limit is analogous to the derivation of Roy et al. (2002). However, the V-groove has a number of unique characteristics that make the thin film approach inapplicable. First, the fluid is confined between two walls and has only one long dimension, rather than being unconfined in two dimensions. Furthermore, the existence of these groove walls creates a unique fluid interface shape, which we will see has a small correction at the first perturbative order due to curvature. This differs from the thin film on a curved substrate, in which the film is conformal to the substrate and experiences capillary pressure due to substrate curvature at zeroth order. A more detailed comparison of the two systems will be presented in Section 7.2.13.

Berthier et al. (2016) performed a preliminary experiment examining flow in open rectangular channels following a curved path, and examined the relative advance of liquid filaments in the channel corners ahead of the bulk flow. The experiment was qualitative in nature, and the curved V-grooves forming the channel corners had different lengths and complex boundary conditions, and were thus not directly comparable. That said, filaments in V-grooves with positive curvature appeared to be thicker than those in grooves with negative curvature. Based on static images in that paper, filaments on the negatively-curved groove appeared longer than those in the positively-curved groove. While strong conclusions cannot be drawn from these results, they indicate that curvature does change the behavior of groove flow, and suggest that an analysis of the problem is worth pursuing.

Wu et al. (2018) performed drop-tower microgravity experiments measuring flow in V-grooves with a curved backbone. The experiments were performed with a relatively large-scale system, having fluid film thickness of approximately 3cm and length of approximately 3-10cm, with groove radii of curvature of approximately 7-27cm. These scales placed the system in a regime in which inertial effects would be relevant and in which the aspect ratio is not slender, unlike this thesis, which considers viscous flow in slender grooves. Wu et al. found that increasing positive curvature enhanced the advance of flow in the groove (no experiments were performed with negative curvature). They further developed a semi-analytic model for flow in V-grooves with a backbone of constant curvature by adding an additional pressure contribution from the backbone, and modifying the friction factor in Weislogel's (1996; 1998) model of viscous, straight, and slender V-grooves to include a correction polynomial in the Dean number, $\mathrm{De} = \mathrm{Re}\sqrt{Dk}$, where Re is the Reynolds number, D the "hydraulic diameter," and k the backbone curvature. This correction was approximated as a polynomial with coefficients derived empirically from computational fluid dynamics (CFD) simulations. Wu et al.'s semi-analytic model qualitatively captured the effect of positive curvature enhancing flow; however, the method of combining an inertia-free ($\mathrm{Re} = 0$) base model with an inertial curvature correction likely limited the accuracy of their model.

In this work, a new physical model for viscous microgravity flow in V-grooves with curved backbones is developed. It is carried out to first perturbative order, at which vertical curvature is relevant but lateral curvature and torsion are not (these would enter as second order effects). The model differs from that of Wu et al. (2018) in three key respects. First, although it is also based on Weislogel's (1996; 1998) straight, viscous V-groove model, all curvature corrections are developed in terms of backbone curvature, rather than inertial factors such as Dean number. Thus, for example, while the model of Wu et al. (2018) would include no flux corrections in a purely viscous ($\mathrm{Re} = 0$) regime, we find through careful derivation that corrections to the flux term are in fact necessary. Second, our model does not require constant backbone curvature, and includes those additional terms which arise in grooves with varying curvature. Third, our model is derived analytically and rigorously from first principles (in a perturbative expansion, following Weislogel [1996; 1998]) and does not rely on ad-hoc addition of terms, or on CFD or empirical parameter fitting. The result is a partial differential equation which is structurally distinct from that of Wu et al. (2018).

The derivation of the model is based on the slender perturbation theory derivation of the straight V-groove equation by Weislogel (1996; 1998), as shown in Chapter 4. However, the backbone curvature is captured by using a generalized nonorthogonal curvilinear coordinate system, resulting in a significantly longer and more challenging derivation. We report this derivation in great detail, with the goal that a student could reproduce or build upon it.

In Section 7.2, we will derive the equations of motion of the new model. Section 7.3 will demonstrate the steady state and self-similar solutions of the model. In Section 7.4, we perform

a nonlinear stability analysis of steady state solutions and a non-normal linear stability analysis of self-similar solutions, as in Chapters 5 and 6. Section 7.5 will discuss numerical methods and caveats of the model.

7.2 Derivation of equations of motion

7.2.1 Assumptions and method of derivation

We use "backbone" to denote the corner of the V-groove. The equations of motion for flow in a V-groove with a straight backbone were first developed independently by Dong and Chatzis (1995), Romero and Yost (1996), and Weislogel and Lichter (1996; 1998), and a full derivation can be found in Chapter 4. The derivation was based upon the slender limit of the incompressible Navier-Stokes equations, which allowed inertial effects to be ignored and reduced the equations to a PDE governing thickness of the fluid in the groove.

The same general framework will be followed when deriving the curved-backbone V-groove equation, although the curvilinear coordinates will change the form of the Navier-Stokes equations, the cross-sectional surface will no longer be circular, and the equation will be expressed in axial arc length units instead of in z.

Several important assumptions underlie the model developed in the following sections, restricting its domain of validity.

The first set of assumptions is exactly those required for the viscous straight V-groove model, described in Chapter 4. The liquid is assumed to be Newtonian and incompressible, as well as isothermal. The geometry is assumed to satisfy the slender limit, in which the slender parameter, $\varepsilon = (d/L)$, satisfies $\varepsilon^2 \ll 1$, where d is the characteristic fluid thickness and L is the characteristic groove length scale. The fluid is assumed to be sufficiently thick that Van der Waals forces between the fluid and wall [which are important in the extremely thin film limit, typically for $d \lesssim O(0.01\ \mu\text{m})$] may be ignored. The region outside the liquid is assumed to be a vacuum, or else a fluid with viscosity much less than that of the liquid in the groove. The liquid is assumed to be purely viscous, i.e., all inertial effects are ignored. This condition is valid when $\varepsilon \mathrm{Re} \Gamma_0 = \varepsilon^2 \rho \gamma d \Phi_0 \Gamma_0 / \mu^2 \ll 1$, where $\varepsilon = (d/L)$ is the slender parameter, ρ is fluid density, γ is surface tension, μ is dynamic viscosity, and Γ_0 is a geometric factor depending on α and θ. $\Phi_0 = \mathrm{Ca}$ is the slender limit capillary number, which will be shown later to reduce to a geometric factor depending only on α and θ. Numerical results show that $\Phi_0 < 0.0335$, a bound which was computed numerically [see Figure 7.7]. In this work, the characteristic fluid thickness d is taken to be the midline fluid thickness at the groove inlet, since no systems are investigated in which the fluid thickness increases significantly beyond the inlet. Furthermore, the thickness of the fluid is assumed to be much smaller than the length scale of axial variations. Note that, given ρ, μ, and γ of a particular liquid, the film being sufficiently thin (i.e., having small enough $d \ll [\mu^2 L^2 / (\Phi_0 \Gamma_0 \gamma \rho)]^{1/3}$) is sufficient to ensure the noninertial condition is satisfied. As an example, consider liquid indium (viscosity $\mu = 1.60 \times 10^{-3}$ Pa s, surface tension $\gamma = 0.57$

N/m, and density $\rho = 7000$ kg/m^3 [Assael et al.; Chentsov et al., 2012; 2011]) and a groove with internal half angle $\alpha = 45°$, fluid contact angle $\theta = 15°$, $d = 5\mu$m, $L = 200\mu$m. Then $\Phi_0 \approx 0.024$, $\Gamma_0 \approx 0.078$, and thus $\varepsilon \mathrm{Re} \approx 0.12$ and $\varepsilon \mathrm{Re} \Gamma_0 \approx 0.009 \ll 1$. Water (viscosity $\mu = 10^{-3}$Pa s, surface tension with air $\gamma = 0.07$ N/m, density $\rho = 1000$ kg/m^3 [Batchelor, 2000]) in a groove of the same dimensions would have $\varepsilon \mathrm{Re} \approx 0.005$ and $\varepsilon \mathrm{Re} \Gamma_0 \approx 0.0004 \ll 1$.

The internal groove half angle, α, is assumed to be constant, as is the liquid contact angle, θ. (Note that we follow Weislogel's convention of α being the internal groove half angle, rather than Romero and Yost's convention of α being the exterior groove angle.) In particular, corrections due to the dynamic variation of θ with fluid velocity are not considered.

Gravitational effects are ignored; specifically, it is assumed that the Bond number $\mathrm{Bo} = \rho g d^2/\gamma \ll \varepsilon \Phi_0$, where g is gravitational acceleration. This can be achieved with a sufficiently thin film, or with a thicker film in a low gravity environment. As an example, again taking values for liquid indium and a groove with $\alpha = 45°$, $\theta = 15°$, $d = 5\mu$m, $L = 200\mu$m, and using Earth gravity of $g = 9.8$ m/s^2, then $\mathrm{Bo}/(\varepsilon \Phi_0) \approx 0.005 \ll 1$. Water in a groove of the same dimensions would have $\mathrm{Bo}/(\varepsilon \Phi_0) \approx 0.006 \ll 1$.

The above assumptions are inherited from the straight V-groove; an additional new set of assumptions is required for the curved V-groove derivation.

It is assumed that the V-groove backbone radius of curvature, $1/k$, must be at least $O(1/\varepsilon)$ larger than the film thickness, i.e., $dk \leq O(\varepsilon)$, and also $O(1/\varepsilon)$ larger than the crosswise radius of curvature of the fluid interface in the groove, i.e., $d\hat{R}k \leq O(\varepsilon)$, where $\hat{R}(\alpha, \theta)$ is the geometric factor relating film midline thickness to interface radius of curvature. In other words, hairpin turns are not described by the model. Note, however, that a hairpin backbone curve regime will re-enter the model regime if the fluid becomes sufficiently thin there. Similarly, the length scale of any torsion or twisting of the groove is assumed to be at least $O(d/\varepsilon)$.

These conditions may equivalently be understood as requiring that the characteristic length scale L be the smallest of $\{$ the groove length of interest, the backbone radius of curvature, and the backbone torsion length scale $\}$, coupled with the aforementioned assumption that $d/L = \varepsilon \ll 1$.

We will further require a limit on the groove half angle, α. The exact value which α must not exceed depends on the slender parameter ε, the fluid contact angle θ, and the pressure correction factor $\widehat{P}_\Upsilon(\theta, \alpha)/\widehat{P}_0(\theta, \alpha)$ which will emerge from the derivation. As an example, for $\theta = 0°$ and $\varepsilon = 0.1$, α must remain below approximately $60°$ (i.e., the full interior angle of the groove must remain below $120°$). Physically, this limitation arises due to the V-groove backbone curvature beginning to dominate the cross-sectional fluid interface curvature when the groove becomes very wide.

We will find through our derivation that torsion and lateral (side-to-side) curvature of the V-groove backbone enter as $O(\varepsilon^2)$ corrections, and thus only vertical (hill-and-valley) curvature

will enter the final expressions.

Note that variables in this work marked with a wide angular hat, such as $\widehat{R}$, are geometric constants, i.e., are functions of α and θ alone and do not depend on spatial or temporal variables. The geometric constants Γ and Φ lack wide angular hats for consistency with the notation of Romero and Yost (1996) and Chapters 4 to 6.

7.2.2 Coordinates and curvature

Backbone coordinates

The line following the interior corner, or backbone, of an arbitrarily curved V-groove can be described as a space curve in $\mathbb{R}^3$ (Figures 7.2 and 7.3). A local coordinate system will first be set up on this curve. This coordinate system will be described in two stages: first, a coordinate triad will be constructed on the backbone; next, these coordinates will be extended to a region around the backbone. This is a common approach for constructing curvilinear coordinate systems around long narrow objects such as rods (Rubin, 2000), and has been used in fluid mechanics to describe flow in curving and twisting pipes (Tuttle, 1990; Wang, 1981b).

Let the backbone be described by a space curve $\vec{\beta}(s)$, where s is an arc-length parametrization. The backbone has a local tangent which makes an obvious choice for one leg of a local coordinate system,

$$\hat{s} = \frac{\partial \vec{\beta}}{\partial s}. \tag{7.1}$$

Note that because s is an arc-length parametrization of $\vec{\beta}$, $\hat{s}$ is a unit vector.

The classical choice of normal and binormal vectors is the Frenet-Serret frame, which is based on the local curvature. This approach was employed, for example, by Wang (1981b) in an analysis of flow in helical pipes with circular cross-sections. The classical theory of space curves defines

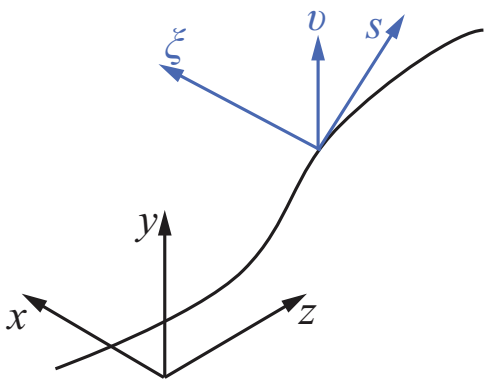

Figure 7.2: The corner, or backbone of the V-groove is described by a space curve, with local coordinates $\{\hat{\xi}, \hat{v}, \hat{s}\}$. Unlike global Cartesian coordinates ($\{x, y, z\}$ in the diagram), local coordinates follow the space curve; $\hat{s}$ is tangent to the curve, while $\hat{\xi}$ and $\hat{v}$ are orthogonal to $\hat{s}$.

total curvature and torsion, which are invariant quantities of the space curve, i.e., quantities which do not depend on coordinate systems. The curvature describes the bending of the curve, or the change in local tangent vector $\hat{s}$. Torsion describes rotation or twisting of the normal and binormal about $\hat{s}$, describing how curves twist out of their local plane. These quantities may be constant or vary in s.

But the V-groove lacks the rotational symmetry of a circular pipe, and thus a more natural choice of coordinates exists, namely, setting $\hat{v}$ to be the normal vector which points "up" in the V, and then defining $\hat{\xi}$ to be $\hat{s} \times \hat{v}$. This way, the V-groove cross section will always look the same in the $\hat{\xi}$-$\hat{v}$ plane at constant s. Note that this set of coordinate vectors is an orthonormal triad on the backbone curve (Figure 7.2). Furthermore, rather than use invariant curvature quantities defined in terms of an unoriented space curve, it becomes natural to use k_v, the curvature projected onto the $\hat{v}$-$\hat{s}$ plane, k_ξ, the curvature projected onto the $\hat{\xi}$-$\hat{s}$ plane, and $\jmath$, the torsion of the v vector. Mathematically,

$$k_\xi = -\hat{s} \cdot \partial_s \hat{\xi}, \tag{7.2a}$$

$$k_v = -\hat{s} \cdot \partial_s \hat{v}, \tag{7.2b}$$

$$\jmath = \hat{v} \cdot \partial_s \hat{\xi} = -\hat{\xi} \cdot \partial_s \hat{v}. \tag{7.2c}$$

k_ξ represents lateral curvature, i.e., curvature of the backbone in the $\hat{\xi}$-$\hat{s}$ plane. k_v represents vertical curvature, i.e., curvature of the backbone in the $\hat{v}$-$\hat{s}$ plane. $\jmath$ describes the torsion or twisting of the V-groove orientation on the backbone curve. Figure 7.3 contains visualizations of k_ξ, k_v, and $\jmath$.

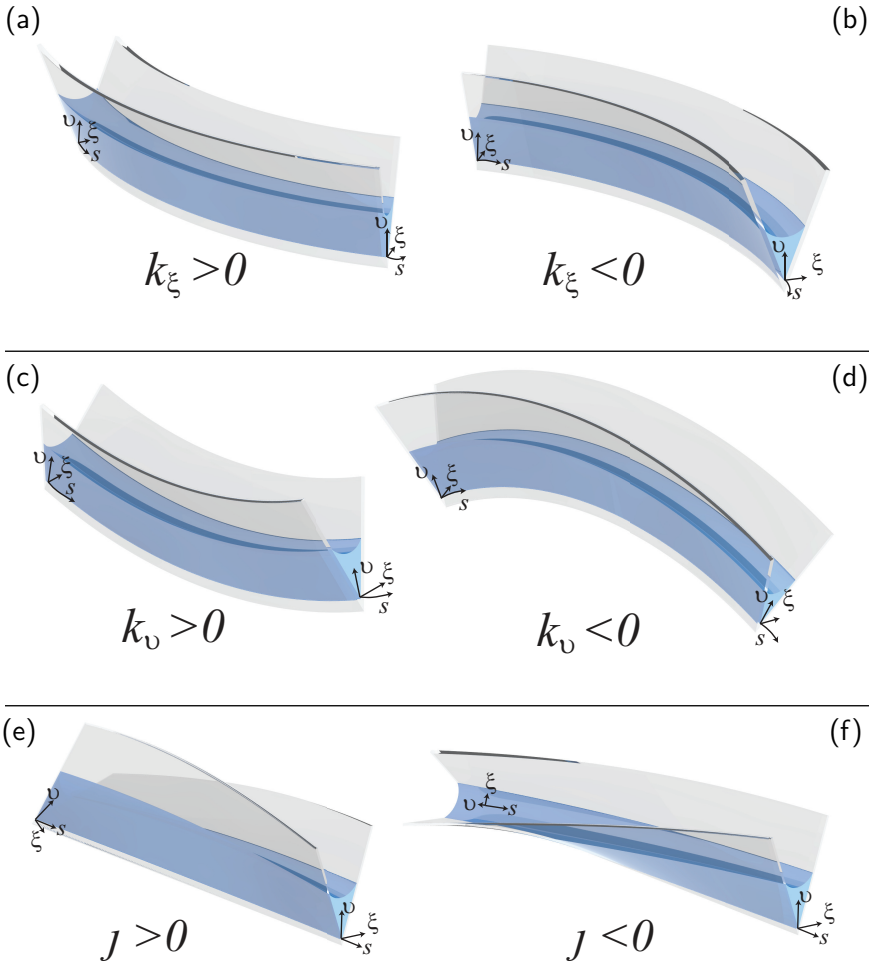

Figure 7.3: Diagrams distinguishing V-groove backbone curvature. (a)-(b): V-grooves with laterally curved backbones. (a) Lateral curvature $k_\xi > 0$; (b) $k_\xi < 0$.
(c)-(d): V-grooves with vertically curved backbones. (c) Vertical curvature $k_\upsilon > 0$; (d) $k_\upsilon < 0$.
(e)-(f): V-grooves with torsion. (e) Torsion $\jmath > 0$; (f) $\jmath < 0$.
Note that the s coordinate follows the backbone (the corner) of the groove, and the υ coordinate (Υ when nondimensionalized) always points "up" from the corner of the V-groove towards the opening of the groove, and the ξ coordinate is orthogonal to the υ coordinate in the cross-sectional plane.

Extended coordinates

Extending the triad off of the backbone in the most natural way leads to the coordinate system definition

$$\vec{x}(\xi, \upsilon, s) = \vec{\beta}(s) + \xi\hat{\xi}(s) + \upsilon\hat{\upsilon}(s). \tag{7.3}$$

While $\hat{\xi}$, $\hat{\upsilon}$, and $\hat{s}$ were previously defined only on the backbone, a new coordinate triad can now be defined that exists in a region near the backbone. Without normalizing, these vectors are

$$\partial_\xi \vec{x} = \hat{\xi}, \tag{7.4a}$$

$$\partial_\upsilon \vec{x} = \hat{\upsilon}, \tag{7.4b}$$

$$\partial_s \vec{x} = \hat{s} + \xi\partial_s\hat{\xi} + \upsilon\partial_s\hat{\upsilon}. \tag{7.4c}$$

Note that $\hat{\xi}$ and $\hat{\upsilon}$ still form two legs of the triad, but $\partial_s\vec{\xi}$ is equal to $\hat{s}$ only when $\xi = \upsilon = 0$, i.e., on the backbone. Therefore, what was an orthonormal coordinate system on the backbone is a nonorthogonal coordinate system elsewhere. However, it will be seen that, to the perturbation order considered in this paper, the nonorthogonality can be ignored.

With these coordinates, a diagram of the curved V-groove can be seen in Figure 7.4. Just as in the straight groove, d is the fluid interface center height (fluid thickness) at the inlet of the groove, L is the characteristic length scale of the groove, α is the half angle of the groove corner, and θ is the contact angle of the groove with the wall. Now, however, υ is the vertical coordinate, ξ is the transverse coordinate, and s is the axial coordinate of the groove.

These coordinates have the convenient property that the scale factor is 1 in ξ and υ. That is, 1 unit of measurement in ξ or υ corresponds to 1 unit in $\mathbb{R}^3$:

$$\partial_\xi \vec{x} \cdot \partial_\xi \vec{x} = \hat{\xi} \cdot \hat{\xi} = 1, \tag{7.5a}$$

$$\partial_\upsilon \vec{x} \cdot \partial_\upsilon \vec{x} = \hat{\upsilon} \cdot \hat{\upsilon} = 1. \tag{7.5b}$$

The scale factor tells how coordinate length relates to physical length. By analogy, in (r, θ) polar coordinates, measuring angular distance in radians is not equivalent to measuring radial distance in, say, meters. In that case, θ has a scale factor of r, since multiplying the local angular distance by the radius gives physical distance. In the case of the curved-backbone V-groove, only the s coordinate has a non-unity scale factor, which will be denoted by f. Computing and simplifying this scale factor requires a few insights. First, since $\hat{\xi}$ and $\hat{\upsilon}$ are unit vectors, then $\partial_s\hat{\xi} \cdot \hat{\xi} = \partial_s\hat{\upsilon} \cdot \hat{\upsilon} = 0$. This means that $\partial_s\hat{\xi}$ and $\partial_s\hat{\upsilon}$ have only the $\hat{s}$ direction in common, so that $\partial_s\hat{\xi} \cdot \partial_s\hat{\upsilon} = (\hat{s} \cdot \partial_s\hat{\xi})(\hat{s} \cdot \partial_s\hat{\upsilon})$. Furthermore, $\partial_s(\hat{\xi} \cdot \hat{\upsilon}) = \partial_s(0) = 0$, so that $\hat{\xi} \cdot \partial_s\hat{\upsilon} = -\hat{\upsilon} \cdot \partial_s\hat{\xi}$. Using these facts,

$$\begin{aligned} f^2 = \partial_s\vec{x} \cdot \partial_s\vec{x} &= \left(\hat{s} + \xi\partial_s\hat{\xi} + \upsilon\partial_s\hat{\upsilon}\right)^2 \\ &= (1 - \xi k_\xi - \upsilon k_\upsilon)^2 + \left(\xi^2 + \upsilon^2\right)\jmath^2 \\ \implies f &= \sqrt{(1 - \xi k_\xi - \upsilon k_\upsilon)^2 + (\xi^2 + \upsilon^2)\,\jmath^2}. \end{aligned} \tag{7.6}$$

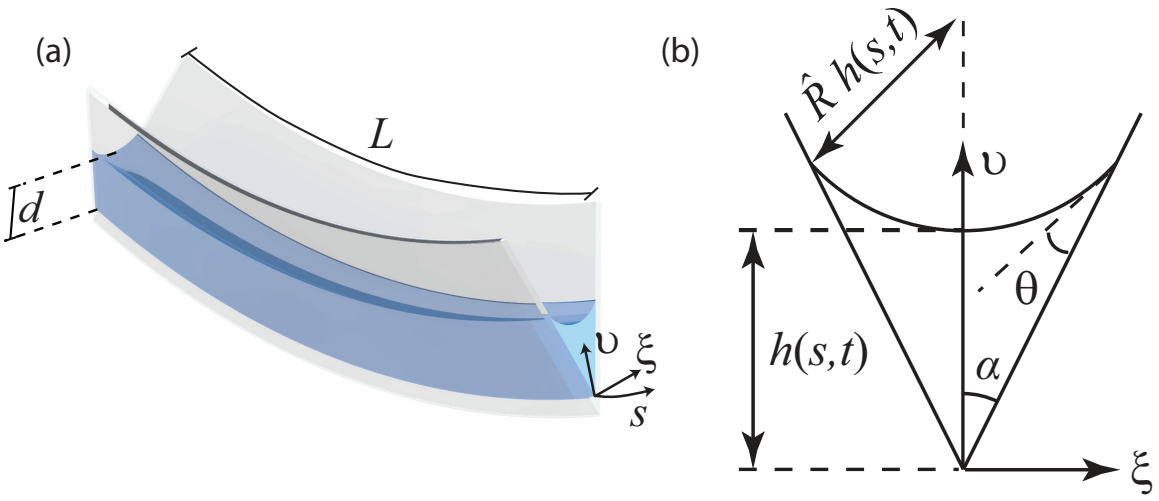

Figure 7.4: Diagrams of curved-backbone V-groove flow system. (a) Schematic of a wetting liquid film ($0 \leq \theta < \pi/2$) flowing within a slender open triangular groove with constant cross-section and curved backbone. The inlet midline film thickness at the origin is denoted by $d = h(\xi = 0, s = 0, t)$ (note that we follow Weislogel's convention of measuring the midline film thickness, rather than Romero and Yost's convention of the film thickness at the wall) and the channel length by L where $d/L \ll 1$. s is an arc length coordinate following the backbone (the corner) of the groove; the υ coordinate points "up" from the corner of the groove to the groove opening; the ξ coordinate is orthogonal to the υ coordinate in the cross-sectional plane. (b) Cross-sectional view of the flow geometry depicted in (a) where $h(s,t)$ denotes the local midline film thickness, α is the groove internal half angle (note that we follow Weislogel's convention of α being the internal groove half angle, rather than Romero and Yost's convention of α being the exterior groove angle), $\widehat{R}h$ is the radius of curvature of the liquid interface and θ is the contact angle of the liquid wetting the channel sidewalls, which is assumed constant.

The nonorthogonality of the system can be shown explicitly:

$$\partial_\xi \vec{x} \cdot \partial_\upsilon \vec{x} = \vec{\xi} \cdot \vec{\upsilon} = 0, \tag{7.7a}$$

$$\partial_\xi \vec{x} \cdot \partial_s \vec{x} = \hat{\xi} \cdot \left(\hat{s} + \xi \partial_s \hat{\xi} + \upsilon \partial_s \hat{\upsilon} \right) = -\upsilon \jmath, \tag{7.7b}$$

$$\partial_\upsilon \vec{x} \cdot \partial_s \vec{x} = \hat{\upsilon} \cdot \left(\hat{s} + \xi \partial_s \hat{\xi} + \upsilon \partial_s \hat{\upsilon} \right) = \xi \jmath. \tag{7.7c}$$

The fact that these dot products vanish at the backbone (where $\xi = \upsilon = 0$) means that the coordinates are orthogonal there. It can be seen that the coordinate nonorthogonality arises not from curvature but from torsion, $\jmath$, just as in Wang's (1981b) curved pipe. Noting this fact, Germano (1982) solved the same curved-pipe problem as Wang (1981b) in a new coordinate system with a frame of reference designed to rotate in such a way that the nonorthogonality was eliminated. Such an approach was effective due to the circular cross-section of the pipe, but would introduce significant challenges in describing a V-groove with a constantly changing orientation. In short, because the inconvenience of a rotating frame of reference in the V-groove would be greater than the inconvenience of a nonorthogonal coordinate system, we accept the latter.

The central methodology of this work is to treat backbone curvature as a first order perturbative correction to the straight V-groove equations of motion. Thus, in order for perturbation theory to be valid, some constraints on the magnitude of the backbone curvature must be enforced. In particular, it will be assumed that $\partial_s\hat{\xi}$ and $\partial_s\hat{v}$ are at most $O(\varepsilon/d)$, where d is the characteristic thickness of fluid in the groove and

$$\varepsilon = \frac{d}{L} \tag{7.8}$$

is the perturbation parameter, "characteristic thickness of fluid"/"characteristic length scale of the groove." This implies that k_ξ, k_v, and $\jmath$ are also $O(\varepsilon/d)$. In other words, the radius of curvature must be much larger than the thickness of the fluid. Due to the symmetry of the problem under reversal of ξ, any corrections to the equations of motion must be at least quadratic in k_ξ, which will lead to k_ξ corrections being $O(\varepsilon^2)$ and thus irrelevant at first order (although k_ξ will be carried through much of the following calculations until it becomes clear exactly where it drops out). Thus, ultimately it will be found that only k_v curvature contributes at first order. Furthermore, it will be seen later that the nonorthogonal terms (i.e., terms containing $\jmath$) contribute only $O(\varepsilon^2)$ corrections to the Navier-Stokes and boundary condition equations, and so these will also be irrelevant.

7.2.3 Covariant notation

Although the nonorthogonality will turn out to be irrelevant after nondimensionalizing the fluid equations, it cannot be left out a priori. The simplest method of performing calculus in nonorthogonal curvilinear coordinates is to use covariant derivatives and Christoffel symbols, i.e., the language of differential geometry (although the background space remains Euclidean). We follow Aris (1989), and the reader is referred to that book for a deeper review of covariant notation, curvilinear coordinates, and nonorthogonal coordinates in fluid mechanics. It should be noted that the scale-factor method found in textbooks such as Batchelor (2000) is useful only for orthogonal coordinate systems.

The language of differential geometry will be used only through Sec. 7.2.7, in which the Navier-Stokes equations, boundary conditions, and the integrated continuity equation are derived. Readers uninterested in the details of coordinate transformations may safely skip to the summary in Sec. 7.2.8, where the continuity and reduced Navier-Stokes equations are listed as Equations 7.50–7.55.

The metric will be denoted by g_{ij} with lowered indices, and its inverse by g^{ij}, with raised indices. Vectors will be denoted by raised indices (e.g., u^i) and are distinct from covectors, denoted with lowered indices ($u_i = \sum_j g_{ij}u^j$). The dot product of two vectors u and v would be represented as $\sum_{i,j} g_{ij}v^iu^j = \sum_j v^ju_j = \sum_j v_ju^j$. Einstein summation notation will not be used; instead, all sums will be written explicitly. Covariant derivatives are defined for scalars, vectors, and

tensors as

$$\nabla_i \phi = \partial_i \phi, \tag{7.9a}$$

$$\nabla_i u^j = \partial_i u^j + \sum_\ell \Gamma^j{}_{i\ell} u^\ell, \tag{7.9b}$$

$$\nabla_i u_j = \partial_i u_j - \sum_\ell \Gamma^\ell{}_{ij} u_\ell, \tag{7.9c}$$

$$\nabla_i T^j{}_k = \partial_i T^j{}_k + \sum_\ell \Gamma^j{}_{i\ell} T^\ell{}_k - \sum_\ell \Gamma^\ell{}_{ik} T^j{}_\ell, \tag{7.9d}$$

and so on, where ∂_i represents the partial derivative with respect to the coordinate i (which is one of ξ, υ, or s), and Christoffel symbols are defined by

$$\Gamma^i{}_{jk} = \frac{1}{2} \sum_\ell g^{i\ell} \left(\partial_j g_{k\ell} + \partial_k g_{\ell j} - \partial_\ell g_{jk} \right) \tag{7.10}$$

(Aris, 1989). For notational convenience, a raised-index covariant derivative will also be defined:

$$\nabla^i = \sum_j g^{ij} \nabla_j. \tag{7.11}$$

For the curved-backbone V-groove system, the metric is defined by

$$g_{ij} = \partial_i \vec{x} \cdot \partial_j \vec{x} = \begin{bmatrix} 1 & 0 & -\upsilon\jmath \\ 0 & 1 & \xi\jmath \\ -\upsilon\jmath & \xi\jmath & f^2 \end{bmatrix}, \tag{7.12}$$

and its inverse (denoted with raised indices) by

$$g^{ij} = \frac{1}{(1 - \xi k_\xi - \upsilon k_\upsilon)^2} \begin{bmatrix} f^2 - \xi^2\jmath^2 & -\xi\upsilon\jmath^2 & \upsilon\jmath \\ -\xi\upsilon\jmath^2 & f^2 - \upsilon^2\jmath^2 & -\xi\jmath \\ \upsilon\jmath & -\xi\jmath & 1 \end{bmatrix}. \tag{7.13}$$

The nonzero Christoffel symbols for this system are

$$\Gamma^{\xi}_{\xi s} = \Gamma^{\xi}_{s\xi} = -\frac{\upsilon k_\xi \jmath}{1 - \xi k_\xi - \upsilon k_\upsilon}, \tag{7.14a}$$

$$\Gamma^{\upsilon}_{\upsilon s} = \Gamma^{\upsilon}_{s\upsilon} = \frac{\xi k_\upsilon \jmath}{1 - \xi k_\xi - \upsilon k_\upsilon}, \tag{7.14b}$$

$$\Gamma^{\xi}_{\upsilon s} = \Gamma^{\xi}_{s\upsilon} = -\frac{(1 - \xi k_\xi)\jmath}{1 - \xi k_\xi - \upsilon k_\upsilon}, \tag{7.14c}$$

$$\Gamma^{\upsilon}_{\xi s} = \Gamma^{\upsilon}_{s\xi} = \frac{(1 - \upsilon k_\upsilon)\jmath}{1 - \xi k_\xi - \upsilon k_\upsilon}, \tag{7.14d}$$

$$\begin{aligned}\Gamma^{\xi}_{ss} =& \frac{-\jmath\upsilon\left(\xi\partial_s k_\xi + \upsilon\partial_s k_\upsilon\right) - \jmath^2\left[\xi - \left(\xi^2 + \upsilon^2\right)k_\xi\right]}{1 - \xi k_\xi - \upsilon k_\upsilon} \\ & - \upsilon\partial_s\jmath + k_\xi(1 - \xi k_\xi - \upsilon k_\upsilon),\end{aligned} \tag{7.14e}$$

$$\begin{aligned}\Gamma^{\upsilon}_{ss} =& \frac{\jmath\xi\left(\xi\partial_s k_\xi + \upsilon\partial_s k_\upsilon\right) - \jmath^2\left[\upsilon - \left(\upsilon^2 + \xi^2\right)k_\upsilon\right]}{1 - \xi k_\xi - \upsilon k_\upsilon} \\ & + \xi\partial_s\jmath + k_\upsilon(1 - \xi k_\xi - \upsilon k_\upsilon),\end{aligned} \tag{7.14f}$$

$$\Gamma^{s}_{\xi s} = \Gamma^{s}_{s\xi} = -\frac{k_\xi}{1 - \xi k_\xi - \upsilon k_\upsilon}, \tag{7.14g}$$

$$\Gamma^{s}_{\upsilon s} = \Gamma^{s}_{s\upsilon} = -\frac{k_\upsilon}{1 - \xi k_\xi - \upsilon k_\upsilon}, \tag{7.14h}$$

$$\Gamma^{s}_{ss} = \frac{\jmath\left(\upsilon k_\xi - \xi k_\upsilon\right) - \xi\partial_s k_\xi - \upsilon\partial_s k_\upsilon}{1 - \xi k_\xi - \upsilon k_\upsilon}. \tag{7.14i}$$

7.2.4 Fluid equations in curvilinear coordinates

When working in non-Cartesian coordinates, it is important to be careful of the scale factor for each coordinate. In particular, given physical velocities u, v, and w, respectively, in the ξ, υ, and s directions, covariant vectors will be denoted as

$$u^\xi = u, \tag{7.15a}$$

$$u^\upsilon = v, \tag{7.15b}$$

$$u^s = \frac{w}{f}, \tag{7.15c}$$

(by analogy, in polar coordinates the physical angular velocity would be measured in meters per second, while the covariant vector component in the θ direction would be multiplied by the scale factor r to give physical velocity).

The continuity equation is then simply

$$\sum_i \nabla_i u^i = 0. \tag{7.16}$$

The Navier-Stokes equations in curvilinear coordinates are defined by

$$\rho\left(\partial_t u^i + \sum_j u^j \nabla_j u^i\right) = \sum_j \nabla_j \tau^{ji}, \tag{7.17}$$

where the stress tensor τ^{ji} is

$$\tau^{ji} = \mu\left(\nabla^j u^i + \nabla^i u^j\right) - p g^{ji} \tag{7.18}$$

(Aris, 1989). It should be noted that these expressions are the same as the usual Navier-Stokes in orthogonal coordinates, except that the derivatives are now covariant and the stress tensor has g^{ij} instead of the identity matrix (in Cartesian coordinates, the metric is the identity). Note also that, from this point forward, gravity will be ignored due to the assumption that it is negligible, i.e., $\mathrm{Bo}/\mathrm{Ca} \ll \varepsilon$, where $\mathrm{Bo} = \rho g d^2/\gamma$ is the Bond number and Ca is the capillary number, which will later be expressed as the purely geometric quantity $\mathrm{Ca} = \Phi_0(\alpha, \theta)$.

A number of alternative formulations of the Navier-Stokes equations in nonorthogonal and curvilinear coordinates are possible, but not used in this work. Hill and Stokes (2018) developed a slightly simpler expression for the viscous term in the Navier-Stokes equations by writing the generalized Laplacian in a simpler form. Applying this methodology would slightly decrease the number of terms in the calculations below but would obscure the role of the stress tensor; we therefore do not take this approach. Voke and Collins (1984) found that writing the Navier-Stokes equations in terms of vorticity decreases the number of Christoffel symbols needed in the inertial terms, but the present work does not rely on those terms. Luo and Bewley (2004) derived the Navier-Stokes equations in general curvilinear *time-dependent* coordinates. While we assume the geometry of the groove is fixed and immobile, their results would be useful in extending this work to a fluid flowing within a flexible, moving groove.

7.2.5 Slender limit of fluid equations

The system will be reduced by taking the slender limit, in which $\varepsilon = d/L$ is taken to be a small parameter and the equations of motion are expanded perturbatively. The coordinates are nondimensionalized following Table 7.1, and terms of order ε^2 are dropped.

One way to proceed would be to take the Navier-Stokes equations [Equation (7.17)], write them all out by substituting in the definitions of covariant derivatives and Christoffel symbols, and then nondimensionalize and take the slender limit by dropping $O(\varepsilon^2)$ terms. However, it is easier to do this in reverse: first nondimensionalize the metric and the Christoffel symbols, and then substitute them into the equations. The result is identical, but this method makes tracking epsilons easier.

The metric tensor and its inverse become

$$g_{ij} = \begin{bmatrix} 1 & 0 & -\varepsilon\Upsilon\mathcal{J} \\ 0 & 1 & \varepsilon\Xi\mathcal{J} \\ -\varepsilon\Upsilon\mathcal{J} & \varepsilon\Xi\mathcal{J} & F^2 + O(\varepsilon^2) \end{bmatrix}, \tag{7.19}$$

$$g^{ij} = \frac{1}{F^2}\begin{bmatrix} F^2 + O(\varepsilon^2) & -\varepsilon^2\Xi\Upsilon\mathcal{J}^2 & \varepsilon\Upsilon\mathcal{J} \\ -\varepsilon^2\Xi\Upsilon\mathcal{J}^2 & F^2 + O(\varepsilon^2) & -\varepsilon\Xi\mathcal{J} \\ \varepsilon\Upsilon\mathcal{J} & -\varepsilon\Xi\mathcal{J} & 1 \end{bmatrix}, \tag{7.20}$$

Quantity	Dimensional variable	Scaling	Rescaled variable
Slender parameter			$\varepsilon = d/L \ll 1$
Coordinates	ξ	d	$\Xi = \xi/d$
(Figures 7.2 and 7.4)	υ	d	$\Upsilon = \upsilon/d$
	s	L	$S = s/L$
Self-similar coord.			$\eta = S/\sqrt{T}$
Characteristic length scale of groove	L	L	
Interface midline thickness at inlet	d	d	
Interface midline thickness	h	d	$H = h(s,t)/d$
Interface shape	σ	d	$\Sigma = \sigma(\xi, s, t)/d$
Cross-sectional area	a	d^2	$A = a/d^2$
Backbone curvature	k_ξ	$1/L$	$K_\Xi = k_\xi L$
	k_υ	$1/L$	$K_\Upsilon = k_\upsilon L$
Backbone torsion	$\jmath$	$1/L$	$\mathcal{J} = \jmath L$
Interface mean curvature	k_{mean}	$1/L$	$K_{\mathsf{mean}} = k_{\mathsf{mean}} L$
Metric scale factor	f	1	$F = 1 - \varepsilon \Xi K_\Xi - \varepsilon \Upsilon K_\Upsilon$
Velocity	u	$u_c = \varepsilon^2 \gamma \mathrm{Ca}/\mu$	$U = u/u_c$
	v	$v_c = \varepsilon^2 \gamma \mathrm{Ca}/\mu$	$V = v/v_c$
	w	$w_c = \varepsilon \gamma \mathrm{Ca}/\mu$	$W = w/w_c$
Stress tensor	τ^{ij}		
Pressure	p	$p_c = \gamma \mathrm{Ca}/(\varepsilon L)$	$P = p/p_c$
Streamwise flux	q	$q_c = w_c d^2$	$Q = q/q_c$
Time	t	$t_c = \mu L/(\varepsilon \gamma \mathrm{Ca})$	$T = t/t_c$
Surface tension	γ		
Liquid density	ρ		
Liquid viscosity	μ		
Slender limit capillary number			$\mathrm{Ca} = \mu w_c/\varepsilon\gamma = \Phi_0$
Reynolds number			$\mathrm{Re} = \rho w_c d/\mu = \varepsilon(\rho\gamma d/\mu^2)\Phi_0$
Bond number			$\mathrm{Bo} = \rho g d^2/\gamma$
Dimensionless interface radius			$\widehat{R} = \sin\alpha/(\cos\theta - \sin\alpha)$

Table 7.1: Characteristic scalings and nondimensional variables used to describe dimensionless system shown in Figures 7.3 and 7.4 .

where

$$F = (1 - \varepsilon \Xi K_\Xi - \varepsilon \Upsilon K_\Upsilon) + O(\varepsilon^2) \tag{7.21}$$

is the nondimensionalization of the scale factor f up to $O(\varepsilon^2)$. The Christoffel symbols become

$$\Gamma^\xi_{\xi s} = \Gamma^\xi_{s\xi} = -\frac{\varepsilon}{L}\,\frac{\Upsilon K_\Xi \mathcal{J}}{F} \tag{7.22a}$$

$$\Gamma^\upsilon_{\upsilon s} = \Gamma^\upsilon_{s\upsilon} = \frac{\varepsilon}{L}\,\frac{\Xi K_\Upsilon \mathcal{J}}{F} \tag{7.22b}$$

$$\Gamma^\xi_{\upsilon s} = \Gamma^\xi_{s\upsilon} = -\frac{1}{L}\,\frac{(1 - \varepsilon \Xi K_\Xi)\mathcal{J}}{F} \tag{7.22c}$$

$$\Gamma^\upsilon_{\xi s} = \Gamma^\upsilon_{s\xi} = \frac{1}{L}\,\frac{(1 - \varepsilon \Upsilon K_\Upsilon)\mathcal{J}}{F} \tag{7.22d}$$

$$\Gamma^\xi_{ss} = -\frac{1}{L}\left[-K_\Xi F + \varepsilon \mathcal{J}^2 \Xi + \varepsilon \Upsilon \partial_S \mathcal{J} + O(\varepsilon^2)\right] \tag{7.22e}$$

$$\Gamma^\upsilon_{ss} = -\frac{1}{L}\left[-K_\Upsilon F + \varepsilon \mathcal{J}^2 \Upsilon - \varepsilon \Xi \partial_S \mathcal{J} + O(\varepsilon^2)\right] \tag{7.22f}$$

$$\Gamma^s_{\xi s} = \Gamma^s_{s\xi} = -\frac{1}{L}\left[\frac{K_\Xi}{1 - \varepsilon \Xi K_\Xi - \varepsilon \Upsilon K_\Upsilon}\right] \tag{7.22g}$$

$$\Gamma^s_{\upsilon s} = \Gamma^s_{s\upsilon} = -\frac{1}{L}\,\frac{K_\Upsilon}{F} \tag{7.22h}$$

$$\Gamma^s_{ss} = \frac{\varepsilon}{L}\,\frac{\mathcal{J}\left(\Upsilon K_\Xi - \Xi K_\Upsilon\right) - \Xi \partial_S K_\Xi - \Upsilon \partial_S K_\Upsilon}{F}. \tag{7.22i}$$

The continuity equation is

$$\begin{aligned} 0 = {} & \partial_\xi u + \partial_\upsilon v + \partial_s \left(\frac{w}{f}\right) + \left(\Gamma^\xi_{\xi\xi} + \Gamma^\upsilon_{\upsilon\xi} + \Gamma^s_{s\xi}\right) u \\ & + \left(\Gamma^\xi_{\xi\upsilon} + \Gamma^\upsilon_{\upsilon\upsilon} + \Gamma^s_{s\upsilon}\right) v + \left(\Gamma^\xi_{\xi s} + \Gamma^\upsilon_{\upsilon s} + \Gamma^s_{ss}\right) \left(\frac{w}{f}\right), \end{aligned} \tag{7.23}$$

which reduces to

$$0 = \partial_\Xi U + \partial_\Upsilon V + \frac{\partial_S W}{F} - \varepsilon K_\Xi U - \varepsilon K_\Upsilon V + O(\varepsilon^2). \tag{7.24}$$

The denominator $F = (1 - \varepsilon \Xi K_\Xi - \varepsilon \Upsilon K_\Upsilon)$ under the $\partial_S W$ term is the scale factor of S, reflecting the fact that outside of a curve is longer than the inside. The $\varepsilon K_\Xi U$ and $\varepsilon K_\Upsilon V$ corrections are due to the $\hat{\upsilon}$ and $\hat{\xi}$ directions depending on s. To see this intuitively, imagine that U and W were 0, and that V were a constant. In such a case, the flow streamlines would not be parallel, but instead diverge or converge, depending on the sign of K_Υ; hence the divergence $\nabla \cdot \vec{u}$ would be nonzero.

The fluid stress tensor is given by

$$\tau^{ji} = \mu \sum_k \left(g^{jk} \partial_k u^i + g^{ik} \partial_k u^j + \sum_\ell \left[g^{jk} \Gamma^i_{k\ell} + g^{ik} \Gamma^j_{k\ell} \right] u^\ell \right) - p g^{ji}. \tag{7.25}$$

In matrix form, and dropping terms of relative order ε^2,

$$\tau^{ij} = \frac{\mu w_c}{L\varepsilon^2}\times \begin{bmatrix} -P & \varepsilon^2\left(\partial_\Xi V + \partial_\Upsilon U + \frac{\Xi\Upsilon\mathcal{J}^2 P}{F^2}\right) & \varepsilon\left(\partial_\Xi\left\{\frac{W}{F}\right\} - \frac{\Upsilon\mathcal{J}P}{F^2}\right) \\ \varepsilon^2\left(\partial_\Xi V + \partial_\Upsilon U + \frac{\Xi\Upsilon\mathcal{J}^2 P}{F^2}\right) & -P & \varepsilon\left(\partial_\Upsilon\left\{\frac{W}{F}\right\} + \frac{\Xi\mathcal{J}P}{F^2}\right) \\ \varepsilon\left(\partial_\Xi\left\{\frac{W}{F}\right\} - \frac{\Upsilon\mathcal{J}P}{F^2}\right) & \varepsilon\left(\partial_\Upsilon\left\{\frac{W}{F}\right\} + \frac{\Xi\mathcal{J}P}{F^2}\right) & -\frac{P}{F^2} \end{bmatrix} \tag{7.26}$$

It will be assumed that the streamwise inertial correction is small enough to be dropped, i.e., $\varepsilon\mathrm{Re}\Gamma_0 = \varepsilon(\rho w_c d/\mu)\Gamma_0 \ll 1$. In other words, inertia is not considered in this problem, which is valid at sufficiently small scales or late times. Note that in the curved pipe problem of Dean (1927), inertial corrections to streamwise velocity enter at $O(\varepsilon\mathrm{Re})$ and corrections to crosswise velocity enter at $O(\varepsilon^2\mathrm{Re})$ [i.e., $O(\mathrm{De}^2)$, De being the so-called Dean number]. In the V-groove, inertial corrections to streamwise velocity due to curvature have $O(\varepsilon^2\mathrm{Re}\Gamma_0)$, and are thus ignored. The three Navier-Stokes equations then lose their inertial terms and are simply described by $\sum_j \nabla_j \tau^{ji} = 0$. Nondimensionalizing,

$$0 = \sum_j \nabla_j \tau^{j\xi} = \frac{1}{\varepsilon^3}\frac{\mu w_c}{L^2}\left[\partial_\Xi P + O(\varepsilon^2)\right], \tag{7.27a}$$

$$0 = \sum_j \nabla_j \tau^{j\upsilon} = \frac{1}{\varepsilon^3}\frac{\mu w_c}{L^2}\left[\partial_\Upsilon P + O(\varepsilon^2)\right], \tag{7.27b}$$

$$0 = \sum_j \nabla_j \tau^{js} = \frac{\mu w_c}{\varepsilon^2 L^2 F}\Big[-\frac{\partial_S P}{F} + \partial_{\Xi\Xi} W + \partial_{\Upsilon\Upsilon} W - \varepsilon\left(K_\Xi \partial_\Xi W + K_\Upsilon \partial_\Upsilon W\right) + O(\varepsilon^2)\Big]. \tag{7.27c}$$

In short, $P = P(S,T)$ and

$$\frac{\partial_S P}{F} = \partial_{\Xi\Xi} W + \partial_{\Upsilon\Upsilon} W - \varepsilon\left[K_\Xi \partial_\Xi W + K_\Upsilon \partial_\Upsilon W\right]. \tag{7.28}$$

The denominator on the left-hand side reflects the fact that the pressure gradient becomes weaker on the outside of a curve, since the outside of a curve is longer than the inside of a curve. On the right-hand side of the equation, the correction is the additional contribution to W diffusion due to the curved geometry. It is not related to W being the S-component of the velocity vector; rather the Laplacian of any scalar would have the same correction at $O(\varepsilon)$. Ultimately, it is due to the $\hat{\upsilon}$ vector varying in s. To draw again from the analogy with polar coordinates, it is the fact that neighboring lines tangent to $\hat{r}$ are not parallel but instead grow apart as r increases that leads to the $r^{-1}\partial_r$ correction in the polar Laplacian.

7.2.6 Boundary conditions

Without loss of generality, the gauge pressure of the vacuum or gas outside the liquid may be set to 0. The boundary conditions across an interface $\upsilon = \sigma(\xi, s)$ are then given by three conditions: the normal stress must be balanced by the surface tension, and the stress must have no tangential

components at the surface (which is two conditions, since there are two independent tangent vectors). Letting γ be the surface tension of the fluid, the boundary conditions are expressed as

$$0 = \sum_{i,j} n_i \tau^{ij} n_j - \gamma k_{\text{mean}}, \tag{7.29a}$$

$$0 = \sum_{i,j} n_i \tau^{ij} t^{(1)}_j, \tag{7.29b}$$

$$0 = \sum_{i,j} n_i \tau^{ij} t^{(2)}_j. \tag{7.29c}$$

Here n^i is the vector normal to the surface, $t^i_{(1)}$ and $t^i_{(2)}$ are vectors tangent to the surface, and n_i, $t^{(1)}_i$, and $t^{(2)}_i$ their corresponding covectors. k_{mean} is the mean surface curvature, defined by

$$k_{\text{mean}} = -\sum_i \left(\nabla_i - n_i \sum_j n_j \nabla^j \right) n^i. \tag{7.30}$$

Although the expression for k_{mean} may appear complicated, it is simply the divergence of the normal vector restricted to the surface σ. The operator in parentheses is known as the surface gradient (frequently denoted ∇_s in the literature, but not here to avoid confusion with the index).

To evaluate these boundary condition expressions, it is first necessary to define tangent and normal vectors to the surface of the fluid. The fluid surface can be written in coordinates as

$$\vec{\sigma} = \begin{pmatrix} \xi \\ \sigma(\xi, s) \\ s \end{pmatrix}. \tag{7.31}$$

Although any two (non-parallel) tangent vectors may be used for $t_{(1)}$ and $t_{(2)}$, it is convenient to choose unit vectors in the directions of $\partial_\xi \vec{\sigma}$ and $\partial_s \vec{\sigma}$:

$$t^i_{(1)} = \frac{\partial_\xi \vec{\sigma}}{\sqrt{\partial_\xi \vec{\sigma} \cdot \partial_\xi \vec{\sigma}}} = \frac{1}{\sqrt{1 + (\partial_\xi \sigma)^2}} \begin{bmatrix} 1 \\ \partial_\xi \sigma \\ 0 \end{bmatrix}, \tag{7.32a}$$

$$t^i_{(2)} = \frac{\partial_s \vec{\sigma}}{\sqrt{\partial_s \vec{\sigma} \cdot \partial_s \vec{\sigma}}} = \frac{1}{\sqrt{f^2 + 2\xi \jmath \partial_s \sigma + (\partial_s \sigma)^2}} \begin{bmatrix} 0 \\ \partial_s \sigma \\ 1 \end{bmatrix}. \tag{7.32b}$$

The normal vector is defined by the cross product of the two tangent vectors. Because the unit tangent vectors are nonorthogonal, their cross product is not a unit vector and must be normalized. Letting ϵ represent the Levi-Civita symbol (not to be confused with the perturbation

parameter ε), the unit normal is

$$\begin{aligned} n^i &= (\text{normalization const.}) \times \sum_{j,k,\ell} g^{i\ell}\epsilon_{\ell jk} t^j_{(2)} t^k_{(1)} \\ &= \frac{1+O(\varepsilon^2)}{\sqrt{1+(\partial_\Xi \Sigma)^2}} \begin{bmatrix} -\partial_\Xi \Sigma \\ 1 \\ -\varepsilon\left(\partial_S \Sigma + \Xi \mathcal{J} + \Upsilon \mathcal{J} \partial_\Xi \Sigma\right)/F^2 \end{bmatrix}. \end{aligned} \tag{7.33}$$

The tangent and normal vectors each have corresponding covectors, given by

$$t^{(1)}_i = \sum_j g_{ij} t^j_{(1)} = \frac{1}{\sqrt{1+(\partial_\Xi \Sigma)^2}} \begin{bmatrix} 1 \\ \partial_\Xi \Sigma \\ \varepsilon \mathcal{J}\left(-\Upsilon + \Xi \partial_\Xi \Sigma\right) \end{bmatrix} \tag{7.34a}$$

$$t^{(2)}_i = \sum_j g_{ij} t^j_{(2)} = \frac{1}{F} \begin{bmatrix} -\varepsilon \mathcal{J} \Upsilon + O(\varepsilon^3) \\ \varepsilon \partial_S \Sigma + \varepsilon \mathcal{J} \Xi + O(\varepsilon^3) \\ F^2 + O(\varepsilon^2) \end{bmatrix} \tag{7.34b}$$

$$n_i = \sum_j g_{ij} n^j = \frac{1}{\sqrt{1+(\partial_\Xi \Sigma)^2}} \begin{bmatrix} -\partial_\Xi \Sigma + O(\varepsilon^2) \\ 1 + O(\varepsilon^2) \\ -\varepsilon \partial_S \Sigma + O(\varepsilon^3) \end{bmatrix}. \tag{7.34c}$$

Substituting these results into Equation (7.30), the mean surface curvature comes out to

$$\begin{aligned} k_{\text{mean}} = \frac{1}{\varepsilon L} \Bigg\{ & \frac{\partial_{\Xi\Xi} \Sigma}{\left[1+(\partial_\Xi \Sigma)^2\right]^{3/2}} \\ & -\varepsilon \frac{K_\Xi \partial_\Xi \Sigma}{\sqrt{1+(\partial_\Xi \Sigma)^2}} + \varepsilon \frac{K_\Upsilon}{\sqrt{1+(\partial_\Xi \Sigma)^2}} + O(\varepsilon^2) \Bigg\}. \end{aligned} \tag{7.35}$$

The first term represents the spanwise curvature of the fluid surface; the two corrective terms express the additional curvature due to the surface following the backbone. The curvature due to axial variations of fluid thickness along the groove (in the S direction) comes in at order $O(\varepsilon^2)$, and so does not contribute[1].

As for the boundary conditions, $0 = \sum_{i,j} n^i \tau_{ij} n^j - \gamma k_{\text{mean}}$ sets the pressure and $0 = \sum_{i,j} n^i \tau_{ij} t^j_{(2)}$ acts as a boundary condition for W. The other condition, $0 = \sum_{i,j} n^i \tau_{ij} t^j_{(1)}$, is a boundary condition on U and V and will not be necessary for the remaining derivation. After some algebra,

[1] For an example of an approach to including axial curvature in V-groove models, see Yang and Homsy (2006). Note, however, that they add it to the model only partially, ignoring some of the additional $O(\varepsilon^2)$ corrections that should arise from the axial curvature.

and making the replacement $\gamma = \varepsilon^{-1}\mu w_c/\mathrm{Ca}$, the two relevant boundary conditions become

$$0 = \frac{\mu w_c}{L\varepsilon^2}\left[-P - \frac{1}{\mathrm{Ca}}\left(\frac{\partial_{\Xi\Xi}\Sigma}{(1+(\partial_\Xi\Sigma)^2)^{3/2}} - \varepsilon\frac{K_\Xi\partial_\Xi\Sigma}{\sqrt{1+(\partial_\Xi\Sigma)^2}} + \varepsilon\frac{K_\Upsilon}{\sqrt{1+(\partial_\Xi\Sigma)^2}}\right) + O(\varepsilon^2)\right], \tag{7.36a}$$

$$0 = \frac{\mu w_c}{L\varepsilon}F\left[\partial_n W + \varepsilon\frac{K_\Upsilon - K_\Xi\partial_\Xi\Sigma}{\sqrt{1+(\partial_\Xi\Sigma)^2}}W + O(\varepsilon^2)\right], \tag{7.36b}$$

where

$$\partial_n = \frac{\partial_\Upsilon - (\partial_\Xi\Sigma)\partial_\Xi}{\sqrt{1+(\partial_\Xi\Sigma)^2}} \tag{7.37}$$

is the outward normal derivative in the Ξ-Υ plane.

7.2.7 Transport equation

The final equation to be derived from the curvilinear coordinate system is the groove transport equation. We first derive the transport equation in a more general form, and then apply it to the curved V-groove.

General metric

Let the local groove coordinates be $\{\xi, \upsilon, s\}$, and the cross-sectional slice of the groove in the ξ-υ plane be denoted $\Omega(s,t)$. Suppose the metric tensor is given by

$$g_{ij} = \begin{bmatrix} 1 & 0 & g_1(\xi,\upsilon,s) \\ 0 & 1 & g_2(\xi,\upsilon,s) \\ g_1(\xi,\upsilon,s) & g_2(\xi,\upsilon,s) & [g_3(\xi,\upsilon,s)]^2 \end{bmatrix}. \tag{7.38}$$

This is not the most general metric tensor possible, but it is sufficient for our purposes. One important feature of this metric is that $\hat{\xi}$ and $\hat{\upsilon}$ are orthogonal, although they are not orthogonal with $\hat{s}$. This means that we can easily switch between the Ω-projected coordinates and the full 3D coordinates.

Normal velocity

The total flux across $\Omega(s,t)$ is $\int_{\Omega(s,t)} \vec{u}\cdot\hat{\nu}d\Xi d\Upsilon$, where $\hat{\nu}$ is normal to the plane of the cross-sectional $\Omega(s,t)$ cut. (Keep in mind that this is distinct from $\hat{n}$, which is the normal to the boundary $\partial\Omega$.) In general, because $\hat{\nu} \neq \hat{s}$, then $\vec{u}\cdot\hat{\nu} \neq w$. Making this distinction between $\vec{u}\cdot\hat{\nu}$ and w when computing integrated flux is necessary only in nonorthogonal coordinate systems (Wang, 1981b). Although the nonorthogonality is $O(\varepsilon^2)$ in our perturbation scheme, we derive the general transport equation here without making assumptions about orthogonality.

In this case, $\xi^i = \{1,0,0\}$ and $\upsilon^i = \{0,1,0\}$. Then, it is clear that the normal vector must have the (lowered) form $\nu_i = \{0,0,c\}$ for some normalization factor c. To be a unit vector, it must be that $\nu_i = \{0,0,\frac{1}{\sqrt{g^{33}}}\}$. Thus,

$$\nu_i = \left\{0, 0, \sqrt{g_3^2 - g_1^2 - g_2^2}\right\} \tag{7.39}$$

$$\nu^i = \frac{1}{\sqrt{g_3^2 - g_1^2 - g_2^2}} \{-g_1, -g_2, 1\} \tag{7.40}$$

$$\vec{u} \cdot \hat{\nu} = u^i \nu_i = \left(\frac{w}{g_3}\right) \sqrt{g_3^2 - g_1^2 - g_2^2}. \tag{7.41}$$

Conservation of mass

We will need the conservation of mass equation in curvilinear coordinates to simplify the transport equation. For an incompressible fluid, this is given by

$$\begin{aligned} 0 = \nabla \cdot \vec{u} &= \sum_k \left(\partial_k + \sum_{i,j} \frac{1}{2} g^{ij} \partial_k g_{ij} \right) u^k \\ &= \frac{1}{\sqrt{\det g_{ij}}} \sum_k \partial_k \left(\sqrt{\det g_{ij}} u^k \right) \\ &= \frac{1}{\sqrt{g_3^2 - g_1^2 - g_2^2}} \sum_k \partial_k \left(\sqrt{g_3^2 - g_1^2 - g_2^2} u^k \right), \end{aligned} \tag{7.42}$$

where $u^i = \{u, v, w/g_3\}$.

General transport equation

Now we substitute these results into the integral transport equation. Note that we will make use of the fact that $\sqrt{\det g_{ij}} = \sqrt{g_3^2 - g_1^2 - g_2^2}$, and in the last step invoke conservation of mass.

$$\begin{aligned} \left.\frac{\partial q}{\partial s}\right|_t &= \left.\frac{\partial}{\partial s}\right|_t \int_{\Omega(s,t)} \hat{u} \cdot \hat{\nu} d\Xi d\Upsilon = \left.\frac{\partial}{\partial s}\right|_t \int_\Omega \left(\frac{w}{g_3}\right) \sqrt{g_3^2 - g_1^2 - g_2^2} dA \\ &= -\left.\frac{\partial}{\partial t}\right|_s \int_\Omega \sqrt{g_3^2 - g_1^2 - g_2^2} dA + \int_\Omega \left.\frac{\partial}{\partial s}\right|_{\vec{x},t} \left[\sqrt{\det g_{ij}} \left(\frac{w}{g_3}\right) \right] dA \\ &\quad + \int_\Omega \left[\partial_\xi \left(\sqrt{\det g_{ij}} u \right) + \partial_\upsilon \left(\sqrt{\det g_{ij}} v \right) \right] \, dA \\ &= -\left.\frac{\partial}{\partial t}\right|_s \int_\Omega \sqrt{g_3^2 - g_1^2 - g_2^2} dA + \int_\Omega \partial_k \left[\sqrt{\det g_{ij}} u^k \right] dA \\ &= -\left.\frac{\partial}{\partial t}\right|_s \int_{\Omega(s,t)} \sqrt{g_3^2 - g_1^2 - g_2^2} dA \ . \end{aligned} \tag{7.43}$$

Transport equation in curved V-groove

Given the cross-sectional slice of the groove in the ξ-υ plane, $\Omega(s,t)$, the flux across that slice is $\int_{\Omega(s,t)} \vec{u} \cdot \hat{\nu} d\xi d\upsilon$, where $\hat{\nu}$ is a unit normal to the slice. (Keep in mind that this is distinct

from $\hat{n}$, which is the normal to the boundary $\partial\Omega$.) Because $\hat{\nu} \neq \hat{s}$, then $\vec{u} \cdot \hat{\nu} \neq w/f$. Instead, $\nu_i = \{0, 0, (1 - \xi k_\xi - \upsilon k_\upsilon)\}$ and

$$\begin{aligned} \vec{u} \cdot \hat{\nu} = u^i \nu_i &= (1 - \xi k_\xi - \upsilon k_\upsilon) \frac{w}{f} \\ &= w_c W + O(w_c \varepsilon^2). \end{aligned} \tag{7.44}$$

Hence the directional corrections to the flux have are of order ε^2, and will be ignored.

Defining the flux

$$q(s,t) = \int_{\Omega(s,t)} u^i \nu_i d\xi d\upsilon, \tag{7.45}$$

the transport equation is

$$\begin{aligned} \left.\frac{\partial q}{\partial s}\right|_t &= \left.\frac{\partial}{\partial s}\right|_t \int_{\Omega(s,t)} \hat{u} \cdot \hat{\nu} d\xi d\upsilon \\ &= -\left.\frac{\partial}{\partial t}\right|_s \int_{\Omega(s,t)} (1 - \xi k_\xi - \upsilon k_\upsilon) d\xi d\upsilon \ . \end{aligned} \tag{7.46}$$

This is analogous to the relation arising in the straight-groove equation, $dq/dz = -da/dt$ (found by Lenormand and Zarcone, 1984, in square capillaries). However, the additional correction comes from the fact that a small volume element in the groove can no longer be expressed simply as $d\mathrm{vol} = a dz$; instead, there is an additional piece of volume on the outside of the curve, and a decrease in volume on the inside. In nondimensional terms, with

$$Q = q/(w_c d^2) \tag{7.47}$$

$$A = a/d^2, \tag{7.48}$$

$$\left.\frac{\partial Q}{\partial S}\right|_T = -\left.\frac{\partial}{\partial T}\right|_S \int_{\Omega(S,T)} (1 - \varepsilon \Xi K_\Xi - \varepsilon \Upsilon K_\Upsilon) d\Xi d\Upsilon \ , \tag{7.49}$$

where $\Omega(S,T)$ is the cross-sectional domain in the Ξ-Υ plane [the nondimensional version of $\Omega(s,t)$].

This concludes the portion of the derivation involving index notation, covariant differentiation, and curvilinear coordinates. The following sections will require only classical calculus.

7.2.8 Summary of continuity, Navier-Stokes equations, and boundary conditions

In summary, the slender limits of the continuity, Navier-Stokes equations, and boundary conditions in curvilinear coordinates are given to $O(\varepsilon^2)$ by

$$0 = \partial_\Xi U + \partial_\Upsilon V + \frac{\partial_S W}{F} - \varepsilon K_\Xi U - \varepsilon K_\Upsilon V, \tag{7.50}$$

$$\frac{\partial_S P}{F} = \partial_{\Xi\Xi} W + \partial_{\Upsilon\Upsilon} W - \varepsilon \left[K_\Xi \partial_\Xi W + K_\Upsilon \partial_\Upsilon W \right], \tag{7.51}$$

$$P = -\frac{1}{\mathrm{Ca}} \left(\frac{\partial_{\Xi\Xi}\Sigma}{\left[1 + (\partial_\Xi \Sigma)^2\right]^{3/2}} - \varepsilon \frac{K_\Xi \partial_\Xi \Sigma}{\sqrt{1 + (\partial_\Xi \Sigma)^2}} + \varepsilon \frac{K_\Upsilon}{\sqrt{1 + (\partial_\Xi \Sigma)^2}} \right), \tag{7.52}$$

$$0 = W|_{\Upsilon = \Xi \cot\alpha}, \tag{7.53}$$

$$0 = \left[\partial_n W + \varepsilon \frac{K_\Upsilon - K_\Xi \partial_\Xi \Sigma}{\sqrt{1 + (\partial_\Xi \Sigma)^2}} W \right]_{\Upsilon = \Sigma(\Xi, S)}, \tag{7.54}$$

and the transport equation is given by

$$\left.\frac{\partial Q}{\partial S}\right|_T = -\left.\frac{\partial}{\partial T}\right|_S \int_{\Omega(S,T)} F d\Xi d\Upsilon \ , \tag{7.55}$$

where $F = (1 - \varepsilon \Xi K_\Xi - \varepsilon \Upsilon K_\Upsilon)$. The first boundary condition on W represents the no-slip walls of the groove; the second represents the zero tangential stress condition at the surface. Note that ∂_n represents the normal derivative restricted to the Ξ-Υ plane; the full expression, including the ε correction, represents the full normal derivative of W to $O(\varepsilon)$.

7.2.9 Cross-sectional interface shape

The internal fluid pressure is determined by the surface curvature, via Equation (7.52). Because P is independent of both Υ and Ξ, then so must be the surface curvature. Combining this fact with the constraint that the surface must meet the wall at a contact angle of θ is sufficient to determine the shape of the surface, to order $O(\varepsilon)$.

The invariance under Ξ and wetting conditions to be satisfied by Σ are

$$0 = \partial_\Xi \left(\frac{\partial_{\Xi\Xi}\Sigma}{\left[1 + (\partial_\Xi \Sigma)^2\right]^{3/2}} - \varepsilon \frac{K_\Xi \partial_\Xi \Sigma}{\sqrt{1 + (\partial_\Xi \Sigma)^2}} + \varepsilon \frac{K_\Upsilon}{\sqrt{1 + (\partial_\Xi \Sigma)^2}} \right) + O(\varepsilon^2), \tag{7.56a}$$

$$\partial_\Xi \Sigma|_{\Sigma = \Xi \cot\alpha} = \cot(\theta + \alpha), \tag{7.56b}$$

$$\partial_\Xi \Sigma|_{\Sigma = -\Xi \cot\alpha} = -\cot(\theta + \alpha). \tag{7.56c}$$

The $O(1)$ solution (i.e., the solution with K_Ξ and K_Υ set to 0) is a section of a circle, as in the

Quantity	Static scaling	Rescaled static variable
Coordinates	$H(S,T)$	$\widetilde{\Xi} = \Xi/H(S,T)$
	$H(S,T)$	$\widetilde{\Upsilon} = \Upsilon/H(S,T)$
Interface shape	$H(S,T)$	$\widetilde{\Sigma}(\widetilde{\Xi}) = \Sigma(\Xi)/H(S,T)$
Interface wall intercept	$H(S,T)$	$\widetilde{I} = I/H(S,T)$
Cross-sectional domain	$H(S,T)$	$\widetilde{\Omega} = \Omega/H(S,T)$
Backbone curvature	$1/H(S,T)$	$\widetilde{K_\Upsilon} = K_\Upsilon H(S,T)$
Streamwise velocity	$H^2(-\partial_S P)$	$\widetilde{W} = W/[H^2(-\partial_S P)]$

Table 7.2: Static variables used in flux computation.

straight V-groove (Weislogel, 1996; Weislogel and Lichter, 1998).

$$\Sigma_0(\Xi) = H(S)\left[1 + \widehat{R} - \sqrt{\widehat{R}^2 - \left(\frac{\Xi}{H(S)}\right)^2}\right], \tag{7.57}$$

$$\implies \frac{\partial_{\Xi\Xi}\Sigma_0}{[1+(\partial_\Xi\Sigma_0)^2]^{3/2}} = \frac{1}{\widehat{R}H(S)}, \tag{7.58}$$

where

$$\widehat{R} = \frac{\sin\alpha}{\cos\theta - \sin\alpha}. \tag{7.59}$$

It is convenient to change into static variables, a summary of which is given in Table 7.2, wherein

$$\widetilde{\Xi} = \frac{\Xi}{H}, \qquad \widetilde{\Upsilon} = \frac{\Upsilon}{H}, \tag{7.60a}$$

$$\widetilde{\Sigma} = \frac{\Sigma}{H}, \qquad \widetilde{K_\Upsilon} = K_\Upsilon H, \tag{7.60b}$$

so that

$$\widetilde{\Sigma}_0(\widetilde{\Xi}) = 1 + \widehat{R} - \sqrt{\widehat{R}^2 - \widetilde{\Xi}^2}, \tag{7.61}$$

$$\frac{\partial_{\widetilde{\Xi}\widetilde{\Xi}}\widetilde{\Sigma}_0}{\left[1+(\partial_{\widetilde{\Xi}}\widetilde{\Sigma}_0)^2\right]^{3/2}} = \frac{1}{\widehat{R}}. \tag{7.62}$$

The backbone curvature K_Ξ and K_Υ then lead to $O(\varepsilon)$ corrections to that circular section.

The K_Ξ surface curvature term is odd in Ξ, which implies that, to order $O(\varepsilon)$, it will add an odd surface correction. This odd correction will end up having no effect on the net pressure or net flux at order $O(\varepsilon)$, and instead will contribute only at $O(\varepsilon^2)$. Hence, from now on, K_Ξ will be dropped and only the effect of K_Υ will be considered.

Decomposing the surface into the sum of the $O(1)$ circular solution $\widetilde{\Sigma}_0(\widetilde{\Xi})$, plus an $O(\varepsilon)$ correction $\varepsilon\widetilde{K_\Upsilon}\widetilde{\Sigma}_\Upsilon(\widetilde{\Xi})$,

$$\widetilde{\Sigma}(\widetilde{\Xi}) = \widetilde{\Sigma}_0(\widetilde{\Xi}) + \varepsilon\widetilde{K_\Upsilon}\widetilde{\Sigma}_\Upsilon(\widetilde{\Xi}) + O(\varepsilon^2). \tag{7.63}$$

Then, Equation (7.56a) gives

$$0 = \partial_{\widetilde{\Xi}}\left\{\frac{\partial_{\widetilde{\Xi}\widetilde{\Xi}}\widetilde{\Sigma}}{\left[1+(\partial_{\widetilde{\Xi}}\widetilde{\Sigma})^2\right]^{3/2}} + \varepsilon\frac{\widetilde{K_\Upsilon}}{\sqrt{1+(\partial_{\widetilde{\Xi}}\widetilde{\Sigma})^2}}\right\} + O(\varepsilon^2), \tag{7.64}$$

$$\implies \frac{(\widehat{R}^2-\widetilde{\Xi}^2)\partial_{\widetilde{\Xi}\widetilde{\Xi}\widetilde{\Xi}}\widetilde{\Sigma}_\Upsilon - 3\widetilde{\Xi}\partial_{\widetilde{\Xi}}\widetilde{\Sigma}_\Upsilon + \widehat{R}^2}{\widehat{R}^3/\sqrt{\widehat{R}^2-\widetilde{\Xi}^2}} = \widehat{P}_\Upsilon, \tag{7.65}$$

where the constant $\widehat{P}_\Upsilon$ has been so named to indicate that it will turn out to be a contribution to the pressure. Integrating the result yields

$$\begin{aligned}\implies \widetilde{\Sigma}_\Upsilon = &-\frac{\widehat{R}^2\widetilde{\Xi}}{2\sqrt{\widehat{R}^2-\widetilde{\Xi}^2}}\tan^{-1}\left(\frac{\widetilde{\Xi}}{\sqrt{\widehat{R}^2-\widetilde{\Xi}^2}}\right)\\ &+\frac{\widehat{P}_\Upsilon\widehat{R}^3 + C_2\widetilde{\Xi}}{\sqrt{\widehat{R}^2-\widetilde{\Xi}^2}} + C_3,\end{aligned} \tag{7.66}$$

where $\widehat{P}_\Upsilon$, C_2 and C_3 must be set by the boundary conditions. The three boundary conditions on $\widetilde{\Sigma}_\Upsilon$ come from choosing to measure thickness at the center, and from the wetting condition on each side of the groove:

$$\widetilde{\Sigma}_\Upsilon(0) = 0, \tag{7.67a}$$

$$\partial_{\widetilde{\Xi}}\widetilde{\Sigma}\Big|_{\widetilde{\Sigma}=\pm\widetilde{\Xi}\cot\alpha} = \pm\cot(\theta+\alpha). \tag{7.67b}$$

The first condition is easily satisfied by setting $C_3 = -\widehat{P}_\Upsilon\widehat{R}^2$. A second is satisfied by enforcing evenness with $C_2 = 0$, leaving

$$\begin{aligned}\widetilde{\Sigma}_\Upsilon = &-\frac{\widehat{R}^2\widetilde{\Xi}}{2\sqrt{\widehat{R}^2-\widetilde{\Xi}^2}}\tan^{-1}\left(\frac{\widetilde{\Xi}}{\sqrt{\widehat{R}^2-\widetilde{\Xi}^2}}\right)\\ &-\widehat{P}_\Upsilon\widehat{R}^2\left(1-\frac{\widehat{R}}{\sqrt{\widehat{R}^2-\widetilde{\Xi}^2}}\right).\end{aligned} \tag{7.68}$$

The remaining constant, $\widehat{P}_\Upsilon$, is set by satisfying the contact angle condition. This is a bit tricky, since rather than a Neumann condition at a specified value of $\widetilde{\Xi}$, it is a Neumann boundary

condition at the point where the surface intercepts the wall, which is not known. So instead of a single equation setting the slope of $\widetilde{\Sigma}$ which can be solved for $\widehat{P}_\Upsilon$, there will instead be a pair of simultaneous equations for two unknowns: $\widehat{P}_\Upsilon$ and the wall intercept location, $\widetilde{I}$.

Letting

$$\widetilde{I}_0 = \widehat{R}\cos(\theta+\alpha) \tag{7.69}$$

be the $O(1)$ wall intercept where $\widetilde{\Sigma}_0(\widetilde{I}_0) = \widetilde{I}_0\cot\alpha$, and

$$\widetilde{I} = \widetilde{I}_0 + \varepsilon\widetilde{K}_\Upsilon\widetilde{I}_\Upsilon \tag{7.70}$$

be the full intercept of $\widetilde{\Sigma}$, then the wall intercept equation $\widetilde{I}\cot\alpha = \widetilde{\Sigma}(\widetilde{I})$ becomes

$$\begin{aligned}\widetilde{I}_0\cot\alpha + \varepsilon\widetilde{K}_\Upsilon\widetilde{I}_\Upsilon\cot\alpha = \widetilde{\Sigma}_0(\widetilde{I}_0) + \varepsilon\widetilde{K}_\Upsilon\widetilde{I}_\Upsilon\partial_{\widetilde{\Xi}}\widetilde{\Sigma}_0(\widetilde{I}_0)\\ + \varepsilon\widetilde{K}_\Upsilon\widetilde{\Sigma}_\Upsilon(\widetilde{I}_0) + O(\varepsilon^2),\end{aligned} \tag{7.71}$$

and hence

$$\widetilde{I}_\Upsilon = \frac{\widetilde{\Sigma}_\Upsilon(\widetilde{I}_0)}{\cot\alpha - \partial_{\widetilde{\Xi}}\widetilde{\Sigma}_0(\widetilde{I}_0)}. \tag{7.72}$$

The second boundary equation, setting the slope of $\widetilde{\Sigma}$ at the intercept, is

$$0 = \partial_{\widetilde{\Xi}}\left[\widetilde{\Sigma}_0 + \varepsilon\widetilde{K}_\Upsilon\widetilde{\Sigma}_\Upsilon\right]_{\widetilde{\Xi}=\widetilde{I}_0+\varepsilon\widetilde{K}_\Upsilon\widetilde{I}_\Upsilon} - \partial_{\widetilde{\Xi}}\widetilde{\Sigma}_0\Big|_{\widetilde{\Xi}=\widetilde{I}_0} \tag{7.73}$$

$$\implies 0 = \varepsilon\widetilde{K}_\Upsilon\left[\widetilde{I}_\Upsilon\partial_{\widetilde{\Xi}\widetilde{\Xi}}\widetilde{\Sigma}_0 + \partial_{\widetilde{\Xi}}\widetilde{\Sigma}_\Upsilon\right]_{\widetilde{\Xi}=\widetilde{I}_0} + O(\varepsilon^2). \tag{7.74}$$

Substituting in the expressions for $\widetilde{I}_\Upsilon$ and $\widetilde{\Sigma}_\Upsilon$ gives a single equation for $\widehat{P}_\Upsilon$:

$$\begin{aligned}0 = &\frac{\widetilde{I}_0\tan^{-1}\left(\widetilde{I}_0/\sqrt{\widehat{R}^2-\widetilde{I}_0^2}\right) + 2\widehat{P}_\Upsilon\left(\sqrt{\widehat{R}^2-\widetilde{I}_0^2}-\widehat{R}\right)}{\cot\alpha\sqrt{\widehat{R}^2-\widetilde{I}_0^2}-\widetilde{I}_0}\\ &+\left[\frac{\widetilde{I}_0\sqrt{\widehat{R}^2-\widetilde{I}_0^2}}{\widehat{R}^2} + \tan^{-1}\left(\frac{\widetilde{I}_0}{\sqrt{\widehat{R}^2-\widetilde{I}_0^2}}\right)\right] - \widehat{P}_\Upsilon\frac{\widetilde{I}_0}{\widehat{R}},\end{aligned} \tag{7.75}$$

which yields

$$\widehat{P}_\Upsilon = \frac{\left(\frac{\pi}{2}-\alpha-\theta\right)\cos\alpha + \cos(\theta+\alpha)\sin\theta}{2(\cos\theta-\sin\alpha)} \tag{7.76}$$

and

$$\widetilde{I}_\Upsilon = -\frac{\sin^3\alpha\left(\frac{\pi}{2}-\alpha-\theta-\cos(\theta+\alpha)\right)(1-\sin(\theta+\alpha))}{2(\cos\theta-\sin\alpha)^3}. \tag{7.77}$$

Because the Concus-Finn condition $(\theta+\alpha) < \pi/2$ is assumed from the start, then $\widehat{P}_\Upsilon > 0$ and $\widetilde{I}_\Upsilon < 0$.

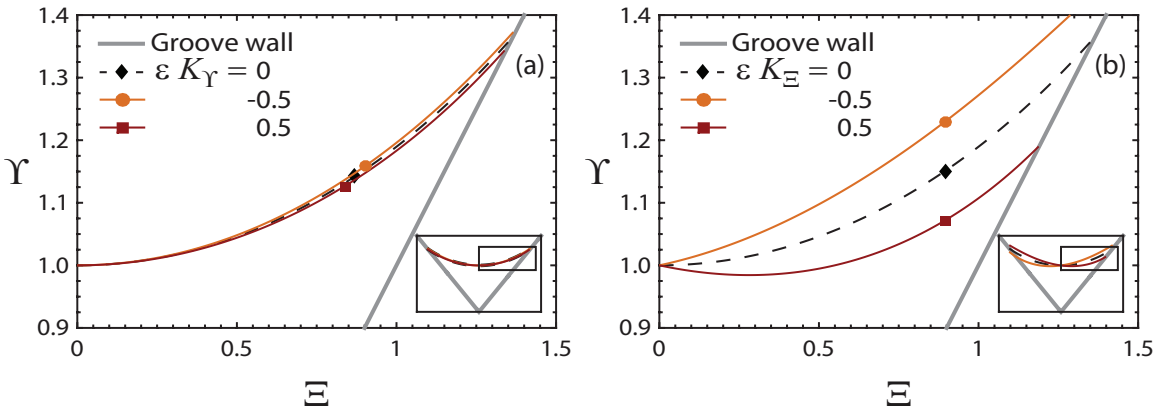

Figure 7.5: Plots showing the influence of positive and negative curvatures K_Υ and K_Ξ on the interface shape $\Sigma(\Xi)$ of a liquid film in a V-groove with internal half angle $\alpha = 45°$ and fluid contact angle $\theta = 15°$., following the formula in Equation (7.68).
(a) Interface shape $\Sigma(\Xi)$ for vertical curvature $K_\Upsilon \in \{-0.5, 0, 0.5\}$ and zero lateral curvature ($K_\Xi = 0$). The correction is even in Ξ, and hence the symmetrical result at $\Xi < 0$ is not shown. Inset: full groove cross-section, with a box to indicate the boundaries of the plot.
(b) Interface shape $\Sigma(\Xi)$ for lateral curvature $K_\Xi \in \{-0.5, 0, 0.5\}$ and zero vertical curvature ($K_\Upsilon = 0$). The correction is odd in Ξ, and hence the antisymmetrical result at $\Xi < 0$ is not shown. Inset: full groove cross-section, with a box to indicate the boundaries of the plot.

The resulting surface correction is shown in Figure 7.5, along with the computed surface correction due to transverse curvature K_Ξ (the derivation of which was not shown). It can be seen that for $K_\Upsilon < 0$, the surface is raised and has a smaller radius of curvature in the center than at the edges, whereas for $K_\Upsilon > 0$, the surface becomes depressed and the center has weaker curvature than the edges. This makes sense intuitively; the vertical backbone curvature leads to a greater curvature at the center of the fluid surface than at the edges, because the edges are closer to parallel with $\hat{v}$. It is also notable that the surface correction for K_Υ is very small, while that for K_Ξ is somewhat larger. In the completed model, this K_Υ surface correction indeed plays only a small role, with most of the correction coming from other terms. Although the K_Ξ surface correction is relatively larger, it is odd, and so it does not modify the pressure or the cross-sectional area at first order.

7.2.10 Pressure

Using the newly constructed surface, the pressure can be computed

$$\begin{aligned} P &= -\frac{1}{\mathrm{Ca}}\left(\frac{\partial_{\Xi\Xi}\Sigma}{[1+(\partial_\Xi\Sigma)^2]^{3/2}} + \varepsilon\frac{K_\Upsilon}{\sqrt{1+(\partial_\Xi\Sigma)^2}}\right) + O(\varepsilon^2) \\ &= -\frac{1}{H\mathrm{Ca}\widehat{R}} - \frac{\varepsilon K_\Upsilon \widehat{P}_\Upsilon}{\mathrm{Ca}} = -\frac{1}{\mathrm{Ca}}\left(\frac{\widehat{P}_0}{H} + \varepsilon\widetilde{K}_\Upsilon\widehat{P}_\Upsilon\right) + O(\varepsilon^2) \\ &= -\frac{\widehat{P}_0}{\mathrm{Ca}}\left(\frac{1}{H} + \varepsilon\widetilde{K}_\Upsilon\frac{\widehat{P}_\Upsilon}{\widehat{P}_0}\right) + O(\varepsilon^2) \end{aligned} \tag{7.78}$$

where

$$\widehat{P}_0 = \frac{1}{\widehat{R}} = \frac{\cos\theta - \sin\alpha}{\sin\alpha} \tag{7.79}$$

is the pressure factor for a straight V-groove, shown in Figure 7.7 (b). The relative pressure correction, $\widehat{P}_\Upsilon/\widehat{P}_0$, can be expressed analytically as

$$\frac{\widehat{P}_\Upsilon}{\widehat{P}_0} = \frac{\{[(\pi/2) - \alpha - \theta]\cos\alpha + \cos(\theta+\alpha)\sin\theta\}\sin\alpha}{2(\cos\theta - \sin\alpha)^2}, \tag{7.80}$$

which is plotted in Figure 7.8 (b). $\widehat{P}_\Upsilon/\widehat{P}_0 > 0$, which implies that negative curvature ($K_\Upsilon < 0$) increases the pressure, and positive curvature ($K_\Upsilon > 0$) decreases the pressure, at a given fixed H. Furthermore, as seen in Figure 7.8 (b), the pressure is larger for wider grooves (large α) and those with large contact angles (large θ). This occurs because the cross-sectional fluid interface has smaller curvature (i.e., is flatter) when α and θ are large; hence the relative effect of backbone curvature (and, to a lesser extent, the interface shape correction) is larger.

7.2.11 Flux computation

Next, the streamwise velocity W must be integrated to determine the flux. To do so, W is determined from the perturbed Poisson equation

$$\frac{\partial_S P}{(1-\varepsilon\Upsilon K_\Upsilon)} = \partial_{\Xi\Xi} W + \partial_{\Upsilon\Upsilon} W - \varepsilon K_\Upsilon \partial_\Upsilon W, \tag{7.81}$$

$$0 = W|_{\Upsilon = \pm \Xi\cot\alpha} \tag{7.82}$$

$$0 = \left[\partial_n W + \varepsilon \frac{K_\Upsilon}{\sqrt{1+(\partial_\Xi \Sigma)^2}} W\right]_{\Upsilon=\Sigma(\Xi,S)}. \tag{7.83}$$

Again, the first boundary condition comes from the no-slip walls of the groove, and the second from the zero tangential stress condition at the boundary. Writing $W = W_0 + \varepsilon K_\Upsilon W_\Upsilon$ and expanding Equation (7.81) to first order yields the two equations

$$\partial_S P = \partial_{\Xi\Xi} W_0 + \partial_{\Upsilon\Upsilon} W_0, \tag{7.84a}$$

$$\Upsilon \partial_S P + \partial_\Upsilon W_0 = \partial_{\Xi\Xi} W_\Upsilon + \partial_{\Upsilon\Upsilon} W_\Upsilon. \tag{7.84b}$$

The first order correction W_Υ is forced by two factors: $\Upsilon\partial_S P$ is the correction due to the pressure gradient being weaker on the outside of a curve and stronger on the inside; $\partial_\Upsilon W_0$ is the correction due to the $O(1)$ Laplacian not accounting for the increased coordinate length away from the groove corner. Interestingly, these two corrections act in opposite directions and their relative strength depends on the geometry. Later it will be seen that for most geometries the pressure term dominates, but in very wide grooves (i.e., large α) the diffusion term can dominate, leading to an opposite sign on the flux correction.

As in the straight V-groove derivation (Weislogel, 1996; Weislogel and Lichter, 1998), we would like to separate out the Poisson problem from its dependence on H, P, and S; this way, instead

of having to numerically solve for W at every time step, we can instead numerically solve a Poisson equation only once and then use the resulting factor as a coefficient in a governing differential equation independent of Ξ and Υ. This suggests the definitions

$$W_0 = H^2(-\partial_S P)\widetilde{W}_0 \tag{7.85a}$$

$$W_\Upsilon = H^3(-\partial_S P)\widetilde{W}_\Upsilon, \tag{7.85b}$$

so that

$$-1 = \partial_{\widetilde{\Xi}\widetilde{\Xi}}\widetilde{W}_0 + \partial_{\widetilde{\Upsilon}\widetilde{\Upsilon}}\widetilde{W}_0, \tag{7.86a}$$

$$-\widetilde{\Upsilon} + \partial_{\widetilde{\Upsilon}}\widetilde{W}_0 = \partial_{\widetilde{\Xi}\widetilde{\Xi}}\widetilde{W}_\Upsilon + \partial_{\widetilde{\Upsilon}\widetilde{\Upsilon}}\widetilde{W}_\Upsilon. \tag{7.86b}$$

These new Poisson equations are indeed independent of H, P, and S.

Applying the same definition to the surface boundary condition, Equation (7.54), gives

$$\begin{aligned} 0 = &\left[\partial_{\widetilde{\Upsilon}}\widetilde{W}_0 + \varepsilon\widetilde{K}_\Upsilon\partial_{\widetilde{\Upsilon}}\widetilde{W}_\Upsilon - \left(\partial_{\widetilde{\Xi}}\widetilde{\Sigma}_0 + \varepsilon\widetilde{K}_\Upsilon\partial_{\widetilde{\Xi}}\widetilde{\Sigma}_\Upsilon\right)\right. \\ &\left.\times\left(\partial_{\widetilde{\Xi}}\widetilde{W}_0 + \varepsilon\widetilde{K}_\Upsilon\partial_{\widetilde{\Xi}}\widetilde{W}_\Upsilon\right) + \varepsilon\widetilde{K}_\Upsilon\widetilde{W}_0\right]_{\Upsilon=\Sigma} + O(\varepsilon^2) \end{aligned} \tag{7.87}$$

$$\begin{aligned} \implies 0 = &\left[\partial_{\widetilde{\Upsilon}}\widetilde{W}_0 - (\partial_{\widetilde{\Xi}}\widetilde{\Sigma}_0)\partial_{\widetilde{\Xi}}\widetilde{W}_0\right]_{\widetilde{\Upsilon}=\widetilde{\Sigma}_0} \\ &+ \varepsilon\widetilde{K}_\Upsilon\left[\partial_{\widetilde{\Upsilon}}\widetilde{W}_\Upsilon - (\partial_{\widetilde{\Xi}}\widetilde{\Sigma}_0)\partial_{\widetilde{\Xi}}\widetilde{W}_\Upsilon - (\partial_{\widetilde{\Xi}}\widetilde{\Sigma}_\Upsilon)\partial_{\widetilde{\Xi}}\widetilde{W}_0 + \widetilde{W}_0\right]_{\widetilde{\Upsilon}=\widetilde{\Sigma}_0} \\ &+ \varepsilon\widetilde{K}_\Upsilon\widetilde{\Sigma}_\Upsilon\left[\partial_{\widetilde{\Upsilon}\widetilde{\Upsilon}}\widetilde{W}_0 - (\partial_{\widetilde{\Xi}}\widetilde{\Sigma}_0)\partial_{\widetilde{\Upsilon}\widetilde{\Xi}}\widetilde{W}_0\right]_{\widetilde{\Upsilon}=\widetilde{\Sigma}_0} + O(\varepsilon^2). \end{aligned} \tag{7.88}$$

In the last step, the prior expression was Taylor-expanded about $\widetilde{\Sigma}_0$ to determine the value at the corrected surface $\widetilde{\Sigma}$, to order $O(\varepsilon)$.

Hence the surface boundary conditions on $\widetilde{W}_0$ and $\widetilde{W}_\Upsilon$ are

$$\left[\partial_{\widetilde{\Upsilon}}\widetilde{W}_0 - (\partial_{\widetilde{\Xi}}\widetilde{\Sigma}_0)\partial_{\widetilde{\Xi}}\widetilde{W}_0\right]_{\widetilde{\Upsilon}=\widetilde{\Sigma}_0} = 0, \tag{7.89a}$$

$$\begin{aligned} &\left[\partial_{\widetilde{\Upsilon}}\widetilde{W}_\Upsilon - (\partial_{\widetilde{\Xi}}\widetilde{\Sigma}_0)\partial_{\widetilde{\Xi}}\widetilde{W}_\Upsilon\right]_{\widetilde{\Upsilon}=\widetilde{\Sigma}_0} = \left[-\widetilde{\Sigma}_\Upsilon\partial_{\widetilde{\Upsilon}\widetilde{\Upsilon}}\widetilde{W}_0 + \right. \\ &\left.\widetilde{\Sigma}_\Upsilon(\partial_{\widetilde{\Xi}}\widetilde{\Sigma}_0)\partial_{\widetilde{\Upsilon}\widetilde{\Xi}}\widetilde{W}_0 + (\partial_{\widetilde{\Xi}}\widetilde{\Sigma}_\Upsilon)\partial_{\widetilde{\Xi}}\widetilde{W}_0 - \widetilde{W}_0\right]_{\widetilde{\Upsilon}=\widetilde{\Sigma}_0}. \end{aligned} \tag{7.89b}$$

$\widetilde{W}_0$ and $\widetilde{W}_\Upsilon$ now have well-defined Poisson equations on the unperturbed domain with surface $\widetilde{\Sigma}_0$. Thus each need be computed only a single time for a given α and θ; once $\widetilde{W}_0$ and $\widetilde{W}_\Upsilon$ are computed, they can be multiplied by the local values of H and $\partial_S P$ to recover W.

Plots of the uncorrected streamwise velocity, $\widetilde{W}_0$, and the first order correction, $\widetilde{W}_\Upsilon$, are shown in Figure 7.6 (a) and (b), respectively, for an example domain with $\alpha = 45°$ and $\theta = 15°$. Since the correction is everywhere positive, a positive curvature enhances the flux and a negative curvature depresses it, for the given geometry parameters. Note also that while $\widetilde{W}_0$ has maximum value (maximum streamwise flow velocity) at the fluid surface, the correction has a maximum within the fluid. Thus, the point of maximum flow is shifted towards the outside of curves, rather than

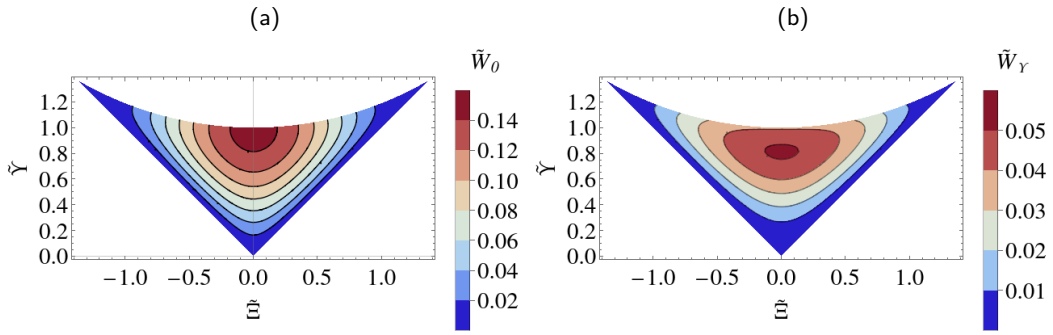

Figure 7.6: Contour plots of streamwise velocity in a slender V-groove with groove half angle $\alpha = 45°$ and fluid contact angle $\theta = 15°$. Results are shown in static variables, $\widetilde{W}_0$ and $\widetilde{W}_\Upsilon$, in which fluid midline thickness and negative pressure gradient are normalized to 1.
(a) Streamwise velocity, $\widetilde{W}_0$, in a straight ($K_\Upsilon = K_\Xi = 0$), torsion-free ($\mathcal{J} = 0$) V-groove, computed according to Equation (7.86a).
(b) $O(\varepsilon K_\Upsilon)$ streamwise velocity correction, $\widetilde{W}_1$, due to nonzero vertical curvature K_Υ in a V-groove with no lateral curvature ($K_\Xi = 0$) and no torsion ($\mathcal{J} = 0$), computed according to Equation (7.86b). Note that the color scales differ between (a) and (b).

towards the inside, as in closed pipes (Chadwick, 1985; Wang, 2012). This is a byproduct of the asymmetry of the V-groove cross-sectional domain and of the free surface. Specifically, it is the $-\widetilde{W}_0$ term which dominates the interface boundary condition [Equation (7.89b)] and forces $\widetilde{W}_\Upsilon$ to have an interior maximum. Closed pipes have no such boundary condition, and furthermore the point of comparison, straight pipes, have centered flow, unlike straight V-grooves.

7.2.12 Integrated flux

To determine the flux, the velocity is integrated over the cross-sectional domain, yielding

$$\begin{aligned} Q = \frac{q}{w_c d^2} &= \frac{1}{w_c d^2}\int_\Omega \hat{u}\cdot\hat{\nu}\, d\xi d\upsilon = H^2 \int_{\widetilde{\Omega}} W\, d\widetilde{\Xi} d\widetilde{\Upsilon} \\ &= H^2\left[\int_{\widetilde{\Omega}_0} \left(W_0 + \varepsilon K_\Upsilon W_\Upsilon\right) d\widetilde{\Xi} d\widetilde{\Upsilon} + \int_{\widetilde{\Omega}\setminus\widetilde{\Omega}_0} W_0 d\widetilde{\Xi} d\widetilde{\Upsilon}\right]. \end{aligned} \tag{7.90}$$

Here Ω denotes the domain in the cross-sectional Ξ-Υ plane, $\widetilde{\Omega}$ is the domain under the static coordinates $\widetilde{\Xi} = \Xi/H$, $\widetilde{\Upsilon} = \Upsilon/H$, and $\widetilde{\Omega}_0$ is the static domain bounded by the $O(1)$ circular surface. In the final expression then, the first term is the order 1 term, the second term is the $O(\varepsilon)$ correction due to integrating W over the domain with the $O(\varepsilon)$ correction to the surface,

and the final term is the $O(\varepsilon)$ term due to the existence of W_Υ. Continuing where we left off,

$$\begin{aligned} Q &= H^4(-\partial_S P)\left[\int_{\widetilde{\Omega}_0} \widetilde{W}_0 d\widetilde{\Xi} d\widetilde{\Upsilon} + \varepsilon K_\Upsilon H \int_{\widetilde{\Omega}_0} \widetilde{W}_\Upsilon d\widetilde{\Xi} d\widetilde{\Upsilon}\right. \\ &\qquad \left. + \varepsilon K_\Upsilon H \int_{-\widetilde{I}_0}^{\widetilde{I}_0} \widetilde{W}_0\left(\widetilde{\Xi}, \widetilde{\Sigma}_\Upsilon(\widetilde{\Xi})\right) \widetilde{\Sigma}_\Upsilon(\widetilde{\Xi}) d\widetilde{\Xi}\right] \qquad (7.91) \\ &= H^4(-\partial_S P)\left(\Gamma_0 + \varepsilon K_\Upsilon H \Gamma_\Upsilon\right) \\ &= -\frac{\Gamma_0 \widehat{P}_0}{\mathrm{Ca}} H^4 \left[\frac{\partial_S H}{H^2} - \varepsilon\left(\frac{\widehat{P}_\Upsilon}{\widehat{P}_0}\partial_S K_\Upsilon - \frac{\Gamma_\Upsilon}{\Gamma_0}\frac{\partial_S H}{H} K_\Upsilon\right)\right]. \qquad (7.92) \end{aligned}$$

Two geometric factors have been introduced here:

$$\Gamma_0 = \int_{\widetilde{\Omega}_0} \widetilde{W}_0 d\widetilde{\Xi} d\widetilde{\Upsilon}, \qquad (7.93)$$

$$\Gamma_\Upsilon = \int_{-\widetilde{I}_0}^{\widetilde{I}_0} \widetilde{W}_0\left(\widetilde{\Xi}, \widetilde{\Sigma}_\Upsilon(\widetilde{\Xi})\right) \widetilde{\Sigma}_\Upsilon(\widetilde{\Xi}) d\widetilde{\Xi} + \int_{\widetilde{\Omega}_0} \widetilde{W}_\Upsilon d\widetilde{\Xi} d\widetilde{\Upsilon}. \qquad (7.94)$$

Γ_0 is the geometric factor Γ as used in Chapters 4 and 5, and, except for a factor due to measuring thickness at the center instead of the edge, equivalent to the Γ of Romero and Yost (1996). [2] Wide grooves (grooves with large half angle α) have larger Γ_0, due to the no-slip walls being farther away from the fluid center. Γ_0 decreases with θ, due to thickness being measured at the fluid midline, so that smaller θ implies a larger cross-sectional area; see Figure 7.7 (c).

The flux has two corrections: the $\widehat{P}_\Upsilon$ term is due to the additional pressure gradient induced by changes in the backbone curvature, and the Γ_Υ term comes from the modification of the flow structure due to the geometry. The Γ_Υ correction itself is made up of two terms, one from integrating W over the additional area due to the $O(\varepsilon)$ modification of the surface, and one from the integral over the entire domain of the additional flow velocity $\widetilde{W}_\Upsilon$. Incidentally, the first of these is very small, only a couple percent the size of the second.

The relative flux correction, Γ_Υ/Γ_0, is plotted in Figure 7.8 (c). It is typically around $O(1)$, and is relatively large and positive in narrow grooves (small α) and decreases to the point of becoming negative in wide grooves (large α). The greater magnitude of Γ_Υ/Γ_0 at small α is a relative effect; rather than Γ_Υ being particularly large there, Γ_0 is particularly small, due to the increased friction between two very close walls. The change in sign occurs as the Poisson equation for the correction, Equation (7.84b), shifts from being dominated by the coordinate correction, $\Upsilon\partial_S P$, to being dominated by the velocity scale factor correction, $\partial_\Upsilon W_0$. For wider and wider grooves (larger and larger α), the streamwise velocity W_0 achieves higher and higher values [reflected in the increase of Γ_0 with α, in Figure 7.7 (c)], and thus $\partial_\Upsilon W_0$ increases in magnitude relative to $\Upsilon\partial_S P$.

[2] The straight-groove flux factor Γ_0 is also related to Ayyaswamy et al.'s (1974) friction factor K_A by the relation $K_\mathrm{A} = 8\widehat{A}_0^3/(\Gamma_0 \widehat{R}_w^2)$, where $\widehat{R}_w = \sqrt{(1+\widehat{R})^2 + \widehat{R}^2 - 2\widehat{R}(1+\widehat{R})\sin(\alpha+\theta)}$ is the diagonal length along the groove wall from corner to interface.

As for the right-hand side of the transport equation [Equation (7.55)],

$$\begin{aligned} A &= \int_{\Omega} (1 - \upsilon k_{\upsilon})\, d\Xi d\Upsilon \\ &= H^2 \int_{\widetilde{\Omega}_0} 1 d\widetilde{\Xi} d\widetilde{\Upsilon} \\ &\quad - \varepsilon K_{\Upsilon} H^3 \left[- \int_{-\widetilde{I}_0}^{\widetilde{I}_0} \widetilde{\Sigma}_{\Upsilon}(\widetilde{\Xi}) d\widetilde{\Xi} + \int_{\widetilde{\Omega}_0} \Upsilon d\widetilde{\Xi} d\widetilde{\Upsilon} \right] + O(\varepsilon^2) \qquad (7.95) \\ &= H^2 \widehat{A}_0 - \varepsilon K_{\Upsilon} H^3 \widehat{A}_{\Upsilon} + O(\varepsilon^2). \qquad (7.96) \end{aligned}$$

Calculating explicitly,

$$\widehat{A}_0 = \frac{\sin\alpha \left\{ \cos\alpha + \cos(\alpha + 2\theta) - [\pi - 2(\theta + \alpha)] \sin\alpha \right\}}{2(\cos\theta - \sin\alpha)^2}, \qquad (7.97)$$

the cross-sectional area of fluid in a straight V-groove, shown in Figure 7.7 (a), and

$$\begin{aligned} \widehat{A}_{\Upsilon} =& \frac{\sin\alpha \left\{ 8\cos^2(\alpha)\cos^3(\theta + \alpha) + \sin\alpha \left[8\cos(\theta + \alpha)\sin\alpha + \sin\theta \right] \right\}}{12(\cos\theta - \sin\alpha)^3} \\ &+ \frac{\sin^2\alpha \sin(4\alpha + 3\theta)}{12(\cos\theta - \sin\alpha)^3} + \frac{\sin^2\alpha\cos\theta \left[-6\pi + 12(\theta + \alpha) + 4\sin(2\theta + 2\alpha) \right]}{12(\cos\theta - \sin\alpha)^3} \\ &- \frac{\sec(\theta + \alpha)\sin^3(\alpha) \left\{ [\pi - 2(\theta + \alpha)]^2 - 4 - 4\cos(2\theta + 2\alpha) \right\}}{4(\cos\theta - \sin\alpha)^3} \\ &- \frac{\sec(\theta + \alpha)\sin^3(\alpha)[\pi - 2(\theta + \alpha)]\sin(2\theta + 2\alpha)}{4(\cos\theta - \sin\alpha)^3} \\ &- \frac{[\pi - 2(\theta + \alpha) - 2\cos(\theta + \alpha)]\sec(\theta + \alpha)\sin^3(\alpha)}{4(\cos\theta - \sin\alpha)^4} \\ &\times \left\{ [\pi - 2(\theta + \alpha)]\sin\alpha - \cos\alpha - \cos(\alpha + 2\theta) \right\} \left[1 - \sin(\theta + \alpha) \right]. \qquad (7.98) \end{aligned}$$

Like Γ_{Υ}, $\widehat{A}_{\Upsilon}$ is composed of two factors: the additional area due to the modified surface and the additional volume element due to the backbone curvature. Again, the former is only a few percent the magnitude of the latter. Thus, the main effects of the backbone curvature come from the curvilinear modifications to the governing Navier-Stokes equations and the additional volume element; not from the slight deviation of the surface from circular. The relative volume element correction, $\widehat{A}_{\Upsilon}/\widehat{A}_0$, is plotted in Figure 7.8 (a). It changes very little across geometries, remaining between approximately 0.65 and 0.9. The extra volume in the volume element is concentrated at large Υ. Thus, the additional volume which can be created is maximized when the cross-sectional domain extends as high above $\Upsilon = 1$ as possible; this occurs when the contact angle θ is small, in which case two "horns" of the domain extend up the sidewalls of the groove. Hence, $\widehat{A}_{\Upsilon}/\widehat{A}_0$ is larger when the contact angle θ is smaller, as seen in Figure 7.8 (a).

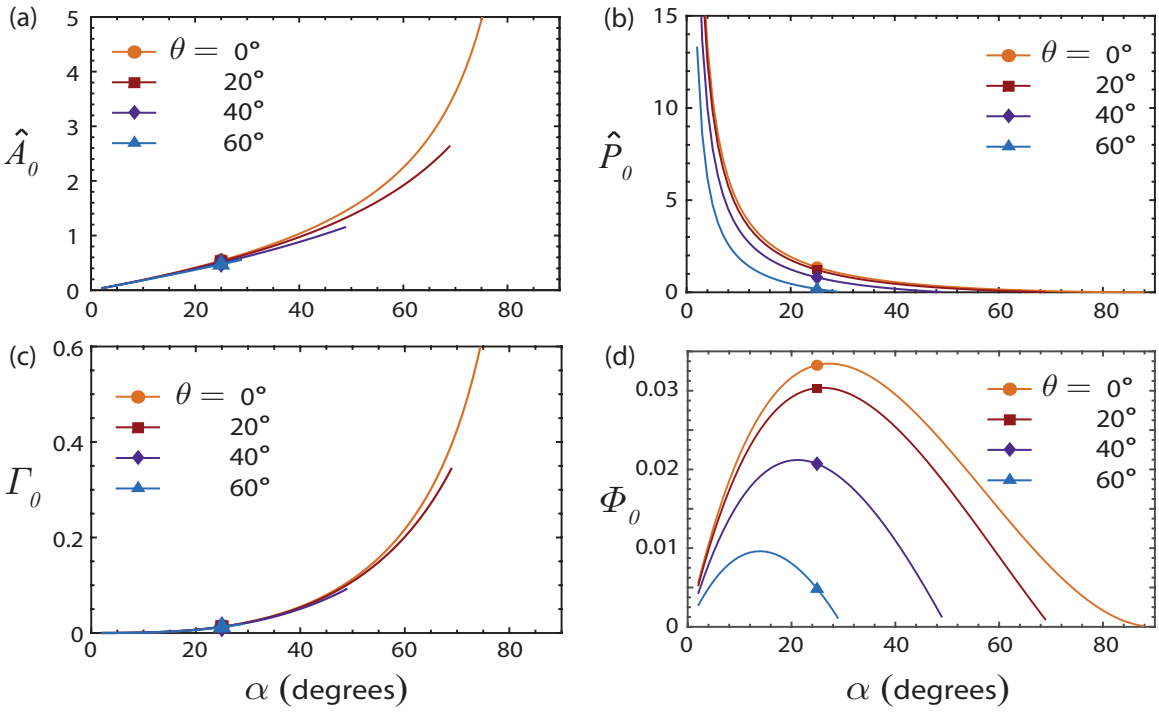

Figure 7.7: Geometric functions pertinent to capillary flow of a Newtonian liquid film with constant contact angle θ in a straight V-groove with no torsion or curvature, with groove half angle α satisfying the Concus-Finn condition $\theta + \alpha < \pi/2$.
(a) $\widehat{A}_0(\theta, \alpha)$, defined by Equation (7.97)
(b) $\widehat{P}_0(\theta, \alpha)$, defined by Equation (7.79)
(c) $\Gamma_0(\theta, \alpha)$, defined by Equation (7.93)
(d) $\Phi_0(\theta, \alpha) = \Gamma_0(\alpha, \theta)\widehat{P}_0(\alpha, \theta)/\widehat{A}_0(\alpha, \theta)$. Note that according to the nondimensionalization scheme of this work, $\mathrm{Ca} = \Phi_0$.
These geometric functions were plotted earlier in Chapter 4, Figure 4.4, and are included again for convenience. Note that because the system satisfies the Concus-Finn condition, data at higher θ is cut off earlier at $\alpha = \pi/2 - \theta$.

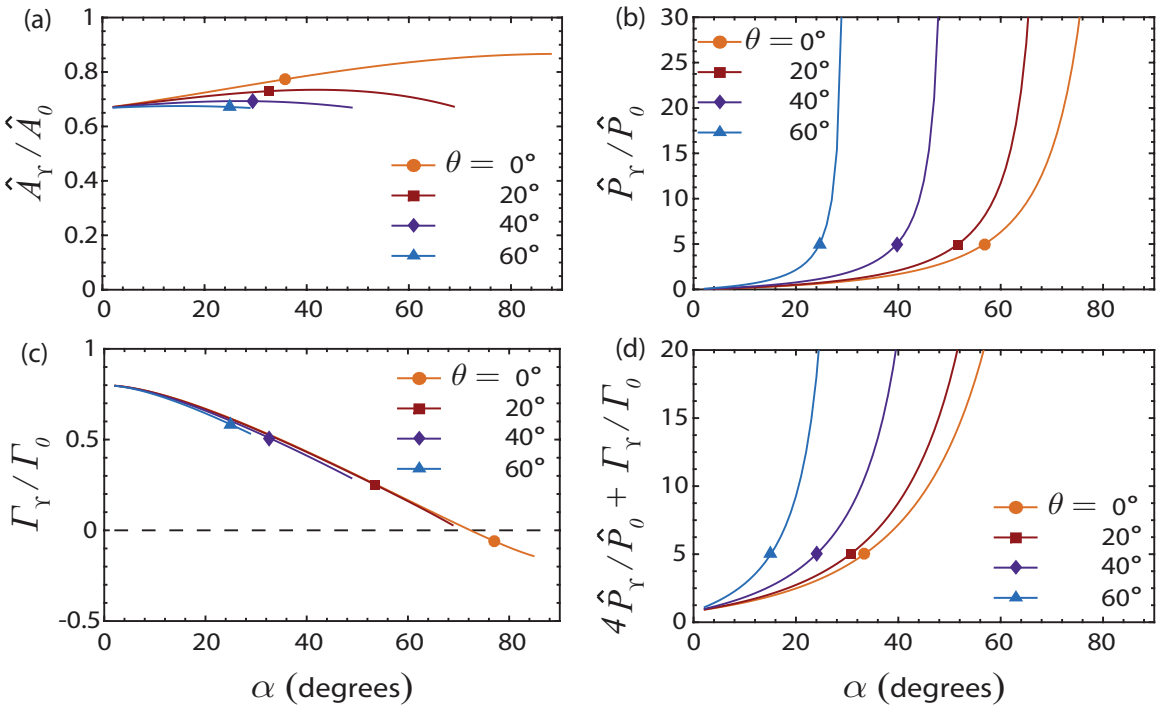

Figure 7.8: Geometric functions pertinent to the capillary flow of a Newtonian liquid film with constant contact angle θ in a slender curved-backbone V-groove with groove half angle α satisfying the Concus-Finn condition $\theta + \alpha < \pi/2$.
(a) $\widehat{A}_\Upsilon(\theta, \alpha)/\widehat{A}_0(\theta, \alpha)$, the relative correction to the cross-sectional area due to backbone curvature. Defined by Equations (7.97) and (7.98).
(b) $\widehat{P}_\Upsilon(\theta, \alpha)/\widehat{P}_0(\theta, \alpha)$, the relative pressure correction due to backbone curvature. Defined by Equations (7.76) and (7.79).
(c) $\Gamma_\Upsilon(\theta, \alpha)/\Gamma_0(\theta, \alpha)$, the relative correction to the flux factor due to backbone curvature. Defined by Equations (7.93) and (7.94).
(d) $4\widehat{P}_\Upsilon(\theta, \alpha)/\widehat{P}_0(\theta, \alpha) + \Gamma_\Upsilon(\theta, \alpha)/\Gamma_0(\theta, \alpha)$, a quantity arising in the correction to overall streamwise flux with fixed Dirichlet pressure boundary conditions, Equation (7.114).

7.2.13 Final reduced equation

Putting all the pieces together,

$$\begin{aligned}
&\frac{\partial a}{\partial t} = -\frac{\partial q}{\partial s} \\
&\implies \frac{d^2}{t_c}\frac{\partial A}{\partial T} = -\frac{w_c d^2}{L}\frac{\partial Q}{\partial S} \\
&\implies \frac{L}{t_c w_c}\frac{\partial}{\partial T}\left(H^2\widehat{A}_0 - \varepsilon K_\Upsilon H^3 \widehat{A}_\Upsilon\right) = \frac{\Gamma_0 \widehat{P}_0}{\mathrm{Ca}} \\
&\times \partial_S\left\{H^4\left[\frac{\partial_S H}{H^2} - \varepsilon\left(\frac{\widehat{P}_\Upsilon}{\widehat{P}_0}\partial_S K_\Upsilon - \frac{\Gamma_\Upsilon}{\Gamma_0}\frac{\partial_S H}{H}K_\Upsilon\right)\right]\right\}.
\end{aligned} \tag{7.99}$$

It is then natural to set the timescale to $t_c = L/w_c = \mu L/(\varepsilon\gamma\mathrm{Ca})$, substituting $w_c = \varepsilon\gamma\mathrm{Ca}/\mu = \varepsilon\gamma\Phi_0/\mu$, where

$$\mathrm{Ca} = \Phi_0(\alpha,\theta) = \frac{\Gamma_0(\alpha,\theta)\widehat{P}_0(\alpha,\theta)}{\widehat{A}_0(\alpha,\theta)}. \tag{7.100}$$

Note that the capillary number, Ca, which measures the ratio between fluid velocity and capillary speed, is reduced to a purely geometric function of the groove half angle, α, and the contact angle θ, due to the velocity being set by viscous-capillary effects alone. This Φ_0 is the same as the Φ of Chapter 4 and introduced by Romero and Yost (1996) (with the difference that Romero and Yost measured fluid thickness at the wall, not at the midline). It is plotted in Figure 7.7 (d).

The equation of motion is then reduced to

$$\frac{\partial}{\partial T}\left(H^2 - \varepsilon K_\Upsilon H^3\frac{\widehat{A}_\Upsilon}{\widehat{A}_0}\right) = \partial_S\left[H^2\partial_S H - \varepsilon\left(\frac{\widehat{P}_\Upsilon}{\widehat{P}_0}H^4\partial_S K_\Upsilon - \frac{\Gamma_\Upsilon}{\Gamma_0}K_\Upsilon H^3\partial_S H\right)\right] + O(\varepsilon^2). \tag{7.101}$$

This final equation is valid to $O(\varepsilon^2, \varepsilon\mathrm{Re}\Gamma_0)$, and was derived rigorously within the framework of slender perturbation theory. The $O(\varepsilon)$ corrections to the straight V-groove equation have been collected into three terms.

First, the $\widehat{A}_\Upsilon/\widehat{A}_0$ term represents the change in the volume element due to backbone curvature. As seen in Figure 7.8 (a), $\widehat{A}_\Upsilon/\widehat{A}_0$ is positive and $O(1)$. Thus the local volume element is smaller when backbone curvature is positive ($K_\Upsilon > 0$) and larger when it is negative $K_\Upsilon < 0$. Conversely, this means that, for a given flux divergence, the fluid film thickness H is affected more in V-grooves with positive curvature and less in those with negative curvature.

The next $O(\varepsilon)$ correction, the $\widehat{P}_\Upsilon/\widehat{P}_0$ term in the flux on the right-hand side of Equation (7.101), is relevant only when the backbone curvature is non-constant. It describes how the connection between backbone curvature and fluid pressure affects the flux. Recall from the pressure-thickness relation, Equation (7.78), that holding the fluid thickness H fixed, a section of a

groove with positive curvature ($K_\Upsilon > 0$) will have lower pressure than one with negative curvature ($K_\Upsilon < 0$). Therefore, a positive gradient in curvature ($\partial_S K_\Upsilon > 0$) induces a negative gradient in pressure ($\partial_S P < 0$), and thus a positive contribution to the flux, Q. Comparing $\widehat{P}_\Upsilon/\widehat{P}_0$ to the other geometric quantities $\widehat{A}_\Upsilon/\widehat{A}_0$ and Γ_Υ/Γ_0 in Figure 7.8, it is immediately clear that this correction has the greatest magnitude for wide grooves; in particular, for grooves with $\alpha \gtrsim 27°$. Thus, this term is often the most important correction for grooves with non-constant curvature.

The last correction is the Γ_Υ/Γ_0 term in the flux on the right-hand side of Equation (7.101). This term combines the effects of the modified interface shape and the curvilinear coordinates on the flux Poisson equation. Note from Figure 7.8 (c) that Γ_Υ/Γ_0 is typically $O(0.1)$ to $O(1)$, and is positive for most grooves but changes sign and becomes negative for very wide grooves ($\alpha \gtrsim 72°$). Thus, for narrow grooves, positive backbone curvature enhances flux for a given H and $\partial_S H$, while negative curvature suppresses it. For wide grooves, this is reversed (keep in mind that this result is predicated on fixed H and $\partial_S H$, and does not describe nonlocal comparisons or pressure boundary conditions).

In the case of constant curvature K_Υ, the system follows the rule that pressure is high when H is high and pressure is low when H is low, so that fluid will flow from high H to low H. When K_Υ varies in S, however, pressure is not necessarily monotonic in fluid thickness.

Unlike $\mathrm{Re} = 0$ flow in circular, rectangular, or elliptical pipes with constant curvature (Chadwick, 1985; Wang, 2012), the flux correction (Γ_Υ/Γ_0 term) arises in the V-groove at $O(\varepsilon)$ and thus scales linearly with the curvature. This occurs because of the asymmetry of the V-groove cross section (as noted earlier, corrections due to torsion or lateral curvature, K_Ξ, arise at second order due to the lateral symmetry of the groove). Furthermore, the pressure correction arising in the V-groove, $\widehat{P}_\Upsilon/\widehat{P}_0$, is entirely absent from closed-pipe analyses because there is no free surface to affect capillary pressure.

Comparison to thin film equation

The curvature corrections arising in Equation (7.101) are qualitatively similar to those in the equation for a thin film coating a curved substrate, first developed by Roy et al. (2002). Because the capillary pressure arises rather differently in the two cases (as the thin film equation has no bounding V-groove walls restricting its interface shape), it is easiest to compare the equations of motion without substituting in the capillary pressure. For the curved V-groove, Equation (7.101) in terms of a general pressure is

$$\frac{\partial}{\partial T}\left(H^2 - \varepsilon K_\Upsilon H^3 \frac{\widehat{A}_\Upsilon}{\widehat{A}_0}\right) = (const.) \times \partial_S \left\{H^4 \left[1 + \varepsilon H \left(\frac{\Gamma_\Upsilon}{\Gamma_0} K_\Upsilon\right)\right] \partial_S P\right\} + O(\varepsilon^2), \quad (7.102)$$

with capillary pressure being

$$P = -\frac{1}{\mathrm{Ca}}\left(\frac{\widehat{P}_0}{H} + \varepsilon \widetilde{K}_\Upsilon \widehat{P}_\Upsilon\right) + O(\varepsilon^2). \quad (7.103)$$

Roy et al.'s (2002) equation of motion for a thin film on a curved substrate (in the form developed in Chapter 8) can be expressed as

$$\frac{\partial}{\partial T}\left(H - \varepsilon K_m H^2\right) = \nabla_\alpha \left\{ \frac{H^3}{3}\left[\widetilde{g}^{\alpha\beta} + \varepsilon H\left(\frac{1}{2}\mathrm{I\!I}^{\alpha\beta} - 2K_m\widetilde{g}^{\alpha\beta}\right)\right]\nabla_\beta P \right\} + O(\varepsilon^2), \quad (7.104)$$

with capillary pressure

$$P = -\frac{1}{\mathrm{Ca}}\left\{2K_m + \varepsilon\left[\nabla_\alpha\nabla^\alpha H + H\left(4{K_m}^2 - 2K_G\right)\right]\right\} + O(\varepsilon^2), \quad (7.105)$$

where H is the fluid thickness normal to the substrate, $\widetilde{g}^{\alpha\beta}$ is the substrate metric tensor, K_m is the substrate mean curvature, K_G is the substrate Gaussian curvature, $\mathrm{I\!I}^{\alpha\beta}$ is the substrate shape tensor (second fundamental form), and ∇ represents the covariant derivative.

In both equations, the time derivative of a volume element is balanced by the divergence of a flux driven by a pressure gradient. The curvature induces a negative correction to the volume element, although the thin film equation lacks the additional contribution due to change in interface shape that arises in the curved V-groove.

Looking at the right-hand side of each equation, in each case the curvature induces a correction to the flux in the form of a multiplier on the pressure gradient, arising from the modified flux integral. In the case of the V-groove, this integral is computed in a confined 2-D cross-section and has contributions both from the modified Poisson equation and from the modified interface shape. In the case of the thin film on the curved substrate, the integral is computed in 1-D but includes cross flow in two-dimensions, making the correction a two dimensional tensor instead of a scalar. In both the curved V-groove and the thin film on a curved substrate, this flux correction can be positive or negative depending on various parameters.

Both equations have a complicated capillary pressure correction which includes a term proportional to the negative mean curvature of the groove or substrate [the $-\varepsilon K_\Upsilon \widehat{P}_\Upsilon$ term in Equation (7.103) and the $-2K_m$ term in Equation (7.105)]. This results in the general rule of thumb that, for a given pressure, fluid in a positively curved V-groove or on a substrate with positive mean curvature will be thicker, and fluid in a negatively curved V-groove or on a substrate with negative mean curvature will be thinner.

Despite this rule of thumb, the differences between the pressure expressions in the two systems lead to substantial differences in behavior. The V-groove pressure is dominated by the effect of the groove walls, inducing the H^{-1} term, while the groove curvature is an $O(\varepsilon)$ correction. Thus, the thinning or thickening effect is tempered by the $O(1)$ pressure term. In particular, groove curvature cannot cause the fluid to thin to the point of breaking, because H^{-1} diverges as $H \to 0$. But in the thin film, substrate curvature is the $O(1)$ effect and the fluid interface thickness variation is the $O(\varepsilon)$ correction. The substrate curvature is thus the dominant effect, and the fluid can become arbitrarily thin in regions of negative mean curvature.

7.3 Results

7.3.1 Steady state solutions

Recall from Chapter 4 that the steady-state solution in a straight V-groove with boundary conditions $H(S_A) = H_A$, $H(S_B) = H_B$, is given by

$$H_{\text{straight}}(S) = \left[H_B^3 \frac{S - S_A}{S_B - S_A} + H_A^3 \frac{S_B - S}{S_B - S_A}\right]^{1/3}. \tag{7.106}$$

The expression for the curved V-groove can be expressed in terms of this result:

$$\begin{aligned} H_{\text{steady}}(S) = H_{\text{straight}}(S) + \frac{\varepsilon}{4H_{\text{straight}}^2(S)} \Bigg\{ \\ \left[4\frac{\widehat{P}_\Upsilon}{\widehat{P}_0} + \frac{\Gamma_\Upsilon}{\Gamma_0}\right] \int_{S_A}^{S} \left[H_{\text{straight}}^4(Z) K_\Upsilon'(Z)\right] dZ + \frac{\Gamma_\Upsilon}{\Gamma_0} H_A^4 K_\Upsilon(S_A) + \\ \left(- \left[4\frac{\widehat{P}_\Upsilon}{\widehat{P}_0} + \frac{\Gamma_\Upsilon}{\Gamma_0}\right] \int_{S_A}^{S_B} \left[H_{\text{straight}}^4(Z) K_\Upsilon'(Z)\right] dZ + \frac{\Gamma_\Upsilon}{\Gamma_0} [H_B^4 K_\Upsilon(S_B) - H_A^4 K_\Upsilon(S_A)] \right) \frac{S - S_A}{S_B - S_A} \\ - \frac{\Gamma_\Upsilon}{\Gamma_0} H_{\text{straight}}^4(S) K_\Upsilon(S) \qquad \Bigg\} + O(\varepsilon^2). \end{aligned} \tag{7.107}$$

The computation of the steady state is thus still expressible in closed form, save for the integrals containing the derivative of K_Υ multiplied by H_{steady}^4. Because $\widehat{P}_\Upsilon/\widehat{P}_0 \gg \Gamma_\Upsilon/\Gamma_0$ for most values of α and θ (see Figure 7.8), it is these integrals that typically contribute most to the deviation of H_{steady} from the result for straight grooves when curvature is non-constant. Intuitively, the varying additional pressure due to the groove curvature is more important in setting the interface shape than is the change in flux due to curvature.

In the special case in which the groove curvature is constant, i.e., $K_\Upsilon(S) = K_0$,

$$\begin{aligned} &H_{\text{steady},K_\Upsilon\text{const.}}(S) = \\ &H_{\text{straight}}(S) + \frac{\varepsilon K_0}{4H_{\text{straight}}^2(S)} \frac{\Gamma_\Upsilon}{\Gamma_0} \left\{ \frac{H_A^4(S_B - S) + H_B^4(S - S_A)}{S_B - S_A} - H_{\text{straight}}^4(S) \right\} + O(\varepsilon^2). \end{aligned} \tag{7.108}$$

It is notable that when K_Υ is constant, the steady state interface equation, Equation (7.108), has only the geometric constant Γ_Υ/Γ_0 and lacks $\widehat{A}_\Upsilon/\widehat{A}_0$ and $\widehat{P}_\Upsilon/\widehat{P}_0$. Because Γ_Υ/Γ_0 is often much less than 1 [see Figure 7.8 (c)], it suppresses the correction, and thus the steady state interface shape is very close to that of a straight V-groove with the same boundary conditions in H. Keep in mind, however, that the similarity in film thickness, H, does *not* imply similarity in pressure, P.

Equations (7.107) and (7.108) were written in terms of Dirichlet conditions in H because that form is more compact than writing in terms of pressure, though the latter could be written out by substituting from Equation (7.78). Indeed, for a given local groove geometry and contact angle, Equation (7.78) expresses a one-to-one relationship between fluid thickness, H, and pressure.

Thus, for a fixed geometry, there is no difference between setting Dirichlet thickness boundary conditions and setting Dirichlet pressure boundary conditions. However, the relationship between H and P is determined by the groove angle, α, the contact angle, θ, and the backbone curvature, K_Υ. Therefore, when comparing grooves with differing geometries, specifying an identical boundary condition in H is not the same as specifying an identical boundary condition in P. We present both comparisons.

We first compare steady states in grooves of differing constant curvature, with Dirichlet pressure (P) boundary conditions. Experimentally, one might prepare two reservoirs of known pressures and set a V-groove to span the reservoirs. Representative plots for such a system with $\alpha = 45^\circ$ and $\theta = 15^\circ$ are shown in Figure 7.9, comparing curvature values $\varepsilon K_\Upsilon \in \{-0.2, -0.1, 0, 0.1, 0.2\}$. In each plot, the boundary condition at $S = 0$ is fixed at $P(S = 0) = -15.217$; the boundary condition at $S = 1$ has values of $P(S = 1) \in \{-12.174, -30.434, -152.17\}$ among the three columns of the figure [these values of P were chosen so that $H(S = 0) = 1$ and $H(S = 1) \in \{1.25, 0.5, 0.1\}$ for the straight groove with $K_\Upsilon = 0$]. Plots (a)-(c) display fluid thickness, H, and (d)-(f) display pressure, P.

Looking at Figure 7.9 (a)-(c), it stands out that the grooves with positive backbone curvature (solid orange and red lines) have much thicker fluid (higher H) than the straight groove (black dashed line) and the negative-curvature grooves (solid blue and teal lines). This phenomenon occurs because a positive-curvature groove has a negative pressure contribution due to the backbone; in order to compensate this negative pressure and achieve the fixed pressure boundary condition, the fluid must become thicker so that its cross-sectional radius of curvature is larger. It is indeed a general rule that, for a given pressure, a groove with positive backbone curvature will contain thicker fluid than a straight groove, which in turn will contain thicker fluid than a groove with negative backbone curvature. A similar phenomenon occurs in thin films coating curved substrates, where fluid thickens in regions of negative mean substrate curvature and thins in regions of positive curvature (Roy et al., 2002).

Examining Figure 7.9 (d)-(f), it can be seen in each plot that while the pressure boundary conditions are fixed, the pressure between $S = 0$ and $S = 1$ varies between the grooves of different curvatures. In particular, the pressure in grooves with positive backbone curvature is greater than that in straight grooves, which in turn is greater than that in negative-curvature grooves. In order to maintain the equal boundary conditions, the pressure in positive-curvature grooves has a gentler slope near the high pressure end and a steeper slope near the low pressure end than the straight and negative-curvature grooves. This phenomenon arises not due to the positive-curvature grooves having thicker films, but due to the ratio of the thicknesses at each end, $H(S = 0) : H(S = 1)$, being more extreme. It will further be shown in the next section that, with identical boundary conditions, the flux in grooves with positive backbone curvature is greater than that in grooves with straight or negative backbone curvature.

We next compare steady states in grooves of differing constant curvature with Dirichlet fluid

thickness (H) boundary conditions. Representative plots for such a system with $\alpha = 45^\circ$ and $\theta = 15^\circ$ are shown in Figure 7.10, comparing curvature values $\varepsilon K_\Upsilon \in \{-0.2, -0.1, 0, 0.1, 0.2\}$. In each plot, the boundary condition at $S = 0$ is fixed at $H(S = 0) = 1$ and the boundary condition at $S = 1$ has values of $H(S = 1) \in \{1.25, 0.5, 0.1\}$ among the three columns of the figure (matching the H boundary of the straight $K_\Upsilon = 0$ groove in Figure 7.9). Plots (a)-(c) display fluid thickness, H, (d)-(f) display the difference between the thickness H and the straight-groove thickness $H_{\text{steady},K_\Upsilon\text{const.}}$, and (g)-(i) display pressure, P.

Because curvature is constant, the equation for steady state fluid thickness, Equation (7.108), has no dependence on $\widehat{P}_\Upsilon/\widehat{P}_0$ or $\widehat{A}_\Upsilon/\widehat{A}_0$, only Γ_Υ/Γ_0. There is therefore little difference between the interface shape between different curvatures [as seen by the visually indistinguishable lines in Figure 7.10 (a)-(c)]. To clarify the difference in interface shapes, Figure 7.10 (d)-(f) show the difference between H and the $H_{\text{steady},K_\Upsilon\text{const.}}$ of a straight groove with $K_\Upsilon = 0$. It can be seen that the grooves with positive curvature (solid orange and red lines) have a slightly greater thickness than those of negative curvature (solid blue and teal lines). The pressure, however, differs substantially between each groove, seen in Figure 7.10 (g)-(i). Grooves with negative curvature (solid blue and teal lines) have higher pressure than the straight groove (black dashed line) or grooves with positive curvature (solid orange and read lines), due to the groove curvature changing the surface curvature, and in turn changing the capillary pressure.

With non-constant curvature, the steady state fluid thickness is described by Equation (7.107), and in particular the $\widehat{P}_\Upsilon/\widehat{P}_0$ term comes into play. Figure 7.11 displays steady state results in a sinusoidal groove, described by a space curve $\vec{\beta} = \{0, 0.001\sin(6\pi z), z\}$. This results in curvature $k_\upsilon = -0.036\pi^2\sin(6\pi z)/[1 + 0.000036\pi^2\cos^2(6\pi z)]^{3/2} \approx -0.3553\sin(6\pi z)$ (i.e., k_υ is sinusoidal to within 0.04%), and the groove height is chosen such that $\varepsilon = 0.1$. Nondimensionalizing yields $\varepsilon K_\Upsilon \approx -0.03553\sin(6\pi S) + O(0.01\%)$; this K_Υ is plotted in Figure 7.11 (a). Steady state plots for such a system with $\alpha = 45^\circ$ and $\theta = 15^\circ$ are shown in Figure 7.11 (b)-(g). In each plot, the boundary condition at $S = 0$ is fixed at $H(S = 0) = 1$ and the boundary condition at $S = 1$ has values of $H(S = 1) \in \{1.25, 0.5, 0.1\}$ among the three columns of the figure. The relatively large value of $\widehat{P}_\Upsilon/\widehat{P}_0$ compared to Γ_Υ/Γ_0 yields a much larger correction to the fluid thickness due to the changing curvature. The correction follows K_Υ: the fluid is thinner where K_Υ is negative and thicker where it is positive. And the correction is larger where the film is thicker. Unlike the fluid thickness, the pressure, P, experiences very little variation. Put another way, the fluid thickness undergoes large variations in order to maintain a relatively smooth pressure.

In a study of flow in circular pipes following sinusoidal paths, Murata et al. (1976) found that, at low Reynolds numbers, the flow centerline (the point of maximum streamwise velocity) shifted towards the inside of each curve, creating a shorter streamline than a line following the pipe center, which aligns with findings in closed pipes of constant curvature (Chadwick, 1985; Wang, 2012). A similar result was found by Wang (1980) in a study of viscous sheet flow in a thin

channel bounded by sinusoidal walls and unbounded in the other dimension. Furthermore, in that system, flux is decreased along the curved path and increased in the perpendicular direction. For the V-groove, as noted in Section 7.2.11, the shift in the point of maximum streamwise velocity occurs in the opposite direction, due to the asymmetry of the domain and the free surface boundary condition. Gravity-driven thin film flow down wavy inclined planes at low Reynolds number was investigated by Tougou (1978) for films of thickness comparable to the magnitude of the sinusoidal substrate variations and by Wang (1981a), with film thickness much greater than the substrate variations. In both cases the steady state film thickness is also found to be sinusoidal plus a constant and has a large (up to $\pi/2$) phase offset from the substrate variations, which occurs due to the interaction of the gravitational and capillary terms in the governing equation. For the sinusoidal V-groove, gravity is ignored, and the fluid thickness is a complicated function which is not simply a sum of the straight groove thickness and a sinusoid. However, the result is clearly periodic and, as seen in Figure 7.11, appears in-phase with the groove curvature. A more extensive study demonstrating the existence or lack of a phase offset is a potential avenue for future research.

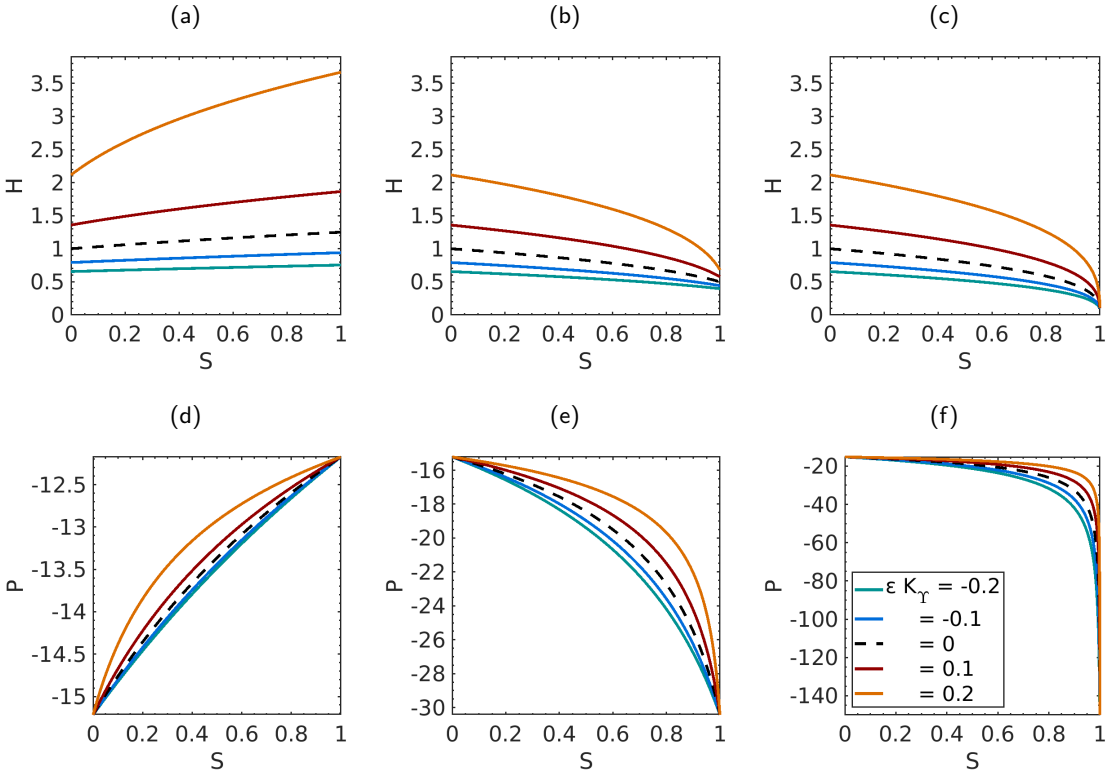

Figure 7.9: Representative steady state solutions of flow in V-grooves of constant curvature with groove half angle $\alpha = 45^\circ$, contact angle $\theta = 15^\circ$, and Dirichlet pressure (P) boundary conditions, according to Equation (7.108). Results are plotted for grooves with 5 different values of vertical curvatures, $\varepsilon K_\Upsilon \in \{-0.2, -0.1, 0, 0.1, 0.2\}$. In each plot, the horizontal axis is S, the nondimensional backbone arc length.
Plots (a)-(c) (top row) display nondimensional fluid midline thickness, H. Plots (d)-(f) (bottom row) display nondimensional pressure, P.
Each column displays a different boundary condition: column 1, (a) and (d), has boundary conditions $P(S = 0) = -15.217$ and $P(S = 1) = -12.174$; column 2, (b) and (e), has boundary conditions $P(S = 0) = -15.217$ and $P(S = 1) = -30.434$; column 3, (c) and (f), has boundary conditions $P(S = 0) = -15.217$ and $P(S = 1) = -152.17$. These values of P were chosen so that the straight groove (with $K_\Upsilon = 0$) would have film midline thickness $H(S = 0) = 1$ and $H(S = 1) \in \{1.25, 0.5, 0.1\}$.

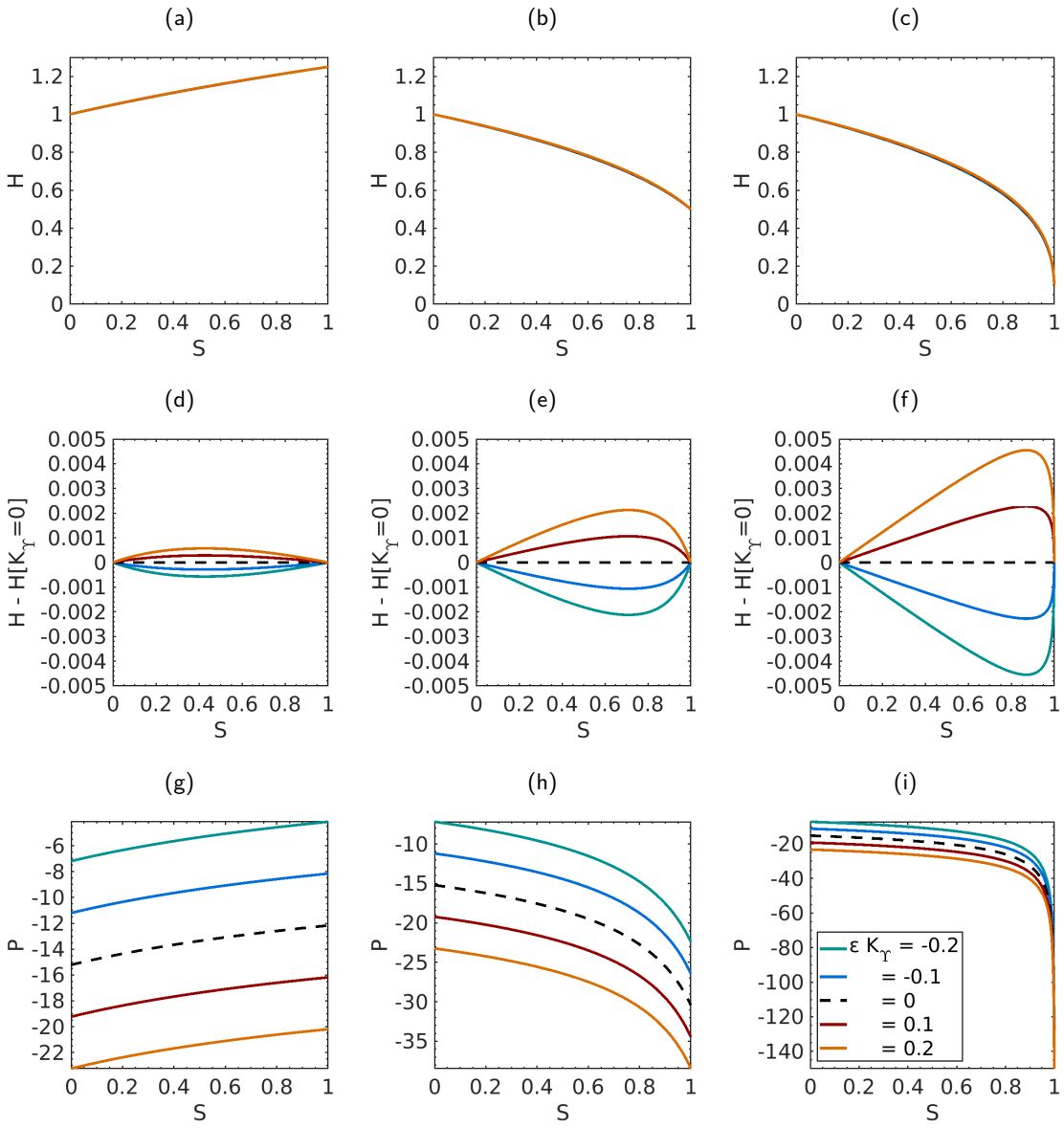

Figure 7.10: Representative steady state solutions of flow in V-grooves of constant curvature with groove half angle $\alpha = 45°$, contact angle $\theta = 15°$, and Dirichlet film thickness (H) boundary conditions, according to Equation (7.108). Results are plotted for grooves with 5 different values of vertical curvatures, $\varepsilon K_\Upsilon \in \{-0.2, -0.1, 0, 0.1, 0.2\}$. In each plot, the horizontal axis is S, the nondimensional backbone arc length.

Plots (a)-(c) (top row) display nondimensional fluid midline thickness, H. Plots (d)-(f) (middle row) display the difference between nondimensional fluid midline thickness, H, and that of a straight V-groove, $H[K_\Upsilon = 0]$. Plots (g)-(i) (bottom row) display nondimensional pressure, P. Each column displays a different boundary condition: column 1 [(a), (d), (g)] has boundary conditions $H(S = 0) = 1$ and $H(S = 1) = 1.25$; column 2 [(b), (e), (h)], has boundary conditions $H(S = 0) = 1$ and $H(S = 1) = 0.5$; column 3 [(c), (f), (i)] has boundary conditions $H(S = 0) = 1$ and $H(S = 1) = 0.1$.

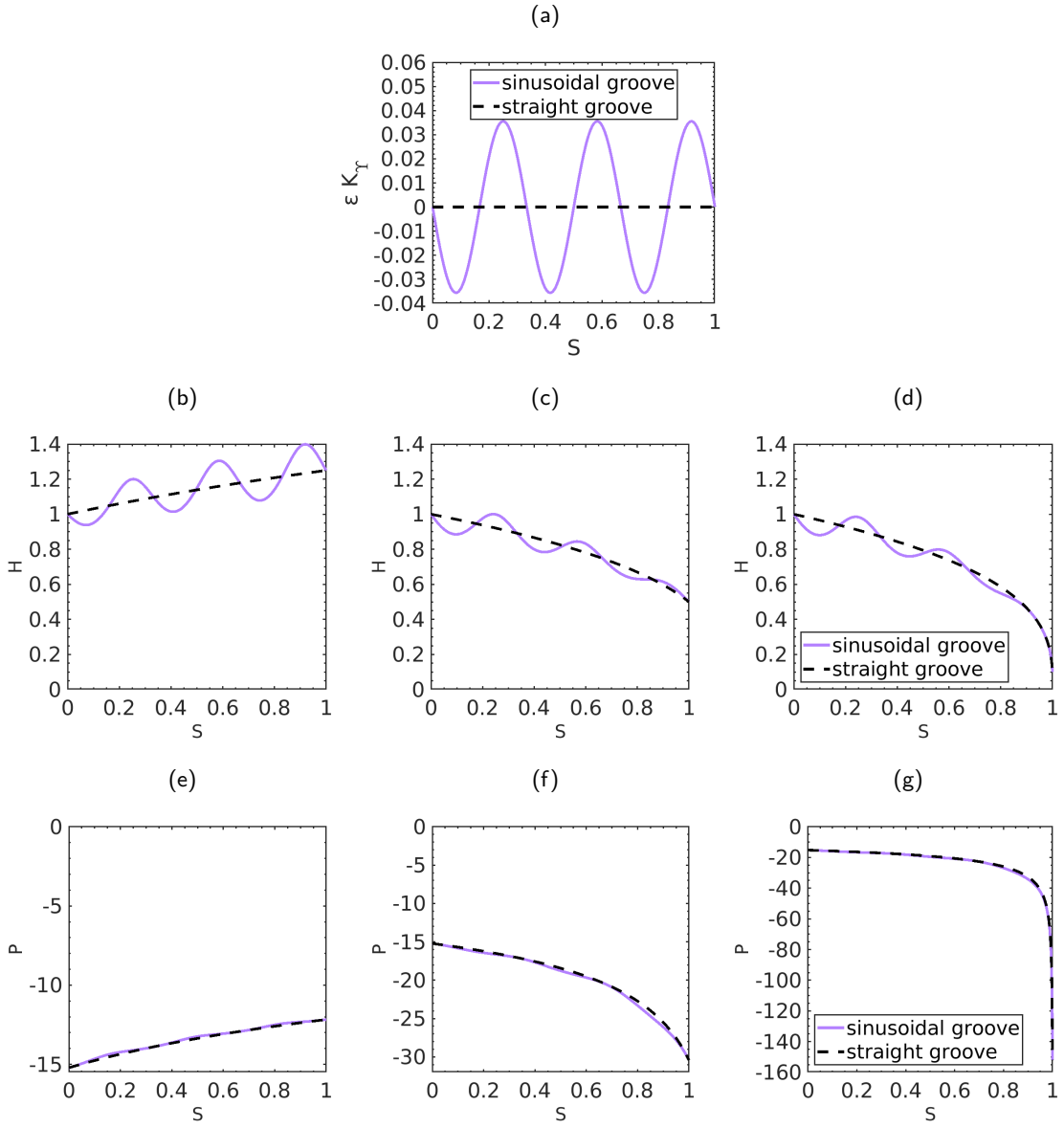

Figure 7.11: Example steady state solution of flow in a V-groove with vertical sinusoidal variation, with groove half angle $\alpha = 45°$, contact angle $\theta = 15°$, and Dirichlet midline thickness (H) boundary conditions, computed by solving Equation (7.101) without time dependence. The groove backbone coordinates are given by $\vec{\beta} = \{0, 0.001\sin(6\pi z), z\}$. Film inlet thickness is chosen such that $\varepsilon = 0.1$, resulting in nondimensional curvature $\varepsilon K_\Upsilon = -0.03553\sin(6\pi S) + O(0.01\%)$, where S is the nondimensional backbone arc length coordinate. Straight ($K_\Upsilon = 0$) V-groove results are also plotted, for comparison.
(a): Nondimensional vertical curvature εK_Υ.
(b)-(d): Nondimensional fluid midline thickness, H. (e)-(g): Nondimensional pressure, P.
Each column displays a different boundary condition: column 1, (b) and (e), has boundary conditions $H(S = 0) = 1$ and $H(S = 1) = 1.25$; column 2, (c) and (f), has boundary conditions $H(S = 0) = 1$ and $H(S = 1) = 0.5$; column 3, (d) and (g), has boundary conditions $H(S = 0) = 1$ and $H(S = 1) = 0.1$.

7.3.2 Steady state flux

One important question which may now be answered is: given pressure boundary conditions $P(S_A) = P_A$ and $P(S_B) = P_B$, what is the steady state flux, and how does it differ from that of a straight groove?

$$Q_0 + \varepsilon Q_1 = H^4 \left(-\partial_S P_0 - \varepsilon \partial_S P_1\right)\left(\Gamma_0 + \varepsilon K_\Upsilon H \Gamma_\Upsilon\right)$$

$$\implies Q_0 = -\left(\frac{\Gamma_0 \widehat{P}_0^4}{\mathrm{Ca}^4}\right)\frac{P_0'(S)}{[P_0(S)]^4}, \tag{7.109a}$$

$$\frac{Q_1}{Q_0} = -4\frac{P_1(S)}{P_0(S)} - \frac{\Gamma_\Upsilon \widehat{P}_0 + 4\Gamma_0 \widehat{P}_\Upsilon}{\mathrm{Ca}\Gamma_0}\,\frac{K_\Upsilon(S)}{P_0(S)} + \frac{P_1'(S)}{P_0'(S)}. \tag{7.109b}$$

Solving for P_0 yields

$$P_0 = \left(\frac{\Gamma_0 \widehat{P_0}^4}{3\mathrm{Ca}^4}\right)^{1/3}(Q_0 S - C_4)^{-1/3}$$

$$= \left(\frac{P_A^{-3}(S_B - S) + P_B^{-3}(S - S_A)}{S_B - S_A}\right)^{-1/3} \tag{7.110}$$

$$\implies Q_0 = \left(\frac{\Gamma_0 \widehat{P_0}^4}{3\mathrm{Ca}^4}\right)\frac{P_B^{-3} - P_A^{-3}}{S_B - S_A} \tag{7.111}$$

$$C_4 = \left(\frac{\Gamma_0 \widehat{P_0}^4}{3\mathrm{Ca}^4}\right)\frac{P_B^{-3} S_A - P_A^{-3} S_B}{S_B - S_A}. \tag{7.112}$$

Then we must solve for P_1, with $P_1(S_A) = P_1(S_B) = 0$, yielding

$$P_1 = -\frac{Q_1}{3Q_0}P_0(S)\left(1 - \left[\frac{P_0(S)}{P_A}\right]^3\right)$$

$$-\frac{\left[\Gamma_\Upsilon \widehat{P}_0 + 4\Gamma_0 \widehat{P}_\Upsilon\right]}{\mathrm{Ca}\Gamma_0} Q_0 \left(\frac{\mathrm{Ca}^4}{\Gamma_0 \widehat{P_0}^4}\right) P_0^4(S) \int_{S_A}^{S} \frac{K_\Upsilon(S)}{P(S)} dS. \tag{7.113}$$

Because $P_1(S_B) = 0$, Q_1 can be solved for, yielding

$$Q_1 = \frac{3Q_0^2 \mathrm{Ca}^3\left[\Gamma_\Upsilon \widehat{P}_0 + 4\Gamma_0 \widehat{P}_\Upsilon\right]}{\Gamma_0^2 \widehat{P}_0^4\left(P_B^{-3} - P_A^{-3}\right)} \int_{S_A}^{S_B} \frac{K_\Upsilon(S)}{-P(S)} dS$$

$$= \frac{\widehat{P}_0^5 \Gamma_0}{3\mathrm{Ca}^5}\left[4\frac{\widehat{P}_\Upsilon}{\widehat{P}_0} + \frac{\Gamma_\Upsilon}{\Gamma_0}\right]\frac{\left(P_B^{-3} - P_A^{-3}\right)}{S_B - S_A}\frac{\int_{S_A}^{S_B} \frac{K_\Upsilon(S)}{-P(S)} dS}{S_B - S_A}. \tag{7.114}$$

Because $\left[4\widehat{P}_\Upsilon/\widehat{P}_0 + \Gamma_\Upsilon/\Gamma_0\right] > 0$ [see Figure 7.8 (d)], $\mathrm{sgn}(P_B^{-3} - P_A^{-3}) = \mathrm{sgn}(Q_0)$, and $P(S) < 0$, then $K_\Upsilon > 0$ enhances flux (i.e., $Q_1 > 0$) and $K_\Upsilon < 0$ suppresses it. Note that in the integral of $K_\Upsilon/(-P)$, $(-P) > 0$.

For all but very narrow grooves (for approximately $\alpha \gtrsim 11^\circ$), the P_Υ/P_0 term dominates Γ_Υ/Γ_0 (visible in Figure 7.8). In this regime, the main effect of the curved backbone is to add a pressure

contribution to the fluid. Thus, to achieve a given pressure, the local fluid thickness must be greater than in a straight groove to counterbalance positive backbone curvature ($K_\Upsilon > 0$), and it must be smaller to counterbalance negative backbone curvature ($K_\Upsilon < 0$). With greater fluid thickness comes a greater flux due to the decreased effect of wall friction (which appeared in the derivation as the no-slip condition). Therefore, the flux-enhancing effect of positive curvature and flux-depressing effect of negative curvature is caused by the thicker and thinner local fluid, respectively. This thickening in regions of positive curvature and thinning in regions of negative curvature is consistent with the same effect in thin films on smoothly curved substrates (Roy et al., 2002). In very narrow grooves, $\Gamma_\Upsilon/\Gamma_0 > 4P_\Upsilon/P_0$. In this regime, the flux enhancement occurs due to the flow structure itself. The relatively fast fluid moving tangent to the free surface is directed into the bulk when curvature is positive, enhancing the flux. Similarly, for negative backbone curvature, the bulk flow feeds the surface flow, slowing it relatively.

Comparing a straight backbone to a curved backbone comes with a choice of how to compare arc length: should it be measured at the base of the groove or at the top? For example, if a groove has positive curvature and a given arc length $S_{\text{tot}} = S_B - S_A$ at its base, then the arc length of the fluid surface is less than S_{tot}. The average distance fluid must traverse to get from one end of the groove to the other is also less than S_{tot}, and the average pressure gradient has greater magnitude than in a straight groove of length S_{tot} with the same boundary conditions. It turns out that this effect is sufficiently small that the flux-enhancing property of positive curvature and flux-depressing property of negative curvature still hold for all but the very narrowest of grooves. To see this, let the arc length of the fluid interface be denoted $\overline{S}$. To first order in ε,

$$\begin{aligned}\overline{S}_{\text{tot}} &= \int_{S_A}^{S_B} (1 - \varepsilon H K_\Upsilon) dS \\ &= S_{\text{tot}} - \varepsilon \int_{S_A}^{S_B} H K_\Upsilon dS \\ &= S_{\text{tot}} - \varepsilon \frac{\widehat{P}_0}{\text{Ca}} \int_{S_A}^{S_B} \frac{K_\Upsilon(S)}{-P(S)} dS. \end{aligned} \tag{7.115}$$

Substituting this into the expression for Q_0, Equation (7.111),

$$\begin{aligned} Q_0 &= \left(\frac{\Gamma_0 \widehat{P_0}^4}{3\text{Ca}^4}\right) \frac{P_B^{-3} - P_A^{-3}}{S_{\text{tot}}} \\ &= \left(\frac{\Gamma_0 \widehat{P_0}^4}{3\text{Ca}^4}\right) \frac{P_B^{-3} - P_A^{-3}}{\overline{S}_{\text{tot}}} - \varepsilon \left(\frac{\Gamma_0 \widehat{P_0}^5}{3\text{Ca}^5}\right) \frac{P_B^{-3} - P_A^{-3}}{\overline{S}_{\text{tot}}} \frac{1}{\overline{S}_{\text{tot}}} \int_{\overline{S}_A}^{\overline{S}_B} \frac{K_\Upsilon(\overline{S})}{-P(\overline{S})} d\overline{S}. \end{aligned} \tag{7.116}$$

Adding the ε correction to Q_1 yields

$$\overline{Q}_1 = \frac{\widehat{P}_0^5 \Gamma_0}{3\text{Ca}^5} \left[4\frac{\widehat{P}_\Upsilon}{\widehat{P}_0} + \frac{\Gamma_\Upsilon}{\Gamma_0} - 1\right] \frac{\left(P_B^{-3} - P_A^{-3}\right)}{\overline{S}_{\text{tot}}} \frac{1}{\overline{S}_{\text{tot}}} \int_{\overline{S}_A}^{\overline{S}_B} \frac{K_\Upsilon(\overline{S})}{-P(\overline{S})} d\overline{S}. \tag{7.117}$$

The quantity $4\widehat{P}_\Upsilon/\widehat{P}_0+\Gamma_\Upsilon/\Gamma_0-1>0$ for $\alpha \gtrsim 4^\circ$ [as seen in the result plotted in Figure 7.8(d)]. Therefore, in all but the very narrowest of grooves, the question of how to compare the arc length to the straight case is irrelevant, and positive curvature is flux-enhancing while negative curvature is flux-depressing.

7.3.3 Self-similar solutions

It has been established earlier that the straight V-groove equation allows for a one-parameter family of self-similar solutions (Vázquez, 2007; Weislogel and Lichter, 1998) under the transformations $B = T^{1-2\beta}H$, $\eta = Z/T^\beta$. The curved-backbone V-groove maintains a self-similar solution only when $K_\Upsilon = C_0 S^\chi$, with C_0 and χ constants. If the curvature satisfies this power-law form then, instead of a family, only one self-similar solution exists, with $\beta = 1/(2+\chi)$, $B = T^{\chi/(2+\chi)}H$, and $\eta = S/T^{1/(2+\chi)}$. Substituting these into the governing equation yields the ordinary differential equation

$$\begin{aligned} 0 = \frac{1}{2+\chi}\eta^{1-2\chi}\partial_\eta\left(\eta^{2\chi}B^2 - \varepsilon C_0\eta^{3\chi}B^3\frac{\widehat{A}_\Upsilon}{\widehat{A}_0}\right) \\ + \partial_\eta\left(B^2\partial_\eta B - \varepsilon C_0\eta^{\chi-1}\left[\chi\frac{\widehat{P}_\Upsilon}{\widehat{P}_0}B^4 - \frac{\Gamma_\Upsilon}{\Gamma_0}\eta B^3\partial_\eta B\right]\right). \end{aligned} \tag{7.118}$$

In the case of a groove with constant curvature, i.e., when $K_\Upsilon = K_0$, $\chi = 0$, $\eta = Z/T^{1/2}$, and the equation simplifies to

$$0 = \frac{1}{2}\eta\partial_\eta\left(H^2 - \varepsilon K_0 H^3\frac{\widehat{A}_\Upsilon}{\widehat{A}_0}\right) + \partial_\eta\left(H^2\partial_\eta H + \varepsilon K_0\frac{\Gamma_\Upsilon}{\Gamma_0}H^3\partial_\eta H\right). \tag{7.119}$$

Thus, a groove with constant curvature still supports $T^{1/2}$ spreading, following the same power law as Washburn filling, just as in the straight-groove case.

Numerical results are shown first for self-similar solutions in grooves of differing constant curvature, with Dirichlet pressure (P) boundary conditions. Representative plots for such a system with $\alpha = 45^\circ$ and $\theta = 15^\circ$ are shown in Figure 7.12, comparing curvature values $\varepsilon K_\Upsilon \in \{-0.2, -0.1, 0, 0.1, 0.2\}$. In each plot, the boundary condition at $\eta = 0$ is fixed at $P(\eta = 0) = -15.217$; the boundary condition at $\eta = 1$ has values of $P(\eta = 1) \in \{-12.174, -30.434, -152.17\}$ among the three columns of the figure [these values of P were chosen so that $H(\eta = 0) = 1$ and $H(\eta = 1) \in \{1.25, 0.5, 0.1\}$ for the straight groove with $K_\Upsilon = 0$]. Plots (a)-(c) display fluid thickness, H, and (d)-(f) display pressure, P.

As seen in the steady state plots (Figure 7.9), grooves with positive curvature (solid orange and red lines) have much thicker fluid than the straight groove (black dashed line), and than those with negative curvature (solid blue and teal lines). This leads to the self-similar front in grooves with positive curvature being farther along in the groove (i.e., the front being at greater η) at any given time than in the straight groove or negatively-curved grooves, an effect arising from the relatively lower friction in the thick film.

We next compare self-similar solutions in grooves of differing constant curvature with Dirichlet fluid thickness (H) boundary conditions. Representative plots for such a system with $\alpha = 45^\circ$ and $\theta = 15^\circ$ are shown in Figure 7.13, comparing curvature values $\varepsilon K_\Upsilon \in \{-0.2,\ -0.1,\ 0,\ 0.1,\ 0.2\}$. In each plot, the boundary condition at $\eta = 0$ is fixed at $H(\eta = 0) = 1$ and the boundary condition at $\eta = 1$ has values of $H(\eta = 1) \in \{1.25,\ 0.5,\ 0.1\}$ among the three columns of the figure (matching the H boundary of the straight $K_\Upsilon = 0$ groove in Figure 7.12). Plots (a)-(c) display fluid thickness, H, and (d)-(f) display pressure, P.

The difference in fluid thickness between grooves of different curvatures is greater than it was in the steady state (Figure 7.10) due to there now being not only a Γ_Υ/Γ_0 correction, but also an $\widehat{A}_\Upsilon/\widehat{A}_0$ corrective term. Still, like the steady state, the interface shapes of grooves with different curvatures are very similar, and the grooves with positive curvature (solid orange and red lines) have lower pressure at a given fluid thickness than the straight groove (dashed black line) or the grooves with negative curvature (solid blue and teal lines). As with the case of Dirichlet pressure boundary conditions, the self-similar front in grooves with positive curvature is farther along in the groove at any given time than in the straight groove or negatively curved grooves, due to the enhanced flux that accompanies positive groove curvature in the given geometry.

As with the straight V-groove, for constant curvature V-grooves there exists a family of terminating self-similar solutions, only one of which has a finite flux at the termination point; the rest have infinite flux at the terminating front, indicating that more physics must be added to the model there (see Chapter 4 for a review of terminating solutions in the straight groove; the unique finite-flux solution in that case was noted by Romero and Yost, 1996, and Weislogel, 1996). Figure 7.14 displays plots of the unique terminating solutions with finite-flux for grooves with $\alpha = 45^\circ$ and $\theta = 15^\circ$, with $\varepsilon K_\Upsilon \in \{-0.2, -0.1, 0, 0.1, 0.2\}$. Plot (a) compares results with a fixed Dirichlet pressure condition $P(\eta = 0) = -15.217$ (chosen so that $H = 1$ for the straight groove), and (b) compares results with a fixed Dirichlet thickness condition $H(\eta = 0) = 1$. As with the non-terminating self-similar spreading solutions (Figures 7.12 and 7.13), grooves with positive curvature (solid orange and red lines) extend farther in the groove at any given time than the straight groove (dashed black line) or grooves with negative curvature (solid blue and teal lines), due to their enhanced flux in the given geometry.

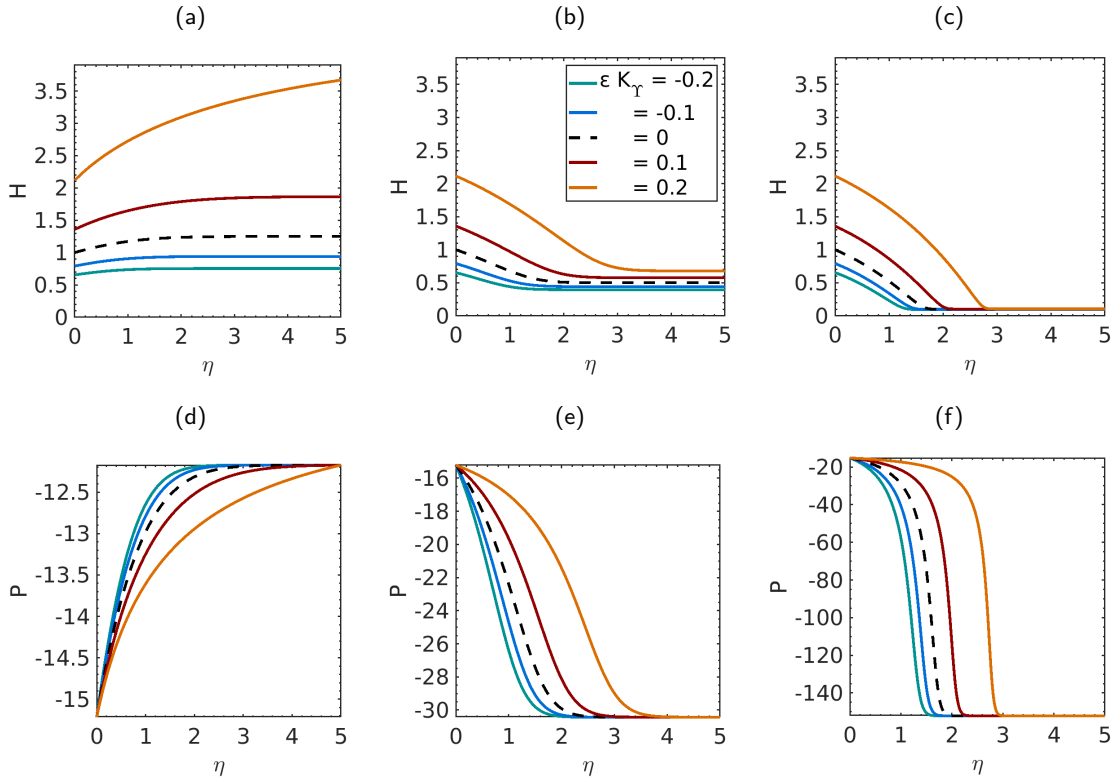

Figure 7.12: Representative self-similar solutions of flow in V-grooves of constant curvature with groove half angle $\alpha = 45°$, contact angle $\theta = 15°$, and Dirichlet pressure (P) boundary conditions, computed according to Equation (7.119). Results are plotted for grooves with 5 different values of vertical curvatures, $\varepsilon K_\Upsilon \in \{-0.2, -0.1, 0, 0.1, 0.2\}$. In each plot, the horizontal axis is the self-similar coordinate $\eta = S/\sqrt{T}$, where S is the nondimensional backbone arc length and T is the nondimensional time.

Plots (a)-(c) (top row) display nondimensional fluid midline thickness, H. Plots (d)-(f) (bottom row) display nondimensional pressure, P.

Each column displays a different boundary condition: column 1, (a) and (d), has boundary conditions $P(\eta = 0) = -15.217$ and $P(\eta = 5) = -12.174$; column 2, (b) and (e), has boundary conditions $P(\eta = 0) = -15.217$ and $P(\eta = 5) = -30.434$; column 3, (c) and (f), has boundary conditions $P(\eta = 0) = -15.217$ and $P(\eta = 5) = -152.17$. These values of P were chosen so that the straight groove (with $K_\Upsilon = 0$) would have film midline thickness $H(\eta = 0) = 1$ and $H(\eta = 5) \in \{1.25, 0.5, 0.1\}$.

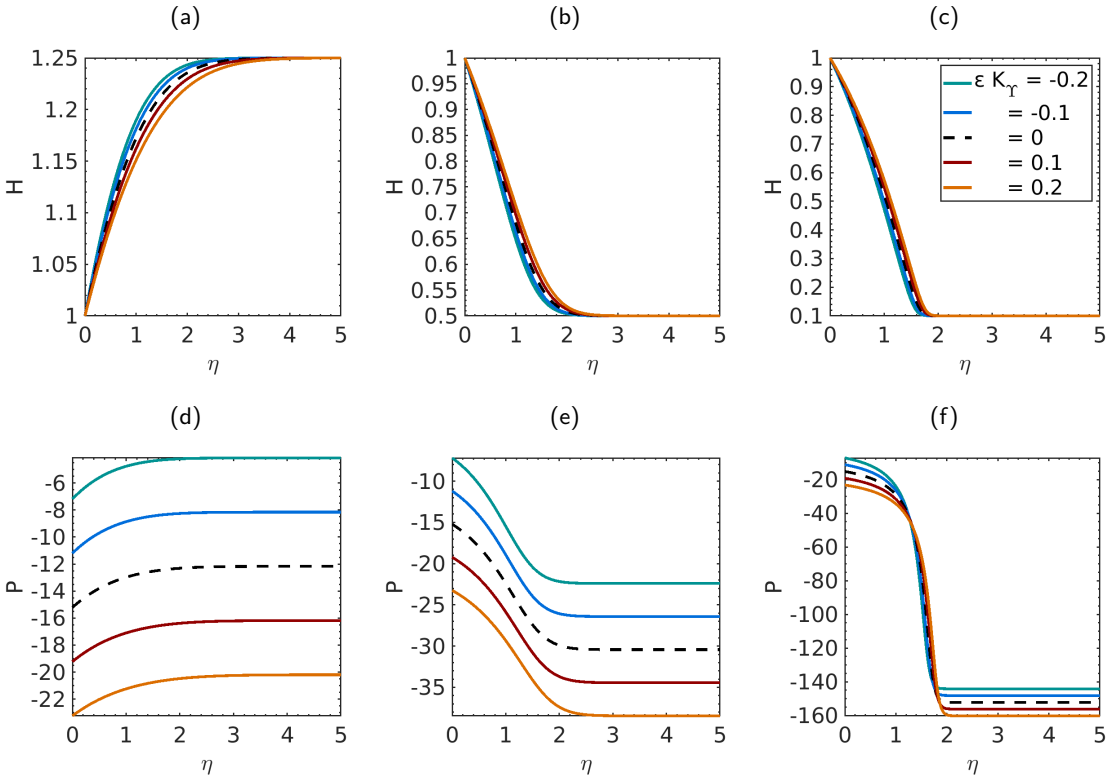

Figure 7.13: Representative self-similar solutions of flow in V-grooves of constant curvature with groove half angle $\alpha = 45°$, contact angle $\theta = 15°$, and Dirichlet midline thickness (H) boundary conditions, computed according to Equation (7.119). Results are plotted for grooves with 5 different values of vertical curvatures, $\varepsilon K_\Upsilon \in \{-0.2, -0.1, 0, 0.1, 0.2\}$. In each plot, the horizontal axis is the self-similar coordinate $\eta = S/\sqrt{T}$, where S is the nondimensional backbone arc length and T is the nondimensional time.

Plots (a)-(c) (top row) display nondimensional fluid midline thickness, H. Plots (d)-(f) (bottom row) display nondimensional pressure, P.

Each column displays a different boundary condition: column 1, (a) and (d), has boundary conditions $H(\eta = 0) = 1$ and $H(\eta = 5) = 1.25$; column 2, (b) and (e), has boundary conditions $H(\eta = 0) = 1$ and $H(\eta = 5) = 0.5$; column 3, (c) and (f), has boundary conditions $H(\eta = 0) = 1$ and $H(\eta = 5) = 0.1$.

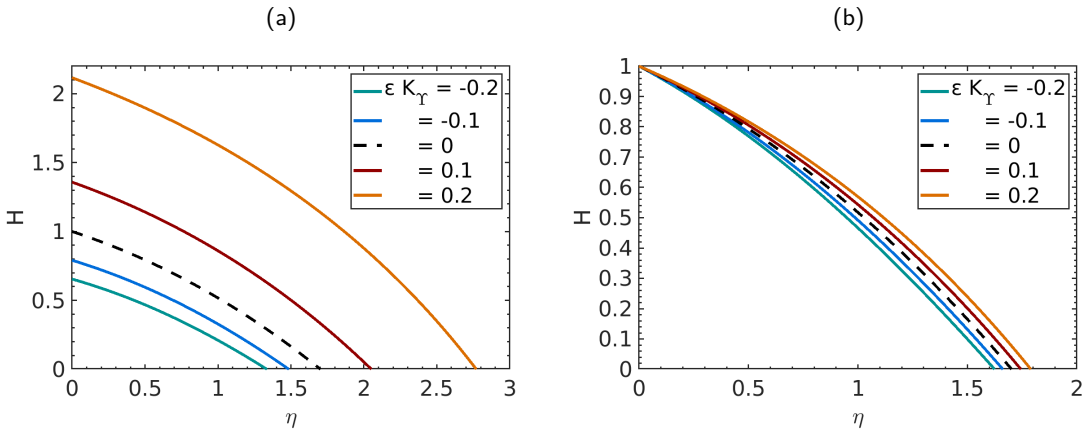

Figure 7.14: Terminating self-similar solutions in V-grooves of constant curvature with groove half angle $\alpha = 45°$, contact angle $\theta = 15°$, computed according to Equation (7.119). Results are plotted for grooves with 5 different values of vertical curvatures, $\varepsilon K_\Upsilon \in \{-0.2, -0.1, 0, 0.1, 0.2\}$. In each plot, the horizontal axis is the self-similar coordinate $\eta = S/\sqrt{T}$, where S is the nondimensional backbone arc length and T is the nondimensional time. The vertical axis is nondimensional fluid midline thickness, H.
(a) Terminating solutions with Dirichlet pressure (P) boundary condition, $P(\eta = 0) = -15.217$, chosen so that the straight groove with $K_\Upsilon = 0$ has film midline thickness $H(\eta = 0) = 1$.
(b) Terminating solutions with Dirichlet midline thickness (H) boundary condition, $H(\eta = 0) = 1$.

7.4 Stability analysis

We now follow the methodology of Chapter 5 to analyze the stability of flow in a curved-backbone V-groove. As with the V-groove under the electric field [Chapter 6], we will be unable to prove stability in general, but will instead consider only special cases. In particular, we consider only grooves with constant backbone curvature.

7.4.1 Nonlinear stability of steady states

For the steady state, we again pursue nonlinear stability, following Section 5.2 and Section 3.2. Note that we are assuming $K_\Upsilon = K_0 = const$. We first rewrite the pressure [Equation (7.78)], flux, and evolution equation [Equation (7.101)] in terms of the volume element $G = H^2 -$

$\varepsilon K_0(\widehat{A}_\Upsilon/\widehat{A}_0)H^3$, whose inverse is $H = \sqrt{G} + (1/2)\varepsilon K_0(\widehat{A}_\Upsilon/\widehat{A}_0)G + O(\varepsilon^2)$.

$$P = -\frac{\widehat{P}_0}{\mathrm{Ca}}\left[\frac{1}{\sqrt{G}} + \varepsilon K_\Upsilon\left(\frac{\widehat{P}_\Upsilon}{\widehat{P}_0} - \frac{1}{2}\frac{\widehat{A}_\Upsilon}{\widehat{A}_0}\right)\right] + O(\varepsilon^2), \tag{7.120}$$

$$\begin{aligned} Q &= -\frac{1}{2}\sqrt{G}\partial_S G + \varepsilon G\left(\left[\frac{\widehat{P}_\Upsilon}{\widehat{P}_0} - \frac{1}{2}\frac{\widehat{A}_\Upsilon}{\widehat{A}_0}\right] G\partial_S K_\Upsilon - \left[\frac{1}{2}\frac{\Gamma_\Upsilon}{\Gamma_0} + \frac{\widehat{A}_\Upsilon}{\widehat{A}_0}\right] K_\Upsilon \partial_S G\right) + O(\varepsilon^2) \\ &= -\frac{1}{2}\sqrt{G}\partial_S G + \varepsilon G\left[\hat{\pi} G\partial_S K_\Upsilon - \hat{\gamma} K_\Upsilon \partial_S G\right] + O(\varepsilon^2) \\ &= -\frac{1}{2}\sqrt{G}\partial_S G - \varepsilon K_0 \hat{\gamma} G\partial_S G + O(\varepsilon^2), \end{aligned} \tag{7.121}$$

$$\frac{\partial G}{\partial T} = -\partial_S Q, \tag{7.122}$$

where we have defined

$$\widehat{\pi} = \frac{\widehat{P}_\Upsilon}{\widehat{P}_0} - \frac{1}{2}\frac{\widehat{A}_\Upsilon}{\widehat{A}_0}, \tag{7.123a}$$

$$\widehat{\gamma} = \frac{1}{2}\frac{\Gamma_\Upsilon}{\Gamma_0} + \frac{\widehat{A}_\Upsilon}{\widehat{A}_0} \tag{7.123b}$$

for brevity.

For a given set of Dirichlet or flux boundary conditions at S_1 and S_2, let G_S be the corresponding steady state solution, with steady state flux $Q_S = const.$ We can then define a Lyapunov free energy by

$$\mathfrak{F}(G) = \int_{S_1}^{S_2}\left[\left(\frac{2}{5}G^{5/2} - GG_S^{3/2} + \frac{3}{5}G_S^{5/2}\right) + \frac{\varepsilon}{2}K_0\widehat{\gamma}(G - G_S)^2(G + 2G_S)\right] dS. \tag{7.124}$$

The $O(\varepsilon^0)$ term of $\mathfrak{F}$ is immediately recognizable as the same free energy we found for the straight V-groove, Equation (5.11). $\mathfrak{F}$ was so chosen because

$$\begin{aligned} \partial_S\left(\frac{\delta\mathfrak{F}}{\delta G}\right) &= \partial_S\left[\left(G^{3/2} - G_S^{3/2}\right) + \frac{\varepsilon}{2}K_0\widehat{\gamma}\,3\left(G^2 - G_S^2\right)\right] \\ &= -3\left(Q - Q_S\right). \end{aligned} \tag{7.125}$$

Note that $\mathfrak{F}(G_S) = 0$, and

$$\delta\mathfrak{F}(G)|_{G_S} = \int_{S_1}^{S_2}\left[\left(G^{3/2} - G_S^{3/2}\right) + \frac{\varepsilon}{2}K_0\widehat{\gamma}\,3\left(G^2 - G_S^2\right)\right]_{G=G_S} dS = 0 \tag{7.126a}$$

$$\delta^2\mathfrak{F}(G)\Big|_{G_S} = \int_{S_1}^{S_2}\left[\frac{3}{2}\sqrt{G_S} + \frac{\varepsilon}{2}K_0\widehat{\gamma}\,6G_S\right] dS \tag{7.126b}$$

$$= \int_{S_1}^{S_2}\frac{3}{2}H_S\left[1 + \varepsilon K_0\left(\frac{\Gamma_\Upsilon}{\Gamma_0} + \frac{3}{2}\frac{\widehat{A}_\Upsilon}{\widehat{A}_0}\right)H_S\right] dS. \tag{7.126c}$$

If $K_0 > 0$, then the second variation is positive, i.e., $\mathfrak{F}$ is convex at $G = G_S$. If $K_0 < 0$, then so long as $|\varepsilon K_0| < (1/2)/\max(H_S)$, $\mathfrak{F}$ will remain convex. This inequality arises

from the fact that $[\Gamma_\Upsilon/\Gamma_0 + (3/2)(\widehat{A}_\Upsilon/\widehat{A}_0)] < 2$ for all values of α and θ. By virtue of our nondimensionalization, H_S should always be $\leq O(1)$; meanwhile we required $|\varepsilon K_0| \ll 1$ for the perturbative expansion to hold in the first place. Thus, we will continue under the assumption that $|\varepsilon K_0| < (1/2)/\max(H_S)$ is satisfied. If K_0 is just on the threshold such that $(1/2)/\max(H_S) < |\varepsilon K_0| < 1$, then the following stability analysis will not hold.

We now must show that the Lyapunov free energy $\mathfrak{F}$ is always decreasing.

$$\begin{aligned}
\frac{\partial \mathfrak{F}}{\partial T} &= \int_{S_1}^{S_2} \frac{\delta \mathfrak{F}}{\delta G}\frac{\partial G}{\partial T} dS \\
&= \int_{S_1}^{S_2} \frac{\delta \mathfrak{F}}{\delta G}\partial_S\left[\frac{1}{3}\partial_S\left(\frac{\delta \mathfrak{F}}{\delta G}\right)\right] dS \\
&= \frac{1}{3}\left[\frac{\delta \mathfrak{F}}{\delta G}\partial_S\left(\frac{\delta \mathfrak{F}}{\delta G}\right)\right]_{S_1}^{S_2} - \frac{1}{3}\int_{S_1}^{S_2} \partial_S\left(\frac{\delta \mathfrak{F}}{\delta G}\right)^2 dS \\
&= \left[\frac{\delta \mathfrak{F}}{\delta G}(Q - Q_S)\right]_{S_1}^{S_2} - \frac{1}{3}\int_{S_1}^{S_2} \partial_S\left(\frac{\delta \mathfrak{F}}{\delta G}\right)^2 dS \\
&= -\frac{1}{3}\int_{S_1}^{S_2} \partial_S\left(\frac{\delta \mathfrak{F}}{\delta G}\right)^2 dS \leq 0.
\end{aligned} \tag{7.127}$$

The boundary term vanishes under either flux (due to the $Q - Q_S$ term) or Dirichlet (due to the $\delta\mathfrak{F}/\delta G$ term) boundary conditions.

Hence, there exists an always-decreasing Lyapunov free energy, which is convex within the accessible region (specifically, for H such that $2\varepsilon K_0 H > -1$), and which has a unique minimum at $H = H_S$. Therefore, the steady states of the V-groove with constant backbone curvature are stable.

7.4.2 Linear stability of self-similar spreading states

Recall from Section 3.1 that, for an autonomous system, the numerical abscissa being negative is sufficient to demonstrate both transient and asymptotic linear stability. While it was possible to analytically prove such stability for the self-similar states of the straight V-groove [Section 5.3], a similar argument for the self-similar states with a curved backbone is not pursued here. Instead, we numerically compute the numerical abscissa for a variety of parameters, demonstrating that, at least within the chosen parameter range, the self-similar spreading and receding states of a V-groove with a constant-curvature backbone exhibit both transient and asymptotic linear stability.

Rewriting Equation (7.101), with constant curvature $K_\Upsilon = K_0$, in self-similar coordinates $\{\eta = H/\sqrt{T}, \tau = \ln T\}$ yields

$$\partial_\tau H = \frac{(1/2)\eta\partial_\eta\left[H^2 - \varepsilon K_0\left(\widehat{A}_\Upsilon/\widehat{A}_0\right)H^3\right] + \partial_\eta\left[H^2\partial_\eta H + \varepsilon K_0\left(\Gamma_\Upsilon/\widehat{\Gamma}_0\right)H^3\partial_\eta H\right]}{H\left[2 - 3\varepsilon K_0\left(\widehat{A}_\Upsilon/\widehat{A}_0\right)H\right]}. \tag{7.128}$$

Note that the numerator on the right-hand side is precisely Equation (7.119).

Taking a non-terminating solution H of Equation (7.119) as the base state, linearizing about Equation (7.128) yields an equation of the form $\partial_\tau \delta H = \mathcal{L}\delta H$, which is extremely long. The transient operator $(\mathcal{L}+\mathcal{L}^\dagger)/2$ is a bit shorter and the operator of interest for computing the numerical abscissa, so only it will be reported here:

$$\begin{aligned}\frac{\mathcal{L}+\mathcal{L}^\dagger}{2} &= \frac{H\left[1+\varepsilon K_0\left(\Gamma_\Upsilon/\widehat{\Gamma}_0\right)H\right]}{2-3\varepsilon K_0\left(\widehat{A}_\Upsilon/\widehat{A}_0\right)H}\partial_{\eta\eta} + \frac{\left[2+4\varepsilon K_0\left(\Gamma_\Upsilon/\widehat{\Gamma}_0\right)H\right]\partial_\eta H}{\left[2-3\varepsilon K_0\left(\widehat{A}_\Upsilon/\widehat{A}_0\right)H\right]^2}\partial_\eta \\ &+ \frac{1}{\left[2-3\varepsilon K_0\left(\widehat{A}_\Upsilon/\widehat{A}_0\right)H\right]^3} \\ &\times\left\{-2\left(1+\partial_{\eta\eta}H\right)+\varepsilon K_0\left[2\left(3\frac{\widehat{A}_\Upsilon}{\widehat{A}_0}+2\frac{\Gamma_\Upsilon}{\widehat{\Gamma}_0}\right)(\partial_\eta H)^2+3\frac{\widehat{A}_\Upsilon}{\widehat{A}_0}H\left(3+5\partial_{\eta\eta}H\right)\right]\right\}.\end{aligned} \tag{7.129}$$

The numerical abscissa is the largest eigenvalue of the transient operator $(\mathcal{L}+\mathcal{L}^\dagger)/2$. A numerical parameter sweep was performed over V-groove geometries $\varepsilon K_0 \in \{-0.2,\ -0.1,\ -0.05,\ 0,\ 0.05,\ 0.1,\ 0.2\}$ and $(\alpha,\theta) \in \{(15°,0°);\ (15°,30°);\ (15°,60°);\ (45°,0°);\ (45°,30°);\ (75°,0°)\}$. These geometries were chosen to give a range of narrow to wide grooves, and a substantial variation in backbone curvature (recall that $\varepsilon K_0 \ll 1$ by assumption, so that 0.2 is considered a very large curvature). This set of seven curvatures and six sets of angles yields 42 distinct geometries. For each geometry, several self-similar spreading and draining solutions were tested. In each case $H(0)=1$. Six different far-field values of the thickness H were tested for each geometry: $H(\eta_{\text{far}}) \in \{0.01,\ 0.1,\ 0.5,\ 1,\ 1.5,\ 2\}$. Far-field values < 1 indicate spreading solutions; the far-field value 1 is the static solution, and far-field values > 1 indicate draining solutions. In each of the 252 cases tested, the numerical abscissa $\beta_{\max}[\mathcal{L}] < -0.25$, indicating transient and asymptotic linear stability of self-similar states within the parameter range tested.

A subset of the numerical abscissa results is plotted in Figure 7.15. Plot (a) shows results for the self-similar spreading solution with $H(0)=1$ and $H(\eta_{far})=0.01$; (b) shows for the self-similar draining solution with $H(0)=1$ and $H(\eta_{far})=1.25$. In each case, the numerical abscissa ω is plotted against the curvature εK_0. Five different groove angles α are shown; the contact angle was fixed at $\theta = 0°$. Each case was nondimensionalized separately, so that varying the angle affects only the curvature contribution.

The spreading results, in Figure 7.15 (a), show no visible difference between the different cases, due to the fact that the majority of the film is extremely thin (0.01); hence the backbone curvature has little effect since it comes in with an extra power of the film thickness. The draining results, in Figure 7.15 (b), have a much more significant variation, as the film is thick (between 1 and 1.25). Positive curvature appears to be more stable than negative curvature, a result which was not obvious a priori, given the complexity of Equation (7.129). This phenomenon may be

due to the non-constant part of the self-similar result near $\eta = 0$ being longer for positively-curved grooves. The groove angle has little effect and depends on the boundary condition. When comparing fixed thickness conditions, as shown in Figure 7.15, wide grooves are more stable for negative curvature and narrow grooves are more stable for positive curvature.

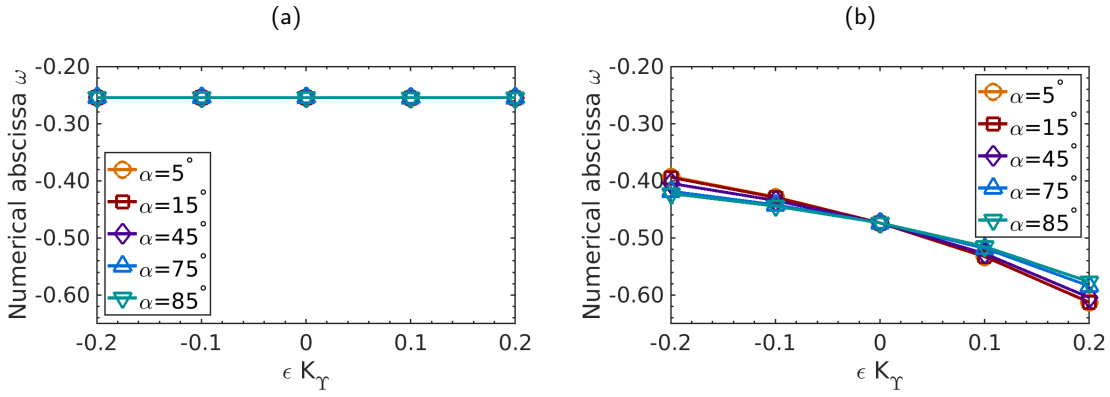

Figure 7.15: Representative numerical abscissae for self-similar solutions of flow in V-grooves with constant vertical backbone curvature and contact angle $\theta = 0°$, computed by finding the largest eigenvalue of the transient linear operator in self-similar coordinates, Equation (7.129). Results for two sets of Dirichlet midline thickness (H) boundary conditions are shown, representing one spreading solution and one draining (receding) solution. Numerical abscissae are computed for interior groove half angle $\alpha \in \{5°, 15°, 45°, 75°, 85°\}$ and vertical backbone curvature $\varepsilon K_\Upsilon \in \{-0.2, -0.1, 0, 0.1, 0.2\}$. Each case is nondimensionalized independently, so that the results with no curvature ($\varepsilon K_0 = 0$) will be identical. Results were computed with domain length 40 and the mesh size was taken to be 0.02, following Chapter 5.
(a) Self-similar spreading solution with $H(0) = 1$ and $H(40) = 0.01$.
(b) Self-similar draining (receding) solution with $H(0) = 1$ and $H(40) = 1.25$.

7.5 Discussion

7.5.1 Numerical methods

Numerical techniques were used to compute the geometric parameters Γ_0 and Γ_Υ (Figures 7.7 and 7.8), to compute the steady state solution on a sinusoidal groove (Figure 7.11), to compute self-similar solutions (Figures 7.12 to 7.14), and to perform linear stability analysis of self-similar solutions (Figure 7.15).

Γ_0 and Γ_Υ were computed by solving the Poisson equations [Equations (7.86a) and (7.86b)] with the appropriate boundary conditions [Equations (7.89a) and (7.89b)] using the finite element method in COMSOL Multiphysics 5.3a (Com, 2017), using the Multiphysics package. Domains were generated for $\alpha \in \{2°, 3°, \cdots, 88°\}$ and $\theta \in \{0°, 5°, \cdots, 85°\}$. A triangular mesh was automatically generated in COMSOL using the constraints of maximum element length 0.05, minimum element length 10^{-5}, curvature factor 0.2, and resolution of narrow regions 2, with a

new mesh constructed for each domain.[3] To ensure that the mesh was sufficiently fine, the area correction integrals $\widehat{A}_\Upsilon$ and $\widehat{A}_0$ were computed in addition to Γ_Υ and Γ_0. Because the exact value of the area corrections is known, the relative error of the numerical integral was computed exactly, and found to be at most 8×10^{-5} (0.008%). The computations of Γ_0 and Γ_Υ could be repeated with a finer mesh to ensure even higher accuracy, but at that point a larger concern would be the size of the $O(\varepsilon^2)$ corrections which were omitted from the model.

Steady state solutions with non-constant curvature were found by solving Equation (7.101) without time dependence using the `ode45` solver in MATLAB (Mat, 2015) on a domain with 2000 points. The system was solved with a shooting method. The boundary condition at $S = 0$ was fixed, a slope $\partial_S H|_{S=0}$ was posited, and the system was solved forward to $S = 5$. The resulting $H(S = 5)$ was compared to the desired boundary condition, and the initial slope was adjusted accordingly. The process was repeated until the absolute error on the $S = 5$ boundary condition thickness was less than 10^{-7}. Self-similar solutions were solved by the same procedure, using Equation (7.119). In order to validate the numerical method, steady state solutions with constant curvature were computed using the same code and compared to the known analytic solutions; the absolute error in fluid thickness was at most 0.0038, and the maximum relative error was at most 0.0023 (0.23%).

Terminating self-similar solutions were computed by solving Equation (7.119) with the `ode45` solver in MATLAB (Mat, 2015) on a domain with 2000 points. The system was solved with a shooting method: first, a termination point η_c was posited, the system was solved backwards from $\eta = \eta_c$ to $\eta = 0$, and the resulting pressure $P(\eta = 0)$ or fluid thickness $H(\eta = 0)$ was compared to the corresponding boundary condition. η_c would then be adjusted, and the process continued until the absolute error on the $\eta = 0$ boundary condition thickness was less than 10^{-7}.

Linear stability analysis was performed in MATLAB by second-order central finite difference on a domain $\eta \in [0, 40]$ with 2000 points, based on the length and mesh fineness found to be sufficient for straight V-grooves in Section 5.3.2. The transient operator was constructed in matrix form using second order finite difference operators, and the maximum eigenvalue was found using MATLAB's built-in `eig` function, which computes exact matrix eigenvalues (the matrices were sufficiently small that approximate eigensystem methods were not required).

7.5.2 Caveats

The slender limit $\varepsilon \ll 1$ is crucial to the validity of this model. In particular, it can be seen from Figure 7.8 (b) that $\widehat{P}_\Upsilon / \widehat{P}_0$ can become quite large when $\theta + \alpha$ is large. In such cases, either ε must be correspondingly small to ensure that $\varepsilon \widehat{P}_\Upsilon / \widehat{P}_0$ is still a perturbative correction, or higher-order corrections must be computed.

[3] The curvature factor is defined as "the ratio between the boundary element size and the curvature radius" (thus a lower number yields a finer mesh) and the resolution of narrow regions as "the number of layers of elements that are created in narrow regions," according to the COMSOL documentation (Com, 2017).

In order to ignore inertia, the model furthermore required that $\varepsilon \mathrm{Re}\Gamma_0 = \varepsilon^2 \rho\gamma d\Phi_0\Gamma_0/\mu^2 \ll 1$. Recall from Chapter 4 that terms of $O(\varepsilon\mathrm{Re})$ appear in the nondimensionalized Navier-Stokes equations, but integrated streamwise flux corrections pick up a factor of $O(\Gamma_0)$. This condition is relatively easy to satisfy for fluids such as water and ethyl alcohol, which have low density and surface tension, but for liquid metals such as indium it requires a small d and large L to hold down the value. In liquid metal systems larger than microscale, inertial effects would need to be included in the model; this could be accomplished perturbatively and is likely a fruitful avenue of future research.

This model assumed that the contact angle θ is equal to the equilibrium (static) contact angle, thus ignoring the effect of a dynamic contact angle dependent on the local capillary number. As discussed in Section 4.4.1, the dynamic contact angle is expected to be a correction of order $\varepsilon^{4/3}$. Although a dynamic contact angle could be included in the model, this complication is beyond the scope of the present work.

It was further assumed that gravity was negligible, specifically, $\mathrm{Bo}/\mathrm{Ca} \ll \varepsilon$. Thus, the model is applicable only to microscale or microgravity systems. In particular, the key application of space-based propellant and fuel management easily satisfies the low gravity requirement.

Because of the symmetry of the groove, the lateral curvature, K_Ξ, and torsion, $\mathcal{J}$, were found to be relevant only at order ε^2 and was thus ignored. Certainly the model could be carried out to higher order to include this effect. When doing so, one must be careful to include the cross-terms, as K_Υ, K_Ξ, and $\mathcal{J}$ effects interact at order ε^2. Furthermore, if $\theta + \alpha$ is very large, then these corrections may become too large for ε to suppress, so more analysis is necessary for the limit of large $\theta + \alpha$.

To extend the curved-backbone model to U-grooves, the interface shape and pressure and area corrections would be similar to those presented here (an additional correction to the interface shape would arise due to the wall curvature, but it would likely be negligibly small). However, the flux factor and corrections thereof would need to be computed numerically for each fluid thickness H, depending on the shape of the U-groove's rounded bottom. The general rule of thumb that positive backbone curvature enhances flux and negative backbone curvature suppresses flux is still expected to apply, although limiting cases (such as a nearly crescent-shaped fluid) might possibly break the rule.

7.6 Conclusion

With this, we conclude our exploration of flow in V-grooves. Building upon the model of Romero and Yost (1996) and Weislogel (1996), we showed in Chapter 5 that steady state flow and self-similar flow in straight V-grooves are very stable against perturbations. In Chapter 6, we developed a new model of flow in a V-groove under an electric field. There we found that electric fields increase fluid flux, and both steady state and self-similar flow under constant electric fields are stable so long as the fluid does not exceed a threshold thickness. And in

the present chapter, Chapter 7, we have developed a new model for flow in a V-groove with a curved backbone. We found that positive curvature diminishes flux and negative curvature enhances flux, and steady state flow and self-similar flow with constant backbone curvature are stable against perturbations. These results provide evidence that V-grooves are indeed a robust transport mechanism for use in the MEP, and furthermore provide a framework for the design of novel compact microfluidic devices.

7.7 Appendix: Additional plots

7.7.1 Steady and self-similar plots in narrow grooves with constant curvature

Figures 7.9, 7.10, 7.12 and 7.13, discussed earlier, displayed steady state and self-similar flow results in grooves of constant curvature with $\alpha = 45^\circ$ and $\theta = 15^\circ$. We now display analogous plots in narrow grooves, with $\alpha = 15^\circ$ and $\theta = 15^\circ$.

Representative plots of steady state flow with Dirichlet pressure (P) boundary conditions, $\alpha = 15^\circ$, and $\theta = 15^\circ$ are shown in Figure 7.16, comparing curvature values $\varepsilon K_\Upsilon \in \{-0.2,\ -0.1,\ 0,\ 0.1,\ 0.2\}$. In each plot, the boundary condition at $S = 0$ is fixed at $P(S = 0) = -101.58$; the boundary condition at $S = 1$ has values of $P(S = 1) \in \{-81.262,\ -203.16,\ -1015.8\}$ among the three columns of the figure [these values of P were chosen so that $H(S = 0) = 1$ and $H(S = 1) \in \{1.25, 0.5, 0.1\}$ for the straight groove with $K_\Upsilon = 0$]. Plots (a)-(c) display fluid thickness, H, and (d)-(f) display pressure, P.

While the results are qualitatively similar to those in wide V-grooves, it stands out that the variation in H in Figure 7.16 is much smaller than in the corresponding figures in wider, $\alpha = 45^\circ$ grooves. This occurs because the pressure correction $\widehat{P}_\Upsilon/\widehat{P}_0$ is smaller in narrow grooves than wide grooves, as seen in Figure 7.8 (b). Intuitively, narrow grooves have a much more strongly curved fluid interface than do wide grooves, and hence the relative effect of adding curvature from the backbone is lessened.

Plots of steady state flow with Dirichlet thickness (H) boundary conditions, $\alpha = 15^\circ$, and $\theta = 15^\circ$ are shown in Figure 7.17, comparing curvature values $\varepsilon K_\Upsilon \in \{-0.2, -0.1, 0, 0.1, 0.2\}$. In each plot, the boundary condition at $S = 0$ is fixed at $H(S = 0) = 1$ and the boundary condition at $S = 1$ has values of $H(S = 1) \in \{1.25, 0.5, 0.1\}$ among the three columns of the figure (matching the H boundary of the straight $K_\Upsilon = 0$ groove in Figure 7.16). Plots (a)-(c) display fluid thickness, H, (d)-(f) display the difference between the thickness H and the straight-groove thickness $H_{\text{steady},K_\Upsilon\text{const.}}$, and (g)-(i) display pressure, P.

With thickness boundary conditions, the narrow grooves experience a *greater* differentiation in H between grooves of different curvatures. Because boundary conditions are set by H, $\widehat{P}_\Upsilon/\widehat{P}_0$ no longer enters the problem, and the difference between steady states of wide and narrow grooves is driven by the flux correction, Γ_Υ/Γ_0, which is larger for narrow grooves [Figure 7.8 (c)]. While the flux correction is complicated, the larger value of Γ_Υ/Γ_0 in narrow grooves is driven by Γ_0 being small due to the higher wall friction in a narrow domain. In other words, the

higher *relative* gain in flux due to backbone curvature because the flux is so low to begin with.

Self-similar solutions in grooves of differing constant curvature, with Dirichlet pressure (P) boundary conditions, $\alpha = 15^\circ$, and $\theta = 15^\circ$ are shown in Figure 7.18, comparing curvature values $\varepsilon K_\Upsilon \in \{-0.2, -0.1, 0, 0.1, 0.2\}$. In each plot, the boundary condition at $\eta = 0$ is fixed at $P(\eta = 0) = -101.58$; the boundary condition at $\eta = 1$ has values of $P(\eta = 1) \in \{-81.262, -203.16, -1015.8\}$ among the three columns of the figure [these values of P were chosen so that $H(\eta = 0) = 1$ and $H(\eta = 1) \in \{1.25, 0.5, 0.1\}$ for the straight groove with $K_\Upsilon = 0$]. Plots (a)-(c) display fluid thickness, H, and (d)-(f) display pressure, P.

And self-similar solutions in grooves of differing constant curvature, with Dirichlet pressure (P) boundary conditions, $\alpha = 15^\circ$, and $\theta = 15^\circ$ are shown in Figure 7.18, comparing curvature values $\varepsilon K_\Upsilon \in \{-0.2, -0.1, 0, 0.1, 0.2\}$. In each plot, the boundary condition at $\eta = 0$ is fixed at $P(\eta = 0) = -101.58$; the boundary condition at $\eta = 1$ has values of $P(\eta = 1) \in \{-81.262, -203.16, -1015.8\}$ among the three columns of the figure [these values of P were chosen so that $H(\eta = 0) = 1$ and $H(\eta = 1) \in \{1.25, 0.5, 0.1\}$ for the straight groove with $K_\Upsilon = 0$]. Plots (a)-(c) display fluid thickness, H, and (d)-(f) display pressure, P.

Self-similar solutions with Dirichlet fluid thickness (H) boundary conditions are shown in Figure 7.19, comparing curvature values $\varepsilon K_\Upsilon \in \{-0.2, -0.1, 0, 0.1, 0.2\}$. In each plot, the boundary condition at $\eta = 0$ is fixed at $H(\eta = 0) = 1$ and the boundary condition at $\eta = 1$ has values of $H(\eta = 1) \in \{1.25, 0.5, 0.1\}$ among the three columns of the figure (matching the H boundary of the straight $K_\Upsilon = 0$ groove in Figure 7.18). Plots (a)-(c) display fluid thickness, H, and (d)-(f) display pressure, P.

As with the steady state results, the self-similar solutions are qualitatively similar to those in wide grooves, but fluid thickness at a given pressure P (and pressure at a given fluid thickness) are less differentiated between grooves of different curvatures, due to the relatively small value of $\widehat{P}_\Upsilon / \widehat{P}_0$ at $\alpha = 15^\circ$. And, with H boundary conditions, the fluid thickness between grooves of different curvatures is more differentiated, due to the larger value of $\Gamma_\Upsilon / \Gamma_0$ at $\alpha = 15^\circ$. Although the self-similar equation [Equation (7.119)] has an additional corrective term, $\widehat{A}_\Upsilon / \widehat{A}_0$, this term varies little with α.

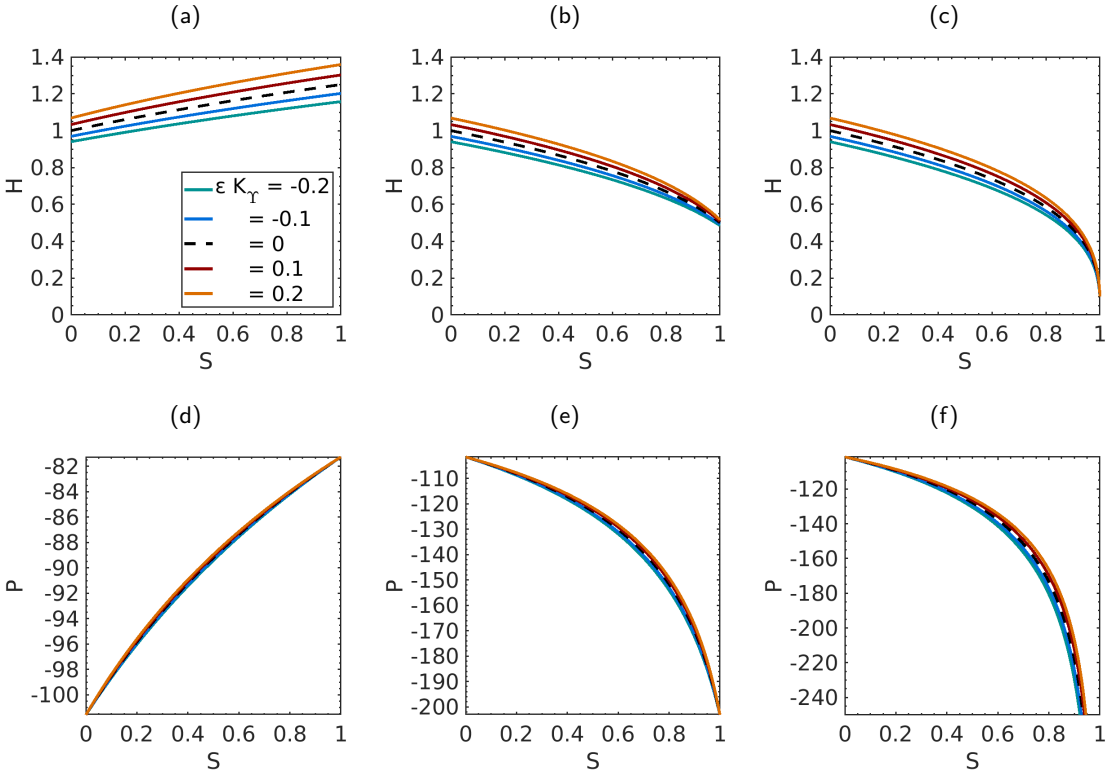

Figure 7.16: Representative steady state solutions of flow in V-grooves of constant curvature with groove half angle $\alpha = 15^\circ$, contact angle $\theta = 15^\circ$, and Dirichlet pressure (P) boundary conditions, according to Equation (7.108). Results are plotted for grooves with 5 different values of vertical curvatures, $\varepsilon K_\Upsilon \in \{-0.2, -0.1, 0, 0.1, 0.2\}$. In each plot, the horizontal axis is S, the nondimensional backbone arc length.

Plots (a)-(c) (top row) display nondimensional fluid midline thickness, H. Plots (d)-(f) (bottom row) display nondimensional pressure, P.

Each column displays a different boundary condition: column 1, (a) and (d), has boundary conditions $P(S = 0) = -101.58$ and $P(S = 1) = -81.262$; column 2, (b) and (e), has boundary conditions $P(S = 0) = -101.58$ and $P(S = 1) = -203.16$; column 3, (c) and (f), has boundary conditions $P(S = 0) = -101.58$ and $P(S = 1) = -1015.8$. These values of P were chosen so that the straight groove (with $K_\Upsilon = 0$) would have film midline thickness $H(S = 0) = 1$ and $H(S = 1) \in \{1.25, 0.5, 0.1\}$.

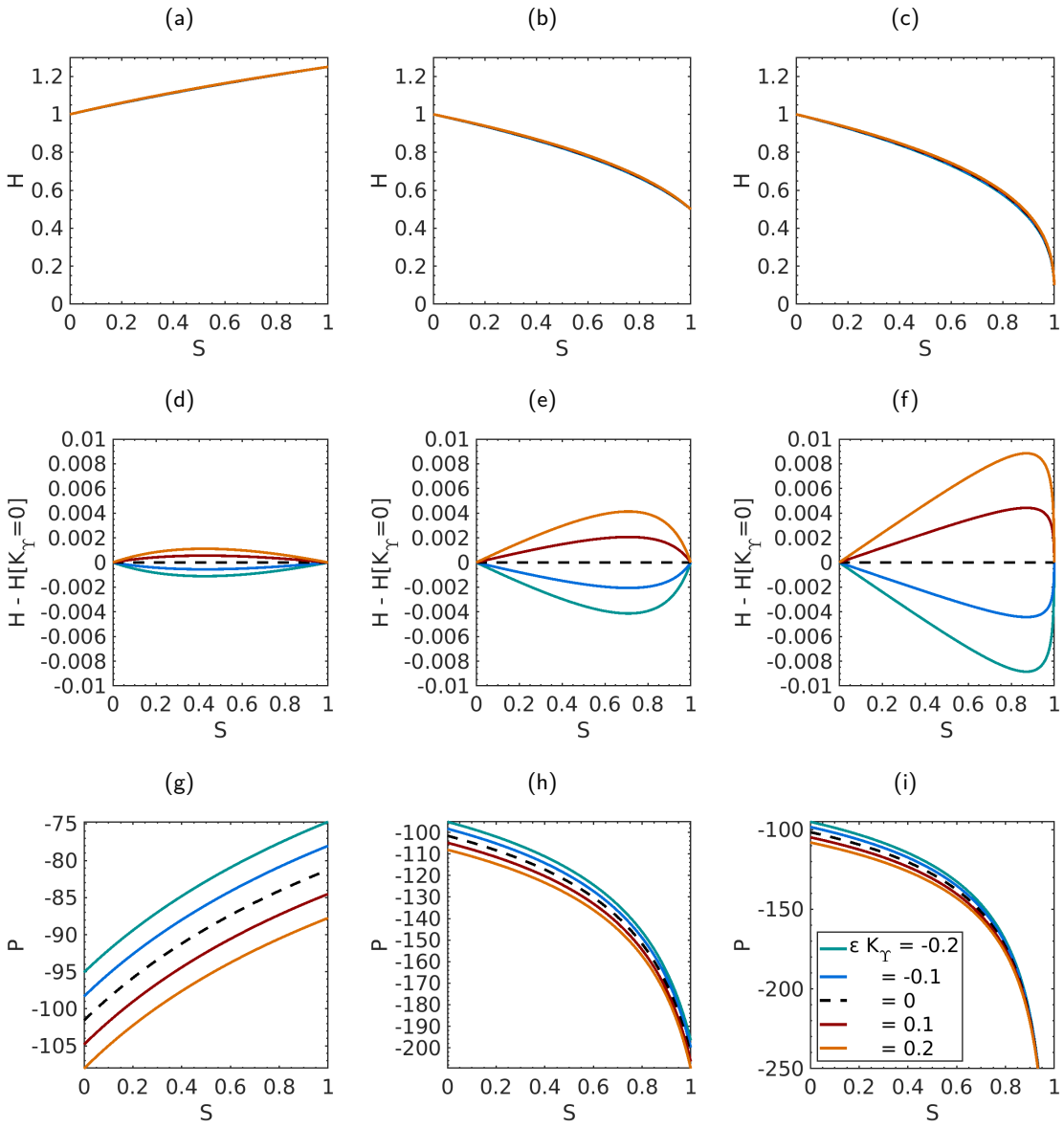

Figure 7.17: Representative steady state solutions of flow in V-grooves of constant curvature with groove half angle $\alpha = 15^\circ$, contact angle $\theta = 15^\circ$, and Dirichlet film thickness (H) boundary conditions, according to Equation (7.108). Results are plotted for grooves with 5 different values of vertical curvatures, $\varepsilon K_\Upsilon \in \{-0.2, -0.1, 0, 0.1, 0.2\}$. In each plot, the horizontal axis is S, the nondimensional backbone arc length.

Plots (a)-(c) (top row) display nondimensional fluid midline thickness, H. Plots (d)-(f) (middle row) display the difference between nondimensional fluid midline thickness, H, and that of a straight V-groove, $H[K_\Upsilon = 0]$. Plots (g)-(i) (bottom row) display nondimensional pressure, P. Each column displays a different boundary condition: column 1 [(a), (d), (g)] has boundary conditions $H(S = 0) = 1$ and $H(S = 1) = 1.25$; column 2 [(b), (e), (h)], has boundary conditions $H(S = 0) = 1$ and $H(S = 1) = 0.5$; column 3 [(c), (f), (i)] has boundary conditions $H(S = 0) = 1$ and $H(S = 1) = 0.1$.

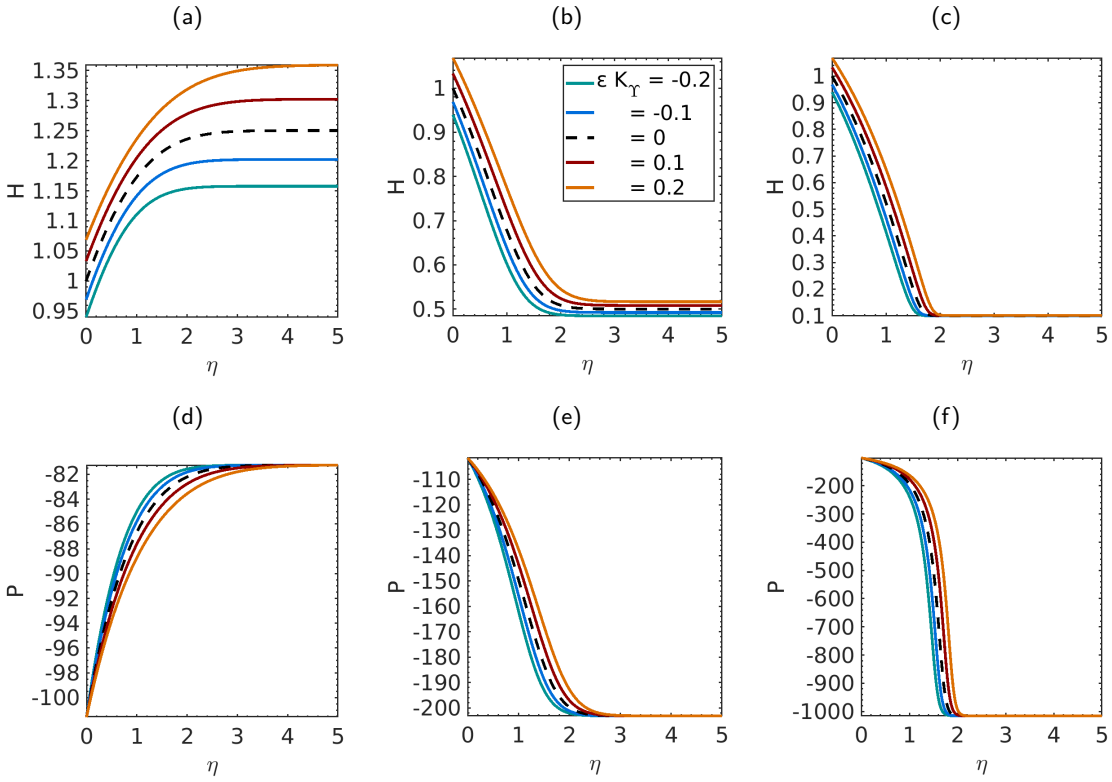

Figure 7.18: Representative self-similar solutions of flow in V-grooves of constant curvature with groove half angle $\alpha = 15°$, contact angle $\theta = 15°$, and Dirichlet pressure (P) boundary conditions, computed according to Equation (7.119). Results are plotted for grooves with 5 different values of vertical curvatures, $\varepsilon K_\Upsilon \in \{-0.2, -0.1, 0, 0.1, 0.2\}$. In each plot, the horizontal axis is the self-similar coordinate $\eta = S/\sqrt{T}$, where S is the nondimensional backbone arc length and T is the nondimensional time.

Plots (a)-(c) (top row) display nondimensional fluid midline thickness, H. Plots (d)-(f) (bottom row) display nondimensional pressure, P.

Each column displays a different boundary condition: column 1, (a) and (d), has boundary conditions $P(\eta = 0) = -101.58$ and $P(\eta = 5) = -81.262$; column 2, (b) and (e), has boundary conditions $P(\eta = 0) = -101.58$ and $P(\eta = 5) = -203.16$; column 3, (c) and (f), has boundary conditions $P(\eta = 0) = -101.58$ and $P(\eta = 5) = -1015.8$. These values of P were chosen so that the straight groove (with $K_\Upsilon = 0$) would have film midline thickness $H(\eta = 0) = 1$ and $H(\eta = 5) \in \{1.25, 0.5, 0.1\}$.

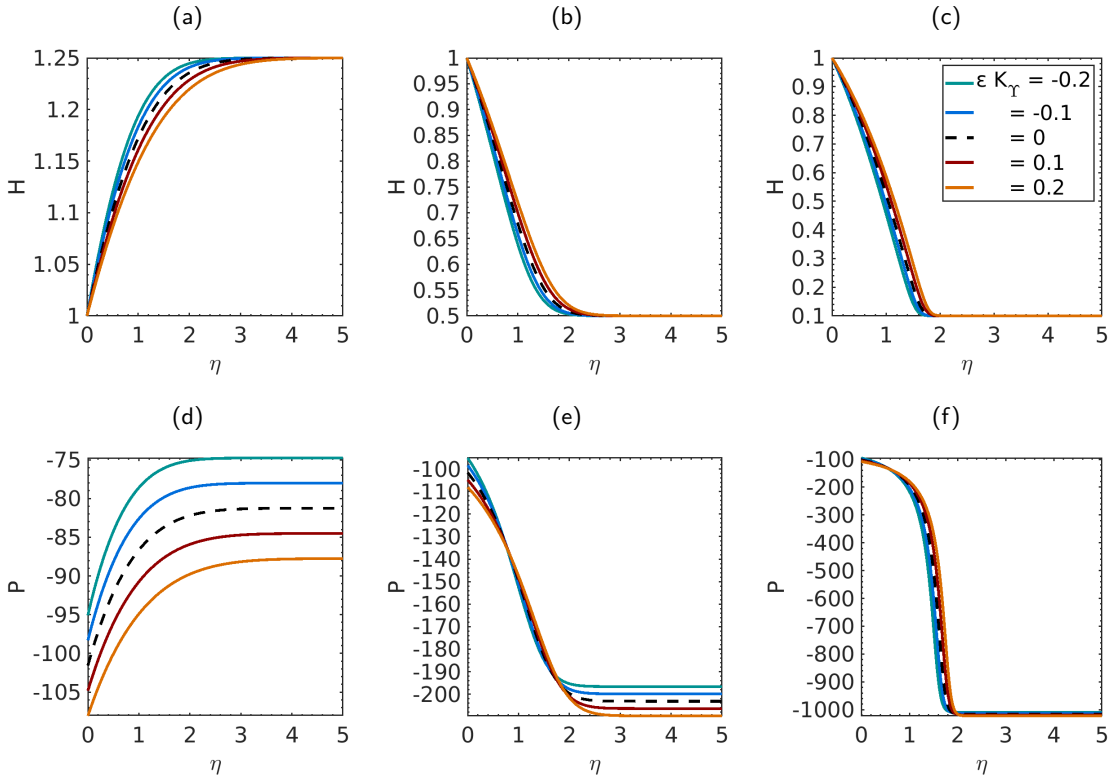

Figure 7.19: Representative self-similar solutions of flow in V-grooves of constant curvature with groove half angle $\alpha = 15^\circ$, contact angle $\theta = 15^\circ$, and Dirichlet midline thickness (H) boundary conditions, computed according to Equation (7.119). Results are plotted for grooves with 5 different values of vertical curvatures, $\varepsilon K_\Upsilon \in \{-0.2, -0.1, 0, 0.1, 0.2\}$. In each plot, the horizontal axis is the self-similar coordinate $\eta = S/\sqrt{T}$, where S is the nondimensional backbone arc length and T is the nondimensional time.
Plots (a)-(c) (top row) display nondimensional fluid midline thickness, H. Plots (d)-(f) (bottom row) display nondimensional pressure, P.
Each column displays a different boundary condition: column 1, (a) and (d), has boundary conditions $H(\eta = 0) = 1$ and $H(\eta = 5) = 1.25$; column 2, (b) and (e), has boundary conditions $H(\eta = 0) = 1$ and $H(\eta = 5) = 0.5$; column 3, (c) and (f), has boundary conditions $H(\eta = 0) = 1$ and $H(\eta = 5) = 0.1$.

7.7.2 Time-dependent numerical simulations

Figures 7.20 to 7.22 show the time evolution of pre-filled grooves with Dirichlet pressure boundary conditions with different backbone curvatures. All cases are shown for grooves with internal half angle $\alpha = 45^\circ$ and contact angle $\theta = 15^\circ$, and pressure conditions $P(S = 0) = -15.217$ and $P(S = 1) = -30.434$ (chosen to make $H(S = 0) = 1$ and $H(S = 1) = 0.5$ for the grooves with zero curvature). Each simulation took an initial condition of a pre-filled groove with uniform fluid thickness except for a small region near $S = 0$ to smoothly connect to the $S = 0$ boundary condition, and simulations were run from $T = 0$ to $T = 10$, a large enough value for the result to be visually indistinguishable from the steady state (the same steady states shown in Figure 7.9 and Figure 7.11). Figure 7.20 compares a positive backbone, with $\varepsilon = 0.1$ and $K_\Upsilon = 1$ to the straight groove; Figure 7.21 does the same with a negative backbone, $\varepsilon = 0.1$ and $K_\Upsilon = -1$; and Figure 7.22 does so with a sinusoidal backbone, $\beta(z) = \{0, 0.001 \sin(6\pi z), z\}$ with $\varepsilon = 0.1$.

As described earlier, grooves with positive curvature at a given pressure P have greater fluid thickness H than straight grooves or grooves with negative curvature. It can be seen from Figure 7.20 that fluid advances faster in a positively-curved groove than a straight groove; Figure 7.21 shows in turn that the fluid advances faster in a straight groove than a negatively-curved groove. This effect is likely due to the increased flux in grooves with positive curvature for given pressure boundary conditions, as computed in Section 7.3.2.

The speed of reaching steady state appears comparable between the sinusoidal groove and the straight groove (Figure 7.22), as the effect of the intermittently positive and negative curvature appears to effectively balance out.

The time-dependent interface evolution equations were also computed with the finite element method in COMSOL (Com, 2017) by solving Equation (7.101) in a domain with elements 0.1% the length of the domain (giving exactly 1000 elements, since this problem has a one-dimensional domain).

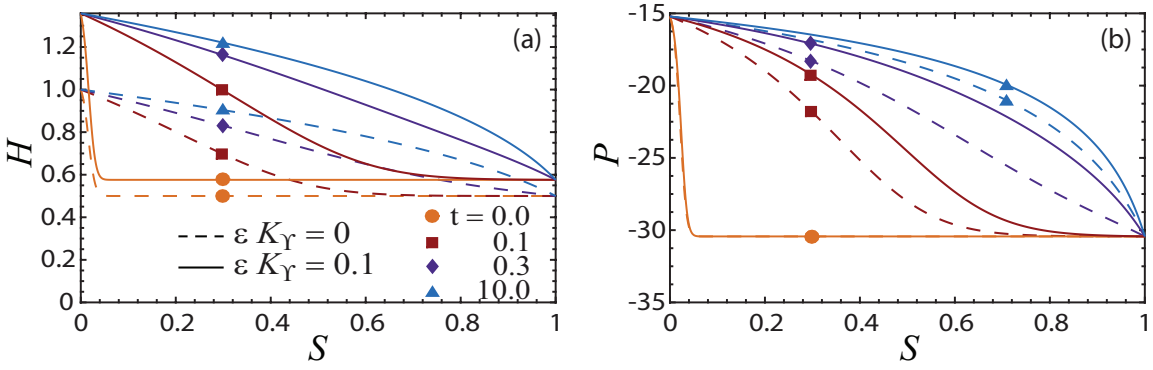

Figure 7.20: Example time-dependent solutions of flow in V-grooves with groove half angle $\alpha = 45°$, contact angle $\theta = 15°$, and Dirichlet pressure (P) boundary conditions, $P(S = 0) = -15.217$, $P(S = 1) = -30.434$, chosen so that a straight V-groove has $H(S = 0) = 1$ and $H(S = 1) = 0.5$. Results are computed following Equation (7.101), and compare a straight ($K_\Upsilon = 0$) V-groove to one with constant positive backbone curvature $\varepsilon K_\Upsilon = 0.1$. Snapshots in time are shown at $t \in \{0.0, 0.1, 0.3, 10.0\}$; by the last time, the flow is visually indistinguishable from the steady state solution. In each plot, the horizontal axis is S, the nondimensional backbone arc length.
(a): Nondimensional fluid midline thickness, H.
(b): Nondimensional pressure, P.

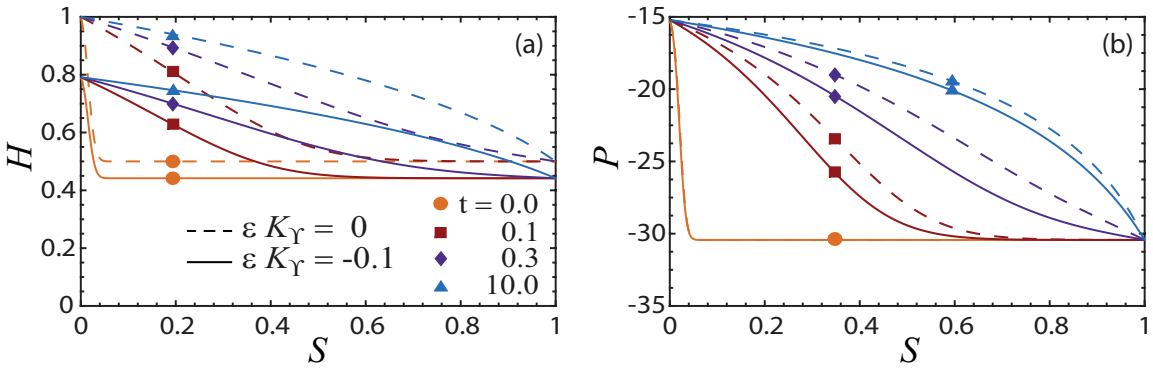

Figure 7.21: Example time-dependent solutions of flow in V-grooves with groove half angle $\alpha = 45°$, contact angle $\theta = 15°$, and Dirichlet pressure (P) boundary conditions, $P(S = 0) = -15.217$, $P(S = 1) = -30.434$, chosen so that a straight V-groove has $H(S = 0) = 1$ and $H(S = 1) = 0.5$. Results are computed following Equation (7.101), and compare a straight ($K_\Upsilon = 0$) V-groove to one with constant negative backbone curvature $\varepsilon K_\Upsilon = -0.1$. Snapshots in time are shown at $t \in \{0.0, 0.1, 0.3, 10.0\}$; by the last time, the flow is visually indistinguishable from the steady state solution. In each plot, the horizontal axis is S, the nondimensional backbone arc length.
(a): Nondimensional fluid midline thickness, H.
(b): Nondimensional pressure, P.

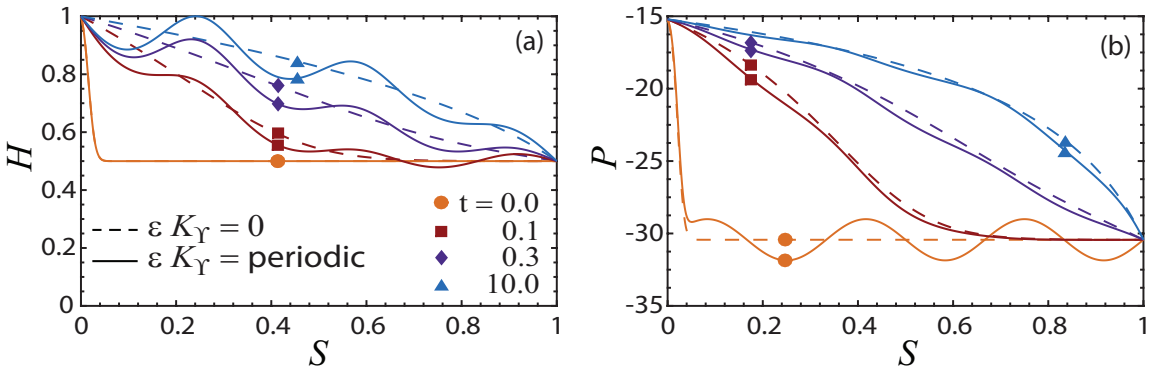

Figure 7.22: Example time-dependent solutions of flow in V-grooves with groove half angle $\alpha = 45°$, contact angle $\theta = 15°$, and Dirichlet pressure (P) boundary conditions, $P(S = 0) = -15.217$, $P(S = 1) = -30.434$, chosen so that a straight V-groove has $H(S = 0) = 1$ and $H(S = 1) = 0.5$. Results are computed following Equation (7.101), and compare a straight ($K_\Upsilon = 0$) V-groove to a V-groove with vertical sinusoidal variation. The sinusoidal V-groove has backbone coordinates $\vec{\beta} = \{0, 0.001\sin(6\pi z), z\}$ and film inlet thickness such that $\varepsilon = 0.1$, resulting in nondimensional curvature $\varepsilon K_\Upsilon \approx -0.03553\sin(6\pi S) + O(0.01\%)$. Snapshots in time are shown at $t \in \{0.0, 0.1, 0.3, 10.0\}$; by the last time, the flow is visually indistinguishable from the steady state solution. In each plot, the horizontal axis is S, the nondimensional backbone arc length.
(a): Nondimensional fluid midline thickness, H.
(b): Nondimensional pressure, P.

References

MATLAB and Statistics Toolbox Release 2015a, The MathWorks, Inc., Natick, MA, USA, 2015. URL `https://www.mathworks.com/products/matlab.html`.

COMSOL Inc. Multiphysics V5.3a, Burlington, MA, USA, 2017. URL `https://www.comsol.com`.

R. Aris. Vectors, Tensors and the Basic Equations of Fluid Mechanics. Dover Publications, New York, 1989. ISBN 9780486661100.

M. J. Assael, I. J. Armyra, J. Brillo, S. V. Stankus, J. Wu, and W. A. Wakeham. Reference data for the density and viscosity of liquid cadmium, cobalt, gallium, indium, mercury, silicon, thallium, and zinc. J. Phys. Chem. Ref. Data, 41(3), 2012. ISSN 0047-2689. doi:10.1063/1.4729873.

P. S. Ayyaswamy, I. Catton, and D. K. Edwards. Capillary flow in triangular grooves. J. Appl. Mech., 41:332–336, 1974. doi:10.1115/1.3423288.

G. K. Batchelor. An Introduction to Fluid Dynamics. Cambridge Mathematical Library. Cambridge University Press, 2000. doi:10.1017/CBO9780511800955.

S. A. Berger, L. Talbot, and L. S. Yao. Flow in curved pipes. Annu. Rev. Fluid Mech., 15(1):461–512, January 1983. ISSN 0066-4189, 1545-4479. doi:10.1146/annurev.fl.15.010183.002333.

J. Berthier, K. A. Brakke, D. Gosselin, F. Navarro, N. Belgacem, and D. Chaussy. Spontaneous capillary flow in curved, open microchannels. Microfluidics and Nanofluidics, 20(7):100, 2016. doi:10.1007/s10404-016-1766-6.

R. S. Chadwick. Slow viscous flow inside a torus—the resistance of small tortuous blood vessels. Quart. Appl. Math., 43(3):317–323, 1985. ISSN 0033-569X, 1552-4485. doi:10.1090/qam/814230.

V. P. Chentsov, V. G. Shevchenko, A. G. Mozgovoi, and M. A. Pokrasin. Density and surface tension of heavy liquid-metal coolants: Gallium and indium. Inorg. Mater. Appl. Res., 2(5): 468–473, 2011. doi:10.1134/S2075113311050108.

P. Concus and R. Finn. On the behavior of a capillary surface in a wedge. Proc. Natl. Acad. Sci. USA, 63(2):292, 1969. doi:10.1073/pnas.63.2.292.

T. P. Cotter. Principles and prospects for micro heat pipes. In Proceedings of the 5th International Heat Pipe Conference, Tsukuba, Ibaraki, Japan, May 14-18, 1984, pages 328–335, Tsukuba, Ibaraki, Japan, 1984. URL `https://www.osti.gov/biblio/5246927`.

W. R. Dean. Note on the motion of fluid in a curved pipe. London Edinburgh Dublin Philos. Mag. J. Sci., 4(20):208–223, July 1927. ISSN 1941-5982, 1941-5990. doi:10.1080/14786440708564324.

M. Dong and I. Chatzis. The imbibition and flow of a wetting liquid along the corners of a square capillary tube. J. Colloid Interface Sci., 172(2):278–288, 1995. doi:10.1006/jcis.1995.1253.

M. Germano. On the effect of torsion on a helical pipe flow. J. Fluid Mech., 125(-1):1, December 1982. ISSN 0022-1120, 1469-7645. doi:10.1017/S0022112082003206.

J. W. Hartwig. A detailed historical review of propellant management devices for low gravity propellant acquisition. In Proceedings of the 52nd AIAA/SAE/ASEE Joint Propulsion Conference, Salt Lake City, UT, July 25-27, 2016, pages AIAA–16–4772. American Institute of Aeronautics and Astronautics, Reston, VA, 2016. doi:10.2514/6.2016-4772.

J. W. Hartwig. Propellant management devices for low-gravity fluid management: Past, present, and future applications. J. Spacecr. Rockets, 54:808–824, 2017. doi:10.2514/1.A33750.

J. M. Hill and Y. M. Stokes. A note on Navier-Stokes equations with nonorthogonal coordinates. ANZIAM J., 59(3):335–348, January 2018. ISSN 1446-1811, 1446-8735. doi:10.1017/S144618111700058X.

D. E. Jaekle. Propellant management device conceptual design and analysis: Vanes. In AIAA/SAE/ASME/ASEE 27th Joint Propulsion Conference, June 24-26, 1991, Sacramento, CA, pages AIAA–91–2172. American Institute of Aeronautics and Astronautics, Reston, VA, 1991. doi:10.2514/6.1991-2172.

R. Lenormand and C. Zarcone. Role of roughness and edges during imbibition in square capillaries. In Proceedings of the 59th Annu. Tech. Conference & Exhibit, Houston, TX, Sept. 16-19, 1984, pages SPE–13264. American Institute of Mining, Metallurgical and Petroleum Engineers, Inc., Englewood, CO, 1984. doi:10.2118/13264-MS.

D. Levine, B. Wise, R. Schulman, H. Gutierrez, D. Kirk, N. Turlesque, W. Tam, M. Bhatia, and D. Jaekle. Surface tension and contact angle analysis with design of propellant measurement apparatus. J. Propul. Power, 31(1):429–443, 2015. doi:10.2514/1.B35213.

H. Luo and T. R. Bewley. On the contravariant form of the Navier–Stokes equations in time-dependent curvilinear coordinate systems. J. Comp. Phys., 199(1):355–375, September 2004. ISSN 00219991. doi:10.1016/j.jcp.2004.02.012.

A. K. Mallik, G. P. Peterson, and M. H. Weichold. On the use of micro heat pipes as an integral part of semiconductor devices. J. Electron. Packaging, 114(4):436–442, 1992. doi:10.1115/1.2905477.

S. Murata, Y. Miyake, and T. Inaba. Laminar flow in a curved pipe with varying curvature. J. Fluid Mech., 73(4):735–752, February 1976. ISSN 0022-1120, 1469-7645. doi:10.1017/S0022112076001596.

M. Norouzi and N. Biglari. An analytical solution for Dean flow in curved ducts with rectangular cross section. Phys. Fluids, 25(5):053602, May 2013. ISSN 1070-6631, 1089-7666. doi:10.1063/1.4803556.

G. P. Peterson, A. B. Duncan, and M. H. Weichold. Experimental investigation of micro heat pipes fabricated in silicon wafers. J. Heat Trans. T. ASME, 115:751–751, 1993. doi:10.1115/1.2910747.

J. Qu, H. Wu, P. Cheng, Q. Wang, and Q. Sun. Recent advances in mems-based micro heat pipes. Int. J. Heat Mass Trans., 110:294–313, 2017. doi:10.1016/j.ijheatmasstransfer.2017.03.034.

J. R. Rollins, R. K. Grove, and D. E. Jaekle. Twenty-three years of surface tension propellant management system design, development, manufacture, test, and operation. In A. I. of Aeronautics and V. Astronautics, Reston, editors, AIAA 21st Joint Propulsion Conference, Monterey, CA, July 8-10, 1985, pages AIAA–85–1199, 1985. doi:10.2514/6.1985-1199.

L. A. Romero and F. G. Yost. Flow in an open channel capillary. J. Fluid Mech., 322:109–129, 1996. doi:10.1017/S0022112096002728.

R. V. Roy, A. J. Roberts, and M. E. Simpson. A lubrication model of coating flows over a curved substrate in space. J. Fluid Mech., 454:235–261, 2002. ISSN 0022-1120. doi:10.1017/S0022112001007133.

M. B. Rubin. Cosserat Theories: Shells, Rods and Points. Solid Mechanics and Its Applications. Springer Netherlands, 2000. doi:10.1007/978-94-015-9379-3.

M. Rumpf and O. Vantzos. Numerical gradient flow discretization of viscous thin films on curved geometries. Math. Models Methods Appl. Sci., 23(05):917–947, 2013. doi:10.1142/S0218202512500649.

L. W. Schwartz and D. E. Weidner. Modeling of coating flows on curved surfaces. J. Eng. Math., 29(1):91–103, 1995. doi:10.1007/BF00046385.

Y. M. Stokes, B. R. Duffy, S. K. Wilson, and H. Tronnolone. Thin-film flow in helically wound rectangular channels with small torsion. Phys. Fluids, 25(8):083103, August 2013. ISSN 1070-6631, 1089-7666. doi:10.1063/1.4818628.

H. Tougou. Long waves on a film flow of a viscous fluid down an inclined uneven wall. J. Phys. Soc. Japan, 44(3):1014–1019, March 1978. ISSN 0031-9015, 1347-4073. doi:10.1143/JPSJ.44.1014.

E. R. Tuttle. Laminar flow in twisted pipes. J. Fluid Mech., 219(-1):545, October 1990. ISSN 0022-1120, 1469-7645. doi:10.1017/S002211209000307X.

J. L. Vázquez. The Porous Medium Equation: Mathematical Theory. Oxford Science Publications. Clarendon Press, 2007. ISBN 9780198569039. doi:10.1093/acprof:oso/9780198569039.001.0001.

P. R. Voke and M. W. Collins. Forms of the generalised Navier-Stokes equations. J. Eng. Math., 18(3):219–233, September 1984. ISSN 0022-0833, 1573-2703. doi:10.1007/BF00039190.

C. Y. Wang. Flow in narrow curved channels. J. Appl. Mech., 47(1):7–10, March 1980. ISSN 0021-8936, 1528-9036. doi:10.1115/1.3153642.

C. Y. Wang. Liquid film flowing slowly down a wavy incline. AIChE J., 27(2):207–212, March 1981a. ISSN 0001-1541, 1547-5905. doi:10.1002/aic.690270206.

C. Y. Wang. On the low-Reynolds-number flow in a helical pipe. J. Fluid Mech., 108:185–194, July 1981b. ISSN 0022-1120, 1469-7645. doi:10.1017/S0022112081002073.

C. Y. Wang. Stokes flow in a curved duct – A Ritz method. Comput. Fluids, 53:145–148, January 2012. ISSN 00457930. doi:10.1016/j.compfluid.2011.10.010.

M. M. Weislogel. Capillary flow in an interior corner. PhD thesis, Northwestern University, June 1996. URL `https://ntrs.nasa.gov/citations/19970010346`. Also published as NASA Technical Memorandum 107364.

M. M. Weislogel and S. Lichter. Capillary flow in an interior corner. J. Fluid Mech., 373: 349–378, 1998. doi:10.1017/S0022112098002535.

Z. Wu, Y. Huang, X. Chen, and X. Zhang. Capillary-driven flows along curved interior corners. Int. J. Multiphase Flow, 109:14–25, 2018. doi:10.1016/j.ijmultiphaseflow.2018.04.004.

L. Yang and G. M. Homsy. Steady three-dimensional thermocapillary flows and dryout inside a v-shaped wedge. Phys. Fluids, 18:042107, 2006. doi:10.1063/1.2193471.

Part III

Thin films on curved substrates

Chapter 8

INTRODUCTION TO THIN FILMS ON CURVED SUBSTRATES

8.1 Background

In Chapter 9, we will perform a novel study of the capillary instabilities arising on a viscous thin film coating a torus, and will find some rather interesting and unintuitive results. The torus study will rely upon a low-order model describing the behavior of thin films on curved substrates, first developed by Roy and Schwartz (1997) and Roy et al. (2002). In the present chapter, we explain and derive that low order model. We present a step-by-step derivation which fills in the gaps missing in the publications of Roy and Schwartz (1997) and Roy et al. (2002). We also employ a covariant notation and, unlike Roy et al. (2002), do not assume any specific parametrization of the substrate.

Recall that the derivation of the V-groove equation (Romero and Yost, 1996; Weislogel, 1996) in Chapter 4 depended upon the *slender limit*, in which one dimension (z) was assumed to be much longer than the other two dimensions (x and y). By considering only long-wavelength phenomena in z (that is, by considering only the infrared limit in z), the Navier-Stokes equations were simplified and a reduced-order model was produced, with the dependent variable being the centerline fluid thickness in the groove. That slender limit derivation owes its origin to the so-called *lubrication limit*, the difference being that in lubrication theory a thin film has not two short dimensions and one long dimension, but instead one short and two long dimensions.

Lubrication theory was first developed (and named) by Reynolds (1886) to describe fluid flow between two solid walls at close proximity, in order to describe the behavior of mechanical devices lubricated with oil. The original paper by Reynolds also discussed lubrication of cylindrical objects, and the following decades saw a variety of extensions developed, considering lubrication between elastic solids, temperature dependent effects, and lubrication of walls with discontinuous steps; an early overview of the field may be found in the textbook on lubrication theory by Pinkus and Sternlicht (1961).

While the original lubrication theory was developed for a fluid bounded by two solids, it can easily be modified to consider a thin film bounded by a solid on one side and a vacuum or second fluid on the other. A reduced-order lubrication model for a thin film with a free surface, with film thickness h as the only dependent variable, was developed by Jeffreys (1930) to describe the flow of a viscous thin film down a vertical plate. Jeffreys's model was driven only by gravity, omitting surface tension and other factors; a similar equation with surface tension as the dominant force was known at least by the time of Orchard (1963), who demonstrated linear

stability for such flows[1]. Many variations on these thin film equations were developed in the following decades, including Van der Waals forces in nanofilms, Marangoni effects (variations in surface tension due to, e.g., surfactants), and thermocapillary effects (variations in surface tension due to temperature gradients); the interested reader is referred to the review article by Oron et al. (1997).

Early lubrication and thin film analyses focused on liquids coating flat or cylindrical substrates (both were discussed in the original work by Reynolds, 1886). Among the first studies considering a more general geometry was a lubrication theory describing a thin film with a free surface flowing over a shallow and long-wavelength but otherwise arbitrary topography, developed independently by Smith (1969a) and Smith (1969b)[2]. The Smiths' theory described slightly bumpy but predominantly flat surfaces; it was not until the work of Schwartz and Weidner (1995) that a model for thin films coating highly curved substrates was developed. Schwartz and Weidner's approach was to write down the capillary-driven thin film equation for a flat substrate and add a correction to the capillary pressure to account for the additional interface curvature induced by the film coating a curved substrate. This model explained phenomena such as the thinning of films coating exterior corners. While effective on a qualitative level, the model did not accurately capture the interfacial curvature and ignored the modifications to the fluid velocity profile caused by flowing over a curved substrate; these shortcomings were addressed in the model of Roy et al. (2002), who carried out a rigorous perturbation expansion of the Navier-Stokes equations using lubrication theory. Roy et al. furthermore included gravity as well as surface tension.

Rumpf and Vantzos (2013) noticed that thin film flow even on curved substrates can be expressed as a gradient flow, and they proceeded to derive the equation of motion for film thickness from variational principles, a process which yielded the same result as Roy et al. (2002). Wray et al. (2017) developed a model with a higher-order expansion to allow for description of relatively thicker films. Roberts and Li (2006) (Roberts being a coauthor on the Roy et al., 2002 paper) later expanded upon their earlier work with a continued perturbation expansion including the Reynolds number.

We will take the approach of Roy and Schwartz (1997) and Roy et al. (2002) in performing a formal perturbation expansion of the Navier-Stokes equations for a viscous film coating a curved substrate in the lubrication limit. Unlike prior work, our derivation will use a general tensorial system and covariant notation. By providing a full, step-by-step derivation, we hope that future students will have an easier time working with and extending the model.

[1] Orchard wrote down the thin film equation $\partial h/\partial t = -(\gamma/\mu)\partial_x(h^3\partial_x^3 h/3)$ and attributes its first stability analysis to a private communication by F. C. Roesler. I have not found an earlier source, but Orchard does not appear to claim discovery of the equation.

[2] Two distinct Smiths appear to have coincidentally derived the same equation and submitted it to the same journal within two weeks of each other.

8.2 Coordinates

8.2.1 Substrate parametrization

The thin film equation will describe the fluid interface as a height field h, measured normal to the curved substrate. One might be concerned that setting up a coordinate normal to the curved substrate could lead to overlap, and this is indeed the case in general. Overlap is avoided, however, if the system remains sufficiently close to the substrate. Specifically, as long as the region of interest normal to the substrate is always less than the local radius of curvature, no coordinate overlap can occur. In fact, the lubrication limit assumption is already going to require that the film thickness be less than the substrate radius of curvature, so the no-overlap condition is automatically satisfied.

The development of local coordinates will proceed in the same manner as in Section 2.1, following the methodology commonly used in shell theory (Niordson, 1985). Consider some two dimensional curved substrate embedded in $\mathbb{R}^3$, specified by $\vec{x}_0(\xi,\zeta)$, i.e., parametrized by the two coordinates ξ and ζ. The induced metric (first fundamental form) on this manifold, is given by

$$\widetilde{g}_{\alpha\beta} = \begin{bmatrix} (\partial_\xi \vec{x}_0 \cdot \partial_\xi \vec{x}_0) & (\partial_\xi \vec{x}_0 \cdot \partial_\zeta \vec{x}_0) \\ (\partial_\zeta \vec{x}_0 \cdot \partial_\xi \vec{x}_0) & (\partial_\zeta \vec{x}_0 \cdot \partial_\zeta \vec{x}_0) \end{bmatrix}. \tag{8.1}$$

Defining a vector normal to the substrate by

$$\hat{\upsilon} \equiv \frac{\partial_\xi \vec{x}_0 \times \partial_\zeta \vec{x}_0}{|\partial_\xi \vec{x}_0 \times \partial_\zeta \vec{x}_0|}, \tag{8.2}$$

the shape tensor, or second fundamental form, can be expressed as

$$\mathrm{I\!I}_{\alpha\beta} = \begin{bmatrix} (\partial_{\xi\xi} \vec{x}_0 \cdot \hat{\upsilon}) & (\partial_{\xi\zeta} \vec{x}_0 \cdot \hat{\upsilon}) \\ (\partial_{\zeta\xi} \vec{x}_0 \cdot \hat{\upsilon}) & (\partial_{\zeta\zeta} \vec{x}_0 \cdot \hat{\upsilon}) \end{bmatrix} = - \begin{bmatrix} (\partial_\xi \vec{x}_0 \cdot \partial_\xi \hat{\upsilon}) & (\partial_\xi \vec{x}_0 \cdot \partial_\zeta \hat{\upsilon}) \\ (\partial_\zeta \vec{x}_0 \cdot \partial_\xi \hat{\upsilon}) & (\partial_\zeta \vec{x}_0 \cdot \partial_\zeta \hat{\upsilon}) \end{bmatrix}. \tag{8.3}$$

This leads to the matrix relation

$$\begin{pmatrix} \partial_\xi \hat{\upsilon} \\ \partial_\zeta \hat{\upsilon} \end{pmatrix} = -\mathrm{I\!I} \widetilde{g}^{-1} \begin{pmatrix} \partial_\xi \vec{x}_0 \\ \partial_\zeta \vec{x}_0 \end{pmatrix}. \tag{8.4}$$

The mean curvature is defined as $\kappa_m \equiv \frac{1}{2} \mathrm{I\!I}^\mu{}_\mu$, and the Gaussian curvature by $\kappa_G \equiv \det(\mathrm{I\!I}^\mu{}_\nu)$. With these definitions, higher powers of $\mathrm{I\!I}$ can be simplified by making use of the quadratic identity

$$\mathrm{I\!I}^{\mu\alpha} \mathrm{I\!I}_{\alpha\nu} = 2\kappa_m \mathrm{I\!I}^\mu{}_\nu - \kappa_G \widetilde{g}^\mu{}_\nu \tag{8.5}$$

(Aris, 1989).

8.2.2 3D coordinates

Introducing a new coordinate υ normal to the substrate allows one to define manifold-centric coordinates: 3D coordinates in $\mathbb{R}^3$ which reduce to the 2D manifold coordinates at $\upsilon = 0$. This is the same setup used in Section 2.1, and in shell theory (Niordson, 1985).

$$\vec{x}(\xi, \zeta, \upsilon) \equiv \vec{x}_0(\xi, \zeta) + \upsilon \hat{v}(\xi, \zeta). \tag{8.6}$$

The metric on the 3D space (denoted by g without a tilde) is

$$\begin{aligned} g_{ij} &= \begin{bmatrix} (\partial_\xi \vec{x}_0 + \upsilon \partial_\xi \hat{v}) \cdot (\partial_\xi \vec{x}_0 + \upsilon \partial_\xi \hat{v}) & (\partial_\xi \vec{x}_0 + \upsilon \partial_\xi \hat{v}) \cdot (\partial_\zeta \vec{x}_0 + \upsilon \partial_\zeta \hat{v}) & 0 \\ (\partial_\xi \vec{x}_0 + \upsilon \partial_\xi \hat{v}) \cdot (\partial_\zeta \vec{x}_0 + \upsilon \partial_\zeta \hat{v}) & (\partial_\zeta \vec{x}_0 + \upsilon \partial_\zeta \hat{v}) \cdot (\partial_\upsilon \vec{x}_0 + \upsilon \partial_\upsilon \hat{v}) & 0 \\ 0 & 0 & \hat{v} \cdot \hat{v} \end{bmatrix} \\ &= \begin{bmatrix} \left(\delta_\alpha{}^\nu - \upsilon \mathrm{I\!I}_\alpha{}^\nu\right) \widetilde{g}_{\nu\rho} \left(\delta^\rho{}_\beta - \upsilon \mathrm{I\!I}^\rho{}_\beta\right) & 0 \\ 0 \quad 0 & 1 \end{bmatrix} \\ &= \begin{bmatrix} \widetilde{g}_{\alpha\beta} - 2\upsilon \mathrm{I\!I}_{\alpha\beta} + \upsilon^2 \mathrm{I\!I}_{\alpha\rho} \mathrm{I\!I}^\rho{}_\beta & 0 \\ 0 \quad 0 & 1 \end{bmatrix} \end{aligned} \tag{8.7}$$

(Niordson, 1985). The inverse metric is

$$\begin{aligned} g^{ij} &= \begin{bmatrix} \frac{\widetilde{g}^{\mu\nu}(1-\upsilon \mathrm{I\!I}^\alpha{}_\alpha)^2 + 2\upsilon \mathrm{I\!I}^{\mu\nu}(1-\upsilon \mathrm{I\!I}^\alpha{}_\alpha) + \upsilon^2 \mathrm{I\!I}^{\mu\alpha} \mathrm{I\!I}_\alpha{}^\nu}{\left[1-\upsilon \mathrm{I\!I}^\alpha{}_\alpha + \upsilon^2 \det\left(\mathrm{I\!I}^\alpha{}_\beta\right)\right]^2} & 0 \\ 0 \quad 0 & 1 \end{bmatrix} \\ &= \begin{bmatrix} \frac{\widetilde{g}^{\mu\nu} + 2\upsilon\left(\mathrm{I\!I}^{\mu\nu} - \mathrm{I\!I}^\alpha{}_\alpha \widetilde{g}^{\mu\nu}\right) + \upsilon^2\left(\mathrm{I\!I}^\alpha{}_\alpha \mathrm{I\!I}^\rho{}_\rho \widetilde{g}^{\mu\nu} - 2\mathrm{I\!I}^\alpha{}_\alpha \mathrm{I\!I}^{\mu\nu} + \mathrm{I\!I}^{\mu\alpha} \mathrm{I\!I}_\alpha{}^\nu\right)}{\left[1-\upsilon \mathrm{I\!I}^\alpha{}_\alpha + \upsilon^2 \det\left(\mathrm{I\!I}^\alpha{}_\beta\right)\right]^2} & 0 \\ 0 \quad 0 & 1 \end{bmatrix} \\ &= \begin{bmatrix} \widetilde{g}^{\mu\nu} + 2\upsilon \mathrm{I\!I}^{\mu\nu} + 3\upsilon^2 \mathrm{I\!I}^{\mu\alpha} \mathrm{I\!I}_\alpha{}^\nu + 4\upsilon^3 \mathrm{I\!I}^{\mu\alpha} \mathrm{I\!I}_{\alpha\beta} \mathrm{I\!I}^{\beta\nu} + O\left((\mathrm{I\!I}\upsilon)^4\right) & 0 \\ 0 \quad 0 & 1 \end{bmatrix}. \end{aligned} \tag{8.8}$$

8.2.3 Covariant derivatives and Christoffel symbols

Unless otherwise stated, Greek indices will be used for tensors on the 2D substrate, such as $\widetilde{g}_{\alpha\beta}$ and $\mathrm{I\!I}_{\alpha\beta}$, and Latin indices for tensors in $\mathbb{R}^3$, such as g_{ij}.

The Christoffel symbols are given below:

$$\Gamma^{\upsilon}_{\upsilon\upsilon} = \Gamma^{\upsilon}_{\alpha\upsilon} = \Gamma^{\alpha}_{\upsilon\upsilon} = 0 \tag{8.9a}$$

$$\begin{aligned}\Gamma^{\upsilon}_{\alpha\beta} &= \frac{1}{2}g^{\upsilon\upsilon}\left(g_{\upsilon\alpha,\beta} + g_{\upsilon\beta,\alpha} - g_{\alpha\beta,\upsilon}\right) = -\frac{1}{2}g_{\alpha\beta,\upsilon} \\ &= \mathrm{I\!I}_{\alpha\beta} - \upsilon \mathrm{I\!I}_{\alpha\rho}\mathrm{I\!I}^{\rho}{}_{\beta} \\ &= \mathrm{I\!I}_{\alpha\beta} - \upsilon\left(2\kappa_m \mathrm{I\!I}_{\alpha\beta} - \kappa_G \widetilde{g}_{\alpha\beta}\right)\end{aligned} \tag{8.9b}$$

$$\begin{aligned}\Gamma^{\alpha}_{\upsilon\beta} &= \frac{1}{2}g^{\alpha\mu}\left(g_{\mu\upsilon,\beta} + g_{\mu\beta,\upsilon} - g_{\beta\upsilon,\mu}\right) = \frac{1}{2}g^{\alpha\mu}g_{\mu\beta,\upsilon} \\ &= -\mathrm{I\!I}^{\alpha}{}_{\beta} - \upsilon \mathrm{I\!I}^{\alpha\mu}\mathrm{I\!I}_{\mu\beta} - \upsilon^2 \mathrm{I\!I}^{\alpha\mu}\mathrm{I\!I}_{\mu\nu}\mathrm{I\!I}^{\nu}{}_{\beta} + O\left((\mathrm{I\!I}\upsilon)^4\right)\end{aligned} \tag{8.9c}$$

$$\begin{aligned}\Gamma^{\alpha}_{\sigma\beta} &= \frac{1}{2}g^{\alpha\mu}\left(g_{\mu\sigma,\beta} + g_{\mu\beta,\sigma} - g_{\beta\sigma,\mu}\right) \\ &= \widetilde{\Gamma}^{\alpha}_{\sigma\beta} - \upsilon\overline{\nabla}^{\alpha}\mathrm{I\!I}_{\sigma\beta} - \upsilon^2 \mathrm{I\!I}^{\alpha\mu}\overline{\nabla}_{\mu}\mathrm{I\!I}_{\sigma\beta} + O\left((\mathrm{I\!I}\upsilon)^3\right),\end{aligned} \tag{8.9d}$$

where $\widetilde{\Gamma}$ denotes the Christoffel symbols of the 2D manifold space.

8.3 Nondimensionalization

Let d be the characteristic film thickness (and thus the characteristic scale in the υ direction), and let L be the minimum radius of curvature of the substrate (providing a characteristic scale in the ξ and ζ directions). Defining $\varepsilon \equiv d/L$, we shall require that $\varepsilon \ll 1$. Expanding the Navier-Stokes equations in small ε is known as lubrication theory, and is the foundation of thin film theory (Oron et al., 1997; Reynolds, 1886). The lubrication limit is very similar to the slender limit seen in Chapter 4, except that here we have one small dimension instead of two.

Based on our definition of L as the minimum substrate radius of curvature, we nondimensionalize the shape tensor by $\mathrm{I\!I} = \mathrm{I\!I}L$. The nondimensional 2D covariant derivative on the manifold will be denoted by $\nabla_\alpha = L\overline{\nabla}_\alpha$ and the 2D Christoffel symbol by $\breve{\Gamma} = L\widetilde{\Gamma}$.

Note that the *dimensional* 3D Christoffel symbols now have the following scalings

$$\Gamma^{\upsilon}_{\upsilon\upsilon} = \Gamma^{\upsilon}_{\alpha\upsilon} = \Gamma^{\alpha}_{\upsilon\upsilon} = 0 \tag{8.10}$$

$$\Gamma^{\upsilon}_{\alpha\beta} = \frac{1}{L}\left[\mathrm{I\!I}_{\alpha\beta} - \varepsilon\Upsilon\mathrm{I\!I}_{\alpha\rho}\mathrm{I\!I}^{\rho}{}_{\beta}\right] \tag{8.11}$$

$$\Gamma^{\alpha}_{\upsilon\beta} = \frac{1}{L}\left[-\mathrm{I\!I}^{\alpha}{}_{\beta} - \varepsilon\Upsilon\mathrm{I\!I}^{\alpha}{}_{\mu}\mathrm{I\!I}^{\mu}{}_{\beta} + O\left(\varepsilon^2\right)\right] \tag{8.12}$$

$$\Gamma^{\alpha}_{\sigma\beta} = \frac{1}{L}\left[\breve{\Gamma}^{\alpha}_{\sigma\beta} - \varepsilon\Upsilon\nabla^{\alpha}\mathrm{I\!I}_{\sigma\beta} + O\left(\varepsilon^2\right)\right]. \tag{8.13}$$

Quantity	Scaling	Rescaled variable
Lubrication parameter		$\varepsilon = d/L \ll 1$
Coordinates	$\xi_c = L$	$\Xi = \xi/\xi_c$
	$\zeta_c = L$	$\mathsf{Z} = \zeta/\zeta_c$
	$\upsilon_c = d$	$\Upsilon = \upsilon/\upsilon_c$
Velocity	u_c	$U^{\Xi} = u^{\xi}/u_c$
	$w_c = u_c$	$U^{\mathsf{Z}} = u^{\zeta}/w_c$
	$v_c = \varepsilon u_c$	$U^{\Upsilon} = u^{\upsilon}/v_c$
Time	$t_c = L/u_c$	$T = t/t_c$
Flux	$q_c = du_c$	$Q^{\alpha} = q^{\alpha}/q_c$
Pressure	$p_c = \mu u_c/(\varepsilon^2 L)$	$P = p/p_c$
Mean curvature	$k_c = 1/L$	$K_m = \kappa_m/k_c$
Gaussian curvature	$k_c = 1/L$	$K_G = \kappa_G/k_c$
Shape tensor	$k_c = 1/L$	$\mathbb{II}_{\alpha\beta} = \mathrm{II}_{\alpha\beta}/k_c$
2D covariant derivative		$\nabla_{\alpha} = L\overline{\nabla}_{\alpha}$
2D Christoffel symbol		$\breve{\Gamma}^{\mu}_{\alpha\beta} = L\widetilde{\Gamma}^{\mu}_{\alpha\beta}$
Interface height	$h_c = d$	$H = h(\xi, \zeta, t)/h_c$
Gravity vector	g_{grav}	$\nabla^{\Upsilon}\Psi = B^{\Upsilon} = b^{\upsilon}/g_{grav}$
		$\nabla^{\alpha}\Psi = B^{\alpha} = b^{\alpha}/g_{grav}$
External tangential stress	$\tau_c^{ext} = \frac{\mu u_c}{d}$	$\mathcal{T}_{\alpha}^{ext} = \tau_{\alpha}^{ext}/\tau_c^{ext}$
Bond number		$\mathrm{Bo} = \rho g_{grav} d^2/(\mu u_c)$
Capillary number		$\mathrm{Ca} = Lp_c/\gamma = \varepsilon^{-2}\mu u_c/\gamma$
Reynolds number		$\mathrm{Re} = \rho u_c d/\mu$

Table 8.1: Characteristic scalings (lower case) and nondimensional variables (uppercase) used to describe dimensionless system.

8.4 Equations of motion

8.4.1 Bulk viscous equations

Recall that the continuity and Navier-Stokes equations are given by

$$\overline{\nabla}_i u^i = 0 \tag{8.14a}$$

$$\rho\left(\partial_t u^i + u^j \overline{\nabla}_j u^i\right) = -\overline{\nabla}^i p + \mu \overline{\nabla}^j \overline{\nabla}_j u^i + \rho b^i, \tag{8.14b}$$

where u^i is velocity, p is pressure, μ is viscosity, ρ is density, and b^i is the acceleration vector of the body force, such as gravity. For a review of the equations of motion of fluid mechanics, see Appendix A. We now nondimensionalize the equations following the scalings in Table 8.1 and perform a perturbation expansion in the lubrication limit.

Nondimensionalizing the continuity equation, Equation (8.14a), yields

$$\begin{aligned}
0 &= \frac{L}{u_c}\left(\partial_i u^i + \Gamma^i_{ji} u^j\right) = \frac{L}{u_c}\left(\partial_\alpha u^\alpha + \partial_\upsilon u^\upsilon + \Gamma^\beta_{\upsilon\beta} u^\upsilon + \Gamma^\beta_{\alpha\beta} u^\alpha\right) \\
&= L\partial_\alpha U^\alpha + \partial_\Upsilon U^\Upsilon - \varepsilon\left(\mathrm{I\!I}^\beta_{\ \beta} + \varepsilon\Upsilon\mathrm{I\!I}^\beta_{\ \mu}\mathrm{I\!I}^\mu_{\ \beta}\right) U^\Upsilon + \left(\breve{\Gamma}^\beta_{\alpha\beta} - \varepsilon\Upsilon\nabla^\beta \mathrm{I\!I}_{\alpha\beta}\right) U^\alpha + O\left(\varepsilon^2\right) \\
&= \nabla_\alpha U^\alpha + \partial_\Upsilon U^\Upsilon - \varepsilon\left[\mathrm{I\!I}^\alpha_{\ \alpha} U^\Upsilon + \Upsilon\left(\nabla^\beta \mathrm{I\!I}_{\alpha\beta}\right) U^\alpha\right] + O\left(\varepsilon^2\right) \\
&= \nabla_\alpha U^\alpha + \partial_\Upsilon U^\Upsilon - 2\varepsilon\left[K_m U^\Upsilon + \Upsilon\left(\nabla_\alpha K_m\right) U^\alpha\right] + O\left(\varepsilon^2\right),
\end{aligned} \tag{8.15}$$

where the last step used the Gauss-Codazzi relation, $\nabla_\alpha \mathrm{I\!I}_{\beta\sigma} = \nabla_\beta \mathrm{I\!I}_{\sigma\alpha} = \nabla_\sigma \mathrm{I\!I}_{\alpha\beta}$ (Aris, 1989). Note that in the process of nondimensionalization, we have converted 3D covariant derivatives to 2D covariant derivatives living on the manifold. Indeed, the ultimate goal of the derivation is to "integrate out" the Υ dimension, resulting in an equation of motion governing fluid thickness as a scalar field on the substrate manifold.

As for the momentum equation, Equation (8.14b),

$$\begin{aligned}
&\rho\left(\partial_t u^i + u^j \overline{\nabla}_j u^i\right) = -g^{ij}\partial_j p + \mu g^{jk}\overline{\nabla}_j \overline{\nabla}_k u^i + \rho b^i \\
&= -g^{ij}\partial_j p + \mu g^{jk}\overline{\nabla}_j\left(\partial_k u^i + \Gamma^i_{kr} u^r\right) + \rho b^i \\
&= -g^{ij}\partial_j p + \mu g^{jk}\left[\partial_j(\partial_k u^i + \Gamma^i_{kr} u^r) + \Gamma^i_{js}(\partial_k u^s + \Gamma^s_{kr} u^r) - \Gamma^s_{jk}(\partial_s u^i + \Gamma^i_{sr} u^r)\right] + \rho b^i \\
&= -g^{ij}\partial_j p + \mu g^{jk}\left[\partial_{jk} u^i + \Gamma^i_{kr}\partial_j u^r + \Gamma^i_{jr}\partial_k u^r - \Gamma^r_{jk}\partial_r u^i + \left(\partial_j \Gamma^i_{kr}\right) u^r\right. \\
&\qquad \left. + \left(\Gamma^i_{js}\Gamma^s_{kr} - \Gamma^s_{jk}\Gamma^i_{sr}\right) u^r\right] + \rho b^i.
\end{aligned} \tag{8.16}$$

Now we consider the normal (υ) term and in-manifold momentum terms separately, and nondimensionalize the results. First, the normal momentum, which we multiply through by $d/p_c =$

$\varepsilon^2 dL/(\mu u_c)$:

$$\left(\frac{d}{p_c}\right)\frac{\rho(\varepsilon u_c)}{L/u_c}\left(\partial_T U^\Upsilon + U^j\nabla_j U^i\right) = -\partial_\Upsilon P + \left(\frac{d}{p_c}\right) g^{\upsilon\upsilon}\partial_\upsilon p$$

$$\begin{aligned}\implies \varepsilon^3\frac{\rho u_c d}{\mu}\left(\partial_T U^\Upsilon + U^j\nabla_j U^\Upsilon\right) &= -\partial_\Upsilon P + \frac{\varepsilon^2 L d}{u_c} g^{jk}\Big[\partial_{jk}u^\upsilon + \Gamma^\upsilon_{kr}\partial_j u^r + \Gamma^\upsilon_{jr}\partial_k u^r \\ &\quad -\Gamma^r_{jk}\partial_r u^\upsilon + \left(\partial_j\Gamma^\upsilon_{kr}\right)u^r + \left(\Gamma^\upsilon_{js}\Gamma^s_{kr} - \Gamma^s_{jk}\Gamma^\upsilon_{sr}\right)u^r\Big] + \mathrm{Bo}\partial_\Upsilon\Psi \\ \implies O(\varepsilon^3\mathrm{Re}) &= -\partial_\Upsilon P + \mathrm{Bo}\partial_\Upsilon\Psi + O(\varepsilon^2),\end{aligned} \tag{8.17}$$

where we have written the body force as $\rho b^i = \rho g_{grav} B^i = \rho g_{grav}\nabla^i\Psi$ for some scalar potential Ψ, with g_{grav} being the characteristic scale of the acceleration. Thus the variation in pressure normal to the substrate is set only by the body force, and not the fluid velocity. This decoupling of pressure and velocity along the short dimension is indeed the same effect found in the slender limit V-groove equation in Chapter 4.

The momentum balance tangent to the substrate is nondimensionalized by multiplying through with $L/p_c = \varepsilon^2 L^2/(\mu u_c)$:

$$\left(\frac{\varepsilon^2 L^2}{\mu u_c}\right)\frac{\rho u_c}{L/u_c}\left(\partial_T U^\alpha + U^j\nabla_j U^\alpha\right) = -\left(\frac{L}{p_c}\right) g^{\alpha\beta}\partial_\beta p + \dots$$

$$\begin{aligned}\implies \varepsilon\frac{\rho u_c d}{\mu}\left(\partial_T U^\alpha + U^j\nabla_j U^\alpha\right) &= -\nabla^\alpha P + \frac{\varepsilon^2 L^2}{u_c} g^{jk}\Big[\partial_{jk}u^\alpha + \Gamma^\alpha_{kr}\partial_j u^r + \Gamma^\alpha_{jr}\partial_k u^r \\ &\quad -\Gamma^r_{jk}\partial_r u^\alpha + \left(\partial_j\Gamma^\alpha_{kr}\right)u^r + \left(\Gamma^\alpha_{js}\Gamma^s_{kr} - \Gamma^s_{jk}\Gamma^\alpha_{sr}\right)u^r\Big] + \mathrm{Bo}\nabla^\alpha\Psi \\ &= -\nabla^\alpha P + d^2 g^{jk}\Big[\partial_{jk}U^\alpha + \varepsilon\Gamma^\alpha_{k\upsilon}\partial_j U^\Upsilon + \varepsilon\Gamma^\alpha_{j\upsilon}\partial_k U^\Upsilon - \Gamma^\upsilon_{jk}\partial_\upsilon U^\alpha + \varepsilon\left(\partial_j\Gamma^\alpha_{k\upsilon}\right)U^\Upsilon \\ &\quad +\varepsilon\left(\Gamma^\alpha_{js}\Gamma^s_{k\upsilon} - \Gamma^s_{jk}\Gamma^\alpha_{s\upsilon}\right)U^\Upsilon + \Gamma^\alpha_{k\beta}\partial_j U^\beta + \Gamma^\alpha_{j\beta}\partial_k U^\beta - \Gamma^\beta_{jk}\partial_\beta U^\alpha \\ &\quad + \left(\partial_j\Gamma^\alpha_{k\beta}\right)U^\beta + \left(\Gamma^\alpha_{js}\Gamma^s_{k\beta} - \Gamma^s_{jk}\Gamma^\alpha_{s\beta}\right)U^\beta\Big] + \mathrm{Bo}\nabla^\alpha\Psi \\ &= -\nabla^\alpha P + d^2 g^{jk}\Big[\partial_{jk}U^\alpha + \Gamma^\alpha_{k\beta}\partial_\upsilon U^\beta\delta^\upsilon{}_j + \Gamma^\alpha_{j\beta}\partial_\upsilon U^\beta\delta^\upsilon{}_k - \Gamma^\upsilon_{jk}\partial_\upsilon U^\alpha\Big] \\ &\quad + \mathrm{Bo}\nabla^\alpha\Psi + O(\varepsilon^2) \\ &= -\nabla^\alpha P + d^2\left[d^{-2}\partial_{\Upsilon\Upsilon}U^\alpha - 2L^{-1}d^{-1}\mathrm{I\!I}^\alpha{}_\beta\partial_\Upsilon U^\beta - L^{-1}d^{-1}\mathrm{I\!I}^\nu{}_\nu\partial_\Upsilon U^\alpha\right] \\ &\quad + \mathrm{Bo}\nabla^\alpha\Psi + O(\varepsilon^2) \\ &= -\nabla^\alpha P + \partial_{\Upsilon\Upsilon}U^\alpha + \mathrm{Bo}\nabla^\alpha\Psi - \varepsilon\left(2\mathrm{I\!I}^\alpha{}_\beta + \mathrm{I\!I}^\nu{}_\nu\delta^\alpha{}_\beta\right)\partial_\Upsilon U^\beta + O(\varepsilon^2).\end{aligned} \tag{8.18}$$

Lowering the index,

$$\begin{aligned}O(\varepsilon\mathrm{Re}) + \nabla_\alpha P = \left(\widetilde{g}_{\alpha\beta} - 2\varepsilon\Upsilon\mathrm{I\!I}_{\alpha\beta}\right)\partial_{\Upsilon\Upsilon}U^\beta - \varepsilon\left(2\mathrm{I\!I}_{\alpha\beta} + \mathrm{I\!I}^\nu{}_\nu\widetilde{g}_{\alpha\beta}\right)\partial_\Upsilon U^\beta \\ + \mathrm{Bo}\nabla_\alpha\Psi + O(\varepsilon^2).\end{aligned} \tag{8.19}$$

Note that at this point we have assumed $\varepsilon\mathrm{Re} = \varepsilon\rho u_c d/\mu$ to be small without specifying a velocity scale. The choice of u_c depends on the dominant driving force of the system, which

may be surface tension, gravity, or other external effects such as Maxwell pressure. We will return to this issue once the full equation has been derived.

The tangential pressure balance includes velocity terms, but they have derivatives only in Υ, the short dimension. The same phenomenon was seen in the V-groove equation of Chapter 4, in which the velocity terms had no derivatives in the Z direction. Having lost all the "long-wavelength" derivatives in α and β, we will soon be able to easily solve Equation (8.19) as an ordinary differential equation in Υ. Before we can do so, we need boundary conditions.

8.4.2 Boundary conditions

Having derived a second order ODE in Υ for U^α, we must determine the boundary conditions in order to solve it. First, we set the no-slip condition at the substrate, i.e. $U^\alpha|_{\Upsilon=0} = 0$.

The surface conditions will be given by

$$n^i \tau_{ij} n^j = -p_{ext}, \tag{8.20}$$

$$t^i_{(\alpha)} \tau_{ij} n^j = \tau^{ext}_\alpha, \tag{8.21}$$

where

$$\tau_{ij} = -p g_{ij} + \mu \left(\overline{\nabla}_i u_j + \overline{\nabla}_j u_i \right) \tag{8.22}$$

is the fluid stress tensor, n^i is the normal to the fluid interface, and $t^i_{(\alpha)}$ is a tangent pair at the interface (not normalized). τ^{ext}_α denotes the external tangential stress, and will be nondimensionalized as $\mathcal{T}^{ext}_\alpha \equiv \tau^{ext}_\alpha/(\mu u_c/d)$. For a review of the interfacial boundary conditions, see Section 2.1. Note that the dimensional tangential stress, τ^{ext}_α, is a tensor and must be multiplied by a scale factor to produce a vector of the correct physical units, $\overline{\tau}^\alpha_{ext} = [\tilde{g}^\alpha_{\ \beta} - h\mathrm{I\!I}^\alpha_{\ \beta} + O(h^2)]\tau^\alpha_{ext}$.

Letting the interface be $\vec{h} = \{\xi, \zeta, h(\xi, \zeta, t)\}$, the tangent and normal vectors at the surface are:

$$t^i_{(\alpha)} = \partial_\alpha \vec{h} = \begin{bmatrix} \delta_{\xi\alpha} \\ \delta_{\zeta\alpha} \\ \partial_\alpha h \end{bmatrix} = \begin{bmatrix} \delta_{\xi\alpha} \\ \delta_{\zeta\alpha} \\ \varepsilon \nabla_\alpha H \end{bmatrix}, \tag{8.23a}$$

$$n_i = \frac{1}{\sqrt{1 + \partial_\alpha h g^{\alpha\beta} \partial_\beta h}} \begin{bmatrix} -\partial_\xi h \\ -\partial_\zeta h \\ 1 \end{bmatrix} = \begin{bmatrix} -\varepsilon \nabla_\Xi H \\ -\varepsilon \nabla_{\mathsf{Z}} H \\ 1 \end{bmatrix} + O(\varepsilon^2), \tag{8.23b}$$

$$n^i = \begin{bmatrix} -\varepsilon \nabla^\Xi H \\ -\varepsilon \nabla^{\mathsf{Z}} H \\ 1 \end{bmatrix} + O(\varepsilon^2), \tag{8.23c}$$

where the last line shows that the raised-index n^i is the same as n_i, to $O(\varepsilon^2)$.

Using these results to compute the normal stress balance,

$$\begin{aligned}
0 &= p_c^{-1}\left(p_{ext} + n^i \tau_{ij} n^j\right) \\
&= (P_{ext} - P) + 2\frac{\mu}{p_c} n^i (\overline{\nabla}_i u^j) n_j \\
&= (P_{ext} - P) + \frac{\varepsilon d}{u_c}\begin{bmatrix} -\varepsilon\nabla^\alpha H \\ 1 \end{bmatrix}^T \begin{bmatrix} 2\overline{\nabla}_\alpha u^\rho & (\overline{\nabla}_\alpha u^\upsilon + \overline{\nabla}^\upsilon u_\alpha) \\ (\overline{\nabla}_\upsilon u^\rho + \overline{\nabla}^\rho u_\upsilon) & 2\overline{\nabla}_\upsilon u^\upsilon \end{bmatrix} \begin{bmatrix} -\varepsilon\nabla_\rho H \\ 1 \end{bmatrix} \\
&= (P_{ext} - P) + \frac{\varepsilon d}{u_c}\begin{bmatrix} -\varepsilon\nabla^\alpha H \\ 1 \end{bmatrix}^T \begin{bmatrix} O(u_c/L) & (u_c/d)\partial_\Upsilon U_\alpha \\ (u_c/d)\partial_\Upsilon U^\rho & 2\varepsilon(u_c/d)\partial_\Upsilon U^\Upsilon \end{bmatrix} \begin{bmatrix} -\varepsilon\nabla_\rho H \\ 1 \end{bmatrix} \\
&= (P_{ext} - P) + O(\varepsilon^2).
\end{aligned} \tag{8.24}$$

Hence the velocity drops out of the normal stress balance, leaving only the hydrodynamic pressure to be set by the external pressure at the interface.

As for the tangential stress balance,

$$\begin{aligned}
0 &= \frac{d}{\mu u_c}\left(-\tau_\alpha^{ext} + t^i_{(\alpha)}\tau_{ij} n^i\right) \\
&= -\mathcal{T}_\alpha^{ext} + \frac{d}{u_c} t^i_{(\alpha)}\left(g_{jk}\overline{\nabla}_i u^k + g_{ik}\overline{\nabla}_j u^k\right) n^j \\
&= -\mathcal{T}_\alpha^{ext} + \frac{d}{u_c}\left[t^i_{(\alpha)}\left(g_{jk}\partial_i u^k + g_{jk}\Gamma^k_{ir}u^r + g_{ik}\partial_j u^k + g_{ik}\Gamma^k_{jr}u^r\right) n^j\right] \\
&= -\mathcal{T}_\alpha^{ext} + \frac{d}{u_c}\Big[t^\upsilon_{(\alpha)}\left(g_{\upsilon k}\partial_\upsilon u^k + g_{\upsilon k}\Gamma^k_{\upsilon r}u^r + g_{\upsilon k}\partial_\upsilon u^k + g_{\upsilon k}\Gamma^k_{\upsilon r}u^r\right) n^\upsilon \\
&\qquad\qquad + t^\mu_{(\alpha)}\left(g_{\upsilon k}\partial_\mu u^k + g_{\upsilon k}\Gamma^k_{\mu r}u^r + g_{\mu k}\partial_\upsilon u^k + g_{\mu k}\Gamma^k_{\upsilon r}u^r\right) n^\upsilon \\
&\qquad\qquad + t^\mu_{(\alpha)}\left(g_{\rho k}\partial_\mu u^k + g_{\rho k}\Gamma^k_{\mu r}u^r + g_{\mu k}\partial_\rho u^k + g_{\mu k}\Gamma^k_{\rho r}u^r\right) n^\rho\Big] + O(\varepsilon^2) \\
&= -\mathcal{T}_\alpha^{ext} + \frac{d}{u_c}\left[O(\varepsilon^2) + \delta^\mu_{\ \alpha}\left(\Gamma^\upsilon_{\mu\beta}u^\beta + g_{\mu\beta}\partial_\upsilon u^\beta + g_{\mu\nu}\Gamma^\nu_{\upsilon\beta}u^\beta\right) + O(\varepsilon^2)\right] + O(\varepsilon^2) \\
&= -\mathcal{T}_\alpha^{ext} + \widetilde{g}_{\alpha\beta}\partial_\Upsilon U^\beta - 2\varepsilon\Upsilon\mathrm{I\!I}_{\alpha\beta}\partial_\Upsilon U^\beta + O(\varepsilon^2).
\end{aligned} \tag{8.25}$$

While this looks a bit complicated, note that raising the index simplifies it significantly: $\mathcal{T}^\alpha_{ext} = \partial_\Upsilon U^\alpha$, exactly the condition which would arise for a flat film. It is useful to express $\mathcal{T}$ as a covector since it is often a derivative. For example, Marangoni stresses have the form $\mathcal{T}_\alpha^{Marangoni} = \nabla_\alpha\gamma = \partial_\alpha\gamma$, where γ is the surface tension.

Summarizing the boundary conditions,

$$P|_{\Upsilon=H} = P_{ext}|_{\Upsilon=H} + O(\varepsilon^2), \tag{8.26a}$$

$$\mathcal{T}_\alpha^{ext} = \left[\widetilde{g}_{\alpha\beta}\partial_\Upsilon U^\beta - 2\varepsilon\Upsilon\mathrm{I\!I}_{\alpha\beta}\partial_\Upsilon U^\beta\right]_{\Upsilon=H} + O(\varepsilon^2). \tag{8.26b}$$

8.4.3 Velocity calculation

Now that we have the reduced forms of the momentum equations and boundary conditions, we can solve the system. Proceeding perturbatively, we write out $U^i = U^i_{(0)} + \varepsilon U^i_{(1)} + O(\varepsilon^2)$, $P = P_{(0)} + \varepsilon P_{(1)} + O(\varepsilon^3)$, etc.

Let us assume a constant body force, such as gravity. In this case, at fixed tangential coordinates (Ξ, Z), the body force potential Ψ must be linear in Υ. Thus it can be written as $\Psi = \Psi_{(0)} + \varepsilon\Upsilon\Psi_{(1)}$, with $\Psi_{(0)}$ and $\Psi_{(1)}$ being independent of Υ. Note that Ψ is not necessarily linear in Ξ or Z.

The 0th order equations can be written as:

$$\partial_\Upsilon P_{(0)} = \varepsilon \mathrm{Bo}\Psi_{(1)}, \tag{8.27a}$$

$$\partial_{\Upsilon\Upsilon} U^\alpha_{(0)} = \widetilde{g}^{\alpha\beta}\left[\nabla_\beta P_{(0)} - \mathrm{Bo}\nabla_\beta\Psi_{(0)} - \varepsilon\mathrm{Bo}\Upsilon\nabla_\beta\Psi_{(1)}\right], \tag{8.27b}$$

$$P_{(0)}|_{\Upsilon=H} = P_{ext}, \tag{8.27c}$$

$$U^\alpha_0|_{\Upsilon=0} = 0, \tag{8.27d}$$

$$\partial_\Upsilon U^\beta_0|_{\Upsilon=H} = \widetilde{g}^{\alpha\beta}\mathcal{T}^{ext}_\alpha, \tag{8.27e}$$

where we have kept the $\Psi_{(1)}$ term together with the $\Psi_{(0)}$ term, despite it being $O(\varepsilon)$, for convenience (this does not change the validity of the perturbation expansion).

Solving the 0th order yields

$$P_{(0)} = P_{ext} + \varepsilon\mathrm{Bo}\Psi_{(1)}\left(\Upsilon - H\right), \tag{8.28a}$$

$$U^\alpha_{(0)} = \widetilde{g}^{\alpha\beta}\left[\mathcal{T}^{ext}_\beta\Upsilon + \left(\nabla_\beta P_{ext} - \mathrm{Bo}\nabla_\beta\Psi_{(0)} - \mathrm{Bo}\nabla_\beta\{\varepsilon\Psi_{(1)}H\}\right)\left(\frac{\Upsilon^2}{2} - \Upsilon H\right)\right]. \tag{8.28b}$$

The 1st order equations are

$$\partial_\Upsilon P_{(1)} = 0 \tag{8.29a}$$

$$P_{(1)}|_{\Upsilon=H} = 0 \tag{8.29b}$$

$$\begin{aligned}\partial_{\Upsilon\Upsilon}U^\alpha_{(1)} &= \widetilde{g}^{\alpha\beta}\nabla_\beta P_{(1)} + 2\Upsilon\mathrm{I\!I}_\beta{}^\alpha\partial_{\Upsilon\Upsilon}U^\beta_{(0)} + \left(2\mathrm{I\!I}_\beta{}^\alpha + 2K_m\delta_\beta{}^\alpha\right)\partial_\Upsilon U^\beta_{(0)}\\ &= \left(2\mathrm{I\!I}^{\alpha\beta} + 2K_m\widetilde{g}^{\alpha\beta}\right)\mathcal{T}^{ext}_\beta + \left[(4\mathrm{I\!I}^\alpha{}_\beta + 2K_m\delta^\alpha{}_\beta)\Upsilon - (2\mathrm{I\!I}^\alpha{}_\beta + 2K_m\delta^\alpha{}_\beta)H\right]\\ &\quad\times\left(\nabla_\beta P_{ext} - \mathrm{Bo}\nabla_\beta\Psi_{(0)} - \mathrm{Bo}\nabla_\beta\{\varepsilon\Psi_{(1)}H\}\right)\end{aligned} \tag{8.29c}$$

$$U^\alpha_1|_{\Upsilon=0} = 0 \tag{8.29d}$$

$$\partial_\Upsilon U^\alpha_1|_{\Upsilon=H} = 2\Upsilon\mathrm{I\!I}^\alpha{}_\beta\partial_\Upsilon U^\beta_{(0)}|_{\Upsilon=H} = 2H\mathrm{I\!I}^{\alpha\beta}\mathcal{T}^{ext}_\beta. \tag{8.29e}$$

Solving the 1st order yields

$$P_{(1)} = 0, \tag{8.30a}$$

$$\begin{aligned}U^\alpha_{(1)} &= \left[\mathrm{I\!I}^{\alpha\beta}\Upsilon^2 + 2K_m\left(\frac{\Upsilon^2}{2} - \Upsilon H\right)\right]\mathcal{T}^{ext}_\beta\\ &\quad + \left[\mathrm{I\!I}^{\alpha\beta}\left(\frac{2\Upsilon^3}{3} - \Upsilon^2 H\right) + K_m\widetilde{g}^{\alpha\beta}\left(\frac{\Upsilon^3}{3} - \Upsilon^2 H + \Upsilon H^2\right)\right]\\ &\quad\times\left(\nabla_\beta P_{ext} - \mathrm{Bo}\nabla_\beta\Psi_{(0)} - \mathrm{Bo}\nabla_\beta\{\varepsilon\Psi_{(1)}H\}\right).\end{aligned} \tag{8.30b}$$

8.4.4 Integrated mass conservation

To construct a flux-volume relation, we integrate conservation of mass over υ. Before doing so, a few relations will be needed. First, note that the kinematic condition, which sets the interface velocity to that of the underlying fluid, is given by

$$[\partial_t h + (\partial_\alpha h) u^\alpha]_{\upsilon=h} = u^\upsilon|_{\upsilon=h} \tag{8.31}$$

(Oron et al., 1997). This condition would not hold if we allowed mass to transfer into or out of the liquid, by evaporation for example, but such effects will not be considered here.

We will also use an identity relating to the covariant derivative, namely,

$$\sqrt{\det g}\overline{\nabla}_i u^i = \partial_i \left(\sqrt{\det g}\ u^i\right) \tag{8.32}$$

(Aris, 1989), which leads to the expansion

$$\sqrt{\det g} = \sqrt{\det \widetilde{g}}\left[1 - \upsilon \mathrm{I\!I}^\mu{}_\mu + \frac{\upsilon^2}{2}\left(\mathrm{I\!I}^\mu{}_\mu \mathrm{I\!I}^\beta{}_\beta - \mathrm{I\!I}^\mu{}_\beta \mathrm{I\!I}^\beta{}_\mu\right)\right] = \sqrt{\det \widetilde{g}}\breve{J}, \tag{8.33}$$

where we are using $\breve{J}$ as shorthand for the term in brackets. Now,

$$\begin{aligned}
0 &= \overline{\nabla}_i u^i \\
\implies 0 &= \int_0^h \sqrt{\det g}\overline{\nabla}_i u^i d\upsilon = \int_0^h \partial_i\left(\sqrt{\det g}\ u^i\right) d\upsilon \\
&= \left[\sqrt{\det g}\ u^\upsilon\right]_{\upsilon=h} + \int_0^h \partial_\alpha\left(\sqrt{\det g}\ u^\alpha\right) d\upsilon \\
&= \sqrt{\det g}|_{\upsilon=h}\partial_t h + \left[\sqrt{\det g}\ u^\alpha \partial_\alpha h\right]_{\upsilon=h} + \int_0^h \partial_\alpha\left(\sqrt{\det g}\ u^\alpha\right) d\upsilon \\
&= \sqrt{\det g}|_{\upsilon=h}\partial_t h + \partial_\alpha \int_0^h \left(\sqrt{\det g}\ u^\alpha\right) d\upsilon \\
&= \sqrt{\det \widetilde{g}}\breve{J}|_{\upsilon=h}\partial_t h + \sqrt{\det \widetilde{g}}\nabla_\alpha \int_0^h \breve{J} u^\alpha d\upsilon \\
\implies \breve{J}|_{\upsilon=h}\partial_t h &= \nabla_\alpha \int_0^h \breve{J} u^\alpha d\upsilon = \nabla_\alpha q^\alpha,
\end{aligned} \tag{8.34}$$

where we have defined the flux q^α as

$$\begin{aligned}
q^\alpha &= \int_0^h \breve{J} u^\alpha d\upsilon \\
&= \int_0^h \left[1 - \upsilon \mathrm{I\!I}^\mu{}_\mu + \frac{\upsilon^2}{2}\left(\mathrm{I\!I}^\mu{}_\mu \mathrm{I\!I}^\beta{}_\beta - \mathrm{I\!I}^\mu{}_\beta \mathrm{I\!I}^\beta{}_\mu\right)\right] u^\alpha d\upsilon,
\end{aligned} \tag{8.35}$$

or, in nondimensional form,

$$Q^\alpha = \frac{1}{du_c} q^\alpha = \int_0^H \left[1 - \varepsilon \Upsilon \mathrm{I\!I}^\mu{}_\mu + \varepsilon^2 \frac{\Upsilon^2}{2}\left(\mathrm{I\!I}^\mu{}_\mu \mathrm{I\!I}^\beta{}_\beta - \mathrm{I\!I}^\mu{}_\beta \mathrm{I\!I}^\beta{}_\mu\right)\right] U^\alpha d\Upsilon. \tag{8.36}$$

We can re-express the mass-conservation result of Equation (8.34) as

$$\frac{\partial}{\partial t}\left(h - K_m h^2 + \frac{1}{3}K_G h^3\right) = -\overline{\nabla}_\alpha q^\alpha, \tag{8.37}$$

or

$$\frac{\partial}{\partial T}\left(H - \varepsilon K_m H^2 + \frac{1}{3}\varepsilon^2 K_G H^3\right) = \frac{\partial V}{\partial T} = -\nabla_\alpha Q^\alpha. \tag{8.38}$$

The left-hand side term in parentheses is the local volume element $\int_0^h \breve{J} d\upsilon = (h - K_m h^2 + (1/3)K_G h^3$, expressing the amount of fluid sitting above a small patch of substrate area (Roy et al., 2002); we have denoted the nondimensional volume element by V. Note that the expression for the volume element is exact; it has not been truncated at $O(\varepsilon^2)$.

8.4.5 Flux

Using the value of U^α just computed, we can express the flux in terms of the external pressure, tangential stress, and body force, as

$$\begin{aligned}
Q^\alpha =& \int_0^H \left(1 - \varepsilon \Upsilon \mathrm{I\!I}^\mu{}_\mu\right) U^\alpha d\Upsilon + O(\varepsilon^2) \\
=& \frac{H^3}{3}\left[-\widetilde{g}^{\alpha\beta} + \varepsilon H\left(2K_m \widetilde{g}^{\alpha\beta} - \frac{1}{2}\mathrm{I\!I}^{\alpha\beta}\right)\right]\nabla_\beta P_{ext} \\
&+ H^2\left[\frac{1}{2}\widetilde{g}^{\alpha\beta} - \frac{1}{3}\varepsilon H\left(4K_m \widetilde{g}^{\alpha\beta} - \mathrm{I\!I}^{\alpha\beta}\right)\right]\mathcal{T}^{ext}_\beta \\
&- \mathrm{Bo}\frac{H^3}{3}\left[-\widetilde{g}^{\alpha\beta} + \varepsilon H\left(2K_m \widetilde{g}^{\alpha\beta} - \frac{1}{2}\mathrm{I\!I}^{\alpha\beta}\right)\right]\nabla_\beta\left(\Psi_{(0)} + \varepsilon\Psi_{(1)}H\right).
\end{aligned} \tag{8.39}$$

8.4.6 Surface tension

The external pressure contribution due to surface tension is $p_{ST} = -2\gamma\kappa_{minterface}$, where $\kappa_{minterface}$ is the mean curvature of the liquid interface [Equation (2.39a)]. This result can be more conveniently computed from the surface divergence of the normal vector, $p_{ST} = \gamma\left(\overline{\nabla}_i - n_i n^j \overline{\nabla}_j\right) n^i = \gamma \overline{\nabla}_i n^i$:

$$\begin{aligned}
P_{ST} = p_c^{-1} p_{ST} &= \frac{\gamma}{p_c}\overline{\nabla}_i n^i|_{\Upsilon=H} \\
&= \frac{\gamma}{p_c}\left[\partial_i n^i + \Gamma^i_{ik} n^k\right]_{\Upsilon=H} \\
&= \frac{\gamma}{p_c}\left[L^{-1}\nabla_\alpha\left(-\varepsilon\nabla^\alpha H\right) + \Gamma^i_{i\upsilon} n^\upsilon + O(\varepsilon^2 L^{-1})\right]_{\Upsilon=H} \\
&= \frac{\gamma}{L p_c}\left[\nabla_\alpha\left(-\varepsilon\nabla^\alpha H\right) + \left(-\mathrm{I\!I}^\alpha{}_\alpha - \varepsilon\Upsilon\mathrm{I\!I}^\alpha{}_\beta\mathrm{I\!I}^\beta{}_\alpha\right) + O(\varepsilon^2)\right]_{\Upsilon=H} \\
&= -\frac{\varepsilon^2\gamma}{\mu u_c}\left[2K_m + \varepsilon\left(\nabla_\alpha\nabla^\alpha H + H\mathrm{I\!I}^\alpha{}_\beta\mathrm{I\!I}^\beta{}_\alpha\right) + O(\varepsilon^2)\right] \\
&= -\mathrm{Ca}^{-1}\left\{2K_m + \varepsilon\left[\nabla_\alpha\nabla^\alpha H + H\left(4{K_m}^2 - 2K_G\right)\right] + O(\varepsilon^2)\right\},
\end{aligned} \tag{8.40}$$

where the last step introduced the capillary number, $\mathrm{Ca} = \mu u_c/(\gamma\varepsilon^2)$. The scaling of the capillary number is chosen so that the dimensionless pressure is $O(\mathrm{Ca}^{-1})$. Thus the definition

differs from the flat-substrate thin-film capillary number, which has no K_m term and thus includes an extra factor of ε^{-1} (Oron et al., 1997). Incidentally it also differs from the capillary number defined in Chapter 4, because V-grooves have an interfacial radius of curvature $O(d)$ rather than $O(L)$.

Thus the dominant contributor to the capillary pressure is the substrate itself, via the $O(1)$ term $2K_m$. Variations in fluid height induce an $O(\varepsilon)$ correction to the capillary pressure: the Laplacian term describes curvature induced by variations in H and is the same as the curvature term found in the classic flat-substrate thin film equation; the second term in H represents the modification to the substrate curvature produced by a uniform layer on top of the substrate.

8.4.7 Final thin film equation

Substituting the flux, Equation (8.39), into the integrated mass conservation equation, Equation (8.38), yields the thin film equation on a curved substrate:

$$\begin{aligned}
&\frac{\partial}{\partial T}\left(H-\varepsilon K_m H^2+\frac{1}{3}\varepsilon^2 K_G H^3\right)=-\nabla_\alpha\Bigg(\\
&\mathrm{Ca}^{-1}\frac{H^3}{3}\left[\widetilde{g}^{\alpha\beta}-\varepsilon H\left(2K_m\widetilde{g}^{\alpha\beta}-\frac{1}{2}\mathrm{I\!I}^{\alpha\beta}\right)\right]\nabla_\beta\left\{2K_m+\varepsilon\left[\nabla_\nu\nabla^\nu H+H\left(4{\kappa_m}^2-2\kappa_G\right)\right]\right\}\\
&+\frac{H^3}{3}\left[-\widetilde{g}^{\alpha\beta}+\varepsilon H\left(2K_m\widetilde{g}^{\alpha\beta}-\frac{1}{2}\mathrm{I\!I}^{\alpha\beta}\right)\right]\nabla_\beta P_{other}\\
&+H^2\left[\frac{1}{2}\widetilde{g}^{\alpha\beta}-\frac{2}{3}\varepsilon H\left(2K_m\widetilde{g}^{\alpha\beta}-\frac{1}{2}\mathrm{I\!I}^{\alpha\beta}\right)\right]\mathcal{T}^{ext}_\beta\\
&+\mathrm{Bo}\frac{H^3}{3}\left[\widetilde{g}^{\alpha\beta}-\varepsilon H\left(2K_m\widetilde{g}^{\alpha\beta}-\frac{1}{2}\mathrm{I\!I}^{\alpha\beta}\right)\right]\nabla_\beta\left(\Psi_{(0)}+\varepsilon\Psi_{(1)}H\right)\\
&\Bigg)+O(\varepsilon^2),
\end{aligned}\tag{8.41}$$

where we have split P_{ext} into the capillary pressure (P_{ST}) and the remainder, P_{other}, which would include, for example, Maxwell pressure. Note that, following the suggestion of Roy et al. (2002), we have retained the $O(\varepsilon^2)$ term in the volume element on the left-hand side. While in principle it could be omitted, the extra term guarantees exact conservation of volume.

The volume element $V\equiv H-\varepsilon K_m H^2+\varepsilon^2\frac{1}{3}K_G H^3$ inverts to

$$H=V+\varepsilon K_m V^2+\varepsilon^2\left(2{K_m}^2-\frac{K_G}{3}\right)V^3+O(\varepsilon^3).\tag{8.42}$$

Rewriting the equation of motion to first order in terms of V gives

$$\frac{\partial V}{\partial T} = -\nabla_\alpha \Bigg(\mathrm{Ca}^{-1}\frac{V^3}{3}\left[\widetilde{g}^{\alpha\beta} + \varepsilon V\left(K_m \widetilde{g}^{\alpha\beta} + \frac{1}{2}\mathrm{I\!I}^{\alpha\beta}\right)\right]\nabla_\beta\left\{2K_m + \varepsilon\left[\nabla_\nu\nabla^\nu V + V\left(4{K_m}^2 - 2K_G\right)\right]\right\} + \frac{V^3}{3}\left[-\widetilde{g}^{\alpha\beta} - \varepsilon V\left(K_m\widetilde{g}^{\alpha\beta} + \frac{1}{2}\mathrm{I\!I}^{\alpha\beta}\right)\right]\nabla_\beta P_{other} + V^2\left[\frac{1}{2}\widetilde{g}^{\alpha\beta} - \frac{1}{3}\varepsilon V\left(K_m\widetilde{g}^{\alpha\beta} - \mathrm{I\!I}^{\alpha\beta}\right)\right]\mathcal{T}^{ext}_\beta + \mathrm{Bo}\frac{V^3}{3}\left[\widetilde{g}^{\alpha\beta} + \varepsilon V\left(K_m\widetilde{g}^{\alpha\beta} + \frac{1}{2}\mathrm{I\!I}^{\alpha\beta}\right)\right]\nabla_\beta\left(\Psi_{(0)} + \varepsilon\Psi_{(1)}V\right) \Bigg) + O(\varepsilon^2). \tag{8.43}$$

Reynolds number and inertial effects

We now return to the issue of the omitted inertial effects, in which we assumed $\varepsilon\mathrm{Re} = \varepsilon\rho u_c d/\mu$ was small enough to drop. The characteristic velocity u_c is determined by which of the terms of Equation (8.41) dominates the dynamics.

Suppose the system is dominated by surface tension. In this case, the left- and right-hand sides of Equation (8.41) are balanced by setting $\mathrm{Ca}^{-1} = \varepsilon^2\gamma/(\mu u_c) = 1$, which implies that $u_c = \varepsilon^2\gamma/\mu$. It follows, then, that $\varepsilon\mathrm{Re} = \varepsilon^3\rho\gamma d/\mu^2$. If this expression is indeed small for a given system, then the perturbation expansion dropping inertial effects was self-consistent. Liquid indium, the material relevant to the MEP, has approximately $\rho = 7\times10^3$ kg/m^3, $\mu = 1.6\times10^{-3}$ Pa·s, and $\gamma = 0.57$ N/m (Assael et al., 2012; Chentsov et al., 2011); hence $\varepsilon\mathrm{Re} \approx 1600\varepsilon^3 \times (d/1 \text{ micron})$. Thus, for a 1 micron thick film of indium, $\varepsilon \lesssim 0.1$ would lead to $\varepsilon\mathrm{Re}$ below of order unity or below.

If the system is dominated by a different external force with characteristic pressure p_c, then Equation (8.41) is similarly balanced by setting $p_c = \mu u_c/(\varepsilon^2 L)$, and hence $u_c = \varepsilon^2 L p_c/\mu$. Therefore, $\varepsilon\mathrm{Re} = \varepsilon^2\rho d^2 p_c/\mu^2$. For example, suppose there is an electric field at the emission strength, $|E| \approx 10^{10}$ V/m, on a liquid indium film (i.e., the local strength of the field at the Taylor cone tip when emission occurs). Then, as the vacuum permittivity is $\epsilon_0 = 8.85\times10^{-12}$ F/m (Tiesinga et al., 2019), we have $p_c = \epsilon_0|E|^2/2 \approx 4\times10^8$ Pa, and thus $\varepsilon\mathrm{Re} \approx 1.2\times 10^6\varepsilon^2 \times (d/1 \text{ micron})^2$. Hence, for this viscous thin film equation to hold at emission field strength would require a very thin film; a 0.1 micron film on a substrate of curvature 10 microns would be just enough.

And if the system is dominated by gravity, then Equation (8.41) is balanced by setting $\mathrm{Bo} = \rho g_{grav} d^2/(\mu u_c)$ to 1, so that $u_c = \rho g_{grav} d^2/\mu$, and $\varepsilon\mathrm{Re} = \varepsilon\rho^2 g_{grav} d^3/\mu^2$.

Comparison with prior work

The capillary and body force terms of Equation (8.41) match the results reported by Roberts (1997), Roy et al. (2002), and Rumpf and Vantzos (2013), up to $O(\varepsilon^2)$ corrections. To see that the results are equivalent requires some additional algebra.

First, note that the assumption of a constant body force allows for further modification of the Bo term. In particular, if B^i is constant in an external Cartesian coordinate system, then $\nabla_\alpha B_\Upsilon = \nabla_\alpha(n^i B_i) = \partial_\alpha(n^i B_i) = \partial_\alpha(n^i)B_i = t_i^{(\beta)}\partial_\alpha(n^i)B_\beta = -\mathrm{I\!I}^\beta{}_\alpha B_\beta$. Hence, the body force term can be written as

$$\nabla_\beta\left(\Psi_{(0)} + \varepsilon\Psi_{(1)}H\right) = \left(\delta^\nu{}_\beta - \varepsilon H\mathrm{I\!I}^\nu{}_\beta\right)B_\nu + \varepsilon B_\Upsilon\nabla_\beta H. \tag{8.44}$$

To recover the equation of Roy et al. (2002), we substitute this expression for the body force into Equation (8.41) and furthermore modify the capillary pressure term by throwing out and adding in some $O(\varepsilon^2)$ terms:

$$\begin{aligned}
\frac{\partial V}{\partial T} &= -\nabla_\alpha\Bigg(\\
&\mathrm{Ca}^{-1}\frac{H^3}{3}\left[\widetilde{g}^{\alpha\beta} - \varepsilon H\left(2K_m\widetilde{g}^{\alpha\beta} - \frac{1}{2}\mathrm{I\!I}^{\alpha\beta}\right)\right]\nabla_\beta\left\{2K_m + \varepsilon\left[\nabla_\nu\nabla^\nu H + H\left(4{K_m}^2 - 2K_G\right)\right]\right\} \\
&+ \mathrm{Bo}\frac{H^3}{3}\left[\widetilde{g}^{\alpha\beta} - \varepsilon H\left(2K_m\widetilde{g}^{\alpha\beta} - \frac{1}{2}\mathrm{I\!I}^{\alpha\beta}\right)\right]\left[\left(\delta^\nu{}_\beta - \varepsilon H\mathrm{I\!I}^\nu{}_\beta\right)B_\nu + \varepsilon B_\Upsilon\nabla_\beta H\right]\Bigg) + O(\varepsilon^2) \\
&= -\frac{1}{3}\mathrm{Ca}^{-1}\nabla_\alpha\Bigg(\\
&H^3\nabla^\alpha\left\{2K_m + \varepsilon\left[\nabla_\nu\nabla^\nu H + H\left(4{K_m}^2 - 2K_G\right)\right]\right\} - \frac{1}{2}\varepsilon H^4\left(4K_m\widetilde{g}^{\alpha\beta} - \mathrm{I\!I}^{\alpha\beta}\right)\nabla_\beta(2K_m) \\
&+ \mathrm{BoCa}\left\{H^3\widetilde{g}^{\alpha\beta}B_\beta - \varepsilon H^4\left(2K_m\widetilde{g}^{\alpha\beta} + \frac{1}{2}\mathrm{I\!I}^{\alpha\beta}\right)B_\beta + \varepsilon H^3 B_\Upsilon\nabla^\alpha H\right\}\Bigg) + O(\varepsilon^2) \\
&= -\frac{1}{3}\mathrm{Ca}^{-1}\nabla_\alpha\Bigg(\\
&H^2V\nabla^\alpha\left\{\frac{2(K_m - \varepsilon HK_G)}{1 - 2\varepsilon HK_m + \varepsilon^2H^2K_G} + \varepsilon\nabla_\nu\nabla^\nu H\right\} - \frac{1}{2}\varepsilon H^4\left(2K_m\widetilde{g}^{\alpha\beta} - \mathrm{I\!I}^{\alpha\beta}\right)\nabla_\beta(2K_m) \\
&+ \mathrm{BoCa}\left\{H^3\widetilde{g}^{\alpha\beta}B_\beta - \varepsilon H^4\left(2K_m\widetilde{g}^{\alpha\beta} + \frac{1}{2}\mathrm{I\!I}^{\alpha\beta}\right)B_\beta + \varepsilon H^3 B_\Upsilon\nabla^\alpha H\right\}\Bigg) + O(\varepsilon^2).
\end{aligned} \tag{8.45}$$

The last step replaced H^3 with $H^2V(1 + \varepsilon K_m H)$ in the leftmost term, and also replaced the capillary pressure (in braces) with the expression

$$\frac{2(K_m - \varepsilon HK_G)}{1 - 2\varepsilon HK_m + \varepsilon^2H^2K_G} + \varepsilon\nabla_\nu\nabla^\nu H, \tag{8.46}$$

which differs only at $O(\varepsilon^2)$. Equation (8.45) is now directly comparable to Eq. 51 in Roy et al. (2002) (note that those authors define their mean curvature with a factor of 2, as $\kappa = \mathrm{I\!I}^\alpha{}_\alpha =$

$2K_m$). Given that our derivation produces a matching result for the capillary pressure, our expression for P_{other} in Equation (8.41) must also be correct, up to errors of $O(\varepsilon^2)$.

Roy et al. (2002) use the above fractional expression of capillary pressure because they found it to give a more accurate solution in a simulation of flow on a cylinder. Since we already chose a different $O(\varepsilon^2)$ truncation by keeping the pressure gradient separate from the mobility, we do not follow them on this issue. Both our Equation (8.41) and Roy et al.'s Equation (8.45) are valid only up to $O(\varepsilon^2)$, and their differences will be at that scale.

On the subject of truncating perturbation expansions, it should be noted that while the methodology of lubrication theory is somewhat ad-hoc, mathematicians have provided more rigorous grounding in recent years. Bertozzi and Pugh (1996) proved the conditions necessary for existence of solutions to the capillary-driven thin film equation. Roberts (1997) (a co-author of Roy et al., 2002) showed that lubrication theory can be viewed as an application of center manifold theory. Giacomelli and Otto (2003) demonstrated that Darcy flow (a simplified model of fluid flow in which the velocity is equal to the gradient of pressure, $u = \overline{\nabla} p$) with a free surface converges to the thin film equation in the limit as the aspect ratio $\varepsilon \to 0$. Although the thin film equation on a curved substrate has not been proven rigorously to be the $\varepsilon \to 0$ limit of the Navier-Stokes equations, we will accept it as the best low-order analytical model available.

Roy and Schwartz (1997) also included tangential stresses on the curved-substrate thin film equation. We have written the tangential stress in Equations (8.41) and (8.43) as a covector, $\mathcal{T}^{ext}_{\beta}$, which is the most convenient form if one wants to include a Marangoni stress of the form $\nabla_\beta \gamma$. If the tangential stress is to be expressed as a vector, the index must be raised, i.e.

$$\mathcal{T}^{ext}_{\beta} = (\widetilde{g}_{\alpha\beta} - 2\varepsilon H \mathrm{I\!I}_{\alpha\beta})\, \mathcal{T}^{\alpha}_{ext} + O(\varepsilon^2), \tag{8.47}$$

in which case the right-hand side tangential stress term of Equation (8.41) becomes:

$$-\nabla_\alpha \left\{ H^2 \left[\frac{1}{2} \widetilde{g}^{\alpha}_{\ \beta} - \frac{1}{3} \varepsilon H \left(4K_m \widetilde{g}^{\alpha}_{\ \beta} + 2\mathrm{I\!I}^{\alpha}_{\ \beta} \right) \right] \mathcal{T}^{\alpha}_{ext} \right\} + O(\varepsilon^2). \tag{8.48}$$

If we then replace $\mathcal{T}^{\alpha}_{ext}$, which is a tensor, with its non-tensorial physical vector counterpart $\overline{\mathcal{T}}^{\alpha}_{ext} = [\widetilde{g}^{\alpha}_{\ \beta} - \varepsilon H \mathrm{I\!I}^{\alpha}_{\ \beta} + O(\varepsilon^2)] \mathcal{T}^{\alpha}_{ext}$ (produced by multiplying by the scale factor), the RHS of Equation (8.41) becomes

$$-\nabla_\alpha \left\{ H^2 \left[\frac{1}{2} \widetilde{g}^{\alpha}_{\ \beta} - \frac{1}{3} \varepsilon H \left(4K_m \widetilde{g}^{\alpha}_{\ \beta} + \frac{1}{2} \mathrm{I\!I}^{\alpha}_{\ \beta} \right) \right] \overline{\mathcal{T}}^{\alpha}_{ext} \right\} + O(\varepsilon^2), \tag{8.49}$$

which is the same result found by Roy and Schwartz (1997). Whether working in covariant notation with tensors or in vector notation with scale factors, one must be very careful when adding tangential stresses. Note, however, that such stresses will not be needed for the applications of this thesis.

References

R. Aris. Vectors, Tensors and the Basic Equations of Fluid Mechanics. Dover Publications, New York, 1989. ISBN 9780486661100.

M. J. Assael, I. J. Armyra, J. Brillo, S. V. Stankus, J. Wu, and W. A. Wakeham. Reference data for the density and viscosity of liquid cadmium, cobalt, gallium, indium, mercury, silicon, thallium, and zinc. J. Phys. Chem. Ref. Data, 41(3), 2012. ISSN 0047-2689. doi:10.1063/1.4729873.

A. L. Bertozzi and M. Pugh. The lubrication approximation for thin viscous films: Regularity and long-time behavior of weak solutions. Commun. Pure Appl. Math., 49(2):85–123, February 1996. ISSN 0010-3640, 1097-0312. doi:https://doi.org/10.1002/(SICI)1097-0312(199602)49:2<85::AID-CPA1>3E3.0.CO;2-2.

V. P. Chentsov, V. G. Shevchenko, A. G. Mozgovoi, and M. A. Pokrasin. Density and surface tension of heavy liquid-metal coolants: Gallium and indium. Inorg. Mater. Appl. Res., 2(5): 468–473, 2011. doi:10.1134/S2075113311050108.

L. Giacomelli and F. Otto. Rigorous lubrication approximation. Interface Free Bound., 5(4): 483–529, 2003. doi:10.4171/ifb/88.

H. Jeffreys. The draining of a vertical plate. Math. Proc. Camb. Philos. Soc., 26(2):204–205, April 1930. ISSN 0305-0041, 1469-8064. doi:10.1017/S0305004100015437.

F. I. Niordson. Shell Theory. Applied Mathematics and Mechanics Series. North-Holland, Amsterdam, 1985. ISBN 9780444876409.

S. E. Orchard. On surface levelling in viscous liquids and gels. Appl. Sci. Res., 11(4-6):451–464, July 1963. ISSN 0003-6994. doi:10.1007/BF03184629.

A. Oron, S. H. Davis, and S. G. Bankoff. Long-scale evolution of thin liquid films. Rev. Mod. Phys., 69(3):931–980, 1997. doi:10.1103/RevModPhys.69.931.

O. Pinkus and B. Sternlicht. Theory of Hydrodynamic Lubrication. McGraw-Hill, New York, 1961.

O. Reynolds. IV. On the theory of lubrication and its application to Mr. Beauchamp Tower's experiments, including an experimental determination of the viscosity of olive oil. Philos. Trans. R. Soc. Lond., 177:157–234, December 1886. ISSN 0261-0523, 2053-9223. doi:10.1098/rstl.1886.0005.

A. J. Roberts. Low-dimensional modelling of dynamics via computer algebra. Comput. Phys. Commun., 100(3):215–230, March 1997. ISSN 00104655. doi:10.1016/S0010-4655(96)00162-2.

A. J. Roberts and Z. Li. An accurate and comprehensive model of thin fluid flows with inertia on curved substrates. J. Fluid Mech., 553(-1):33–73, April 2006. ISSN 0022-1120, 1469-7645. doi:10.1017/S0022112006008640.

L. A. Romero and F. G. Yost. Flow in an open channel capillary. J. Fluid Mech., 322:109–129, 1996. doi:10.1017/S0022112096002728.

R. V. Roy and L. W. Schwartz. Coating flow over a curved substrate. In Proc. 2nd European Coating Symposium, pages 18–27, Université Louis Pasteur, Strasbourg, 1997. P. G. Bourgin.

R. V. Roy, A. J. Roberts, and M. E. Simpson. A lubrication model of coating flows over a curved substrate in space. J. Fluid Mech., 454:235–261, 2002. ISSN 0022-1120. doi:10.1017/S0022112001007133.

M. Rumpf and O. Vantzos. Numerical gradient flow discretization of viscous thin films on curved geometries. Math. Models Methods Appl. Sci., 23(05):917–947, 2013. doi:10.1142/S0218202512500649.

L. W. Schwartz and D. E. Weidner. Modeling of coating flows on curved surfaces. J. Eng. Math., 29(1):91–103, 1995. doi:10.1007/BF00046385.

P. Smith. On steady long waves on a viscous liquid at small Reynolds number. J. Eng. Math., 3(3):181–187, July 1969a. ISSN 0022-0833, 1573-2703. doi:10.1007/BF01535167.

S. H. Smith. A non-linear analysis of steady surface waves on a thin sheet of viscous liquid flowing down an incline. J. Eng. Math., 3(3):173–179, July 1969b. ISSN 0022-0833, 1573-2703. doi:10.1007/BF01535166.

E. Tiesinga, P. Mohr, D. Newell, and B. Taylor. 2018 codata recommended values of the fundamental constants of physics and chemistry, 2019-06-03 04:06:00 2019. URL `https://tsapps.nist.gov/publication/get_pdf.cfm?pub_id=928211`.

M. M. Weislogel. Capillary flow in an interior corner. PhD thesis, Northwestern University, June 1996. URL `https://ntrs.nasa.gov/citations/19970010346`. Also published as NASA Technical Memorandum 107364.

A. W. Wray, D. T. Papageorgiou, and O. K. Matar. Reduced models for thick liquid layers with inertia on highly curved substrates. SIAM J. Appl. Math., 77(3):881–904, January 2017. ISSN 0036-1399, 1095-712X. doi:10.1137/16M1060686.

Chapter 9

GENERALIZED STABILITY OF VISCOUS THIN FILM CAPILLARY FLOW ON THE SURFACE OF A TORUS

9.1 Background

In this chapter, we consider the problem of viscous thin-film flow on a torus, driven only by capillary forces. While the torus may seem to be a rather simple shape, the base state and stability behaviors of a thin film coating its exterior turn out to be significantly more complex than those of films coating spheres or cylinders, and some of the results are initially counterintuitive.

We base our work on the curved-substrate viscous thin film equation driven by capillary forces alone, first developed by Roy and Schwartz (1997) [an improvement on an earlier model by Schwartz and Weidner (1995), including conservation of fluid volume] and expanded upon by Roy et al. (2002) (for a review of the derivation, see Chapter 8). Roy and Schwartz (1997) simulated the viscous thin film equation on the exterior of a torus, finding that an initially uniform film will thin on the outside of the torus and thicken on the inside (this phenomenon is depicted in Figure 9.1). (We use "outside" to refer to the side away from the center and "inside" to refer to the sides adjacent to the central hole. We will always think of the torus as a solid object with the film coating the exterior.) This behavior is to be expected, as the mean substrate curvature is more negative (and thus the capillary pressure more positive) on the outside than the inside. Roy et al. (2002) repeated the computation using a Galerkin method and with a governing equation differing by $O(\varepsilon^2)$, where ε is the characteristic film thickness over the characteristic length scale of variations, and finding a qualitatively similar result. Howell (2003) modified the curved-substrate viscous thin film equation of Roy and Schwartz (1997) by dropping pressure terms due to film interface variation; keeping only constant capillary pressure terms induced by substrate curvature. Howell showed that without the smoothing effect of fluid interface curvature, the interface experiences finite-time blowup; Howell went on to predict the blowup time for thin films coating the exterior of a torus and those coating the interior of a hollow torus. Reintroducing film curvature effects prevents blowup, but introduces an intermediate length scale between the fluid thickness and the substrate curvature length scale.

The analyses just mentioned were axisymmetric. However, Roy and Schwartz (1997) performed a simulation whose initial state was a uniform film with non-axisymmetric noise added. They found that, over time, a periodic disturbance appeared; with their simulation parameters of [major torus radius / minor torus radius] $= B = 10$ and [initial film thickness / minor torus radius] $= \varepsilon = 0.05$, the periodic pattern which emerged formed 4 ridges and 4 troughs, i.e., had wavenumber $k = 0.4$. Roy and Schwartz did not investigate this phenomenon further. We will do so with a linear stability analysis, and the result of which will confirm that $k = 0.4$ is an expected instability wavenumber with these parameters. Rumpf and Vantzos (2013) rederived the equation of Roy

and Schwartz (1997), expressing it as a gradient flow. In a later work, Vantzos et al. (2017) displayed the results of the thin film equation with gravity on a variety of curved substrates, including a torus. Beginning with a uniform thin film with "small perturbations," a symmetry breaking instability forms a periodic ring of droplets at the bottom of the torus (the authors did not provide parameter details or discuss the phenomenon further). We will ignore gravity in our work.

The study of capillary-induced instability of fluids has a long history, beginning with the Plateau-Rayleigh instability, according to which the surface of a cylindrical column of an inviscid fluid is unstable and forms undulations of a characteristic wavelength, and may break up into drops. Plateau (1873) computed the critical wavelength at which a perturbation becomes unstable, finding it to be 2π times the fluid radius. He verified the result with experiments in which a cylindrical thread of oil was suspended between two plates, observing that if the plates were separated by a distance of 6 to 8 times thread's radius, an undulation would indeed appear on the surface. Rayleigh (1878) performed a linear stability analysis of the problem, and found that besides the critical wavelength being 2π times the radius of the thread, the fastest-growing wavelength is approximately 9.02 times the radius.

While the Plateau-Rayleigh instability ignores viscosity, the phenomenon occurs in viscous fluids as well, where it is known as the Rayleigh-Tomotika instability. Rayleigh (1892) revisited the problem of fluid column instability with a linear stability analysis of a viscous and inertia-free fluid surrounded by vacuum, finding that the critical wavelength remains the same (2π times the column radius), but that there is no finite fastest-growing wavelength; longer wavelengths are monotonically more and more unstable. Tomotika (1935) extended the result by supposing that the cylindrical fluid column is surrounded not by vacuum but by another viscous fluid; in this case the fastest-growing wavelength is finite and a function of the ratio of the viscosities.

Variations on the Plateau-Rayleigh and Rayleigh-Tomotika instabilities can occur in fluid tori. Interest in tori of fluid appears to have begun with the study of ring bubbles, like those famously produced for recreation by dolphins (Marten et al., 1996). Perhaps the first experimental study of ring bubbles without cetaceans was performed by Walters and Davidson (1963), who then modeled them theoretically as inviscid vortex rings and thus found a relation between bubble radius and velocity. A symmetry-breaking instability is visible in the photographs taken by Walters and Davidson, but not addressed in their work. Lundgren and Mansour (1991) argued that the circulation of fluid around vortex ring bubbles should diminish the Plateau-Rayleigh instability; their simulations of ring bubbles revealed instead an axisymmetric instability in which the radius of the ring oscillates.

Pairam and Fernández-Nieves (2009) created smaller fluid tori a few millimeters across by a different process, injecting a stream of water into a rotating bath of oil. They observed a qualitatively Rayleigh-Tomotika-like instability in narrow tori, with fastest-growing wavelength proportional to the minor radius of the torus. Thick tori, i.e., those with a large minor radius,

shrank and formed droplets without holes before any symmetry-breaking instability was observed. Fragkopoulos et al. (2018) plotted the experimental results of Pairam and Fernández-Nieves (2009) against the Rayleigh-Tomotika dispersion curve and found them to be fairly close (within about 20%), suggesting that the observed instability was perhaps indeed related to the Rayleigh-Tomotika instability. McGraw et al. (2010) created even smaller liquid tori, around 30 microns in diameter, by melting small rings of solid polystyrene suspended in methanol; they also reported an instability with fastest-growing wavelength proportional to the torus minor radius. Mehrabian and Feng (2013) performed numerical simulations of an inertia-free, viscous fluid torus suspended in another viscous fluid, and performed a stability analysis by imposing a sinusoidal perturbation on the surface and numerically tracking the perturbations' growth. They found thick tori to be more stable than thin tori at early times; at later times, the complicated shrinkage of the tori prevented assessment of perturbation growth. For one example aspect ratio, they found a fastest-growing wavelength to be nearly exactly that of the cylinder predicted by Tomotika.

Unlike the work just described, our focus is not on pure fluid systems, but instead on thin films coating solid substrates. The linear instability of a thin film on the exterior of a straight cylinder was apparently first derived by Goren (1962), who found the most unstable wavelength for viscous and inviscid, and thick and thin film regimes. In the viscous thin-film regime, the fastest-growing wavelength is $2\sqrt{2}\pi \approx 8.89$ times the cylinder radius. Hammond (1983) carried out a numerical investigation of the full nonlinear thin film equation coating the *interior* of a cylindrical tube, finding that the fluid breaks up into a pattern of large and small droplets. Johnson et al. (1991) extended Hammond's analysis to include inertial effects and predicted the timescale at which a liquid bridge would form across the tube for various values of Reynolds number.

Unlike the case of a cylinder, the base state of thin film initially uniformly coating a torus is time-dependent, and the linearization of the governing equation is non-normal. In the limit as $T \to \infty$, the system approaches a stationary state, and in that limit a modal analysis can be conducted. At earlier times, a generalized linear stability analysis is required, which we will conduct following the generalized linear stability analysis methodology of Farrell and Ioannou (1996a,b) and Goldhirsch et al. (1987).

Generalized linear stability analysis has been applied to the problem of thin viscous films coating curved substrates under the influence of capillary forces and gravity by Balestra et al. (2016, 2018a,b). Those authors investigated a fluid coating the interior of cylindrical and spherical substrates, which produced periodic patterns of droplets as gravity and surface tension oppose each other. While the linearization of the curved thin film equation for a thin film uniformly coated cylinder of sphere without gravity is normal, the addition of gravity and a non-uniform initial condition resulted in non-normal and nonautonomous operators, necessitating a generalized linear stability analysis. Balestra et al. found in both cases that the system underwent large transient growth due to the non-orthogonal eigenfunctions; on spheres this was followed by

decay (decreasing amplitude) of disturbances at late times, while on a cylinder the disturbances continued to grow but at more slowly than at early times. They computed optimal disturbances using an adjoint method (Schmid, 2007); an overview of this method is given in Appendix B of this thesis. The problem of a thin film coating a torus without gravity is different in that the force driving evolution of the film is purely capillary, arising from the balance between outside and inside substrate curvatures, in addition to film interface curvature. The linear operator is also non-normal and nonautonomous.

We carry out a linear stability analysis of thin viscous films on tori. We concentrate on initial time ($T = 0$) and late times ($T \to \infty$). The non-normality of the operator leads us to compute both normal modes and optimal non-normal transient disturbances at $T = 0$, while at late times a modal analysis is sufficient. We also carry out a full, time-dependent generalized linear stability analysis for certain cases. We use comparisons to the cylinder instability to gain insight into the torus, though a few key differences should be kept in mind. First, the linearization of the governing equation on the torus yields a non-normal operator, rather than the normal operator that arises in the cylindrical case. Second, the base state of the film on the torus is moving, necessitating nonautonomous stability analysis. And, third, the periodic boundary conditions of the torus limit the admissible wavenumbers of the instability. While one might initially expect that the value of the fastest-growing wavelength should converge to that of the uniformly-coated cylinder as the major radius of the torus approaches infinity, that turns out to be the case only at $T = 0$. We show analytically and numerically that in the limit of large radius and late times, the fastest-growing wavelength does converge to a finite and well-defined value, and we explain why it does not equal that of the uniformly-coated cylinder.

The chapter is organized as follows. Section 9.2 will introduce the thin film equation on a toroidal substrate, and Section 9.3 will discuss the base state evolution. Section 9.4 will discuss the general linear stability analysis methodology. Section 9.5 will analytically explore limiting cases. While the general case is not analytically tractable, results will be found in the limiting cases of large major radius, and of extremely thin films, and these will be sufficient to provide explanation of much of the observed behavior. Numerical results for a variety of parameters will then be presented in Section 9.6.

9.1.1 Key model assumptions

Several important assumptions underlie the model developed in the following sections, restricting its domain of validity. The liquid film is assumed to be Newtonian and incompressible. Furthermore, gravity is ignored; specifically it is assumed that the Bond number $\mathrm{Bo} = \rho g L^2/\gamma \ll 1$, where ρ is fluid density, g is gravitational acceleration, L is the length scale of the substrate variations (taken to be the minor radius of the torus), and γ is the surface tension.

The liquid is assumed to be purely viscous, and all inertial effects are ignored. This condition is valid when the velocity is sufficiently small or the film is sufficiently thin. Specifically, epsilon

times the Reynolds number must be small, i.e., $\varepsilon \mathrm{Re} = \varepsilon(\rho u_c d/\mu) \ll 1$, where $\varepsilon = d/L$ is the lubrication parameter representing the ratio of the length scale of the film thickness normal to the substrate to the minor torus radius, ρ is the fluid density, u_c is the characteristic fluid velocity, and μ is the dynamic viscosity of the fluid. In the curved-substrate thin film problem, $u_c = \varepsilon^2\gamma/\mu$, where γ is surface tension, yielding the inertia-free condition $\varepsilon^3\rho\gamma d/\mu^2 \ll 1$. Furthermore, the thickness of the fluid is assumed to be much smaller than the length scale of tangential variations. These two conditions allow the fluid to be modeled by the viscous thin film equation on a curved substrate, first developed by Roy and Schwartz (1997).

Because we work exclusively in nondimensional coordinates, there is no concern about the zero gravity or noninertial requirements being unmet. However, the lubrication requirement must be checked continuously, as the characteristic length scale of fluid variations does not always equal that of the substrate (Howell, 2003). Therefore, we ensure that $(h/L)^2 = \varepsilon^2 H^2 \ll 1$, $(\partial_\theta h/L)^2 = \varepsilon^2(\partial_\theta H)^2 \ll 1$, and $(h\partial_{\theta\theta}h/L^2) = \varepsilon^2(H\partial_{\theta\theta}H) \ll 1$ at all times, where h is the normal film thickness and $H = h/d$ is the dimensionless normal film thickness. We find that this condition is satisfied so long as the initial uniform film thickness satisfies $\varepsilon < 0.15$ and the dimensionless major torus radius $B = b/L$ satisfies $B \geq 5$. For tori with smaller radius, a thick film analysis such as that of Wray et al. (2017) may be applicable. Roy and Schwartz (1997) and Roy et al. (2002) show base state results for only $B = 2$, $\varepsilon = 0.1$, which we exclude due to violation of our lubrication limit requirements. Our model differs from theirs at $O(\varepsilon^2)$ (and both are accurate only to ε^2 in the first place), and thus does not give the same results in the thick film regime $h/L \gtrsim 0.3$. In the thin film regime, for $h/L \lesssim 0.3$, the results for the $B = 2$, $\varepsilon = 0.1$ case match well, with typical difference $< 1\%$ and worst-case difference of 5% (see Section 9.6.4).

It should also be noted that the solid torus substrate is assumed to be perfectly smooth, with no roughness or grooving. Furthermore, Van der Waals effects, which become important for very thin films, are ignored, and no rupturing processes will be considered.

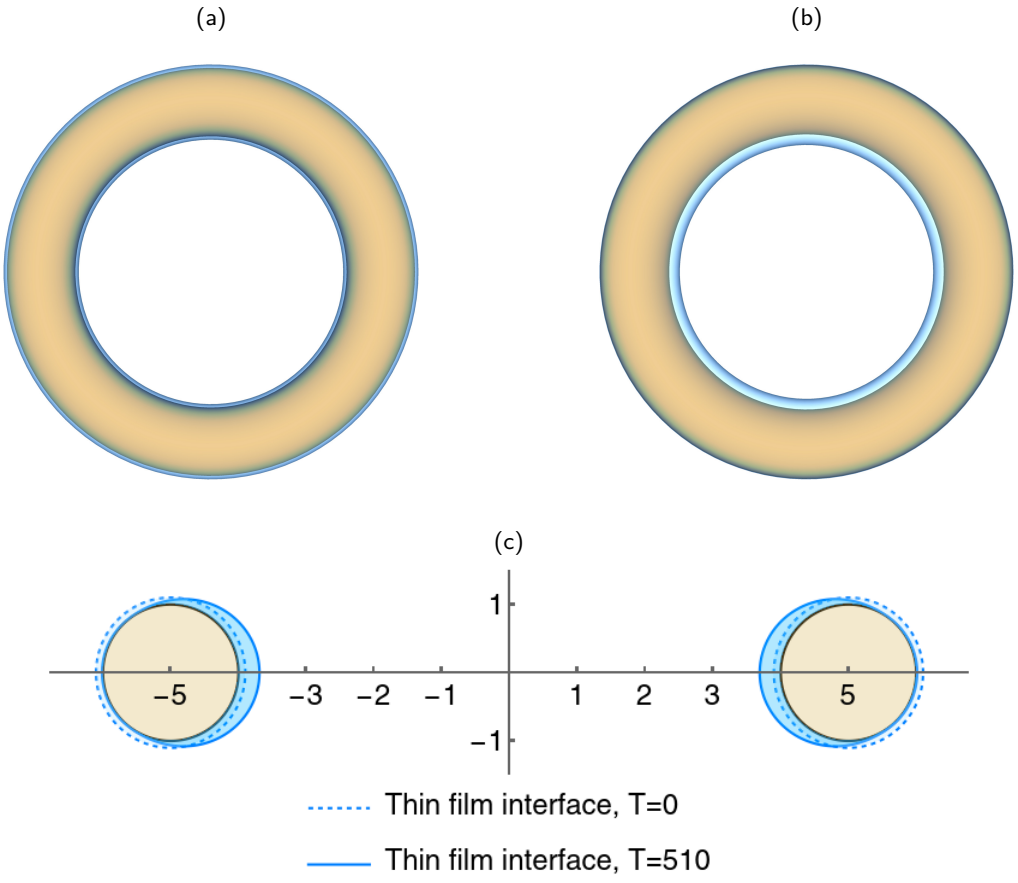

Figure 9.1: Evolution of initially uniform base state film $H_{\text{base}}(\theta, T)$ for a torus with minor radius 1, major radius $B = 5$ and initial uniform film thickness $0.1\times$ the minor radius (i.e., $\varepsilon = 0.1$), according to the thin film equation on a torus, Equations (9.17) and (9.18). Plots depict the uniform condition, $H_{\text{base}}(\theta, T = 0)$, and a late time $H_{\text{base}}(\theta, T = T_{\text{late}} = 510)$ at which the system has reached a quasi-stationary state. Numerical results were computed using a finite difference method, described in Section 9.6.1. See Table 9.1 for an overview of variable definitions relevant to this system.
(a) Overhead view of torus at initial time $T = 0$.
(b) Overhead view of torus at late time $T = T_{\text{late}} = 510$, by which point the fluid has reached a quasi-stationary state in which it has thickened on the inside and thinned on the outside.
(c) Cross-sectional view displaying thin film interface at $T = 0$ (dotted blue line) and $T = T_{\text{late}} = 510$ (solid blue line).

9.2 Thin film equation on a torus

Consider a torus (doughnut) coated by an initially uniform thin film of a viscous, incompressible Newtonian liquid. Over time, the film will thicken around the central hole, while thinning on the outside (Figure 9.1). Furthermore, a linear stability analysis reveals that an undulating disturbance to the film surface around the central hole may grow in time. The purpose of this work is to elucidate the nature of this instability. In this derivation, we will use the term "inside"

to refer to region proximal to the central hole of the torus, where the Gaussian curvature is negative, and "outside" to refer to the distal region where the Gaussian curvature is positive. These terms should *not* be confused with the exterior or interior of a hollow, tubular torus; our tori will always be solid and the liquid film will lie only on the exterior.

9.2.1 Thin film equation on a general curved substrate

The fluid is modeled by the viscous thin film equation on a curved substrate, first developed by Roy and Schwartz (1997), given for a general curved substrate by

$$\frac{\partial}{\partial t}\left(h-\kappa_m h^2+\frac{1}{3}\kappa_G h^3\right)=-\frac{1}{3\mu}\overline{\nabla}_\alpha\left\{h^3\left[-\delta^\alpha{}_\beta+h\left(2\kappa_m\delta^\alpha{}_\beta-\frac{1}{2}\mathrm{I\!I}^\alpha{}_\beta\right)\right]\overline{\nabla}^\beta p\right\}+O(\varepsilon^2), \tag{9.1}$$

where h is the film thickness measured normal to the substrate, $\mathrm{I\!I}^\alpha{}_\beta$ is the substrate shape tensor, or second fundamental form, $\kappa_m=(1/2)\mathrm{I\!I}^\alpha{}_\alpha$ is the substrate mean curvature, $\kappa_G=\det[\mathrm{I\!I}^\alpha{}_\beta]$ is the substrate Gaussian curvature, t is time, p is pressure at the fluid interface, and $\varepsilon=d/L$, with d being the characteristic film thickness and L being the characteristic length scale of variations in the substrate. The derivatives $\overline{\nabla}_\alpha$ are covariant derivatives, defined on the substrate surface.

The system is nondimensionalized as described in Chapter 8; an overview of the dimensionless variables is given in Table 9.1. In dimensionless variables, Equation (9.1) may be written as

$$\frac{\partial}{\partial T}\left(H-\varepsilon K_m H^2+\frac{1}{3}\varepsilon^2 K_G H^3\right)=-\frac{1}{3}\nabla_\alpha\left\{H^3\left[-\delta^\alpha{}_\beta+\varepsilon H\left(2K_m\delta^\alpha{}_\beta-\frac{1}{2}\mathrm{I\!I}^\alpha{}_\beta\right)\right]\nabla^\beta P\right\}+O(\varepsilon^2), \tag{9.2}$$

where $H=h/d$ is the dimensionless film thickness, $K_m=\kappa_m L$ is the dimensionless substrate mean curvature, $K_G=\kappa_G L$ is the dimensionless substrate Gaussian curvature, $\mathrm{I\!I}=\mathrm{I\!I}L$ is the dimensionless substrate shape tensor, and the covariant derivatives $\nabla_\alpha=L\overline{\nabla}_\alpha$ have been nondimensionalized by L. $P=p/p_c=p/(\gamma/L)$ is the dimensionless pressure, which has been nondimensionalized by the characteristic capillary pressure γ/L, γ being the surface tension. The dimensionless time is $T=t/t_c=t(\varepsilon^2\gamma)/(\mu L)$.

It is convenient to work not in film thickness H measured normal to the substrate surface, but in volumetric film thickness $V=[H-\varepsilon K_m H^2+(1/3)\varepsilon^2 K_G H^3]$, which measures the total volume of fluid above an infinitesimal patch of substrate surface. Besides simplifying the left-hand side of Equation (9.2), working in volumetric film thickness makes tracking the redistribution of fluid more intuitive. If a small volume of fluid is added to the outside of the torus, it will change the normal thickness H differently than if that same volume were added to the inside of the torus, because of the curvature of the substrate. But the volumetric thickness V increases in response to an additional volume of fluid by the same amount, regardless of where on the substrate that volume is added. The dimensionless thin film equation in terms of volumetric thickness is

$$\frac{\partial V}{\partial T}=-\frac{1}{3}\nabla_\alpha\left\{V^3\left[-\delta^\alpha{}_\beta-\varepsilon V\left(K_m\delta^\alpha{}_\beta+\frac{1}{2}\mathrm{I\!I}^\alpha{}_\beta\right)\right]\nabla^\beta P\right\}+O(\varepsilon^2)=-\nabla_\alpha Q^\alpha, \tag{9.3}$$

Quantity	Scaling	Rescaled variable
Minor torus radius	L	1
Major torus radius	L	$B = b/L$
Lubrication parameter		$\varepsilon = d/L \ll 1$
Normal film thickness	d	$H(\theta, S, T) = h(\theta, s, t)/d$
Normal film thickness at $t = 0$	d	$H(\theta, S, 0) = h(\theta, s, 0)/d = 1$
Volumetric film thickness	d	$V(\theta, S, T) = v(\theta, s, t)/d$
Base state normal film thickness	d	$H_{\mathsf{base}}(\theta, S, T) = h_{\mathsf{base}}(\theta, s, t)/d$
Base state volumetric film thickness	d	$V_{\mathsf{base}}(\theta, S, T) = v_{\mathsf{base}}(\theta, s, t)/d$ $= [H - \varepsilon K_m H^2 + (1/3)\varepsilon^2 K_G H^3]$
Coordinates	L	$S = s/L = B\phi$ ϕ θ
Wavenumber	L^{-1}	$k = \tilde{k}L$
Velocity	$u_c = \varepsilon^2\gamma/\mu$	
Time	$t_c = L/u_c = L\mu/(\varepsilon^2\gamma)$	$T = t/t_c$
Late time		$T_{\mathsf{late}} = 5\varepsilon^{-1/3}\pi^2 B(1 - B^{-2})$
Pressure	$p_c = \gamma/L$	$P = p/p_c$
Mean curvature	$k_c = 1/L$	$K_m = \kappa_m/k_c$
Gaussian curvature	$k_c = 1/L$	$K_G = \kappa_G/k_c$
Shape tensor	$k_c = 1/L$	$\mathbb{II}_{\alpha\beta} = \mathrm{II}_{\alpha\beta}/k_c$
Covariant derivative	$1/L$	$\nabla_\alpha = L\overline{\nabla}_\alpha$
Lubrication limit capillary number		$\mathrm{Ca} = \varepsilon^{-2}\mu u_c/\gamma = Lp_c/\gamma = 1$
Reynolds number		$\mathrm{Re} = \rho u_c d/\mu = \varepsilon^2\rho\gamma d/\mu^2$
Bond number		$\mathrm{Bo} = \rho g_{grav} L^2/\gamma$
Shorthand geometric factor f		$f = B^{-1}\cos\theta$

Table 9.1: Characteristic scalings (lower case) and nondimensional variables (uppercase) used to describe dimensionless system depicted in Figure 9.2.

where Q^α is the flux, a vector quantity tangential to the substrate which is the result of integrating the tangential fluid velocity normally from the substrate to the fluid interface. The flux can be understood as the net amount of fluid passing through a line which extends normally from a point on the surface. The pressure P is the capillary pressure, which is given by

$$\begin{aligned} P &= \mathrm{Ca}^{-1}\left[-\mathrm{I\!I}^\alpha_\alpha - \varepsilon\left(\nabla_\mu\nabla^\mu V + V\mathrm{I\!I}^\alpha_\mu\mathrm{I\!I}^\mu_\alpha\right)\right] + O(\varepsilon^2) \\ &= -\mathrm{Ca}^{-1}\left[2K_m + \varepsilon\left(\nabla_\mu\nabla^\mu V + V\left\{4{K_m}^2 - 2K_G\right\}\right)\right] + O(\varepsilon^2) \\ &= -\left[2K_m + \varepsilon\left(\nabla_\mu\nabla^\mu V + V\left\{4{K_m}^2 - 2K_G\right\}\right)\right] + O(\varepsilon^2) \end{aligned} \tag{9.4}$$

and Ca the capillary number. We have taken the characteristic velocity to be the capillary velocity, $u_c = \gamma/\mu$, so that $\mathrm{Ca} = 1$ and the time scale is $t_c = L/u_c = L\mu/\gamma$. Because inertial effects are neglected and the only force is that of surface tension, μ and γ have no effect on the equation other than to set the time scale. The base state and instability behavior of the system do not otherwise depend on the viscosity or surface tension constant.

Equation (9.3) can be understood as describing how a local volume element, a parcel of fluid above a small patch of substrate surface, changes in response to flux divergence. If the divergence of flux is positive at some point on the substrate surface, i.e., $\nabla_\alpha Q^\alpha > 0$, then fluid is on the net flowing away from that point, and the local volume element (and local film height) will decrease. The flux is essentially the negative gradient of pressure (with some multiplicative corrections due to the curved coordinates); in particular, fluid is driven from high pressure to low pressure. The capillary pressure is determined by the mean curvature of the fluid interface. The film is assumed to be thin compared to the substrate radius of curvature, and thus at lowest order may be considered to be conformal to the substrate. Therefore, the dominant contribution to the mean curvature of the fluid interface is simply the mean curvature of the substrate; the film thickness and variations thereof induce $O(\varepsilon)$ corrections to the interfacial curvature, as seen in Equation (9.4). For a detailed derivation of Equations (9.2) to (9.4), see Chapter 8.

9.2.2 Torus geometry

Let the minor radius of the torus be denoted L, and the major radius b, with the major radius measured to the center of the solid portion of the torus (Figure 9.2). Nondimensionalizing with the minor radius L as the characteristic length, the dimensionless minor radius is 1 and the dimensionless major radius is $B = b/L$. The major radius, B, must satisfy $B > 1$ to avoid self-intersection. In all cases, we will take the initial condition of the film to be a coating of uniform thickness d, which is nondimensionalized as a small parameter $\varepsilon = d/L$.

In order to define Equation (9.3) on a toroidal substrate of minor radius 1 and major radius B, we choose to express the substrate parametrically in terms of a minor coordinate $\theta \in [0, 2\pi)$

and major coordinate $S \in [0, 2\pi B)$ as:

$$\vec{X} = \begin{pmatrix} (B + \cos\theta)\cos\phi \\ (B + \cos\theta)\sin\phi \\ \sin\theta \end{pmatrix} = \begin{pmatrix} (B + \cos\theta)\cos\left(\frac{S}{B}\right) \\ (B + \cos\theta)\sin\left(\frac{S}{B}\right) \\ \sin\theta \end{pmatrix}. \tag{9.5}$$

This is the same parametrization used by Roy and Schwartz (1997), Roy et al. (2002), and Howell (2003), except that we choose S instead of ϕ as our major coordinate. Since we have designated the minor radius as 1, then θ is both an angular measure and an arc length measure. Note that $\theta = 0$ on the outside of the torus, and $\theta = \pi$ on the inside. The other coordinate, S, measures arc length of the major coordinate, and $\phi = S/B$ is the major angular measure (see Figure 9.2). We use the coordinate S instead of ϕ in order to simplify comparisons to the cylindrical case, where $B \to \infty$ and ϕ becomes ill-defined.

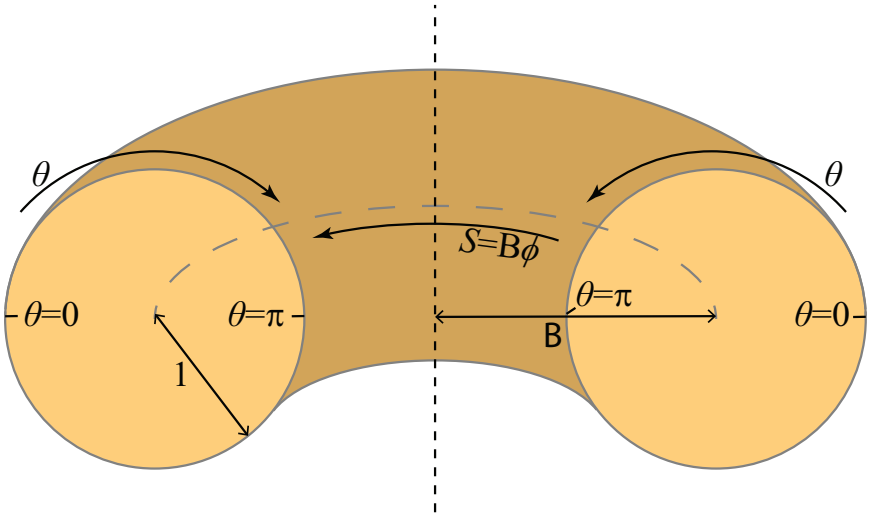

Figure 9.2: Coordinate system on a torus of minor radius 1 and major radius B (diagram depicts only toroidal substrate, omitting coating liquid film).

The local metric is then

$$\widetilde{g}_{\alpha\beta} = (\nabla\vec{X})^T \cdot (\nabla\vec{X}) = \begin{bmatrix} 1 & 0 \\ 0 & (1 + B^{-1}\cos\theta)^2 \end{bmatrix}, \tag{9.6}$$

$$\widetilde{g}^{\alpha\beta} = \begin{bmatrix} 1 & 0 \\ 0 & (1 + B^{-1}\cos\theta)^{-2} \end{bmatrix}, \tag{9.7}$$

$$\sqrt{\det\widetilde{g}} = 1 + B^{-1}\cos\theta. \tag{9.8}$$

The surface tangent and normal vectors are

$$\hat{N} = \begin{pmatrix} \cos\theta\cos\phi \\ \cos\theta\sin\phi \\ \sin\theta \end{pmatrix} \quad \hat{T}_\theta = \begin{pmatrix} -\sin\theta\cos\phi \\ -\sin\theta\sin\phi \\ \cos\theta \end{pmatrix}, \quad \hat{T}_s = \begin{pmatrix} -(1 + B^{-1}\cos\theta)\sin\phi \\ (1 + B^{-1}\cos\theta)\cos\phi \\ 0 \end{pmatrix}. \tag{9.9}$$

The shape tensor, or second fundamental form, can then be derived, along with the mean and Gaussian curvatures

$$\begin{aligned}\mathrm{I\!I}_{\alpha\beta} &= \begin{bmatrix} (\partial_\theta \hat{T}_\theta)\cdot\hat{N} & (\partial_\theta \hat{T}_S)\cdot\hat{N} \\ (\partial_S \hat{T}_\theta)\cdot\hat{N} & (\partial_S \hat{T}_S)\cdot\hat{N} \end{bmatrix} \\ &= \begin{bmatrix} -1 & 0 \\ 0 & -(1+B^{-1}\cos\theta)B^{-1}\cos\theta \end{bmatrix} = \begin{bmatrix} -1 & 0 \\ 0 & -f(1+f) \end{bmatrix}, \end{aligned} \tag{9.10}$$

$$\mathrm{I\!I}^{\alpha}_{\ \beta} = \widetilde{g}^{\alpha\delta}\mathrm{I\!I}_{\delta\beta} = \begin{bmatrix} -1 & 0 \\ 0 & -\frac{B^{-1}\cos\theta}{(1+B^{-1}\cos\theta)} \end{bmatrix} = \begin{bmatrix} -1 & 0 \\ 0 & -\frac{f}{1+f} \end{bmatrix}, \tag{9.11}$$

$$\mathrm{I\!I}^{\alpha\beta} = \mathrm{I\!I}^{\alpha}_{\ \delta}\widetilde{g}^{\delta\beta} = \begin{bmatrix} -1 & 0 \\ 0 & -\frac{B^{-1}\cos\theta}{(1+B^{-1}\cos\theta)^3} \end{bmatrix} = \begin{bmatrix} -1 & 0 \\ 0 & -\frac{f}{(1+f)^3} \end{bmatrix}, \tag{9.12}$$

$$K_m = \frac{1}{2}\mathrm{I\!I}^{\alpha}_{\ \alpha} = -\frac{1+2B^{-1}\cos\theta}{2(1+B^{-1}\cos\theta)} = -\frac{1+2f}{2(1+f)}, \tag{9.13}$$

$$K_G = \det\left(\mathrm{I\!I}^{\alpha}_{\ \beta}\right) = \frac{B^{-1}\cos\theta}{(1+B^{-1}\cos\theta)} = \frac{f}{1+f}, \tag{9.14}$$

$$\mathrm{I\!I}^{\alpha}_{\ \beta}\mathrm{I\!I}^{\beta}_{\ \alpha} = \left(4{K_m}^2 - 2K_G\right) = 1 + \frac{(B^{-1}\cos\theta)^2}{(1+B^{-1}\cos\theta)^2} = 1 + \left(\frac{f}{1+f}\right)^2, \tag{9.15}$$

where we have defined

$$f = B^{-1}\cos\theta \tag{9.16}$$

for convenience. The curvature does not depend on ϕ, since the torus is symmetrical in ϕ. The mean curvature, K_m, is clearly negative on the outside, where $\theta = 0$, and lower there than on the inside, where $\theta = \pi$. For sufficiently small B (i.e., sufficiently "fat" tori) where $B < 2$, K_m becomes positive on the inside; at larger B, it is negative. As for the Gaussian curvature, it is positive on the outside and negative on the inside.

Using the differential geometry identity $\sqrt{\det\widetilde{g}}\nabla_\alpha v^\alpha = \partial_\alpha(\sqrt{\det\widetilde{g}}v^\alpha)$, the thin film equation on a torus can be written explicitly:

$$\begin{aligned}\frac{\partial V}{\partial T} =& \frac{1}{\sqrt{\det\widetilde{g}}}\partial_\alpha\left\{\sqrt{\det\widetilde{g}}\frac{V^3}{3}\left[\widetilde{g}^{\alpha\beta} + \varepsilon V\left(K_m\widetilde{g}^{\alpha\beta} + \frac{1}{2}\mathrm{I\!I}^{\alpha\beta}\right)\right]\partial_\beta P\right\} + O(\varepsilon^2) \\ =& \frac{1}{1+f}\partial_\theta\left\{(1+f)\frac{V^3}{3}\left[1 - \varepsilon V\frac{(2+3f)}{2(1+f)}\right]\partial_\theta P\right\} \\ &+ \partial_S\left\{\frac{V^3}{3}\left[\frac{1}{(1+f)^2} - \varepsilon V\frac{(1+3f)}{2(1+f)^3}\right]\partial_S P\right\} + O(\varepsilon^2), \end{aligned} \tag{9.17}$$

with

$$\begin{aligned}P &= \frac{1+2f}{1+f} - \varepsilon\left\{\nabla_\mu\nabla^\mu V + V\left[1 + \left(\frac{f}{1+f}\right)^2\right]\right\} + O(\varepsilon^2) \\ &= \frac{1+2f}{1+f} - \varepsilon\left\{\partial_{\theta\theta}V + \frac{\partial_\theta f}{1+f}\partial_\theta V + \frac{\partial_{SS}V}{(1+f)^2} + \left[1 + \left(\frac{f}{1+f}\right)^2\right]V\right\} + O(\varepsilon^2), \end{aligned} \tag{9.18}$$

where again $f = B^{-1}\cos\theta$. By comparison, the thin film equation on a cylinder is computed by taking the limit $B \to \infty$, or $f \to 0$:

$$\frac{\partial V}{\partial T} = \partial_\theta \left\{ \frac{V^3}{3} \left[1 - \varepsilon V\right] \partial_\theta P_{\text{cylinder}} \right\} + \partial_S \left\{ \frac{V^3}{3} \left[1 - \frac{1}{2}\varepsilon V\right] \partial_S P_{\text{cylinder}} \right\} + O(\varepsilon^2), \tag{9.19}$$

$$P_{\text{cylinder}} = 1 - \varepsilon \left\{ \partial_{\theta\theta} V + \partial_{SS} V + V \right\} + O(\varepsilon^2). \tag{9.20}$$

In this cylindrical case, the substrate contribution to the pressure is constant (the leading 1), while the thin film adds pressure both by its own surface curvature ($\partial_{\theta\theta}V + \partial_{SS}V$) and by its thickness changing the radius of curvature about the substrate (the V term). Because the substrate pressure is constant on the cylinder, the dynamics will be entirely driven by film surface effects; on the torus, the non-constant substrate curvature drives film redistribution even without taking into account the film's curvature contribution.

9.3 Base state evolution

In this work, we consider the evolution of thin films which initially uniformly coat tori. Specifically, we set initial condition

$$H_{\text{base}}(\theta, S, T = 0) = H_0 = 1, \tag{9.21a}$$

$$\implies V_{\text{base}}(\theta, S, T = 0) = V_0(\theta) = 1 - \varepsilon K_m + \frac{\varepsilon^2}{3} K_G = 1 + \varepsilon \frac{1 + 2f}{2(1+f)} + \frac{\varepsilon^2}{3} \frac{f}{1+f}, \tag{9.21b}$$

where H_{base} and V_{base} denote the base-state solutions to Equations (9.17) and (9.18) given the uniform initial condition specified above. Note in particular that the initial condition specified in Equation (9.21) is axisymmetric, i.e., independent of S. The evolution of this base state thus remains axisymmetric at all times T.

There is no stationary (time-independent) solution to Equations (9.17) and (9.18) without fluid rupture or bridging the inner hole. This situation arises due to the lack of axisymmetric surfaces of topological genus > 0 (i.e., with holes) with constant mean curvature (Delaunay, 1841); a result which also explains why the pure fluid tori of Pairam and Fernández-Nieves (2009) collapsed into droplets. However, an axisymmetric surface of constant mean curvature does exist if rupture is allowed, and this is the state which the initially uniformly-coated torus system approaches. Because rupture or, alternatively, Van der Waals forces, are not included in our model, the system approaches rupture without actually achieving it, simply becoming very thin and never reaching $H = 0$. Due to the large viscous stresses in regions where the film becomes extremely thin, fluid redistribution slows down and the interface very gradually approaches the ruptured stationary state. The speed of interface movement at late times slows to far below the rate of growth of instabilities, and hence can be considered a quasi-stationary state.

9.3.1 Numerical methodology

By virtue of the base state being axisymmetric, the evolution equations [Equations (9.17) and (9.18)] become a 1+1 dimensional PDE. The base state was integrated in MATLAB R2018B

(Mat, 2018) by first manually discretizing the spatial derivatives and then using the built-in `ode15s` solver to integrate the result in time.

The spatial discretization was performed with 4th order central differences on an equispaced mesh $\theta \in [0, 2\pi)$, with periodic boundary conditions. For $\varepsilon \geq 0.01$, $N_{\text{mesh}} = 100$ mesh points were used. For thinner films, the mesh spacing was set to be ceil$[50 \times 2\pi/(0.15\varepsilon^{1/3})]/50$ to ensure that narrow regions around $\theta = \pi$ were adequately captured; specifically, N_{mesh} was

ε	≥ 0.01	0.005	0.001	5×10^{-4}	10^{-4}	5×10^{-5}	10^{-5}
N_{mesh}	100	250	450	550	950	1150	1950
ε	5×10^{-6}	10^{-6}	5×10^{-7}	10^{-7}			
N_{mesh}	2450	4200	5300	9050			

.

For the case of $B = 200$, a finer mesh of $N_{\text{mesh}} = 200$ was used, even for $\varepsilon \geq 0.01$. These mesh sizes were sufficient to capture fluid thickness variations; in particular, $\Delta\theta < |V/\partial_\theta V|$ and $\Delta\theta < \sqrt{|V/\partial_{\theta\theta} V|}$ in all simulations.

Due to the varying geometry, there is no canonically "correct" timescale for comparing results of different simulations. The integration time T_{late} was simply chosen to be long enough to ensure that the base state was close to the stationary state. For simplicity, a single T_{late} expression was chosen and used across all simulations, with

$$T_{\text{late}} = 10\varepsilon^{-1/3} \frac{\pi^2}{P_0(\theta = 0) - P_0(\theta = \pi)} = 10\varepsilon^{-1/3} \frac{\pi^2(1 - B^{-2})}{2B^{-1}}, \tag{9.22}$$

where P_0 refers to the substrate-induced pressure. In other words, the timescale was chosen to be the distance between inside and outside (π) squared over the nondimensional $O(\varepsilon^0)$ pressure difference between inside and outside. This choice is made from Equation (9.2), as a coarse scaling with $H \approx 1$ gives it the form roughly $1/T \sim \nabla^2 P$. A correction $\varepsilon^{-1/3}$ is included to ensure that sufficient time is allotted due to the singular perturbation effect (Section 9.5.2), and a factor of 10 is added. Time-dependent simulations were run for $\varepsilon \geq 0.05$ (very small ε simulations were run only to determine $T = 0$ results). In all cases, the velocity of the fluid interface was much lower than both the initial velocity and the spectral abscissa $\beta(T_{\text{late}})$ (see Section 9.4). Specifically, $|\partial_T V(\theta = \pi, T = T_{\text{late}})|/|\partial_T V(\theta = \pi, T = 0)| < 5 \times 10^{-3}$ and $[\beta(T_{\text{late}})]^{-1}|[\partial_T V(\theta = \pi, T = T_{\text{late}})]/V(\theta = \pi, T = T_{\text{late}})| < 10^{-3}$. T_{late} is thus judged to be a sufficiently long time as to consider the base state to be quasi-stationary.

The intermediate time T_{mid} was chosen to be the point at which the fluid thickness at $\theta = \pi$ had grown to 25% of the distance between its initial state and its late state. That is, $H(\theta = \pi, T = T_{\text{mid}}) = H(\theta = \pi, T = 0) + 0.25[H(\theta = \pi, T = T_{\text{late}}) - H(\theta = \pi, T = 0)]$. Typically, $T_{\text{mid}} \approx O(0.01 T_{\text{late}})$.

Individual time steps were chosen automatically by `ode15s` to ensure stable integration (the alternative built-in MATLAB solvers `ode23s`, `ode23t`, and `ode23tb` were tested for $B = 10$ and $\varepsilon = 0.1$ and gave nearly identical results, with maximum absolute difference $\max_{T,\theta}$

$|H_{\text{ode15s}}(T,\theta) - H_{\text{ode23x}}(T,\theta)| = 0.0066$ and maximum relative difference $\max_{T,\theta} |H_{\text{ode15s}}(T,\theta)$ / $H_{\text{ode23x}}(T,\theta) - 1| = 0.53\%$).

Note that because we conduct numerical simulations of Equations (9.17) and (9.18) in the volumetric thickness variable V rather than the normal thickness variable H, the total volume is automatically conserved (this was confirmed numerically as well).

9.3.2 Numerical results

Examples of base state evolution are shown in Figure 9.3, for $\varepsilon = 0.1$ and major radii $B = 5$ (a)-(b), $B = 10$ (c)-(d), and $B = 100$ (e)-(f). Plots display the normal thickness $H_{\text{base}}(\theta, T)$ plotted against θ, and a cross-section plot showing the growth of $H_{\text{base}}(\theta, T)$ as it appears on the curved substrate. Plots show evolution until a late time at which the film is quasi-stationary. In all cases, fluid thins on the outside of the torus and thickens on the inside; this phenomenon was described by Howell (2003); Roy and Schwartz (1997); Roy et al. (2002) as well. There appear to be two stagnation points where the fluid thickness remains nearly constant in time as fluid is transferred from the outside to the inside. This stagnation point is near $\pm\pi/2$, but is not exactly at that value; it occurs at approximately $\theta = \{1.77, 1.70, 1.59\}$ for $B = \{5, 10, 100\}$, respectively.

The $B = 100$ case (Figure 9.3 (e)-(f)] approaches a state which is nearly a simple shifting of the entire fluid surface: where it was a circle of radius $(1+0.1)$ centered around the substrate at $T = 0$, at later times it is close to a circle of radius $(1+0.1)$ shifted inwards (f). In the linear plot (e), the shifted circle corresponds to a nondimensional film thickness of $H_{\text{base}} \approx [1 - \cos(\theta)]$.

The cases of $B = 5$, (a)-(b), and $B = 10$, (c)-(d), look different. The thickening on the inside is much greater and narrower, and the fluid forms an egg shape around the substrate. Although at first glance this appears to violate conservation of volume, it does not; because the inside circumference $2\pi(B-1)$ is much less than the outside circumference $2\pi(B+1)$, a greater fluid thickness is needed $\theta = \pi$ to store the same volume of liquid. It is also notable that as the major radius B is decreased, the point of presumable future rupture moves inwards. Thus, the stationary state being approached is one of two distinct regions, one mass of fluid on the inside of the torus and a second mass on the outside of the torus. As B decreases, the size of the outer mass appears to increase. This phenomenon appeared in the results of Howell (2003); Roy et al. (2002) as well, both of whom considered $B = 2$.

We next fix the major radius at $B = 10$ and vary the initial uniform film thickness, such that $\varepsilon \in \{0.05, 0.1, 0.15\}$, results of which are shown in Figure 9.4. The difference between these three cases is somewhat similar to that between the cases of different B. Thin initial films (small ε) have a greater thickening around $\theta = \pi$ and a narrow peak, with the stagnation points at approximately $\theta = \pm\{1.79, 1.70, 1.66\}$ for $\varepsilon = \{0.05, 0.1, 0.15\}$, respectively. This phenomenon occurs because a thinner film requires a larger second derivative in order for the variation in its interface curvature to balance that of the substrate.

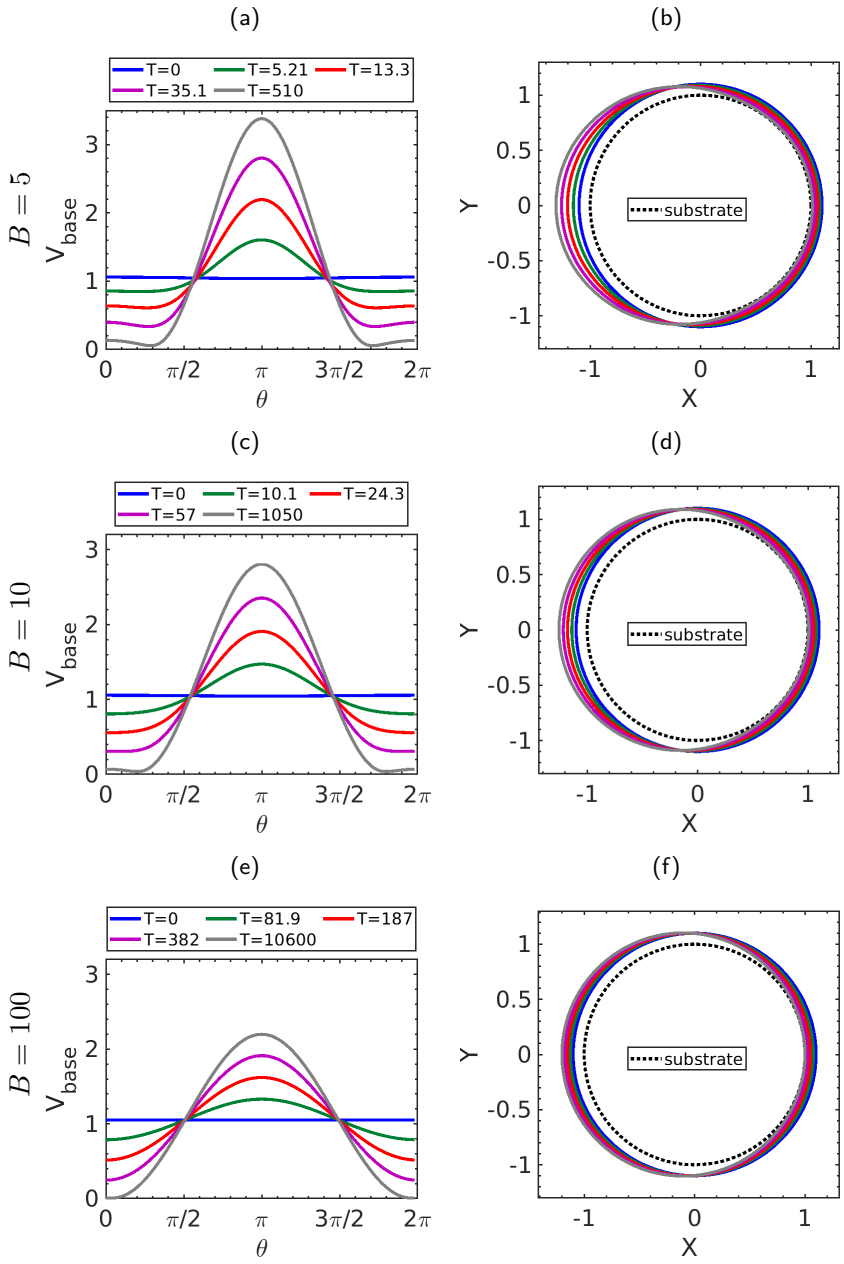

Figure 9.3: Evolution of base state volumetric film thickness $V_{\text{base}}(\theta, T)$ for tori with uniform initial film thickness such that $\varepsilon = 0.1$, according to the thin film equation on a torus, Equations (9.17) and (9.18). Each plot depicts five time steps, chosen such that the film thickness at $\theta = \pi$ is equispaced between $T = 0$ and the late time, $T = T_{\text{late}}$. The left column depicts volumetric film thickness against θ; the right column depicts a cross-sectional view of the fluid coating the circular substrate (black dotted line).
(a)-(b): Major radius $B = 5$, shown at time steps $T \in \{0, 5.21, 13.3, 35.1, 510\}$.
(c)-(d): Major radius $B = 10$, shown at time steps $T \in \{0, 10.1, 24.3, 57.0, 1050\}$.
(e)-(f): Major radius $B = 15$, shown at time steps $T \in \{0, 81.9, 187, 382, 10600\}$.

The similarity between the effects of varying B and varying ε arises because the film growth is controlled by the competing effects of substrate curvature, which is $O(1/B)$, and thin film interface curvature, which is $O(\varepsilon)$. The ratio of these two factors is thus $O(\varepsilon B)$. That is, increasing B or ε increases the relative effect of the film interface curvature, and vice versa. While this argument captures the main effect, there are additional factors of B and ε in the governing equations which cannot be collapsed into a single parameter (εB).

Additional plots of the base states may be found in this chapter's appendix (Section 9.9).

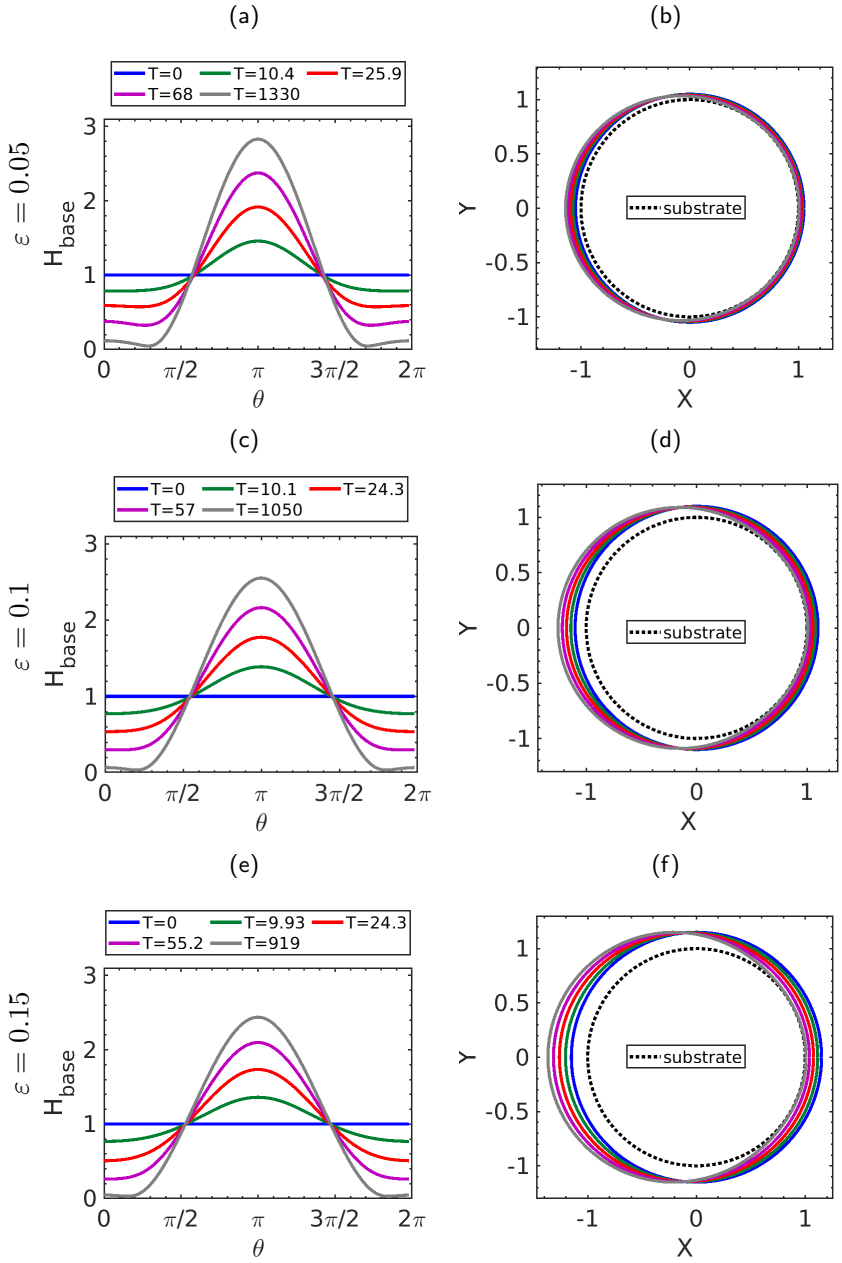

Figure 9.4: Evolution of base state volumetric film thickness $V_{\text{base}}(\theta, T)$ for tori with major radius $B = 10$, and various uniform initial film thicknesses such that $\varepsilon \in \{0.05, 0.1, 0.15\}$, according to the thin film equation on a torus, Equations (9.17) and (9.18). Each plot depicts five time steps, chosen such that the film thickness at $\theta = \pi$ is equispaced between $T = 0$ and the late time, $T = T_{\text{late}}$. The left column depicts volumetric film thickness against θ; the right column depicts a cross-sectional view of the fluid coating the circular substrate (black dotted line).
(a)-(b): $\varepsilon = 0.05$, shown at time steps $T \in \{0, 10.4, 25.9, 68.0, 1330\}$.
(c)-(d): $\varepsilon = 0.1$, shown at time steps $T \in \{0, 10.1, 24.3, 57.0, 1050\}$.
(e)-(f): $\varepsilon = 0.15$, shown at time steps $T \in \{0, 9.93, 24.3, 55.2, 919\}$.

9.4 Linear stability analysis

We next perform a linear stability analysis of viscous, capillary-driven thin-film flow on tori which are initially uniformly coated with a film. The initial condition is given by Equation (9.21), i.e., $H_0 = 1$, $V_0(\theta) = 1 + \varepsilon(1+2f)/[2(1+f)] + \varepsilon^2 f/[3(1+f)]$.

Letting the perturbed volumetric thickness be

$$V(\theta, S, T) = V_{\mathsf{base}}(\theta, T) + \delta V(\theta, S, T), \tag{9.23}$$

where δV is an infinitesimal perturbation, the linearization of Equations (9.17) and (9.18) is

$$\frac{\partial \delta V}{\partial T} = \mathcal{L}[V_{\mathsf{base}}]\delta V, \tag{9.24}$$

where

$$\begin{aligned}
\mathcal{L}[V_{\mathsf{base}}] = &-\frac{\varepsilon}{3}V_{\mathsf{base}}^3\partial_\theta^4 - \frac{\varepsilon}{3}V_{\mathsf{base}}^2\left[\frac{2(\partial_\theta f)V_{\mathsf{base}} + 3(1+f)\partial_\theta V_{\mathsf{base}}}{1+f}\right]\partial_\theta^3 \\
&- \frac{\varepsilon}{3}V_{\mathsf{base}}^2\left[\frac{V_{\mathsf{base}}[1-(\partial_\theta f)^2] + 3(1+f)(\partial_\theta f)(\partial_\theta V_{\mathsf{base}})}{(1+f)^2}\right]\partial_\theta^2 \\
&+ V_{\mathsf{base}}^2\left\{\frac{\partial_\theta f}{(1+f)^2} - \frac{\varepsilon}{3}\left[\frac{[4+18f+(2+\sec^2\theta)f^2]V_{\mathsf{base}}(\partial_\theta f)}{(1+f)^2}\right.\right. \\
&\quad \left.\left. + \frac{6[1+f+\cos(2\theta)\sec^2(\theta)f^2]\partial_\theta V_{\mathsf{base}}}{(1+f)^2} + \frac{3(\partial_\theta f)(\partial_\theta^2 V_{\mathsf{base}})}{1+f} - 3\partial_\theta^3 V_{\mathsf{base}}\right]\right\}\partial_\theta \\
&- \frac{2\varepsilon}{3}\left[\frac{V_{\mathsf{base}}^3}{(1+f)^2}\right]\partial_\theta^2\partial_S^2 + \frac{\varepsilon}{3}\left[\frac{2V_{\mathsf{base}}(\partial_\theta f) - 3(1+f)(\partial_\theta V_{\mathsf{base}})}{(1+f)^3}\right]\partial_\theta\partial_S^2 \\
&- \frac{\varepsilon}{3}V_{\mathsf{base}}^2\left[\frac{(1+4f+4f^2\sec^2\theta)V_{\mathsf{base}} - 6(1+f)(\partial_\theta f)(\partial_\theta V_{\mathsf{base}})}{(1+f)^4}\right]\partial_S^2 \\
&- \frac{\varepsilon}{3}\left[\frac{V_{\mathsf{base}}^3}{(1+f)^4}\right]\partial_S^4 \\
&- \frac{V_{\mathsf{base}}}{3}\left\{\frac{3f(1+f\sec^2\theta)V_{\mathsf{base}} + 6f(1+f)\tan(\theta)\partial_\theta V_{\mathsf{base}}}{(1+f)^3}\right. \\
&\quad + \varepsilon\left[\frac{-4f - 2f^2[3+6\cos(2\theta)+7f]\sec^2\theta}{(1+f)^4}V_{\mathsf{base}}^2\right. \\
&\quad + \frac{[12+3f(18+2f+f\sec^2\theta)](\partial_\theta f)(\partial_\theta V_{\mathsf{base}})V_{\mathsf{base}}}{(1+f)^3} + \frac{3[1-(\partial_\theta f)^2]V_{\mathsf{base}}\partial_\theta^2 V_{\mathsf{base}}}{(1+f)^2} \\
&\quad + \frac{6[1+f+\cos(2\theta)f^2\sec^2\theta](\partial_\theta V_{\mathsf{base}})^2}{(1+f)^2} + \frac{6(\partial_\theta f)(\partial_\theta V_{\mathsf{base}})(\partial_\theta^2 V_{\mathsf{base}})}{1+f} \\
&\quad \left.\left. + \frac{6V_{\mathsf{base}}(\partial_\theta f) + 6(1+f)(\partial_\theta V_{\mathsf{base}})}{(1+f)}\partial_\theta^3 V_{\mathsf{base}} + 3V_{\mathsf{base}}\partial_\theta^4 V_{\mathsf{base}}\right]\right\}.
\end{aligned} \tag{9.25}$$

This linear operator is rather complicated, but a few key features stand out. First, because it contains the time-dependent base state $V_{\mathsf{base}}(\theta, T)$, it is nonautonomous.

Second, the operator is non-normal. Specifically, defining the adjoint $\mathcal{L}^\dagger[V_{\text{base}}]$ by

$$\int_0^{2\pi B}\int_0^{2\pi}\sqrt{\det\widetilde{g}}\;u\mathcal{L}[V_{\text{base}}]v d\theta dS = \int_0^{2\pi B}\int_0^{2\pi}\sqrt{\det\widetilde{g}}\;v\mathcal{L}^\dagger[V_{\text{base}}]u d\theta dS \tag{9.26}$$

for all test functions u and v, $\mathcal{L}[V_{\text{base}}]$ and $\mathcal{L}^\dagger[V_{\text{base}}]$ do not commute[1]. Because the operator is both non-normal and nonautonomous, interaction between non-orthogonal eigenfunctions can cause transient growth behavior not predicted by a modal analysis. Therefore, a generalized linear stability analysis is necessary to analyze the system. However, in the limit of $T\to\infty$ and the system approaches a stationary state, a modal analysis will be sufficient.

It is notable that there is no S-dependence in the operator except in the presence of the 2nd- and 4th-order S derivatives, ∂_S^2 and ∂_S^4. Therefore, defining the partial adjoint in S, $\mathcal{L}^{S*}[V_{\text{base}}]$ by

$$\int_0^{2\pi B} u\mathcal{L}v dS = \int_0^{2\pi B} v\mathcal{L}^{S*}u dS \tag{9.27}$$

for test functions u and v, it is apparent that $\mathcal{L}[V_{\text{base}}]=\mathcal{L}^{S*}[V_{\text{base}}]$ (this can be seen by inspection, as ∂_S^2 and ∂_S^4 are self-adjoint). That is, the linear operator is self-adjoint and normal in the S coordinate, and non-normal in the θ coordinate. We can therefore perform a Fourier transform in S. Without loss of generality, we perform a cosine transform, and define a given perturbation as

$$\delta V(\theta,S,T)=\delta V_k(\theta,T)\cos(kS) \tag{9.28}$$

(although k is lowercase, it is a nondimensional wavenumber). The linear operator then becomes

$$\begin{aligned}
\mathcal{L}_k[V_{\text{base}}] = {}& -\frac{\varepsilon}{3}V_{\text{base}}^3\partial_\theta^4 - \frac{\varepsilon}{3}V_{\text{base}}^2\left[\frac{2(\partial_\theta f)V_{\text{base}}+3(1+f)\partial_\theta V_{\text{base}}}{1+f}\right]\partial_\theta^3\\
&-\frac{\varepsilon}{3}V_{\text{base}}^2\left[\frac{V_{\text{base}}[1-(\partial_\theta f)^2]+3(1+f)(\partial_\theta f)(\partial_\theta V_{\text{base}})}{(1+f)^2}\right]\partial_\theta^2\\
&+V_{\text{base}}^2\left\{\frac{\partial_\theta f}{(1+f)^2}-\frac{\varepsilon}{3}\left[\frac{[4+18f+(2+\sec^2\theta)f^2]V_{\text{base}}(\partial_\theta f)}{(1+f)^2}\right.\right.\\
&\left.\left.+\frac{6[1+f+\cos(2\theta)\sec^2(\theta)f^2]\partial_\theta V_{\text{base}}}{(1+f)^2}+\frac{3(\partial_\theta f)(\partial_\theta^2 V_{\text{base}})}{1+f}-3\partial_\theta^3 V_{\text{base}}\right]\right\}\partial_\theta\\
&+k^2\frac{2\varepsilon}{3}\left[\frac{V_{\text{base}}^3}{(1+f)^2}\right]\partial_\theta^2-k^2\frac{\varepsilon}{3}\left[\frac{2V_{\text{base}}(\partial_\theta f)-3(1+f)(\partial_\theta V_{\text{base}})}{(1+f)^3}\right]\partial_\theta\\
&+k^2\frac{\varepsilon}{3}V_{\text{base}}^2\left[\frac{(1+4f+4f^2\sec^2\theta)V_{\text{base}}-6(1+f)(\partial_\theta f)(\partial_\theta V_{\text{base}})}{(1+f)^4}\right]\\
&-k^4\frac{\varepsilon}{3}\left[\frac{V_{\text{base}}^3}{(1+f)^4}\right]
\end{aligned}$$

[1] Given the complexity of the $\mathcal{L}[V_{\text{base}}]$ and the time dependence of V_{base}, one could conclude from inspection that the operator is almost certainly non-normal. Proving that it is indeed non-normal can be done by directly evaluating the commutator, $\mathcal{L}\mathcal{L}^\dagger-\mathcal{L}^\dagger\mathcal{L}$, and determining that it is nonzero. This is a long computation which was performed, but is not shown here.

$$
\begin{aligned}
&- \frac{V_{\text{base}}}{3}\left\{\frac{3f(1+f\sec^2\theta)V_{\text{base}} + 6f(1+f)\tan(\theta)\partial_\theta V_{\text{base}}}{(1+f)^3}\right. \\
&+\varepsilon\left[\frac{-4f - 2f^2[3+6\cos(2\theta)+7f]\sec^2\theta}{(1+f)^4}V_{\text{base}}^2\right. \\
&+\frac{[12+3f(18+2f+f\sec^2\theta)](\partial_\theta f)(\partial_\theta V_{\text{base}})V_{\text{base}}}{(1+f)^3} + \frac{3[1-(\partial_\theta f)^2]V_{\text{base}}\partial_\theta^2 V_{\text{base}}}{(1+f)^2} \\
&+\frac{6[1+f+\cos(2\theta)f^2\sec^2\theta](\partial_\theta V_{\text{base}})^2}{(1+f)^2} + \frac{6(\partial_\theta f)(\partial_\theta V_{\text{base}})(\partial_\theta^2 V_{\text{base}})}{1+f} \\
&\left.\left.+\frac{6V_{\text{base}}(\partial_\theta f)+6(1+f)(\partial_\theta V_{\text{base}})}{(1+f)}\partial_\theta^3 V_{\text{base}} + 3V_{\text{base}}\partial_\theta^4 V_{\text{base}}\right]\right\}. \qquad (9.29)
\end{aligned}
$$

The key differentiating factor between normal and non-normal operators is that the eigenfunctions of non-normal operators are non-orthogonal. Thus, a superposition of two eigenfunctions may grow at a faster rate than the eigenfunctions individually, a phenomenon which is impossible for normal operators with orthogonal eigenfunctions (for a review of generalized linear stability theory, see Chapter 3). But $\mathcal{L}[V_{\text{base}}]$ is normal in the S coordinate and non-normal in the θ coordinate, and can be decomposed into eigenfunctions of the form $v(\theta)\cos(kS)$. Thus, selecting any two eigenfunctions with $k = k_1$ and $k = k_2$, then if $k_1 = k_2$ the eigenfunctions are not necessarily orthogonal, but if $k_1 \neq k_2$ then they will be orthogonal. That is, perturbations with different values of k are orthogonal and cannot interfere with each other. We can therefore perform a Fourier transform in S, and perform a generalized stability analysis of each family of perturbations with a given k.

All disturbances must satisfy the periodic boundary condition of the torus, $\delta V(0,S,T) = \delta V(2\pi,S,T)$. Because the domain is finite, the spectrum is discrete; specifically, the only accessible wavenumbers are $k = n/B$, with $n \in \mathbb{Z}_{\geq 0}$. Note that we limit our investigation to $k \leq 1$. Larger wavenumbers (indicating smaller wavelengths) are expected to be increasingly stable, as such disturbances would be dominated by film curvature rather than substrate curvature. This is borne out by numerical simulations. Furthermore, the lubrication assumption required that variations be at least $O(L)$, which is equivalent to $k < O(1)$. Note also that there is no additional scaling of k with B. Wavenumbers k may be directly compared across tori of different major radii.

The analysis follows the methodology developed by Farrell and Ioannou (1996a) and Goldhirsch et al. (1987) for nonautonomous generalized linear stability analysis, as introduced in Section 3.1.2. We will present instantaneous normal (modal) results for comparison with the nonautonomous non-normal results. Because of the non-normality and time-dependence of the linear operator, the fastest growing modes at $T = 0$ are different from the modes which experience the greatest amplitude growth over long periods of time.

We first define instantaneous modal operators and spectral abscissae. Note that each will be defined in terms of specific wavenumber k. Let the least-stable normal mode at time T at

wavenumber k be defined as

$$W_k(T) = \underset{\text{eigenvectors}}{\arg\max}\ \text{real}(\text{eigenvalue}\mathcal{L}_k[V_{\text{base}}(\theta,T)]). \tag{9.30}$$

That is, $W_k(T)$ represents the eigenvector of $\mathcal{L}_k[V_{\text{base}}(\theta,T)]$ whose corresponding eigenvalue has maximum real part. The real part of the corresponding eigenvalue is denoted the spectral abscissa,

$$\beta_k(T) = \max \text{real}(\text{eigenvalue}\mathcal{L}_k[V_{\text{base}}(T)]). \tag{9.31}$$

Note that both $W_k(T)$ and $\beta_k(T)$ are instantaneous quantities; they are determined based on $V_{\text{base}}(\theta,T)$ without taking into account the history of the base state's evolution.

Because $\mathcal{L}_k[V_{\text{base}}(\theta,T)]$ is non-normal and time-dependent, one can define quantities that describe how perturbations introduced at $T=0$ grow and change over time. First, it is useful to define a linear propagation operator $\Phi_k(T)$ by

$$\Phi_k(T=0) = 1, \tag{9.32a}$$

$$\frac{d\Phi_k(T)}{dT} = \mathcal{L}_k[V_{\text{base}}]\Phi_k(T), \tag{9.32b}$$

where 1 represents the identity operator. $\Phi_k(T)$ can be represented explicitly by a time-ordered exponential series; for a review of the subject, see Farrell and Ioannou (1996a). The linear evolution of an infinitesimal perturbation δV_k can then be described as

$$\delta V_k(\theta,T) = \Phi_k(T)\delta V_k(\theta,0). \tag{9.33}$$

The optimal input and output disturbances are defined as

$$V_k^{\text{in}}(\theta,T) = \underset{y_k(\theta,0)}{\arg\max}\ \frac{\|\Phi_k(T)y_k(\theta,0)\|}{\|y_k(\theta,0)\|} \tag{9.34a}$$

and

$$U_k^{\text{out}}(\theta,T) = \frac{\Phi_k(T)V_k^{\text{in}}(\theta,T)}{\|\Phi_k(T)V_k^{\text{in}}(\theta,T)\|}, \tag{9.34b}$$

respectively, where $\|\cdot\|$ denotes the L_2 norm,

$$\|u\|^2 = \int_0^{2\pi B}\int_0^{2\pi}\sqrt{\det\widetilde{g}}\ u^2 d\theta dS = \int_0^{2\pi B}\int_0^{2\pi}\left(1+B^{-1}\cos\theta\right)\ u^2 d\theta dS. \tag{9.35}$$

In other words, $V_k^{\text{in}}(\theta,T)$ is the infinitesimal initial disturbance of wavenumber k which experiences the greatest amplitude of growth between time 0 and T, and $U_k^{\text{out}}(\theta,T)$ is the resulting form which $V_k^{\text{in}}(\theta,T)$ evolves into over that time. Both V_k^{in} and U_k^{out} are normalized; the optimal disturbance amplitude is defined separately as

$$G_k(T) = \frac{\|\Phi_k(T)V_k^{\text{in}}(\theta,T)\|}{\|V_k^{\text{in}}(\theta,T)\|} = \max_{y_k(\theta,0)}\frac{\|\Phi_k(T)y_k(\theta,0)\|}{\|y_k(\theta,0)\|} = \|\Phi_k(T)\|, \tag{9.36}$$

where $\|\cdot\|$ in the last expression represents the operator norm. Thus,

$$\Phi_k(T)V_k^{\mathsf{in}}(\theta,T) = G_k(T)U_k^{\mathsf{out}}(\theta,T). \tag{9.37}$$

Note that $G_k(0) = 1$, and thus at $T = 0$

$$\begin{aligned} V_k^{\mathsf{in}}(\theta,0) = U_k^{\mathsf{out}}(\theta,0) &= \lim_{T\to 0} \underset{y_k(\theta,0)}{\arg\max} \frac{\|\Phi_k(T)y_k(\theta,0)\|}{\|y_k(\theta,0)\|} \\ &= \underset{\text{eigenvectors}}{\arg\max}\ \text{eigenvalue} \left\{ \frac{\mathcal{L}_k[V_{\mathsf{base}}(T=0)] + \mathcal{L}_k^\dagger[V_{\mathsf{base}}(T=0)]}{2} \right\}, \end{aligned} \tag{9.38}$$

i.e., the optimal input and output disturbances at $T = 0$ are identical and equal to the eigenvector of the transient operator, $(\mathcal{L}_k[V_{\mathsf{base}}] + \mathcal{L}_k^\dagger[V_{\mathsf{base}}])/2|_{T=0}$, with greatest value. While $V_k^{\mathsf{in}}(\theta,T)$ and $U_k^{\mathsf{out}}(\theta,T)$ describe the input and output disturbances which experience the greatest total amplitude of growth from 0 to T, in the limit as $T \to 0$, they instead describe the disturbance with the fastest growth rate at $T = 0$.

Our preferred measure of growth at intermediate times will not be $G_k(T)$ itself but rather the time-dependent Lyapunov exponent (Goldhirsch et al., 1987),

$$\lambda_k(T) = \frac{\ln\|\Phi_k(T)\|}{T} = \frac{\ln G_k(T)}{T}. \tag{9.39}$$

$\lambda_k(T)$ can be understood as the average exponential growth rate of the optimal disturbance between times 0 and T. Note that the $T = 0$ numerical abscissa, ω_k, representing the fastest growth rate of any disturbance at $T = 0$, is given by the maximum eigenvalue of the transient operator and is equal to

$$\omega_k = \max \text{eigenvalue} \left\{ \frac{\mathcal{L}_k[V_{\mathsf{base}}(T=0)] + \mathcal{L}_k^\dagger[V_{\mathsf{base}}(T=0)]}{2} \right\} = \lambda_k(0). \tag{9.40}$$

Note that at $T = 0$, the optimal input and output disturbances coincide. This disturbance will be labeled $X_k(\theta)$, the optimal transient disturbance, and represents the fastest growing disturbance at $T = 0$.

$$X_k(\theta) = U_k^{\mathsf{out}}(\theta, T=0) = V_k^{\mathsf{in}}(\theta, T=0). \tag{9.41}$$

In autonomous systems (i.e., systems in which the linear operator is time independent),

$$\lim_{T\to\infty} \lambda_k(T) = \beta_k = \max \text{eigenvalue}\,\{\mathcal{L}_k\}, \tag{9.42}$$

i.e., the time-dependent Lyapunov exponent converges to the spectral abscissa (Farrell and Ioannou, 1996b). Because V_{base} varies more and more slowly in time, $\mathcal{L}_k[V_{\mathsf{base}}]$ approaches autonomy at late times. It is therefore expected that $\lim_{T\to\infty}\lambda_k(T) = \lim_{T\to\infty}\beta_k(T)$. That

is, the time-dependent Lyapunov exponent is expected to converge to the instantaneous spectral abscissa as time goes to infinity; similarly, the optimal output disturbance is expected to converge to the fastest growing normal mode, i.e., $\lim_{T\to\infty} U_k^{\text{out}}(\theta,T) = \lim_{T\to\infty} X_k(\theta,T)$. Note also that while autonomous systems satisfy $\lambda_k(T) \geq \beta_k(T)$ at all times, this is not true for nonautonomous systems.

The numerical abscissa represents the fastest instantaneous growth rate of any disturbance and is always greater than or equal to the spectral abscissa, which represents the fastest instantaneous growth rate of any eigenfunction (Farrell and Ioannou, 1996b). Hence, $\lambda_k(T=0) = \omega_k(T=0) \geq \beta_k(T=0)$. At later times, however, $\lambda_k(T)$ represents the average exponential growth rate of the disturbance with greatest total amplitude increase between 0 and T and is not necessarily greater or less than the spectral abscissa.

Note that we have defined everything in Fourier space, in terms of wavenumber k. Thus, for example, ω_k is the numerical abscissa *for wavenumber* k.

We denote the peak wavenumbers representing the fastest growing normal modes and optimal disturbances by

$$k_{\text{peak}}^{\text{normal}}(T) = \arg\max_k \beta_k(T) \tag{9.43a}$$

$$k_{\text{peak}}^{\text{non-normal}}(T) = \arg\max_k \lambda_k(T). \tag{9.43b}$$

We denote the fastest growing normal modes and optimal disturbances over all k by

$$W(\theta,S,T) = W_k(\theta,T)\cos(kS)|_{k=k_{\text{peak}}^{\text{normal}}(T)}, \tag{9.44a}$$

$$X(\theta,S) = X_k(\theta)\cos(kS)|_{k=k_{\text{peak}}^{\text{non-normal}}(T=0)}, \tag{9.44b}$$

$$V^{\text{in}}(\theta,S,T) = V_k^{\text{in}}(\theta,T)\cos(kS)|_{k=k_{\text{peak}}^{\text{non-normal}}(T)}, \tag{9.44c}$$

$$U^{\text{out}}(\theta,S,T) = U_k^{\text{out}}(\theta,T)\cos(kS)|_{k=k_{\text{peak}}^{\text{non-normal}}(T)}. \tag{9.44d}$$

A summary of the variable definitions related to linear stability analysis is given in Table 9.2. In all cases, W, X, V^{in}, and U^{out} refer to disturbances of volumetric fluid thickness V, not normal fluid thickness H.

Variable	Definition
k	Dimensionless wavenumber from performing Fourier transform in S; all disturbances and eigenfunctions of interest contain the term $\cos(kS)$.
$k_{\text{peak}}^{\text{normal}}(T)$	Wavenumber of fastest growing normal mode at time T: $\arg\max_k \beta_k(T)$
$k_{\text{peak}}^{\text{non-normal}}(T)$	Wavenumber of optimal input and output disturbance with maximal amplitude at time T: $\arg\max_k \lambda_k(T)$
$\mathcal{L}_k[V_{\text{base}}(T)]$	Linear operator; linearization of Eqns. 9.17 and 9.18 about base state $V_{\text{base}}(\theta, T)$, Fourier-transformed in S. Defined by Eqn. 9.29
$V_k^{\text{in}}(\theta, T)$	Optimal input disturbance of wavenumber k, defined by Eqn. 9.34a
$V^{\text{in}}(\theta, S, T)$	Optimal input disturbance, defined by Eqn. 9.44
$U_k^{\text{out}}(\theta, T)$	Optimal output disturbance of wavenumber k, defined by Eqn. 9.34b
$U^{\text{out}}(\theta, S, T)$	Optimal output disturbance, defined by Eqn. 9.44
$X_k(\theta)$	Optimal transient disturbance of wavenumber k at $T = 0$, defined by Eqn. 9.41
$X(\theta, S)$	Optimal transient disturbance at $T = 0$, defined by Eqn. 9.44
$W_k(\theta, T)$	Fastest growing normal mode of wavenumber k at time T,
$W(\theta, S, T)$	Fastest growing normal mode, defined by Eqn. 9.44
	defined by Eqn. 9.31
$G_k(T)$	Optimal disturbance amplitude of wavenumber k at time T, defined by Eqn. 9.36
$\beta_k(T)$	Spectral abscissa: growth rate of fastest growing normal mode W_k at time T; defined by Eqn. 9.31
$\lambda_k(T)$	Time-dependent Lyapunov exponent: average growth rate of optimal disturbance from time 0 to T; defined by Eqn. 9.39
ω_k	Numerical abscissa: fastest growth rate of any disturbance at $T = 0$; defined by Eqn. 9.40

Table 9.2: Variables arising in linear stability analysis of a thin viscous film coating a torus.

9.5 Linear stability analysis: Analytical and semi-analytical results

We begin by addressing analytically tractable limits of the linear stability of a thin viscous film coating a torus. Our main result will be to show that in the large-major-radius limit $B \to \infty$, the wavenumber of the fastest growing normal mode at $T = 0$ is $k_{\text{peak}}^{\text{normal}}(T = 0) = 1/\sqrt{2} \approx 0.707$, but at late times converges to $k_{\text{peak}}^{\text{normal}}(T \to \infty) \approx 0.566$. To understand this result, we will first analyze thin films coating cylinders.

We will next compute analytically the peak wavenumbers of fastest growing normal and transient non-normal modes at $T = 0$, $k_{\text{peak}}^{\text{normal}}(T = 0)$ and $k_{\text{peak}}^{\text{non-normal}}(T = 0)$ to $O(B^{-2})$ for tori with large major radius such that $B\varepsilon \gg 1$.

Finally, we will determine the power-law dependence of ω (the numerical abscissa) on ε, finding that $\omega = B^{-1}/[2(1 - B^{-1})^2] - const. \times \varepsilon^{1/3}$ in the limit of small ε.

9.5.1 Analysis of cylinder

Uniform film coating a cylinder

The case of a straight cylinder corresponds to the limit $B \to \infty$, i.e., $(1/B) \to 0$ or $f \to 0$. The normal stability analysis for a uniform film coating a cylinder was first carried out by Goren (1962). In this case,

$$P = \{1 - \varepsilon \left[V + \partial_{\theta\theta} V + \partial_{SS} V\right]\} + O(\varepsilon^2). \tag{9.45}$$

The first term, 1, comes from the azimuthal (θ-coordinate) curvature of the cylindrical substrate. The next term, $-\varepsilon V$, is the correction to the azimuthal curvature due to a film of thickness V. A thicker film implies a greater radius of curvature, and hence a lower pressure. The next two terms, the Laplacian of the film thickness, describe the additional curvature due to azimuthal and axial (S-coordinate) variations in the film itself.

Consider adding a perturbation of the form $\delta V = \cos(ks)$ to an initially flat film (see Figure 9.5). At the peaks of δV, the pressure will decrease due to the azimuthal curvature correction, but increase due to the axial curvature correction; vice versa at the troughs. To see this competition clearly, we can write out the corrected pressure as $\delta P = \varepsilon(-1 + k^2)\cos(ks)$.

If $k > 1$, then $(-1 + k^2) > 0$, and so δP is positive at peaks and negative at troughs. Introducing such a perturbation will thus lead to a pressure gradient driving fluid from the peaks to the troughs, smoothing out the film again. That is, at large wavenumbers, the axial curvature dominates azimuthal curvature and suppresses perturbations. But if $k < 1$, then $(-1 + k^2) < 0$ and the peaks have lower pressure than the troughs. Such a perturbation will be unstable, as fluid will be driven from the troughs to the peaks, enhancing the perturbation. For these small wavenumbers, the azimuthal curvature dominates the axial curvature.

Performing the computations explicitly, the equation of motion is

$$\frac{\partial V}{\partial T} = \partial_\theta \left\{ \frac{V^3}{3} \left[1 - \varepsilon V\right] \partial_\theta P \right\} + \partial_S \left\{ \frac{V^3}{3} \left[1 - \frac{\varepsilon}{2} V\right] \partial_S P \right\} + O(\varepsilon^2). \tag{9.46}$$

Linearizing about the constant-thickness initial condition $V = V_0 = H_0 + \frac{1}{2}\varepsilon H_0^2$,

$$\frac{\partial \delta V}{\partial T} = -\varepsilon \frac{H_0^3}{3}\left[\partial_\theta^2 + \partial_S^2 + \partial_\theta^4 + \partial_\theta^2 \partial_S^2 + \partial_S^4\right] \delta V + O(\varepsilon^2). \tag{9.47}$$

We immediately find that indeed $\delta V = \cos(ks)$ is an eigenfunction with eigenvalue corresponding to the spectral abscissa

$$\beta_k = (\varepsilon H_0^3/3)k^2(1 - k^2) \tag{9.48}$$

[see Figure 9.6 (b)]. Hence, the critical wavenumber is $k = 1$, and the most unstable mode has $k_{\text{peak}} = 1/\sqrt{2} \approx 0.707$ and wavelength $2\sqrt{2}\pi \approx 8.89$. These results agree with Goren (1962). Note that although there exists another set of eigenfunctions of the form $\cos(a\theta + const)\sin(ks + const)$, these are all stable (decaying).

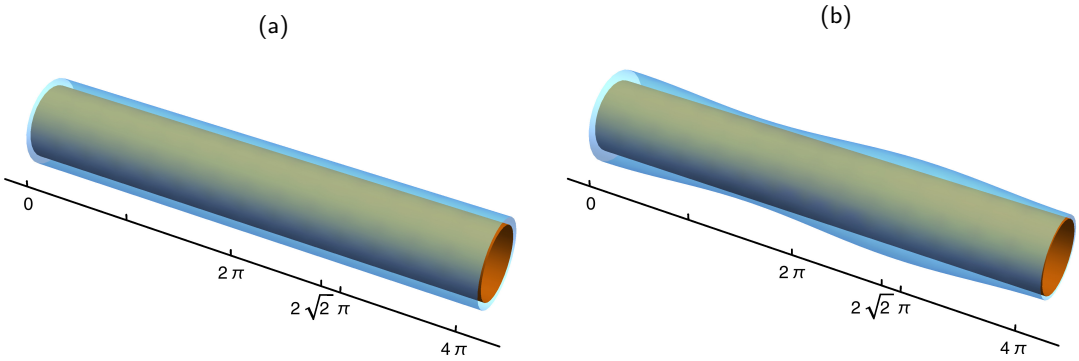

Figure 9.5: Viscous-capillary instability of a thin film coating a cylinder. (a) Cylinder (orange) of radius 1 coated with uniform film (blue) of thickness 0.2.
(b) Cylinder of radius 1 coated by uniform film with a sinusoidal disturbance, exhibiting the wavenumber $k = 1/\sqrt{2}$ and wavelength $2\sqrt{2}\pi$ corresponding to the most unstable normal mode.

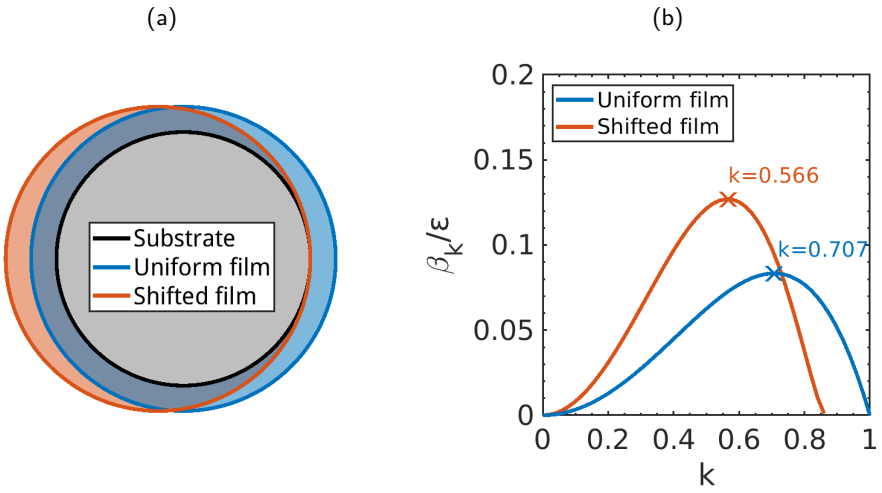

Figure 9.6: Geometry and dispersion of uniform and shifted thin films coating a cylinder. (a) Diagram displaying a cylindrical cross-section (gray) coated by a uniform thin film (blue) and a shifted thin film (red).
(b) Dispersion curves, β_k, normalized by ε and corresponding to a uniform film coating a cylinder (blue) described by Equation (9.48) and to a shifted film coating a cylinder (red) described by the real parts of the eigenvalues of Equation (9.49).

Shifted film coating a cylinder

Consider now a shifted film on a cylinder (see Figure 9.6 a). Recall from Section 9.3 that for tori with large major radii B, the base state effectively translates the entire fluid surface inward relative to the substrate. Indeed, in the $B \to \infty$ cylinder limit, a static fluid with circular cross-section is a stationary state, regardless of the substrate's location within it. The shifted film cylinder turns out to have a very different dispersion pattern from the uniform film cylinder, and represents the $T \to \infty, B \to \infty$ limit of the torus system.

Substituting the base state $H_0 = [1 - \cos(\theta)]$ into Equations (9.19) and (9.20) and linearizing yields

$$\begin{aligned}\frac{\partial \delta V}{\delta T} &= -\frac{4}{3}\varepsilon\left[2\sin^6\left(\frac{\theta}{2}\right)\left(\partial_\theta^2 + \partial_s^2\right) + 3\sin(\theta)\sin^4\left(\frac{\theta}{2}\right)\partial_\theta\right]\left[1 + \partial_\theta^2 + \partial_s^2\right]\delta V \\ &= -\frac{4}{3}\varepsilon\left[2\sin^6\left(\frac{\theta}{2}\right)\left(\partial_\theta^2 - k^2\right) + 3\sin(\theta)\sin^4\left(\frac{\theta}{2}\right)\partial_\theta\right]\left[1 - k^2 + \partial_\theta^2\right]\delta V, \qquad (9.49)\end{aligned}$$

where the second line has been Fourier transformed in the S-dimension. This linearized equation is non-normal, but we are interested in it as a late-time limit of the torus system. Therefore, the relevant quantity of interest is the spectral abscissa, β, and not the numerical abscissa, ω. While Equation (9.49) has no simple analytic solution, it can easily be computed numerically; the resulting dispersion relation is shown in Figure 9.6 (b). Note in particular that the most unstable wavenumber is approximately $k_{\text{peak}} = 0.566$, which is less than the uniform film result of $k_{\text{peak}} = 1/\sqrt{2} \approx 0.707$.

To understand the decreased peak k physically, recall the effect of a sinusoidal perturbation δV on a cylinder with a uniform coating: at the peaks of δV, the pressure will decrease due to the azimuthal curvature correction, but increase due to the axial curvature correction, and vice versa at the troughs. A sinusoidal disturbance on a shifted film has a similar change in pressure due to the azimuthal effect, as the circular surface is expanding just as much as before at each peak. But the axial curvature is concentrated on one side, and hence is around twice as large as it would be on a uniform film. Therefore, high-frequency undulations are more strongly suppressed than before, and so the peak shifts to lower frequencies. There are some additional complicating factors; most importantly, the peak eigenfunction is not really a uniform expansion of the circular interface. If we were to make a back-of-the-envelope approximation by doubling the axial curvature, we would find a dispersion proportional to $k^2(1-2k^2)$, yielding an approximate peak k of 0.5, which is indeed lower than that of the uniformly-coated cylinder. This physical argument is likely the dominant reason for the shift in peak k.

9.5.2 Analysis of torus

Unlike the cylinder, the base state of the torus evolves in time; in particular, the film on the inside of the torus thickens while that on the outside thins. At early times, this evolution is accelerating, which causes the fastest-growing transient mode to have $k_{\text{peak}}^{\text{non-normal}}(T=0)=0$, reflecting the base state's evolution. At late times, the base state's evolution decelerates and k_{peak} shifts to above 0.

The torus system has two particular limits which are amenable to some analysis. Large-radius or thick-film tori, satisfying $1 \ll \varepsilon B$, experience capillary effects dominated by the film surface rather than the substrate curvature; such tori can be viewed as a perturbation of the cylindrical case. Small-radius or thin-film tori, satisfying $\varepsilon B \ll 1$, experience capillary effects dominated by the substrate curvature; these tori are highly non-cylindrical and display a different behavior. Note that although the quantity (εB) determines the regime of the torus at a coarse level, ε and B remain independent and cannot be reduced into one parameter.

Large-radius torus at late times

As even the shifted-film cylinder dispersion curve could only be computed numerically, the late-time behavior of the torus is not analytically tractable. That said, we can make a 0th order estimate for the relationship between the peak wavenumber and the radius B. Beginning with the peak wavenumber of the shifted-film cylinder ($k=0.566$) and including a correction to account for the inner circumference of the torus being shorter than $2\pi B$, we approximate

$$\lim_{T\to\infty} k_{\text{peak}}^{\text{normal}}(T) \approx 0.566(B-1)/B. \tag{9.50}$$

This approximation is shown in Figure 9.7, along with the peak wavenumbers $k_{\text{peak}}^{\text{normal}}(T = T_{\text{late}})$ found in numerical simulations. The plot shows the peak wavenumber without imposing boundary conditions; including boundary conditions, the results would be rounded to the nearest

$1/B$. The crude approximation captures the general trend line for large B, suggesting that the physical intuition is correct; however, it is not sufficiently accurate to capture the variation in results due to varying ε.

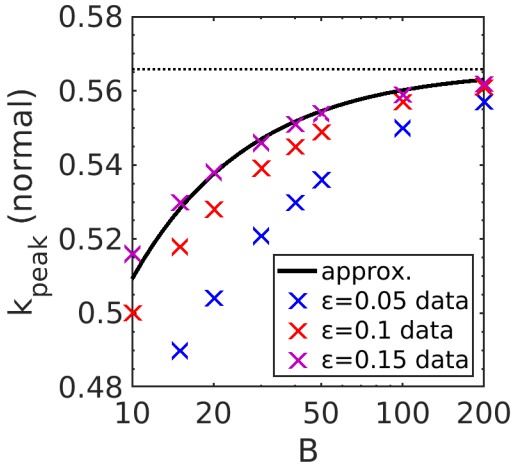

Figure 9.7: Comparison of the analytic approximation of $\lim_{T\to\infty} k_{\text{peak}}^{\text{normal}}(T)$ for large B (black solid line), described by Equation (9.50), to numerically computed $k_{\text{peak}}^{\text{normal}}(T = T_{\text{late}})$ (crosses). The black dotted line indicates 0.566, representing $k_{\text{peak}}^{\text{normal}}$ of the shifted cylinder (see Figure 9.6). The horizontal axis displays major radius B on a log scale; the vertical axis displays $k_{\text{peak}}^{\text{normal}}$ on a linear scale. Colors indicate film thickness ε; $\varepsilon = 0.05$ (blue), $\varepsilon = 0.1$ (red), and $\varepsilon = 0.15$ (purple). Numerical results are given for $B \in \{10, 15, 20, 30, 40, 50, 100, 200\}$, computed at $T = T_{\text{late}} = 5\varepsilon^{-1/3}\pi^2 B(1 - B^{-2})$ using a finite difference method (Section 9.6.1). $k_{\text{peak}}^{\text{normal}}$ is computed without boundary conditions; including boundary conditions would round the data points to the nearest $1/B$.

Large-radius torus at T=0

We next consider $T = 0$. Substituting the initial condition $H(T = 0) = H_0 = 1$ [i.e., $V_0 = H_0 + \frac{1}{2}\varepsilon H_0^2 + O(\varepsilon^2) = 1 + \varepsilon/2 + O(\varepsilon^2)$] into Equations (9.17) and (9.18) and linearizing yields

$$\begin{aligned}\frac{\partial \delta V}{\partial T} =& \mathcal{L}\delta V = -\frac{1}{3}\left\{\varepsilon\partial_\theta^4 - \frac{2\varepsilon B^{-1}\sin\theta\,\partial_\theta^3}{(1+B^{-1}\cos\theta)} + \frac{\varepsilon\left(1-2k^2-B^{-2}\sin^2\theta\right)\partial_\theta^2}{(1+B^{-1}\cos\theta)^2}\right.\\ &+\frac{B^{-1}\sin\theta\left[3-2\varepsilon k^2-\varepsilon-2B^{-2}\varepsilon+3B^{-1}(1-4\varepsilon)\cos\theta-B^{-2}\varepsilon\cos(2\theta)\right]\partial_\theta}{(1+B^{-1}\cos\theta)^3}\\ &-\frac{\varepsilon\left(1-k^2+4B^{-2}+4B^{-1}\cos\theta\right)k^2}{(1+B^{-1}\cos\theta)^4}\\ &\left.+\frac{3(3-\varepsilon)B^{-2}+2B^{-1}[3-\varepsilon+(3-8\varepsilon)B^{-2}]\cos\theta+3B^{-2}(1-5\varepsilon)\cos(2\theta)}{2(1+B^{-1}\cos\theta)^4}\right\}\delta V,\end{aligned} \tag{9.51}$$

where the result has been Fourier transformed in S, with wavenumber k. This is equivalent to Equation (9.29), substituting in $V_0 = H_0 + \frac{1}{2}\varepsilon H_0^2 + O(\varepsilon^2) = 1 + \varepsilon/2 + O(\varepsilon^2)$.

The transient operator is then[2]

$$\begin{aligned}\frac{\mathcal{L}+\mathcal{L}^\dagger}{2} =& -\frac{1}{3}\left\{\varepsilon\partial_\theta^4 - \varepsilon\frac{2B^{-1}\sin\theta}{1+B^{-1}\cos\theta}\partial_\theta^3 + \frac{\varepsilon\left(1-2k^2-B^{-2}\sin^2\theta\right)}{(1+B^{-1}\cos\theta)^2}\partial_\theta^2\right.\\ &-\frac{B^{-1}\sin\theta\varepsilon\left[2B^{-2}+2k^2+4B^{-1}\cos\theta+B^{-2}\cos(2\theta)\right]}{(1+B^{-1}\cos\theta)^3}\partial_\theta\\ &-\frac{\varepsilon\left(1-k^2+4B^{-2}+4B^{-1}\cos\theta\right)k^2}{(1+B^{-1}\cos\theta)^4}\\ &\left.+\frac{3B^{-2}(3-\varepsilon)+2B^{-1}\left[3-\varepsilon+(3-8\varepsilon)B^{-2}\right]\cos\theta+3B^{-2}(1-5\varepsilon)\cos(2\theta)}{4(1+B^{-1}\cos\theta)^4}\right\}.\end{aligned} \tag{9.52}$$

These linear operators are quite complicated and it should come as no surprise that they have no simple closed-form eigenfunctions. Therefore, we must work in limiting cases. For the large-radius torus satisfying $B^{-1} \ll \varepsilon$, we expand to second order in B^{-1} yielding

$$\begin{aligned}\mathcal{L} =& \frac{\varepsilon}{3}\left\{-\partial_\theta^4-(1-2k^2)\partial_\theta^2+k^2(1-k^2)\right\}\\ &+\frac{B^{-1}}{3}\left\{\sin\theta\left[2\varepsilon\partial_\theta^3-(3-\varepsilon-2k^2\varepsilon)\partial_\theta\right]+\cos\theta\left[(2-4k^2)\varepsilon\partial_\theta^2-(3-\varepsilon-4k^4\varepsilon)\right]\right\}\\ &+\frac{B^{-2}}{6}\left\{\sin(2\theta)\left[-2\varepsilon\partial_\theta^3+3(2+3\varepsilon-2k^2\varepsilon)\partial_\theta\right]-2\varepsilon\left[1-3k^2+(2-3k^2)\cos(2\theta)\right]\partial_\theta^2\right.\\ &\left.+\left[3-(1-2k^2+10k^4)\varepsilon+(9+\{11-6k^2-10k^4\}\varepsilon)\cos(2\theta)\right]\right\}+O(B^{-3}),\end{aligned} \tag{9.53}$$

$$\begin{aligned}\frac{\mathcal{L}+\mathcal{L}^\dagger}{2} =& \frac{\varepsilon}{3}\left\{-\partial_\theta^4-(1-2k^2)\partial_\theta^2+k^2(1-k^2)\right\}\\ &+\frac{B^{-1}}{6}\left\{4\varepsilon\sin\theta\left[\partial_\theta^3+k^2\partial_\theta\right]+\cos\theta\left[4(1-2k^2)\varepsilon\partial_\theta^2-(3-\varepsilon-8\varepsilon k^4)\right]\right\}\\ &+\frac{B^{-2}}{12}\left\{-4\varepsilon\sin(2\theta)\left[\partial_\theta^3-(2-3k^2)\partial_\theta\right]-4\varepsilon\left[1-3k^2+(2-3k^2)\cos(2\theta)\right]\partial_\theta^2\right.\\ &\left.+\left[3-\varepsilon(1-4k^2+20k^4)+9\cos(2\theta)+\varepsilon(11-12k^2-20k^4)\cos(2\theta)\right]\right\}+O(B^{-3}).\end{aligned} \tag{9.54}$$

Though still ugly, the lack of complicated denominators gives these operators analytic eigenfunctions. The first eigenfunctions δV_{normal} and eigenvalues (dispersion) β of the operator $\mathcal{L}$ are given by

$$\begin{aligned}\delta V_{\text{normal}} =& 1-(\varepsilon B)^{-1}\frac{3-\varepsilon(1+4k^4)}{2k^2}\cos\theta\\ &+(\varepsilon B)^{-2}\frac{9-\varepsilon 18k^4-\varepsilon^2(1-14k^2+8k^4-2k^6-8k^8)}{8k^2(3+2k^2)}\cos(2\theta)+O(\varepsilon B)^{-3},\end{aligned} \tag{9.55a}$$

$$\beta = \frac{\varepsilon}{3}k^2(1-k^2)-B^{-2}\frac{1}{3}k^2\left[3-(2-3k^2+4k^4)\varepsilon\right]+O(B^{-3}), \tag{9.55b}$$

[2]Note: when computing the adjoint, be sure to include the integration weight $\sqrt{\det\widetilde{g}} = (1+B^{-1}\cos\theta)$.

leading to a peak wavenumber of

$$k_{\text{peak}}^{\text{normal}}(T=0) = \frac{1 - B^{-2}(1.5\varepsilon^{-1} - 1)}{\sqrt{2}} + O(B^{-3}) \tag{9.56}$$

and a critical wavenumber $k = 1-(3/2)B^{-2}(\varepsilon^{-1}-1)$. Thus the peak and critical wavenumbers for the normal solution at $T = 0$ are shifted to lower k, as compared to the cylinder.

As for the fastest-growing non-normal mode at $T = 0$, the first set of eigenfunctions $\delta V_{\text{non-normal}}$ and eigenvalues (dispersion) ω is given by

$$\begin{aligned}\delta V_{\text{non-normal}} &= 1 - (\varepsilon B)^{-1}\frac{3-\varepsilon(1+8k^4)}{4k^2}\cos\theta \\ &+ (\varepsilon B)^{-2}\frac{9+6\varepsilon(3-8k^4)-\varepsilon^2(7-56k^2+96k^4-16k^6-64k^8)}{64k^2(3+2k^2)}\cos(2\theta) + O(\varepsilon B)^{-3},\end{aligned} \tag{9.57a}$$

$$\begin{aligned}\omega &= \frac{\varepsilon}{3}k^2(1-k^2) \\ &+ B^{-2}\varepsilon^{-1}\frac{9-6\varepsilon(1+8k^4)+\varepsilon^2(1+32k^4-48k^6+64k^8)}{48k^2} + O(B^{-3}),\end{aligned} \tag{9.57b}$$

yielding a peak wavenumber

$$k_{\text{peak}}^{\text{non-normal}}(T=0) = \frac{1 - B^{-2}(1.125\varepsilon^{-2} + 0.75\varepsilon^{-1} - 0.875)}{\sqrt{2}} + O(B^{-3}) \tag{9.58}$$

and a critical wavenumber $k = 1 + B^{-2}\varepsilon^{-2}(9 - 54\varepsilon + 49\varepsilon^2)/32$. Thus the peak wavenumber is shifted down, and the critical wavenumber up. These analytic approximations for peak wavenumber are plotted in Figure 9.8, along with the numerical result from simulations (numerical methods are described in the next section). For $\varepsilon B \gtrsim 4$ (e.g., $\varepsilon = 0.1$ and $B \geq 40$, or $\varepsilon = 0.2$ and $B \geq 20$), the analytic approximation is fairly close to the numerical solution.

It is notable that both $T = 0$ and late time analytical results reflect the general rule that $k_{\text{peak}}^{\text{normal}}$ and $k_{\text{peak}}^{\text{non-normal}}$ increase with B and ε. The relationship with B is most intuitive. Effectively, the ratio of the circumference of the inner hole of the torus, $2\pi(B-1)$, to the central circumference, $2\pi B$, is given by $(B-1)/B = 1-B^{-1}$, a quantity which increases with B. Thus, a disturbance of the form $\cos(kS)$ has wavelength $2\pi/k$ in the solid center of the torus, but wavelength $(2\pi/k)(B-1)/B$ around the inner hole. The effective wavenumber is thus decreased from k to $kB/(B-1)$. The correction to the value of k_{peak} from the cylindrical value depends on the relative strength of the $O(1/B)$ substrate curvature and the $O(\varepsilon)$ film interface curvature; the ratio of which is of the form (εB). Thus, increasing ε or B has the same effect of increasing the relative strength of the interface curvature over the substrate curvature, and vice versa for decreasing ε or B.

Fixing B, thinner films (with smaller ε) have a decreased k_{peak} for a reason similar to that of the shifted cylinder having a lower k_{peak} than the uniform cylinder. As ε gets smaller, the eigenfunction (normal or transient) has a taller peak around $\theta = \pi$. The extra height of this peak

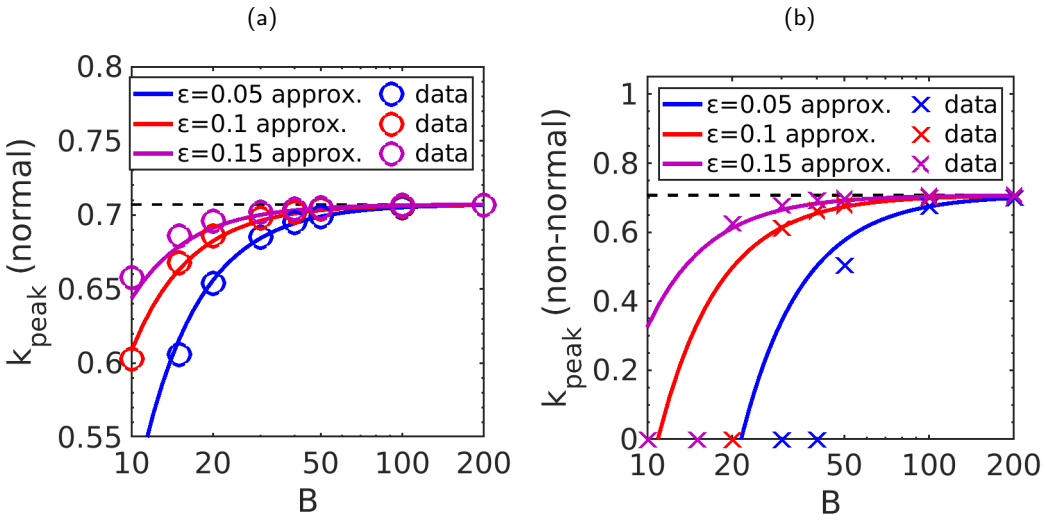

Figure 9.8: Comparisons of analytic approximations of $k_{\text{peak}}^{\text{normal}}(T=0)$ and $k_{\text{peak}}^{\text{non-normal}}(T=0)$ for large B to numerically computed results. The black dashed line indicates 0.707, representing $k_{\text{peak}}^{\text{normal}}$ of the uniformly coated cylinder (see Figure 9.6). The horizontal axis displays major radius B on a log scale; the vertical axis displays $k_{\text{peak}}^{\text{normal}}$ on a linear scale. Colors indicate film thickness ε; $\varepsilon = 0.05$ (blue), $\varepsilon = 0.1$ (red), and $\varepsilon = 0.15$ (purple). Numerical results are given for $B \in \{10, 15, 20, 30, 40, 50, 100, 200\}$, computed at $T = 0$ using a finite difference method (Section 9.6.1). $k_{\text{peak}}^{\text{normal}}$ is computed without boundary conditions; including boundary conditions would round the data points to the nearest $1/B$.
(a) Analytic approximation of $k_{\text{peak}}^{\text{normal}}(T=0)$ for large B (solid lines), described by Equation (9.56), and numerically computed results (circles).
(b) Analytic approximation of $k_{\text{peak}}^{\text{non-normal}}(T=0)$ for large B (solid lines), described by Equation (9.58), and numerically computed results (crosses).

results in a greater pressure being produced by undulations in the S coordinate. To compensate, the peak k is therefore reduced.

Thin-film torus at T=0

Taking the limit $\varepsilon \to 0$ of Equation (9.52) yields an operator with no derivatives; only a multiplicative constant $-(1/2)(B^{-1}\cos\theta)/(1-B^{-1}\cos\theta)^2$. Such a non-constant multiplicative operator has no eigenfunctions. Thus the $\varepsilon \to 0$ limit of the curved thin film equation is a singular perturbation problem (Bender and Orszag, 1999), as noted by Howell (2003). It is clear from the numerical results that the eigenfunctions are maximized around $\theta = \pi$, and hence that is where the inner region should be defined. Setting the inner region variable $\eta = (\theta - \pi)/\varepsilon^{1/6}$, Equation (9.52) becomes [3]

$$\left[\frac{\mathcal{L}+\mathcal{L}^\dagger}{2}\right]_{\text{inner}} = \frac{B^{-1}}{2\left(1-B^{-1}\right)^2} - \varepsilon^{1/3}\left[\frac{1}{3}\partial_\eta^4 + \frac{B^{-1}(1+3B^{-1})\eta^2}{4(1-B^{-1})^3}\right] + O(\varepsilon^{2/3}). \qquad (9.59)$$

The equation $[(\mathcal{L}+\mathcal{L}^\dagger)/2]u = \omega u$ does not appear to have a simple closed form solution. For the case $\omega = 0$, it can be solved using computer algebra, yielding a result in terms of a sum of hypergeometric functions. Instead of pursuing an exact solution, we can glean some information directly from the equation.

Note that we expect $k_{\text{peak}}^{\text{non-normal}}(T=0) = 0$ for sufficiently small B (numerical results shown in the next section suggest this is true for $B \leq 20$ and $\varepsilon \leq 0.1$), and hence can proceed without k dependence. The remaining interesting quantity to determine is therefore ω, the numerical abscissa, representing the growth rate of the fastest-growing disturbance. Clearly, in the limit $\varepsilon \to 0$, $\omega_0 = B^{-1}/[2(1-B^{-1})^2]$. As the film thickness increases, the growth rate should have a correction that scales as $\varepsilon^{1/3}$. Figure 9.9 shows a comparison between the growth rate found in numerical simulations (blue crosses) and the relation $\omega_0 - const. \times \varepsilon^{1/3}$, where the constant is selected by a numerical fit, for $B = 10$. The numerical results appear to match the predicted power law well for $\varepsilon \lesssim 10^{-3}$.

[3] Because we are considering an eigensystem problem, constants added to the operator do not affect the eigenvector. Therefore, the inner region is not a balance between $\varepsilon\partial_\theta^4$ and the ε^0 constant term, as one might at first be tempted to assume (and which would yield a scaling of $[\theta-\pi]/\varepsilon^{1/4}$), but instead between $\varepsilon\partial_\theta^4$ and the $\cos(\theta)$ term in Equation (9.52). $\cos(\theta)$ expands to a constant plus θ^2, and hence balances $\varepsilon\partial_\theta^4$ if $\eta = (\theta-\pi)/\varepsilon^{1/6}$.

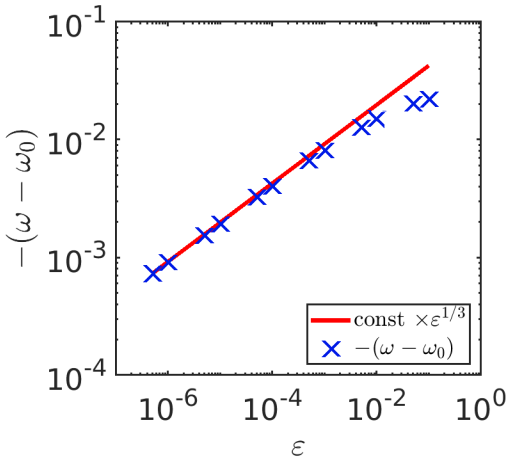

Figure 9.9: Plot of $T = 0$ numerical abscissa, $\omega_{k=0}$, on a torus with $B = 10$ and initial uniform film thickness such that $\varepsilon \in \{5\times10^{-7}, 10^{-6}, 5\times10^{-6}, 10^{-5}, 5\times10^{-5}, 10^{-4}, 5\times10^{-4}, 10^{-3}, 5\times10^{-3}, 10^{-2}, 5\times10^{-2}, 10^{-1}\}$. The horizontal axis shows ε on a log scale; the vertical axis shows $-(\omega-\omega_0)$ on a log scale, where $\omega_0 = B^{-1}/[2(1-B^{-1})^2] \approx 0.0617$. Crosses denote numerically computed results which were computed at $T = 0$ using a finite difference method (Section 9.6.1). The red line displays the power law $\varepsilon^{1/3}$ for reference.

9.6 Linear stability analysis: Numerical results

We next numerically compute normal modes and optimal transient disturbances for a variety of parameters. We concentrate on $T = 0$ and late times, though some results for intermediate times will be shown. Because V_{base} approaches a stationary state as $T \to \infty$ and thus varies more and more slowly in time, $\mathcal{L}_k[V_{\text{base}}]$ approaches autonomy at late times. We therefore show both non-normal and normal results at $T = 0$, but at $T = T_{\text{late}}$ we show only normal results. Comparisons will be made among systems with fixed initial film thickness and varying major radius B, and among systems with fixed major radius B and varying initial film thickness. All results are shown in nondimensional variables.

9.6.1 Numerical methodology

Linear stability analysis was performed in MATLAB, using the nonautonomous methodology described in Section 9.4. Discretized linear operators $\mathcal{L}_k$ were constructed according to Equation (9.29) using 4th order central finite differences on the same equispaced mesh used for the base state. The propagation matrix was constructed by defining $\Phi_k(0)$ to be the identity matrix and integrating $\Phi_k(T)$ in time according to the differential equation, Equation (9.32). Integration was performed using the implicit trapezoid method (Trefethen, 1996)

$$\frac{\Phi_k^{n+1} - \Phi_k^n}{T_{n+1} - T_n} = \frac{1}{2}\left[\mathcal{L}_k^{n+1}\Phi_k^{n+1} + \mathcal{L}_k^n\Phi_k^n\right]. \tag{9.60}$$

Time steps were chosen to be $T_n \in \{0, 10^{-7}, [1,2,3,\cdots]\times10^{-4}\}\times T_{\text{late}}$. In order to efficiently compute non-normal modes over longer timescales or with smaller time steps, it may be

preferable to use adjoint methods instead of direct computation of the propagator matrix (see Appendix B.2 and references therein).

Normal modes, $W_k(\theta, T)$, and the corresponding spectral abscissae $\beta_k(T)$ were computed simply by determining the eigenvector of $\mathcal{L}_k(T)$ whose eigenvalue had maximum real part. The transient mode $X_k(\theta) = U_k^{\text{out}}(\theta, T = 0) = V_k^{\text{in}}(\theta, T = 0)$ and numerical abscissa $\omega_k(T = 0)$ were computed by determining the maximum eigenvalue eigenvector pair of the transient operator $[\mathcal{L}_k(T = 0), \mathcal{L}_k^\dagger(T = 0)]/2$. Optimal input and output modes and the corresponding amplitude $G_k(T)$ were determined by computing the SVD of $\Phi_k(T)$, by which

$$\Phi_k(T) = U_k^{\text{all}}(T)\Sigma(T)V_k^{\text{all}\,\dagger}(T) \tag{9.61}$$

$U_k^{\text{out}}(T)$, $V_k^{\text{in}}(T)$, and $G_k(T)$ were the entries of $U_k^{\text{all}}(T)$, $\Sigma(T)$, and $V_k^{\text{all}}(T)$ corresponding to the maximum singular value (Farrell and Ioannou, 1996a). The time-dependent Lyapunov exponent was then $\lambda_k(T) = \ln G_k(T)/T$, as defined in Equation (9.39).

9.6.2 Normal modes and optimal disturbances at $T = 0$ and $T = T_{\text{late}}$

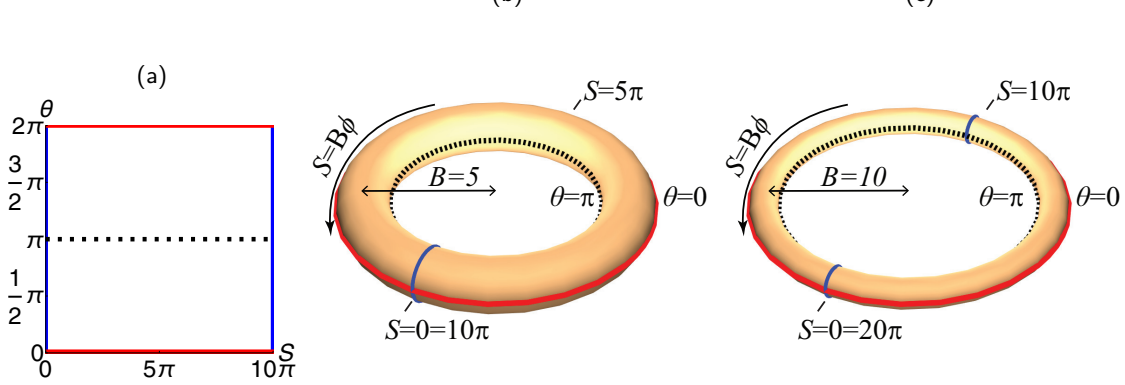

Figure 9.10: Diagram to demonstrate how flat contour plots map to the surface of a torus. The outside of a torus (red line) is mapped to $\theta = 0$ and $\theta = 2\pi$ which are the top and bottom of the contour plot. The inside of the torus (black dashed line) maps to the center of the contour plot, at $\theta = \pi$.
Contour plots will depict $\theta \in [0, 2\pi]$ and $S \in [0, 10\pi]$, the domain shown in (a).
For the torus of major radius $B = 5$ shown in (b), $S \in [0, 10\pi]$ spans the entire torus.
For a torus of major radius $B > 5$, such as the $B = 10$ torus shown in (c), the region $S \in [0, 10\pi]$ does not span the entire torus.

Contour plots of the optimal transient disturbance $X(\theta, S)$ and fastest growing normal modes $W(\theta, S, T)$ at $T = 0$ and $T = T_{\text{late}}$ are shown in Figure 9.11 for a cylinder, and Figures 9.12 and 9.13 for tori of various parameters. In each case, the vertical axis plots θ, the minor angular measure, while the horizontal axis plots S, the arc-length distance around the torus or along the cylinder axis. To simplify comparison between different cases, S is plotted in the range $[0, 10\pi]$. For the $B = 5$ torus, this represents the entire domain of S; for $B > 5$ tori, this is a subset

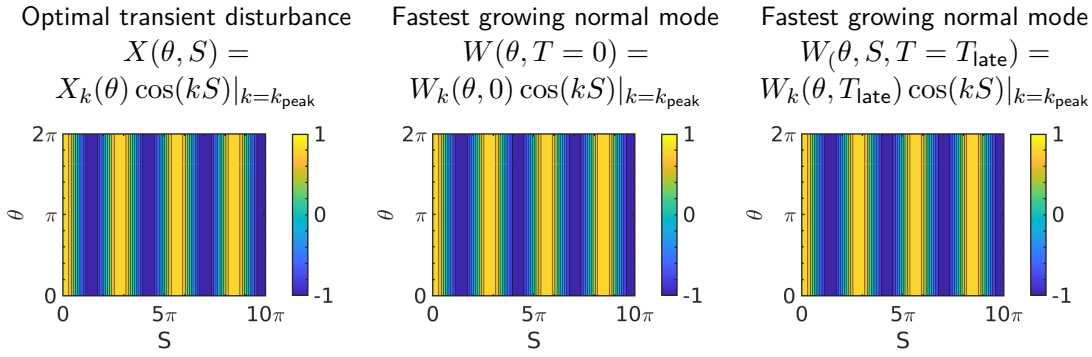

Figure 9.11: Optimal transient disturbance of volumetric fluid thickness, $X(\theta,S)$, fastest growing normal mode at $T=0$, $W(\theta,S,0)$, and fastest growing normal mode at a late time $W(\theta,S,T_{\text{late}}=10)$, described by Eqn. 9.44, for a thin film uniformly coating a cylinder with $\varepsilon=0.1$. The wavenumber of all disturbances shown is $k_{\text{peak}}=1/\sqrt{2}\approx 0.707$. Disturbances are normalized to $[-1,1]$, without loss of generality due to the scaling freedom of linear stability theory. Results were computed numerically using a finite difference method described in Section 9.6.1.
Because the linear operator on a uniformly coated cylinder is normal and autonomous, $X(\theta,S)=W(\theta,T)\ \forall T$.

of the domain, $S\in[0,10\pi]\subset[0,2\pi B]$. The extrema $\theta=0$ and $\theta=2\pi$ represent the outside of the torus, while the center of the plot, $\theta=\pi$ is the inside of the torus. An overview of the plotting domain is given in Figure 9.10. All results are normalized to have peaks and troughs between -1 and 1. Because these are results of linear stability (not nonlinear stability), every disturbance can be freely multiplied by a constant factor without changing the result. Because $U^{\text{out}}(\theta,S,T)$ converges to $W(\theta,S,T)$ at late times, only $W(\theta,S,T_{\text{late}})$ is shown [see Section 9.9 for plots of $U^{\text{out}}(\theta,S,T_{\text{late}})$ and $V^{\text{in}}(\theta,S,T_{\text{late}})$].

Figure 9.11 displays $X(\theta,S)$, $W(\theta,S,0)$, and $W(\theta,S,T=10)$ for a cylinder. Because the linear operator on the cylinder is normal and time-independent, there is no difference between the optimal transient disturbance or fastest growing normal modes at different times. As shown in Section 9.5.1, $X(\theta,S)=W(\theta,S,T)=\cos(S/\sqrt{2})$. Note that the results on the cylinder are symmetric in θ; there is no sense of an "inside" and "outside" as with the torus.

Figure 9.12 displays $X(\theta,S)$, $W(\theta,S,0)$, and $W(\theta,S,T=T_{\text{late}})$ for tori of identical initial film thickness such that $\varepsilon=0.1$, but varying major radius B (recall that the system has been nondimensionalized so that the minor radius is fixed at 1). The top row, with $B=100$, clearly has similar wavenumber and structure to the cylinder at $T=0$, although the normal and output modes are concentrated around the inside of the torus ($\theta=\pi$). At $T=T_{\text{late}}=10600$, however, the fastest growing normal mode W clearly has a longer wavelength, with $k_{\text{peak}}^{\text{non-normal}}(T=T_{\text{late}})=0.56$, and is even more concentrated around $\theta=\pi$. These results accord with the analysis in Section 9.5.2, in which it was found that tori with large B have $k_{\text{peak}}(T=0)$ near the cylinder value of $1/\sqrt{2}$, while at late times k_{peak} approaches the lower

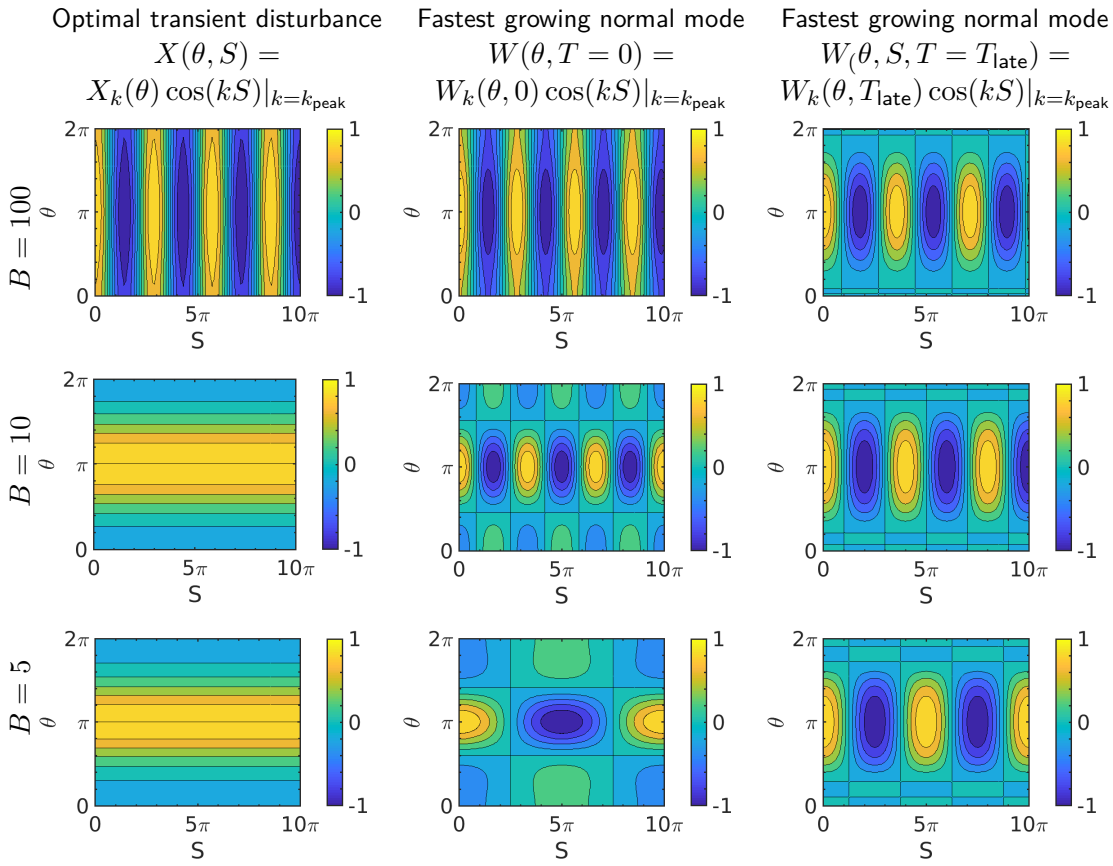

Figure 9.12: Optimal transient disturbance of volumetric fluid thickness, $X(\theta, S)$, fastest growing normal mode at $T = 0$, $W(\theta, S, 0)$, and fastest growing normal mode at a late time $W(\theta, S, T_{\text{late}})$, described by Eqn. 9.44, for a thin film initially uniformly coating tori with $\varepsilon = 0.1$. Results are shown for tori of various major radii $B \in \{5, 10, 15\}$. Disturbances are normalized to $[-1, 1]$, without loss of generality due to the scaling freedom of linear stability theory. Results were computed numerically using a finite difference method described in Section 9.6.1.
Row 1: $B = 100$. $k_{\text{peak}}^{\text{non-normal}}(0) = 0.70$; $k_{\text{peak}}^{\text{normal}}(0) = 0.71$; $k_{\text{peak}}^{\text{normal}}(T_{\text{late}} = 10600) = 0.56$.
Row 2: $B = 10$. $k_{\text{peak}}^{\text{non-normal}}(0) = 0$; $k_{\text{peak}}^{\text{normal}}(0) = 0.6$; $k_{\text{peak}}^{\text{normal}}(T_{\text{late}} = 1050) = 0.5$.
Row 3: $B = 5$. $k_{\text{peak}}^{\text{non-normal}}(0) = 0$; $k_{\text{peak}}^{\text{normal}}(0) = 0.2$; $k_{\text{peak}}^{\text{normal}}(T_{\text{late}} = 510) = 0.4$.

shifted-film cylinder value of 0.566. The next row displays $B = 10$. In this case, the optimal transient disturbance $X(\theta, S)$ has wavenumber $k = 0$, implying that the accelerating transfer of fluid from outside to inside of the torus dominates symmetry-breaking instability at $T = 0$. The wavenumber of the fastest growing normal modes at $T = 0$ and $T = T_{\text{late}} = 1050$ are slightly lower than those of the $B = 100$ torus, and more concentrated around $\theta = \pi$. This again accords with the analysis performed earlier, in which it was predicted that both $k_{\text{peak}}(T = 0)$ and $k_{\text{peak}}(T = T_{\text{late}})$ should decrease with B. The last row displays $B = 5$. As with $B = 10$, the optimal transient disturbance has wavenumber $k_{\text{peak}}^{\text{non-normal}}(T = 0) = 0$. And the fastest growing normal modes have $k_{\text{peak}}^{\text{normal}}(T = 0)$ and $k_{\text{peak}}^{\text{normal}}(T = T_{\text{late}} = 510)$ smaller than those of $B = 10$, reflecting the general rule that k_{peak} should decrease as B decreases, due to the

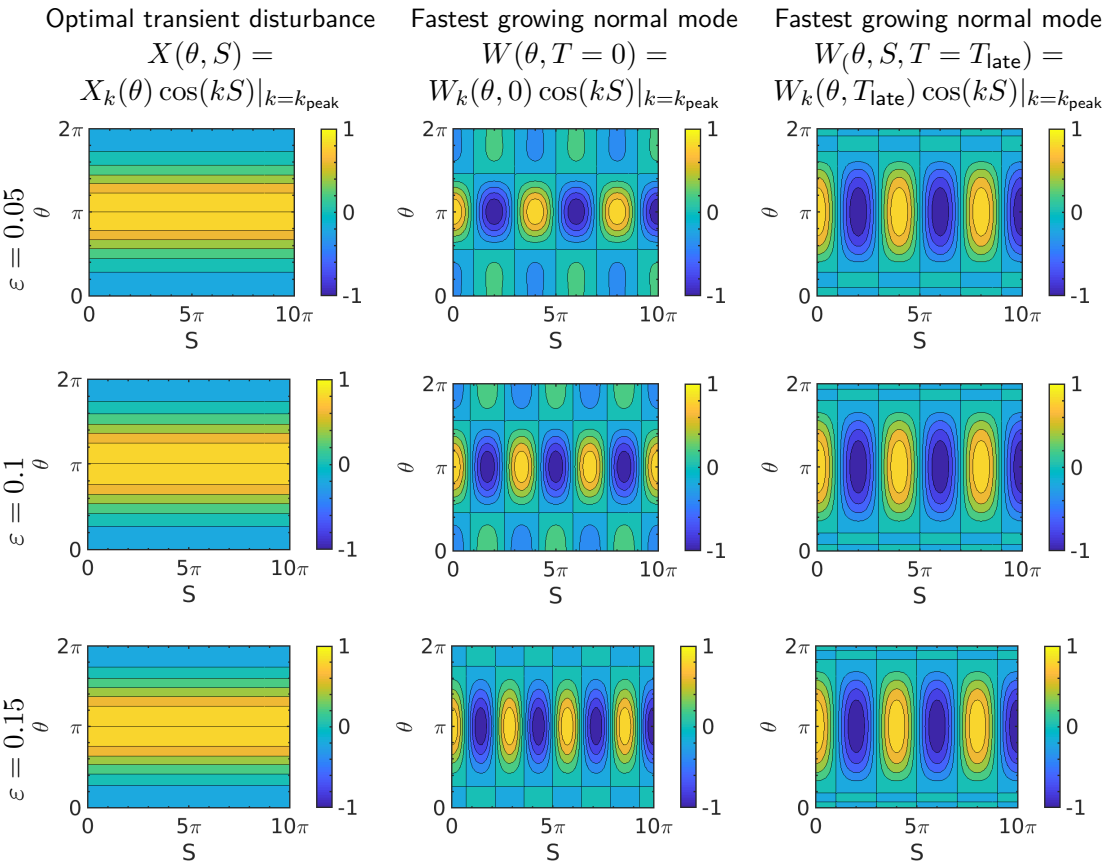

Figure 9.13: Optimal transient disturbance of volumetric fluid thickness, $X(\theta,S)$, fastest growing normal mode at $T=0$, $W(\theta,S,0)$, and fastest growing normal mode at a late time $W(\theta,S,T_{\text{late}})$, described by Eqn. 9.44, for a thin film initially uniformly coating tori with $B=10$ and $\varepsilon \in \{0.05, 0.1, 0.15\}$. Disturbances are normalized to $[-1,1]$, without loss of generality due to the scaling freedom of linear stability theory. Results were computed numerically using a finite difference method described in Section 9.6.1.
Row 1: $\varepsilon = 0.05$. $k_{\text{peak}}^{\text{non-normal}}(0) = 0$; $k_{\text{peak}}^{\text{normal}}(0) = 0.5$; $k_{\text{peak}}^{\text{normal}}(T_{\text{late}} = 1330) = 0.5$.
Row 2: $\varepsilon = 0.1$. $k_{\text{peak}}^{\text{non-normal}}(0) = 0$; $k_{\text{peak}}^{\text{normal}}(0) = 0.6$; $k_{\text{peak}}^{\text{normal}}(T_{\text{late}} = 1050) = 0.5$.
Row 3: $\varepsilon = 0.15$. $k_{\text{peak}}^{\text{non-normal}}(0) = 0$; $k_{\text{peak}}^{\text{normal}}(0) = 0.7$; $k_{\text{peak}}^{\text{normal}}(T_{\text{late}} = 919) = 0.5$.

relatively smaller circumference of the inner hole. But, unlike with higher B, the $B=5$ case has $k_{\text{peak}}^{\text{normal}}(T=0) < k_{\text{peak}}^{\text{normal}}(T=T_{\text{late}})$. The general trend of disturbances concentrating more around $\theta=\pi$ as B decreases is similar to the increasingly sharply peaked base states generated as B is decreased, seen in Figure 9.3.

Figure 9.13 displays $X(\theta,S)$, $W(\theta,S,0)$, and $W(\theta,S,T=T_{\text{late}})$ for tori of identical major radius B and varying initial film thickness, such that $\varepsilon \in \{0.05, 0.1, 0.15\}$. In each case, the optimal transient disturbance $X(\theta,S)$ has wavenumber $k_{\text{peak}}^{\text{non-normal}}(T=0)=0$, reflecting axisymmetric transfer of fluid from the outside of the torus to the inside. The fastest growing normal modes $W(\theta,S,T=0)$ display increasing wavenumber $k_{\text{peak}}^{\text{normal}}(T=0)$ (decreasing wavelength) as ε

increases. This accords with the analysis of Section 9.5.2. Intuitively, the peak wavenumber is determined by a balance of curvature in θ and S coordinates. The eigenfunctions for thin films (smaller ε) are more concentrated, and have a taller peak, around $\theta = \pi$. A sinusoidal disturbance in the S-coordinate therefore produces a greater curvature and greater effect on pressure for small ε, decreasing k_{peak} in compensation. At $T = T_{\text{late}}$ ($T_{\text{late}} = 1330$ for $\varepsilon = 0.05$, 1050 for $\varepsilon = 0.1$, and 919 for $\varepsilon = 0.15$), $k_{\text{peak}}^{\text{normal}}(T = T_{\text{late}})$ is identical; i.e., any difference in $k_{\text{peak}}^{\text{normal}}$ is less than $1/B = 0.1$. Thinner films (smaller ε) appear to be more concentrated around $\theta = \pi$, an effect similar to the sharper base states of thinner films (Figure 9.4).

9.6.3 Dispersion curves

We now examine dispersion relations of the spectral abscissa $\beta_k(T)$ [representing the growth rate of the fastest growing normal mode at T, Equation (9.31)] and the time-dependent Lyapunov exponent $\lambda_k(T)$ [representing the average growth rate of the disturbance which has experiences greatest amplitude growth from 0 to T, Equation (9.39)]. We begin with a torus with $B = 10$ and $\varepsilon = 0.1$.

Figure 9.14 displays dispersion relations (plots against k) of $\lambda_k(T)$ and $\beta_k(T)$ for $T \in \{0,\ 10.1,\ 24.3,\ 57.0,\ T_{\text{late}} = 1050\}$. These times were chosen to be those at which the normal film thickness at $\theta = \pi$, $H(\pi, T)$ had risen to approximately $\{0,\ 0.25,\ 0.5,\ 0.75,\ 1\}$ of the distance between $H(\pi, 0)$ and $H(\pi, T_{\text{late}})$ (the same times were shown in base state plots, Figure 9.3 c-d). Dots indicate the accessible wavenumbers ($k = n/B = n/10$, for integer n). At $T = 0$, $\lambda_k(0) = \omega_k$ is monotonically decreasing in k, with $k_{\text{peak}}^{\text{non-normal}}(T = 0) = 0$, reflecting the accelerating growth of the base state as fluid is transferred from the outside to the inside of the torus. As time progresses and the base state slows, the entire dispersion relation decreases (indicating that the average growth rate of disturbances at all k decreases over time for $0 \leq T \leq 57$). The average growth rate of small k declines faster, resulting in a shift from $k_{\text{peak}}^{\text{non-normal}}(T = 0) = 0$ to $k_{\text{peak}}^{\text{non-normal}}(10.1) = 0.3$, and $k_{\text{peak}}^{\text{non-normal}}(T \geq 24.3) = 0.5$. At late times, the average growth rate $\lambda_0(T_{\text{late}})$ of the optimal $k = 0$ disturbance drops to near 0, but the growth rate of the peak increases again. At late times, $\lambda_k(T_{\text{late}})$ appears very similar to the spectral abscissa $\beta_k(T_{\text{late}})$, although there is a small discrepancy for $k \gtrsim 0.8$. Although for nonautonomous systems there is no requirement that $\lambda_k(T)$ be greater than $\beta_k(T)$, this discrepancy may be due to the numerics; the slow convergence of $\lambda_k(T)$ with $k \geq 0.8$ as timesteps are decreased is discussed in Section 9.6.4, reflecting the challenge of capturing decaying exponents over long periods of time. This issue does not arise in the unstable ($\lambda_k > 0$) portion of the dispersion relation, or at earlier times.

The dispersion of the spectral abscissa, $\beta_k(T)$, follows a different path. At $T = 0$, $k_{\text{peak}}^{\text{normal}}(0) = 0.6$; as time progresses, it first decreases to $k_{\text{peak}}^{\text{normal}}(T = 10.1) = k_{\text{peak}}^{\text{normal}}(T = 24.3) = 0.4$ before increasing again to $k_{\text{peak}}^{\text{normal}}(T \geq 57) = 0.5$. The general trend of $k_{\text{peak}}^{\text{normal}}(T = 0) > k_{\text{peak}}^{\text{normal}}(T = T_{\text{late}})$ is expected, as fluid gathers on the inside of the torus, making it more similar to a shifted-film cylinder than a uniform cylinder (discussed in Section 9.5.1). The increase in

$k_{\text{peak}}^{\text{normal}}$ at intermediate times is difficult to assess intuitively, but is likely related to the relative sharpening of the base state at later times (see Figure 9.3).

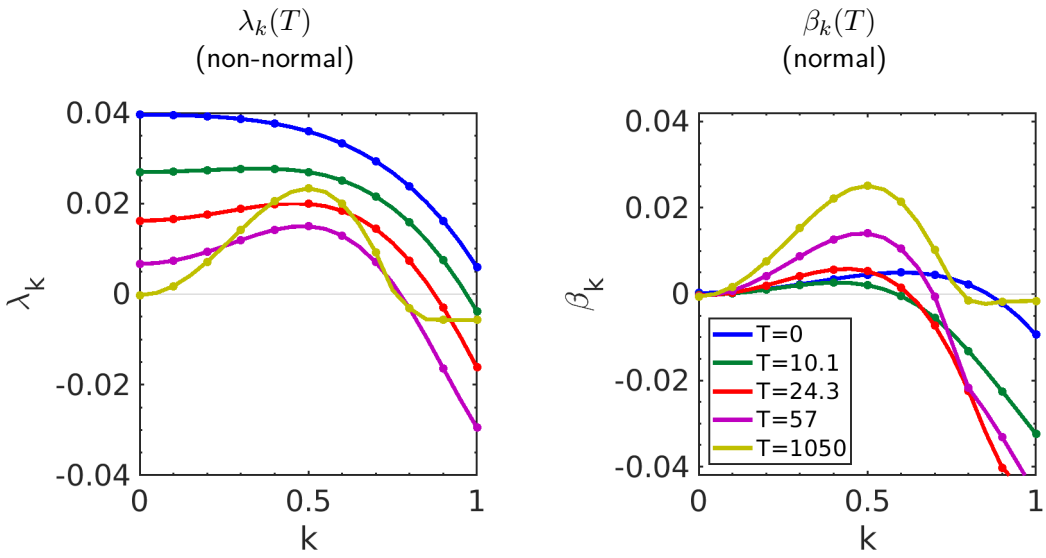

Figure 9.14: Dispersion relations, plotting time-dependent Lyapunov exponent $\lambda_k(T)$, defined by Equation (9.39) and spectral abscissa $\beta_k(T)$, defined by Equation (9.31), against k for a torus with $B = 10$ and $\varepsilon = 0.1$. Each plot depicts five time steps $T \in \{0, 10.1, 24.3, 57.0, 1050\}$, chosen such that the film thickness at $\theta = \pi$ is equispaced between $T = 0$ and the late time, $T = T_{\text{late}} = 1050$. λ_k and β_k are expected to converge at late times, and appear to do so. The discrepancy between $\lambda_k(1050)$ and $\beta_k(1050)$ in the stable portion of the dispersion relation, at $k \geq 0.8$, may be due to the numerics; the slow convergence of $\lambda_k(T)$ with $k \geq 0.8$ as timesteps are decreased is discussed in Section 9.6.4, reflecting the challenge of capturing decaying exponents over long periods of time. This issue does not arise in the unstable ($\lambda_k > 0$) portion of the dispersion relation, or at earlier times.

Having seen in Figure 9.14 that $k_{\text{peak}}^{\text{non-normal}}$ begins at 0 and increases to 0.3 and then 0.5, for the torus with $B = 10$ and $\varepsilon = 0.1$, we plot the optimal disturbance amplitude, $G_k(T)$, at each of these wavenumbers in Figure 9.15. Figure 9.15 (a) shows a long time period, $T \in [0, 600]$, with $G_k(T)$ on a log scale; (b) shows a shorter time frame $T \in [0, 20]$ with $G_k(T)$ on a linear scale. Although the $G_0(T)$ has the fastest growth at $T = 0$, it is not much faster than $G_{k=0.3}$ and $G_{k=0.5}$. At $T = 10.1$, $G_{k=0.3}$ is larger than $G_{k=0.5}$, but the difference is almost imperceptible [note that the dispersion of $\lambda_k(T = 10.1)$, shown in Figure 9.14 (a), is close to flat for $k \leq 0.5$]. It is only over long periods of time that the $k = 0.5$ disturbance pulls ahead of the others. In a realistic system, in which noise is added to an initial state, it is therefore expected that it is only at late times that a single dominant $k = 0.5$ mode would be preferred over other modes; at earlier times before the fluid has approached stationary state thickness, it is likely that small random variations could lead to either $k = 0.5$, $k = 0.3$, or other modes being dominant. Plot (a) also shows a line proportional to $\exp[\beta(T_{\text{late}})T]$ (dashed black line), demonstrating that the optimal disturbance amplitude converges towards the growth rate of the spectral abscissa at

late times.

Although there is a hand-off of $k_{\text{peak}}^{\text{non-normal}}$ from 0 at $T = 0$, to 0.3 and $T = 10.1$, and finally to 0.5, there does not appear to be a transient disturbance with another wavenumber significantly more unstable than the late-time $k_{\text{peak}}^{\text{non-normal}}(T_{\text{late}}) = 0.5$ wavenumber.

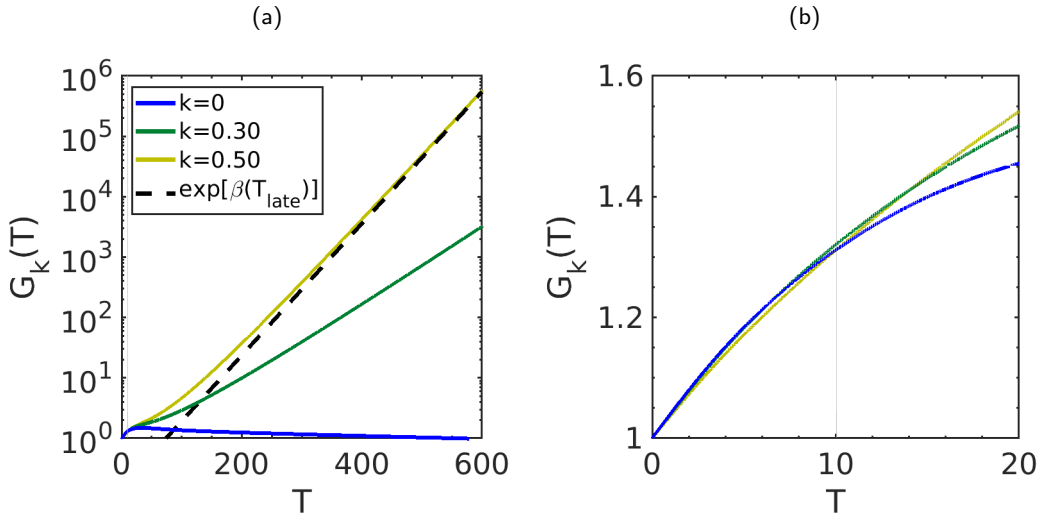

Figure 9.15: Plots over time of optimal disturbance amplitude, $G_k(T)$, defined by Equation (9.36), for a torus with $B = 10$ and $\varepsilon = 0.1$. Three wavenumbers are shown: $k = k_{\text{peak}}^{\text{non-normal}}(T = 0) = 0$ (blue), representing the fastest growing transient disturbance at $T = 0$; $k = k_{\text{peak}}^{\text{non-normal}}(T = 10.1) = 0.3$ (green), representing the disturbance with greatest amplitude growth between $T = 0$ and $T = 10.1$; and $k = k_{\text{peak}}^{\text{non-normal}}(T = T_{\text{late}} = 1050) = 0.5$ (yellow), representing the disturbance with greatest amplitude growth between $T = 0$ and $T = T_{\text{late}}$.
(a) Plot of $G_k(T)$ with linear horizontal axis T and log vertical axis $G_k(T)$. The dashed black line indicates $const. \times \exp[\beta(T_{\text{late}})]$, where $\beta(T_{\text{late}}) = \beta_{k=0.5}(T_{\text{late}})$ is the spectral abscissa at late times, defined by Equation (9.31). $G_k(T)$ is expected to converge to $const. \times \exp[\beta(T_{\text{late}})]$ at late times.
(b) Plot of $G_k(T)$ over a shorter time range with linear axes. $G_{k=0}(T)$ has greater slope than $G_{k=0.3}(T)$ and $G_{k=0.5}(T)$ at $T = 0$ because it is the amplitude of the fastest growing transient disturbance at that time. At $T = 10.1$, $G_{k=0.3}(T) > G_{k=0.5}(T)$ and $G_{k=0}(T)$. At later times, $G_{k=0.5}(T)$ exceeds the other two.

We next look at tori with different initial film thickness and major radius B parameters, comparing dispersion relations of the numerical abscissa at $T = 0$, ω_k [representing the growth rate of the fastest growing disturbances at $T = 0$, Equation (9.40)], the spectral abscissa at $T = 0$ [representing the growth rate of the fastest growing normal mode at $T = 0$, Equation (9.31)], and $\beta_k(T = T_{\text{late}})$ [representing the growth rate of the fastest growing normal mode at $T = T_{\text{late}}$, Equation (9.31)]. Having seen in Figure 9.14 that β_k and λ_k appear to converge at late times, we show only the former.

Figure 9.16 shows dispersion relations of ω_k, $\beta_k(T=0)$, and $\beta_k(T=T_{\text{late}})$ for tori of identical initial film thickness such that $\varepsilon = 0.1$, and varying major radius $B \in \{5, 10, 50, 100, 200\}$. Note that $T_{\text{late}} = \{510, 1050, 5310, 10600, 21300\}$, respectively. In all cases, the general rule of k_{peak} increasing as B increases is maintained. Tori with smaller radii, $B \in \{5, 10\}$, have $k_{\text{peak}}^{\text{non-normal}}(0) = 0$ due to the accelerating base state which transfers fluid from the outside to the inside of the torus. At larger radii, $B \in \{50, 100, 200\}$, the base state motion is slower, and hence the disturbances similar to those on the cylinder with wavenumber $k_{\text{peak}} = 0.707$ (dashed line) are able to grow faster. Dispersion of $\beta_k(T=0)$ similarly has a small $k_{\text{peak}}^{\text{normal}}$ for $B \in \{5, 10\}$ and $k_{\text{peak}}^{\text{normal}}$ near the cylindrical value for large B. It is notable that $\beta_k(T=0)$ increases with B, i.e., normal modes grow faster at large B than small B, while ω_k has the opposite effect. This gap reflects the large non-normality of the linear operator at small B; while at large B the linear operator approaches that of the cylinder and becomes closer to normal. At late times, the $k_{\text{peak}}^{\text{normal}}(T=T_{\text{late}})$ approaches the shifted-cylinder peak of ≈ 0.566 (dotted line). At smaller B, the peak wavenumber is lower. Furthermore, $\beta_k(T=T_{\text{late}})$ is larger for small B than large B, i.e., disturbances grow faster at late times on small-B tori than large-B tori.

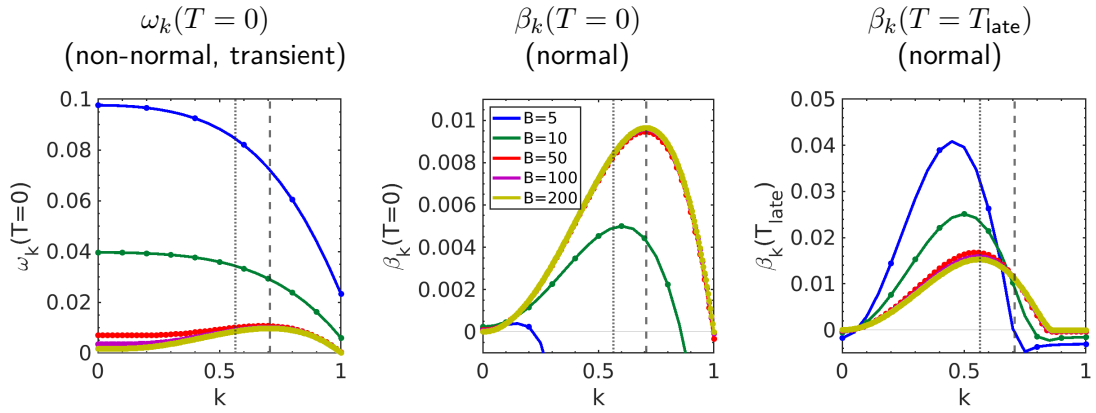

Figure 9.16: Dispersion relations of numerical abscissa ω_k at $T=0$, defined by Equation (9.40), spectral abscissa $\beta_k(T=0)$ defined by Equation (9.31), and spectral abscissa at late times $\beta_k(T=T_{\text{late}})$, for a tori with identical uniform film thickness such that $\varepsilon = 0.1$, and varying major radii $B \in \{5, 10, 50, 100, 200\}$, for which $T_{\text{late}} = \{510, 1050, 5310, 10600, 21300\}$, respectively. The dispersion relations are discrete, and accessible wavenumbers are indicated by dots. The continuous dispersion relation connecting the accessible wavenumbers was included to simplify the visual presentation. Dashed vertical line indicates $k = 1/\sqrt{2} \approx 0.707$, the peak wavenumber on a uniformly coated cylinder. Dotted vertical line indicates $k = 0.566$, the peak wavenumber on a cylinder coated by a shifted film (see Figure 9.6). Numerical results were computed using a finite difference method (Section 9.6.1).

Figure 9.17 shows dispersion relations of ω_k, $\beta_k(T=0)$, and $\beta_k(T=T_{\text{late}})$ for tori of identical major radius $B = 10$ and varying initial film thickness such that $\varepsilon \in \{0.05, 0.1, 0.15\}$. Note that $T_{\text{late}} = \{1330, 1050, 919\}$, respectively. The general rule of $k_{\text{peak}}^{\text{normal}}$ increasing as B increases is maintained; although, $k_{\text{peak}}^{\text{non-normal}}(T=0) = 0$ for all film thicknesses. The dispersion of the numerical abscissa ω_k at $T=0$ appears similar for all cases, as the growth is driven by

the base state. Thinner films have higher ω_k, following the $\omega_k \sim \varepsilon^{-1/3}$ relation discussed in Section 9.5.2. At $T = T_{\text{late}}$, the film has approached the stationary state at which the interface curvature balances the substrate curvature, and so disturbances induce pressure variations of $O(\varepsilon)$, and the scaling should thus be $\beta_k(T_{\text{late}}) \propto \varepsilon$. This explains the relative magnitudes of $\beta_k(T = T_{\text{late}})$. It is interesting that the spectral abscissa at $T = 0$, $\beta_k(T = 0)$, has scaling similar to $\beta_k(T = T_{\text{late}})$, rather than similar to ω_k. It is thus likely that a normal mode analysis effectively picks up only the $O(\varepsilon)$ pressure variations, and is relatively unaffected by the substrate pressure which drives the base state and optimal transient disturbances. In the case of the thickest film, $\varepsilon = 0.15$, $\beta_k(T = 0)$ begins to develop a secondary peak at wavenumber $k = 0$. While it is still lower than the peak at $k = 0.7$, it suggests that as the film gets thicker the $k = 0$ mode (similar to the optimal transient disturbance) becomes more important. For very thick films, it may be that $k_{\text{peak}}^{\text{normal}}(T = 0)$ is 0 instead of having a value near 0.707; such an analysis could be conducted using a thicker film model such as that of Wray et al. (2017), but is beyond the scope of the present work.

Note that $B = 10$, $\varepsilon = 0.05$ is the parameter set used by Roy and Schwartz (1997) in their nonlinear simulation of a thin film with noise added to a uniform initial condition, which evolved into a periodic disturbance with wavenumber $k = 0.4$. According to our linear stability analysis, $\beta_{k=0.4}(T_{\text{late}}) = 0.0101$ and $\beta_{k=0.5}(T_{\text{late}}) = 0.0104$; thus, although $\beta_{k=0.5}$ is slightly higher, the results are very close (approximately 3% apart) and the appearance of a $k = 0.4$ disturbance is in agreement with our results.

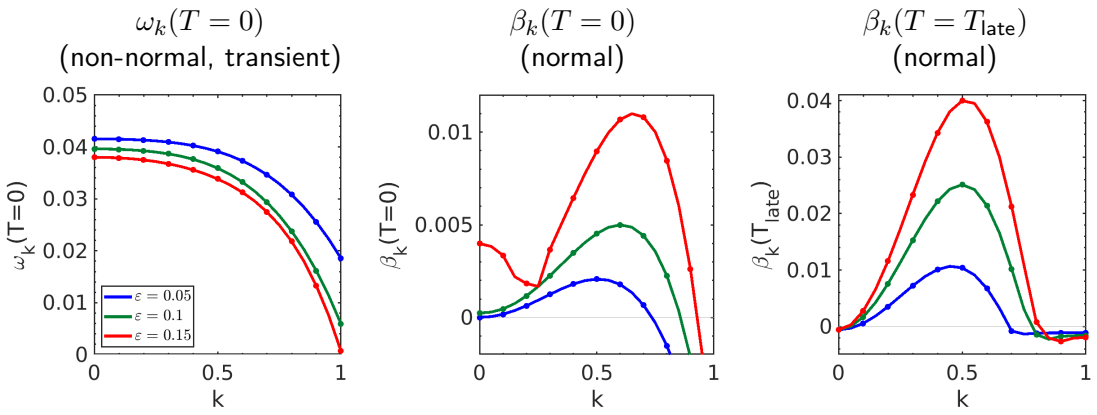

Figure 9.17: Dispersion relations of numerical abscissa ω_k at $T = 0$, defined by Equation (9.40), spectral abscissa $\beta_k(T = 0)$ defined by Equation (9.31), and spectral abscissa at late times $\beta_k(T = T_{\text{late}})$, for a tori with major radius $B = 10$ and varying initial uniform film thickness such that $\varepsilon \in \{0.05, 0.1, 0.15\}$, for which $T_{\text{late}} = \{1330, 1050, 919\}$, respectively. The dispersion relations are discrete, and accessible wavenumbers are indicated by dots. The continuous dispersion relation connecting the accessible wavenumbers was included to simplify the visual presentation. Dashed vertical line indicates $k = 1/\sqrt{2} \approx 0.707$, the peak wavenumber on a uniformly coated cylinder. Dotted vertical line indicates $k =\approx 0.566$, the peak wavenumber on a cylinder coated by a shifted film (see Figure 9.6). Numerical results were computed using a finite difference method (Section 9.6.1).
Note the increase in $\beta_k(T = 0)$ for $\varepsilon = 0.15$ (red) around $k = 0$. Simulations conducted at $\varepsilon = 0.2$ indicate that the $k = 0$ peak of $\beta_k(T = 0)$ grows even further; these results were not shown due to the system violating the lubrication assumption at intermediate and late times. It may be that for sufficiently thick films, the $k = 0$ peak of $\beta_k(T = 0)$ could surpass the $k > 0$ peak, resulting in $k^{\text{normal}}_{\text{peak}}(T = 0) = 0$.

9.6.4 Numerical validation tests

The good agreement between numerical and analytic results in large-B and small-ε limits, suggest that the numerical method is likely accurate; additional tests are carried out to ensure that this is the case.

We first compare our base state result to that of Roy et al. (2002), whose equation of motion differs from ours at $O(\varepsilon^2)$. The authors only provided results for a torus of $B = 2$, $\varepsilon = 0.1$, a parameter set which we exclude due to violation of the lubrication condition; in such a situation, the designated $\varepsilon = 0.1$ is not reflective of the actual ratio (h/L), and we should expect $O([h/L]^2)$ difference instead. However, we compute results at these parameters in order to compare our results to those of Roy et al.. Figure 9.18 displays $\varepsilon H_{\text{base}}(\theta, T)$ superimposed on the corresponding plot from Roy et al. (2002). At the peaks, the difference is approximately $0.5(h/L)^2 = 0.5h^2$, in line with the expected $O([h/L]^2)$ difference. For $H_{\text{base}} \lesssim 3$, the results match well; the difference is typically less than 1% and reaches a worst case of 5% at the peak near $\theta = \pi$. In order to avoid issues with violation of lubrication limits, all results in the present work satisfy $H_{\text{base}} < 3.1$. In order to study thicker films, a model such as that of Wray et al.

(2017) would be needed.

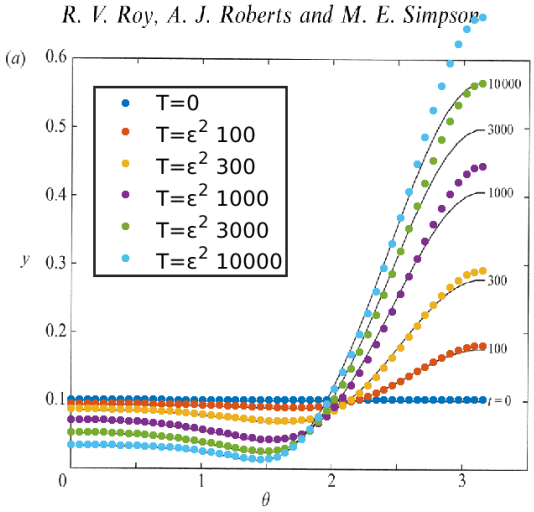

Figure 9.18: Evolution of base state normal film thickness $h_{\text{base}}(\theta, T) = \varepsilon H_{\text{base}}(\theta, T)$ for torus with $B = 2$, $\varepsilon = 0.1$, according to the thin film equation on a torus, Equations (9.17) and (9.18). Data is superimposed on the evolution plot from the publication of Roy et al. (2002). Results are shown at times $T \in \{0, 100, 300, 1000, 3000, 10000\}\varepsilon^2$, corresponding to the times shown by Roy et al.. The difference betwen the models is expected to have $O(h^2/L^2)$. In this case, $L = 1$, and the maximum difference at the fluid peaks is indeed approximately $0.5h^2$. Note that the results are very close for $h \lesssim 0.3$ (i.e., $H \lesssim 3$); all results in the present work satisfy $H_{\text{base}} < 3.1$.

In order to further validate the numerical results, we confirm that the results converge as the spatial mesh size is refined, as the time step is decreased, and also that the results are unchanged if a spectral differentiation scheme is used instead of finite difference. Numerical tests are performed for the parameter $B = 10$, $\varepsilon = 0.1$. Comparisons of base state and dispersion relations are made at times $T = 0$, $T = T_{\text{mid}} = 10.1$, and $T = T_{\text{late}} = 1050$.

We first perform a mesh refinement test, with results shown in Figure 9.19. Simulations are run with N_{mesh} mesh points in the range $\theta \in [0, 2\pi)$, where $N_{\text{mesh}} = 25 \times 2^{j-1} \in \{25, 50, 100, 200\}$. The relative difference between the base state film thickness with mesh size j, $H_j(\theta, T_{\text{late}})$, and that of mesh size $j + 1$ is compared: $\|H_{j+1}(\theta, T_{\text{late}}) - H_j(\theta, T_{\text{late}})\| \;/\; \|H_{j+1}(\theta, T_{\text{late}})\|$, where $\|\cdot\|$ indicates the L_2 norm on the domain $\theta \in [0, 2\pi]$. The result is plotted in Figure 9.19 (a). The relative difference between subsequent mesh refinements is small ($< 1\%$ for all cases tested), and decreases for $j = 1, 2, 3$.

A similar test is performed for the normal and non-normal dispersion curves. Letting a given dispersion curve be denoted $\sigma(k)$, the comparison $\|\sigma(k)_{j+1} - \sigma(k)_j\|/\|\sigma(k)_{j+1}\|$ is performed, where $\|\cdot\|$ indicates the L_2 norm on the domain $k \in [0, 1]$. A second comparison of the

maximum difference, $\max_k |\sigma(k)_{j+1} - \sigma(k)_j|$ is also computed. This comparison is performed for normal modes [i.e., $\sigma(k) = \beta_k$] at $T = 0, T_{\text{mid}}, T_{\text{late}}$ and non-normal modes at $T = 0$ [for which $\sigma(k) = \omega_k$] and at $T = T_{\text{mid}}$ [for which $\sigma(k) = \lambda_k$, the time-dependent Lyapunov exponent]. Note that intermediate-time non-normal results were not computed for $N_{\text{mesh}} = 200$, due to computational constraints. The results are plotted in Figure 9.19, (b)-(c). Under moth measures, the difference decreases monotonically as the mesh size is decreased. The relative norm difference of normal mode dispersion, shown in (b), is at most 2.4% between $N_{\text{mesh}} = 100$ and $N_{\text{mesh}} = 200$; non-normal mode dispersion has relative norm difference of at most 0.12% between $N_{\text{mesh}} = 50$ and $N_{\text{mesh}} = 100$. We therefore conclude that the choice of $N_{\text{mesh}} = 100$ is reasonable.

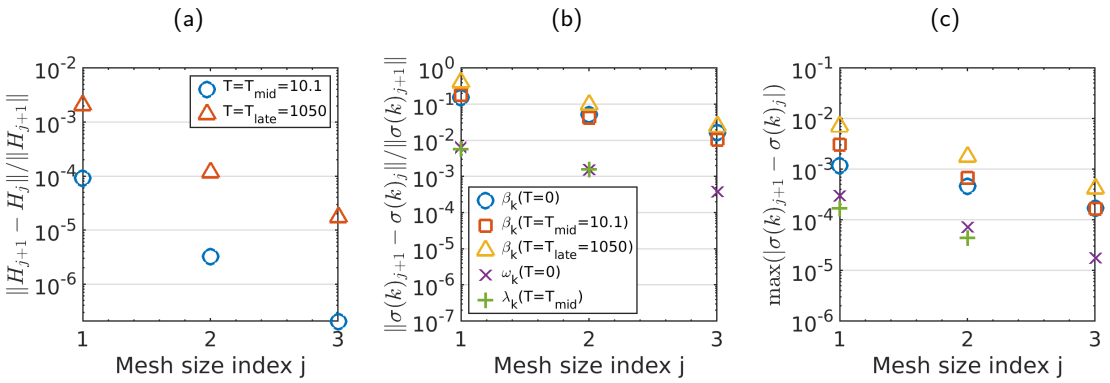

Figure 9.19: Convergence of base state film thickness and dispersion relations as mesh is refined. Simulations are run for the parameter $B = 10$, $\varepsilon = 0.1$ to time $T = T_{\text{mid}} = 10.1$ and $T = T_{\text{late}} = 1050$, with N_{mesh} mesh points in the range $\theta \in [0, 2\pi)$, where $N_{\text{mesh}} = 25 \times 2^{j-1} \in \{25, 50, 100, 200\}$.
(a) Relative norm difference between the base state film thickness with mesh size j, $H_j(\theta, T_{\text{late}})$, and that of mesh size $j+1$: $\|H_{j+1}(\theta, T_{\text{late}}) - H_j(\theta, T_{\text{late}})\|/\|H_{j+1}(\theta, T_{\text{late}})\|$, where $\|\cdot\|$ indicates the L_2 norm on the domain $\theta \in [0, 2\pi]$.
(b) Relative norm difference, $\|\sigma(k)_{j+1} - \sigma(k)_j\|/\|\sigma(k)_{j+1}\|$, between mesh sizes of the dispersion curves $\sigma(k) \in \{\beta_k(T = 0), \beta_k(T = T_{\text{mid}}), \beta_k(T = T_{\text{late}}), \omega_k(T = 0), \lambda_k(T = T_{\text{mid}})\}$, defined by Equations (9.31), (9.39) and (9.40).
(c) Maximum absolute difference, $\max_k(|\sigma(k)_{j+1} - \sigma(k)_j|)$, between mesh sizes of the dispersion curves $\sigma(k) \in \{\beta_k(T = 0), \beta_k(T = T_{\text{mid}}), \beta_k(T = T_{\text{late}}), \omega_k(T = 0), \lambda_k(T = T_{\text{mid}})\}$.
Note that $\lambda_k(T = T_{\text{mid}})$ was not computed for $N_{\text{mesh}} = 200$, due to computational expense.

Next, the convergence of non-normal dispersion curves $\sigma(k)$ is computed with decreasing time steps. The generalized linear stability analysis is performed with time steps of size $\Delta T = \{5, 2, 1, 0.5, 0.25\} \times 10^{-4} T_{\text{late}}$. The comparison $\|\lambda(k)_{i+1} - \lambda(k)_i\|/\|\lambda(k)_{i+1}\|$ is performed, where $\|\cdot\|$ indicates the L_2 norm on the domain $k \in [0, 1]$, and $\lambda(k)$ represents the time-dependent Lyapunov exponent. We also compute the maximum difference $|\lambda(k)_{i+1} - \lambda(k)_i|$. Finally, noting that the dispersion is positive (unstable) for $k \leq 0.77$, we also compute differences for $k \in [0, 0.8]$.

The results are plotted in Figure 9.20. The relative difference decreases monotonically as the time steps are decreased. At $T_{\text{mid}} = 10.1$, the relative norm difference between dispersion relations $\lambda_k(T = T_{\text{mid}})$ with $\Delta T = 2 \times 10^{-4} T_{\text{late}}$ and $\Delta T = 10^{-4} T_{\text{late}}$ is below 0.003%. At $T_{\text{late}} = 1050$, the relative difference between $\lambda_k(T = T_{\text{late}})$ is 4.3%. But restricting the domain of interest to positive k with $k \in [0, 0.8]$, the relative difference is only 0.00003%. Thus, a finer time step would be required to achieve high accuracy in the stable portion of the dispersion relation at $k > 0.8$. Based on these results, we choose a standard timestep of $\Delta T = 10^{-4} T_{\text{late}}$. For $B = 10$, $\varepsilon = 0.1$, we use $\Delta T = 0.5 \times 10^{-4} T_{\text{late}}$, as a simulation with that short timestep was produced for the convergence test.

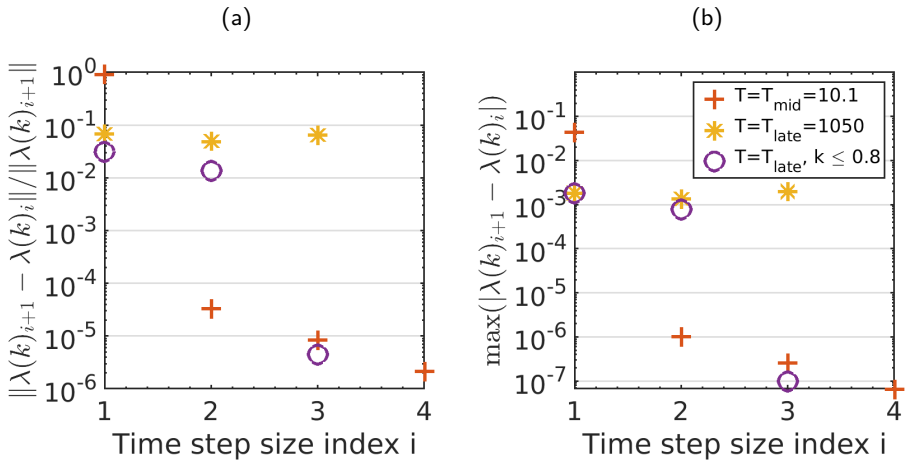

Figure 9.20: Convergence of time-dependent Lyapunov exponent dispersion relations as timestep is refined. Simulations are run for the parameter $B = 10$, $\varepsilon = 0.1$ to time $T = T_{\text{mid}} = 10.1$ and $T = T_{\text{late}} = 1050$, with time steps of size $\Delta T = \{5, 2, 1, 0.5, 0.25\} \times 10^{-4} T_{\text{late}}$. Results are shown for time-dependent Lyapunov exponent λ_k, defined by Equation (9.39), at $T = T_{\text{mid}} = 10.1$ on the domain $k \in [0, 1]$ (red pluses), $T = T_{\text{late}} = 1050$ on the domain $k \in [0, 1]$ (yellow stars), and $T = T_{\text{late}} = 1050$ on the domain $k \in [0, 0.8]$ (purple circles).
(b) Relative norm difference, $\|\lambda(k)_{j+1} - \lambda(k)_j\| / \|\lambda(k)_{j+1}\|$, between time steps of the time-dependent Lyapunov exponent λ_k, where $\|\cdot\|$ represents the L_2 norm.
(c) Maximum absolute difference, $\max_k(|\lambda(k)_{j+1} - \lambda(k)_j|)$, between time steps of the time-dependent Lyapunov exponent λ_k.
Note that late time convergence is slow on the entire domain, $k \in [0, 1]$, but fast on $k \in [0, 0.8]$. Because $\lambda_{k>0.8} < 0$, the slow-converging portion of the dispersion relation is stable. I.e., the unstable portion of the dispersion relation, which is the region of interest, converges quickly with time step refinement.

Results were computed using fourth-order central finite differences, on an equispaced mesh with periodic boundary conditions. As a check on the robustness of the numerical method, we compute results with a spectral differentiation method as well. A mesh of size $N_{\text{mesh}} = 100$ points covering $\theta \in [0, 2\pi)$ is used, as with the finite difference case, so that $\theta_j = 2\pi(j-1)/N_{\text{mesh}}$, with $1 \le j \le N_{\text{mesh}}$. Discrete wavenumbers are defined by $k_j = 1 - (N_{\text{mesh}}/2) + j$; let the diagonal matrix $\hat{K}$ be defined by $\hat{K}_{jj} = k_j$. The discrete Fourier transform matrix, $\hat{F}$, is constructed by

$\hat{F}_{j\ell} = (2\pi/\sqrt{N_{\text{mesh}}})\exp(-ik_j\theta_\ell)$, and inverse by $\hat{F}^{-1}_{j\ell} = (2\pi/\sqrt{N_{\text{mesh}}})^{-1}\exp(ik_\ell\theta_j)$. Differentiation matrices are then defined by $\hat{\partial}_\theta = \hat{F}^{-1}(i\hat{K})\hat{F}$, $\hat{\partial}_{\theta\theta} = \hat{F}^{-1}(i\hat{K})^2\hat{F}$, $\hat{\partial}^m_\theta = \hat{F}^{-1}(i\hat{K})^m\hat{F}$.

Comparisons between finite difference and spectral method results are computed for $B = 10$, $\varepsilon = 0.1$, for base state $H(\theta, T)$ and for dispersion relations $\sigma(k, T)$. Base state solutions showed little difference with maximum absolute difference $\max_{T,\theta}|H_{\text{fin.diff.}}(T,\theta) - H_{\text{spectral}}(T,\theta)| = 0.00018$ and maximum relative difference $\max_{T,\theta}|H_{\text{fin.diff.}}(T,\theta)/H_{\text{spectral}}(T,\theta) - 1| = 0.31\%$.

Dispersion relations of normal modes $\beta_k(T=0), \beta_k(T = T_{\text{mid}} = 10.1), \beta_k(T = T_{\text{late}} = 1050)$ and non-normal modes, ω_k at $T = 0$, $\lambda_k(T = T_{\text{mid}} = 10.1)$, $\lambda_k(T = T_{\text{late}} = 1050)$ were similar between the two cases. Letting $\sigma(k)$ represent the dispersion relation, the maximum relative norm difference was $\|\sigma_{\text{fin.diff.}}(k) - \sigma_{\text{spec}}(k)\|/\|\sigma_{\text{fin.diff.}}(k)\| = 0.034$, except for the time-dependent Lyapunov exponential $\lambda_k(T = T_{\text{late}})$, which had relative norm difference 0.12. But, as with the time convergence test, the error was concentrated at $k > 0.8$, the stable region of the dispersion relation (note the visible difference in Figure 9.21 f). When the stable region is excluded, the relative norm difference is at most 0.037. Plots of the dispersion relations $\beta_k(T=0)$, ω_k, $\beta_k(T = T_{\text{mid}})$, $\lambda_k(T = T_{\text{mid}})$, $\beta_k(T = T_{\text{late}})$, $\lambda_k(T = T_{\text{late}})$ for finite difference and spectral methods are shown in Figure 9.21. Note that in order for the spectral method to converge, a smaller time step of $5 \times 10^{-6}T_{\text{late}}$ was used for $T \in [0, 0.01T_{\text{late}}]$, instead of the $10^{-4}T_{\text{late}}$ used for the finite difference case.

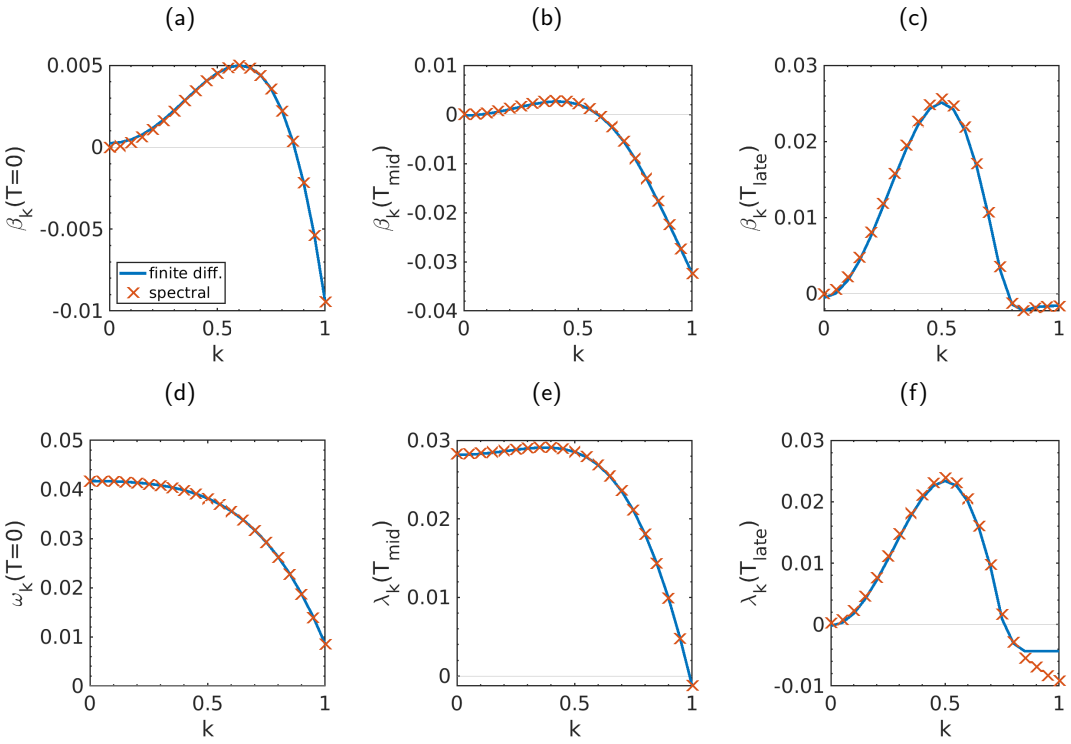

Figure 9.21: Comparison of dispersion relations of the spectral abscissa $\beta_k(T)$, defined by Equation (9.31) and the time-dependent Lyapunov exponent $\lambda_k(T)$, defined by Equation (9.39), between finite difference and spectral differentiation methods. Results are computed on a torus of $B = 10$ and $\varepsilon = 0.1$, at times $T = 0$, $T = T_{\text{mid}} = 10.1$, and $T = T_{\text{late}} = 1050$.
(a) $\beta_k(T = 0)$ (b) $\beta_k(T = T_{\text{mid}} = 10.1)$ (c) $\beta_k(T = T_{\text{late}} = 1050)$ (d) $\omega_k(T = 0) = \lambda_k(T = 0)$ (e) $\lambda_k(T = T_{\text{mid}} = 10.1)$ (f) $\lambda_k(T = T_{\text{late}} = 1050)$
The results in all cases show good agreement, with the exception of $\lambda_k(T_{\text{late}})$ for $k > 0.8$, representing the stable portion of the $\lambda_k(T_{\text{late}})$ dispersion relation. Using a finer time step would likely lead to convergence in this region, but was not possible due to computational expense.

9.7 Discussion

The thin film model ignored inertial effects, requiring in particular that $\varepsilon\rho d u_c/\mu = \varepsilon^3\rho\gamma d/\mu^2 \ll 1$ [an alternative condition specific to the torus was suggested by Roy et al. (2002), namely, $\varepsilon^4\rho\gamma d/(6\mu^2 B) \ll 1$] . If a real system has a large length scale, or a large density, then this requirement might be violated, making the results invalid. Similarly, gravity has not been taken into account; the effect of gravity would depend on the orientation of the torus relative to the gravitational field. Given the droplet formation results for a thin film coating a torus with gravity reported by Vantzos et al. (2017), a stability analysis of that case may be an interesting future research direction. Because all simulations were conducted in nondimensional variables, with no specific choice of physical length scales or materials, there is no concern of the simulations violating the noninertial or zero gravity assumptions.

Over time, the liquid film thins on the outside of the torus, and the stationary state approached is that of a ruptured film. Therefore, it may be worthwhile to conduct additional studies either explicitly allowing the film to rupture or including Van der Waals forces where the film is very thin. However, it is expected that the late-time dynamics are largely driven by the inside, where the fluid is thick, and a Van der Waals correction to the dynamics where the fluid is extremely thin would likely not have a very large effect on the results.

It should also be noted that the linear stability analysis is valid only for infinitesimal perturbations. Given that the governing thin film equation is highly nonlinear, large perturbations to the film interface should not necessarily be expected to follow the predictions of the linear system. The study was performed in two dimensions, time and θ, while the dimension s was factored out by a Fourier transform; this simplified the numerical method considerably. To further validate the predictions of the linear stability analysis, it may be worthwhile to perform full nonlinear simulations with noisy initial conditions. Such a simulation was performed for one set of parameters by Roy and Schwartz (1997), resulting in an instability with wavenumber matching our linear stability analysis; however, a wider range of parameters could be tested. It may be interesting to compute pseudospectra and other quantifiers of the non-normality of the linear operator $\mathcal{L}$. In order to achieve higher resolution results, one could use the approach of Balestra et al. (2016, 2018b) and apply an adjoint method (Schmid, 2007) to determine optimal disturbances. See Appendix B of this thesis for an overview of both pseudospectral analysis and adjoint methods for computing optimal disturbances.

9.8 Conclusion

The instability behavior of viscous thin films coating tori of various sizes has been computed. The result differed from the behavior of thin films on cylinders, due to the moving base state and non-normality of the linear operators on tori. We have shown that in the limit of infinite major radius, $B \to \infty$, the most unstable disturbance converges to wavenumber $k = 0.566$ at late times, which is that of the shifted film on a cylinder, not the $k = 0.707$ found on a centered cylinder as in Goren (1962). We further developed approximate analytic expressions for the $T = 0$ dispersion relations of both normal modes and fastest-growing transient disturbances in the large-radius and thin-film limits.

This study focused on only a few torus sizes and film thicknesses, and on $T = 0$ and late times. By choosing this simplified set of parameters to consider, analytically tractable results were able to be determined and compared to the numerics. It is hoped that this work opens the door to future research considering larger parameter ranges and additional effects such as inertia and gravity.

9.9 Appendix: Additional plots

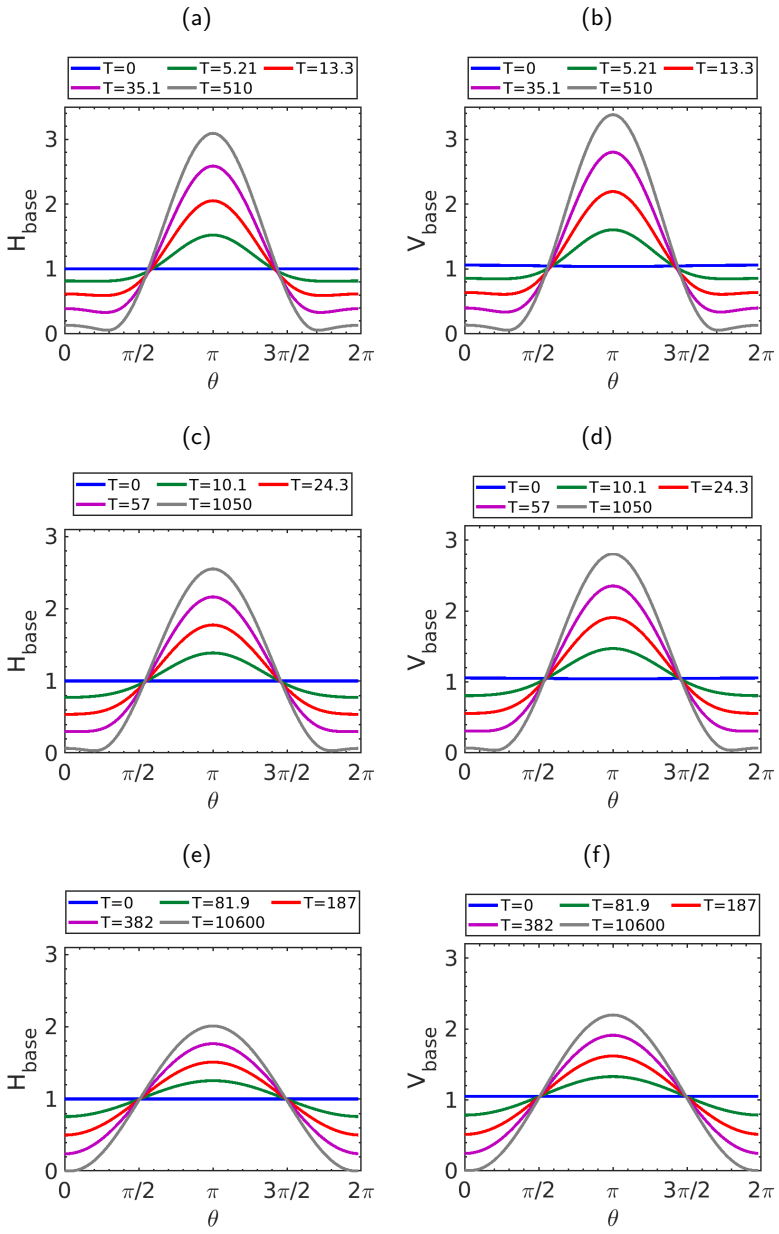

Figure 9.22: Evolution of base state normal film thickness $H_{\text{base}}(\theta, T)$ and volumetric film thickness $V_{\text{base}}(\theta, T) = H_{\text{base}} - \varepsilon K_m H_{\text{base}}^2 + (1/3)\varepsilon^2 K_G H_{\text{base}}^3$, for tori with uniform initial film thickness such that $\varepsilon = 0.1$ and major radius $B \in \{5, 10, 100\}$. Note that because the mean curvature $K_m < 0$ at all points on the torus, $V_{\text{base}} > H_{\text{base}}$. Each plot depicts five time steps, chosen such that the film thickness at $\theta = \pi$ is equispaced between $T = 0$ and the late time, $T = T_{\text{late}}$. The left column depicts $H_{\text{base}}(\theta, T)$ against θ; the right column depicts $V_{\text{base}}(\theta, T)$. Simulations were conducted in V; results in H were computed by the inverse relation $H = V + \varepsilon K_m V^2 + (1/3)\varepsilon^2(6{K_m}^2 - K_G)V^3$.
(a)-(b): Major radius $B = 5$, shown at time steps $T \in \{0, 5.21, 13.3, 35.1, 510\}$.
(c)-(d): Major radius $B = 10$, shown at time steps $T \in \{0, 10.1, 24.3, 57.0, 1050\}$.
(e)-(f): Major radius $B = 15$, shown at time steps $T \in \{0, 81.9, 187, 382, 10600\}$.

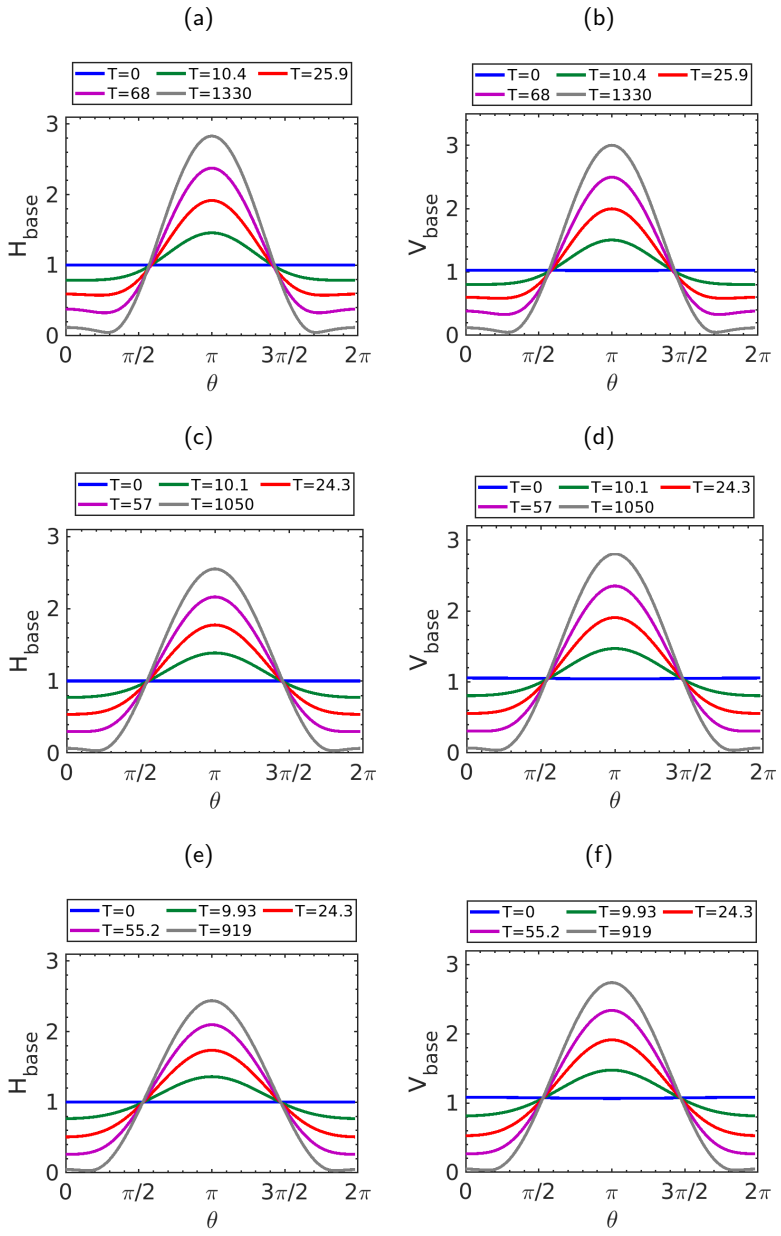

Figure 9.23: Evolution of base state normal film thickness $H_{\text{base}}(\theta, T)$ and volumetric film thickness $V_{\text{base}}(\theta, T) = H_{\text{base}} - \varepsilon K_m H_{\text{base}}^2 + (1/3)\varepsilon^2 K_G H_{\text{base}}^3$, for tori with major radius $B = 10$, and various uniform initial film thicknesses such that $\varepsilon \in \{0.05, 0.1, 0.15\}$. Note that because the mean curvature $K_m < 0$ at all points on the torus, $V_{\text{base}} > H_{\text{base}}$. Each plot depicts five time steps, chosen such that the film thickness at $\theta = \pi$ is equispaced between $T = 0$ and the late time, $T = T_{\text{late}}$. The left column depicts $H_{\text{base}}(\theta, T)$ against θ; the right column depicts $V_{\text{base}}(\theta, T)$. Simulations were conducted in V; results in H were computed by the inverse relation $H = V + \varepsilon K_m V^2 + (1/3)\varepsilon^2(6{K_m}^2 - K_G)V^3$.
(a)-(b): $\varepsilon = 0.05$, shown at time steps $T \in \{0, 10.4, 25.9, 68.0, 1330\}$.
(c)-(d): $\varepsilon = 0.1$, shown at time steps $T \in \{0, 10.1, 24.3, 57.0, 1050\}$.
(e)-(f): $\varepsilon = 0.15$, shown at time steps $T \in \{0, 9.93, 24.3, 55.2, 919\}$.

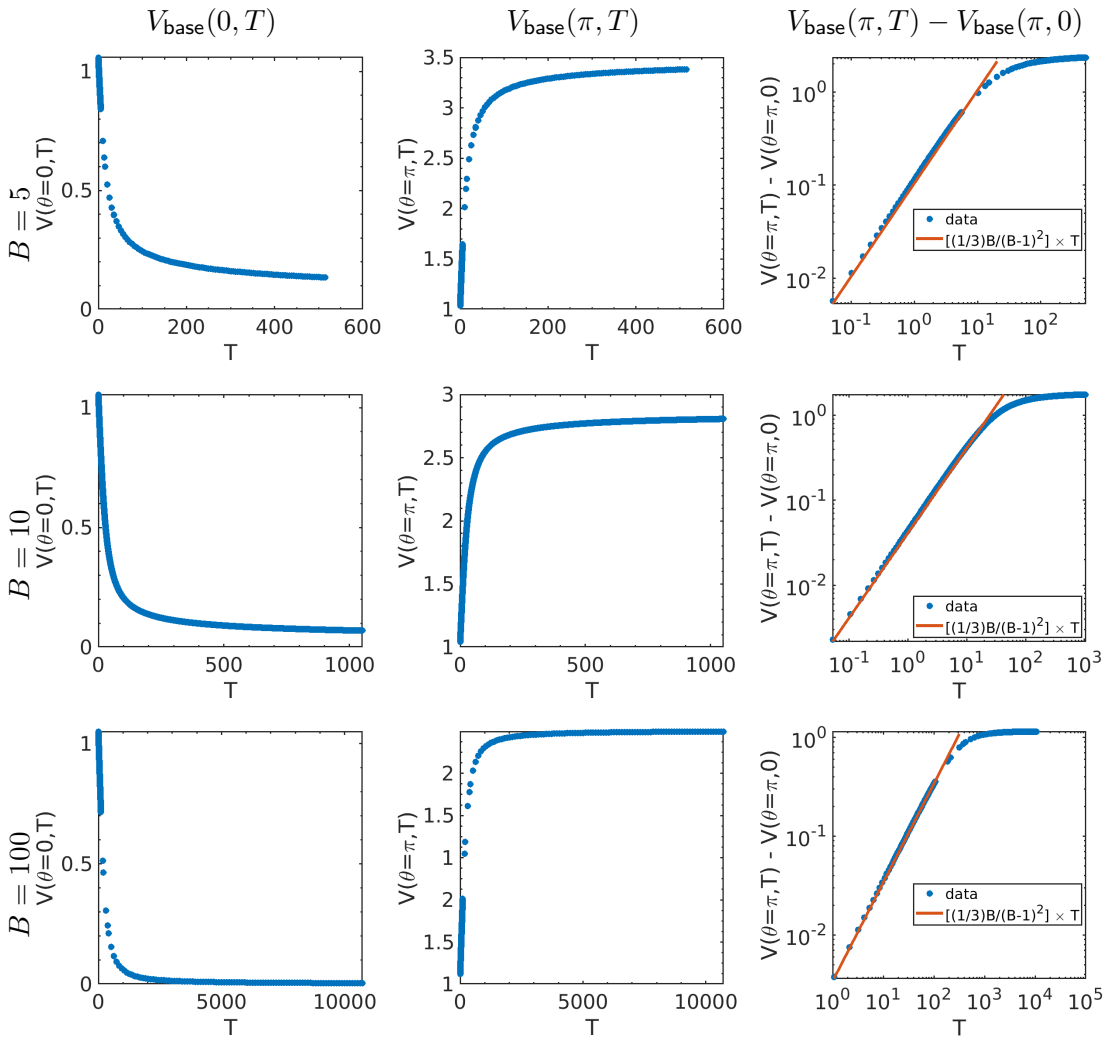

Figure 9.24: Evolution of base state volumetric film thickness $V_{\text{base}}(\theta, T)$ at $\theta = \{0, \pi\}$, for tori with uniform initial film thickness such that $\varepsilon = 0.1$ and major radius $B \in \{5, 10, 100\}$. Result were computed from $T = 0$ to $T = T_{\text{late}} \in \{510, 1050, 10600\}$, respectively. The left column shows $V_{\text{base}}(\theta = 0, T)$, the middle column $V_{\text{base}}(\pi, T)$, and the right column shows $V_{\text{base}}(\pi, T) - V_{\text{base}}(\pi, 0)$ on a log-log plot, along with a linear $[(1/3)B/(B-1)^2] \times T^1$ line for reference, indicating the linear growth of V_{base} at early times.

The constant term $[(1/3)B/(B-1)^2]$ was derived by substituting in $\theta = \pi$ and $V = 1$ to Equations (9.17) and (9.18), and dropping terms of $O(\varepsilon)$. In that case, the Laplacian of the substrate pressure is $\partial_{\theta\theta} P = B/(B-1)^2 + O(\varepsilon)$.

Note that dots represent results at requested output times from the MATLAB solver, not the time steps used for integration.

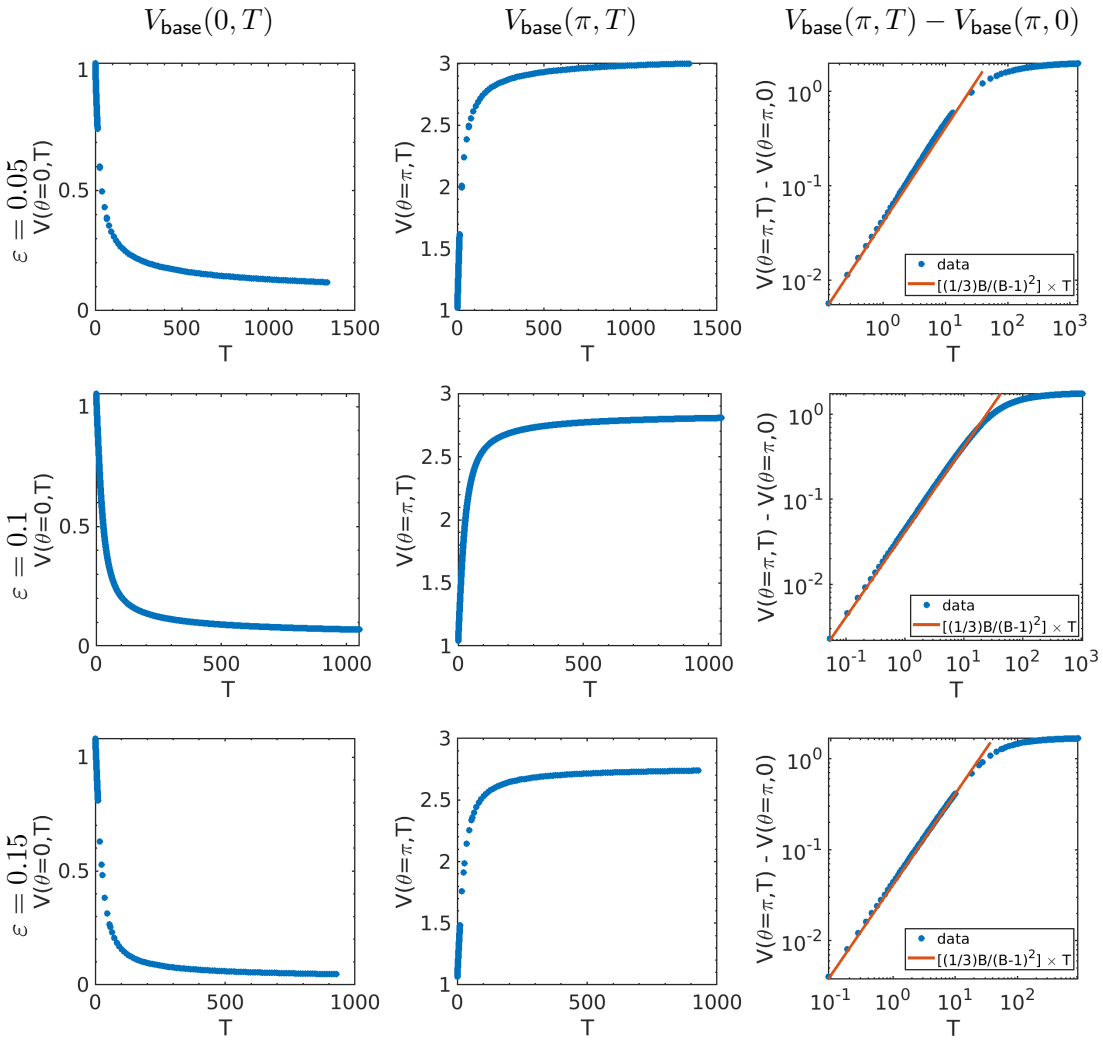

Figure 9.25: Evolution of base state volumetric film thickness $V_{\text{base}}(\theta, T)$ at $\theta = \{0, \pi\}$, for tori with major radius B and varying uniform initial film thickness such that $\varepsilon \in \{0.05, 0.1, 0.15\}$. Result were computed from $T = 0$ to $T = T_{\text{late}} \in \{1330, 1050, 919\}$, respectively. The left column shows $V_{\text{base}}(\theta = 0, T)$, the middle column $V_{\text{base}}(\pi, T)$, and the right column shows $V_{\text{base}}(\pi, T) - V_{\text{base}}(\pi, 0)$ on a log-log plot, along with a linear $[(1/3)B/(B-1)^2] \times T^1$ line for reference, indicating the linear growth of V_{base} at early times.
Note that dots represent results at requested output times from the MATLAB solver, not the time steps used for integration.

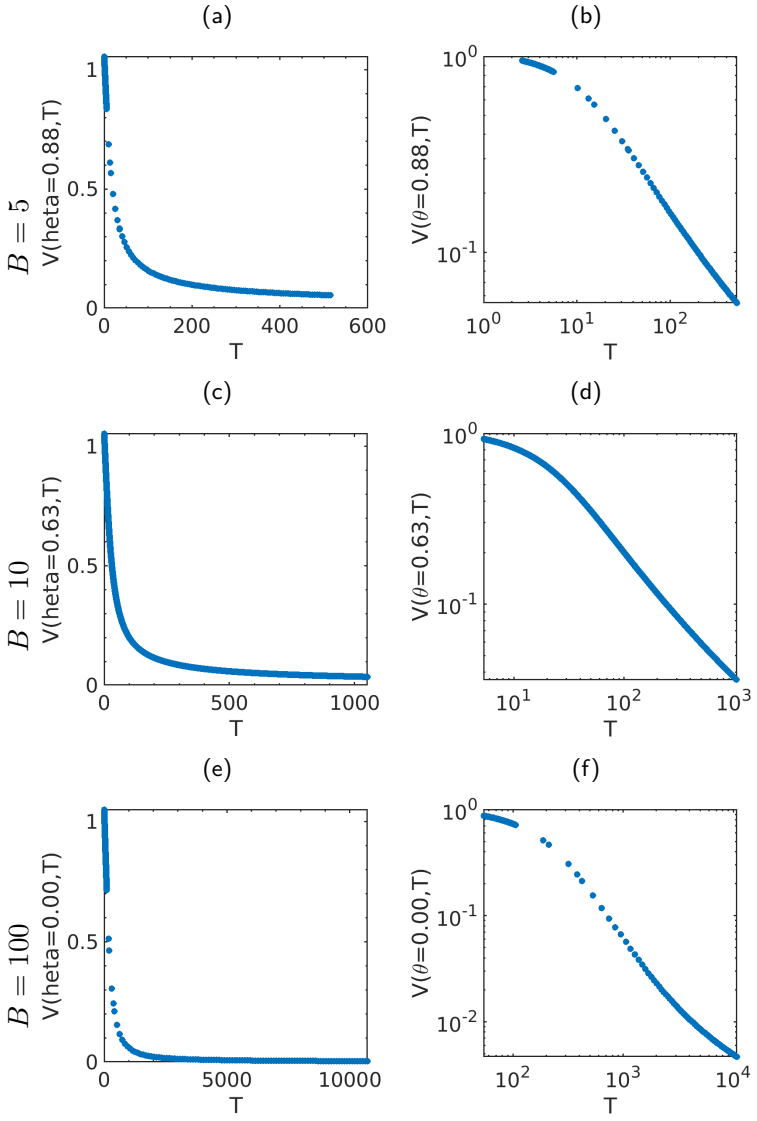

Figure 9.26: Evolution of base state volumetric film thickness $V_{\text{base}}(\theta, T)$ at the thinning point, for tori with uniform initial film thickness such that $\varepsilon = 0.1$ and major radius $B \in \{5, 10, 100\}$. Result were computed from $T = 0$ to $T = T_{\text{late}} \in \{510, 1050, 10600\}$, respectively. Note that dots represent results at requested output times from the MATLAB solver, not the time steps used for integration.
(a) $B = 5$, $\varepsilon = 0.1$, thinning point $\theta = 0.88 = 0.28\pi$. Linear axes. (b) Log axes.
(c) $B = 10$, $\varepsilon = 0.1$, thinning point $\theta = 0.63 = 0.20\pi$. Linear axes. (d) Log axes.
(c) $B = 100$, $\varepsilon = 0.1$, thinning point $\theta = 0$. Linear axes. (d) Log axes.

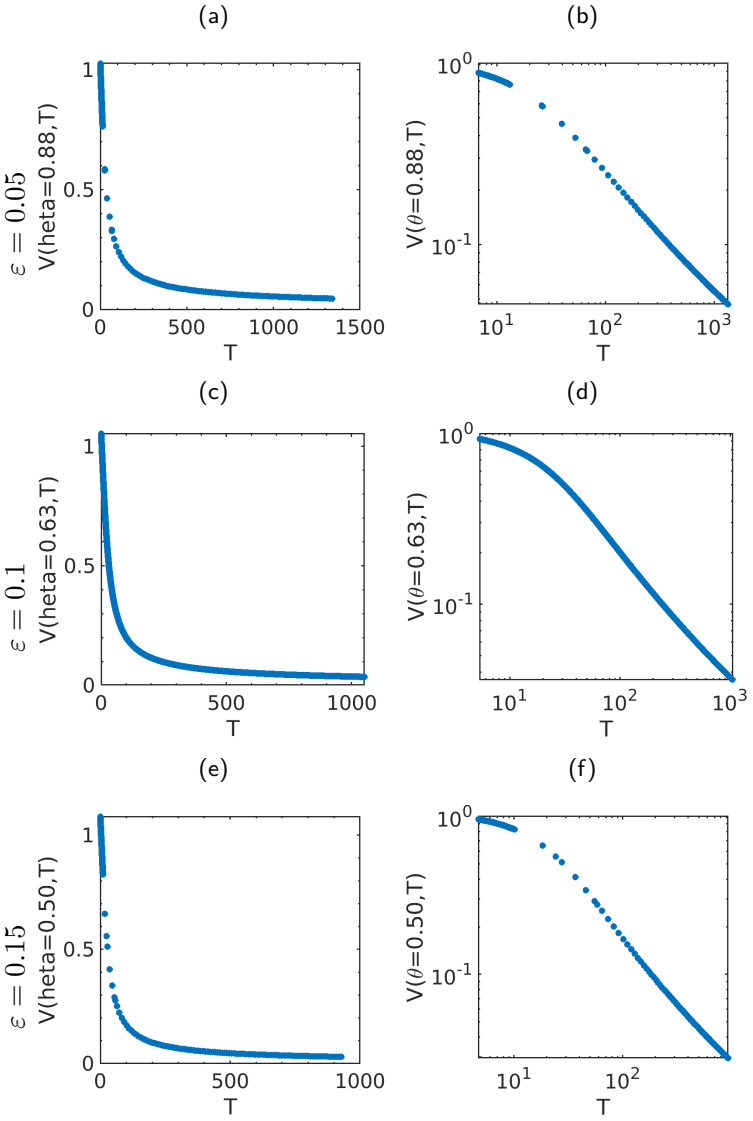

Figure 9.27: Evolution of base state volumetric film thickness $V_{\text{base}}(\theta, T)$ at the thinning point, for tori with major radius $B = 10$ and uniform initial film thickness such that $\varepsilon = \in \{0.05, 0.1, 0.15\}$. Result were computed from $T = 0$ to $T = T_{\text{late}} \in \{1330, 1050, 919\}$, respectively. Note that dots represent results at requested output times from the MATLAB solver, not the time steps used for integration.
(a) $B = 10$, $\varepsilon = 0.05$, thinning point $\theta = 0.88 = 0.28\pi$. Linear axes. (b) Log axes.
(c) $B = 10$, $\varepsilon = 0.1$, thinning point $\theta = 0.63 = 0.20\pi$. Linear axes. (d) Log axes.
(c) $B = 10$, $\varepsilon = 0.15$, thinning point $\theta = 0.50 = 0.16\pi$. Linear axes. (d) Log axes.

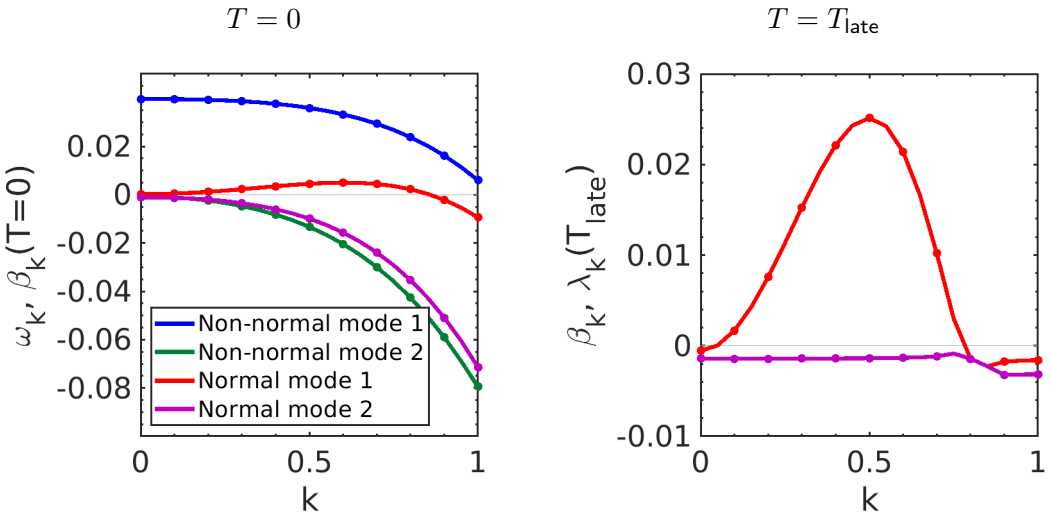

Figure 9.28: Dispersion relation of first and second normal modes (i.e., the two eigenvalues with maximum real part of $\mathcal{L}_k[V_{\text{base}}]$, defined in Equation (9.29)) and first and second transient disturbances (i.e., the two eigenvalues with maximum real part of $(\mathcal{L}_k[V_{\text{base}}] + \mathcal{L}_k^\dagger[V_{\text{base}}])/2$) at $T = 0$, and of the first and second normal modes at $T = T_{\text{late}} = 1050$, for a torus with $B = 10$ and $\varepsilon = 0.1$.

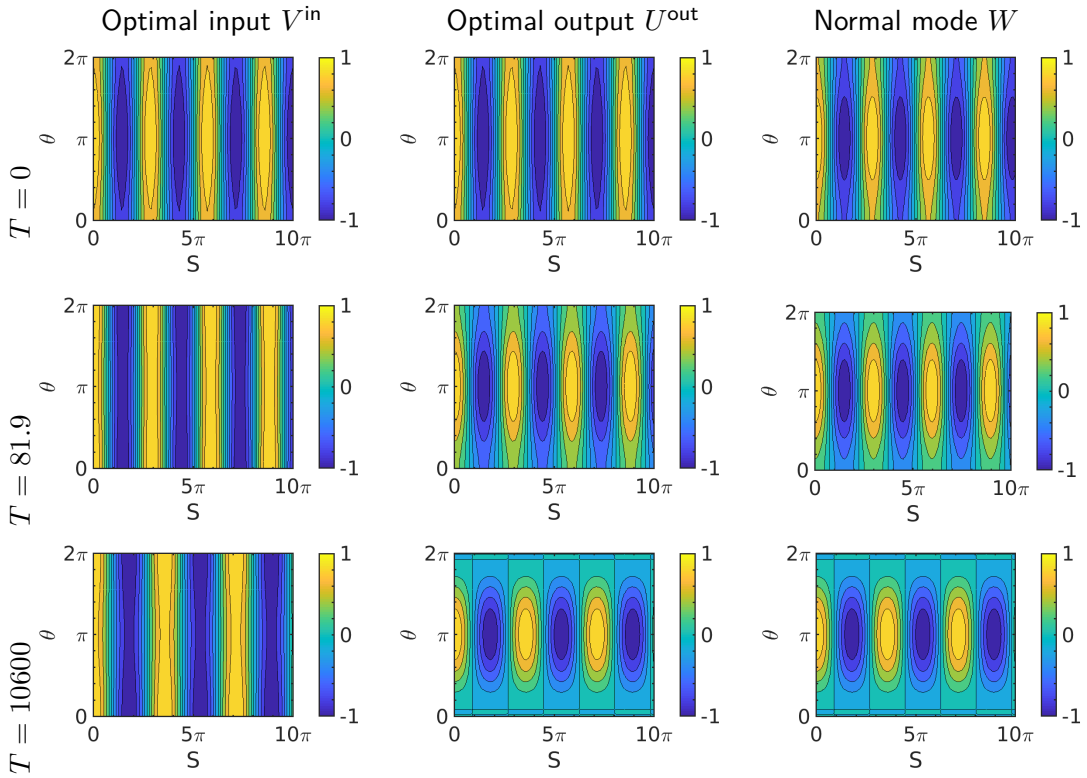

Figure 9.29: Optimal input disturbance of volumetric fluid thickness, $V^{\text{in}}(\theta, S, T)$, optimal output disturbance $U^{\text{out}}(\theta, S, T)$, and fastest growing normal mode $W(\theta, S, T)$, described by Eqn. 9.44, for a thin film initially uniformly coating a torus with $B = 100$ and $\varepsilon = 0.1$. Results are shown at $T = 0$, $T = T_{\text{mid}} = 81.9$ (the time at which the film thickness at $\theta = \pi$ is $1/4$ of the way from its initial thickness to its $T = T_{\text{late}}$ thickness), and $T = T_{\text{late}} = 10600$. Disturbances are normalized to $[-1, 1]$, without loss of generality due to the scaling freedom of linear stability theory. Results were computed numerically using a finite difference method described in Section 9.6.1. Note that at $T = 0$, $V^{\text{in}}(\theta, S, 0) = U^{\text{out}}(\theta, S, 0) = X(\theta, S)$. At $T = T_{\text{late}}$, $U^{\text{out}}(\theta, S, T_{\text{late}})$ has converged to the normal mode $W(\theta, S, T_{\text{late}})$.
Row 1: $T = 0$. $k_{\text{peak}}^{\text{non-normal}}(0) = 0.70$; $k_{\text{peak}}^{\text{normal}}(0) = 0.71$.
Row 2: $T = T_{\text{mid}} = 81.9$. $k_{\text{peak}}^{\text{non-normal}}(T_{\text{mid}}) = 0.68$; $k_{\text{peak}}^{\text{normal}}(T_{\text{mid}}) = 0.67$.
Row 3: $T = T_{\text{late}} = 10600$. $k_{\text{peak}}^{\text{non-normal}}(T_{\text{late}}) = k_{\text{peak}}^{\text{normal}}(T_{\text{late}}) = 0.56$.

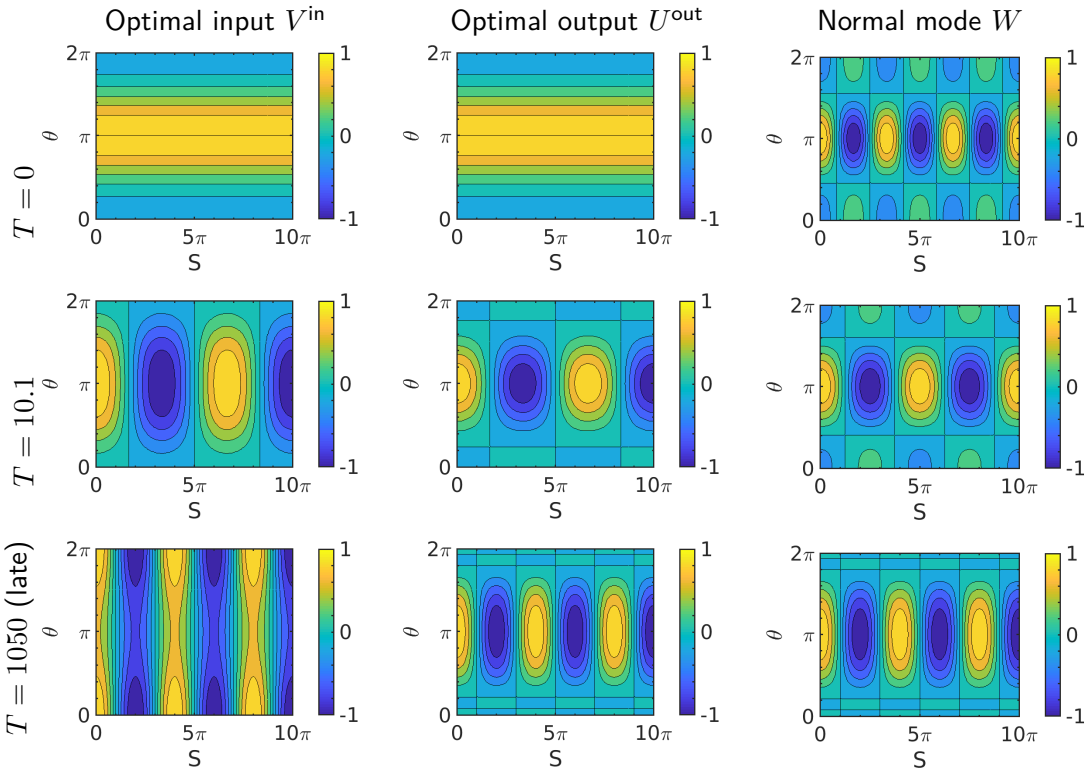

Figure 9.30: Optimal input disturbance of volumetric fluid thickness, $V^{\text{in}}(\theta, S, T)$, optimal output disturbance $U^{\text{out}}(\theta, S, T)$, and fastest growing normal mode $W(\theta, S, T)$, described by Eqn. 9.44, for a thin film initially uniformly coating a torus with $B = 10$ and $\varepsilon = 0.1$. Results are shown at $T = 0$, $T = T_{\text{mid}} = 10.1$ (the time at which the film thickness at $\theta = \pi$ is $1/4$ of the way from its initial thickness to its $T = T_{\text{late}}$ thickness), and $T = T_{\text{late}} = 1050$. Disturbances are normalized to $[-1, 1]$, without loss of generality due to the scaling freedom of linear stability theory. Results were computed numerically using a finite difference method described in Section 9.6.1. Note that at $T = 0$, $V^{\text{in}}(\theta, S, 0) = U^{\text{out}}(\theta, S, 0) = X(\theta, S)$. At $T = T_{\text{late}}$, $U^{\text{out}}(\theta, S, T_{\text{late}})$ has converged to the normal mode $W(\theta, S, T_{\text{late}})$.
Row 1: $T = 0$. $k_{\text{peak}}^{\text{non-normal}}(0) = 0$; $k_{\text{peak}}^{\text{normal}}(0) = 0.6$.
Row 2: $T = T_{\text{mid}} = 10.1$. $k_{\text{peak}}^{\text{non-normal}}(T_{\text{mid}}) = 0.3$; $k_{\text{peak}}^{\text{normal}}(T_{\text{mid}}) = 0.4$.
Row 3: $T = T_{\text{late}} = 1050$. $k_{\text{peak}}^{\text{non-normal}}(T_{\text{late}}) = k_{\text{peak}}^{\text{normal}}(T_{\text{late}}) = 0.5$.

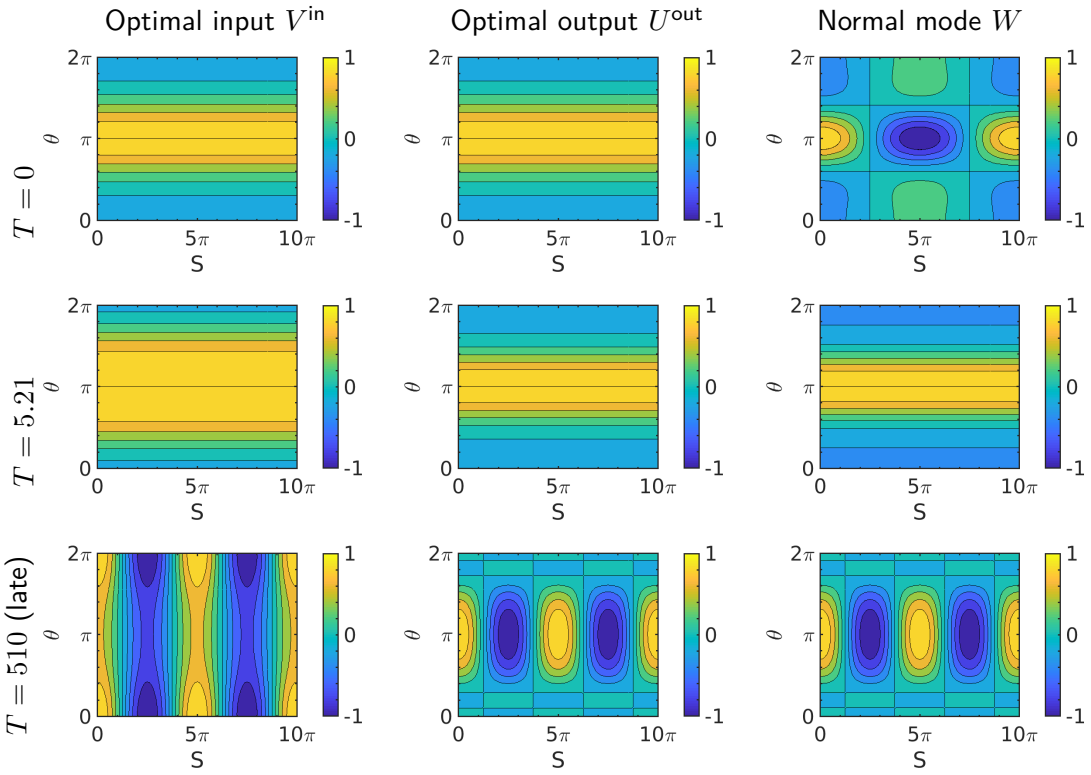

Figure 9.31: Optimal input disturbance of volumetric fluid thickness, $V^{\text{in}}(\theta, S, T)$, optimal output disturbance $U^{\text{out}}(\theta, S, T)$, and fastest growing normal mode $W(\theta, S, T)$, described by Eqn. 9.44, for a thin film initially uniformly coating a torus with $B = 5$ and $\varepsilon = 0.1$. Results are shown at $T = 0$, $T = T_{\text{mid}} = 5.21$ (the time at which the film thickness at $\theta = \pi$ is $1/4$ of the way from its initial thickness to its $T = T_{\text{late}}$ thickness), and $T = T_{\text{late}} = 510$. Disturbances are normalized to $[-1, 1]$, without loss of generality due to the scaling freedom of linear stability theory. Results were computed numerically using a finite difference method described in Section 9.6.1. Note that at $T = 0$, $V^{\text{in}}(\theta, S, 0) = U^{\text{out}}(\theta, S, 0) = X(\theta, S)$. At $T = T_{\text{late}}$, $U^{\text{out}}(\theta, S, T_{\text{late}})$ has converged to the normal mode $W(\theta, S, T_{\text{late}})$.
Row 1: $T = 0$. $k_{\text{peak}}^{\text{non-normal}}(0) = 0$; $k_{\text{peak}}^{\text{normal}}(0) = 0.2$.
Row 2: $T = T_{\text{mid}} = 5.21$. $k_{\text{peak}}^{\text{non-normal}}(T_{\text{mid}}) = 0$; $k_{\text{peak}}^{\text{normal}}(T_{\text{mid}}) = 0$.
Row 3: $T = T_{\text{late}} = 510$. $k_{\text{peak}}^{\text{non-normal}}(T_{\text{late}}) = k_{\text{peak}}^{\text{normal}}(T_{\text{late}}) = 0.4$.

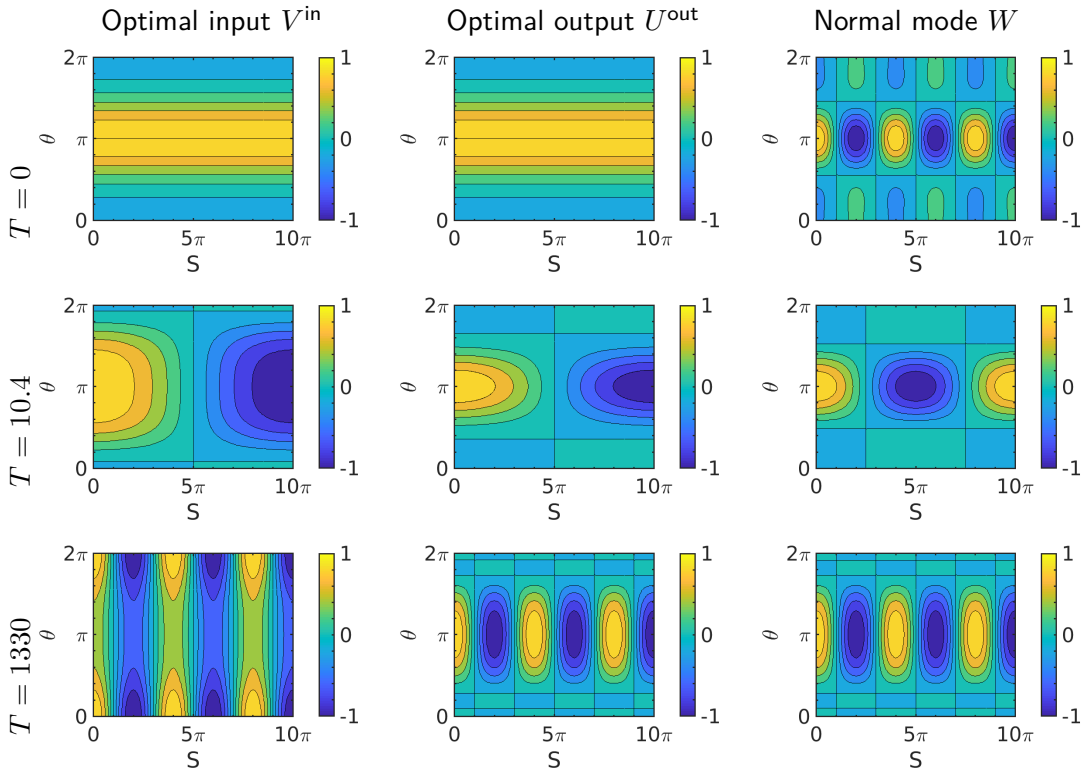

Figure 9.32: Optimal input disturbance of volumetric fluid thickness, $V^{\text{in}}(\theta, S, T)$, optimal output disturbance $U^{\text{out}}(\theta, S, T)$, and fastest growing normal mode $W(\theta, S, T)$, described by Eqn. 9.44, for a thin film initially uniformly coating a torus with $B = 10$ and $\varepsilon = 0.05$. Results are shown at $T = 0$, $T = T_{\text{mid}} = 10.4$ (the time at which the film thickness at $\theta = \pi$ is $1/4$ of the way from its initial thickness to its $T = T_{\text{late}}$ thickness), and $T = T_{\text{late}} = 1330$. Disturbances are normalized to $[-1, 1]$, without loss of generality due to the scaling freedom of linear stability theory. Results were computed numerically using a finite difference method described in Section 9.6.1. Note that at $T = 0$, $V^{\text{in}}(\theta, S, 0) = U^{\text{out}}(\theta, S, 0) = X(\theta, S)$. At $T = T_{\text{late}}$, $U^{\text{out}}(\theta, S, T_{\text{late}})$ has converged to the normal mode $W(\theta, S, T_{\text{late}})$.
Row 1: $T = 0$. $k_{\text{peak}}^{\text{non-normal}}(0) = 0$; $k_{\text{peak}}^{\text{normal}}(0) = 0.5$.
Row 2: $T = T_{\text{mid}} = 10.4$. $k_{\text{peak}}^{\text{non-normal}}(T_{\text{mid}}) = 0.1$; $k_{\text{peak}}^{\text{normal}}(T_{\text{mid}}) = 0.2$.
Row 3: $T = T_{\text{late}} = 1330$. $k_{\text{peak}}^{\text{non-normal}}(T_{\text{late}}) = k_{\text{peak}}^{\text{normal}}(T_{\text{late}}) = 0.5$.

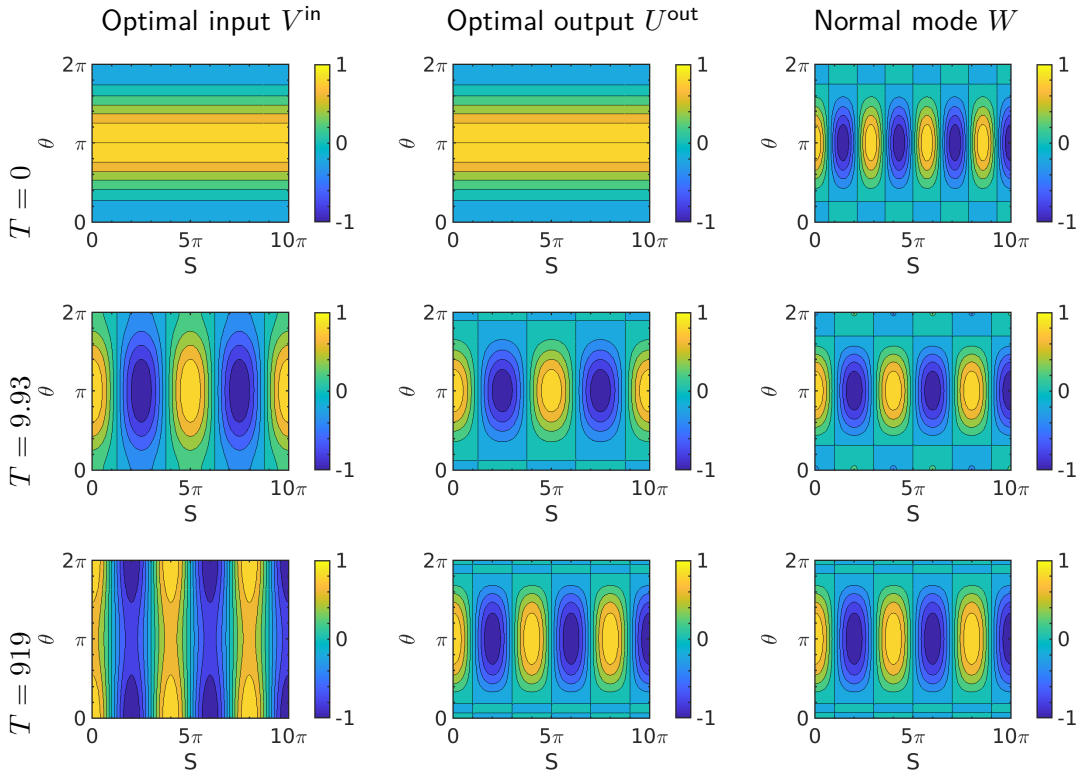

Figure 9.33: Optimal input disturbance of volumetric fluid thickness, $V^{\text{in}}(\theta, S, T)$, optimal output disturbance $U^{\text{out}}(\theta, S, T)$, and fastest growing normal mode $W(\theta, S, T)$, described by Eqn. 9.44, for a thin film initially uniformly coating a torus with $B = 10$ and $\varepsilon = 0.15$. Results are shown at $T = 0$, $T = T_{\text{mid}} = 9.93$ (the time at which the film thickness at $\theta = \pi$ is $1/4$ of the way from its initial thickness to its $T = T_{\text{late}}$ thickness), and $T = T_{\text{late}} = 919$. Disturbances are normalized to $[-1, 1]$, without loss of generality due to the scaling freedom of linear stability theory. Results were computed numerically using a finite difference method described in Section 9.6.1. Note that at $T = 0$, $V^{\text{in}}(\theta, S, 0) = U^{\text{out}}(\theta, S, 0) = X(\theta, S)$. At $T = T_{\text{late}}$, $U^{\text{out}}(\theta, S, T_{\text{late}})$ has converged to the normal mode $W(\theta, S, T_{\text{late}})$.
Row 1: $T = 0$. $k_{\text{peak}}^{\text{non-normal}}(0) = 0$; $k_{\text{peak}}^{\text{normal}}(0) = 0.7$.
Row 2: $T = T_{\text{mid}} = 9.93$. $k_{\text{peak}}^{\text{non-normal}}(T_{\text{mid}}) = 0.4$; $k_{\text{peak}}^{\text{normal}}(T_{\text{mid}}) = 0.5$.
Row 3: $T = T_{\text{late}} = 919$. $k_{\text{peak}}^{\text{non-normal}}(T_{\text{late}}) = k_{\text{peak}}^{\text{normal}}(T_{\text{late}}) = 0.5$.

References

MATLAB and Statistics Toolbox Release 2015a, The MathWorks, Inc., Natick, MA, USA, 2018. URL `https://www.mathworks.com/products/matlab.html`.

G. Balestra, P.-T. Brun, and F. Gallaire. Rayleigh-Taylor instability under curved substrates: An optimal transient growth analysis. Phys. Rev. Fluids, 1(8):083902, 2016. doi:10.1103/PhysRevFluids.1.083902.

G. Balestra, N. Kofman, P.-T. Brun, B. Scheid, and F. Gallaire. Three-dimensional Rayleigh–Taylor instability under a unidirectional curved substrate. J. Fluid Mech., 837: 19–47, 2018a. doi:10.1017/jfm.2017.817.

G. Balestra, D. M.-P. Nguyen, and F. Gallaire. Rayleigh-Taylor instability under a spherical substrate. Phys. Rev. Fluids, 3(8), August 2018b. ISSN 2469-990X. doi:10.1103/PhysRevFluids.3.084005.

C. M. Bender and S. A. Orszag. Advanced Mathematical Methods for Scientists and Engineers I: Asymptotic Methods and Perturbation Theory. Advanced Mathematical Methods for Scientists and Engineers. Springer, 1999. ISBN 9780387989310. doi:10.1007/978-1-4757-3069-2.

C. Delaunay. Sur la surface de révolution dont la courbure moyenne est constante. J. Math. Pure. Appl., 6:309–314, 1841.

B. F. Farrell and P. J. Ioannou. Generalized Stability Theory. Part II: Nonautonomous operators. J. Atmos. Sci., pages 2041–2053, 1996a. doi:10.1175/1520-0469(1996)053<2041:GSTPIN>2.0.CO;2.

B. F. Farrell and P. J. Ioannou. Generalized Stability Theory. Part I: Autonomous operators. J. Atmos. Sci., 53(14):2025–2040, 1996b. doi:10.1175/1520-0469(1996)053<2025:GSTPIA>2.0.CO;2.

A. A. Fragkopoulos, E. Pairam, E. Berger, and A. Fernandez-Nieves. Toroidal droplets: Growth rates, dispersion relations, and behavior in the thick-torus limit. Langmuir, 34(3):1218–1224, January 2018. ISSN 0743-7463, 1520-5827. doi:10.1021/acs.langmuir.7b02280.

I. Goldhirsch, P.-L. Sulem, and S. A. Orszag. Stability and Lyapunov stability of dynamical systems: A differential approach and a numerical method. Physica D: Nonlin. Phen., 27(3): 311–337, August 1987. ISSN 01672789. doi:10.1016/0167-2789(87)90034-0.

S. L. Goren. The instability of an annular thread of fluid. J. Fluid Mech., 12(02):309, February 1962. ISSN 0022-1120, 1469-7645. doi:10.1017/S002211206200021X.

P. S. Hammond. Nonlinear adjustment of a thin annular film of viscous fluid surrounding a thread of another within a circular cylindrical pipe. J. Fluid Mech., 137:363–384, December 1983. ISSN 0022-1120, 1469-7645. doi:10.1017/S0022112083002451.

P. D. Howell. Surface-tension-driven flow on a moving curved surface. J. Eng. Math., 45(3-4): 283–308, 2003. doi:10.1023/A:1022685018867.

M. Johnson, R. D. Kamm, L. W. Ho, A. Shapiro, and T. J. Pedley. The nonlinear growth of surface-tension-driven instabilities of a thin annular film. J. Fluid Mech., 233:141–156, December 1991. ISSN 0022-1120, 1469-7645. doi:10.1017/S0022112091000423.

T. S. Lundgren and N. N. Mansour. Vortex ring bubbles. J. Fluid Mech., 224:177–196, March 1991. ISSN 0022-1120, 1469-7645. doi:10.1017/S0022112091001702.

K. Marten, K. Shariff, S. Psarakos, and D. J. White. Ring Bubbles of Dolphins. Sci. Am., 275 (2):82–87, August 1996. ISSN 0036-8733. doi:10.1038/scientificamerican0896-82.

J. D. McGraw, J. Li, D. L. Tran, A.-C. Shi, and K. Dalnoki-Veress. Plateau-Rayleigh instability in a torus: Formation and breakup of a polymer ring. Soft Matter, 6(6):1258, 2010. ISSN 1744-683X, 1744-6848. doi:10.1039/b919630g.

H. Mehrabian and J. J. Feng. Capillary breakup of a liquid torus. J. Fluid Mech., 717:281–292, February 2013. ISSN 0022-1120, 1469-7645. doi:10.1017/jfm.2012.572.

E. Pairam and A. Fernández-Nieves. Generation and Stability of Toroidal Droplets in a Viscous Liquid. Phys. Rev. Lett., 102(23), June 2009. ISSN 0031-9007, 1079-7114. doi:10.1103/PhysRevLett.102.234501.

J. A. F. Plateau. Statique expérimentale et théorique des liquides soumis aux seules forces moléculaires, volume 2. Gauthier-Villars, Paris, 1873.

L. Rayleigh. On the instability of jets. Proc. Lond. Math. Soc., s1-10(1):4–13, November 1878. ISSN 00246115. doi:10.1112/plms/s1-10.1.4.

L. Rayleigh. XVI. On the instability of a cylinder of viscous liquid under capillary force. London Edinburgh Dublin Philos. Mag. J. Sci., 34(207):145–154, August 1892. ISSN 1941-5982, 1941-5990. doi:10.1080/14786449208620301.

R. V. Roy and L. W. Schwartz. Coating flow over a curved substrate. In Proc. 2nd European Coating Symposium, pages 18–27, Université Louis Pasteur, Strasbourg, 1997. P. G. Bourgin.

R. V. Roy, A. J. Roberts, and M. E. Simpson. A lubrication model of coating flows over a curved substrate in space. J. Fluid Mech., 454:235–261, 2002. ISSN 0022-1120. doi:10.1017/S0022112001007133.

M. Rumpf and O. Vantzos. Numerical gradient flow discretization of viscous thin films on curved geometries. Math. Models Methods Appl. Sci., 23(05):917–947, 2013. doi:10.1142/S0218202512500649.

P. J. Schmid. Nonmodal stability theory. Annu. Rev. Fluid Mech., 39:129–62, 2007. ISSN 0824307399. doi:10.1146/annurev.fluid.38.050304.092139.

L. W. Schwartz and D. E. Weidner. Modeling of coating flows on curved surfaces. J. Eng. Math., 29(1):91–103, 1995. doi:10.1007/BF00046385.

S. Tomotika. On the instability of a cylindrical thread of a viscous liquid surrounded by another viscous fluid. Proc. R. Soc. Lond. A, 150(870):322–337, June 1935. ISSN 0080-4630, 2053-9169. doi:10.1098/rspa.1935.0104.

L. N. Trefethen. Finite Difference and Spectral Methods for Ordinary and Partial Differential Equations. Lloyd N. Trefethen, 1996.

O. Vantzos, O. Azencot, M. Wardeztky, M. Rumpf, and M. Ben-Chen. Functional thin films on surfaces. IEEE Trans. Visual Comput. Graphics, 23(3):1179–1192, March 2017. ISSN 1077-2626. doi:10.1109/TVCG.2016.2605083.

J. K. Walters and J. F. Davidson. The initial motion of a gas bubble formed in an inviscid liquid. J. Fluid Mech., 17(03):321, November 1963. ISSN 0022-1120, 1469-7645. doi:10.1017/S0022112063001373.

A. W. Wray, D. T. Papageorgiou, and O. K. Matar. Reduced models for thick liquid layers with inertia on highly curved substrates. SIAM J. Appl. Math., 77(3):881–904, January 2017. ISSN 0036-1399, 1095-712X. doi:10.1137/16M1060686.

Part IV

Additional results in mathematical physics and cosmology

Chapter 10

THE ROLE OF VARIATIONAL SYMMETRIES IN GRADIENT FLOW PDES

10.1 Introduction

It is a well-known result of multivariable calculus that a scalar quantity's gradient vector is orthogonal to its level sets (see, e.g., Marsden and Tromba, 2003). This fact is the basis for discrete gradient descent techniques such as the Newton-Raphson method, which sequentially take steps in the direction of the gradient to seek local minima. In the limit of infinitesimally short steps, Newton-Raphson descent can be described as an ordinary differential equation (ODE) in gradient flow form (Jordan, 2017), in which case the evolution progresses in a direction orthogonal to the level sets. An example of finite-dimensional gradient flow is shown in Figure 10.1; red arrows depict the evolution vectors, which are orthogonal to the blue level set tangent vectors.

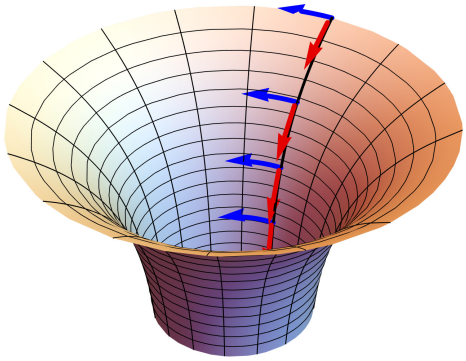

Figure 10.1: Depiction of gradient flow in a finite-dimensional functional landscape. Red arrows depict evolution vectors, and point in the direction of the gradient of the functional. Blue arrows depict the tangent vectors of level sets (sets of constant value), and are orthogonal to the evolution.

Generalizing such gradient flow ODEs from finite dimensions to infinite-dimensional functional spaces allows definition of gradient flow partial differential equations (PDEs), which evolve by following gradients of a governing functional (Naito, 1988). It is natural, then, to ask whether the intuition of evolution orthogonal to level sets can be extended to the case of PDE gradient flow and, if so, under what conditions and what definition of orthogonality. In this paper, we demonstrate how such intuition indeed holds: in particular, generalized symmetries of the governing functional describe vectors tangent to level sets, and we apply Noether's Theorem to show that the gradient flow is orthogonal to those symmetries under an inner product which depends on the form of the gradient flow equation.

The one-to-one correspondence between the generalized symmetries of Lagrangian systems and

conservation laws was first discovered by Noether (1918), in a foundational result of modern mathematical physics. Since that time, analogous results have been produced by studying the role played in other partial differential equations by Noether's generalized symmetries (which are sometimes referred to as Lie-Bäcklund symmetries, although Olver [1986] points out that credit is due to Noether). Olver (1980) found the relationship between generalized symmetries and conserved quantities of Hamiltonian systems, a result which was subsequently extended to a larger class of skew-symmetric evolution equations by Strampp (1982). Fokas (1979) demonstrated that single-variable evolution equations of the form $du(x,t)/dt = K[u(x,t)]$, where $dK[u]/dx$ is the Euler-Lagrange equation for some Lagrangian, also have an exact correspondence between their generalized symmetries and conserved quantities.

It is the goal of this paper to instead consider the role of generalized symmetries in gradient flow PDEs, of the type described by Otto (2001). In contrast to prior work on evolution equations, we will consider symmetries not of the full PDE, but only of the functional driving the gradient flow. Furthermore, the main result will be a correspondence not between symmetries and conservation laws, but between symmetries and functions orthogonal to the evolution of the system. The result can be understood as a generalization of the finite-dimensional result that, for a finite-dimensional gradient flow $d\vec{x}/dt = \nabla F$, the variable $\vec{x}$ evolves in a direction orthogonal to the level sets of F. Special cases leading to conservation laws will also be discussed.

One practical application of Noether's Theorem in Lagrangian systems is to verify numerical simulations. After performing a simulation, one can confirm that it satisfies conservation of, e.g., energy or angular momentum. Similarly, the evolution of gradient flows orthogonal to their functionals' symmetries may be used to measure the accuracy of different numerical schemes. For example, suppose one is computing the evolution of a gradient flow equation whose governing functional satisfies rotational symmetry on a circular domain. If the meshing or discretization of the domain is too coarse, then one may be concerned about the numerical error due to the discretization asymmetry. Computing the numerical solution's orthogonality to the relevant rotational symmetry characteristic provides one metric for that error.

In Section 10.2, we will review definitions of continuous symmetries and Noether's Theorem. Section 10.3 will relate the main theorem regarding evolutionary constraints, as well as a corollary describing the special conditions for a conserved quantity to arise. Section 10.4 demonstrates the results by computing the evolutionary constraints of a thermocapillary thin film flow. An example of a gradient flow whose symmetry leads to a conserved quantity is also related.

10.2 Background

We begin by reviewing some definitions, and the statement of Noether's Theorem. For brevity, details such as smoothness requirements will be omitted. All functions will be assumed to be sufficiently smooth, and the interested reader is referred to Olver (1986) for a more rigorous approach. For the duration of this work, we will consider functionals of scalar functions

$u(x_1, \cdots, x_k)$, the with u defined on a k-dimensional space Ω. Furthermore, we will ignore boundary terms, assuming that all relevant terms vanish on $\partial\Omega$. The requirements for boundary terms to vanish will be shown for specific examples in Section 10.4.

10.2.1 Variational derivatives and the Euler operator

The *Fréchet derivative* of a function or functional $\mathscr{F}$ is the differential operator defined such that its action on a function m is given by

$$\mathsf{D}_{\mathscr{F}}(m) = \left(\frac{d}{d\varepsilon}\mathscr{F}[u + \varepsilon m]\right)_{\varepsilon=0} \tag{10.1}$$

(Olver, 1986).

The *variational derivative* of a functional $\mathscr{F}[u] = \int_\Omega \mathcal{F}[u]d^k x$ with respect to a function u will be denoted $\delta_u\mathscr{F}$, defined by satisfying

$$\int_\Omega \delta_u\mathscr{F}[u] \cdot m d^k x = \mathsf{D}_{\mathscr{F}}(m) = \left(\frac{d}{d\varepsilon}\mathscr{F}[u + \varepsilon m]\right)_{\varepsilon=0} \tag{10.2}$$

for all sufficiently smooth functions m (Olver, 1986). Note that $\delta_u\mathscr{F}$ is a vector with the same dimension as u; this work will assume u is a scalar, so $\delta_u\mathscr{F}$ will also be a scalar.

Let J denote the multi-index $J = \{j_1, j_2, \cdots, j_k\}$, each j_i being a nonnegative integer, and let $|J| = \sum_i j_i$ be the size of J. Let d_J denote the differential operator $d_J = d^{j_1+j_2+\ldots+j_k}/dx_1^{j_1}dx_2^{j_2}\cdots dx_k^{j_k}$. Then the *Euler operator* is defined as

$$\begin{aligned} E_u &= \sum_J (-1)^{|J|} d_J \frac{\partial}{\partial(d_J u)} \\ &= \frac{\partial}{\partial u} - \sum_{i=1}^{k} \frac{d}{dx_i}\frac{\partial}{\partial(du/dx_i)} + \sum_{i=1}^{k}\sum_{\ell=i}^{k} \frac{d^2}{dx_i dx_\ell}\frac{\partial}{\partial(d^2u/dx_i dx_\ell)} - \cdots, \end{aligned} \tag{10.3}$$

where the sum in the first expression extends over all sets of multi-indices J (Olver, 1986). Note in particular that

$$\delta_u\mathscr{F} = E_u[\mathcal{F}]; \tag{10.4}$$

that is, the variational derivative of a functional is equal to the Euler operator applied to the functional density (Olver, 1986). Furthermore, if $\mathscr{F}$ is a Lagrangian (and hence $\mathcal{F}$ is a Lagrangian density), then $E_u[\mathcal{F}]$ is the corresponding Euler-Lagrange equation.

10.2.2 Symmetries and characteristics

A *classical variational symmetry group* of a functional $\mathscr{F} = \int_\Omega \mathcal{F}[u]d^k x$ with $\vec{x} \in \omega$ and $u \in U$ is a group G of local transformations $g : \Omega \times U \to \Omega \times U$

$$\int_{\Omega_1} \mathcal{F}[g \cdot u]d^k g \cdot x = \int_{\Omega_1} \mathcal{F}[u]d^k x \tag{10.5}$$

for all $\Omega_1 \subset \Omega$ (Olver, 1986). Note that defining the action of g on u and x is sufficient to determine its action on derivatives of u, via the prolongation equation.

A continuous symmetry group is a Lie group and hence may be described in terms of a set of *infinitesimal generators*

$$\vec{v} = \sum_{i=1}^{k} \xi^i[x,u]\frac{\partial}{\partial x_i} + \phi[x,u]\frac{\partial}{\partial u}. \tag{10.6}$$

The action of $\vec{v}$ on derivatives of u is determined self-consistently by the vector prolongation formula (Olver, 1986). Note that the factors of ξ^i and ϕ may depend both on u and on derivatives of u. For brevity, we will occasionally refer to $\vec{v}$ as a "symmetry," although, being precise, it is the generator of a symmetry group.

An infinitesimal generator $\vec{v}$ as in Equation (10.6) generates a classical variational symmetry group of $\mathscr{F}$ if and only if

$$\vec{v}(\mathcal{F}) + \mathcal{F}\nabla \cdot \xi = 0 \tag{10.7}$$

(Olver, 1986). Note that while the infinitesimal generator of a symmetry group of a differential equation $\mathcal{A}$ satisfies simply $\vec{v}(\mathcal{A}) = 0$, a functional $\mathscr{F} = \int_\Omega \mathcal{F} d^k x$ has a total of k extra multiplicative factors of x due to the integral, and hence requires the factor of $\mathcal{F}\nabla \cdot \xi$ in the infinitesimal generator equation.

An infinitesimal generator $\vec{v}$ as in Equation (10.6) generates a *generalized variational symmetry* group of $\mathscr{F}$ if and only if

$$\vec{v}(\mathcal{F}) + \mathcal{F}\nabla \cdot \xi = \nabla \cdot \vec{A} \tag{10.8}$$

for some $\vec{A}$ (Olver, 1986). While a generalized variational symmetry does not necessarily leave a functional $\mathscr{F}$ invariant, it does leave the Euler-Lagrange equation of that functional invariant. That is, it adds a term to $\mathcal{F}$ which is in the kernel of E_u. For the remainder of this work, the term *variational symmetry* will be used to refer to generalized variational symmetries.

The *characteristic* of a symmetry generated by $\vec{v}$ as in Equation (10.6) is given by

$$Q = \phi[x,u] - \sum_{i=1}^{k} \xi^i[x,u]\frac{\partial u}{\partial x_i} \tag{10.9}$$

(Olver, 1986). Note that a specific solution $u_{\text{spec.}}$ is invariant under the group generated by $\vec{v}$ iff $Q[u_{\text{spec.}}] = 0$ (Hydon, 2000).

The *evolutionary representative* of a generator $\vec{v}$ with characteristic Q is the generator $\vec{v}_Q = Q\partial_u$. $\vec{v}$ is a variational symmetry of a functional $\mathscr{F}$ if and only if $\vec{v}_Q$ is a variational symmetry of said functional. In this sense, $\vec{v}$ and $\vec{v}_Q$ are equivalent (Olver, 1986). Note that this equivalence holds only for generalized variational symmetries, and not for classical variational symmetries,

due to the fact that $\vec{v}(\mathcal{F}) + \mathcal{F}\nabla \cdot \xi - \vec{v}_Q(\mathcal{F}) = \nabla \cdot (\xi\mathcal{F})$ which does not in general vanish. Furthermore, regardless of whether or not $\vec{v}$ is a symmetry of $\mathcal{F}$,

$$\vec{v}_Q(\mathcal{F}) = E_u[\mathcal{F}]Q + \nabla \cdot \vec{A} \tag{10.10}$$

for some $\vec{A}$ (Olver, 1986).

10.2.3 Noether's Theorem

Theorem 1 (Noether's Theorem)**.** *A functional $\mathscr{L}[u]$ has a variational symmetry with characteristic Q if and only if $\exists \vec{B}$ such that $E_u[\mathscr{L}]Q = \nabla \cdot \vec{B}$. In particular, when $E_u[\mathscr{L}]$ vanishes, then $\nabla \cdot \vec{B} = 0$, i.e., $\vec{B}$ is a conserved flux (Olver, 1986).*

The typical application of Noether's Theorem in physics is to Lagrangian problems, in which $\mathscr{L} = \int \mathcal{L} d^n x dt$ is a Lagrangian integrated over both space and time. On shell, $E_u[\mathscr{L}] = 0$, so that $0 = \nabla \cdot \vec{B} = \partial_t B^{(t)} + \nabla_i B^{(i)}$, where we have separated the time and space components of $\vec{B}$. Integrating the result over a time-independent spatial domain yields $\partial_t \int B^{(t)} d^n x = 0$, the classic conservation law. This last result holds only if the boundary conditions are such that the boundary terms vanish. In the derivation below, we will similarly ignore boundary conditions, assuming they are vanishing; boundary conditions will be discussed in the specific examples in Section 10.4.

10.3 Noether's theorem applied to gradient flow

In the following results, $\langle \cdot, \cdot \rangle_{L^2}$ will denote the L^2 inner product, while $\langle \cdot, \cdot \rangle_{\mathcal{G}}$ will denote the inner product $\langle w, y \rangle_{\mathcal{G}} \equiv \langle w, \mathcal{G}y \rangle_{L^2} = \langle \mathcal{G}w, y \rangle_{L^2}$, where $\mathcal{G} : V \to L^2$ is a self-adjoint linear operator which is assumed to be surjective. Often, $\mathcal{G}$ will be the identity, in which case $V = L^2$, or else an elliptic operator such as a modified Laplacian, in which case V will be a subset of L^2 subject to appropriate smoothness constraints. Other choices of $\mathcal{G}$ are also possible.

A pseudoinverse $\mathcal{G}^{-1} : L^2 \to V$ is defined by choosing a representative element of V for every element of L^2 (more precisely, $\mathcal{G}^{-1} = \mathcal{P}[\mathcal{G}/\ker(\mathcal{G})]^{-1}$, where $\mathcal{P}$ takes elements from the equivalence class produced by quotienting $\mathcal{G}$ by its kernel and projects them onto V). When $\mathcal{G}$ is a differential operator, the imposition of vanishing boundary conditions may be enough to uniquely select representative elements. Otherwise, another rule may be defined. The uniqueness of $\mathcal{G}^{-1}$'s definition is not important to the results which follow. Because $\mathcal{G}$ is surjective, a pseudoinverse may be defined; that is all that is needed. The $\mathcal{G}^{-1}$ inner product will be defined by $\langle w, y \rangle_{\mathcal{G}^{-1}} \equiv \langle w, \mathcal{G}^{-1} y \rangle = \langle \mathcal{G}^{-1} w, y \rangle$.

A gradient flow PDE will be defined following Otto (2001), as an equation of the form

$$\langle \partial_t u, w \rangle_{L^2} = \langle \delta_u \mathscr{F}, w \rangle_{\mathcal{G}} \,. \tag{10.11}$$

10.3.1 Main result: Evolutionary constraints of gradient flow PDEs

Proposition 1. *Let $\vec{v}$ be a variational symmetry of the functional $\mathscr{F}$, with characteristic Q. If u is governed by a gradient flow equation $\langle \partial_t u, w\rangle_{L^2} = \langle \delta_u \mathscr{F}, w\rangle_{\mathcal{G}}$, then $\partial_t u$ is orthogonal to Q under the $\mathcal{G}^{-1}$ inner product, $\langle \partial_t u, Q\rangle_{\mathcal{G}^{-1}} = 0$, given appropriate boundary conditions.*

Proof. By Noether's Theorem, $\langle \delta_u \mathscr{F}, Q\rangle_{L^2} = \int_\Omega E_u[\mathcal{F}]Q d^k x = \int_\Omega \nabla \cdot \vec{B} d^k x = \oint_{\partial\Omega} \vec{B} \cdot d\hat{n}$, where $\hat{n}$ is the normal vector. If the boundary conditions are such that $\oint \vec{B} \cdot d\hat{n}$ vanishes, then $\langle \delta_u \mathscr{F}, Q\rangle_{L^2} = 0$. Given such boundary conditions, $0 = \langle \delta_u \mathscr{F}, \mathcal{G}^{-1}Q\rangle_{\mathcal{G}} = \langle \partial_t u, \mathcal{G}^{-1}Q\rangle_{L^2} = \langle \partial_t u, Q\rangle_{\mathcal{G}^{-1}}$. □

One interesting aspect of this result is that it reverses the usual importance of the terms in Noether's Theorem. In Lagrangian systems, where $E_u[\mathscr{L}]Q = \nabla \cdot \vec{B}$, the $E_u[\mathscr{L}]Q$ term vanishes on-shell and it is the $\vec{B}$ term which is nontrivial and describes the conserved quantity. But for gradient flow, it is the $\vec{B}$ term which vanishes and the $E_u[\mathscr{F}]Q$ term which is relevant to the final result.

In the finite dimensional case, we know that the gradient of a scalar function f is orthogonal to contours of constant f. In particular, a symmetry of f defines contours of constant f, and so the gradient must be orthogonal to the symmetry. In the infinite dimensional gradient flow, Proposition 1 defines the sense in which the evolution is orthogonal to any variational symmetry.

10.3.2 Conserved quantities

The evolutionary constraints do not lead to conserved quantities except under certain circumstances, which should not be expected to arise frequently. We show here the conditions under which conserved quantities do arise.

Corollary 1. *Let $\vec{v}$ be a variational symmetry of the functional $\mathscr{F}$, with characteristic Q. Let u be governed by a gradient flow equation $\langle \partial_t u, w\rangle_{L^2} = \langle \delta_u \mathscr{F}, w\rangle_{\mathcal{G}}$. If $Q = \mathcal{G}\delta_u \mathscr{R}$ for some $\mathscr{R} = \int \mathcal{R} d^k x$, then $\mathscr{R}$ is a conserved quantity under the gradient flow, i.e., $\partial_t \mathscr{R} = \partial_t \int \mathcal{R} d^k x = 0$, given appropriate boundary conditions.*

Proof. It was established in Proposition 1 that $\langle \partial_t u, Q[u]\rangle_{\mathcal{G}^{-1}} = 0$. Hence, $0 = \langle \partial_t u, Q[u]\rangle_{\mathcal{G}^{-1}}$ $= \langle \partial_t u, \mathcal{G}\delta_u \mathscr{R}\rangle_{\mathcal{G}^{-1}} = \langle \partial_t u, \delta_u \mathscr{R}\rangle_{L^2} = \partial_t \int \mathcal{R} d^k x$. □

The question of when $Q = \mathcal{G}\delta_u \mathscr{R}$ then arises. Although it is difficult to determine in general, an easily-checked condition exists for the special case where $\mathcal{G}$ has no u dependence and $\mathcal{G}^{-1}Q$ has no integral operators.

Corollary 2. *Let $\vec{v}$ be a variational symmetry of the functional $\mathscr{F}$, with characteristic Q. Let u be governed by a gradient flow equation $\langle \partial_t u, w\rangle_{L^2} = \langle \delta_u \mathscr{F}, w\rangle_{\mathcal{G}}$. Further assume that $\mathcal{G}$ is independent of u, and that $\mathcal{G}^{-1}Q$ is expressible without integral operators. If D_Q is self-adjoint*

under the $\mathcal{G}^{-1}$ inner product (i.e., $\mathsf{D}_Q\mathcal{G} = \mathcal{G}\mathsf{D}_Q^*$, where D_Q is the Fréchet derivative of Q and D_Q^* is its adjoint), then $Q = \mathcal{G}\delta_u\mathscr{R}$ for some $\mathscr{R} = \int \mathcal{R} d^k x$, and $\mathscr{R}$ is a conserved quantity under the gradient flow, given appropriate boundary conditions.

Proof. It can be shown that an expression M is the variational derivative of some quantity N (i.e., $M = \delta_u N$ for some N) if and only if $\mathsf{D}_M = \mathsf{D}_M^*$, where D_M is the Fréchet derivative of M and D_M^* its adjoint under the L^2 inner product (Olver, 1986). Therefore, $Q = \mathcal{G}\delta_u\mathcal{R}$ for some $\mathscr{R}$ if and only if $\mathsf{D}_{\mathcal{G}^{-1}Q} = [\mathsf{D}_{\mathcal{G}^{-1}Q}]^*$. If $\mathcal{G}$ is independent of u, then it commutes with the Fréchet derivative, and hence the condition becomes $\mathsf{D}_Q\mathcal{G} = \mathcal{G}\mathsf{D}_Q^*$, where we used the fact that $\mathcal{G}$ is self-adjoint. Equivalently, $Q = \mathcal{G}\delta_u\mathscr{R}$ if and only if D_Q is self-adjoint under the $\mathcal{G}^{-1}$ inner product, because $\langle u, \mathsf{D}_Q v\rangle_{\mathcal{G}^{-1}} = \langle \mathcal{G}^{-1}u, \mathsf{D}_Q v\rangle_{L^2} = \left\langle \mathcal{G}\mathsf{D}_Q^*\mathcal{G}^{-1}u, v\right\rangle_{\mathcal{G}^{-1}}$. □

10.4 Examples

10.4.1 Example 1: Thermocapillary thin film equation

Gradient flow form and symmetries

Consider the thermocapillary thin film equation,

$$\partial_t h = -\nabla\cdot\left\{\frac{h^3}{3}\nabla\nabla^2 h + \frac{\mathsf{Ma}}{3}\frac{h^2}{(1-h)^2}\nabla h\right\} = \nabla\cdot\left\{\frac{h^3}{3}\nabla p\right\}, \tag{10.12}$$

$$p = -\nabla^2 h - \mathsf{Ma}\left[\frac{1}{1-h} + \ln\left(\frac{h}{1-h}\right)\right] \tag{10.13}$$

where h is nondimensional film thickness, Ma is the thermocapillary Marangoni constant, and p is the effective nondimensional pressure (Oron and Rosenau, 1992). This equation describes the evolution of a thin film on a flat substrate held at a constant temperature, with a second plate parallel to the substrate and having a different temperature held above the fluid interface. The first term in the pressure is the capillary pressure; we have seen this in the curved-substrate thin film derivation of Chapter 8. The second term arises due from tangential stresses induced by the temperature-dependence of the thin film's surface tension.

Oron and Rosenau (1992) showed that the equation may be expressed in gradient flow form as

$$\langle \partial_t h, w\rangle_{L^2} = \left\langle \nabla^2 h + \mathsf{Ma}\left[\frac{1}{1-h} + \ln\left(\frac{h}{1-h}\right)\right], w\right\rangle_{\mathcal{G}} = \langle \delta_h \mathscr{F}, w\rangle_{\mathcal{G}}\,, \tag{10.14}$$

where

$$\langle u, v\rangle_{\mathcal{G}} = \left\langle -\nabla\cdot\left(\frac{h^3}{3}\nabla u\right), v\right\rangle_{L^2} \tag{10.15}$$

and

$$\mathscr{F} = -\frac{1}{2}\nabla h\cdot\nabla h + \mathsf{Ma}\, h\ln\left(\frac{h}{1-h}\right). \tag{10.16}$$

Hence, by Proposition 1, if Q is a variational symmetry characteristic of $\mathscr{F}$ then

$$\langle \partial_t h, Q \rangle_{\mathcal{G}^{-1}} = \int_\Omega (\partial_t h) u \, dxdy = 0, \tag{10.17}$$

$$\text{with } u \text{ defined by } \nabla \cdot (h^3 \nabla u) = Q. \tag{10.18}$$

Just as Noether's theorem in Lagrangian systems provides quantities which are conserved in time only with the appropriate boundary conditions, the symmetry characteristics of the gradient flow functional will be orthogonal to the evolution vector only with the appropriate boundary conditions. In this case specifically, the required boundary condition on u for the boundary terms to vanish is

$$\int_{\partial\Omega} \left[(\partial_t h) h^3 \partial_n u - \partial_n \left(h^3 \partial_t h \right) u \right] = 0 \tag{10.19}$$

where ∂_n denotes $\hat{n} \cdot \nabla$, the gradient normal to the domain boundary. In particular, if the thin film equation is solved with Dirichlet boundary conditions, then u may be chosen to satisfy homogeneous Dirichlet boundary conditions $u|_{\partial\Omega} = 0$. And if the thin film equation is solved with Neumann boundary conditions, then u may be restricted to homogeneous Neumann conditions $\partial_n u|_{\partial\Omega} = 0$.

Performing a variational symmetry analysis on $\mathscr{F}$, we find three symmetries:

1. $\vec{v}_1 = \partial_x$, corresponding to translation in x. The characteristic is $Q_1 = -\partial_x h$.
2. $\vec{v}_2 = \partial_y$, corresponding to translation in y. The characteristic is $Q_2 = -\partial_y h$.
3. $\vec{v}_3 = x\partial_y - y\partial_x$, corresponding to rotation in the x-y plane. The characteristic is $Q_3 = y\partial_x h - x\partial_y h$.

Numerical example

We now demonstrate the results with a numerical example, computed using the finite element method in COMSOL (Com, 2017). Let us consider as an example $\vec{v}_3$, the rotational symmetry. This symmetry is valid if the domain Ω is circular and h satisfies a rotationally symmetric boundary condition, such as $\partial_n h = const$. Therefore, the function $(y\partial_x h - x\partial_y h)$ is always orthogonal to the evolution $\partial_t h$ under the $\mathcal{G}^{-1}$ norm,

$$\langle \partial_t h, y\partial_x h - x\partial_y h \rangle_{\mathcal{G}^{-1}} = 0. \tag{10.20}$$

Note in particular that the initial condition is *not* required to be rotationally symmetrical for this orthogonality to hold; it is sufficient for the domain shape and boundary condition to satisfy rotational symmetry.

We will numerically solve the thermocapillary thin film equation on a circle of radius 1, with boundary conditions $\partial_n h|_{\partial\Omega} = \partial_n p|_{\partial\Omega} = 0$. We set $\mathrm{Ma} = 10$, and an arbitrary initial condition maintaining $h(t = 0) \in [0.1, 0.11]$.

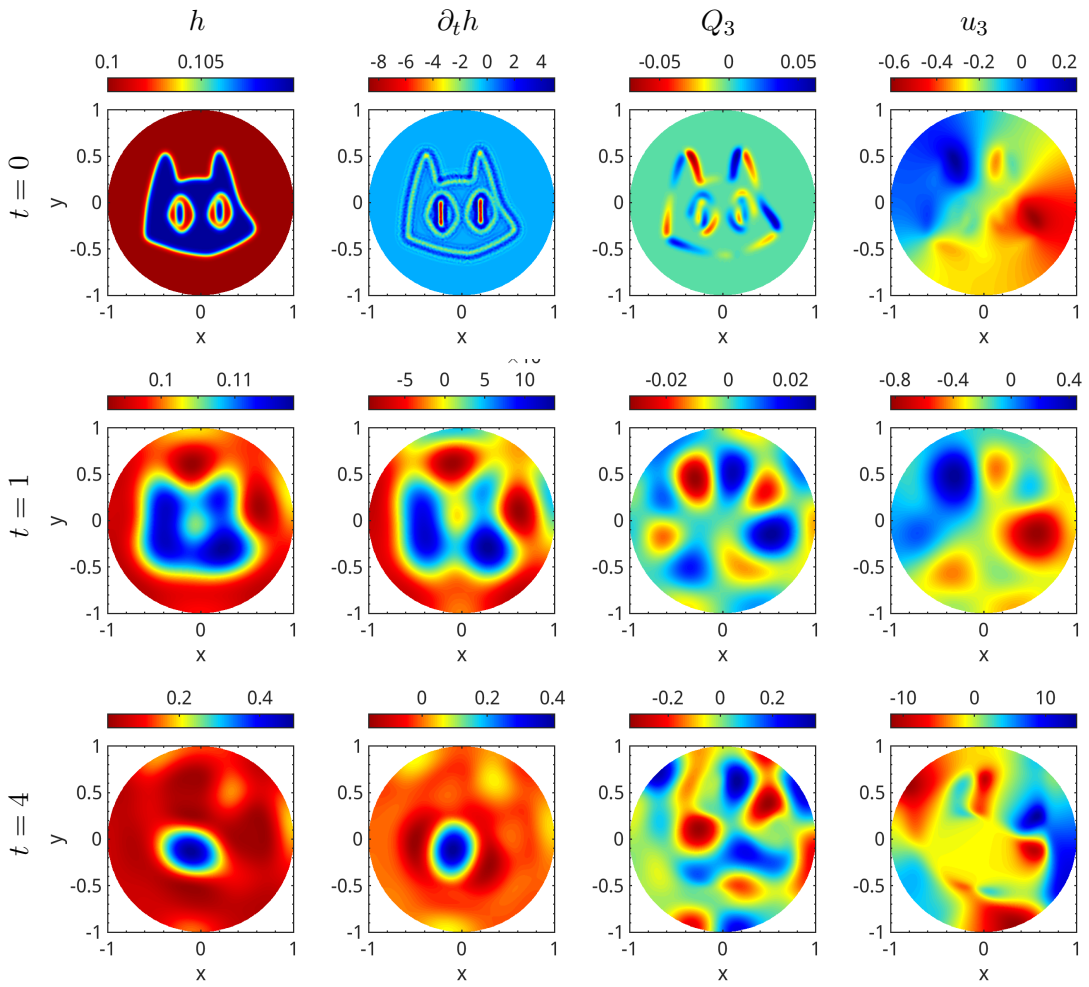

Figure 10.2: Plots of fluid film thickness h, evolution vector $\partial_t h$, rotational symmetry characteristic Q_3, and orthogonal function $u_3 = \mathcal{G}^{-1}Q_3$ at various times ($t \in \{0, 1, 4\}$) during the evolution of the thermocapillary thin film equation, Equation (10.12), for a finite element simulation with mesh element size 0.02. Note that the scale of the color bar varies between plots.

The evolution of the thermocapillary thin film equation with the example initial condition in a circular domain of radius 1 is shown in Figure 10.2. The columns display fluid height h, evolution vector $\partial_t h$, rotational symmetry characteristic Q_3, and orthogonal function $u_3 = \mathcal{G}^{-1}Q_3$. Each row shows a different time in the evolution; the first row is the initial condition at $t = 0$, the second row displays $t = 1$, and the final row displays $t = 4$. Note that the color bars are not consistent between times as the scale of the fluid surface varies significantly.

The symmetry characteristic, Q_3, would vanish if the data (h) satisfied the symmetry; that is, if h were rotationally symmetric, Q_3 would be identically zero. Q_3 (as seen in column 3 of Figure 10.2) thus provides a local measure of the deviation of h from rotational symmetry. $u_3 = \mathcal{G}^{-1}Q_3$ would thus also vanish if h were rotationally symmetric; however, it is not a local

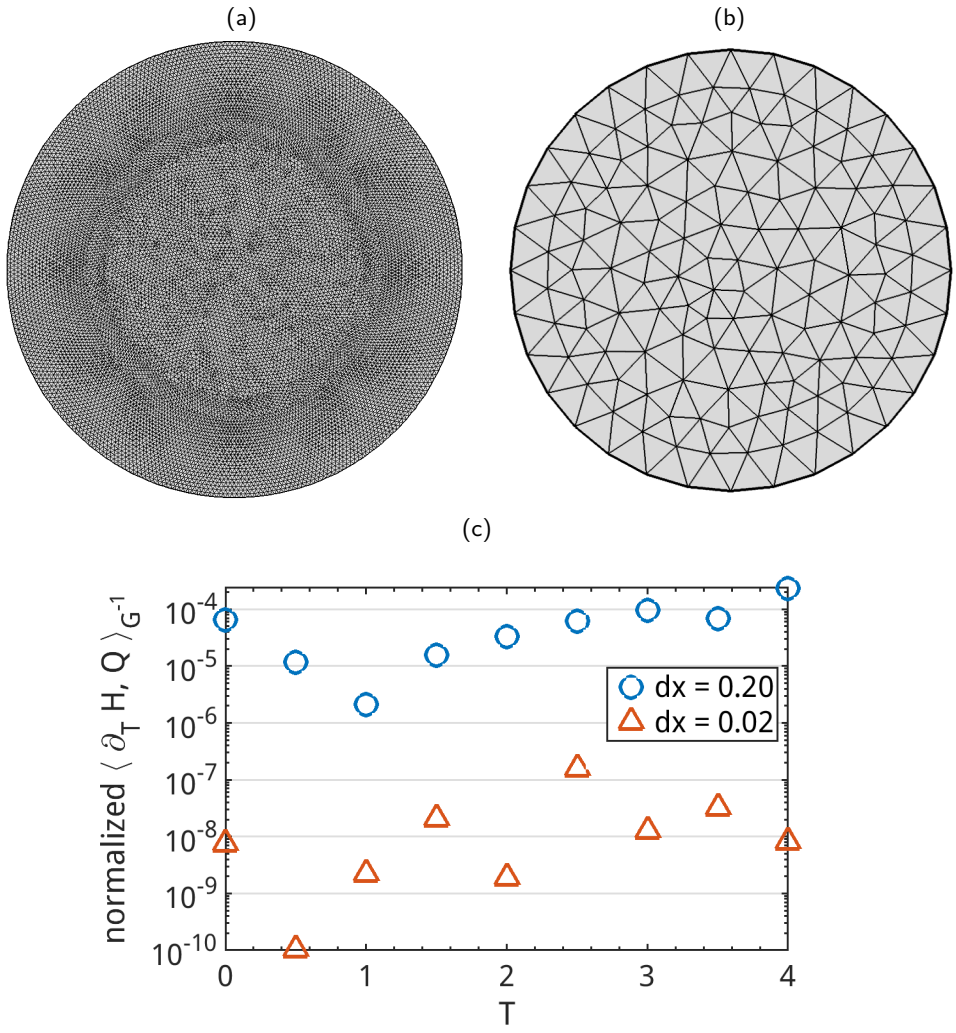

Figure 10.3: Comparison of symmetry condition violation between coarse and fine meshes. (a)-(b): Fine and coarse meshes on a circle of radius 1. Fine mesh (a) has maximum mesh element length $dx = 0.02$ and 25,970 elements; coarse mesh (b) has maximum mesh element length $dx = 0.2$ and 250 elements.
(c): Normalized inner product of the evolution vector and the rotational symmetry characteristic, $|\langle \partial_t h, Q_3 \rangle_{\mathcal{G}^{-1}}| / \sqrt{\langle \partial_t h, \partial_t h \rangle \langle u_3, u_3 \rangle}$, where $u_3 = \mathcal{G}^{-1} Q_3$. Vertical axis is a log axis, and displays the normalized inner product value. Horizontal axis is linear and tracks time.

descriptor of deviation from the symmetry, but a nonlocal one, as $\mathcal{G}^{-1}$ is a nonlocal operator.

As the film evolves, it should be the case that $\partial_t h$ and Q_3 are orthogonal under the $\mathcal{G}^{-1}$ norm, and that $\partial_t h$ and u_3 are orthogonal under the L_2 norm. Keep in mind that this must hold even though the initial condition is not rotationally symmetric. As with the application of Noether's Theorem to Lagrangian problems, the symmetry is a quality of the governing equations, not of the data.

The thermocapillary thin film simulation with the displayed initial condition was performed using

the finite element method two times; once with a fine mesh (the results of which were shown in Figure 10.2), and once with a coarse mesh. The fine mesh had maximum mesh element length $dx = 0.02$ and 25,970 elements, while the coarse mesh had maximum mesh element length $dx = 0.2$ and 250 elements; both meshes are shown in Figure 10.3. In both cases, the orthogonality of $\partial_t h$ to Q_3 in the $\mathcal{G}^{-1}$ norm was computed in order to test how well the simulations avoided violating the symmetry condition. While the value $\langle \partial_t h, Q_3 \rangle_{\mathcal{G}^{-1}}$ could be used as a metric of orthogonality, its magnitude will scale with $\partial_t h$ and Q_3. It is hence reasonable to instead take a normalized measure of orthogonality as $\langle \partial_t h, Q_3 \rangle_{\mathcal{G}^{-1}} / \sqrt{\langle \partial_t h, \partial_t h \rangle \langle u_3, u_3 \rangle}$; this result is plotted in Figure 10.3. The normalized violation of orthogonality is much lower for the fine mesh than the coarse mesh; the former has values ranging from approximately 10^{-10} to 10^{-7}, while the latter has values ranging from approximately 10^{-6} to 10^{-4}. A portion of the difference may be due to COMSOL selecting shorter time steps on the finer mesh, in addition to the mesh itself being finer. These results suggest that the symmetry condition may indeed be a useful quantitative metric to assess the quality of a simulation; if the violation is too large, one may wish to use a finer mesh or timestep, or change the numerical method.

10.4.2 Example 2: A gradient flow equation with a conservation law

Although the evolutionary constraints of gradient flow problems do not typically lead to conserved quantities, Corollary 1 showed that it can sometimes occur. Consider the gradient flow equation

$$\partial_t u = \partial_x \left\{ \frac{\partial_x \left[f\left(\partial_x^4 u\right) \right]}{\partial_x^3 u} \right\} = \partial_x \left[\frac{f'\left(\partial_x^4 u\right)}{\partial_x^3 u} \partial_x^5 u \right] \tag{10.21}$$

$$\implies \langle \partial_t u, w \rangle_{L^2} = \left\langle \partial_x^4 u, w \right\rangle_{\mathcal{G}}, \quad \mathcal{G} = \partial_x \left[\frac{f'\left(\partial_x^4 u\right)}{\partial_x^3 u} \partial_x \right]. \tag{10.22}$$

One variational symmetry of $\mathscr{F}$ is given by

$$\vec{v} = -\left(\partial_x^5 u\right) f''\left(\partial_x^4 u\right) \partial_u = \left[\mathcal{G} \delta_u \frac{(\partial_x u)^2}{2} \right] \partial_u. \tag{10.23}$$

It is then straightforward to show that $(\partial_x u)^2/2$ is indeed a conserved quantity of Equa-

tion (10.21), so long as the appropriate boundary conditions are met:

$$\begin{aligned}
\partial_t \int \frac{1}{2}\left(\partial_x u\right)^2 dx &= \left[(\partial_t u)(\partial_x u)\right]_{\text{boundary}} - \int (\partial_t u)\partial_{xx} u \; dx \\
&= \left[(\partial_t u)(\partial_x u)\right]_{\text{boundary}} - \int \partial_x \left\{ \frac{\partial_x \left[f\left(\partial_x^4 u\right)\right]}{\partial_x^3 u} \right\} \partial_{xx} u \; dx \\
&= \left[(\partial_t u)(\partial_x u) - \frac{\partial_x \left[f\left(\partial_x^4 u\right)\right]}{\partial_x^3 u} \partial_{xx} u \right]_{\text{boundary}} + \int \frac{\partial_x \left[f\left(\partial_x^4 u\right)\right]}{\partial_x^3 u} \partial_x^3 u \; dx \\
&= \left[(\partial_t u)(\partial_x u) - \frac{\partial_x \left[f\left(\partial_x^4 u\right)\right]}{\partial_x^3 u} \partial_{xx} u \right]_{\text{boundary}} + \int \partial_x \left[f\left(\partial_x^4 u\right) \right] \; dx \\
&= \left[(\partial_t u)(\partial_x u) - \frac{\partial_x \left[f\left(\partial_x^4 u\right)\right]}{\partial_x^3 u} \partial_{xx} u + f\left(\partial_x^4 u\right) \right]_{\text{boundary}} \\
&= 0 \text{ , if boundary term vanishes.}
\end{aligned} \tag{10.24}$$

This example is clearly somewhat contrived; in general, conservation laws should not be expected to arise out of variational symmetries of gradient flow PDEs.

10.5 Conclusion

We have demonstrated how the continuous symmetry characteristics of gradient flow functionals produce a constraint on the evolution vector of that flow. We have described the special case in which symmetries give rise to conserved quantities in gradient flow PDEs, and provided an example of such a system. And we have given a practical example in which the obedience of a simulation of the thermocapillary thin film equation to this constraint was measured in order to provide a metric of the validity of the numerical method.

The application of this result to validation of numerical methods is expected to be the primary domain in which it is useful. However, the most important takeaway of this work should be that Noether's Theorem is not confined to Lagrangian systems or conservation laws. Indeed, any time one works with a variational problem, Noether's Theorem can likely provide some useful insight.

References

COMSOL Inc. Multiphysics V5.3a, Burlington, MA, USA, 2017. URL `https://www.comsol.com`.

A. S. Fokas. Generalized symmetries and constants of motion of evolution equations. Lett. Math. Phys., 3(6):467–473, November 1979. ISSN 0377-9017, 1573-0530. doi:10.1007/BF00401927.

P. E. Hydon. Symmetry Methods for Differential Equations: A Beginner's Guide. Cambridge Texts in Applied Mathematics. Cambridge University Press, 2000. ISBN 9780521497862. doi:10.1017/CBO9780511623967.

M. I. Jordan. On gradient-based optimization: Accelerated, distributed, asynchronous and stochastic. In Computational Challenges in Machine Learning. Simons Institute, May 2017. doi:10.1145/3143314.3078506.

J. E. Marsden and A. J. Tromba. Vector Calculus. W. H. Freeman and Company, New York, 5th edition, 2003. ISBN 9780716749929.

H. Naito. A stable manifold theorem for the gradient flow of geometric variational problems associated with quasi-linear parabolic equations. Compos. Math., 68(2):221–239, 1988. URL http://www.numdam.org/item/CM_1988__68_2_221_0/.

E. Noether. Invariante variationsprobleme. Göttingen Nachr., 1918:235–257, 1918.

P. J. Olver. On the Hamiltonian structure of evolution equations. Math. Proc. Camb. Philos. Soc., 88(01):71, July 1980. ISSN 0305-0041, 1469-8064. doi:10.1017/S0305004100057364.

P. J. Olver. Applications of Lie groups to differential equations. Graduate Texts in Mathematics. Springer-Verlag New York, 1986. ISBN 9780387962504. doi:10.1007/978-1-4684-0274-2.

A. Oron and P. Rosenau. Formation of patterns induced by thermocapillarity and gravity. J. Phys. II, 2(2):131–146, 1992. doi:10.1051/jp2:1992119.

F. Otto. The geometry of dissipative evolution equations: The porous medium equation. Commun. Part. Diff. Eq., 26(1-2):101–174, 2001. doi:10.1081/PDE-100002243.

W. Strampp. On the correspondence between symmetries and conservation laws of evolution equations. Lett. Math. Phys., 6(2):113–121, March 1982. ISSN 0377-9017, 1573-0530. doi:10.1007/BF00401736.

Chapter 11

ROBUST COMPUTATION OF CUBIC GALILEON GRAVITY POTENTIAL FIELD AT SOLAR SYSTEM SCALES

Note: This chapter is adapted from published work (White et al., 2020).

11.1 Introduction

Researchers continue to debate whether dark energy or modified gravity is responsible for the apparent accelerating expansion of the universe. This debate underscores our current lack of understanding of gravitational physics at large scales (de Rham, 2012; Koyama and Silva, 2007; Schmidt, 2009; Schmidt et al., 2010). In order to explain cosmological expansion at large scales while also maintaining consistency with the observed lack of a strong "fifth force" on bodies at sub-solar-system scales, modified gravity theories often take the form of phenomenological scalar field theories incorporating screening mechanisms. Such screening mechanisms can be classified broadly as depending on the local value, the first derivative, or the second derivative of the scalar potential field (Joyce et al., 2015). Examples of the first class, in which the fifth force is screened when the gravitational potential exceeds some critical value, include the Symmetron (Hinterbichler and Khoury, 2010; Olive and Pospelov, 2008), Chameleon (Khoury and Weltman, 2004), and dilaton (Brax et al., 2011; Damour and Polyakov, 1994) screening mechanisms. Models such as k-mouflage (Babichev et al., 2009) fall into the second class for which the screening is engaged once the gradient of the potential field exceeds some bound. Vainshtein screening mechanisms (Vainshtein, 1972) fall into a third class, in which the fifth force is screened in regions of space where the local curvature of the field exceeds some value. The popular cubic, quartic and quintic Galileon models (de Rham, 2012; Nicolis et al., 2009) all incorporate such a Vainshtein mechanism. A comprehensive review of screening mechanisms and modified gravity theories may be found in Joyce et al. (2015) and references therein. In this work, we focus exclusively on the cubic Galileon gravity (CGG) form of the Vainshtein mechanism, which was first identified in the context of the Dvali-Gabadadze-Porrati (DGP) braneworld model (Dvali et al., 2000). The cubic and higher-order Galileon terms have been included in various other models of massive gravity (a review can be found in Sakstein, 2018 and references therein). These effective field theories have also been proposed as an alternative to dark matter rather than dark energy (Chan and Hui, 2018).

In scalar field models that incorporate Vainshtein screening, the standard quadratic kinetic term in the Lagrangian is augmented by a higher-order nonlinearity and the system is forced by the trace of the stress-energy tensor. The resulting governing equation includes a linear d'Alembertian term, which dominates at long distances (based on a length scale derived from the forcing of the given system), and a nonlinear term, which suppresses the field at small

distances (de Rham, 2012). A particularly simple manifestation of the Vainshtein mechanism, and the one investigated in this study, is one in which the Lagrangian contains a cubic interaction term, hence leading to an equation that is quadratic in the field and higher derivatives.

One notable example giving rise to such a cubic Lagrangian is the DGP model, in which the universe is regarded as a 4D brane embedded in a 5D Minkowski bulk space. The corresponding action contains two Einstein-Hilbert terms, one for the bulk and one for the brane, each with its own Planck mass setting the strength of the gravity, which may be denoted M_4 and M_5, respectively. These two mass scales induce a crossover length scale $r_c = (\hbar/c)M_4^2/\left(2M_5^3\right)$, where $\hbar$ denotes Planck's constant and c is the speed of light, which characterizes the distance over which metric fluctuations propagating on the brane dissipate into the bulk, above which 5D gravity is dominant and below which 4D gravity is dominant (Dvali et al., 2000). Metric perturbations can then be linearized as scalar fields acting on the brane in the decoupling limit. These perturbations to the metric describe leakage of gravitons from the 4D brane universe (Lue and Starkman, 2003). The resulting equation of motion is dominated by linear terms at scales above the Vainshtein radius r_V, and nonlinear terms below r_V, where $r_V \sim r_c^{1/3}$ and is also dependent on details of the local density. To make contact with current cosmological models, r_c is typically expressed in terms of the current Hubble rate H_0 and matter density parameter Ω_m^0 such that $r_c = cH_0^{-1}\left(1-\Omega_m^0\right)^{-1}$ (Chan and Scoccimarro, 2009; Deffayet, 2001). The crossover length evaluates to approximately 1.8×10^{23} km or 6×10^3 Mpc using the constants reported by Carroll and Ostlie (2017).

Scalar field models are ultimately constrained by comparison to direct observations at cosmological or galactic scales (e.g., Mpc scales) at which the field is still relatively strong. Model predictions are often based on density perturbation analyses and n-body simulations. So far, analytic approaches have mostly yielded field equations for large-scale density perturbations (Deffayet, 2002; Koyama and Maartens, 2006; Koyama and Silva, 2007; Lue et al., 2004; Schmidt et al., 2010; Scoccimarro, 2009). Numerical simulations of large-scale structure evolution in the quasi-static approximation have also been conducted using spectral (Chan and Scoccimarro, 2009) and position-space (Barreira et al., 2013; Li et al., 2013; Schmidt, 2009) methods which sequentially solve for the scalar field and update the local mass density distribution, represented as discrete particles. These large-scale simulations have predicted perturbative density growth rates, power spectra of mass distribution, and parameter values for dark matter halos. Besides large-scale structure formation, the dynamics and radiation of binary pulsars under a Galileon scalar field have also been studied and shown to influence orbital periods due to Vainshtein screening (Dar et al., 2018; de Rham et al., 2013a,b). Analysis of the dependence of the Vainshtein radius on the radii of bodies has also demonstrated that the relative strength of the cubic Galileon fifth force to gravity is greater around infinite cylindrical bodies than around spherical bodies (Bloomfield et al., 2015), indicating potential advantages in obtaining measurements in regions lacking spherical symmetry in order to better discriminate signals from the fifth force.

On the experimental side, advances in instrumentation, such as atom interferometry, have introduced unprecedented sensitivity in force measurements (Chiow et al., 2015, 2016; Williams et al., 2016), so much so that there now exists the possibility of direct detection of a "fifth force" due to modified gravity; indeed, detection schemes for Chameleon (Burrage et al., 2015; Chiow and Yu, 2018; Hamilton et al., 2015) and Symmetron (Chiow and Yu, 2020) models have already been proposed. Direct detection experiments of the cubic Galileon scalar field at solar system scales may soon provide parameter constraints supplementing those arising from astrophysical observations, where in particular a significant tension has been found with data from the Integrated Sachs-Wolfe effect (Barreira et al., 2014; Renk et al., 2017). Efforts on validating modified gravity models at solar system scales are summarized by Sakstein (2018), in which the cubic Galileon field for only a single spherical object was analyzed. A comprehensive solution of the scalar field potential must include contributions from multiple planetary bodies to enable realistic mission design and data analysis as well as utilization of planetary ephemeris for constraining the cubic Galileon model, an approach similar to that of Bernus et al. (2019) on graviton mass bounds. To determine fully accurate solutions of the field around multiple bodies, 3D numerical simulations are required.

Numerical investigation of the 3D Galileon potential field at solar system scales described by the CGG model carries some inherent challenges. In contrast to the behavior at large-scales, the linear term at small distances is essentially negligible, such that the field equation becomes strongly nonlinear in the second derivative terms. Methods based on the finite element technique therefore become difficult to apply. Unlike the large-scale n-body regime, the solar system regime contains mass sources with compact support, such as the Sun and planets, which introduces difficulties for spectral methods, and further suggests modeling mass density as a field rather than as discrete particles. And since the radii of bodies tend to be orders of magnitude smaller than their separation distances, the multiple scales inherent in this system must be managed effectively to prevent numerical artifacts. Furthermore, since the CGG equation is quadratic, it harbors both attractive and repulsive solutions; care must be taken in isolating solutions iterating toward two separate global minima. Despite these challenges, some numerical studies have successfully elucidated aspects at small scales within the Vainshtein radii of the relevant bodies. For example, the anomalous precession of bodies such as Mercury beyond the correction to GR has been computed (Iorio, 2012; Lue and Starkman, 2003) as has solution of the Green's functions for corrections to a massive, spherically-symmetric body, with perturbative corrections computed to several orders (Andrews et al., 2013; Chu and Trodden, 2013).

While prior work had concentrated on large-scale cosmological simulations, Hiramatsu *et al.* (Hiramatsu et al., 2013) realized the importance of studying the very different small-scale regime as well and carried out the first significant numerical study of the static scalar potential field equation at small scales. Their study considered an idealized system containing two spherical bodies with mass ratio comparable to Earth and the Moon but positioned within very close range, using a finite difference technique coupled with a successive over-relaxation method. The

system considered was within the nonlinear regime subject to strong screening since the two bodies were both well within each other's Vainshtein radius. In this case, the authors were able to take advantage of the fact that despite the presence of a strong nonlinear term, the solution at distances close to a massive body must be dominated by that body. (We note the use of the term "screening" by Hiramatsu et al., 2013, to describe this effect should not be confused with the Vainshtein screening mechanism). Recent studies have also examined masses contained within spherical shells or voids which become subject to a force, in contrast to masses subject purely to Newtonian gravity (Belikov and Hu, 2013). Numerical simulations of disks containing holes have revealed how cavities reduce the screening force (Ogawa et al., 2019). In these examples, the numerical iteration scheme converges well so long as the initial trial solution is sufficiently close to the true solution.

The goal of this current work therefore is to provide an accurate and rapidly convergent numerical scheme for solution of the static scalar potential field of the cubic Galileon model at solar system scales for systems containing multiple dense compact mass sources. We present a numerical method based on finite differences for solution of the static CGG scalar field for a 2D axisymmetric Sun-Earth system and a 3D Cartesian Sun-Earth-Moon system. The method relies on gradient descent of an integrated residual based on the normal attractive branch of the CGG equation. The algorithm is shown to be stable, accurate and rapidly convergent toward the global minimum state. While the computation of observational constraints is beyond the scope of this work, the results presented below nonetheless offer useful guidelines for the positioning of space-based detection schemes to obtain measurements at solar system scales.

This paper is organized as follows: Section 11.2 describes the model system and non-dimensionalization of the governing equation to identify dominant and subdominant terms; Section 11.3 outlines the iteration scheme with application to solution of the Galileon potential fields for the axisymmetric Sun-Earth system and 3D Sun-Earth-Moon system along with discussion of results. Following the conclusion, we provide in the Appendices detailed explanations of the numerical method along with validation tests. Included there are download links to the data and software for the interested reader.

11.2 Analytic model and rescalings

In what follows, we follow the derivations in Refs. (Schmidt et al., 2010) and (Nicolis and Rattazzi, 2004) and review features of the CGG model equation. In particular, we discuss the known analytic solution for a spherically-symmetric single body at length scales above and far below the Vainshtein limit. The CGG equation are then non-dimensionalized to highlight relative strengths of the linear and nonlinear terms at solar system scales and to facilitate numerical investigation.

The cubic Galileon Lagrangian is given by

$$\mathfrak{L} = 3\phi\Box\phi - \frac{r_c^2}{c^2}\left(\partial_\alpha\phi\right)\left(\partial^\alpha\phi\right)\Box\phi + 16\pi G c^{-2} T^\alpha_{\ \alpha}\phi, \tag{11.1}$$

where $\Box$ is the d'Alembertian operator, ∂_α is the 4D covariant derivative, $\phi(\vec{r})$ is the scalar field, G is the gravitational constant, and $T^\alpha_{\ \alpha}$ is the trace of the stress-energy tensor (de Rham, 2012; Nicolis and Rattazzi, 2004). Eq. 11.1 was derived for a Minkowski (flat) 4D space; in a Friedmann background, the Lagrangian can instead be written as

$$\mathfrak{L}_{\rm Fr} = 3\frac{\beta}{a^2}\phi\Box\phi - \frac{r_c^2}{a^4 c^2}\left(\partial_\alpha\phi\right)\left(\partial^\alpha\phi\right)\Box\phi + 16\pi G c^{-2} T^\alpha_{\ \alpha}\phi, \tag{11.2}$$

where a is the cosmological scale factor and $\beta = 1 \pm 2H_0 c^{-1} r_c[1 + (\partial_t H_0)/(3H_0^2)]$, where ∂_t denotes the time derivative. In the DGP model there is an unstable self-accelerating branch, corresponding to the positive branch of β, and a stable "normal" non-accelerating attractive branch (Charmousis et al., 2006; Deffayet, 2001), corresponding to the negative branch of β (Koyama and Silva, 2007; Schmidt et al., 2010). We consider only the normal branch. By definition, $a = 1$ at the present day and, depending on the deceleration factor of the Universe, β may be estimated by a value of 2–4. Following Hiramatsu et al. (2013), we approximate $\beta \approx 1$ and proceed with the Lagrangian defined in Equation (11.1).

The resulting equation of motion is given by

$$3\Box\phi + \frac{r_c^2}{c^2}\left[(\Box\phi)^2 - \partial_{\alpha\mu}\phi\partial^{\alpha\mu}\phi\right] = -8\pi G c^{-2} T^\alpha_{\ \alpha}, \tag{11.3}$$

whose static potential field satisfies the nonlinear equation

$$3\nabla^2\phi + \frac{r_c^2}{c^2}\left[\left(\nabla^2\phi\right)^2 - \sum_{i,j}\left(\nabla_i\nabla_j\phi\right)^2\right] = 8\pi G\widetilde{\rho}, \tag{11.4}$$

where $\widetilde{\rho}$ denotes the local mass density difference from the cosmological mean and ∇_i is the 3D gradient operator. We note henceforth that the Einstein summation convention no longer applies. The scalar field can be regarded as static since the configuration of solar system bodies changes very slowly in comparison with the speed of light.

In the vicinity of dense bodies, the nonlinear term is dominant due to size of the coefficient r_c; at long scales above the Vainshtein radius, the linear term is dominant. The transition in solution behavior that results, is evident, for example, in the spherically-symmetric solution $\phi(r)$ for a single mass source, for which Equation (11.4) reduces to the form (Schmidt et al., 2010)

$$\frac{6}{r}\partial_r\phi + 3\partial_{rr}\phi + \frac{r_c^2}{c^2}\frac{2}{r^2}\left(\partial_r\phi\right)\left(\partial_r\phi + 2r\partial_{rr}\phi\right) = 8\pi G\widetilde{\rho}. \tag{11.5}$$

Schmidt et al. (2010) showed that the solution $\phi(r)$ for a single spherical body of radius $r_{\rm ref}$, density $\rho_{\rm ref}$ and total mass $M_{\rm ref} = (4/3)\pi\rho_{\rm ref} r_{\rm ref}^3$ can be written in terms of the hypergeometric

function ${}_2F_1$, where

$$\phi(r) = \frac{3c^2}{8}\begin{cases} \left(\frac{r}{r_c}\right)^2\left[\sqrt{1+\left(\frac{r_V}{r_{\rm ref}}\right)^3}-1\right] + \left(\frac{r_{\rm ref}}{r_c}\right)^2\left({}_2F_1\left[-\frac{1}{2},-\frac{2}{3};\frac{1}{3};-\left(\frac{r_V}{r_{\rm ref}}\right)^3\right] - \sqrt{1+\left(\frac{r_V}{r_{\rm ref}}\right)^3}\right), \\ \qquad\qquad\qquad\qquad\qquad\qquad\qquad\qquad\qquad\qquad\qquad\qquad r \le r_{\rm ref}; \\ \left(\frac{r}{r_c}\right)^2\left({}_2F_1\left[-\frac{1}{2},-\frac{2}{3};\frac{1}{3};-\left(\frac{r_V}{r}\right)^3\right]-1\right), \quad r > r_{\rm ref}; \end{cases} \tag{11.6}$$

and the Vainshtein radius is given by (Deffayet, 2002)

$$r_V = \frac{4}{3} r_{\rm ref}\left(\pi\frac{G}{c^2}\rho_{\rm ref} r_c^2\right)^{1/3} = \left(\frac{16}{9}\frac{G}{c^2}M_{\rm ref} r_c^2\right)^{1/3}. \tag{11.7}$$

The constant of integration incorporated into this form, which ensures $\lim\phi(r\to\infty) = 0$, does not affect the resulting force since the addition of a constant to the potential is a gauge freedom.

Given the complex nature of this solution, it is useful to examine instead the resulting force on a test body, which yields the simpler expression (Nicolis and Rattazzi, 2004; Schmidt et al., 2010):

$$\partial_r\phi(r) = \frac{3c^2 r}{4r_c^2}\begin{cases} \sqrt{1+\frac{64}{27}\pi\frac{G}{c^2}\rho_{\rm ref} r_c^2} - 1, & r \le r_{\rm ref}, \\ \sqrt{1+\frac{64}{27}\pi\frac{G}{c^2}\rho_{\rm ref} r_c^2\left(\frac{r_{\rm ref}}{r}\right)^3} - 1, & r > r_{\rm ref}, \end{cases} \tag{11.8}$$

or equivalently,

$$\partial_r\phi(r) = \frac{3c^2 r}{4r_c^2}\begin{cases} \sqrt{1+\left(\frac{r_V}{r_{\rm ref}}\right)^3} - 1, & r \le r_{\rm ref}, \\ \sqrt{1+\left(\frac{r_V}{r}\right)^3} - 1, & r > r_{\rm ref}. \end{cases} \tag{11.9}$$

This solution corresponding to the positive square root identifies the attractive solution which correctly matches the $r\to\infty$ linear-dominated limit of Equation (11.4).

At short distances where $r_{\rm ref} < r \ll r_V$, wherein the nonlinear terms dominate, the first-order solution becomes (Nicolis and Rattazzi, 2004; Schmidt et al., 2010):

$$\lim_{r_{\rm ref}<r\ll r_V}\partial_r\phi(r) = \frac{3c^2 r_V}{4r_c^2}\left[\left(\frac{r}{r_V}\right)^{-1/2} + O\left(\frac{r}{r_V}\right)\right]. \tag{11.10}$$

At long distances $r \gg r_V$ in which the linear term is instead dominant, the solution to first order becomes harmonic and reduces to (Nicolis and Rattazzi, 2004; Schmidt et al., 2010):

$$\lim_{r\gg r_V}\partial_r\phi(r) = \frac{3c^2 r_V}{8r_c^2}\left[\left(\frac{r}{r_V}\right)^{-2} + O\left(\frac{r}{r_V}\right)^{-4}\right]. \tag{11.11}$$

11.2.1 Non-dimensionalization of scalar potential equation

We introduce here scalings for non-dimensionalization of the governing scalar potential equation in order to clarify the relative importance of the linear term at small scales and to simplify the numerical method. The rescaling is based on a suitable length scale of interest, d, and a reference spherical mass of radius r_{ref} and density ρ_{ref}. These choices yield a characteristic scale for the potential field ϕ_{ref} and a dimensionless coefficient k preceding the linear term, where

$$\phi_{\text{ref}} = \left(\frac{3}{2}\right)^{3/2} \frac{c^2 d^{1/2} r_V^{3/2}}{r_c^2} = \sqrt{(8\pi G\rho_{\text{ref}}) \frac{d\, c^2\, r_{\text{ref}}^3}{r_c^2}}, \tag{11.12a}$$

$$k = \sqrt{\frac{8}{3}} \left(\frac{d}{r_V}\right)^{3/2} = \sqrt{\frac{9}{8\pi} \left(\frac{d^3\, c^2}{G\rho_{\text{ref}} r_{\text{ref}}^3 r_c^2}\right)}. \tag{11.12b}$$

The resulting non-dimensional equation for the scalar field $\Phi(\vec{R})$ becomes

$$k\nabla^2\Phi + \left[\left(\nabla^2\Phi\right)^2 - \sum_{i,j} \left(\nabla_i \nabla_j \Phi\right)^2\right] = \rho, \tag{11.13}$$

where the reduced density $\rho = \widetilde{\rho}/(\rho_{\text{ref}} r_{\text{ref}}^3/d^3)$ and dimensionless reference body radius is $R_{\text{ref}} = r_{\text{ref}}/d$. All other scalings and definitions can be found in Table 11.1.

The solution in Equation (11.6) can now be recast in dimensionless form for a spherically symmetric body of radius $R_b = r_b/d$ and density $\rho_b = \widetilde{\rho}_b/(\rho_{\text{ref}} r_{\text{ref}}^3/d^3)$:

$$\Phi(R) = \frac{kR_b^2}{8} \begin{cases} \left(\dfrac{R}{R_b}\right)^2 \left[\sqrt{1 + \dfrac{8\rho_b}{3k^2}} - 1\right] + {}_2F_1\left[-\dfrac{1}{2}, -\dfrac{2}{3}; \dfrac{1}{3}; -\dfrac{8\rho_b}{3k^2}\right] - \sqrt{1 + \dfrac{8\rho_b}{3k^2}}, & R \le R_b; \\ \left(\dfrac{R}{R_b}\right)^2 \left({}_2F_1\left[-\dfrac{1}{2}, -\dfrac{2}{3}; \dfrac{1}{3}; -\dfrac{8\rho_b}{3k^2}\left(\dfrac{R_b}{R}\right)^3\right] - 1\right), & R > R_b. \end{cases} \tag{11.14}$$

In regions close to a dense mass such as a planet, the reference density ρ_{ref} will typically be tens of orders of magnitude greater than the cosmological average density (Ryden, 2016); hence even if the surrounding space has an underdensity, it will tend to be negligibly small. The empty space close to a dense mass may therefore be assumed to have a value $\rho \ge 0$.

The chosen scalings help distinguish between solutions characterized by k large and k small and in turn make evident whether the linear or nonlinear term in Equation (11.13) is dominant at a given distance. The scalings above derive from consideration of a single body with spherically symmetry, but may be applied to the case of multiple bodies by choosing an appropriate distance d and either one body or a combination of the bodies for the reference mass and radius. In the case of one massive body which dominates the fields of all other bodies, such as the Sun in the solar system, the massive body is the natural reference choice. In the highly nonlinear regime characterized by negligibly small values of k, the governing equation for $\Phi(\vec{R})$ retains only the

nonlinear terms, thereby simplifying to the form

$$\left[\left(\nabla^2\Phi\right)^2 - \sum_{i,j}\left(\nabla_i\nabla_j\Phi\right)^2\right] = \rho. \tag{11.15}$$

The single-body spherically-symmetric solution in this nonlinear regime is then given by

$$\Phi(R) = \sqrt{\frac{M_b R_b}{32\pi}} \begin{cases} \left(\dfrac{R}{R_b}\right)^2 + \text{const.}\,, & R \le R_b \\ 4\sqrt{\dfrac{R}{R_b}} - 3 + \text{const.}\,, & R > R_b, \end{cases} \tag{11.16}$$

where $M_b = (4/3)\pi\rho_b R_b^3$ is the dimensionless reduced body mass. This result corresponds to the limit of small r derived by Schmidt et al. (2010). The choice of additive constant is arbitrary and may be chosen to match the full single-body solution.

Returning to Equation (11.13), we note that the coefficient k corresponding to the two-body Sun-Earth system is in fact negligibly small. For example, with the Sun as the reference body and a reference distance $d = 1$ AU, $k \approx 10^{-11}$. The distance 1 AU is well within the Vainshtein radii of the Sun, Earth, and Moon, which are approximately 3×10^7 AU, 4×10^5 AU, and 1×10^5 AU, respectively. For comparison, the apogee of Pluto's orbit is around 50 AU and the Oort cloud extends to at most 2×10^5 AU from the Sun. Furthermore, comparison between the analytic one-body solutions for the force field caused by the Sun, $\partial_r\Phi_{\rm S}$, for $k = 0$ and $k \neq 0$ reveals that the linear term is indeed irrelevant in the Sun-Earth system, as the relative difference at 1 AU is only of the order of 10^{-11}.

Smaller masses such as satellites or individual atoms have much smaller Vainshtein radii. However, so long as they are within the solar system, their potential fields will be dominated by the Sun or other planets at short distances below the Vainshtein radii of the smaller objects. For example, a hydrogen atom has a Vainshtein radius of approximately 0.4 m, but the fifth force it would exert on an object one angstrom away is still tens of orders of magnitude smaller than the fifth force exerted by the Sun on an object at a distance of 1 AU. Similarly, a spherical satellite of mass 10^4 kg has a Vainshtein radius of approximately 10^{10} m. However, at a distance of 1 AU from the Sun, the force the satellite would exert on a nearby mass is comparable to the fifth force exerted by the Sun at a millionth of an angstrom away. The magnitude of the Laplacian of its scalar field is comparable to that of the Sun at a distance of about 250 meters, still many orders of magnitude below the satellite's Vainshtein radius. In the present work, focusing on solar system scales, the coefficient k of the linear term in Equation (11.13) was set to 0 in all simulations, although the numerical method should remain valid for arbitrary $k > 0$.

11.3 Scalar potential solution for the axisymmetric Sun-Earth and 3D Sun-Earth-Moon systems

Although Equations (11.13) and (11.15) have been solved analytically for the case of single body with spherical symmetry, as shown above, exact analytic solutions for asymmetric systems

consisting of two or more bodies have remained intractable. By noting that the governing equation remains invariant to the addition of terms represented by constant gradients to Φ (so-called Galilean invariance), Hui et al. (2009) suggested that the influence of a distant mass on a local system could be approximated by first solving for the local system in isolation and then adding the linearized potential of the field of the distant mass. For an axisymmetric two-body problem, an analytic perturbation expansion based on this assumption has been developed (Cutler). To achieve higher accuracy for the two-body problem or to solve complex systems containing many bodies or non-spherical masses, it becomes necessary to turn to numerical solution techniques.

The success of the numerical method used in this work relies on an important observation by Chan and Scoccimarro (2009). Recasting Equation (11.13) or Equation (11.15) as a quadratic equation in terms of the Laplacian $\nabla^2\Phi$ allows one to isolate the solution which correctly matches the large-scale limiting behavior by selecting the corresponding positive or negative square root. While they used a discriminant splitting technique to avoid complex roots in the residual function of trial solutions in large-scale cosmological simulations containing both over- and under-densities, we find that the method without splitting is particularly useful for simulations like ours at distances below the Vainshtein radius containing dense and compact mass sources, i.e., cases in which underdensities can be ignored. In particular, we show that in this small scale regime, the residual error landscape of the solved quadratic form of Equation (11.13) or Equation (11.15) has no local minima, implying that an iteration scheme following gradient descent will locally converge to the global minimum representing the true solution. The main analytic aspects of the iteration scheme used in the numerical simulations are discussed in Section 11.3.1, while a detailed explanation of the implementation and numerical method of central finite differences with nested meshes is contained in Section 11.5.

Unlike previous studies incorporating compact mass sources (Belikov and Hu, 2013; Hiramatsu et al., 2013), the Vainshtein radii in our studies are many orders of magnitude larger than the radii and separation distance of the solar system bodies of interest. The scalar potential field is therefore computed well within the Vainshtein radii of the dominant bodies, without having to extend the computational domain to the far field region dominated by the linear term. In addition, the boundary conditions applied along the edges of the computational domain derive from the values of the spherically-symmetric solution given by Equation (11.14) forced by a spherical average of the mass sources, in contrast to boundary conditions corresponding to superposition of single-body solutions. The reader will find in Section 11.3.1 a more detailed explanation of the boundary conditions and validation tests are presented in Section 11.6.2.

Experimental detection relying on force measurements would allow quantification of the Galileon force $\nabla\Phi$, and its spatial variation in the form of the Laplacian $\nabla^2\Phi$. At solar system scales, $\nabla\Phi$ is many orders of magnitude smaller than the force of Newtonian gravity. Directly measuring the small additional Galileon force would require exact computation of the gravitational field to

the same precision, and is therefore one of the key obstacles to detection. However, because the Laplacian of the Newtonian gravitational field always vanishes, measurement of the Laplacian will reveal only non-Newtonian forces associated with the background scalar field. For this reason, we concentrate in this work mostly on the gradient and Laplacian functions of Φ for the two-body Sun-Earth system and the three-body Sun-Earth-Moon system.

In Sections 11.3.2 and 11.3.3, we contrast the full numerical solutions for the 2D axisymmetric Sun-Earth and 3D Cartesian Sun-Earth-Moon system, with the solution to the single body Sun case, and naïve solutions based on simple superposition of the independent scalar fields. The results of the Sun-Earth-Moon system are further compared to the superposition of the two body Earth-Moon system with the single body Sun solution. Because the Sun's field has nearly a constant gradient in the region surrounding Earth and the Moon, the latter solution closely represents the approximation proposed by Hui et al. (2009). Simulation parameters are listed in Table 11.1. We note that although our numerical simulations were all based on the non-dimensionalized form of the governing equation and corresponding boundary conditions, the results that follow are presented in dimensional variables for the convenience of those readers interested in experimental scales and verification.

Quantity	Scaling	Rescaled variable
Current Hubble rate constant	$H_0 = 71\,\mathrm{km/s/Mpc}$ (Carroll and Ostlie, 2017)	
Matter density parameter	$\Omega_m^0 = 0.27\,\mathrm{km/s/Mpc}$ (Carroll and Ostlie, 2017)	
Speed of light in vacuum	$c = 2.998 \times 10^8$ m s^{-1}	
Crossover length scale	$r_c = cH_0^{-1}\left(1-\Omega_m^0\right)^{-1}$	
	$= 1.8 \times 10^{23}$ km	
Gravitational constant	$G = 6.674 \times 10^{-11}$ m^3 kg^{-1} s^{-2}	
Sun density	$\widetilde{\rho}_\mathsf{S} = 1,408$ kg m^{-3}	$\rho_\mathsf{S} = \widetilde{\rho}_\mathsf{S}/\rho_\mathrm{ref} = 1$
Sun radius	$r_\mathsf{S} = 0.6957 \times 10^6$ km	$R_\mathsf{S} = r_\mathsf{S}/d = 1$
Sun Vainshtein radius	$r_{V,\mathsf{S}} = \left[(64\pi/27)Gc^{-2}\widetilde{\rho}_\mathsf{S} r_\mathsf{S}^3 r_c^2\right]^{1/3}$	
	$= 4.396 \times 10^{15}$ km	$R_{V,\mathsf{S}} = r_{V,\mathsf{S}}/d = 6.318 \times 10^9$
Sun coordinates	$x_\mathsf{S} = 0$	$X_\mathsf{S} = x_\mathsf{S}/d = 0$
	$y_\mathsf{S} = 0$	$Y_\mathsf{S} = y_\mathsf{S}/d = 0$
	$z_\mathsf{S} = 0.5$ AU	$Z_\mathsf{S} = z_\mathsf{S}/d = 107.5$
	$= 74.80 \times 10^6$ km	
Earth density	$\widetilde{\rho}_\mathsf{E} = 5,515$ kg m^{-3}	$\rho_\mathsf{E} = \widetilde{\rho}_\mathsf{E}/\rho_\mathrm{ref} = 3.917$
Earth radius	$r_\mathsf{E} = 0.006371 \times 10^6$ km	$R_\mathsf{E} = r_\mathsf{E}/d = 9.158 \times 10^{-3}$
Earth Vainshtein radius	$r_{V,\mathsf{E}} = 6.346 \times 10^{13}$ km	$R_{V,\mathsf{E}} = r_{V,\mathsf{E}}/d = 9.121 \times 10^7$
Earth coordinates	$x_\mathsf{E} = 0$	$X_\mathsf{E} = x_\mathsf{E}/d = 0$
	$y_\mathsf{E} = 0$	$Y_\mathsf{E} = y_\mathsf{E}/d = 0$

	$z_{\mathsf{E}} = -74.80 \times 10^6$ km	$Z_{\mathsf{E}} = z_{\mathsf{E}}/d = -107.5$
Moon density	$\widetilde{\rho}_{\mathsf{M}} = 3,344$ kg m^{-3}	$\rho_{\mathsf{M}} = \widetilde{\rho}_{\mathsf{M}}/\rho_{\mathrm{ref}} = 2.375$
Moon radius	$r_{\mathsf{M}} = 0.001737 \times 10^6$ km	$R_{\mathsf{M}} = r_{\mathsf{M}}/d = 2.497 \times 10^{-3}$
Moon Vainshtein radius	$r_{V,\mathsf{M}} = 1.464 \times 10^{13}$ km	$R_{V,\mathsf{M}} = r_{V,\mathsf{M}}/d = 2.105 \times 10^7$
Moon coordinates	$x_{\mathsf{M}} = 0$	$X_{\mathsf{M}} = x_{\mathsf{M}}/d = 0$
	$y_{\mathsf{M}} = -0.3850 \times 10^6$ km	$Y_{\mathsf{M}} = y_{\mathsf{M}}/d = -0.5534$
	$z_{\mathsf{M}} = -74.80 \times 10^6$ km	$Z_{\mathsf{M}} = z_{\mathsf{M}}/d = -107.5$
Reference distance	$d = 0.6957 \times 10^6$ km $= r_S$	$(X, Y, Z, R) = (x, y, z, r)/d$
Reference body density	$\rho_{\mathrm{ref}} = 1,408$ kg m^{-3} $= \widetilde{\rho}_{\mathrm{S}}$	$\rho = \widetilde{\rho}/\rho_{\mathrm{ref}}$
Reference body radius	$r_{\mathrm{ref}} = 0.6957 \times 10^6$ km $= r_{\mathrm{S}}$	$R_{\mathrm{ref}} = r_{\mathrm{ref}}/d = 1$
Reference scalar field value	$\phi_{\mathrm{ref}} = \sqrt{(8\pi G\rho_{\mathrm{ref}})\, c^2 d r_{\mathrm{ref}}^3/r_c^2}$	
	$= 1.2 \times 10^{-3}$ m^2 s^{-2}	$\Phi = \phi/\phi_{\mathrm{ref}}$
Linear coeff. of Equation (11.13)	$k = \sqrt{(9d^3c^2)/(8\pi G\rho_{\mathrm{ref}} r_{\mathrm{ref}}^3 r_c^2)}$	
	$= 3.2 \times 10^{-15}$	$k = 0$ in simulations
Gravitational potential field	$\psi_{\mathrm{G}}: \quad \nabla^2\psi_{\mathrm{G}} = 4\pi G\widetilde{\rho}(\vec{r})$	$\Psi_{\mathsf{G}} = \psi_{\mathrm{G}}/\phi_{\mathrm{ref}}$
Quantity normalized by gravity	$\|\cdot\|_G = \|\cdot\|/\|\nabla\psi_{\mathrm{G}}\|$	
Arbitrary body density	$\widetilde{\rho}_{\mathsf{B}}$	$\rho_{\mathsf{B}} = (\widetilde{\rho}_{\mathsf{B}}/\rho_{\mathrm{ref}})(d/r_{\mathrm{ref}})^3$
Arbitrary body radius	r_{B}	$R_{\mathsf{B}} = r_{\mathsf{B}}/d$
Computational domain size	$\ell = 64$ AU	$L = \ell/d = 1.376 \times 10^4$
	$= 9,574 \times 10^6$ km	
3D simulation bounds	$(x, y, z) \in [-\ell, \ell] \times [-\ell, \ell] \times [-\ell, \ell]$	
2D simulation bounds	$(r, z) \in [0, \ell] \times [-\ell, \ell]$	
Iteration number	n	

Table 11.1: Parameter values and scalings for the numerical simulations (unless otherwise specified). In this work, the reference distance d, reference body density ρ_{ref}, and reference body radius r_{ref} were set equal to the Sun values, resulting in a reference scalar field, ϕ_{ref}, based on the Sun.

11.3.1 Solution scheme

The numerical solution scheme for obtaining the CGG scalar potential field at solar system scales is based on inclusion of mass sources far denser than any local cosmological underdensities. Under this assumption, the mass density term ρ of Equation (11.13) can be assumed to be non-negative, which allows formulation of a robust iteration scheme with rapid convergence regardless of the initial trial solution. The accuracy and convergence of this iteration scheme are examined next.

Analytic properties of implemented iteration scheme

The solution to the general governing nonlinear equation given by Equation (11.13) can be accurately approximated by iterative linearization. Given a nonlinear residual function $\mathcal{R}[\Phi]$ quantifying the difference of an interim solution from the actual solution Φ, the numerical approximation scheme is recast as an optimization problem by minimizing the value of the integrated residual over the volume of interest, namely $\|\mathcal{R}[\Phi]\|^2 = \int \mathcal{R}^2[\Phi] dV$. The initial trial function for Φ is then made to evolve via gradient descent toward a minimum of the residual, where the gradient operator is defined by the functional derivative $\mathcal{L}[\Phi] = \delta\mathcal{R}[\Phi]/\delta\Phi$. A variety of algorithms exist in the literature for speeding the computations involving gradient descent and seeking global minima amidst a residual landscape potentially populated by many local minima, all the while ensuring accuracy and stability (Kelley, 1995).

The choice of residual function is not unique and ultimately establishes the details of the residual landscape, which can complicate identification of the global minimum. The most straightforward option based simply on collection of all terms in Equation (11.13) yields a direct residual function $\mathcal{R}_{\text{direct}}$ and direct linear gradient operator $\mathcal{L}_{\text{direct}}$ given by

$$\mathcal{R}_{\text{direct}}[\Phi] = k\nabla^2\Phi + \left[\left(\nabla^2\Phi\right)^2 - \sum_{i,j}\left(\nabla_i\nabla_j\Phi\right)^2\right] - \rho, \tag{11.17}$$

$$\mathcal{L}_{\text{direct}}[\Phi] = k\nabla^2 + 2\left(\nabla^2\Phi\right)\nabla^2 - 2\sum_{i,j}\left(\nabla_i\nabla_j\Phi\right)\nabla_i\nabla_j. \tag{11.18}$$

This choice of residual and linear operator has previously been shown to produce convergence in cases where the initial trial function was chosen to be close to the true solution (Belikov and Hu, 2013; Hiramatsu et al., 2013; Ogawa et al., 2019) or in cases where the governing equation was restricted to the large-scale regime where the linear term is dominant (Schmidt, 2009). The difficulty in applying this choice of residual function to finding solutions of Equation (11.13) is that its quadratic form can yield two solution branches, leading to a residual landscape containing at least two global minima [we say "at least," because proof that there exist only two solutions to Equation (11.13) would require analysis beyond the scope of this paper]. Furthermore, our numerical tests have found that if the trial solution is not sufficiently close to the true solution, then gradient descent with this direct residual can yield solutions which settle into minima far from the true solution. Such local minima can occur when the local solution in one region of space iterates toward the repulsive branch of Equation (11.13) while the solution in a different region iterates towards the attractive branch.

Chan and Scoccimarro (2009) made the critical observation that upon solving Equation (11.13) as a quadratic equation in $\nabla^2\Phi$, one can explicitly select a solution branch and thus avoid the potential problem of different points converging to the undesired branch when the starting trial solution is not close enough to the true solution. With that insight, the positive branch is given

by

$$\nabla^2\Phi = \sqrt{\sum_{i,j}\left(\nabla_i\nabla_j\Phi\right)^2 + \rho + \left(\frac{k}{2}\right)^2} - \frac{k}{2}. \tag{11.19}$$

This then leads to the following natural choice for the residual function and gradient operator:

$$\mathcal{R}[\Phi] = \sqrt{\sum_{i,j}\left(\nabla_i\nabla_j\Phi\right)^2 + \rho + \left(\frac{k}{2}\right)^2} - \nabla^2\Phi - \frac{k}{2}, \tag{11.20}$$

$$\mathcal{L}[\Phi] = \frac{\sum_{i,j}\left(\nabla_i\nabla_j\Phi\right)\nabla_i\nabla_j}{\sqrt{\sum_{\ell,m}\left(\nabla_\ell\nabla_m\Phi\right)^2 + \rho + \left(\frac{k}{2}\right)^2}} - \nabla^2. \tag{11.21}$$

For any solution Φ of Equation (11.13), the discriminant in the square root will be positive. However, when evaluating the residual for a trial solution which is not a true solution, the discriminant will not necessarily be positive if $\rho < 0$. At galactic and cosmological scales, such $\rho < 0$ underdensities must be considered, so Chan and Scoccimarro used a discriminant splitting method to ensure that the residual could be evaluated for any trial solution. In the small-scale case around dense bodies, underdensities can be ignored, i.e., $\rho \geq 0$, and hence splitting the discriminant is unnecessary.

As we demonstrate next, this reformulation introduces a significant advantage for computation in that all critical points of $\mathcal{R}[\Phi]^2$ are global minima, due to the fact that $\mathcal{R}[\Phi]$ is a convex function unbounded from below. The convexity of $\mathcal{R}[\Phi]$ is evident from inspection of the second functional derivative of $\mathcal{R}$ acting on an arbitrary function ξ, which is always non-negative:

$$\begin{aligned}\frac{\delta^2\mathcal{R}}{\delta\Phi^2}[\xi,\xi] &= \frac{\left[\rho + \left(\frac{k}{2}\right)^2 + \sum_{i,j}\left(\nabla_i\nabla_j\Phi\right)^2\right]\sum_{i,j}\left(\nabla_i\nabla_j\xi\right)^2 - \left[\sum_{i,j}\left(\nabla_i\nabla_j\Phi\right)\left(\nabla_i\nabla_j\xi\right)\right]^2}{\left[\sum_{\ell,m}\left(\nabla_\ell\nabla_m\Phi\right)^2 + \rho + (k/2)^2\right]^{3/2}} \\ &\geq \frac{\left[\rho + \left(\frac{k}{2}\right)^2\right]\left[\sum_{i,j}\left(\nabla_i\nabla_j\xi\right)^2\right]}{\left[\sum_{\ell,m}\left(\nabla_\ell\nabla_m\Phi\right)^2 + \rho + (k/2)^2\right]^{3/2}} \geq 0.\end{aligned} \tag{11.22}$$

The functional second derivative vanishes only when ξ is a constant or a linear function. Both forms of ξ represent a gauge freedom of Φ since any constant or linear function can be added to a solution of Equation (11.13) and remain a solution; hence, $\mathcal{R}$ is convex. The unboundedness of $\mathcal{R}$ from below can be shown by considering the ansatz function $\Phi = (c/2)(x^2 + y^2 + z^2)$ representing solutions close to an extremum. Then $\nabla^2\Phi = 3c$ and $\sum_{i,j}(\nabla_i\nabla_j\Phi)^2 = 3c^2$. If $c \gg k$ and $c \gg \rho$, then $\mathcal{R}[\Phi] \approx (\sqrt{3} - 3)c$, which can assume arbitrarily large values for arbitrarily large coefficient values c.

Because $\mathcal{R}$ is a convex function unbounded from below, $\mathcal{R}^2$ has the property that the only critical points are global minima. This can be seen immediately by noting that $\delta\mathcal{R}^2/\delta\Phi = 2\mathcal{R}(\delta\mathcal{R}/\delta\Phi)$, which can vanish only if $\delta\mathcal{R}/\delta\Phi = 0$ or $\mathcal{R} = 0$. But the existence of an extremum satisfying

$\delta\mathcal{R}/\delta\Phi = 0$ would contradict the unboundedness of $\mathcal{R}$, and hence the only critical points of $\mathcal{R}^2$ correspond to points at which $\mathcal{R} = 0$, which represent global minima of $\mathcal{R}^2$. Furthermore, this implies that so long as $\mathcal{R}$ is sufficiently smooth, the global minima of $\mathcal{R}^2$ must be connected, in the sense that one solution can be continuously deformed into another while satisfying the global minimum condition $\mathcal{R}^2 = 0$. Were there to exist two separated minima, there would then have to exist a non-minimum critical point on a line connecting them, resulting in a contradiction.

The properties of $\mathcal{R}$ and $\mathcal{R}^2$ so far described represent local behavior. However, the residual function of interest, which represents a global constraint, is represented by the integral L_2 norm of $\mathcal{R}$, namely $\|\mathcal{R}[\Phi]\|^2 = \int \mathcal{R}^2[\Phi]dV$. Because the global minima of $\mathcal{R}^2$ are connected within sufficiently smooth regions of $\mathcal{R}$, then if boundary conditions allow a global solution to exist, the quantity $\|\mathcal{R}[\Phi]\|^2$ is also expected to have no minima aside from the global minimum. Rigorous proof is beyond the scope of this paper, as is proof of the existence and uniqueness of solutions to $\mathcal{R}[\Phi] = 0$ subject to Dirichlet boundary conditions. Furthermore, the strong concavity of the landscape requires $k > 0$; if k is taken to be 0 then there are no local minima but there may be saddle points. That said, we have found that in practice the numerical convergence of $\|\mathcal{R}[\Phi]\|^2$ is accurate, stable, and rapidly convergent even in the $k = 0$ limit, suggesting that the local properties of $\mathcal{R}^2$ yield a residual landscape for $\|\mathcal{R}[\Phi]\|^2$, whose geometry is highly favorable to gradient descent techniques and rapid identification of the global minimum.

Boundary conditions in numerical simulations

Solution of Equation (11.19), which is second-order, requires specification of a condition at each point on the boundary. For the axisymmetric Sun-Earth simulations, we invoked a Neumann condition reflecting symmetry about the $R = 0$ axis such that $\partial_R\Phi(R = 0, Z) = 0$. With regard to the remaining far field boundary conditions in R and Z, (or in X, Y, and Z, for the 3D Sun-Earth-Moon simulations based on Cartesian geometry), we note the following reasoning for the choice of Dirichlet conditions.

When simulations of Equation (11.19) are conducted in a computational domain whose size is much larger than the Vainshtein radii of the interior bodies, the equation becomes dominated by the linear term along the far field exterior boundaries. In this case, boundary conditions based on superposition of the individual analytic single-body solutions may represent a good choice (Hiramatsu et al., 2013). In the present study, however, the Vainshtein radii are prohibitively large and all simulations were conducted within a computational domain whose size represents relatively small scales such that the nonlinear term in Equation (11.19) is dominant. For such a nonlinear equation, there is no reason to expect that the boundary conditions applied along the domain boundaries should be accurately represented by simple superposition of single-body solutions. However, it is expected that so long as the domain edges are sufficiently far from the included bodies, they should together act as a point source or equivalently, the scalar potential function should behave as though it is driven by a single point mass.

Since in our simulations all bodies were confined to the interior of the computational domain, we adopted far field Dirichlet conditions obtained from the value of the scalar potential given by Equation (11.16) for a point mass equal to the total mass of all interior bodies positioned at the center of mass of those bodies. Were the computational domain to be spherical, this boundary condition would be a constant applied on the domain boundaries. But because the computational domain was either spherical or cubic, the spherically-symmetric solution was used to determine the values at each point of the boundary, resulting in a non-constant boundary condition. In what follows, we refer to this choice of boundary condition as the point source boundary condition (PSBC) and its dimensional value denoted by $\phi_\infty(\vec{r})$ [or dimensionless value $\Phi_\infty(\vec{R})$]. It should also be noted that for a spherically-symmetric system whose density field has compact support, the scalar potential field in the external vacuum depends only on the total mass and not its spatial distribution. Thus, a point mass and an arbitrary compact spherically-symmetric mass distribution are indistinguishable beyond their radii, and the point mass boundary condition is equivalent to the solution of the scalar potential equation forced by a spherical average of the density field. The point source boundary condition is therefore the natural physical choice for the scalar potential field at distances much greater than the separation distances of the interior bodies. For the solar system, the Sun is so massive that the relative difference between the point source solution and the linear superposition of single-body solutions is of the order of 10^{-6} and therefore essentially negligible. However, it seems inappropriate to impose far field boundary conditions based on linear superposition of individual single-body potential fields when solving a nonlinear equation.

11.3.2 Results of axisymmetric Sun-Earth system

Shown in Figure 11.1 are far-field and near-field views about the Earth body of the dimensional axisymmetric Sun-Earth Galileon field $\phi_{\rm SE}(r,z)$ $\mathrm{m}^2/\mathrm{s}^2$ for Sun (S) and Earth (E) bodies positioned on the axis of symmetry $r=0$. The body coordinates were chosen to be ($r_{\rm S}=0, z_{\rm S}=+74.80\times10^6\,\mathrm{km}=+0.5\,\mathrm{AU}$) and ($r_{\rm E}=0, z_{\rm E}=-74.80\times10^6\,\mathrm{km}=-0.5\,\mathrm{AU}$). The boundary conditions applied along the exterior edges of the cylindrical domain were $\partial_r\phi_{\rm SE}(r=0,-64\,\mathrm{AU}\le z\le+64\,\mathrm{AU})=0$, $\phi_{\rm SE}(r=+64\,\mathrm{AU},-64\,\mathrm{AU}\le z\le+64\,\mathrm{AU})=\phi_\infty(r,z)$ and $\phi_{\rm SE}(0\le r\le 64\,\mathrm{AU}, z=\pm64\,\mathrm{AU})=\phi_\infty(r,z)$. The strong spherical symmetry of the solution about the Sun body evident in Figure 11.1(a) is indicative of the fact that the field is dominated by the massive Sun. Shown in Figure 11.1(b) is a magnified view of the field about the Earth body. The results in Figure 11.1(c) and the magnified view in (d) depict the field values along the axis of symmetry near the Earth body. The results show a slight reduction in the field value near the location of the Earth body. Shown for comparison is the single-body Sun solution $\phi_{\rm S}(0,z)$ and the combined solution from linear superposition of the single-body Sun and Earth solutions $\phi_{\rm S+E}(0,z)$. At the scales shown about the Earth body, the full numerical solution $\phi_{\rm SE}(0,z)$ and the solution obtained by linear superposition of single-body solutions $\phi_{\rm S+E}(0,z)$ are virtually indistinguishable but differ from the single-body Sun solution $\phi_{\rm S}(0,z)$.

Whereas $\phi_{\rm S}(0,z)$ appears nearly linear throughout the range shown, the full solution given by $\phi_{\rm SE}$ contains a visible bend within a distance of approximately $O(10^5$ km) of the Earth center.

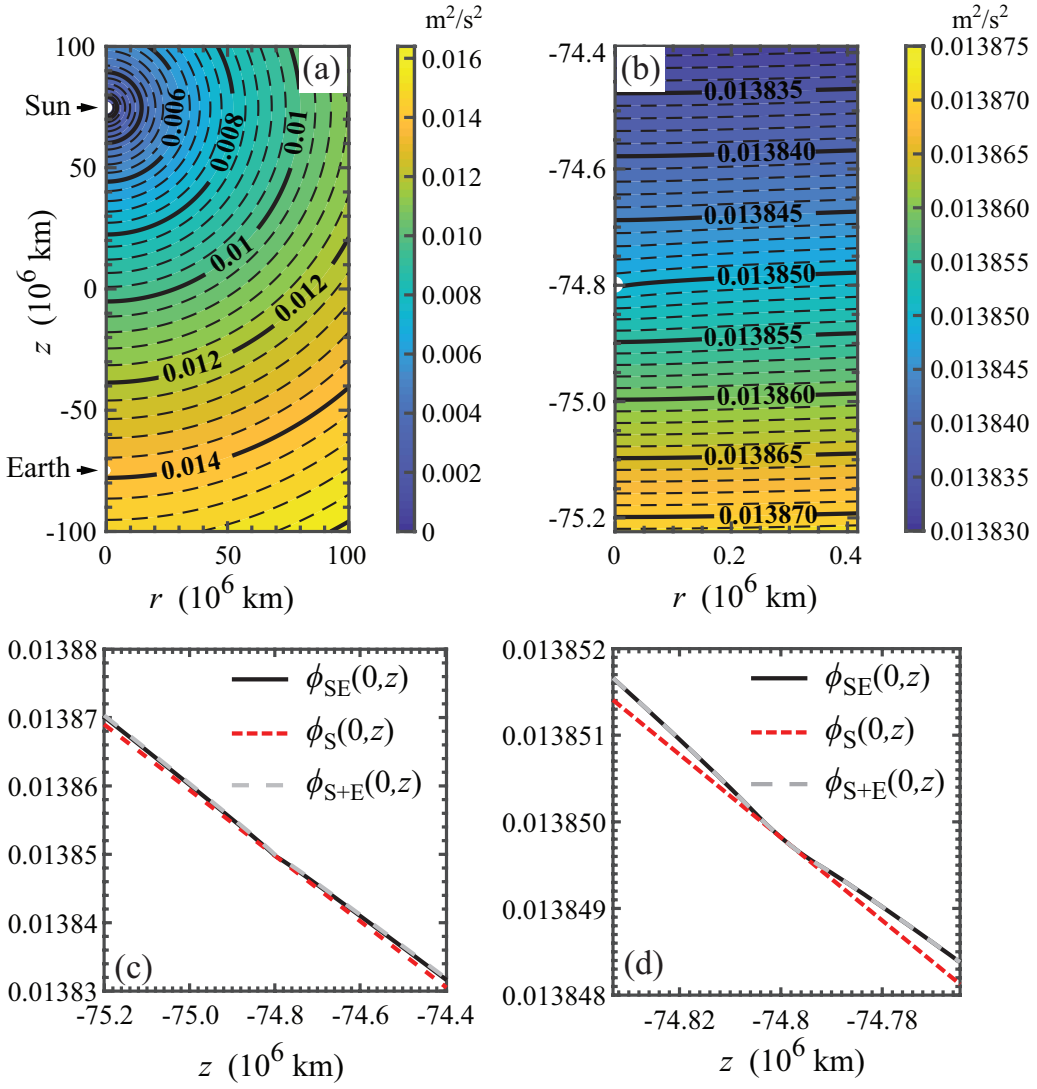

Figure 11.1: Numerical solutions for the axisymmetric Sun-Earth (SE) Galileon potential field $\phi_{\rm SE}(r,z)$ m^2/s^2. Magnitudes indicated on solid contour lines (black) correspond to major divisions on color bar; dashed contour lines represent 1/5 intermediate color bar values. Sun and Earth bodies shown in white. (a) Contour plot for region containing Sun (S) and Earth (E) bodies positioned at coordinate values ($r_{\rm S}=0, z_{\rm S}=+74.80\times10^6{\rm km}=+0.5\,{\rm AU}$) and ($r_{\rm E}=0, z_{\rm E}=-74.80\times10^6{\rm km}=-0.5\,{\rm AU}$). (b) Magnified view of (a) showing solution about the Earth center. (c) Comparison of three solutions in the vicinity of the Earth body along the line connecting the Sun and Earth bodies: full solution $\phi_{\rm SE}$ (solid black line), single-body Sun solution $\phi_{\rm S}$ (dashed red line) and combined solution $\phi_{\rm S+E}$ (dashed gray line) from linear superposition of single-body Earth and Sun solutions. Span in z equals a distance 4.17×10^5 km about Earth. (d) Magnified view of solutions in (c). Span in z equals a distance 3.48×10^4 km about Earth.

Shown in Figure 11.2 is a large scale view and near field views about the Earth body of the relative strength of the fifth force to the force of Newtonian gravity, $\|\nabla\phi_{\rm SE}(r,z)\|_G = \|\nabla\phi_{\rm SE}(r,z)\|/\|\nabla\psi_{\rm G}\|$, where $\|\cdot\|$ denotes the vector norm. These data correspond to the simulation runs shown in Figure 11.1. Here $\psi_{\rm G}$, the Newtonian potential, is the solution of $\nabla^2\psi_{\rm G}(\vec{r}) = 4\pi G\rho(\vec{r})$. The strong spherical symmetry about the massive Sun body is evident in Figure 11.2(a). The magnified plots in Figure 11.2(b) and (c) also indicate high spherical symmetry about the Earth body with only slight elongation along the z axis. The results in Figure 11.2(d) and the magnified view in (e) depict the spatial variation in the field along the axis of symmetry near the Earth body. The plots shown exclude results within the regions interior to the Earth body where the gravitational force vanishes. The results show a very slight depression near the location of the Earth body with a slight asymmetry about its center. Shown for comparison is the single-body Sun solution and the combined solution from superposition of the single-body Sun and Earth solutions. At the scales about the Earth body indicated, the full numerical solution and the superposed solution are virtually indistinguishable but differ from the single-body Sun solution. The visible asymmetry between the solutions reflects the fact that the Sun's and Earth's force fields oppose each other on the side of Earth facing the Sun and supplement each other on the side of Earth away from the Sun.

Shown in Figure 11.3 are the results for the dimensional axisymmetric Sun-Earth (SE) Laplacian field $\nabla^2\phi_{\rm SE}(r,z)$ s^{-2} plotted on a logarithmic scale for the runs shown in Figure 11.1. The strong spherical symmetry of the solution about the massive Sun body is evident in Figure 11.3(a). The magnified plots in Figure 11.3(b) and (c) make evident the anisotropy along the z axis due to the Sun body. The Laplacian field magnitude undergoes rapid decay with increasing distance from either body. The results in Figure 11.1(d) and the magnified view in (e) depict the Laplacian field values along the axis of symmetry near the Earth body. Shown for comparison is the single-body Sun solution and the superposed single-body Sun and Earth solutions. At the scales about the Earth body indicated, the full numerical solution and the superposed solution are virtually indistinguishable but differ significantly from the single-body Sun solution in form and magnitude. In particular, the Laplacian field of the single-body Sun solution is uniformly negligible by comparison. Also evident from Figure 11.1(d) is the fact that the solution obtained from superposition everywhere slightly underestimates the correct magnitude, with the discrepancy increasing with distance from the Earth body. Figure 11.1(e) shows that the Laplacian field for the Sun-Earth system within the radius of the Earth is approximately constant, beyond which it undergoes rapid decay in accord with the single-body solution given by Equation (11.16).

Shown in Figure 11.4 are numerical solutions of the normalized differences for the Galileon force and Laplacian fields, namely $\|\nabla\phi_{\rm SE}(r,z) - \nabla\phi_{\rm S+E}(r,z)\|/\|\nabla\phi_{\rm SE}(r,z)\|$ (top panel) and $[\nabla^2\phi_{\rm SE}(r,z) - \nabla^2\phi_{\rm S+E}(r,z)]/[\nabla^2\phi_{\rm SE}(r,z)]$ (bottom panel), plotted on a logarithmic scale. The relative errors are smaller near the Sun body than the Earth body. As evident from Figs. 11.4(a) and (d), these smaller errors in the vicinity of the Earth are caused by the fact that the

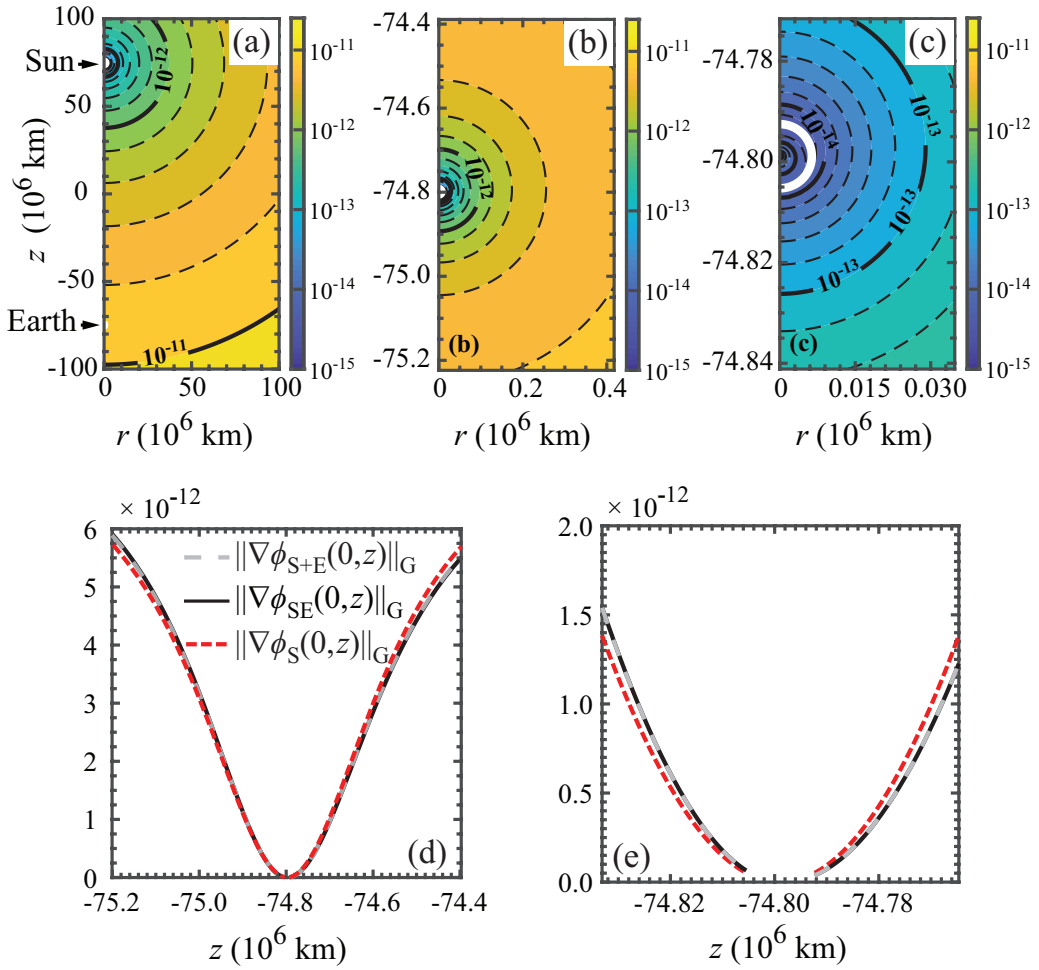

Figure 11.2: Numerical solutions for the axisymmetric Sun-Earth (SE) force field normalized by the force of gravity (G), $\|\nabla\phi_{\rm SE}(r,z)\|_G = \|\nabla\phi_{\rm SE}(r,z)\|/\|\nabla\psi_{\rm G}(r,z)\|$, where $\psi_{\rm G}(r,z)$ is the Newtonian gravitational potential. Magnitudes plotted on a logarithmic scale and indicated by solid contour lines (black) correspond to major divisions on color bar; dashed contour lines represent 1/5 intermediate color bar values. Sun and Earth bodies shown in white. (a) Contour plot in region containing Sun (S) and Earth (E) bodies positioned at coordinate values ($r_{\rm S} = 0, z_{\rm S} = +74.80 \times 10^6{\rm km} = +0.5\,{\rm AU}$) and ($r_{\rm E} = 0, z_{\rm E} = -74.80 \times 10^6{\rm km} = -0.5\,{\rm AU}$). Magnitudes plotted on a logarithmic scale. (b) Magnified view of solution in (a) centered about the Earth body. Span in z is 10% larger than the Moon's orbit radius. (c) Further magnified view of contour plot in (b). Earth body outlined in white. (d) Comparison of three solutions in the vicinity of the Earth body along the line connecting the Sun and Earth bodies: full solution $\|\nabla\phi_{\rm SE}\|_G$ (solid black line), single-body Sun solution $\|\nabla\phi_{\rm S}\|_G$ (dashed red line) and combined solution $\|\nabla\phi_{\rm S+E}\|_G$ (dashed gray line) from linear superposition of the single-body Earth and Sun solutions. Span in z equals a distance 4.17×10^5 km about Earth. (e) Magnified view of solutions in (d). Span in z equals a distance 3.48×10^4 km about Earth.

more massive Sun body has a relatively larger influence on the field about the Earth than vice versa. As evident also from Figs. 11.4(c) and (f), for distances close to the Earth body, the relative error in the force field is of the order of 0.1% while that for the Laplacian field is of

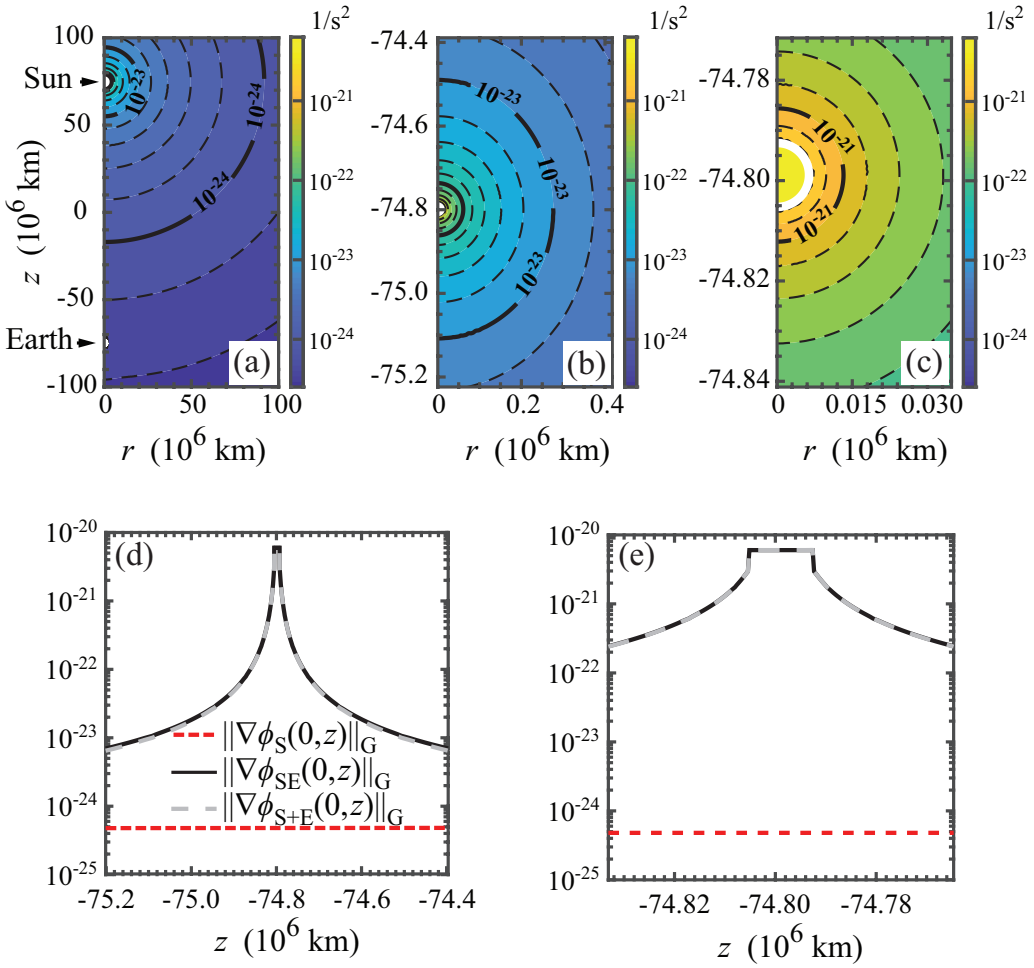

Figure 11.3: Contour plots showing the axisymmetric Sun-Earth (SE) Laplacian field distribution $\nabla^2\phi_{\rm SE}(r,z)$ s^{-2} plotted on a logarithmic scale. Magnitudes plotted on a logarithmic scale and indicated by solid contour lines (black) correspond to major divisions on color bar; dashed contour lines represent $1/5$ intermediate color bar values. Sun and Earth bodies shown in white. (a) Solution in region containing both Sun (S) and Earth (E) bodies positioned at coordinate values $(r_{\rm S}=0, z_{\rm S}=+74.80\times10^6{\rm km}=+0.5\,{\rm AU})$ and $(r_{\rm E}=0, z_{\rm E}=-74.80\times10^6{\rm km}=-0.5\,{\rm AU})$. (b) Magnified view of solution in (a) centered about the Earth body. Span in z is 10% larger than the Moon's orbit radius. (c) Magnified view of solution in (b). Earth body outlined in white. (d) Comparison of three solutions in the vicinity of the Earth body along the line connecting the Sun and Earth bodies: full solution $\nabla^2\phi_{\rm SE}$ (solid black line), single-body Sun solution $\nabla^2\phi_{\rm S}$ (dashed red line) and combined solution $\nabla^2\phi_{\rm S+E}$ (dashed gray line) from linear superposition of the single-body Earth and Sun solutions. Span in z equals a distance 4.17×10^5 km about Earth. (e) Magnified view of solutions in (d). Span in z equals a distance 3.48×10^4 km about Earth.

the order of 1%. At a distance of 4×10^5 km from Earth, these differences become larger—the relative error in the Laplacian field can exceed 15%, as shown in (e). In general too, the superposition approximation tends to underestimate the value of the Laplacian field along the

central Sun-Earth axis and to overestimate the value away from this axis.

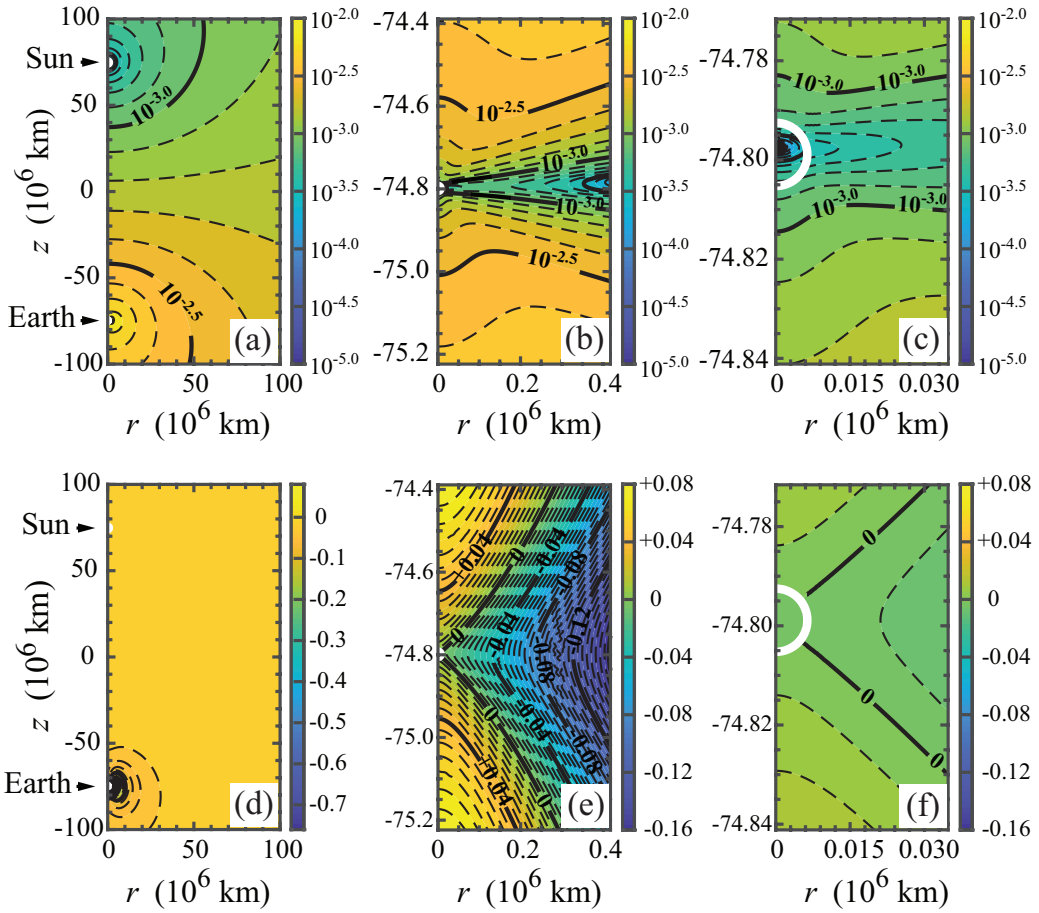

Figure 11.4: Contour plots showing the normalized differences $\|\nabla\phi_{\rm SE}(r,z) - \nabla\phi_{\rm S+E}(r,z)\|/\|\nabla\phi_{\rm SE}(r,z)\|$ (top panel) and $[\nabla^2\phi_{\rm SE}(r,z) - \nabla^2\phi_{\rm S+E}(r,z)]/[\nabla^2\phi_{\rm SE}(r,z)]$ (bottom panel) plotted on a logarithmic scale. Magnitudes indicated by solid contour lines (black) (logarithmic scale in top panel; linear scale on bottom panel) correspond to major divisions on corresponding color bar; dashed contour lines represent 1/5 intermediate color bar values. Sun and Earth bodies shown in white. (a) and (d) Solutions in region containing Sun (S) and Earth (E) bodies positioned at the coordinate values $(r_{\rm S} = 0, z_{\rm S} = +74.80 \times 10^6 {\rm km} = +0.5\,{\rm AU})$ and $(r_{\rm E} = 0, z_{\rm E} = -74.80 \times 10^6 {\rm km} = -0.5\,{\rm AU})$. (b) and (e) Magnified view of solutions in (a) and (d) centered about the Earth body. Span in r and z is 10% larger than the Moon's orbit radius. (c) and (f) Magnified view of solutions in (b) and (d) in close vicinity of the Earth body. Span in r equals a distance 3.48×10^4 km about Earth.

11.3.3 Results of Sun-Earth-Moon system

In this section, we review results of 3D simulations for the three-body Sun-Earth-Moon system computed in a cubic domain (Cartesian coordinates). The Sun (S) and Earth (E) bodies were positioned on the z axis and the Moon (M) located at a point in its orbit forming a 90° angle with the Earth and Sun. The actual coordinates used in the simulations were as follows: $(x_{\rm S} = 0, y_{\rm S} = 0, z_{\rm S} = +74.80 \times 10^6\,{\rm km} = +0.5\,{\rm AU})$, $(x_{\rm E} = 0, y_{\rm E} = 0, z_{\rm E} = -74.80 \times 10^6\,{\rm km} =$

$-0.5\,\mathrm{AU})$ and $(x_\mathrm{M} = 0, y_\mathrm{M} = -0.3845 \times 10^6\,\mathrm{km} = -0.00257\,\mathrm{AU}, z_\mathrm{M} = -74.80 \times 10^6\,\mathrm{km} = -0.5\,\mathrm{AU})$. The Dirichlet boundary conditions applied along the exterior edges of the cubic domain $-64\,\mathrm{AU} \leq (x, y, z) \leq +64\,\mathrm{AU}$ equaled those values given by Equation (11.16) for a point particle with a mass equal to the total mass of the three individual bodies positioned at the location of the three-body center of mass.

Shown in Figure 11.5 are the numerical solutions for the Sun-Earth-Moon (SEM) scalar potential field $\phi_\mathrm{SEM}(x, y, z)$ $\mathrm{m}^2/\mathrm{s}^2$. The strong spherical symmetry of the solution about the Sun body is evident in Figure 11.5(a), indicative of the fact that the potential field is dominated by that of the massive Sun. Shown in Figure 11.5(b) is a magnified view of the potential field near the Earth and Moon showing how their presence slightly distorts the local potential field. The plots in (c) and (e) show magnified views at distances close to the Earth body for the potential field along the line joining the Sun and Earth. There is no visible difference between the plots in (c) and (e) and the values plotted in Figure 11.1 (c) and (d), except for the addition of an overall constant which has no effect on the force. The results in (c) and (e) also show a slight reduction in the field near the Earth body. Shown for comparison is the single-body Sun and combined solution from superposition of the single-body Sun, Earth and Moon solutions. At the scales shown about the Earth body, the full numerical solution and the solution obtained by linear superposition are quite close but differ from the single-body Sun solution. While the single-body solution exhibits linear behavior, the full solution contains a visible bend centered about the Earth body. The results in (d) and (f) clearly show the influence of the Moon on the potential field solution in close proximity to the Earth. Here, the deviations of the full and linear superposition solutions from the single-body Sun solution are more evident. In particular, the influence of the Moon is clearly visible by the kink appearing on the curve at $y = -0.385 \times 10^6$ km. Close inspection also reveals that the full solution differs somewhat from the superposition solution. The latter appears to underestimate the correct field value near the Moon and to overestimate the value on the side of the Earth farthest from the Moon.

Figure 11.6 shows, on a logarithmic scale, large scale and near field views about the Earth body of the relative strength of the fifth force to the force of Newtonian gravity, $\|\nabla\phi_\mathrm{SE}(x, y, z)\|_G = \|\nabla\phi_\mathrm{SE}(r, z)\|/\|\nabla\psi_\mathrm{G}\|$ for the runs shown in Figure 11.5, where $\psi_\mathrm{G}(r, z)$ is the Newtonian gravitational potential. The normalized values of the force in the vicinity of the Earth and Moon bodies is on the order of 10^{-12}. As shown in (a)–(d), beyond the confines of each body, the contours are nearly spherically symmetric, with value increasing with distance from each body. The results in Figure 11.6 (e) and (f) depict the spatial variation in the normalized force field along the axis connecting the Sun and Earth bodies and the Moon and Earth bodies, respectively, centered about the Earth body. Curves exclude results within the regions interior to the Earth and Moon bodies where the gravitational force vanishes. The curves indicate a very slight reduction near the Earth body and slight asymmetry about its center. Shown for comparison is the single-body Sun solution and the combined solution from linear superposition of the single-body Sun, Earth and Moon solutions. At the scales about the Earth body shown,

the full numerical solution and the superposed solution are virtually indistinguishable and fairly close to the Sun solution, though the approximate solutions have opposing errors. In Figure 11.6 (f), all three solutions yield the same result when viewed at distances on the order of 10^6 km.

Figure 11.7 shows solutions of the Sun-Earth-Moon (SEM) Laplacian field $\nabla^2\phi_{\rm SEM}(x,y,z)$ s^{-2} for the runs in Figure 11.5, plotted on a logarithmic scale. The magnitudes about the Earth and Moon span roughly 10^{-23} to $10^{-21}\,\mathrm{s}^{-2}$, decreasing rapidly with distance from each body. Contours of the Laplacian field along the axis connecting the Earth and Moon in (b) and centered about the Moon in (c) exhibit some elongation. [The small ripples visible in some of the contours adjacent to the Moon and Earth surface boundaries in (c) and (d) are numerical artifacts due to meshing and not physical phenomena.] Shown also are close up views of the spatial variation in the Laplacian field in the vicinity of the Earth body along the line connecting the Sun and Earth (e) and Earth and Moon (f). For comparison, shown are the single-body Sun solution and the combined solution from linear superposition of the single-body Sun, Earth and Moon solutions. At the scales about the Earth body indicated in (e), the full numerical solution and the solution based on linear superposition are virtually indistinguishable and differ significantly from the uniform single-body Sun solution shown. The rapid decay with increasing distance from each body in (e) accords with the single-body solution given by Equation (11.16). The data in (f) indicate that the approximate solution based on linear superposition tends to overestimate the correct solution with increasing distance from the Earth and Moon bodies.

The contour plots depicted in Figure 11.8 show the normalized residuals for the runs in Figure 11.5 of the force field—$\|\nabla\phi_{\rm SEM} - \nabla\phi_{\rm S+E+M}\|/\|\nabla\phi_{\rm SEM}\|$ (left column) and $\|\nabla\phi_{\rm SEM} - \nabla\phi_{\rm EM} - \nabla\phi_{\rm S}\|/\|\nabla\phi_{\rm SEM}\|$ (right column)—displayed in the $x = 0$ plane on a logarithmic scale. As is the case with the residual errors for the two-body Sun-Earth system shown in Figure 11.4, the relative errors for the three-body system in Figure 11.8 are nowhere more than 1%. These errors become even smaller when the full solution is compared against the solution based on the sum of the two-body Earth-Moon ($\phi_{\rm EM}$) and single-body Sun solution, as evident in the right panel.

The contour plots in Figure 11.9 show the normalized residuals for the corresponding Laplacian fields—$(\nabla^2\phi_{\rm SEM} - \nabla^2\phi_{\rm S+E+M})/(\nabla^2\phi_{\rm SEM})$ (left column) and $(\nabla^2\phi_{\rm SEM} - \nabla^2\phi_{\rm EM} - \nabla^2\phi_{\rm S})/(\nabla^2\phi_{\rm SEM})$ (right column). The relative errors corresponding to $(\nabla^2\phi_{\rm SEM} - \nabla^2\phi_{\rm S+E+M})/(\nabla^2\phi_{\rm SEM})$ (left column) are of the order of 1% within distances of about 10^5 km from the Earth body but increase to about 80% at distances of about 2×10^5 km from the Moon. The relative errors corresponding to $(\nabla\phi_{\rm SEM} - \nabla\phi_{\rm EM} - \nabla\phi_{\rm S})/(\nabla\phi_{\rm SEM})$ (right column) are smaller though still reach values of 15% at a distances of about 2×10^5 km from the Moon. We note that the small-scale undulations visible on some of the contour lines are numerical artifacts due to the mesh size, which can be resolved by enforcing much finer meshes in the vicinity of the respective masses shown.

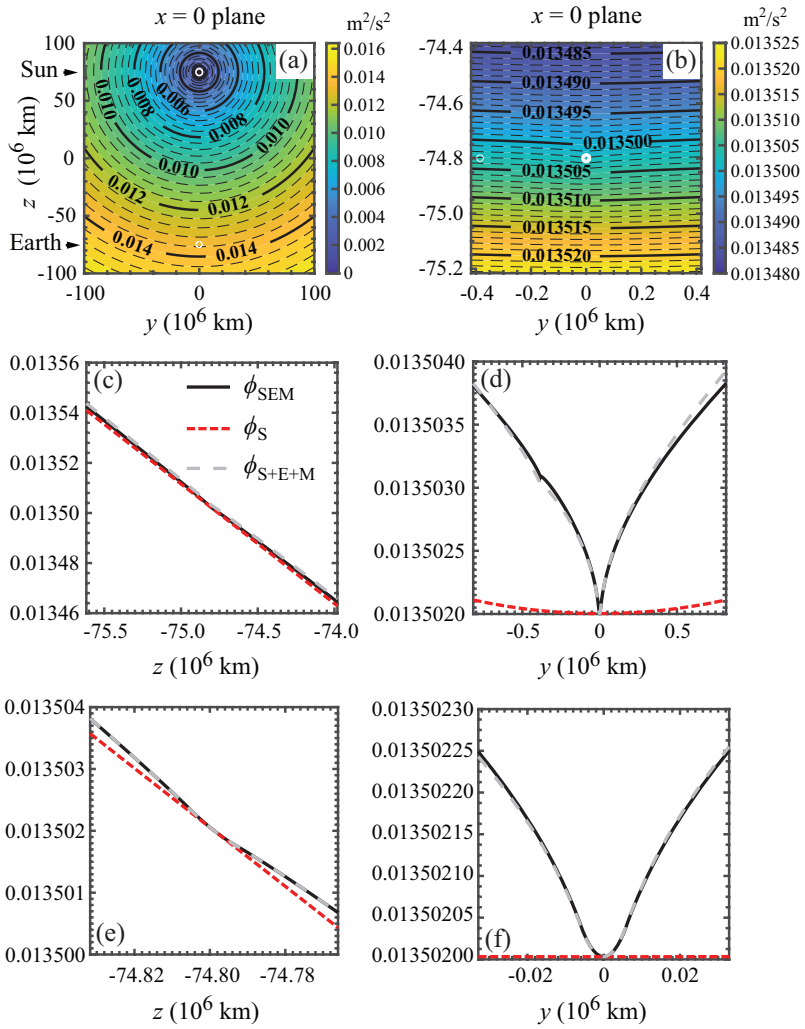

Figure 11.5: Numerical solutions for the Sun-Earth-Moon (SEM) scalar potential field $\phi_{\rm SEM}(x,y,z)$ [m^2/s^2] displayed in the $x = 0$ plane. Magnitudes indicated on solid contour lines (black) correspond to major divisions on color bar; dashed contour lines represent $1/5$ intermediate color bar values. Sun, Earth and Moon bodies shown in white. (a) Contour plot in region containing Sun (S), Earth (E) and Moon (M) bodies positioned at the coordinate values $(x_{\rm S} = 0, y_{\rm S} = 0, z_{\rm S} = +74.80\times10^6\,{\rm km} = +0.5\,{\rm AU})$, $(x_{\rm E} = 0, y_{\rm E} = 0, z_{\rm E} = -74.80\times10^6\,{\rm km} = -0.5\,{\rm AU})$ and $(x_{\rm M} = 0, y_{\rm M} = -0.3845\times10^6\,{\rm km} = -0.00257\,{\rm AU}, z_{\rm M} = -74.80\times10^6\,{\rm km} = -0.5\,{\rm AU})$. (b) Magnified view of solution in (a) centered about the Earth body with the Moon to its left. (c) Comparison of three solutions in the vicinity of the Earth body along the line connecting the Sun and Earth bodies: full solution $\phi_{\rm SEM}$ (solid black), single-body Sun solution $\phi_{\rm S}$ (dashed red) and combined solution $\phi_{\rm S+E+M}$ (dashed gray) from linear superposition of the single-body Earth, Sun and Moon solutions. Span in z equals a distance 8.35×10^5 km about Earth. (d) Comparison of three solutions in the vicinity of the Earth body along the line connecting the Earth and Moon: full solution $\phi_{\rm SEM}$, single-body Sun solution $\phi_{\rm SEM}$ and combined solution $\phi_{\rm S+E+M}$ from linear superposition of the single-body Earth, Sun and Moon solutions. (e) Magnified view of solutions in (c) in the vicinity of the Earth body. (f) Magnified view of solutions in (d) in the vicinity of the Earth body.

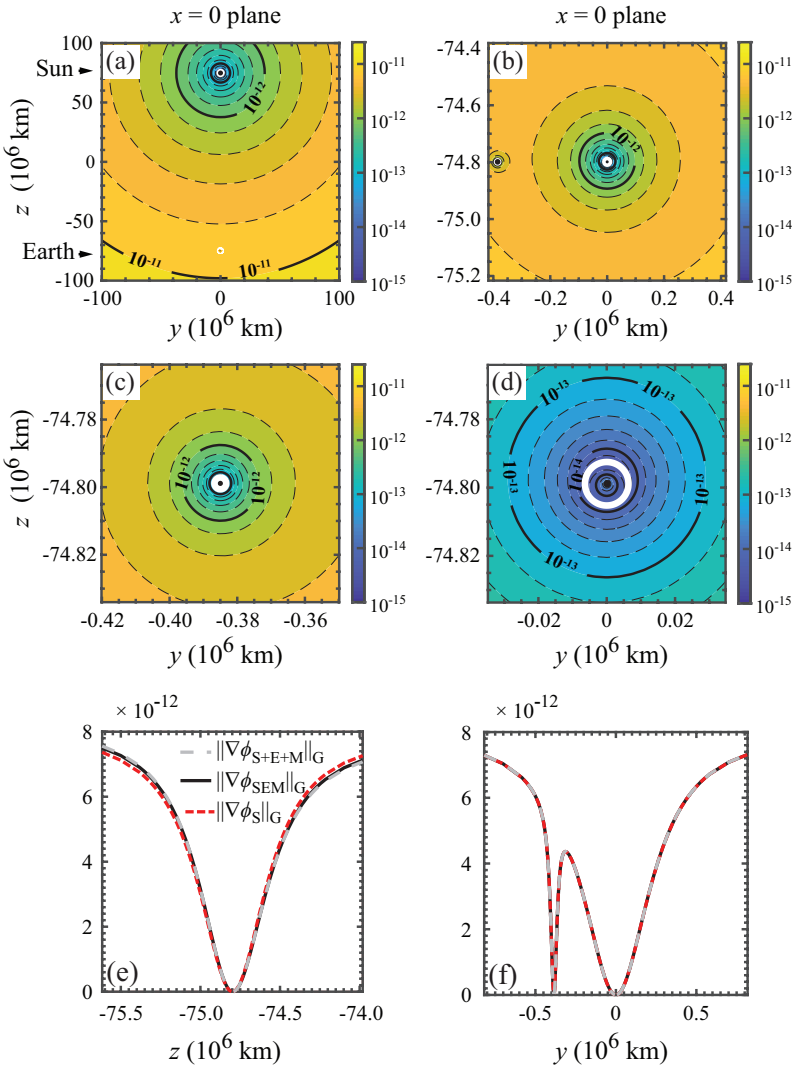

Figure 11.6: Numerical solutions for the Sun-Earth-Moon (SEM) force field normalized by gravity (G), $\|\nabla\phi_{\rm SEM}(x,y,z)\|_G = \|\nabla\phi_{\rm SEM}(x,y,z)\|/\|\nabla\psi_{\rm G}(x,y,z)\|$ displayed in the $x = 0$ plane and on a logarithmic scale, corresponding to the simulation runs in Figure 11.5. Magnitudes indicated by solid contour lines (black) correspond to major divisions on color bar; dashed contour lines represent 1/5 intermediate color bar values. Sun, Earth and Moon bodies shown in white. The plots exclude regions interior to the Earth and Moon bodies where the gravitational force vanishes. (a) Contour plot showing Sun (S), Earth (E) and Moon (M) bodies positioned at coordinate values $(x_{\rm S} = 0, y_{\rm S} = 0, z_{\rm S} = +74.80\times10^6{\rm km} = +0.5\,{\rm AU})$, $(x_{\rm E} = 0, y_{\rm E} = 0, z_{\rm E} = -74.80\times10^6{\rm km} = -0.5\,{\rm AU})$ and $(x_{\rm M} = 0, y_{\rm M} = -0.3845\times10^6{\rm km} = -0.00257\,{\rm AU}, z_{\rm M} = -74.80\times10^6{\rm km} = -0.5\,{\rm AU})$. (b) Magnified view of solution in (a) centered about Earth body with the Moon to its left. (c) Magnified view of solution in (b) centered about the Moon body. (d) Magnified view of solution in (b) centered about Earth body (surface outlined in white). (e) Comparison of three solutions in the vicinity of the Earth body along the line connecting the Sun and Earth bodies: full solution $\|\nabla\phi_{\rm SEM}\|_G$ (solid black), single-body Sun solution $\|\nabla\phi_{\rm S}\|_G$ (dashed red) and combined solution $\|\phi_{\rm S+E+M}\|_G$ from linear superposition of the single-body Earth, Sun and Moon solutions (dashed gray). Span in z equals a distance 8.35×10^5 km about Earth. (f) Comparison of three solutions in the vicinity of the Earth body along the line connecting the Earth and Moon: full solution, single-body Sun solution and combined solution.

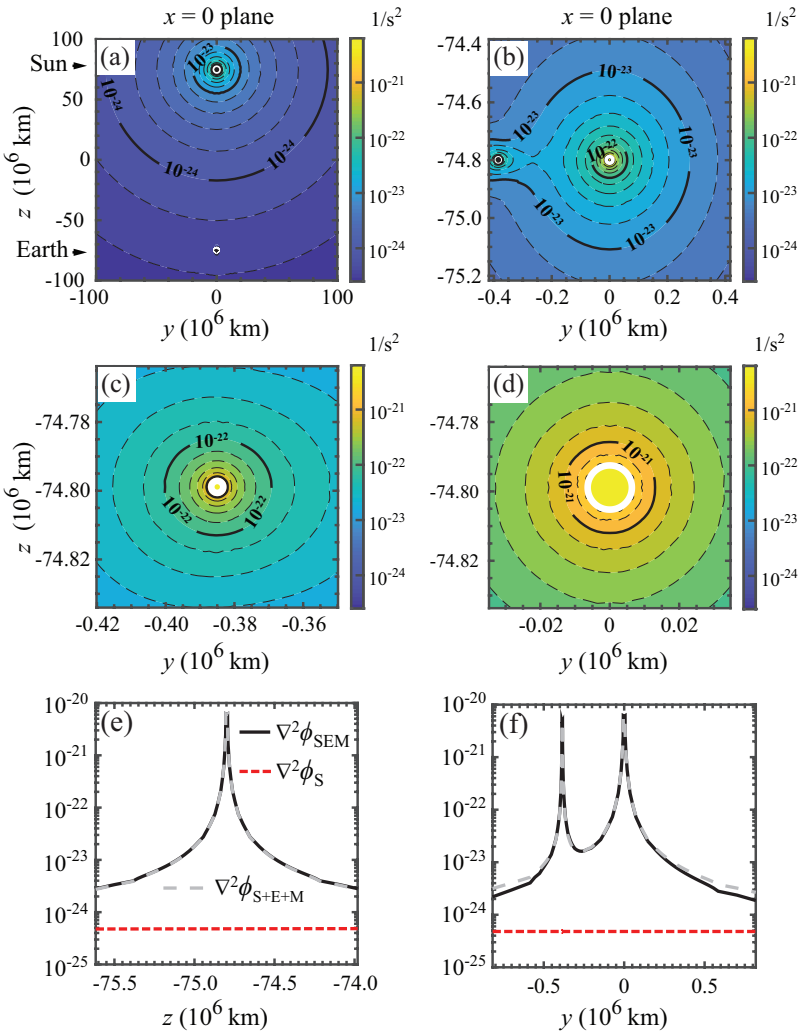

Figure 11.7: Numerical solutions for the Sun-Earth-Moon (SEM) Laplacian field $\nabla^2\phi_{\rm SEM}(x,y,z)$ s^{-2} on a logarithmic scale, corresponding to the simulation runs in Figure 11.5. Magnitudes indicated by solid contour lines (black) correspond to major divisions on color bar; dashed contour lines represent 1/5 intermediate color bar values. Sun, Earth and Moon bodies shown in white. (a) Contour plot in region containing Sun (S), Earth (E) and Moon (M) bodies positioned at the coordinate values $(x_{\rm S}=0, y_{\rm S}=0, z_{\rm S}=+74.80\times10^6{\rm km}=+0.5\,{\rm AU})$, $(x_{\rm E}=0, y_{\rm E}=0, z_{\rm E}=-74.80\times10^6{\rm km}=-0.5\,{\rm AU})$ and $(x_{\rm M}=0, y_{\rm M}=-0.3845\times10^6{\rm km}=-0.00257\,{\rm AU}, z_{\rm M}=-74.80\times10^6{\rm km}=-0.5\,{\rm AU})$. (b) Magnified view of (a) centered about the Earth body with the Moon body to its left. (c) Magnified view of (b) centered about the Moon. (d) Magnified view of (b) centered about Earth. (e) Comparison of solutions in the vicinity of the Earth body along the line connecting the Sun and Earth: full solution $\nabla^2\phi_{\rm SEM}$ (solid black), single-body Sun solution $\nabla^2\phi_{\rm S}$ (dashed red) and combined solution $\nabla^2\phi_{\rm S+E+M}$ (dashed gray) from linear superposition of the single-body Earth, Sun and Moon solutions. Span in z equals a distance 8.35×10^5 km about the Earth. (f) Comparison of three solutions in the vicinity of the Earth body along the line connecting the Moon and Earth: full solution, single-body Sun solution and combined solution.

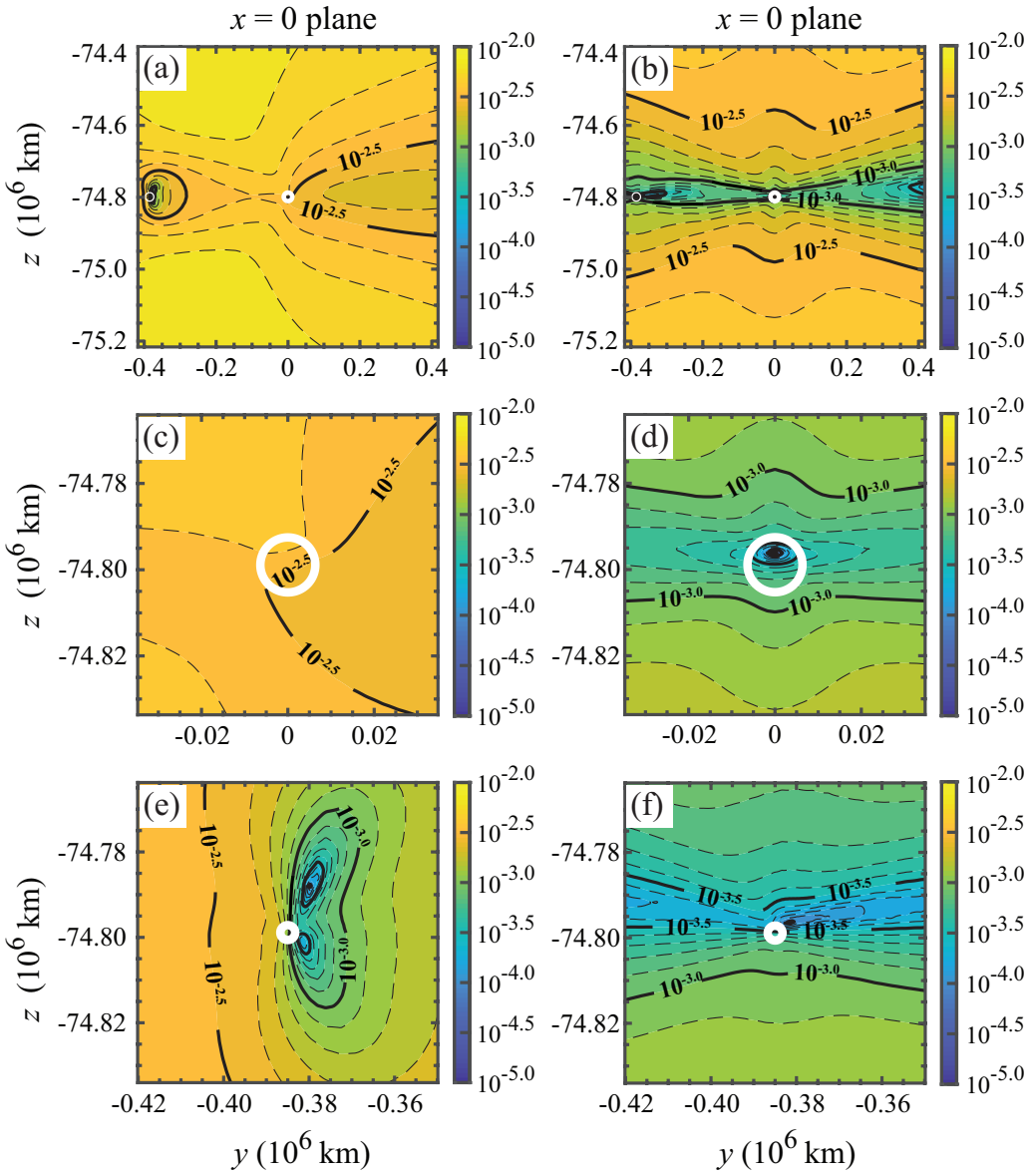

Figure 11.8: Contour plots showing normalized residuals of the force field - $\|\nabla\phi_{\mathrm{SEM}} - \nabla\phi_{\mathrm{S+E+M}}\|/\|\nabla\phi_{\mathrm{SEM}}\|$ (left column) and $\|\nabla\phi_{\mathrm{SEM}} - \nabla\phi_{\mathrm{EM}} - \nabla\phi_{\mathrm{S}}\|/\|\nabla\phi_{\mathrm{SEM}}\|$ (right column) - displayed in the $x = 0$ plane on a logarithmic scale, corresponding to the simulation runs in Figure 11.5. Magnitudes indicated by solid contour lines (black) correspond to major divisions on color bar; dashed contour lines represent 1/5 intermediate color bar values. Earth and Moon bodies shown in white. (a) and (b) Contour plots showing Earth body with Moon to its left. Body coordinates values are $(x_{\mathrm{S}} = 0, y_{\mathrm{S}} = 0, z_{\mathrm{S}} = +74.80 \times 10^6\mathrm{km} = +0.5\,\mathrm{AU})$, $(x_{\mathrm{E}} = 0, y_{\mathrm{E}} = 0, z_{\mathrm{E}} = -74.80 \times 10^6\mathrm{km} = -0.5\,\mathrm{AU})$ and $(x_{\mathrm{M}} = 0, y_{\mathrm{M}} = -0.3845 \times 10^6\mathrm{km} = -0.00257\,\mathrm{AU}, z_{\mathrm{M}} = -74.80 \times 10^6\mathrm{km} = -0.5\,\mathrm{AU})$. (c) and (d) Magnified view of solutions in (a) and (b) centered about the Earth body (surface outlined in white). (e) and (f) Magnified view of solutions in (a) and (b) centered about the Moon body (shaded in white).

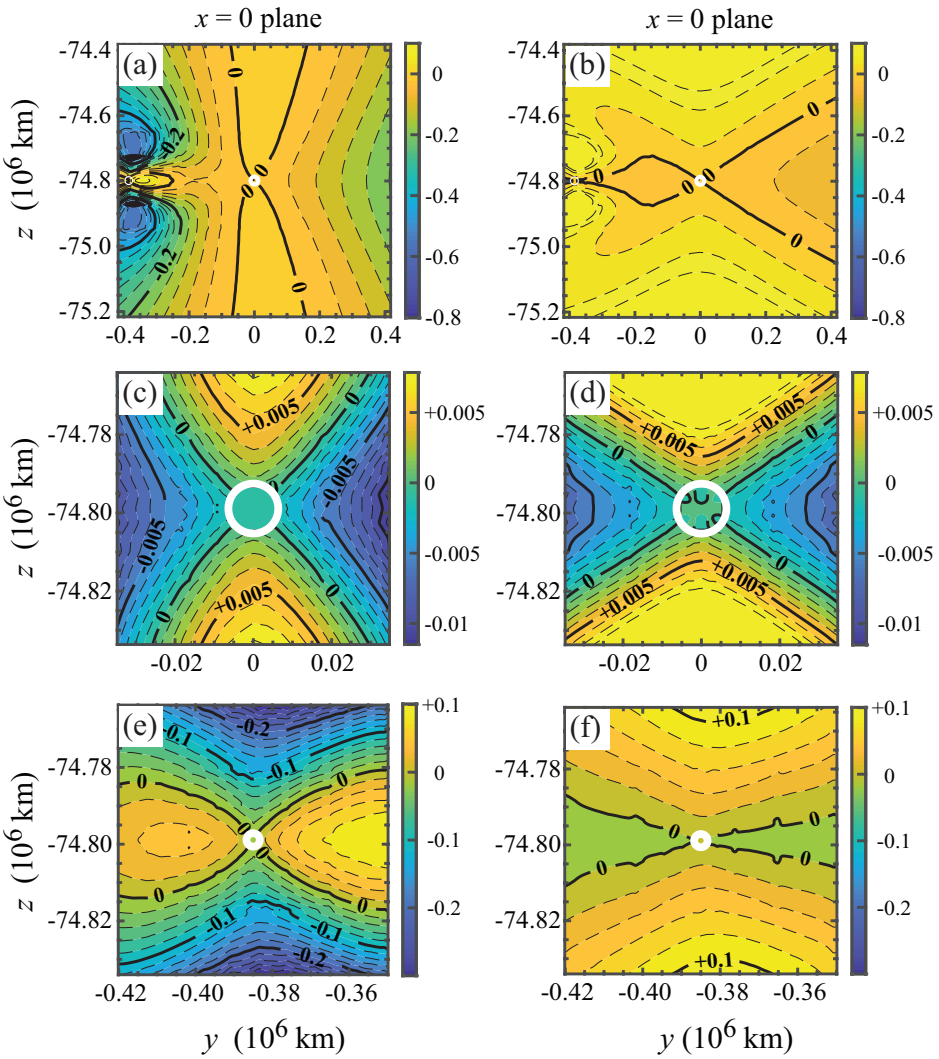

Figure 11.9: Contour plots showing the normalized residuals of the Laplacian fields—$(\nabla^2\phi_{\rm SEM} - \nabla^2\phi_{\rm S+E+M})/(\nabla^2\phi_{\rm SEM})$ (left column) and $(\nabla^2\phi_{\rm SEM} - \nabla^2\phi_{\rm EM} - \nabla^2\phi_{\rm S})/(\nabla^2\phi_{\rm SEM})$ (right column)—displayed in the $x = 0$ plane on a linear scale, corresponding to the simulation runs in Figure 11.5. Magnitudes indicated by solid contour lines (black) correspond to major divisions on color bar; dashed contour lines represent $1/5$ intermediate color bar values. Earth and Moon bodies shown in white. (a) and (b) Contour plots showing Earth body with Moon to its left. Body coordinates values are $(x_{\rm S} = 0, y_{\rm S} = 0, z_{\rm S} = +74.80 \times 10^6{\rm km} = +0.5\,{\rm AU})$, $(x_{\rm E} = 0, y_{\rm E} = 0, z_{\rm E} = -74.80 \times 10^6{\rm km} = -0.5\,{\rm AU})$ and $(x_{\rm M} = 0, y_{\rm M} = -0.3845 \times 10^6{\rm km} = -0.00257\,{\rm AU}, z_{\rm M} = -74.80 \times 10^6{\rm km} = -0.5\,{\rm AU})$. (c) and (d) Magnified view of solutions in (a) and (b) centered about the Earth body (surface outlined in white). (e) and (f) Magnified view of solutions in (a) and (b) centered about the Moon body (shaded in white).

11.3.4 Discussion

The results presented were obtained from numerical simulations of 2D axisymmetric and 3D Cartesian scalar potential fields at solar system scales in the cubic Galileon gravity model given by Equation (11.15) in the limit where the coefficient of the linear Laplacian term vanishes ($k = 0$). These studies for the two-body Sun-Earth system indicate that despite the nonlinearity of the governing equation, linear superposition of the individual Sun and Earth potential fields satisfying Equation (11.16) for a single-body, spherically symmetric mass provides a satisfactory first-order approximation to the correct scalar field. Inspection of the corresponding differences for higher-order derivatives such as the force and Laplacian fields, both critical to experimental measurements, indicate significant deviations away from the two bodies. These results highlight that despite their sizable separation distance, the nonlinear couplings between the Earth and Sun bodies play a significant role. For the studies involving the three-body Sun-Earth-Moon system, we find that linear superposition of the individual Sun, Earth and Moon potential fields satisfying Equation (11.16) for a single-body, spherically symmetric mass do not provide a satisfactory first-order approximation to the correct scalar field. Differences between the correct solution and approximations based on superposition fields for the force and Laplacian become unacceptably large.

These phenomena can be simply traced to the relatively small distance separating the Earth and Moon and the large distance separating the Earth and Sun. For the two-body Sun-Earth system, the field is dominated by the massive Sun body and its corresponding force field is practically constant in the vicinity of the Earth. This background force field (i.e., the gradient of the Sun potential field) near the Earth does not affect solutions to Equation (11.13) due to Galilean invariance. By contrast, the Earth and Moon are closer in mass and distance, and therefore the single-body potential field of each is stronger and the corresponding gradient functions (forces) no longer relatively constant. The two-body Earth and Moon system is therefore expected to exhibit stronger nonlinear coupling than the two-body Sun and Earth system. Indeed, the approximate solutions for the force fields and Laplacian fields based on linear superposition of the two-body Earth-Moon system and the single-body Sun solution (see right columns of Figs. 11.8 and 11.9) show an accuracy comparable to that of the superposition solution for the two-body Sun-Earth system.

Based on our findings, we recommend that space-based detection schemes for measurements at solar system scales, which are designed around the fact that the Laplacian field for Newtonian gravity vanishes identically, will be best served by relying on predictions based on three-body Sun-Earth-Moon simulations (Yu et al., 2018). This will avoid potentially large errors in the range of 10-15 % near the Earth-Moon region reported in this study. We also recommend that such detection missions be positioned in regions where the fifth force is relatively strong compared to Newtonian gravity. Our results in Figure 11.6 (f) indicate that this ratio achieves a local maximum between the Earth and Moon body, corresponding to the location where their individual gravitational fields nearly cancel. This then provides an optimal location for

detection of the fifth force. In fact, the results in Figure 11.7 (b) showing significant elongation of the Laplacian field along the axis connecting the two bodies suggest that the location choice based on a local maximum in the force can also be balanced against regions exhibiting strong modulation in the Laplacian field in order to seek optimal orbits for detection and measurement.

11.4 Conclusion

In this work, we provide an accurate, stable and rapidly convergent numerical scheme for solution of the 2D axisymmetric and 3D Cartesian scalar potential fields at solar system scales in the cubic Galileon gravity model given by Equation (11.15). The method should be equally effective for non-vanishing k. The approach taken derives from the fact that the solar system must be treated differently from systems modeled at galactic and cosmological scales since dense mass sources have compact support and the distances relevant to solar system bodies fall well within the Vainshtein radii.

We illustrate the numerical method by obtaining solutions for the 2D axisymmetric Sun-Earth system and 3D Cartesian Sun-Earth-Moon system. The iteration scheme is based on gradient descent of a residual function representing the positive (attractive) branch of the governing equation, which is quadratic in the Laplacian field. Due to the assumption that the dense mass sources dominate local underdensities, the algorithm converges rapidly toward the global minimum, regardless of the initial trial solution. This behavior is confirmed by a simple analytic argument. The proposed iteration scheme is therefore robust against initial trial solutions and converges rapidly to the global minimum representing the correct two-body and three-body solutions. Generally speaking, the results of our simulations indicate that the approximate solutions based on linear superposition of fields of individual bodies may be an acceptable zero order approximation to the correct solution. But even in cases where the full 2D or 3D Galileon potential solutions do not deviate too strongly from the solutions obtained by linear superposition, higher derivatives of the scalar field, namely the force and Laplacian fields, always show unacceptable discrepancy. And since current detection schemes are being designed around measurement of the Laplacian field, we discourage use of approximate solutions based on linear superposition as a substitute for the correct solution.

Regarding the choice of boundary conditions used in such simulations, we offer the following suggestions as well. The validation studies provided in Section 11.6.2 offer good evidence that the far field boundary condition we applied is acceptable so long as the boundaries of the computational domain are placed sufficiently far from the location of all interior bodies. This boundary condition mimics the influence of an interior point source mass equal to the total mass of all interior bodies positioned at the center of mass of those bodies. Sensitivity studies to investigate the influence of choice of far field boundary condition should also be conducted in order to quantify how boundary perturbations affect the solution in the interior domain. In addition to this issue, even more realistic simulations can be conducted by attributing density profiles to massive bodies with spatial variation. Of course, for even more accurate predictions of

the scalar, force and Laplacian fields for detection missions, even finer meshes are recommended. One could also consider a different parameter r_c or include a non-unity β term. Doing so would only multiply the results by a constant factor, giving a different estimate for the relative strength of the Galileon force and Newtonian gravity, but otherwise having no effect on our conclusions.

We anticipate that our methodology can be adopted in support of future detection missions seeking to validate the Vainshtein screening mechanism at small scales. To this end, we hope the results of this study can better guide the design of future instrumentation and bounds on precision required for such missions. To facilitate distribution of our software code and encourage further testing, we provide the following link `https://www.github.com/nwhite-math/small-GaPS`, where this material can be freely downloaded.[1]

11.5 Details of implemented iteration scheme

11.5.1 Algorithm

We present the numerical scheme used in the numerical simulations along with tests conducted to verify accuracy, stability and convergence. Note that all computations were performed in dimensionless variables according to Table 11.1; however, results are presented here in dimensional form for convenience.

The iteration scheme mentioned in Section 11.3.1 was carried out in MATLAB (Mat, 2015) using central finite difference discretization. The mesh consisted of a discrete set of points describing a series of nested rectilinear grids described in more detail in Section 11.5.2. All quantities of interest were therefore defined on mesh points. Each mesh point was specified by a unique number ranging from 1 to N_{mesh}, the latter denoting the total number of mesh points. Each quantity of interest, such as Φ or ρ, was stored as a vector of length N_{mesh}, where the ith component defined its value at mesh point i.

The density field $\rho(\vec{r})$ for each body mass was constructed by setting all mesh points within the interior equal to the relevant density value listed in Table 11.1. All mesh points in empty space between and around bodies were set to zero. The boundary surfaces were therefore defined to within a mesh length. The initial trial solution for the non-dimensional scalar field, $\Phi^{(n=0)}$, was then constructed from the summation of the single-body solutions obtained from Equation (11.16) according to their respective masses. As discussed in Section 11.3.1, however, any other trial solution is acceptable. The values of $\Phi^{(n=0)}$ at the boundaries were then set to the required boundary conditions. For the 2D axisymmetric Sun-Earth simulations, we applied a Neumann condition along the symmetry axis $R = 0$ such that $\partial_R \Phi(R = 0, Z) = 0$. With regard to the remaining far field boundary conditions in R and Z, and for the far field boundary conditions chosen for the 3D Sun-Earth-Moon simulations based on Cartesian geometry, we adopted Dirichlet conditions obtained from the value of the scalar potential given by Equation (11.16).

[1] An archived version including both code and data is available at `https://dataverse.harvard.edu/dataverse/nwhite-cubic-galileon-sun-earth-moon`.

Because the initial trial solution was always made to satisfy the boundary condition, iterative corrections were computed using homogeneous boundary conditions.

Discrete differential operators $\widehat{\partial}_r$, $\widehat{\partial}_r^2$, $\widehat{\partial}_z$, and $\widehat{\partial}_z^2$ for the 2D axisymmetric simulations and $\widehat{\partial}_x$, $\widehat{\partial}_x^2$, $\widehat{\partial}_y$, $\widehat{\partial}_y^2$, $\widehat{\partial}_z$, and $\widehat{\partial}_z^2$ for the 3D Cartesian simulations (where $\widehat{\partial}$ denotes the discrete version of ∂) were constructed according to the central difference scheme described in Section 11.5.2. Each of these operators was stored as an $N_{\text{mesh}} \times N_{\text{mesh}}$ matrix.

At each iteration step n, the corresponding discrete residual function for Equation (11.20) given by

$$\mathcal{R}^{(n)} = \sqrt{\sum_{i,j} \left(\widehat{\partial}_i \widehat{\partial}_j \Phi^{(n)}\right)^2 + \rho + \left(\frac{k}{2}\right)^2} - \sum_i \widehat{\partial}_i^2 \Phi^{(n)} - \frac{k}{2}, \tag{11.23}$$

and the discrete linear operator for Equation (11.21) given by

$$\widehat{\mathcal{L}}^{(n)} = \frac{\sum_{i,j} \left(\widehat{\partial}_i \widehat{\partial}_j \Phi^{(n)}\right) \widehat{\partial}_i \widehat{\partial}_j}{\sqrt{\sum_{\ell,m} \left(\widehat{\partial}_\ell \widehat{\partial}_m \Phi^{(n)}\right)^2 + \rho + \left(\frac{k}{2}\right)^2}} - \sum_i \widehat{\partial}_i^2 \tag{11.24}$$

were computed. Here we include the linear term with coefficient k. For $i \neq j$, the term $\widehat{\partial}_i \widehat{\partial}_j$ was computed by matrix multiplication since even in discrete form, the product is commutative. The term $\widehat{\partial}_i^2$ was computed using its own stencil instead of multiplying together the two first-order derivative operators. We refer to Section 11.5.2 for further explanation. Like the $\widehat{\partial}_i$ operator matrix, the linear operator $\widehat{\mathcal{L}}^{(n)}$ was also stored as an $N_{\text{mesh}} \times N_{\text{mesh}}$ matrix.

The correction step $\xi^{(n)}$ was then computed by solving the equation

$$\widehat{\mathcal{L}}^{(n)} \xi^{(n)} = -\mathcal{R}^{(n)}. \tag{11.25}$$

This step, based on a linear solver, is described in more detail below. The correction $\xi^{(n)}$ was then added to the current value of $\Phi^{(n)}$ to yield the updated solution $\Phi^{(n+1)}$, namely

$$\Phi^{(n+1)} = \Phi^{(n)} + \nu \xi^{(n)}. \tag{11.26}$$

Had the classical Newton-Raphson method been used instead, the gradient step size ν would have equalled 1 (Householder, 1953), but convergence would not have been guaranteed. Dynamically reducing ν to be less than 1 ensured that the integrated residual decreased at every iteration (Broyden, 1965). In the present implementation, ν was chosen to be 1 whenever possible. If $\int (\mathcal{R}^{(n+1)}[\Phi^{(n)} + \xi^{(n)}])^2 dV > \int (\mathcal{R}^{(n)}[\Phi^{(n)}])^2 dV$ (i.e., the residual error did not decrease), then ν was halved to a value of 0.5. If this smaller step size still did not reduce the residual error, ν was halved yet again. In this manner, the step size ν was continually decreased by powers of two until either the residual decreased or attained a limiting value of 10^{-10}. Once

a value of ν was found which successfully reduced the residual, the iteration loop was allowed to continue, i.e., $\mathcal{R}^{(n+1)}$, $\widehat{\mathcal{L}}^{(n+1)}$, $\xi^{(n+1)}$, etc were constructed. If no step size ν could be found which reduced the residual, then the iteration loop was either aborted or switched to a different linear solver, as described below.

The boundary conditions were handled in two different ways. Whenever the iteration loop for a minimum step size ν did not reduce the value of the residual, the algorithm was switched to an alternate linear solver that applied the boundary conditions differently. This approach was found to improve the final value of the residual by a few percent in comparison to results obtained using either solver alone.

Some additional notation is required before describing these linear solvers. Let $B \subset \{1, \ldots, N_{\text{mesh}}\}$ denote the set of mesh points on the boundary of the computational domain, and I denote the mesh points within the domain interior, so that $I \cup B = \{1, \ldots, N_{\text{mesh}}\}$. Let square brackets denote indexing, so that for example, $\xi^{(n)}[I]$ denotes the subvector of $\xi^{(n)}$ defined on interior mesh points and $\widehat{\mathcal{L}}^{(n)}[I \cup B, I]$ denotes the rectangular submatrix of $\widehat{\mathcal{L}}^{(n)}$ consisting of rows corresponding to all nodes and columns corresponding only to interior nodes.

The first linear solver relied only on the interior points such that

$$\begin{aligned} \xi^{(n)}[B] &= 0, \\ \widehat{\mathcal{L}}^{(n)}[I, I]\xi^{(n)}[I] &= -\mathcal{R}^{(n)}[I]. \end{aligned} \tag{11.27}$$

Since the matrix $\widehat{\mathcal{L}}^{(n)}[I, I]$ is square and invertible, a solution was guaranteed, which was obtained using the direct solver in MATLAB `mldivide` based on least squares. This was the approach taken for most of the runs conducted. For cases involving large 3D meshes, the iterative biconjugate gradient solver `bicgstab` in MATLAB was used instead, with the diagonal of $\widehat{\mathcal{L}}^{(n)}[I, I]$ used as a preconditioner. When the process `bicgstab` failed to converge, the algorithm was made to revert back to the direct solver `mldivide`. The second linear solver relied on the fact that $\mathcal{R}^{(n)}$ is defined on both interior and boundary nodes such that the equation could be solved immediately as a least squares problem using `mldivide`, according to which

$$\begin{aligned} \xi^{(n)}[B] &= 0, \\ \xi^{(n)}[I] &= \underset{\xi^{(n)}[I]}{\arg\min} \left(\widehat{\mathcal{L}}^{(n)}[I \cup B, I]\xi^{(n)}[I] + \mathcal{R}^{(n)}[I \cup B] \right)^2. \end{aligned} \tag{11.28}$$

11.5.2 Nested grid finite difference scheme

One of the challenges in simulating the scalar potential field over solar system distances is the range of length scales which must be resolved numerically. For example, the radius of the Sun is approximately 5×10^{-3} AU, while the radius of Earth is only about 4×10^{-5} AU. Constructing a uniform 3D rectilinear mesh covering one cubic AU, with mesh spacing of one Earth radius, would easily demand about 10^{13} points, clearly not an effective use of computational resources. One alternative is to construct a rectilinear mesh with variable mesh spacing, the approach used

by Hiramatsu et al. (2013). Constraining variable mesh spacings to be rectilinear, however, inevitably leads to distorted spacings of high aspect ratio in regions where the mesh is fine along one coordinate axis but coarse along another. When possible, it is preferable instead to implement local mesh refinement.

To resolve this issue without introducing an entirely unstructured mesh, a system of nested rectilinear meshes was employed. This choice led to two types of mesh points: interior points which were not on a boundary between coarse and fine regions, and boundary points. Derivatives on interior points were then computed at second order using a 3-point central difference scheme, while boundary points involved a more complex stencil to include interpolated "halo points" (Figueroa and Löhner, 2019). A diagram outlining this nested mesh scheme (confined to 2D for simplicity) is shown in Figure 11.10. The solid circles (blue) denote mesh points on a fine mesh with spacing of h, the solid squares (red) denote mesh points on an exterior coarser mesh with spacing of $2h$, and the open diamonds (white) denote interpolated halo points.

We illustrate this scheme for the 3D Cartesian system. Let x, y and z coordinates be indexed by i, j, k so that $\{i+1, j, k\}$ is the point immediately adjacent to $\{i, j, k\}$ along the x-axis. Let $f_{i,j,k}$ denote the value of a scalar function f on the mesh point $\{i, j, k\}$ where $x_{i,j,k}$ denotes the value of the coordinate x at that point, and so on. Let then $x_{i,j,k} - x_{i-1,j,k} = h_1$ and $x_{i+1,j,k} - x_{i,j,k} = h_2$. In Figure 11.10, $h_1 = h$ and $h_2 = 2h$.

All derivatives were computed to second order. Variations in the scale function f along the x axis, for example, are given by

$$\frac{\widehat{\partial} f}{\widehat{\partial} x} = \frac{h_1^2 \left(f_{i+1,j,k} - f_{i,j,k}\right) + h_2^2 \left(f_{i,j,k} - f_{i-1,j,k}\right)}{h_1 h_2 (h_1 + h_2)}, \tag{11.29}$$

$$\frac{\widehat{\partial}^2 f}{\widehat{\partial} x^2} = 2\frac{h_1 \left(f_{i+1,j,k} - f_{i,j,k}\right) - h_2 \left(f_{i,j,k} - f_{i-1,j,k}\right)}{h_1 h_2 (h_1 + h_2)} \tag{11.30}$$

(Sundqvist and Veronis, 1970), and similarly for y and z. On the interior of each submesh, points are equispaced and the derivatives reduce to central difference. At the outer edges of the outermost mesh, derivatives are computed to $O(h^2)$ using two neighboring points. For example, letting $x_{2,j,k} - x_{1,j,k} = h_2$ and $x_{3,j,k} - x_{1,j,k} = h_3$,

$$\frac{\widehat{\partial} f}{\widehat{\partial} x} = \frac{1}{h_3 - h_2}\left[h_3 \frac{f_{2,j,k} - f_{1,j,k}}{h_2} - h_2 \frac{f_{3,j,k} - f_{1,j,k}}{h_3}\right], \tag{11.31}$$

$$\frac{\widehat{\partial}^2 f}{\widehat{\partial} x^2} = \frac{2}{h_3 - h_2}\left[\frac{f_{3,j,k} - f_{1,j,k}}{h_3} - \frac{f_{2,j,k} - f_{1,j,k}}{h_2}\right]. \tag{11.32}$$

Similarly for derivatives along the y and z axes.

The above scheme, of course, relies on every point having neighboring points. However, certain points on the boundary of fine submeshes will not have a neighboring point in the exterior mesh. In Figure 11.10 for example, the mesh point $\{i, j, k\}$ has no neighbor to the right along the x axis and $\{i-1, j+1, k\}$ has no neighboring point above it along the y axis. To compute

a second order x derivative at $\{i, j, k\}$, for example, information from the surrounding points $\{i, j+1, k\}$, $\{i+1, j+1, k\}$, $\{i, j-1, k\}$, $\{i+1, j-1, k\}$ and $\{i-1, j, k\}$ is required. The information from all these surrounding points can be incorporated through the introduction of a halo point at $\{i+1, j, k\}$. To illustrate this from Figure 11.10, the halo point is defined as

$$f_{i+1,j,k} = f_{i,j,k} + 2h\times \\ \frac{1}{2}\left[\frac{f_{i+1,j+1,k} - f_{i,j+1,k}}{2h} + \frac{f_{i+1,j-1,k} - f_{i,j-1,k}}{2h}\right]. \tag{11.33}$$

The halo point is therefore defined by linear interpolation of nearby points. In particular, the x-derivative is approximated by a weighted average of first order derivatives at $f_{i,j-1,k}$ and $f_{i,j+1,k}$, and the result multiplied by $2h$ to extrapolate from $f_{i,j,k}$ to $f_{i+1,j,k}$. The 3D analogue is identically computed except that the neighboring points $f_{i,j,k-1}$ and $f_{i,j,k+1}$ along the z axis are also used in the weighted average. Multiple derivatives for different variables, such as $\widehat{\partial}^2 f/(\widehat{\partial}x\widehat{\partial}y)$, are constructed directly by first computing $\widehat{\partial}f/\widehat{\partial}x$ and then $\widehat{\partial}/\widehat{\partial}y$ at each mesh point.

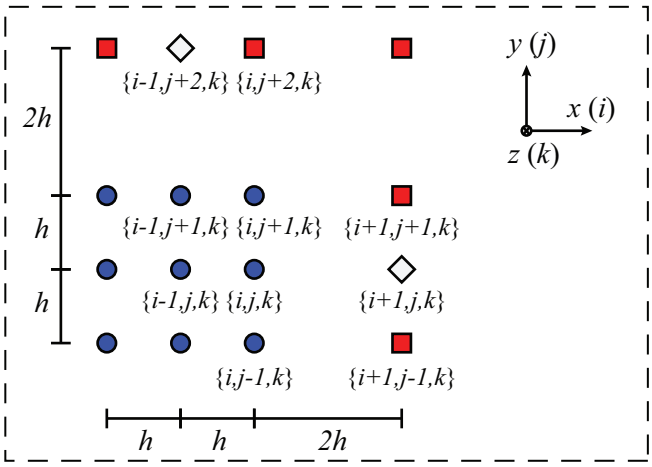

Figure 11.10: Diagram of nested mesh structure used in numerical simulations. Filled circles (blue) indicate points on a fine mesh with periodic spacing h. Filled squares (red) indicate points on an exterior coarser mesh with periodic spacing $2h$. Open diamonds (white) indicate interpolated halo points.

11.5.3 Meshes used in simulations

The 2D axisymmetric Sun-Earth simulations included 26 nested rectangular meshes, each twice as long in the $\hat{z}$ direction compared to the $\hat{r}$ direction. Each mesh consisted of $(n+1)$ points per side along $\hat{r}$ and $(2n+1)$ points per side along $\hat{z}$, with $n = 32$ for all but one of the submeshes which contained $n = 64$. The submeshes were divided into 7 outer meshes centered at the midpoint of the Sun and Earth bodies and containing both, 6 Sun body centered meshes containing only the Sun, and 13 Earth body centered meshes containing only Earth. The outer meshes extended over a radial distance from the origin equal to 2^p AU and a total longitudinal

distance equal to 2^{p+1} AU for $0 \leq p \leq 6$. The system for $p = 0$ required extra mesh points ($n = 64$) since there was no outer mesh of size 0.5 AU, as such a mesh would have bifurcated the Sun and Earth bodies. The Sun-centered meshes were constructed to have a radial range of 2^{-2} AU, 2^{-3} AU, ..., 2^{-7} AU, the last representing a distance roughly 1.7 times the radius of the Sun. The Earth-centered meshes were constructed to have a radial range of 2^{-2} AU, ..., 2^{-14} AU, the last roughly 1.4 times the radius of Earth.

The 3D Cartesian Sun-Earth-Moon simulations were constructed similarly and included 32 nested cubic meshes, each with $(n + 1)$ points per side along each of the $\hat{x}$, $\hat{y}$ and $\hat{z}$ axes. All but two of the meshes were designed with $n = 10$; two submeshes were designed with $n = 20$. The submeshes consisted of the following collection: 7 outer meshes centered at the midpoint of the Sun and Earth bodies, 6 centered about the Sun containing only the Sun, 7 centered about the Earth containing both the Earth and Moon bodies, 5 additional meshes centered about the Earth containing only the Earth body, and 7 centered about the Moon containing only the Moon. The outer meshes had side lengths 2^{p+1} AU for $0 \leq p \leq 6$. The $p = 0$ system required extra mesh points ($n = 20$), again due to the fact that there was no outer mesh of side length 1 AU. The Sun-centered meshes had side lengths 2^{-1} AU, 2^{-2} AU, ..., 2^{-6} AU, the last roughly 1.7 times the diameter of the Sun. The Earth-centered meshes had side extent 2^{-1} AU, ..., 2^{-7} AU and 2^{-9} AU, ... 2^{-13} AU, the last roughly 1.4 times the diameter of the Earth. The choice 2^{-8} AU was not implemented, since the edge of such a mesh would have bifurcated the Moon body. Instead, double the number of mesh points was used for the runs with side lengths 2^{-7} AU. The Moon-centered meshes had side lengths 2^{-9} AU, ..., 2^{-15} AU, the last roughly 1.3 times the diameter of the Moon.

11.6 Validation and benchmarking of numerical algorithm

The analysis in Section 11.3.1 describes the iteration scheme from an analytic standpoint, and the proofs therein cannot be applied exactly to a discretized approximation. That said, we observed fast convergence even in the finite difference implementation and encountered no numerical instabilities. In this section, we provide results of numerical tests to validate the implementation of our algorithm.

11.6.1 Solution convergence study

The arguments presented in Section 11.3.1 indicate that the numerical simulations should converge rapidly regardless of choice of initial trial function for the scalar field potential. Convergence tests were therefore conducted to quantify approach to the global minimum representing the solution to Equation (11.15). A variety of initial trial solutions was tested which included a uniform zero field, as well as nine distributions representing both white and red noise, each initiated from a different seed.

The (non-dimensional) white noise trial function was represented by values on each mesh node extracted from a normal distribution with zero mean and a standard deviation of 270.3, reflecting

the range in values of the single body Sun solution $\Phi(R)$ given by Equation (11.16) evaluated within a distance of 512 AU from the Sun body. The (non-dimensional) red noise trial function was represented by

$$\Phi^{(n=0)} = 270.3 \sum_{j=1}^{100} a_j \prod_{X_i=\{X,Y,Z\}} \frac{\sin(\kappa_{j,i} X_i + \theta_{j,i})}{\sqrt{\kappa_{j,X}^2 + \kappa_{j,Y}^2 + \kappa_{j,Z}^2}}. \tag{11.34}$$

Here, j denotes the 100 wave numbers along each coordinate direction selected uniformly from a logarithmic distribution ranging from $10^{-3} - 10^{3}$ where the wave numbers for the 2D axisymmetric case are labeled $\kappa_{j,R}$ and $\kappa_{j,Z}$ and for the 3D Cartesian case $\kappa_{j,X}$, $\kappa_{j,Y}$ and $\kappa_{j,Z}$. The corresponding amplitudes a_j were chosen from a normal distribution with zero mean and normalized to unity such that $\sum_j a_j^2 = 1$. The phase offsets represented by $\theta_{j,X}$ and the like were chosen uniformly from the range $[0, 2\pi]$.

Figure 11.11 shows results of the volume averaged integration of the dimensionless residual error squared computed after each iteration step n according to Equation (11.23). Within just a few iterations, the integrated residual decays rapidly by many orders of magnitude, followed by a second substantial drop, and is observed to asymptote rapidly to values below 10^{-4}. Indeed, the results of Figure 11.11 confirm that in both the 2D and 3D systems studied, the integrated residual error for all test cases converged to the same small value within no more than 25 iterations.

Although the analytical argument suggests that the integrated residual error should rapidly decay to zero, this cannot occur, or course, since the solution domain is represented by a discretized mesh. Because all points on domain boundaries are fixed by Dirichlet boundary conditions and only internal mesh points are free to vary, there are not enough degrees of freedom to achieve a pointwise residual of zero. Furthermore, the gradient descent step computed from the equation $\mathcal{L}[\Phi]\xi = -\mathcal{R}[\Phi]$ is a discrete approximation. However, higher accuracy can be achieved by implementation of other higher order finite difference schemes on even finer meshes than the basic implementation outlined in Appendix 11.5.2.

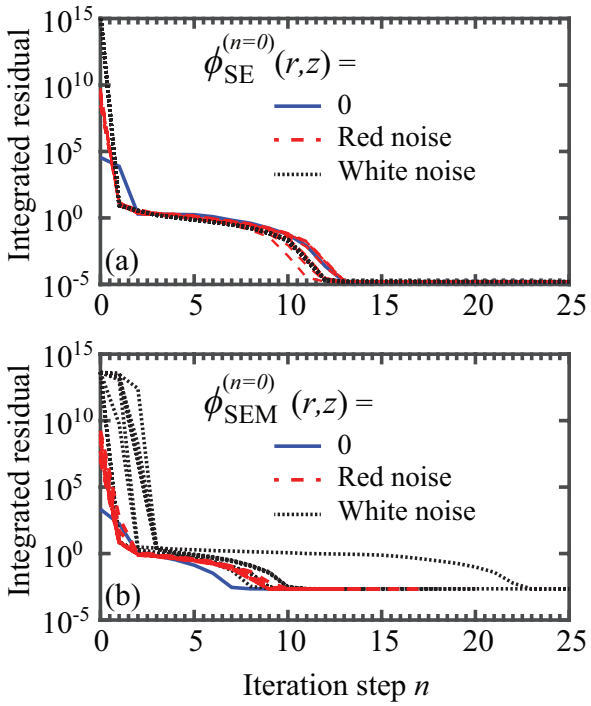

Figure 11.11: Results of volume averaged integration of the (dimensionless) residual error squared $d^{-3}\int(\mathcal{R}^{(n)}[\Phi])^2 dV$ computed after each iteration step n according to Equation (11.23). (a) Results for 2D axisymmetric Sun-Earth potential field $\phi_{\mathrm{SE}}(r,z)$. (b) Results for Sun-Earth-Moon potential field $\phi_{\mathrm{SEM}}(x,y,z)$. Shown are three types of initial trial functions: $\phi^{(n=0)}=0$ (solid blue line), red noise (long dashed red line) and white noise (short dashed black line). White noise and red noise distributions were generated from nine different seeds each. Further detail provided in Section 11.6.1.

11.6.2 Finite size study

Far beyond the Vainshtein radius of the largest body in a collection of bodies, the Galileon scalar potential is expected to vanish (Chu and Trodden, 2013) such that $\lim(R\to\infty)\Phi(\vec{R})=0$. In contrast to previous studies (Hiramatsu et al., 2013), our computational domain falls well within the Vainshtein radii of all included bodies, and we therefore argue that it is natural to apply the approximate boundary condition set by the values of the Galileon field given by Equation (11.16). This seems a valid choice so long as all computational boundaries are positioned at distances far greater than any internal length scales such as body separation distances. To validate this choice and to quantify finite size effects, we carried out simulations with domain boundaries positioned increasingly distant from the massive bodies. These simulations were carried out for the 2D axisymmetric Sun-Earth and 3D Cartesian Sun-Earth-Moon systems, which are the subject of the current work, as well as the idealized two-body system investigated by Hiramatsu et al. (2013). The origin of each coordinate system was positioned halfway between the two bodies for the idealized cases, and halfway between the Sun and Earth bodies for the solar system cases.

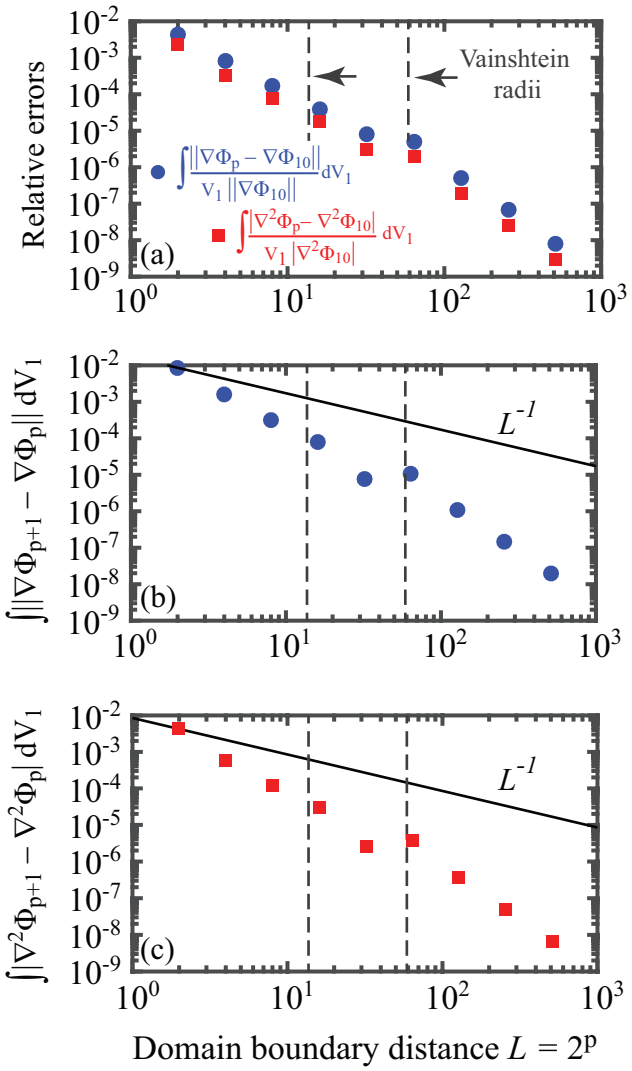

Figure 11.12: Results of convergence tests carried out in a cylindrical domain for increasing domain boundary distance L for the Galileon field of an idealized axisymmetric two body system. The parameter values were obtained from the study by Hiramatsu et al. (2013) according to which the dimensionless radii and densities of the two bodies equalled $(0.3, 1.0)$ and $(0.1, 0.3375)$, the separation distance equalled one, $k = 5.93 \times 10^{-4}$ and the Vainshtein radii (vertical dashed lines) equalled 58.9 and 13.7, respectively. Additional details can be found in Section 11.6.2. (a) Log-log plot showing the volume averaged relative errors in field strength $\int \|\nabla\Phi_{\rm p} - \nabla\Phi_{10}\|/(V_1\|\nabla\Phi_{10}\|)dV_1$ (solid blue circles) and Laplacian field $\int |\nabla^2\Phi_{\rm p} - \nabla^2\Phi_{10}|/(V_1|\nabla^2\Phi_{10}|)dV_1$ (solid red squares) for increasing domain size $L^{2{\rm p}}$ for integer values $1 \leq {\rm p} \leq 10$. (b) Log-log plot of $\int \|\nabla\Phi_{\rm p+1} - \nabla\Phi_{\rm p}\|dV_1$ for increasing domain size. (c) Log-log plot of $\int |\nabla^2\Phi_{\rm p+1} - \nabla^2\Phi_{\rm p}|dV_1$ for increasing domain size. Shown in (b) and (c) for comparison is the decay function L^{-1}.

In Figure 11.12, our results for the same two-body system examined by Hiramatsu et al. (2013) are plotted in non-dimensional form. In Figure 11.13 for the Sun-Earth (SE) and Sun-Earth-Moon (SEM) systems, our results are plotted in dimensional form for the convenience of experi-

mentalists. The non-dimensional length scale $L = 2^{\mathrm{p}}$ refers to the radius of a cylindrical domain of volume $V_{\mathrm{p}} = \pi \times (2^{\mathrm{p}})^2 \times 2^{\mathrm{p}+1}$ for integer values $1 \leq \mathrm{p} \leq 10$ used to compute the non-dimensional Galileon field potential $\Phi_p(R, Z)$. The dimensional length scale $\ell = 2^{\mathrm{p}}\,\mathrm{AU}$ refers instead to the distance from the origin of the computational domain to its nearest boundary. For those simulations carried out in cylindrical domains, this distance ℓ equaled the radius of a cylinder of volume $V_{\mathrm{p}} = \pi \times (2^{\mathrm{p}})^2 \times 2^{\mathrm{p}+1}\,\mathrm{AU}^3$. For simulations carried out in a cubic domain, this distance ℓ equaled the half length of the edge of a cube of volume $V_{\mathrm{p}} = 2^{\mathrm{p}+1} \times 2^{\mathrm{p}+1} \times 2^{\mathrm{p}+1}\,\mathrm{AU}^3$ for integer values $1 \leq \mathrm{p} \leq 9$. The actual simulations to determine the potential fields $\phi_{\mathrm{p}}(\vec{r})$ $\mathrm{m}^2/\mathrm{s}^2$ for the SE and SEM systems were, of course, carried out in dimensionless coordinates, with the results then plotted in dimensional form. For proper comparison, all differences reported were evaluated only within the smallest volume common to all volumes tested for a given system, namely $V_{\mathrm{p}=1}$. All relative errors are reported in comparison to the solutions obtained for the largest domain size tested.

For the idealized two-body system, we used the parameter values given by Hiramatsu *et al.* (Hiramatsu et al., 2013). Accordingly, body A was assigned a radius and density of $(0.3, 1.0)$, respectively, and body B was assigned the values $(0.1, 0.3375)$. The two bodies were given a separation distance of 1.0. These choices yielded a non-dimensional value for the linear coefficient in Equation (11.13) $k = 5.93 \times 10^{-4}$ and Vainshtein radii of 58.9 and 13.7, respectively. The results in Figure 11.12(a) demonstrate just how small are the relative errors for the force and Laplacian fields when compared to the results for the largest domain. The comparison in (b) and (c) of the results for the gradient and Laplacian fields to the decay function L^{-1} also confirm rapid convergence. The results in (b) showing the mean relative difference in the force field for the smallest domain V_1 (where L falls well within the Vainshtein radii) and the largest domain V_{10} (where L far exceeds the Vainshtein radii) is only about 0.43%. The corresponding mean relative difference for the Laplacian field, shown in (c), is only about 0.23 %. There does appear a region around the larger Vainshtein radius at which the convergence stalls, but the relative error subsequently continues to decrease as the size of the computational domain increases. A more comprehensive study of boundary conditions is required to determine whether this stall is spurious.

The results in Figure 11.13 show convergence of the solar system simulations with increasing domain size. The Sun-Earth (3D Cartesian) and Sun-Earth-Moon (3D Cartesian) results are indistinguishable to two significant digits. The results in (a) and (b) demonstrate rapid convergence with increasing ℓ when compared to the decay function ℓ^{-1}. The results in (c) and (d) evidence numerical consistency with increasing ℓ, as expected. Quantitatively, in the SE (cylindrical) simulations, the mean relative gradient difference between the simulations carried out with $\ell = 2\,\mathrm{AU}$ and $\ell = 256\,\mathrm{AU}$ was only 0.075% and between the $\ell = 64\,\mathrm{AU}$ and $\ell = 256\,\mathrm{AU}$ simulations only 0.00033%. The corresponding mean relative Laplacian difference was 0.16% and 0.000060%, respectively. Likewise for the Sun-Earth (3D Cartesian) and Sun-Earth-Moon (3D Cartesian) simulations, the mean relative gradient difference between the simulations car-

ried out with $\ell = 2\,\mathrm{AU}$ and $\ell = 256\,\mathrm{AU}$ was only 0.33% and between the $\ell = 64\,\mathrm{AU}$ and $\ell = 256\,\mathrm{AU}$ simulations only 0.00071%. The corresponding mean relative Laplacian difference was 1.7% and 0.0010%, respectively.

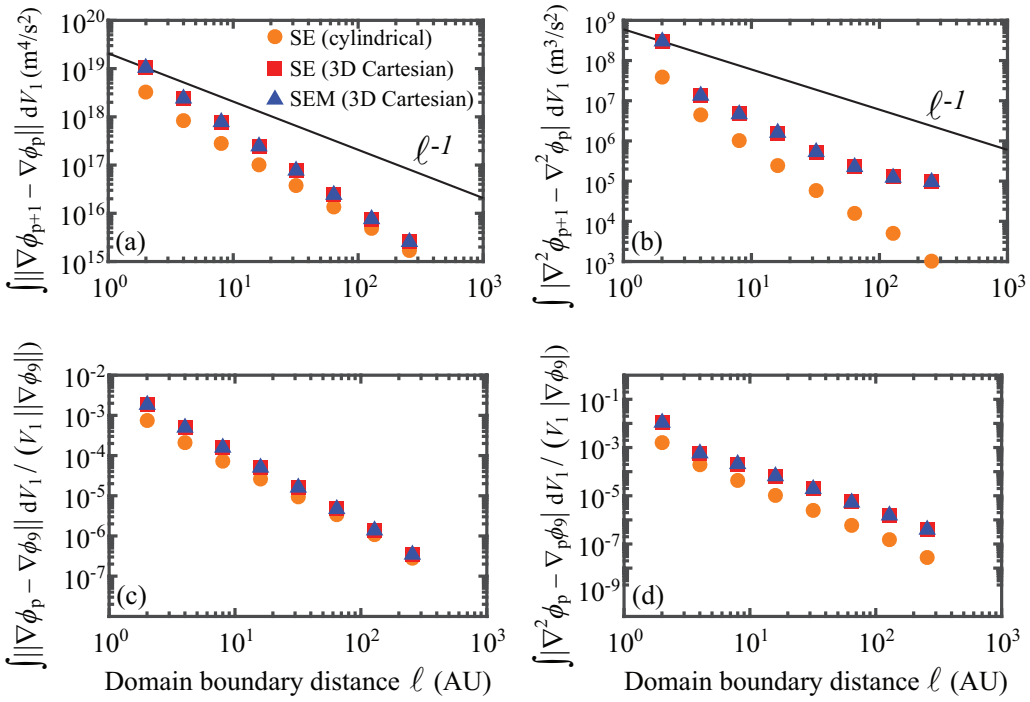

Figure 11.13: Results of convergence tests for increasing domain boundary distance $\ell\,\mathrm{AU}$ for the Galileon force and Laplacian fields corresponding to the Sun-Earth (SE) (cylindrical), Sun-Earth (SE) (3D Cartesian) and Sun-Earth-Moon (SEM) (3D Cartesian) solutions. The largest domain boundary distance is $\ell = 2^{\mathrm{p}=9}\,\mathrm{AU} = 512\,\mathrm{AU}$. Additional details can be found in Section 11.6.2. Shown for comparison in (a) and (b) is a line with a fall off rate of $1/\ell$. (a) Log-log plots of $\int \|\nabla\phi_{\mathrm{p}+1} - \nabla\phi_{\mathrm{p}}\| dV_1\ m^4/s^2$. (b) Log-log plots of $\int |\nabla^2\phi_{\mathrm{p}+1} - \nabla^2\phi_{\mathrm{p}}| dV_1\ m^4/s^2$. (c) Log-log plots of $\int \|\nabla\phi_{\mathrm{p}} - \nabla\phi_9\| dV_1$ normalized by $V_1\|\nabla\phi_9\|$. (d) Log-log plots of $\int |\nabla^2\phi_{\mathrm{p}} - \nabla^2\phi_9| dV_1$ normalized by $V_1|\nabla^2\phi_9|$.

Based on these results, we chose a domain boundary distance of 64 AU, measured from the midpoint of the axis connecting the Sun-Earth bodies, as the standard domain boundary distance for the main computations presented in the body of this work. The improved convergence seen in Figure 11.13 for the SE (cylindrical) system is likely due to the finer meshes used there. In particular, when comparing the slope of the curves in Figure 11.13(b) connecting the final two points, we find for the SE (3D Cartesian) system yields a value slightly greater than -1 while the SE (cylindrical) yields a value closer to -1.5, indicating more rapid convergence.

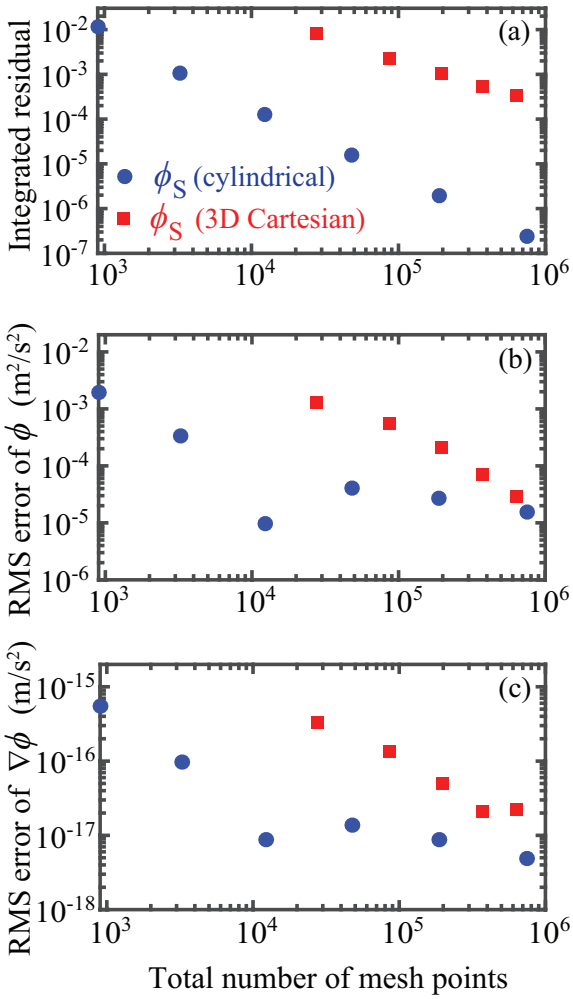

Figure 11.14: Mesh refinement study quantifying the difference between the single-body Sun solutions, $\phi_{\rm S}$ and $\nabla\phi_{\rm S}$, and the exact analytical result given by Equation (11.20), namely $\phi_{\rm theor}$. Results were carried out with a cylindrical and cubic domain of boundary distance 64 AU and volume V_6. Since the computational volume for each geometry was held constant, increasing number of mesh points reflects smaller mesh lengths. (a) Integrated residual value $d^{-3}\int(\mathcal{R}^{(n)}[\Phi])^2 dV_6$. (b) Root mean square error (RMS) of ϕ given by $[\int(\phi_S-\phi_{\rm theor})^2 dV_6/V_6]^{1/2}$. (c) RMS value of $\nabla\phi$ given by $[\int\|\nabla\phi_S-\nabla\phi_{\rm theor}\|^2 dV_6/V_6]^{1/2}$.

11.6.3 Convergence with mesh refinement

A mesh refinement study was conducted comparing the difference between the numerical solution $\phi_{\rm S}(\vec{r})$ and the analytic solution for the Galileon field $\phi_{\rm theor}(\vec{r})$ of the single-body Sun system given by Equation (11.16). Both cylindrical and 3D Cartesian volumes were used with boundary distance $\ell = 64$ (i.e. $V_6\,\mathrm{AU}^3$). The cylindrical volume contained 26 submeshes and the 3D Cartesian volume contained 32 submeshes. For the cylindrical coordinate system, the underlying rectangular mesh elements contained $(n+1)\times(2n+1)$ mesh points per side for $n = 4$, 8, 16, 32, 64 and 128. For the 3D Cartesian system, the underlying cubic mesh elements contained

$(2n+1)$ mesh points per side for $n = 4$, 6, 8, 10 and 12. The total number of mesh points was therefore approximately $m \times (2n+1)(n+1)$ for the cylindrical volume and $m \times (2n+1)^3$ for the 3D cubic volume. These numbers are not exact because some points are shared between submeshes and some submeshes contained $(4n+1)$ points per side instead of $(2n+1)$ for the reasons described in Section 11.5.3.

The results in Figure 11.14 for either geometry at constant volume confirm that the integrated residual error decreases monotonically with increasing mesh refinement as shown in (a), indicating that the numerical results approach the analytical results as the total number of mesh points is increased. The root-mean-square (RMS) error for Φ in (b) and $\nabla\Phi$ in (c) also decreases, though not entirely monotonically. In particular, two somewhat odd features are apparent. Firstly, the simulations conducted within a cylindrical volume exhibit a dip of about an order of magnitude at the third mesh refinement step. This is likely a spurious effect, perhaps reflecting that the distribution of points at that mesh size better captures the spherical contours about the Sun center. Regardless, the error continues to decrease monotonically upon further mesh refinement. Secondly, the RMS error of $\nabla\Phi$ for the 3D Cartesian system increases slightly at the final mesh refinement step, while that of the cylindrical system continues to drop. This suggests that the simulation results may become more accurate far from the Sun and slightly less accurate near the Sun. However, this behavior may also arise from numerical issues in connection with the fact that the linear problem was solved approximately by using the MATLAB `bicg` biconjugate gradient solver instead of the direct linear solver. Additional tests conducted using even finer meshes will help resolve this issue.

11.6.4 Study of computational times

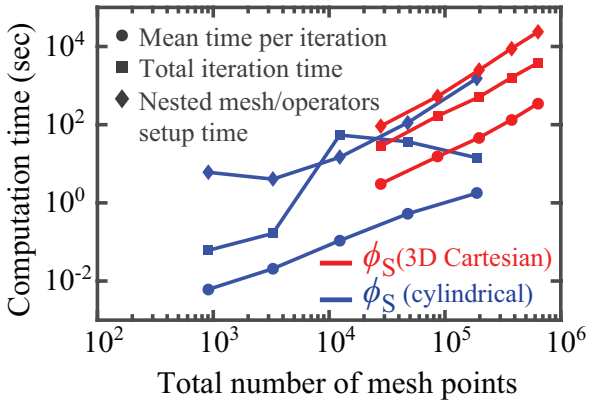

Figure 11.15: Mean time per iteration, total iteration time and nested mesh/differential operator setup time for the single-body potential field $\phi_S(\vec{r})$ with increasing total number of mesh points. The volume of the cylindrical and cubic domains was V_6. Additional details given in Section 11.6.4.

Simulations were also conducted to quantify the mean time per iteration, total iteration time and time for constructing nested mesh differential operators for the single-body field $\phi_S(\vec{r})$ by

increasing the number of total mesh points with a cylindrical and a cubic domain referenced to a volume V_6. The computations were performed on a Dell Power Edge R430 server with two 10-core Intel Xeon E5-2630 v4 2.2GHz processors and 112GB of RAM [including 25M Cache, 8.0 GT/s QPI, Turbo, HT, 10C/20T, Max Mem 2133 MHz]. Our software code was not parallelized although some matrix operations in MATLAB automatically run in parallel across multiple cores. The initial trial function for this study was chosen to be the analytic solution given by Equation (11.16), which of course is not an exact solution once discretized. The total number of mesh points ranged from 903 for the cylindrical domains with the coarsest meshes to $635,941$ for the cubic domains with the finest meshes.

The results in Figure 11.15 show that for the cylindrical volume, the mean time per iteration scales approximately linearly with the total number of mesh points, while the cubic volume scales somewhere closer to a quadratic. The total iteration time in either case does not increase monotonically due to the variable number of iterations required for the residual to cease to decrease. The time required to set up the initial nested meshes and discrete differential operators appears to scale somewhat between linear and quadratic for both geometries. The results in the main body of this paper were obtained with 47,985 mesh points for the cylindrical volumes with a radius measuring $2^6 = 64$ AU, resulting in computation times on the order of one or two minutes, and 374,411 mesh points for the cubic volumes of side half-length measuring $2^6 = 64$ AU, resulting in computation times on the order of thirty minutes.

Acknowledgments

NCW gratefully acknowledges financial support from a 2017 NASA Space Technology Research Fellowship (80NSSC17K0139). This research was carried out in part at the Jet Propulsion Laboratory, California Institute of Technology (Caltech), under a contract with the National Aeronautics and Space Administration (80NM0018D0004). SMT and NCW wish to thank Dr. Peter Thompson for his efforts in designing and implementing the computing cluster used for the simulations. Jérôme Gleyzes, Jason Rhodes, Olivier Doré, Eric Huff, and Kristofer Pardo are also acknowledged for valuable discussions of dark energy and modified gravity.

References

MATLAB and Statistics Toolbox Release 2015a, The MathWorks, Inc., Natick, MA, USA, 2015. URL `https://www.mathworks.com/products/matlab.html`.

M. Andrews, Y.-Z. Chu, and M. Trodden. Galileon forces in the solar system. Phys. Rev. D, 88 (8):084028, 2013. doi:10.1103/PhysRevD.88.084028.

E. Babichev, C. Deffayet, and R. Ziour. k-mouflage gravity. Int. J. Mod. Phys. D, 18(14): 2147–2154, 2009. doi:10.1142/S0218271809016107.

A. Barreira, B. Li, W. A. Hellwing, C. M. Baugh, and S. Pascoli. Nonlinear structure formation in the cubic Galileon gravity model. J. Cosmol. Astroparticle Phys., 2013(10):027–027, 2013. doi:10.1088/1475-7516/2013/10/027.

A. Barreira, B. Li, C. M. Baugh, and S. Pascoli. The observational status of Galileon gravity after Planck. J. Cosmol. Astroparticle Phys., 2014(08):059, 2014. doi:10.1088/1475-7516/2014/08/059.

A. V. Belikov and W. Hu. Equivalence principle violation in weakly Vainshtein-screened systems. Phys. Rev. D, 87(8):084042, 2013. doi:10.1103/PhysRevD.87.084042.

L. Bernus, O. Minazzoli, A. Fienga, M. Gastineau, J. Laskar, and P. Deram. Constraining the mass of the graviton with the planetary ephemeris INPOP. Phys. Rev. Lett., 123:161103, 2019. doi:10.1103/PhysRevLett.123.161103.

J. K. Bloomfield, C. Burrage, and A.-C. Davis. Shape dependence of Vainshtein screening. Phys. Rev. D, 91(8):083510, 2015. doi:10.1103/PhysRevD.91.083510.

P. Brax, C. van de Bruck, A.-C. Davis, B. Li, and D. J. Shaw. Nonlinear structure formation with the environmentally dependent dilaton. Phys. Rev. D, 83:104026, 2011. doi:10.1103/PhysRevD.83.104026.

C. G. Broyden. A class of methods for solving nonlinear simultaneous equations. Math. Comput., 19(92):577–593, 1965. doi:10.1090/S0025-5718-1965-0198670-6.

C. Burrage, E. J. Copeland, and E. A. Hinds. Probing dark energy with atom interferometry. J. Cosmol. Astroparticle Phys., 2015(03):042–042, 2015. doi:10.1088/1475-7516/2015/03/042.

B. W. Carroll and D. A. Ostlie. An Introduction to Modern Astrophysics. Cambridge University Press, 2017. ISBN 9781108390248. doi:10.1017/9781108380980.

K. C. Chan and R. Scoccimarro. Large-scale structure in brane-induced gravity. II. Numerical simulations. Phys. Rev. D, 80(10):104005, 2009. doi:10.1103/PhysRevD.80.104005.

M. H. Chan and H. K. Hui. Testing the Cubic Galileon Gravity model by the Milky Way rotation curve and SPARC data. Astrophys. J., 856(2):177, 2018. doi:10.3847/1538-4357/aab3e6.

C. Charmousis, R. Gregory, N. Kaloper, and A. Padilla. DGP specteroscopy. J. High Energy Phys., 2006(10):066, 2006. doi:10.1088/1126-6708/2006/10/066.

S.-w. Chiow and N. Yu. Multiloop atom interferometer measurements of chameleon dark energy in microgravity. Phys. Rev. D, 97(4):044043, 2018. doi:10.1103/PhysRevD.97.044043.

S.-w. Chiow and N. Yu. Constraining symmetron dark energy using atom interferometry. Phys. Rev. D, 101:083501, 2020. doi:10.1103/PhysRevD.101.083501.

S.-w. Chiow, J. Williams, and N. Yu. Laser-ranging long-baseline differential atom interferometers for space. Phys. Rev. A, 92:063613, 2015. doi:10.1103/PhysRevA.92.063613.

S.-w. Chiow, J. Williams, and N. Yu. Noise reduction in differential phase extraction of dual atom interferometers using an active servo loop. Phys. Rev. A, 93:013602, 2016. doi:10.1103/PhysRevA.93.013602.

Y.-Z. Chu and M. Trodden. Retarded Green's function of a Vainshtein system and Galileon waves. Phys. Rev. D, 87(2):024011, 2013. doi:10.1103/PhysRevD.87.024011.

C. J. Cutler. (unpublished).

T. Damour and A. M. Polyakov. The string dilation and a least coupling principle. Nucl. Phys. B, 423(2):532–558, 1994. doi:10.1016/0550-3213(94)90143-0.

F. Dar, C. de Rham, J. T. Deskins, J. T. Giblin, Jr., and A. J. Tolley. Scalar gravitational radiation from binaries: Vainshtein mechanism in time-dependent systems. Classical Quant. Grav., 36(2):025008, 2018. doi:10.1088/1361-6382/aaf5e8.

C. de Rham. Galileons in the sky. Comptes Rendus Physique, 13(6-7):666–681, 2012. doi:10.1016/j.crhy.2012.04.006.

C. de Rham, A. Matas, and A. J. Tolley. Galileon radiation from binary systems. Phys. Rev. D, 87(6):064024, 2013a. doi:10.1103/PhysRevD.87.064024.

C. de Rham, A. J. Tolley, and D. H. Wesley. Vainshtein mechanism in binary pulsars. Phys. Rev. D, 87(4):044025, 2013b. doi:10.1103/PhysRevD.87.044025.

C. Deffayet. Cosmology on a brane in Minkowski bulk. Phys. Lett. B, 502(1-4):199–208, 2001. doi:10.1016/S0370-2693(01)00160-5.

C. Deffayet. On brane world cosmological perturbations. Phys. Rev. D, 66(10):103504, 2002. doi:10.1103/PhysRevD.66.103504.

G. Dvali, G. Gabadadze, and M. Porrati. 4D gravity on a brane in 5D Minkowski space. Phys. Lett. B, 485(1-3):208–214, 2000. doi:10.1016/S0370-2693(00)00669-9.

A. Figueroa and R. Löhner. Postprocessing-based interpolation schemes for nested Cartesian finite difference grids of different size. Int. J. Num. Method Fluids, 89(6):196–215, 2019. doi:10.1002/fld.4689.

P. Hamilton, M. Jaffe, P. Haslinger, Q. Simmons, H. Müller, and J. Khoury. Atom-interferometry constraints on dark energy. Science, 349(6250):849–851, 2015. doi:10.1126/science.aaa8883.

K. Hinterbichler and J. Khoury. Screening long-range forces through local symmetry restoration. Phys. Rev. Lett., 104(23):231301, 2010. doi:10.1103/PhysRevLett.104.231301.

T. Hiramatsu, W. Hu, K. Koyama, and F. Schmidt. Equivalence principle violation in Vainshtein screened two-body systems. Phys. Rev. D, 87(6):063525, 2013. doi:10.1103/PhysRevD.87.063525.

A. S. Householder. Principles of Numerical Analysis. McGraw-Hill Book Company, Inc., 1953.

L. Hui, A. Nicolis, and C. W. Stubbs. Equivalence principle implications of modified gravity models. Phys. Rev. D, 80(10):104002, 2009. doi:10.1103/PhysRevD.80.104002.

L. Iorio. Constraints on Galileon-induced precessions from solar system orbital motions. J. Cosmol. Astroparticle Phys., 2012(07):001–001, 2012. doi:10.1088/1475-7516/2012/07/001.

A. Joyce, B. Jain, J. Khoury, and M. Trodden. Beyond the cosmological standard model. Phys. Rep., 568:1–98, 2015. doi:10.1016/j.physrep.2014.12.002.

C. T. Kelley. Iterative Methods for Linear and Nonlinear Equations. Frontiers in Applied Mathematics. Society for Industrial and Applied Mathematics, 1995. ISBN 9780898713527. doi:10.1137/1.9781611970944.

J. Khoury and A. Weltman. Chameleon fields: Awaiting surprises for tests of gravity in space. Phys. Rev. Lett., 93(17):171104, 2004. doi:10.1103/PhysRevLett.93.171104.

K. Koyama and R. Maartens. Structure formation in the Dvali-Gabadadze-Porrati cosmological model. J. Cosmol. Astroparticle Phys., 2006(01):016–016, 2006. doi:10.1088/1475-7516/2006/01/016.

K. Koyama and F. P. Silva. Nonlinear interactions in a cosmological background in the Dvali-Gabadadze-Porrati braneworld. Phys. Rev. D, 75(8):084040, 2007. doi:10.1103/PhysRevD.75.084040.

B. Li, G.-B. Zhao, and K. Koyama. Exploring Vainshtein mechanism on adaptively refined meshes. J. Cosmol. Astroparticle Phys., 2013(05):023–023, 2013. doi:10.1088/1475-7516/2013/05/023.

A. Lue and G. Starkman. Gravitational leakage into extra dimensions: Probing dark energy using local gravity. Phys. Rev. D, 67(6):064002, 2003. doi:10.1103/PhysRevD.67.064002.

A. Lue, R. Scoccimarro, and G. D. Starkman. Probing Newton's constant on vast scales: Dvali-Gabadadze-Porrati gravity, cosmic acceleration, and large scale structure. Phys. Rev. D, 69 (12):124015, 2004. doi:10.1103/PhysRevD.69.124015.

A. Nicolis and R. Rattazzi. Classical and quantum consistency of the DGP model. J. High Energy Phys., 2004(06):059–059, 2004. doi:10.1088/1126-6708/2004/06/059.

A. Nicolis, R. Rattazzi, and E. Trincherini. Galileon as a local modification of gravity. Phys. Rev. D, 79(6):064036, 2009. doi:10.1103/PhysRevD.79.064036.

H. Ogawa, T. Hiramatsu, and T. Kobayashi. Anti-screening of the Galileon force around a disk center hole. Modern Phys. Lett. A, 34(02):1950013, 2019. doi:10.1142/S0217732319500135.

K. A. Olive and M. Pospelov. Environmental dependence of masses and coupling constants. Phys. Rev. D, 77(4):043524, 2008. doi:10.1103/PhysRevD.77.043524.

J. Renk, M. Zumalacárregui, F. Montanari, and A. Barreira. Galileon gravity in light of ISW, CMB, BAO and H0 data. J. Cosmol. Astroparticle Phys., 2017(10):020, 2017. doi:10.1088/1475-7516/2017/10/020.

B. Ryden. Introduction to Cosmology. Cambridge University Press, 2nd edition, 2016. ISBN 9781316889404. doi:10.1017/9781316651087.

J. Sakstein. Tests of gravity with future space-based experiments. Phys. Rev. D, 97:064028, 2018. doi:10.1103/PhysRevD.97.064028.

F. Schmidt. Self-consistent cosmological simulations of DGP braneworld gravity. Phys. Rev. D, 80(4):043001, 2009. doi:10.1103/PhysRevD.80.043001.

F. Schmidt, W. Hu, and M. Lima. Spherical collapse and the halo model in braneworld gravity. Phys. Rev. D, 81(6):063005, 2010. doi:10.1103/PhysRevD.81.063005.

R. Scoccimarro. Large-scale structure in brane-induced gravity. I. Perturbation theory. Phys. Rev. D, 80(10):104006, 2009. doi:10.1103/PhysRevD.80.104006.

H. Sundqvist and G. Veronis. A simple finite-difference grid with non-constant intervals. Tellus, 22(1):26–31, 1970. doi:10.1111/j.2153-3490.1970.tb01933.x.

A. I. Vainshtein. To the problem of nonvanishing gravitation mass. Phys. Lett. B, 39(3):393–394, 1972. doi:10.1016/0370-2693(72)90147-5.

N. C. White, S. M. Troian, J. B. Jewell, C. J. Cutler, S.-w. Chiow, and N. Yu. Robust numerical computation of the 3D scalar potential field of the cubic Galileon gravity model at solar system scales. Phys. Rev. D, 102:024033, 2020. doi:10.1103/PhysRevD.102.024033.

J. Williams, S. wey Chiow, N. Yu, and H. Müller. Quantum test of the equivalence principle and space-time aboard the international space station. New J. Phys., 18(2):025018, 2016. doi:10.1088/1367-2630/18/2/025018.

N. Yu, S.-w. Chiow, J. Gleyzes, P. Bull, O. Doré, J. Rhodes, J. Jewell, E. Huff, and H. Muller. Direct probe of dark energy interactions with a solar system laboratory. phase 1 final report; NASA Innovative Advanced Concepts (NIAC). Technical report, NASA Headquarters; Washington, DC, United States, 2018. URL `https://ntrs.nasa.gov/citations/20190002500`.

Appendix A

BRIEF NOTES ON COVARIANT NOTATION AND FLUID MECHANICS

A.1 Brief notes on covariant notation

In several sections of this work (Chapter 2, Chapter 7, Chapter 8), we will find it convenient to use covariant notation for our results on curved lines and surfaces. Here we review a few features that will be relevant. Note that we will use the Einstein summation convention in which repeated indices are summed.

For a given coordinate system, a metric tensor g_{ij} defines how vectors are measured. In flat space with Cartesian coordinates, the metric tensor is simply the identity matrix. But in curved space or in a flat space with non-Cartesian coordinates (e.g., spherical or cylindrical coordinates), the metric tensor is nontrivial. The inverse of the metric tensor is written with raised indices, as $[g_{ij}]^{-1} = g^{ij}$. This then allows a convenient convention of raising indices by multiplying with g^{ij} and lowering them by multiplying by g_{ij}. For example, a vector $v^i = g^{ij}v_j$, and a covector $v_i = g_{ij}v^j$ (Aris, 1989).

Such notation makes it easy to compute dot products without getting confused about the coordinate system. While in Cartesian coordinates one can simply write $\vec{u} \cdot \vec{v}$, summing the product of each component of the vectors, in more general coordinates the dot product is given by $u^i g_{ij} v^j = u_j v^j$. While vectors and tensors have different representations in different coordinate systems, scalars do not; any expression which has no hanging indices (e.g., $u_j v^j$) will have the same value regardless of coordinate system (Aris, 1989).

The covariant derivative ∇_j is defined for scalars simply as the partial derivative:

$$\nabla_j f = \partial_j f. \tag{A.1}$$

For vectors and covectors, it is defined with an additional correction,

$$\nabla_j v^i = \partial_j v^i + \Gamma^i_{jk} v^k \tag{A.2}$$

$$\nabla_j v_i = \partial_j v_i - \Gamma^k_{ji} v_k, \tag{A.3}$$

where $\Gamma^i{}_{jk}$ is the Christoffel symbol of the second kind. Each additional index of a tensor introduces a similar correction. E.g., for second rank tensors,

$$\nabla_j T^{ik} = \partial_j T^{ik} + \Gamma^i_{j\ell} T^{\ell k} + \Gamma^k_{j\ell} T^{i\ell} \tag{A.4}$$

$$\nabla_j T^i_{\ k} = \partial_j T^{ik} + \Gamma^i_{j\ell} T^\ell_{\ k} - \Gamma^\ell_{jk} T^i_{\ \ell}, \tag{A.5}$$

etc. The Christoffel symbols are defined by

$$\Gamma^i{}_{jk} = \frac{1}{2} g^{i\ell} \left(\partial_k g_{j\ell} + \partial_j g_{\ell k} - \partial_\ell g_{jk} \right). \tag{A.6}$$

The covariant derivative makes it easy to convert between different coordinate systems. For example, the Laplacian of a scalar is written as $\nabla_j \nabla^j f$, an expression which is valid in any coordinate system. For example, the Laplacian in cylindrical coordinates is $\partial_{zz} f + \partial_{rr} f + (1/r)\partial_r f + (1/r^2)\partial_{\theta\theta} f$, which is fully captured by the covariant expression $\nabla_j \nabla^j f$. The covariant derivative commutes with the metric tensor, so that $\nabla_i v^j = g^{jk} \nabla_i v_k$, for example. In curved space, covariant derivatives do not commute with themselves; in particular, $\nabla_i \nabla_j v^k = \nabla_j \nabla_i v^k + R_{\ell}{}^{k}{}_{ji} v^{\ell}$, where $R_{\ell}{}^{k}{}_{ji}$ is the Riemann curvature tensor (Aris, 1989).

A.1.1 Curved surfaces in Cartesian space

In this work, we will be interested in curved lines and surfaces embedded in a flat bulk space. Given a 2D manifold $\mathcal{M}$ parametrized by ξ and ζ, $\vec{\sigma}(\xi, \zeta) \in \mathbb{R}^3$, the metric tensor on the manifold may be computed as

$$g_{\mu\nu} = \begin{bmatrix} (\partial_\xi \vec{\sigma} \cdot \partial_\xi \vec{\sigma}) & (\partial_\xi \vec{\sigma} \cdot \partial_\zeta \vec{\sigma}) \\ (\partial_\zeta \vec{\sigma} \cdot \partial_\xi \vec{\sigma}) & (\partial_\zeta \vec{\sigma} \cdot \partial_\zeta \vec{\sigma}) \end{bmatrix}. \tag{A.7}$$

This metric allows computation of vector lengths for vectors in the tangent bundle of the manifold (Aris, 1989).

The shape tensor, or second fundamental form, describes the curvature of $\mathcal{M}$ and can be expressed as

$$\mathrm{I\!I}_{\mu\nu} = \begin{bmatrix} (\partial_{\xi\xi} \vec{\sigma} \cdot \hat{n}) & (\partial_{\xi\zeta} \vec{\sigma} \cdot \hat{n}) \\ (\partial_{\zeta\xi} \vec{\sigma} \cdot \hat{n}) & (\partial_{\zeta\zeta} \vec{\sigma} \cdot \hat{n}) \end{bmatrix} = - \begin{bmatrix} (\partial_\xi \vec{\sigma} \cdot \partial_\xi \hat{n}) & (\partial_\xi \vec{\sigma} \cdot \partial_\zeta \hat{n}) \\ (\partial_\zeta \vec{\sigma} \cdot \partial_\xi \hat{n}) & (\partial_\zeta \vec{\sigma} \cdot \partial_\zeta \hat{n}) \end{bmatrix}, \tag{A.8}$$

where $\hat{n}$ is a normal vector on $\mathcal{M}$ (note that the shape tensor will switch sign depending on which direction the normal is chosen to have). The eigenvectors of $\mathrm{I\!I}_{\mu\nu}$ give the directions of principal curvature, while the eigenvalues give the magnitude of the principal curvature. The mean curvature is then given by $\kappa_m = (1/2)\mathrm{I\!I}^{\mu}{}_{\mu}$ and the Gaussian curvature by $\kappa_G = \det[\mathrm{I\!I}^{\mu}{}_{\nu}]$. For example, on the surface of a cylinder of radius R, one principal curvature is $1/R$, while the other is 0 (there is no curvature axially along the cylinder). Thus the mean curvature is $1/(2R)$ and the Gaussian curvature is 0 (Aris, 1989).

The mean curvature is an extrinsic quantity, i.e., it depends on the embedding of the manifold in the bulk space, and the sign of the mean curvature depends upon the choice of normal direction. The Gaussian curvature is intrinsic; it depends only on the metric and not the embedding. Intuitively, the difference can be understood by considering a surface which moves isometrically (without bending or stretching). A flat sheet of paper (with mean curvature 0 and Gaussian curvature 0) can be rolled up into a cylinder, giving it (extrinsic) mean curvature $1/(2R)$ but maintaining its (intrinsic) Gaussian curvature (Misner et al., 1973).

A.2 Brief notes on fluid mechanics

A portion of this work describes the flow of liquids in various micro-scale geometries. These liquids will be assumed to be Newtonian, incompressible, and well-described by the continuum

approximation. Frequently, they will also be assumed to have negligible inertia. In this section, the equations of motion governing such fluids will be briefly derived, and the associated assumptions discussed.

A.2.1 Conservation and the Navier-Stokes equations

In relativistic mechanics, conservation of energy and momentum are expressed by $\nabla_\Xi T^{\Xi\Lambda}$ (with Einstein summation) and conservation of angular momentum by $T^{\Xi\Lambda} = T^{\Lambda\Xi}$, where $T^{\Xi\Lambda}$ is the stress-energy tensor and the indices (for which we will use capital Greek letters) span the four dimensions space and time (Misner et al., 1973). While the nonrelativistic limit of the stress-energy tensor is not uniquely defined, due to the decoupling of mass and energy and of time and space (Duval and Künzle, 1978), it will be sufficient for our purposes to write down a version which tracks only mass and momentum (Vinokur, 1974):

$$T^{\Xi\Lambda} = \begin{bmatrix} -\rho & -\rho u^i \\ -\rho u^j & T^{ij} \end{bmatrix}, \tag{A.9}$$

$$T^{ij} = \tau^{ij} + \tau^{ij}_{\text{add.}} - p g^{ij} - \rho u^i u^j, \tag{A.10}$$

where lowercase Latin letters index the three spatial coordinates, ρ denotes the local fluid density, u^i denotes local fluid velocity, p denotes pressure, g^{ij} denotes the three-dimensional spatial metric tensor, τ^{ij} denotes the viscous stress tensor, and $\tau^{ij}_{\text{add.}}$ denotes any additional contributions to the stress tensor, such as electric fields and conservative forces, like gravity. (Not including the t terms of the electromagnetic stress tensor means that we disallow transfer between mass and electromagnetic energy, which is expected in nonrelativistic systems.) The first row (or column) of the stress-mass tensor, $T^{t\Lambda}$, is recognizable as the negative of the nonrelativistic four-momentum of a piece of fluid.

The conservation of mass and momentum can then be written as

$$\nabla_\Xi T^{\Xi\Lambda} = f^\Lambda, \tag{A.11}$$

where $f^\Lambda = \{0, f^i\}$ represents any external nonconservative forces acting on the system. Writing out the t-component (mass conservation) and spatial components (momentum conservation) separately,

$$0 = \partial_t \rho + \nabla_i \left(\rho u^i \right), \tag{A.12}$$

$$\begin{aligned} 0 &= \partial_t \left(\rho u^j \right) - \nabla_i \left[\tau^{ij} + \tau^{ij}_{\text{add.}} - p g^{ij} - \rho u^i u^j \right] - f^j \\ &= \rho \left(\partial_t u^j + u^i \nabla_i u^j \right) - \nabla_i \left(\tau^{ij} + \tau^{ij}_{\text{add.}} - p g^{ij} \right) - f^j, \end{aligned} \tag{A.13}$$

where the momentum conservation equation was simplified by substituting in the mass conservation result. Equation (A.13) is known as Cauchy's equation of motion (Marsden and Tromba, 2003). The operator $(\partial_t + u^i \nabla_i)$ is sometimes called the material derivative (or advective derivative, convective derivative, total derivative, etc.), and represents the time derivative of a

fixed "particle" of fluid, taking into account that particle's motion. (Note that we implicitly assumed $\partial_t \sqrt{\det g} = 0$, i.e., the coordinate system does not shrink or grow in time).

Setting $\tau^{ij} = 0$ represents a fluid with no viscous dissipation and is often used as an approximation to model certain high-speed or low-viscosity fluids. Equation (A.13) with $\tau^{ij} = 0$ is known as the Euler equations (Landau and Lifshitz, 1987).

In order to close the equations for a viscous fluid, a constitutive relation defining the relationship between τ^{ij} and u^i is necessary. Clearly, a fluid for which u^i is a constant or which is undergoing rigid-body rotation should have no viscous dissipation (Landau and Lifshitz, 1987). The most general linear constitutive relation which does not depend on higher derivatives of u^j then has the form

$$\tau_{ij} = \mu \left(\nabla_i u_j + \nabla_j u_i \right) + \left(\zeta - \frac{2}{3}\mu \right) g_{ij} \nabla_k u^k, \tag{A.14}$$

where μ is the dynamic viscosity and ζ the second viscosity of the fluid (Landau and Lifshitz, 1987). This describes so-called Newtonian fluids, and is the most commonly used constitutive relation in fluid dynamics. Other constitutive relations exist for non-Newtonian fluids, including those for shear-thickening fluids (which solidify as shear stress is applied) and shear-thinning fluids (which become less viscous as shear stress is applied). Shear-thinning fluids include blood, paint, and foods like mayonnaise, and are often modeled as Bingham plastics or Casson fluids (Larson, 1999). In this work, only Newtonian fluids will be considered.

Substituting the Newtonian stress tensor, Equation (A.14), into the Cauchy equation, Equation (A.13), yields the Navier-Stokes equations:

$$\rho \left(\partial_t u^j + u^i \nabla_i u^j \right) = -\nabla^j p + f^j + \mu \left(\nabla_i \nabla^i u^j + R^j{}_i u^i \right) + \left(\zeta + \frac{1}{3}\mu \right) \nabla^j \nabla_i u^i. \tag{A.15}$$

Here $R^j{}_i$ is the Ricci curvature tensor describing the curvature of the background space. Because we work only in the nonrelativistic limit, our bulk equations will always be in flat space and lack the extra curvature term. It should be noted that the restriction of the Navier-Stokes equations to 2D membranes does include that term, and it is thus relevant for flows confined to fluid interfaces (Aris, 1989).

Liquids which move very slowly compared to the speed of sound may be assumed to be incompressible, i.e., $(\partial_t + u_i \nabla^i)\rho = 0$ (Landau and Lifshitz, 1987). This incompressibility assumption must be expressed with the material derivative, to imply that a small convecting parcel of fluid has constant density. Under this assumption, the incompressible continuity (mass conservation) and Navier-Stokes equations are

$$\nabla_i u^i = 0, \tag{A.16}$$

$$\rho \left(\partial_t u^j + u^i \nabla_i u^j \right) = -\nabla^j p + f^j + \mu \nabla_i \nabla^i u^j. \tag{A.17}$$

It is worth noting at this point that we have assumed from the start that a fluid may be modeled as a continuum. This assumption breaks down when the mean free path or the length scale of intermolecular forces is comparable to the relevant length scale of interest, e.g., the diameter of the bounding channel. Such a situation arises in liquids at very small scales, typically $\lesssim O(\text{nm})$, or at larger scales in dilute gases (Bird et al., 2002). Neither of these regimes will be considered in this work.

A.2.2 Reynolds number

Setting a length scale L and characteristic velocity scale u_c, along with a characteristic time scale $t_c = L/u_c$ and pressure scale $p_c = \mu u_c/L$, and defining dimensionless quantities $U_j = u_j/u_c$, $T = t/t_c$, $P = p/p_c$, the Navier-Stokes equations can be rewritten as

$$\mathrm{Re}\left(\partial_T U^j + U^i \overline{\nabla}_i U^j\right) = -\overline{\nabla}^j P + \frac{f^j}{p_c/L} + \overline{\nabla}_i \overline{\nabla}^i U^j, \tag{A.18}$$

$$\mathrm{Re} = \frac{\rho u_c L}{\mu}. \tag{A.19}$$

Re is called the Reynolds number (Landau and Lifshitz, 1987). When Re is large, inertia is relatively important compared to viscous dissipation, and vice-versa.

Fluids typically become turbulent above a critical Reynolds number, which varies depending on the flow geometry but typically has order of magnitude 10^2 to 10^3 (Trefethen et al., 1993)[1]. High viscosity, slow flow, or small scales all decrease the Reynolds number. We will rely on the small scales (a few microns) of our problems of interest to keep Re low enough to ignore, and hence we will not consider turbulence.

A.2.3 Bond number and capillary number

Two other nondimensional numbers which will be encountered in this work are the Bond number[2] and capillary number. The Bond number measures the relative strength of gravity to capillary (surface tension) pressure, and is defined as

$$\mathrm{Bo} = \frac{\rho g L}{\gamma/L} = \frac{\rho g L^2}{\gamma}, \tag{A.20}$$

where ρ is density, g is gravitational acceleration, γ is surface tension, and L is the relevant length scale (Probstein, 1994). The numerator of the first expression is the hydrostatic gravitational pressure and the denominator the capillary pressure, for the given length scale. Assuming it was defined with the relevant length scales, then a large Bond number $\mathrm{Bo} \gg 1$ indicates that gravity dominates surface tension, and a small Bond number $\mathrm{Bo} \ll 1$ indicates that surface tension dominates gravity. In this work, we will typically remain in the small Bond number regime, as we not only consider very small systems but also are interested in applications in space. The Bond

[1] For example, Trefethen et al. (1993) cite turbulent transition for flow driven by a moving flat plate to occur at $\mathrm{Re} \approx 350$, and for pressure-driven flow in a pipe to occur at $\mathrm{Re} \approx 1000$.

[2] Note that the value of the Bond number depends on the system and is not, in fact, fixed at 007.

number is discussed, however, in the derivation of the V-groove equations of motion (Chapter 4) and the thin film equation for a curved substrate (Chapter 8).

The capillary number measures the scale of viscous forces to capillary forces, and is defined as

$$\mathrm{Ca} = \frac{\mu u_c / L}{\gamma / L} = \frac{\mu u_c}{\gamma}, \tag{A.21}$$

where μ is viscosity, u_c is the velocity scale, γ is the surface tension, and L is the relevant length scale (Probstein, 1994). The first expression makes clear that the numerator is the scale of the normal viscous stress and the denominator the scale of the capillary pressure. Keep in mind that, despite its name, the capillary number is inversely proportional to surface tension: a large capillary number implies relatively small surface tension, and vice versa. Because this work deals with phenomena which are dominated by surface tension, we typically nondimensionalize with a velocity scale u_c proportional to the capillary velocity γ/μ, and hence the capillary number is factored out.

A.2.4 Wall boundary condition

For this work, we will take the no-slip boundary condition against solid surfaces. This implies that the fluid immediately adjacent to a solid boundary is stationary (with respect to that boundary); not only does it not move normal to the boundary, but also does not move tangent to it. This no-slip condition is widely used in fluid mechanics (Landau and Lifshitz, 1987), but does break down at very small scales. In particular, the assumption of a no-slip condition at the contact line of two fluids and a solid (or a fluid, a vacuum, and a solid) leads to a stress singularity; introducing a small slip between the fluid and solid allows computation of a contact line configuration without a singularity (Cox, 1986). However, the slip condition is not always easy to predict and depends on the form of intermolecular potentials and microscopic wall roughness (Thompson and Troian, 1997). Therefore, this work considers only the no-slip boundary condition, although the results could certainly be rederived for slip boundary conditions.

References

R. Aris. Vectors, Tensors and the Basic Equations of Fluid Mechanics. Dover Publications, New York, 1989. ISBN 9780486661100.

R. B. Bird, E. N. Lightfoot, and W. E. Stewart. Transport Phenomena. J. Wiley & Sons, Inc., New York, 2002. ISBN 9780471364740.

R. G. Cox. The dynamics of the spreading of liquids on a solid surface. part 1. viscous flow. J. Fluid Mech., 168:169–194, 1986. doi:10.1017/S0022112086000332.

C. Duval and H. P. Künzle. Dynamics of continua and particles from general covariance of newtonian gravitation theory. Rep. Math. Phys., 13(3):351–368, June 1978. ISSN 00344877. doi:10.1016/0034-4877(78)90063-0.

L. D. Landau and E. M. Lifshitz. Fluid Mechanics, volume 6 of Course of Theoretical Physics. Butterworth-Heinemann, 2nd edition, 1987.

R. G. Larson. The Structure and Rheology of Complex Fluids. Topics in Chemical Engineering. Oxford University Press, Oxford, 1999. ISBN 9780195121971.

J. E. Marsden and A. J. Tromba. Vector Calculus. W. H. Freeman and Company, New York, 5th edition, 2003. ISBN 9780716749929.

C. W. Misner, K. S. Thorne, and J. A. Wheeler. Gravitation. W. H. Freeman, 1973. ISBN 9780716703440. doi:10.1002/asna.19752960110.

R. F. Probstein. Physicochemical Hydrodynamics: An Introduction. John Wiley & Sons, New York, 1994. ISBN 9780471010111.

P. A. Thompson and S. M. Troian. A general boundary condition for liquid flow at solid surfaces. Nature, 389(6649):360–362, September 1997. ISSN 0028-0836, 1476-4687. doi:10.1038/38686.

L. N. Trefethen, A. E. Trefethen, S. C. Reddy, and T. A. Driscoll. Hydrodynamic stability without eigenvalues. Science, 261:30, 1993. doi:10.1126/science.261.5121.578.

M. Vinokur. A new formulation of the conservation equations of fluid dynamics. Technical Report NASA-TM-X-62415, NASA Ames Research Center Moffett Field, CA, United States, 1974. URL `https://ntrs.nasa.gov/citations/19750011505`.

Appendix B

RELATED STABILITY ANALYSIS TECHNIQUES

B.1 Introduction

The methods in this section relate to the generalized linear stability analysis, but were not employed for the new research in this thesis. They are mentioned here because they are expected to be useful for future extensions of this work.

Appendix B.2 discusses adjoint and variational methods of computing optimal input and output modes, which can be far more computationally efficient than the naïve direct computation of the propagator (the method used in this thesis). In particular, adjoint methods are likely necessary to extend the stability results for thin films on curved substrates (Chapter 9) to finer resolution or to non-axisymmetric substrates. Appendix B.3 discusses pseudospectral analysis, which provides analytic techniques for bounding transient growth, as well as a way of understanding the response of non-normal operators to forcing. It was not needed for the results in this thesis, as all systems were either shown to be stable using Lyapunov techniques or the numerical abscissa alone, or else were nonautonomous and hence out of the purview of pseudospectroscopy. But future variations on the V-groove equation which are not amenable to Lyapunov's direct method[1] may be best addressed with pseudospectral or resolvent techniques.

B.2 Adjoint and variational methods

Another method for studying the growth of perturbations in a linearized system is the adjoint method (Schmid, 2007). The adjoint method is a general term for a variety of analyses which consider the sensitivity of later-time outputs to initial-time inputs. For example, consider some vector $v_i(t)$ which is propagated in time by the linear operator $\Phi(t,s)$, so that $v_i(t) = \Phi_{ij}(t,0)v_j(0)$. Given some function $f[v_i(t)]$ which measures some property of the output $v_i(t)$, we can compute the sensitivity of f to the input $v_i(0)$ explicitly (Johnson, 2006):

$$\frac{\partial f}{\partial v_j(0)} = \frac{\partial f}{\partial v_i(t)}\frac{\partial v_i(t)}{\partial v_j(0)} = \frac{\partial f}{\partial v_i(t)}\frac{\partial \Phi_{ik}(t,0)v_k(0)}{\partial v_j(0)} = \frac{\partial f}{\partial v_i(t)}\Phi_{ij}(t,0) = [\Phi(t,0)]^T_{ji}\frac{\partial f}{\partial v_i(t)}. \tag{B.1}$$

The sensitivity of f to perturbations in the initial state $v_i(0)$ is equal to the product of the adjoint propagator and the sensitivity of f to perturbations in the output state $v_i(t)$. This result in itself is not especially interesting; we are already familiar with the propagator $\Phi(t,s)$ from generalized linear stability analysis, and so we could use it to compute any desired sensitivity to initial conditions. Unfortunately, the propagator is in general computationally expensive to

[1] For example, coupling an electric field to a dielectric liquid in a groove would lead to a reduced V-groove equation with tangential stresses for which it may be challenging to find a Lyapunov functional.

compute; even for an autonomous equation where $\Phi(t,0) = \exp(At)$, the matrix exponential must be computed, an operation which is cubic in the number of rows or columns of A (Moler and Van Loan, 2003).

The adjoint method provides a way around the inefficiency of matrix operations by using backwards propagation of sensitivities. Given a linear (possibly nonautonomous) equation $\partial_t v_i(t) = A_{ij}(t)v_j(t)$ with $v_i(t) = \Phi_{ij}(t,s)v_j(s)$, then

$$\partial_\tau \widetilde{v}_i(t-\tau) = [A(t-\tau)]^T_{ij}\widetilde{v}_j(t-\tau) \implies \widetilde{v}_i(t-\tau) = [\Phi(t,t-\tau)]^T_{ij}\widetilde{v}_j(t). \tag{B.2}$$

That is, the adjoint propagator applied to a vector $\widetilde{v}_j(t)$ is described by the solution of the backwards-time evolution equation controlled by A^T. In particular, the sensitivity $\partial f/\partial v_i(0)$ can be computed by starting with the adjoint initial condition $\widetilde{v}_i(t) = \partial f/\partial v_i(t)$ and integrating the differential equation of Equation (B.2) from $\tau = 0$ to $\tau = t$. Rather than compute the entire propagator which contains the solutions to the evolution equation for every possible vector, it becomes necessary only to compute one solution backwards in time.

However, there is still a catch. The adjoint method provides a way to get from $\partial f/\partial v_i(t)$ to $\partial f/\partial v_i(0)$ with a relatively cheap computation, but $\partial f/\partial v_i(t)$ is not necessarily known. This situation arises in particular when using the adjoint method to optimize an output variable, so that $v_i(t)$ is not known a priori. In such cases, an iteration is typically performed in which an initial input $v_i(0)$ is guessed and propagated forward in time to get $v_i(t)$; $\partial f/\partial v_i(t)$ is then computed and propagated backwards. A condition based on the optimization being performed is used to update the guess of $v_i(0)$, which is again propagated forward, and so on (Schmid, 2007).

The adjoint method can be used to determine maximally growing perturbations by formulation a variational optimization problem. We will first relate a simplification the example given by (Schmid, 2007), and then show how the result is equivalent to that obtained by generalized linear stability theory with a known propagator. Consider a (possibly nonautonomous) linear system $\partial_t v_i(t) = A_{ij}(t)v_j(t)$ with the Euclidean inner product. The maximum perturbation growth $\max_{v_i(0)} \|v_i(t)\|/\|v_i(0)\|$ at some time t may be computed by treating $v_i(t)$ and $v_i(0) = v_i^{(0)}$ as independent vectors and relying on Lagrange multipliers to enforce their evolutionary relationship, yielding the Lagrangian (Schmid, 2007)

$$L(v,\widetilde{v},v^{(0)},\widetilde{v}^{(0)}) = \frac{\|v(t)\|^2}{\|v^{(0)}\|^2} - \int_0^t [\widetilde{v}(s)]^T \left(\frac{\partial}{\partial s}v(s) - A(s)v(s)\right) ds - [\widetilde{v}^{(0)}]^T \left(v(0) - v^{(0)}\right), \tag{B.3}$$

where indices have been dropped for brevity. Here $\widetilde{v}(s)$ is a Lagrange multiplier enforcing the evolution equation and $\widetilde{v}^{(0)}$ a Lagrange multiplier enforcing the initial condition. Maximizing L by differentiating with respect to $\widetilde{v}(s)$, $\widetilde{v}^{(0)}$, $v(s)$ (with $0 < s < t$), $v(t)$, $v(0)$ and $v^{(0)}$ gives the

equations (Schmid, 2007)

$$\frac{\partial}{\partial s}v(s) = -A(s)v(s), \tag{B.4a}$$

$$v(0) = v^{(0)}, \tag{B.4b}$$

$$\frac{\partial}{\partial s}\widetilde{v}(s) = -[A(s)]^T\widetilde{v}(s), \tag{B.4c}$$

$$\widetilde{v}(t) = 2\frac{v(t)}{\|v^{(0)}\|^2}, \tag{B.4d}$$

$$\widetilde{v}(0) = \widetilde{v}^{(0)}, \tag{B.4e}$$

$$\widetilde{v}^{(0)} = 2\frac{\|v(t)\|^2}{\|v^{(0)}\|^4}v^{(0)}. \tag{B.4f}$$

The iteration procedure to determine $v(t)$ and $v^{(0)}$ is then fully specified. Starting with a guess $v^{(0)} = v(0)$, propagate forward in time using Equation (B.4a) until $v(t)$ is attained. Then compute $\widetilde{v}(t)$ with Equation (B.4d) and propagate it backwards in time with Equation (B.4c) until $\widetilde{v}(0) = \widetilde{v}^{(0)}$ is attained. An updated guess of $v^{(0)}$ is then set by Equation (B.4f), and the whole process is repeated until convergence is achieved.

To see that this result is the same as that achieved by generalized linear stability theory, we use the propagator Φ, which is defined by $v(t) = \Phi v(0)$ and $\widetilde{v}(0) = \Phi^T\widetilde{v}(t)$. Plugging in the values from Equations (B.4d) and (B.4f),

$$\begin{aligned} v(t) = \Phi v(0) &= \Phi\frac{\|v(0)\|^4}{2\|v(t)\|^2}\widetilde{v}(0) = \Phi\frac{\|v(0)\|^4}{2\|v(t)\|^2}\Phi^T\widetilde{v}(t) = \Phi\frac{\|v(0)\|^4}{2\|v(t)\|^2}\Phi^T\frac{2v(t)}{\|v(0)\|^2} \\ &= \frac{\|v(0)\|^2}{\|v(t)\|^2}\Phi\Phi^T v(t). \end{aligned} \tag{B.5}$$

Thus, the optimal output vector $v(t)$ is an eigenvector of $\Phi\Phi^T$ with eigenvalue $\|v(t)\|^2/\|v(0)\|^2$. The SVD gives $\Phi = V\Lambda U^T$, so that $\Phi\Phi^T = V\Lambda^2V^T$; i.e., the eigenvectors of $\Phi\Phi^T$ are precisely the output modes computed with generalized linear stability theory. Thus the adjoint method provides a way to determine optimal input and output modes without explicitly computing the propagation matrix. The downside is that these optimal perturbations are computed only for a specific time t; the whole iterative procedure must be repeated for each time of interest.

Farazmand and Sapsis (2017) apply a similar variational approach to determine the instantaneously fastest-growing perturbations at each time, corresponding to the numerical abscissae. Although computing only numerical abscissae gives less information than computing the optimal perturbations over a period of time, it is less computationally expensive as there is no need even for reverse time propagation of the adjoint. They apply the analysis to a nonautonomous system with "intermittent bursts" of large perturbation growth to identify the fastest-growing mode associated with each burst, and suggest that, once identified, such modes be tracked in order to detect future bursts of growth early in their onset.

B.3 Pseudospectral and resolvent analysis

Key to classical modal stability analysis is the spectrum σ of an operator $\mathcal{L}$, defined as the set of its eigenvalues. One way of identifying eigenvalues is as values z such that the *resolvent* $(z-\mathcal{L})^{-1}$ does not exist; that is, $z-\mathcal{L}$ is not invertible (Trefethen and Embree, 2005). The spectrum can then be extended to the concept of a pseudospectrum, which consists of all points which are in a specific sense close to eigenvalues. Specifically, the ε-pseudospectrum is defined as

$$\sigma_\varepsilon(\mathcal{L}) = \left\{ z \in \mathbb{C} \,\middle|\, \|z-\mathcal{L}\|^{-1} > \varepsilon^{-1} \right\} \tag{B.6}$$

or, equivalently,

$$\sigma_\varepsilon(\mathcal{L}) = \left\{ z \in \mathbb{C} \,\middle|\, \|(z-\mathcal{L})v\| < \varepsilon \text{ for some unit vector } v \right\} \tag{B.7}$$

(Trefethen and Embree, 2005). The second definition in particular makes it clear that σ_ε includes all z which are "almost" eigenvalues in the sense that there are certain "almost" eigenvectors v which satisfy $\mathcal{L}v = zv + O(\varepsilon)$.

It turns out that the ε-pseudospectra for normal matrices simply describe circles of radius ε around the eigenvalues, while the ε-pseudospectra of non-normal matrices can be much more complicated. Specifically, using the L_2 norm,

$$\sigma_\varepsilon(\mathcal{L}) = \left\{ z \in \mathbb{C} \,\middle|\, |z-\sigma(\mathcal{L})| < \varepsilon \right\} \text{ if } \mathcal{L} \text{ is normal,} \tag{B.8}$$

$$\sigma_\varepsilon(\mathcal{L}) \supseteq \left\{ z \in \mathbb{C} \,\middle|\, |z-\sigma(\mathcal{L})| < \varepsilon \right\} \text{ if } \mathcal{L} \text{ is non-normal.} \tag{B.9}$$

Along with the ε-pseudospectrum, the ε-pseudospectral abscissa is defined by $\beta_\varepsilon(\mathcal{L}) = \max\{ \mathrm{re}(z) | z \in \sigma_\varepsilon(\mathcal{L})\}$ (here re refers to the real part, not the Reynolds number).

An example comparing ε-pseudospectra for normal and non-normal matrices is given in Figure B.1, based on the non-normal example in the previous section. Note that the pseudospectra of the normal matrix (left) describe perfect circles around the spectrum. Besides the non-normal having a more ellipsoid shape, each ε-pseudospectrum of the non-normal matrix is clearly much larger than its normal counterpart. We can also see clearly that while $\beta_{\varepsilon=0.5} \approx -0.5$ for the normal matrix, $\beta_{\varepsilon=0.5} \approx +0.4$ for the non-normal one.

A number of theorems describe various upper and lower bounds on transient growth based on pseudospectra; two notable ones will be related here. First, an upper bound. Letting L_ε be the arc length of the boundary or convex hull of $\sigma_\varepsilon(\mathcal{L})$,

$$\|\exp(t\mathcal{L})\| \leq \frac{L_\varepsilon \exp\left(t\beta_\varepsilon(\mathcal{L})\right)}{2\pi\varepsilon} \tag{B.10}$$

(Trefethen and Embree, 2005). Note that for a normal matrix, $L_\varepsilon = 2\pi\varepsilon$ for sufficiently small ε, and so the statement trivially implies $\|\exp(t\mathcal{L})\| = \exp[t\beta_{\max}(\mathcal{L})] \leq \exp[t\beta_{\max}(\mathcal{L}) + t\varepsilon]$.

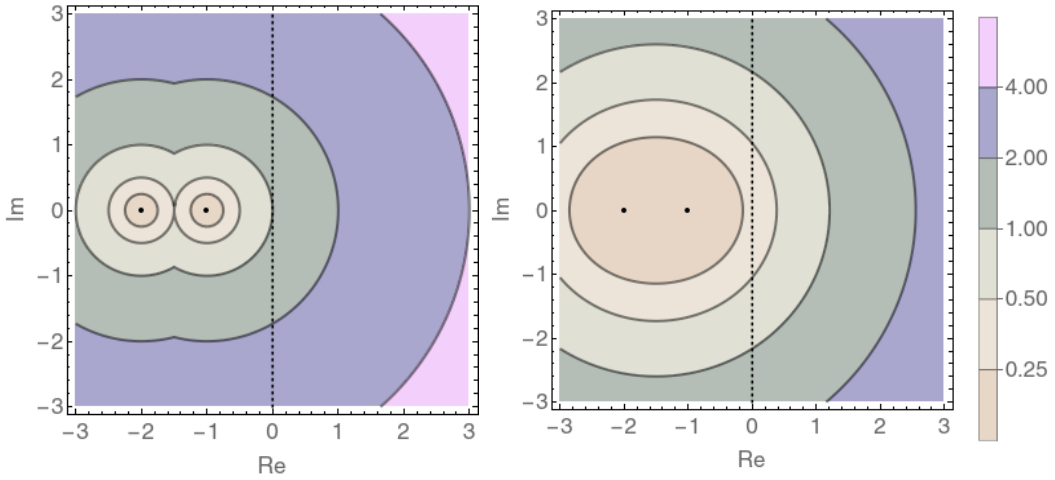

Figure B.1: Depiction of ε-pseudospectra with $\varepsilon = \{0.25, 0.5, 1, 2, 4\}$ for a normal matrix $\{-1, 0; 0, -2\}$ (left) and a non-normal matrix $\{-1, 6; 0, -2\}$ (right). Vertical axis is imaginary and horizontal axis real; the dotted black line indicates the imaginary axis $\mathrm{re}(z) = 0$. Black dots indicate eigenvalues.

Furthermore, the fact that the ε-pseudospectrum of a non-normal matrix always contains the ball of radius ε around the spectrum, then non-normal matrices always satisfy $L_\varepsilon \geq 2\pi\varepsilon$.

Next, a lower bound. Defining the *Kreiss constant* $\mathfrak{K}(\mathcal{L})$ by

$$\mathfrak{K}(\mathcal{L}) = \sup_{\varepsilon>0} \frac{\beta_\varepsilon(\mathcal{L})}{\varepsilon} = \sup_{\mathrm{re}(z)>0} \mathrm{re}(z)\|z - \mathcal{L}\|^{-1}, \tag{B.11}$$

then

$$\sup_{t>0} \|\exp(t\mathcal{L})\| \geq \mathfrak{K}(\mathcal{L}) \tag{B.12}$$

(Trefethen and Embree, 2005). Again, it is easy to see that for a normal matrix, $\mathfrak{K}(\mathcal{L})$ is equal to 1 if $\beta_{\max} < 0$ and ∞ if $\beta_{\max} > 0$. Unfortunately this bound is not always sharp, and a variety of more complicated bounds can be constructed; the interested reader is referred to Trefethen and Embree (2005), an entire book devoted exclusively to pseudospectral analysis.

The discussion so far has been limited to the behavior of perturbations introduced at a single specific time whose evolution is then tracked, but another question one might ask is how a non-normal linear system responds to forcing (either deterministic or stochastic). The resolvent matrix described earlier proves critical to analyzing such behavior. Suppose we have a forced linear system

$$\partial_t u = \mathcal{L}u + f. \tag{B.13}$$

Performing a Fourier transform in time, so that $\hat{u}(\omega) = \int_{-\infty}^{\infty} u(t)\exp(-i\omega t)d(t/2\pi)$, and similarly for f, one immediately finds that

$$\hat{u} = (i\omega - \mathcal{L})^{-1}\hat{f}, \tag{B.14}$$

where $(i\omega - \mathcal{L})^{-1}$ is the resolvent matrix used earlier to derive the pseudospectrum, with $i\omega$ playing the role of what we called z before (Farrell and Ioannou, 1996). Recalling that the pseudospectrum of a non-normal matrix may cover a large area, i.e., there may be a large range of ω for which $\|i\omega - \mathcal{L}\|^{-1} > \varepsilon^{-1}$ for a given ε, it is thus immediately clear that non-normal operators can have large "pseudoresonant" responses even at frequencies ω quite far from the eigenvalues of $\mathcal{L}$ (Trefethen et al., 1993). McKeon and Sharma (2010) built upon these results to construct a nonlinear model of turbulent fluctuations. Rather than assuming small perturbations and discarding nonlinear terms when linearizing the Navier-Stokes equations, they retain the quadratic fluctuation terms to be used as the forcing $\hat{f}$ in Equation (B.14).

References

M. Farazmand and T. P. Sapsis. A variational approach to probing extreme events in turbulent dynamical systems. Sci. Adv., 3(9):e1701533, September 2017. ISSN 2375-2548. doi:10.1126/sciadv.1701533.

B. F. Farrell and P. J. Ioannou. Generalized Stability Theory. Part I: Autonomous operators. J. Atmos. Sci., 53(14):2025–2040, 1996. doi:10.1175/1520-0469(1996)053<2025:GSTPIA>2.0.CO;2.

S. Johnson. Notes on adjoint methods for 18.335, Spring 2006.

B. J. McKeon and A. S. Sharma. A critical-layer framework for turbulent pipe flow. J. Fluid Mech., 658:336–382, 2010. ISSN 0022-1120. doi:10.1017/S002211201000176X.

C. Moler and C. Van Loan. Nineteen dubious ways to compute the exponential of a matrix, twenty-five years later. SIAM Rev., 45(1):3–49, 2003. ISSN 00361445. doi:10.1137/S00361445024180.

P. J. Schmid. Nonmodal stability theory. Annu. Rev. Fluid Mech., 39:129–62, 2007. ISSN 0824307399. doi:10.1146/annurev.fluid.38.050304.092139.

L. N. Trefethen and M. Embree. Spectra and Pseudospectra: The Behavior of Nonnormal Matrices and Operators. Princeton University Press, Princeton and Oxford, 2005. ISBN 9780691119465.

L. N. Trefethen, A. E. Trefethen, S. C. Reddy, and T. A. Driscoll. Hydrodynamic stability without eigenvalues. Science, 261:30, 1993. doi:10.1126/science.261.5121.578.

Appendix C

V-GROOVES IN OTHER REGIMES

C.1 Introduction

This section sketches out how the V-groove equation would be extended to capture other regimes, such as the presence of gravity perpendicular to the flow, and inertial regimes. These are not full derivations (which would be very lengthy), but blueprints; it is hoped that they are sufficient to make it fairly easy for another student to construct the models.

C.2 V-grooves with perpendicular gravity

The equation of motion for flow in V-grooves when gravity acts parallel to Z (i.e., parallel to the flow) was found by Weislogel (1996) and discussed in Chapter 4. Recall that gravity in such cases can be ignored when $\mathrm{Bo}/(\varepsilon\Phi) \ll 1$, where $\mathrm{Bo} = \rho g d^2/\gamma$ is the Bond number.

When gravity acts perpendicular to the flow (i.e., in the X-Y plane), it has a smaller effect, and can be ignored when $\mathrm{Bo}/\Phi \ll 1$. For water, which has $\rho_{\text{water}} = 10^3$ kg/m^3 and surface tension $\gamma \approx 0.072$ N/m (Dean, 1999), and for a groove with $\alpha = 45°$, $\theta = 15°$, $\mathrm{Bo}/\Phi \approx 5.6 \times 10^6 d^2$, with d measured in meters. Thus, $\mathrm{Bo}/\Phi = 1$ when $d \approx 0.42$mm. Many lab-on-a-chip devices are likely oriented perpendicular to gravity, specifically with gravity in the y-axis, and reach such a scale. Determining the equation of motion with gravity in the y-direction is thus a natural next step. Doing so is a bit more involved than when gravity acts in z; an overview of the procedure is given here.

Following the derivation in Chapter 4, when gravity acts in the y-axis, the reduced Navier-Stokes and continuity equations are:

$$\frac{\partial U}{\partial X} + \frac{\partial V}{\partial Y} + \frac{\partial W}{\partial Z} = 0, \tag{C.1a}$$

$$\frac{\partial P}{\partial X} = 0, \tag{C.1b}$$

$$\frac{\partial P}{\partial Y} = B, \tag{C.1c}$$

$$\frac{\partial P}{\partial Z} = \frac{\partial^2 W}{\partial X^2} + \frac{\partial^2 W}{\partial Y^2}, \tag{C.1d}$$

where

$$B = \frac{\mathrm{Bo}}{\mathrm{Ca}} G_y \tag{C.2}$$

is the y-rescaled Bond number (note that this differs from the z-rescaled Bond number in the earlier chapter).

Hence,

$$P = P_0(Z) + BY. \tag{C.3}$$

C.2.1 Interface correction

The normal interface boundary condition reduces to

$$0 = -P - \mathrm{Ca}^{-1}\left(\frac{\partial_X^2 \Sigma}{[1+(\partial_X \Sigma)^2]^{3/2}}\right) + O(\varepsilon^2). \tag{C.4}$$

In static variables ($\widetilde{X} = X/H$, $\widetilde{Y} = Y/H$, $\widetilde{\Sigma} = \Sigma/H$, etc.), and letting $P_0 = -\widehat{P}/H$,

$$\mathrm{Ca}\widehat{P} = \left(\frac{\partial_{\widetilde{X}}^2 \widetilde{\Sigma}}{[1+(\partial_{\widetilde{X}} \widetilde{\Sigma})^2]^{3/2}}\right) + \mathrm{Ca}BH^2\widetilde{\Sigma} + O(\varepsilon^2). \tag{C.5}$$

Thus, the fluid interface is no longer a circular section. Unfortunately there does not seem to be a general analytic solution, so $\widetilde{\Sigma}$ must be computed numerically for each value of the three parameters: $\{\alpha, \theta, \mathrm{Ca}BH^2\}$. (If, however, the gravity is very small compared to the capillary pressure, then a perturbative approach can be taken, following Chapter 7, yielding an analytic surface correction). This interface defines a cross-sectional domain $\widetilde{\Omega}(\alpha, \theta, \mathrm{Ca}BH^2)$ which likewise depends on all three parameters.

C.2.2 Flux computation

The flux does not have any bulk corrections; as before, the static velocity variable can be defined as $\widetilde{W}(\widetilde{X}, \widetilde{Y}) = \left[-H^2\partial_Z P\right]^{-1} W$. $\widetilde{W}$ is then solved for by the Poisson equation $\nabla^2 \widetilde{W} = -1$ on the domain $\widetilde{\Omega}(\alpha, \theta, \mathrm{Ca}BH^2)$, and the flux by

$$Q = \int_\Omega W dX dY = H^2\left[-H^2\partial_Z P\right]\int_{\widetilde{\Omega}} \widetilde{W} d\widetilde{X} d\widetilde{Y} \tag{C.6}$$

$$= -H^4 \Gamma(\alpha, \theta, \mathrm{Ca}BH^2)\partial_Z\left[-\frac{\widehat{P}(\alpha, \theta, \mathrm{Ca}BH^2)}{H}\right]. \tag{C.7}$$

C.2.3 Final equation

Finally, using the conservation of mass relation $\partial_T A = -\partial_Z Q$ yields the equation of motion

$$\partial_T\left[H^2 \widehat{A}(\alpha, \theta, \mathrm{Ca}BH^2)\right] = \partial_Z\left\{H^4 \Gamma(\alpha, \theta, \mathrm{Ca}BH^2)\partial_Z\left[-\frac{\widehat{P}(\alpha, \theta, \mathrm{Ca}BH^2)}{H}\right]\right\}. \tag{C.8}$$

These three geometric factors, $\widehat{A}$, $\widehat{P}$, and Γ, now depend on the third parameter $\mathrm{Ca}BH^2$, and each must be computed numerically. In the weak-gravity limit, each could be computed perturbatively to linear order in B.

Because the corrective factors depend only on H and not on derivatives thereof, the equation still has a self-similar solution with $\eta = Z/T^{1/2}$; i.e., Washburn-like $T^{1/2}$ spreading and draining is retained. Furthermore, the equation can be put into nonlinear diffusion form.

C.3 V-grooves with inertia

In a regime such that $\varepsilon \mathrm{Re}\Gamma < O(1)$, inertial terms can be added perturbatively to the V-groove system. The methodology is analogous to the perturbative addition of inertial terms to the thin film equation, an overview of which may be found in the review article by Oron et al. (1997).

From Chapter 4, the reduced Navier-Stokes and continuity equations without gravity are given by

$$0 = \frac{\partial U}{\partial X} + \frac{\partial V}{\partial Y} + \frac{\partial W}{\partial Z}, \tag{C.9a}$$

$$\frac{\partial P}{\partial X} = 0 + O(\varepsilon^3 \mathrm{Re}) \tag{C.9b}$$

$$\frac{\partial P}{\partial Y} = 0 + O(\varepsilon^3 \mathrm{Re}) \tag{C.9c}$$

$$\varepsilon \mathrm{Re}\left[\partial_T W + U\partial_X W + V\partial_Y W + W\partial_Z W\right] = -\frac{\partial P}{\partial Z} + (\partial_{XX} + \partial_{YY})W + O(\varepsilon^2). \tag{C.9d}$$

Note that P is, as in the inertia-free groove, constant in each cross-section. Hence the circular interface is maintained.

Let

$$W = W_0 + \varepsilon \mathrm{Re} W_1, \tag{C.10}$$

where W_0 is the streamwise velocity in the purely viscous V-groove (i.e., W_0 is the solution described in Chapter 4), which satisfies $-\partial_Z P = (\partial_{XX} + \partial_{YY})W_0$. The W_1 correction is then computed by

$$(\partial_{XX} + \partial_{YY})W_1 = \left[\partial_T W_0 + U_0\partial_X W_0 + V_0\partial_Y W_0 + W_0\partial_Z W_0\right], \tag{C.11}$$

with $W_1 = 0$ on the walls and $\partial_n W_1 = 0$ at the free surface.

To determine W_1, we switch to static variables, with $\widetilde{X} = X/H$, $\widetilde{Y} = Y/H$, and $\widetilde{W}_0 = W/(-H^2\partial_Z P)$. Note first that static forms of U_0 and V_0 must be split in two:

$$U_0 = H^3(-\partial_{ZZ}P)\widetilde{U}_A + H^2(\partial_Z H)(-\partial_Z P)\widetilde{U}_B \tag{C.12a}$$

$$V_0 = H^3(-\partial_{ZZ}P)\widetilde{V}_A + H^2(\partial_Z H)(-\partial_Z P)\widetilde{V}_B. \tag{C.12b}$$

The continuity equation then splits into

$$0 = \partial_{\widetilde{X}}\widetilde{U}_A + \partial_{\widetilde{Y}}\widetilde{V}_A + \widetilde{W}_0, \tag{C.13a}$$

$$0 = \partial_{\widetilde{X}}\widetilde{U}_B + \partial_{\widetilde{Y}}\widetilde{V}_B + 2\widetilde{W}_0 - \widetilde{X}\partial_{\widetilde{X}}\widetilde{W}_0 - \widetilde{Y}\partial_{\widetilde{Y}}\widetilde{W}_0, \tag{C.13b}$$

while $\widetilde{U}_A$, $\widetilde{U}_B$, $\widetilde{V}_A$, and $\widetilde{V}_B$ are harmonic, zero at the walls, and obey the relevant surface boundary condition.

Plugging these values into Equation (C.11) yields a variety of coefficients involving different derivatives of P and H. The corrective W_1 must then be written as a sum of three parts:

$$W_1 = H^6(\partial_Z P)(\partial_{ZZ}P)\widetilde{W}_A(\widetilde{X},\widetilde{Y}) + H^5(\partial_Z H)(\partial_Z P)^2\widetilde{W}_B(\widetilde{X},\widetilde{Y}) + H^4(-\partial_{ZT}P)\widetilde{W}_C(\widetilde{X},\widetilde{Y}), \tag{C.14}$$

resulting in the three Poisson equations:

$$\widetilde{\nabla}^2\widetilde{W}_A = -\frac{\Gamma_0}{\widehat{A}}\widetilde{W}_0 + \widetilde{W}_0^2 + \left[\widetilde{U}_A + \frac{\Gamma_0}{\widehat{A}}\frac{\widetilde{X}}{2}\right]\partial_{\widetilde{X}}\widetilde{W}_0 + \left[\widetilde{V}_A + \frac{\Gamma_0}{\widehat{A}}\frac{\widetilde{Y}}{2}\right]\partial_{\widetilde{Y}}\widetilde{W}_0, \tag{C.15a}$$

$$\widetilde{\nabla}^2\widetilde{W}_B = -4\frac{\Gamma_0}{\widehat{A}}\widetilde{W}_0 + 2\widetilde{W}_0^2 + \left[\widetilde{U}_B + 2\frac{\Gamma_0}{\widehat{A}}\widetilde{X} - \widetilde{X}\widetilde{W}_0\right]\partial_{\widetilde{X}}\widetilde{W}_0 + \left[\widetilde{V}_B + 2\frac{\Gamma_0}{\widehat{A}}\widetilde{Y} - \widetilde{Y}\widetilde{W}_0\right]\partial_{\widetilde{Y}}\widetilde{W}_0, \tag{C.15b}$$

$$\widetilde{\nabla}^2\widetilde{W}_C = \widetilde{W}_0, \tag{C.15c}$$

where $\widetilde{\nabla}^2 = \left(\partial_{\widetilde{X}\widetilde{X}} + \partial_{\widetilde{Y}\widetilde{Y}}\right)$. Upon integrating the result, the corrected flux is given by

$$Q = -\Gamma_0 H^4\partial_Z P + \varepsilon\mathrm{Re}H^2\left[\Gamma_A H^6(\partial_Z P)(\partial_{ZZ}P) + \Gamma_B H^5(\partial_Z H)(\partial_Z P)^2 + \Gamma_C H^4(-\partial_{ZT}P)\right]. \tag{C.16}$$

Recalling that $\widetilde{\nabla}^2\widetilde{W}_0 = -1$ yielded an integrated factor of Γ_0, we then expect that $\Gamma_A, \Gamma_B \approx O(\Gamma_0^3)$ and $\Gamma_C \approx O(\Gamma_0^2)$. This Q can then be substituted into $\partial_T A = -\partial_Z Q$ to get the equation of motion.

We have until now kept P as an unknown quantity, in order to more easily allow inertia to be added to, e.g., a V-groove with an electric field. Let us focus on the straight groove with pressure set purely by capillary effects, i.e., $P = -(\Phi\widehat{R}H)^{-1}$. In this case,

$$\begin{aligned}
\widehat{A}^{-1}Q &= -H^2\partial_Z H \\
&+ \varepsilon\mathrm{Re}\frac{1}{\Phi^2\widehat{A}\widehat{R}^2}H^2\left[\Gamma_A H^6(\partial_Z H^{-1})(\partial_{ZZ}H^{-1}) + \Gamma_B H^5(\partial_Z H)(\partial_Z H^{-1})^2 + \Gamma_C H^4(\partial_{ZT}H^{-1})\right] \\
&= -H^2H' + \varepsilon\mathrm{Re}\left\{\frac{\Gamma_A\widehat{A}}{\Gamma_0^2}H^3H'[-2(H')^2 + HH''] \right. \\
&\qquad \left. + \frac{\Gamma_B\widehat{A}}{\Gamma_0^2}H^3(H')^3 + \frac{1}{2}\frac{\Gamma_C}{\Gamma_0}\left[4(H')^3 - 3HH'H'' - H^2H'''\right]\right\},
\end{aligned} \tag{C.17}$$

and finally,

$$\begin{aligned}
\partial_T H^2 = \partial_Z\left(-H^2H' + \varepsilon\mathrm{Re}\left\{\frac{\Gamma_A\widehat{A}}{\Gamma_0^2}H^3H'[-2(H')^2 + HH''] \right.\right. \\
\left.\left. + \frac{\Gamma_B\widehat{A}}{\Gamma_0^2}H^3(H')^3 + \frac{1}{2}\frac{\Gamma_C}{\Gamma_0}\left[4(H')^3 - 3HH'H'' - H^2H'''\right]\right\}\right).
\end{aligned} \tag{C.18}$$

Recalling that $\widehat{A} = O(1)$, the corrective term is thus expected to have $O(\varepsilon\mathrm{Re}\Gamma_0)$.

All that remains is to do the work of numerically computing $\widetilde{U}_A$, $\widetilde{U}_B$, $\widetilde{W}_A$, $\widetilde{W}_B$, $\widetilde{W}_C$, $\Gamma_A(\alpha,\theta)$, $\Gamma_B(\alpha,\theta)$, and $\Gamma_C(\alpha,\theta)$. We leave this as an exercise for the reader.

References

J. A. Dean. Lange's Handbook of Chemistry. McGraw-Hill, New York, 15th edition, 1999. ISBN 0070163847.

A. Oron, S. H. Davis, and S. G. Bankoff. Long-scale evolution of thin liquid films. Rev. Mod. Phys., 69(3):931–980, 1997. doi:10.1103/RevModPhys.69.931.

M. M. Weislogel. Capillary flow in an interior corner. PhD thesis, Northwestern University, June 1996. URL `https://ntrs.nasa.gov/citations/19970010346`. Also published as NASA Technical Memorandum 107364.